UNIVERSITY OF CALIFORNIA, SAN DIEGO

Blast Simulator Wall Tests: Experimental Methods and Mitigation Strategies for Reinforced Concrete and Concrete Masonry

A dissertation submitted in partial satisfaction of the

requirements for the degree Doctor of Philosophy

in

Structural Engineering

by

Michael G. Oesterle

Committee in charge:

Professor Gilbert A. Hegemier, Chair
Professor David J. Benson
Professor Vitali Nesterenko
Professor Jose Restrepo
Professor Frieder Seible
Professor Peter M. Shearer

2009

The dissertation of Michael G. Oesterle is approved, and it is acceptable in quality and form for publication on microfilm and electronically:

_____

_____

_____

_____

_____

_____

Chair

University of California, San Diego

2009

DEDICATION

To my wife and son.

TABLE OF CONTENTS

LIST OF ABBREVIATIONS

ACI	American Concrete Institute
ASCE	American Society of Civil Engineers
ASTM	ASTM International (American Society for Testing and Materials)
BG	Blast Generator
CFD	Computational Fluid Dynamics
CFRP	Carbon Fiber Reinforced Polymer
CMU	Concrete Masonry Unit
COR	Coefficient of Restitution
DIF	Dynamic Increase Factor
EMRTC	Energetic Materials Research and Testing Center
ESEC	Englekirk Structural Engineering Center
FE	Finite Element
FPWA	Frangible Panel Wall Analysis
FRP	Fiber Reinforced Polymer
GFRP	Glass Fiber Reinforced Polymer
HE	High Explosive
LHPOST	Large High Performance Outdoor Shake Table
LVDT	Linear Variable Displacement Transducer
MDOF	Multi Degree of Freedom
MTS	MTS Systems Corporation
RC	Reinforced Concrete
SDOF	Single Degree of Freedom
TEMA	Track Eye Motion Analysis
TNT	Trinitrotoluene
TSWG	Technical Support Working Group
UCSD	University of California, San Diego
UFC	Unified Facilities Criteria
URM	Unreinforced Masonry
VCE	Vapor Cloud Explosion

LIST OF SYMBOLS

Lower Case Latin Characters

a Depth of compression zone

a_i Accelerations measured by i^{th} accelerometers

a_{0y}, a_{1y}, a_{2y} Constants of yield failure surface

a_{0m}, a_{1m}, a_{2m} Constants of maximum failure surface

a_{1f}, a_{2f} Constants of residual failure surface

a_o Speed of sound in ambient conditions

$\bar{a}$ Distance from top of section to centroid of nonlinear stress profile

b Width of wall

b_{eff} Effective thickness of polyurea at connection

b_p Width of polyurea lining

b_{ps} Shear stress factor

b_{sn} Width of programmer sub module

b_t Tie width

b_w Waveform parameter

c Depth of neutral axis

c_1, c_2, c_3 Parameters for dynamic modification function

d Depth to tension steel in reinforced concrete section

d' Depth to compression steel in reinforced concrete section

d_{cfb} Distance to bottom CFRP from of section

d_h Diameter of bolt holt

ds Distance to steel from top of section

$d\bar{\varepsilon}^p$ Effective plastic strain

E_c Modulus of elasticity for concrete

f'_c Compressive strength of concrete

f'_{cb} Compressive strength of concrete block

f'_{cc} Compressive strength of confined concrete

f'_g Compressive strength of grout

f'_m Compressive strength of masonry

f'_r Modulus of rupture

f_{cu} Ultimate stress in concrete

g Gravity constant

h_{sn} height of programmer sub module

i- Impulse of negative phase

i_r Reflected impulse

i_s Side-on specific impulse

k_1 and k_2 Coefficients for shape modification factor

k_c Factor defining softening in masonry and concrete uniaxial stress-strain model

k_{eq} Equivalent stiffness for generalized SDOF

l_{cr} Critical development length of tie in polyurea

l_{dtp} Development length of tie in polyurea

l_s Length of polyurea in connection subject to shear

m Mass

m_{BG} Mass of BG impact plate

m_{eq} equivalent mass for generalized SDOF

n Number of elements

n_a Number of accelerometers

n_c Factor defining hardening in masonry and concrete uniaxial stress-strain model

n_r Modular ratio

p Pressure load

p_{eq} Equivalent applied load for generalized SDOF

p_o Ambient pressure

p_{peak} Peak pressure

p_r Reflected pressure

p_s Peak side-on overpressure

p_{sc} pressure on wall after clearing of reflected load

p_{so} Peak side-on pressure

p-$_{so}$ Minimum underpressure

$\bar{p}$ Non-dimensional pressure for Baker-Strehlow method

q_s Dynamic gas pressure

r_{cb}	Ratio of net CMU block area to gross CMU block area
s	Arc length
s_n	Shape factor for programmer sub module
s_o	Initial arc length
s_t	Tie spacing
t	Time
t_a	Time of arrival of shock front
t_c	Clearing time
t_r	"Fictitious" duration of reflected pressure pulse
t_L	Load duration
t_n	Thickness of the programmer sub module
t_{of}	Duration of idealized positive phase
t_{of}-	Duration of idealized positive phase and negative phase
t_p	Thickness of frangible panel
t_{pl}	Thickness of polyurea lining
t_t	Thickness of steel tie
t_w	Positive phase duration
u	Displacement
u^p	Predictor displacement
u_s	Particle velocity behind wave front
v	Velocity
v_{11}	Initial velocity of mass 1 in two body collision
v_{12}	Final velocity of mass 1 in two body collision
v_{21}	Initial velocity of mass 2 in two body collision
v_{22}	Final velocity of mass 2 in two body collision
w	Load per length
w_i	Weights for Gaussian quadrature rule
w_l	Weight normalized by loaded area
w_m	Weight density of masonry
w_{pc}	Weight of wall with frangible panel normalized by concrete core area
x	Coordinate along longitudinal axis of one-way bending wall

x_i Locations for evaluation of function for Gaussian quadrature rule

$\overline{x}$ Distance to centroid

y Distance from neutral axis to extreme fiber of cross-section

y_t Distance from neutral axis to extreme tension fiber of cross-section

Upper Case Latin Characters

A Area

A_b Cross-sectional area of bolt

A_c Area of concrete

A_{cfb} Cross-sectional area of bottom CFRP

A_{cft} Cross-sectional area of top CFRP

A_e Effective area

A_s Cross-sectional area of steel

A_s' Area of compression steel

A_{sh} Shear area of polyurea

$A_{t,net}$ Net cross-sectional area of tie

C Damping coefficient

C_c Compressive force in concrete

C_{cft} Compressive force in top CFRP

C_D Drag coefficient

C_{dl} Development length coefficient for tie in polyurea

C_m Compressive force in masonry

C_{mu} Ultimate compressive strength of masonry

C_r speed of sound in reflected region

$C_{r\alpha}$ Coefficient for oblique reflections of shock fronts

C_s Compressive force in steel

C_v Shear capacity factor

D Dynamic modification factor

D_p Deformation in programmer

E Modulus of elasticity

E_c Modulus of elasticity for concrete

EI	Flexural stiffness
E_m	Modulus of elasticity for masonry
E_s	Modulus of elasticity for steel
E_t	Energy of fuel air mixture
F	Force in element
F_{BG}	Force-deformation function for BG programmers
F_{cfb}	Stress in bottom CFRP
F_{cft}	Stress in top CFRP
F_p	Stress in polyurea
F_{pb}	Baseline force for programmer
F_{pc}	Strength of polyurea connection
F_{pd}	Dynamic baseline force with shape modification
F_{pn}	Shape modified baseline force
F_s	Stress in steel
F_u	Ultimate stress
F_y	Yield stress
F_{yb}	Yield stress of bolt
F_{yp}	Yield stress of polyurea
F_{yt}	Yield stress of tie
F_s'	Stress in compression steel
G_f	Fracture energy
H_c	Height of charge
H_{ce}	Volumetric combustion energy
H_f	Heat of combustion of fuel
H_s	Height of a structure
H_{TNT}	Detonation energy of TNT
KE	Kinetic energy
I_1	First invariant of principle stress
I_{bar}	Non-dimensional impulse
I_s	Moment of inertia of a cross-section
I_t	Moment of inertia of a transformed cross-section

$\bar{I}$ Non-dimensional impulse for Baker-Strehlow method

J_2 Second invariant of deviatoric stress

J_3 Second invariant of deviatoric stress

K Initial slope of resistance function

K_L Load factor

K_{LM} Load-mass factor

K_M Mass factor

K_r Coefficient for boundary condition

K_S Stiffness factor

L Length

L_o Initial length

L_w Wave length of the positive phase

M Bending moment

M_{co} Moment in concrete section when stress in extreme fiber reaches peak stress

M_{cr} Cracking moment

M_f Flame speed

M_u Moment associated with formation of yield hinge

M_y Moment in concrete section when steel yields

N_n Number of programmer sub modules

R Resistance

R_1 Resistance associated with formation of first yield hinge for pinned-fixed beam

R_2 Resistance associated with formation of second yield hinge for pinned-fixed beam

R_b Resistance of bolt

R_{br} Required resistance of bolt

R_c Standoff distance from charge to target

R_d Diagonal distance from charge to target

R_{eq} Equivalent resistance for generalized SDOF

R_g Horizontal standoff distance from charge to target

R_{pc} Strength of polyurea connection

R_t Resistance of tie

R_u Peak resistance

R_v Shear resistance

R_{wall} Resistance function for wall

$\bar{R}$ Scaled distance for Baker-Strehlow method

S Clearing distance

S_n Shape modification factor to the baseline force

S_{sh} Strain hardening factor for polyurea

S_{sr} Strain rate factor for polyurea

T Tensile force

T_{cfb} Tensile force in bottom CFRP

T_s Tensile force in steel

U Shock front velocity

V Transverse shear

V_m Shear capacity of masonry

V_n Shear capacity of wall

V_s shear capacity of web reinforcement

W Charge weight in equivalent units of TNT

W_{int} Internal work

W_{EXP} Weight of explosive

W_f Weight of fuel

W_s Width of a structure

Z Scaled distance

Greek Characters

α Strain rate parameter

α_{cb} Strain rate parameter for concrete block

α_e is the TNT equivalency based on energy

α_{fu} Strain rate parameter for ultimate strength of steel

α_{fy} Strain rate parameter for yield strength of steel

α_g Strain rate parameter for grout

α_i Angle of incidence for oblique reflections

α_p Coefficient for effective width of polyurea/steel tie connection

β Parameter for numeric integration

β_p Prying coefficient

β_1 Factor relation neutral axis depth to depth of compression zone

δu Virtual displacement

δW_e External work

δW_i Internal work

Δ Deformation

Δ_p Plastic deformation

Δ_y Deformation associated with formation of yield hinge for simply-supported beam

Δ_1 Deformation associated with formation of first yield hinge for pinned-fixed beam

Δ_2 Deformation associated with formation of second hinge for pinned-fixed beam

Δt Time step

Δu Increment of displacement

Δv Change in velocity

ΔH_{EXP} Specific energy of explosive

ΔH_{TNT} Specific energy of TNT

$\Delta\sigma$ Current failure surface

$\Delta\sigma_m$ Failure surface corresponding to maximum strength of concrete

$\Delta\sigma_r$. Failure surface corresponding to residual strength of concrete

$\Delta\sigma_y$ Failure surface corresponding to limit of elastic behavior of concrete

$\dot{\Delta}$ Deformation rate

ε Strain

ε_c Strain in concrete

ε_{cfb} Strain in CFRP at bottom of section

ε_{cft} Strain in CFRP at top of section

ε_{co} Strain associated with peak stress in concrete

ε_{cu} Ultimate strain in concrete

ε_d Strain in frangible panel

ε_m Strain in masonry

ε_{mo} Strain associated with peak stress in masonry

ε_{oct} Octahedral strain

ε_{p} Strain in polyurea

ε_{s} Strain in steel

ε_{sh} Strain corresponding to initiation of strain hardening

ε_{u} Strain corresponding to ultimate stress

ε_{y} Yield strain

ε_{ij}^{p} Plastic strain tensor

ε_{s}' Strain in compression steel

$\dot{\varepsilon}$ Strain rate

$\dot{\varepsilon}_{s}$ Quasi-static strain rate

ϕ Curvature

ϕ_{p} Curvature associated with plastic hinge formation

ϕ_{cr} Curvature associated with cracking of cross-section

ϕ_{y} Curvature associated with steel yielding

γ Parameter for numeric integration

γ_{h} Specific heat ratio

γ_{p} Non-dimensional deformation rate

μ Ductility

θ Angle

ρ_{b} Balanced reinforcement ratio

ρ_{s} Density of air

ρ_{st} Reinforcement ratio

σ Stress

σ_{oct} Octahedral stress

σ_{d} Stress in frangible panel

ψ Shape function for SDOF analysis

ψ_{ff} Shape function for one-way fixed-fixed boundary conditions

ψ_{pf} Shape function for one-way pinned-fixed boundary conditions

ψ_{ss} Shape function for one-way simple-supported boundary conditions

ψ_1, ψ_2, ψ_3 Dynamic reaction coefficients

Matrices and Arrays

u Displacement array

C Damping matrix

F Force array

M Mass matrix

P Load array

General Notation

$\dot{(\bullet)}$ Differentiation with respect to time

$(\bullet)'$ Differentiation with respect to a variable other than time

$(\bullet)_{i+1}$ or $(\bullet)_i$ Iteration of a variable

$(\bullet)_{max}$ Maximum value

LIST OF FIGURES

LIST OF TABLES

ACKNOWLEDGEMENTS

I would first like to thank my parents and sisters for their constant support, love, and encouragement. I have often relied on them and they have always been there for me.

I would like to thank my research advisor, Dr. Gilbert Hegemier for giving me the opportunity to work on this research and for providing me with funding and guidance throughout the course of my graduate career at UCSD. Dr. Karen Arnett also deserves acknowledgement for her management of the research project that I have been involved with. I thank Technical Support Working Group for providing the funding to conduct my research.

I would like thank the staff at the Englekirk Structural Engineering Center and Powell Structural Labs for their dedicated work that supported my research. I am also grateful to Ken Morrill, Joe Magallanes and Dr Shengrui Lan from Karagozian and Case for their consultation on my research.

I would like to thank fellow graduate students, Anna Lang, Don Phillippi, Janet Wolfson, Johnson Lee Lauren Stewart, Matt Schoettler, Peter Huson, and Tona Rodriguez with whom I have shared this experience. In particular I would like to thank Lauren Stewart for the occasional frozen yogurt distraction and more importantly for all the advice that she offered me as I worked on this research.

Finally, I would like to thank my wife Nani for all of her love and patience throughout this journey. Without her unconditional love and support I could have never completed this work.

VITA

2001	Bachelor of Science, University of Notre Dame
2001-2003	Research Assistant, Virginia Polytechnic Institute
2003	Master of Science, Virginia Polytechnic Institute
2003-2009	Research Assistant, University of California, San Diego
2004	Teaching Assistant, University of California, San Diego
2009	Doctor of Philosophy, University of California, San Diego

PUBLICATIONS

Conference Proceedings

Oesterle, M.G., Hegemier, G.A., and Morrill, K. (2009). "Response of Concrete Masonry Walls to Simulated Blast Loads." *ASCE Structures Congress 2009*, Austin, TX, May.

Hegemier, G., Seible, F., Karbhari, V., Lee, C. Rodriguez-Nikl, T., Oesterle, M.G., Morrill, K. and Crawford, J. (2007). "The Use of Fiber Reinforced Polymers to Mitigate Natural and Man-Made Hazards." *8th International Symposium on Fiber Reinforced Polymer Reinforcement for Concrete Structures (FRPRCS-08),* Patras, Greece, July 16-18th.

Hegemier, G., Seible, F., Arnett, K., Rodriguez-Nikl, T., Oesterle, M.G., Wolfson, J., Gram, M., and Clark, A. (2006). "The UCSD Blast Simulator." *77th Shock and Vibration Symposium (SAVIAC)*, Monterey, CA, March.

Technical Reports

Oesterle, M.G., Hegemier, G.A. and Seible, F. (2008). "Blast Simulator Testing of CMU Walls with CFRP Retrofits." *TSWG Contract Deliverable*, University of California, San Diego, Department of Structural Engineering, La Jolla, CA.

Oesterle, M.G., Hegemier, G.A., and Seible, F. (2008). "Response of Dynablok™ Walls to Simulated Blast Loads Part II." *TSWG Contract Deliverable*, University of California, San Diego, Department of Structural Engineering, La Jolla, CA.

Oesterle, M.G., Hegemier, G.A., and Seible, F. (2008). "Response of Dynablok™ Walls to Simulated Blast Loads." *TSWG Contract Deliverable*, University of California, San Diego, Department of Structural Engineering, La Jolla, CA.

Rodriguez-Nikl, T., Gram, M.M., Oesterle, M.G., Hegemier, G.A., Seible, F., and Arnett, K. (2008). "The UCSD Blast Simulator: Experimental Methodology." Report No. SSRP 2007/05, University of California, San Diego, Department of Structural Engineering, La Jolla, CA.

Hegemier, G. A., Seible, F., Oesterle, M.G. and Rodriguez-Nikl, T. (2006). "Quick Look Report - CFRP Retrofitted and As-Built RC Columns," *TSWG Contract Deliverable*, University of California, San Diego, Department of Structural Engineering, La Jolla, CA.

Seible, F., Hegemier, G.A., and Oesterle, M.G. (2006). "Quick Look Report – Unreinforced Masonry (URM) Wall Tests," *TSWG Contract Deliverable*, University of California, San Diego, Department of Structural Engineering, La Jolla, CA.

ABSTRACT OF THE DISSERTATION

Blast Simulator Wall Tests: Experimental Methods and Mitigation Strategies for Reinforced Concrete and Concrete Masonry

by

Michael G. Oesterle

Doctor of Philosophy in Structural Engineering

University of California, San Diego, 2009

Professor Gilbert A. Hegemier, Chair

. Loads generated in explosions that result from terrorist attacks and industrial accidents create devastating hazards for buildings and their occupants. The objective of this dissertation is to develop design guidelines and methodologies for protective/hardening strategies used to mitigate blast hazards in reinforced concrete and concrete masonry walls. Commonly, guidelines and methodologies are developed from experimental data. Field testing with live explosive is a reliable experimental method for demonstrating the performance of blast resistant concepts, but it is expensive, time consuming, and often produces low quality data. Static testing is another experimental

method that allows researchers to clearly observe behavior and failure modes of structural components; however this too is limited because it cannot account for the rate effects associated with blast loads. The UCSD Blast Simulator was developed to offers an alternative method for testing structures to loads generated in an explosion without the difficulties and limitations associated with field and static testing.

For this dissertation, tests were conducted with the blast simulator to study reinforced concrete walls protected with frangible panels, concrete masonry walls strengthened with carbon fiber reinforced polymer composite, and unreinforced masonry walls retrofitted with polyurea catcher systems. The objective of the dissertation was achieved through a succession of tasks that included; the development of a test protocol, validation and implementation of numerical models to predict loads delivered to specimens during blast simulator tests, development of method to correlate blast simulator loads to air blast loads, generation of high quality data on specimens with mitigation strategies for validation of numerical models to predict response of hardened/protected reinforced concrete and concrete masonry walls, and investigation of design variables with parametric studies.

The investigation of concrete masonry walls demonstrated that the addition of carbon fiber reinforced polymers can increase the resistance to blast loads, but may result in a brittle failure mode. The study of reinforced concrete walls showed that frangible panels can improve the response by adding mass to the system. Finally, the research performed on unreinforced masonry walls with polyurea catcher emphasized the need for proper connection detailing.

1 INTRODUCTION

Explosions resulting from terrorist attacks and industrial accidents generate loading environments that create devastating hazards for buildings and their occupants. The mitigation of these hazards often requires innovative hardening/protective technologies that have been proven experimentally. Application of these strategies to new and existing structures by engineers also require numerical tools and guidelines to aid in their design. These motivations led to the development of the University of California, San Diego (UCSD) Blast Simulator, which provides a method for characterizing the response of structural components and testing innovative hardening technologies to simulated blast loads in a laboratory environment [1]. The blast simulator produces high fidelity data that aids in the validation of numerical models used to simulate the response of the structural members to explosive loads.

Field testing with live explosive is the most reliable method for demonstrating the effectiveness or lack there of for a structural component to a blast events. However, these types of test are expensive, time consuming, and often do not produce quality data due to the harsh environment for the instrumentation and the variability in the specified loads. Furthermore, when using actual explosives, a fireball is created that prevents qualitative observations to be made during the test, which can be extremely useful for understanding the behavior of the test specimen.

The blast simulator overcomes the difficulties associated with testing in the field by using an array hydraulic oil/nitrogen driven actuators to impact the specimens simultaneously, thereby delivering a significant amount of energy to the specimen in a

manner similar to an explosion. The blast simulator does not produce the harsh environment experienced during an actual blast event, therefore the damage done to the instruments, cables, and data acquisition is relatively small. The blast simulator does not produce a fireball and the entirety of test can be captured by high speed cameras. The video that is recorded is useful for understanding the behavior of concrete because it visualizes the crack formation, spallation, and brittle failures that occur due to the blast loads. Blast simulator tests are controlled experiments that produce repeatable loads which is often unattainable when using actual explosives. The blast simulator requires only a short setup time and several tests can be run in a short time period depending on the specimen type and its condition.

The focus of the research in this dissertation is the experimental methods and mitigation strategies to simulated blast loads for reinforced concrete (RC), reinforced concrete masonry unit (CMU), and unreinforced concrete masonry (URM) walls. Reinforced concrete is a building material used world wide and a mitigation strategy to improve its response was investigated. The system that was studied uses frangible blast panels that are attached to the exterior of the wall during constructions. CMU and URM wall construction is commonly used for in-fill and load bearing walls in low to mid-rise buildings. These walls have low resistance to out-of-plane loads and are susceptible to catastrophic failure modes including collapse and fragmentation that threaten building occupants. Carbon fiber reinforced polymer (CFRP) composite was studied as a retrofit solution for strengthening CMU walls. URM walls were investigated with a polyurea retrofit that served as a catcher system.

The overall objectives of the research described in this dissertation are as follows:

- Provide methodologies and guidelines for performing blast simulator tests on reinforced concrete and concrete masonry walls.
- Provide numerical tools to aid in the study of reinforced concrete and concrete masonry walls tested with the blast simulator
- Investigate the effectiveness of different protective strategies for reinforced concrete, reinforced concrete masonry, and unreinforced concrete masonry walls
- Validate numerical models of reinforced concrete and concrete masonry walls that have been tested with the blast simulator
- Develop guidelines for the use of the protective strategies investigated with the blast simulator and with the validated numerical models.

The dissertation is divided into six chapters. Chapter 2 provides background information on topics that relate to the remainder of the dissertation. It discusses the methods used to determine design loads generated in high explosive (HE) blasts and in vapor cloud explosions (VCEs). Also included is a discussion of simple analysis techniques used to estimate the response of one-way bending walls to blast loads. Finally, a general discussion of concrete behavior is presented and a model used in finite element analysis that simulates concrete behavior is described.

Chapter 3 provides a full description of the UCSD Blast Simulator Laboratory. The description includes information on the experimental and analytical methods that are

employed to study the response of reinforced concrete and concrete masonry to simulated blast loads. The different methods and models discussed in the chapter were used in later chapters to investigate the effectiveness of different mitigation strategies.

Chapter 4 presents a research study conducted on CMU walls retrofitted with carbon fiber reinforced polymer composite. The study included an experimental portion using the blast simulator and an analytical study using models validated with the data generated by the experiments. The analytical study focused on CFRP retrofit design for used on CMU walls subject to loads generated in HE and VCE blasts.

Chapter 5 presents a research study that was conducted on reinforced concrete walls with frangible panels. This study consisted of two tests series that included blast simulator testing and quasi-static tests. The data generated in the experiments was used to develop and validate a one-dimensional model of the frangible panel/reinforced concrete wall system. This validated model was then used in a parametric study that investigated the effectiveness of the panels. Also included in the chapter is a discussion of a finite element model of the frangible panel/reinforced concrete wall system that was also validated with the blast simulator test data.

Chapter 6 presents a test program on URM walls with polyurea retrofits catcher systems. In the experimental portion of this study the response of the walls with the retrofit strategy was compared to an as-built wall. An investigation of connection details was also included in the experiment work. Observations from these experiments led to a set of proposed design equations for the connection design which are also presented in this chapter. Finally, the data generated in the blast simulator tests was used for

comparisons with FE models that simulate the behavior of the as-built and retrofitted URM walls.

The seventh and final chapter concludes the dissertation. Appendices are included at the end of the document. They include test data and comparisons between finite element analyses and experimental results which were not included in the main body of the text.

2 BACKGROUND

2.1 INTRODUCTION

This chapter of the dissertation is included to provide background information on topics which are important for the design of reinforced concrete and concrete masonry walls. The first section of this chapter focuses on fundamentals of blast loading for conventional explosives and for vapor cloud explosions. The next section provides information on single degree-of-freedom (SDOF) modeling of one-way bending structural members subject to blast loads. The final section of this chapter presents basic information on the behavior of reinforced concrete. The section also includes a discussion of the concrete model that is used in later chapters of the dissertation to model concrete walls in the blast simulator tests. A modified version of the concrete model is also used in the dissertation to simulate the response of concrete masonry walls to blast loading; thus making it important to understand the original version.

2.2 FUNDAMENTALS OF BLAST LOADING

This section summarizes the fundamentals of air blast to provide background information on the methods used to determine the blast load parameters used to design a protected structure. Detonation of the explosive affects any surrounding medium such as air, water, and the ground. In the design of concrete and concrete masonry walls discussed in this dissertation only blast waves generated in the air will be considered. When a high explosive is initiated in air the following sequence of events occurs [2]-[3]

- Detonation of the high explosive is initiated
- High temperature and large pressure gas is created in the detonation of the explosive
- Gas expands violently and pushes surrounding air out of the volume that it occupies
- The air that is pushed out is now in a compressed state and forms a blast wave in front of the gas from the explosive reaction. The blast wave contains most of the energy released by the explosion
- The blast wave travels outward from the source and air pressure at the blast wave front decays with distance
- Eventually the gas and air cools and the pressure falls below atmospheric pressure before it returns to a state of equilibrium where there is no gas or air being pushed away from the source
- The drop in pressure below atmospheric is a result of the gas molecules having a certain amount of momentum when the pressure returns to zero and a negative pressure is generated and reverses the direction of the flow back towards the source in order to achieve a state of equilibrium

Blast loads can be classified as unconfined or confined explosions. Confined explosions occur when the blast initiates inside of a structure and the load is comprised of

the shock load that can be amplified with reflections off of the internal surfaces and a quasi-static gas pressure that results from the increase in temperature and the production of gas in the explosion [4].

Unconfined explosions occur when the explosive is detonated in an open source and the blast waves propagate away from the source towards the structure. Unconfined explosions can be further classified as free air burst explosions, air burst explosions, and surface burst explosions. A free burst denotes the situation when the shock wave produced by the detonation propagates away from the source and impinges on the structure without any amplification. An air burst explosion describes the situation when the detonation occurs a certain distance above and away from the structure so that the blast wave reflects off the ground before it reaches the structure. Finally, a surface burst explosion describes the case where the detonation occurs near the ground and the initial shock wave is amplified at this point by the reflections off of the ground [4]. The effects of unconfined explosives are of interest in the research detailed in this dissertation; hence only the effects of unconfined explosives will be discussed herein.

2.2.1 FREE AIR BURST EXPLOSIONS

The parameters of the blast wave in a free air burst explosion are important for characterizing the loads that will be used to design a structure. Numerical analysis by Brode [5] produced the following relations between peak side-on overpressure, p_s, and scaled distance, Z; in the near field when p_s is greater than 10 bar and in the mid to far field when p_s is between 0.1 and 10 bar.

$$p_s = \frac{6.7}{Z^3} + 1 \quad \textbf{(}p_s \textbf{> 10 bar)} \tag{2.1}$$

$$p_s = \frac{0.975}{Z} + \frac{1.455}{Z^2} + \frac{5.85}{Z^3} - 0.019 \quad \textbf{(0.1 <} p_s \textbf{< 10 bar)} \tag{2.2}$$

where the scaled distance, Z, is given by

$$Z = \frac{R_c}{W^{1/3}} \tag{2.3}$$

and R_c is the distance from the center of the (spherical) charge and W is the charge mass in of TNT (trinitrotoluene).

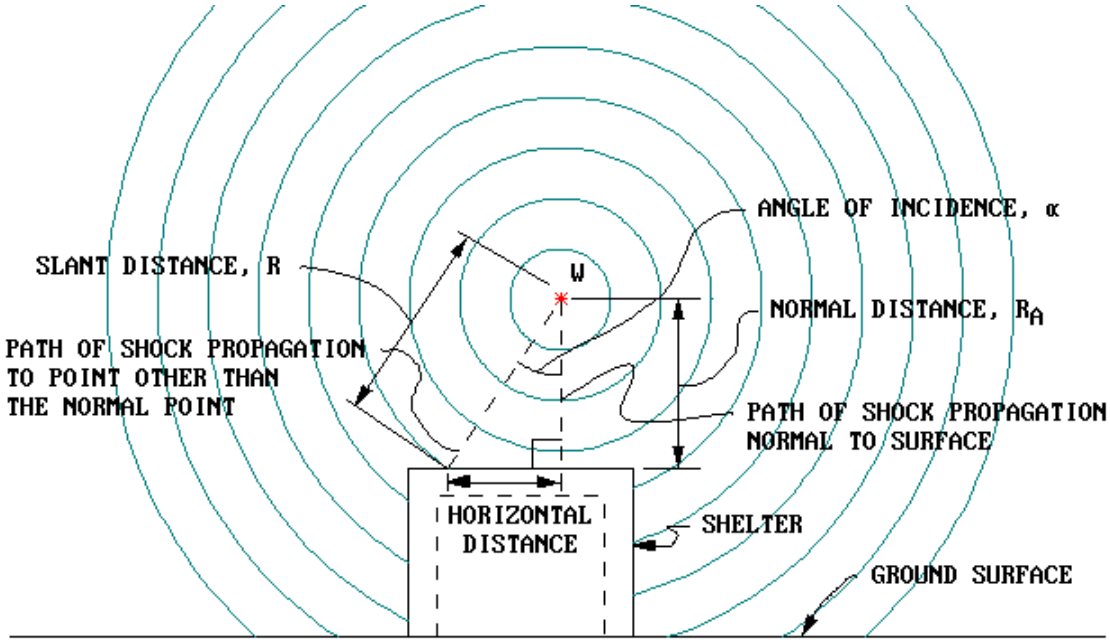

Figure 2.1: Free air burst wave front (reproduced from [6])

TNT is the universal reference explosive used in the determination of the scaled distance, Z. When determining the blast wave parameters generated by an explosive

other than TNT the initial step is to convert the mass of the explosive to an equivalent mass of TNT. Common practice is to calculate the equivalent mass of TNT, W_{TNT}, by scaling the mass of the explosive, W_{EXP}, by a conversion factor that is based on its specific energy, ΔH_{EXP} and the specific energy of TNT, ΔH_{TNT} as shown below:

$$W = \frac{\Delta H_{EXP}}{\Delta H_{TNT}} W_{EXP} \tag{2.4}$$

A different approach is to use a scale factor that matches either the peak overpressure or the impulse depending on which parameter is desired. Table 2.1 is reproduced from ASCE [4] and lists the conversions factors for several different explosives. Included in the table are pressure ranges for which the factors are applicable.

Table 2.1: Conversion factors for explosives (from [4])

Explosive	Equivalent Weight, Pressure [lbs]	Equivalent Weight, Impulse [lbs]	Pressure Range [psi]
ANFO	0.82	--	1-100
Composition A-3	1.09	1.076	5-50
Composition B	1.11 1.20	0.98 1.3	5-50 100-1,000
Composition C-4	1.37	1.19	10-100
Cyclotol (70/30)	1.14	1.09	5-50
HBX-1	1.17	1.16	5-20
HBX-3	1.14	0.97	5-25
H-6	1.38	1.15	5-100
Minol II	1.20	1.11	3-20
Octol (70/30, 75/25)	1.06	--	E
PBX-9010	1.29	--	5-30
PETN	1.27	--	5-100
Pentolite	1.42 1.38 1.50	1.00 1.14 1.00	5-100 5-600 100-1,000
Picratol	0.90	0.93	--
Tetryl	1.07	--	3-20
Tetrytol (Tetry/TNT) (75/25, 70/30, 65/35)	1.06	--	E
TNETB	1.36	1.10	5-100
TNT	1.00	1.00	Standard
TRITONAL	1.07	0.96	5-100

Table 2.2: Conversion factors for pressure and impulse (from [4])

Explosive	Equivalent pressure	Equivalent impulse
Compound B (60% RDX 40% TNT)	1.11	0.98
Pentolite	1.40	1.07
TNT	1.00	1.00

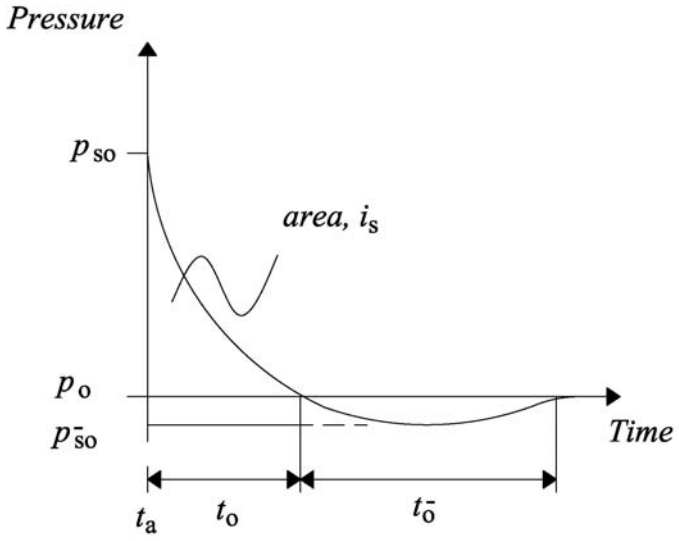

Figure 2.2: Typical pressure time-history for blast wave in free air

A typical pressure time-history plot for a blast wave in air is shown in Figure 2.2. At the time of arrival, t_a, the pressure has an "instantaneous" increase from ambient pressure, p_o, to peak side-on overpressure, p_{so}, and then decays to a minimum underpressure p^-_{so} before returning ambient conditions. The duration of the positive phase, t_d, occurs in the time span where the pressure remains greater than ambient. This pressure profile is described by the Friedlander equation [2, 3]:

$$p(t) = p_{so}(1-\frac{t}{t_o})\exp(-\frac{bt}{t_o}) \tag{2.5}$$

where b is called the waveform parameter. The side-on specific impulse, i_s, is the time area of the pressure-time curve for the duration of the positive phase and can be found with the following equation

$$i_s = \int_{t_a}^{t_a+t_o} p_{so}(t)dt \tag{2.6}$$

The duration of the blast wave profile when the pressure dips below than ambient pressure is called the negative phase. According to Brode [5], the minimum underpressure, p^-_{so}, of the negative phase can be determined with the following expression:

$$p^-_{so} = -\frac{0.35}{Z} \tag{2.7}$$

where the pressure is in bar and the scaled distance is greater than 1.6. The impulse of the negative phase is denoted i^- and can be found with

$$i^- \approx i_s\left[1-\frac{1}{2Z}\right] \tag{2.8}$$

The parameters of the negative phase are often unimportant in the design of structural components because the positive phase pressures and impulses for threats of interest are significantly higher and have a more significant effect on the structural response. However, several of the reinforced concrete and masonry walls studied in this dissertation are affected by the negative pressures and impulses, thus they will be considered when appropriate. Other important parameters of the blast wave are the shock

front velocity, U, the wave length of the positive phase, L_w, reflected pressure p_r, and reflected impulse, i_r.

Graphical methods are convenient for determining the blast wave parameters described above. Several references, including [6], provide plots of the parameters for a free air burst versus the scaled distance. Figure 2.3 is a plot of the positive phase blast wave parameters versus the scaled distance, Z.

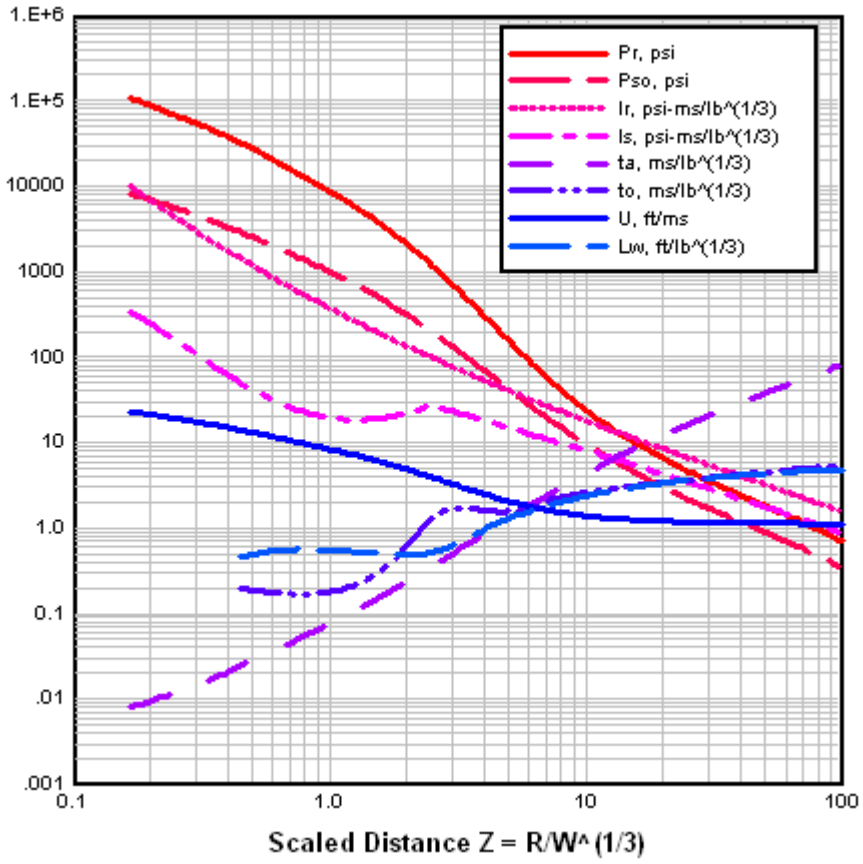

Figure 2.3: Positive phase free air burst blast wave parameters vs. scaled distance (reproduced from [6])

In the plot p_r and i_r are the reflected pressure and the reflected specific impulse. These parameters apply for a blast wave that has reflected off a surface. The magnitude

of the reflected pressure and impulse will be greater than the side-on pressure and impulse. The enhancement is because in addition to the potential energy stored as a pressure differential in the blast wave, the air particles that comprise the blast wave have velocity and therefore, kinetic energy. In the case when the wave encounters an infinitely large rigid wall wherein the particles are brought to rest and are compressed at the surface resulting in an increase in pressure.

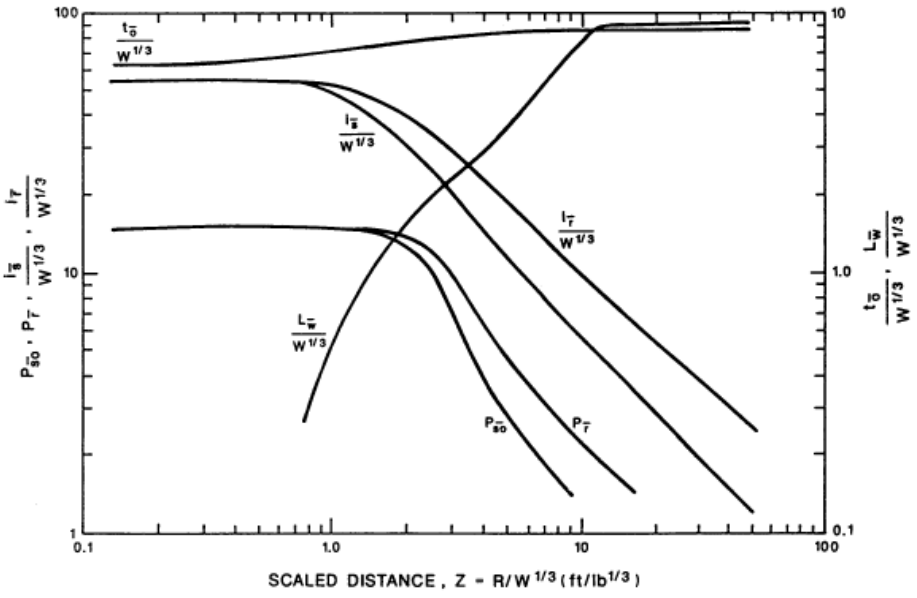

Figure 2.4: Negative phase free air burst blast wave parameters vs. scaled distance (reproduced from [6])

For the case when the angle of incidence is zero the peak reflected pressure can be given by the Rankine-Hugoniot prediction [3]:

$$p_r = 2p_{so} + (\gamma + 1)q_s \tag{2.9}$$

where γ is the specific heat ratio of a real gas and q_s is the dynamic pressure which can be found by

$$q_s = \frac{1}{2}\rho_s u_s^2 \tag{2.10}$$

and ρ_s is the density of the air and u_s is the particle velocity behind the wave front. The particle velocity can be found with

$$u_s = \frac{a_o p_s}{\gamma_h p_o}\left[1+\left[\frac{\gamma_h+1}{2\gamma_h}\right]\frac{p_s}{p_o}\right]^{-\frac{1}{2}} \tag{2.11}$$

where a_o is the speed of sound at ambient conditions. Substitutions of equations (2.10) and (2.11) into (2.9) yields

$$p_r = 2p_s\left[\frac{7p_o+4p_s}{7p_o+p_s}\right] \tag{2.12}$$

when $\gamma = 1.4$ for air. The reflected pressure will be twice the incident side-on pressure for the case when p_s is small relative to p_o; which arises when the explosion is small and at long range. The reflected pulse can be as much as eight times the incident side-on pressure for the case when the p_s is large compared to p_o which arises when the charge is large and close in. It should be noted that these equations are only applicable when Z is greater than 0.134 ft/lb$^{1/3}$ (0.053 m/kg$^{1/3}$) which represents the radius of a spherical TNT explosive and, therefore, the surface of the explosive [3].

TM 5-1300 [6] calculates peak reflected pressure for a normally reflected wave in a free air burst using a graphical method shown in Figure 2.5. This method predicts that the reflected pressure will be double the incident at low incident pressure. In the case of high peak incident pressure the reflected peak could be nearly 13 times the peak incident.

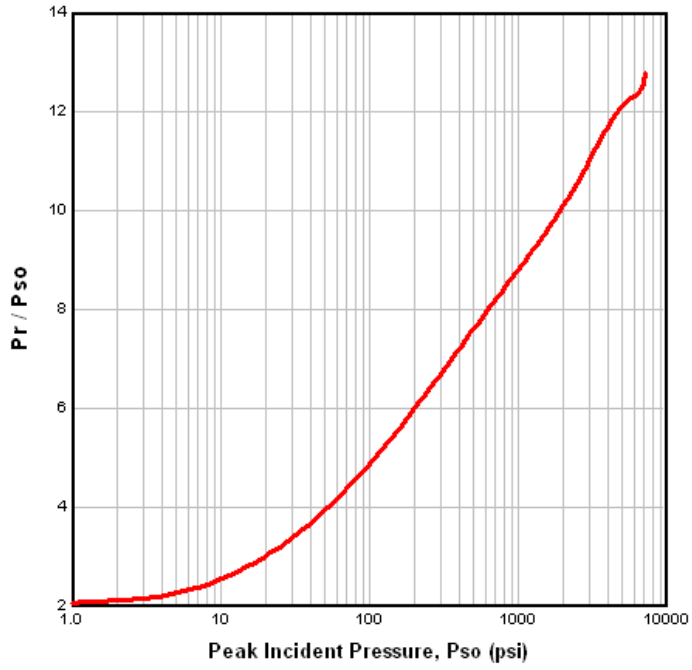

Figure 2.5: Peak incident pressure versus ratio of peak normally reflected pressure to peak incident pressure for free air burst (reproduced from[6])

When the wave front from a free air burst is not normal to the reflecting surface, but instead there is an angle of incidence then, according to [6], the peak reflected pressure and the peak reflected impulse can be found with Figure 2.6 and Figure 2.7. In these plots the peak pressure is a function of incident angle and scaled height which is similar to the scaled distance found with equation (2.3), except that the range is replaced with the height of the charge above the surface. The remaining parameters of the blast wave can be found with Figure 2.3 and Figure 2.4 using the slant distance for the range.

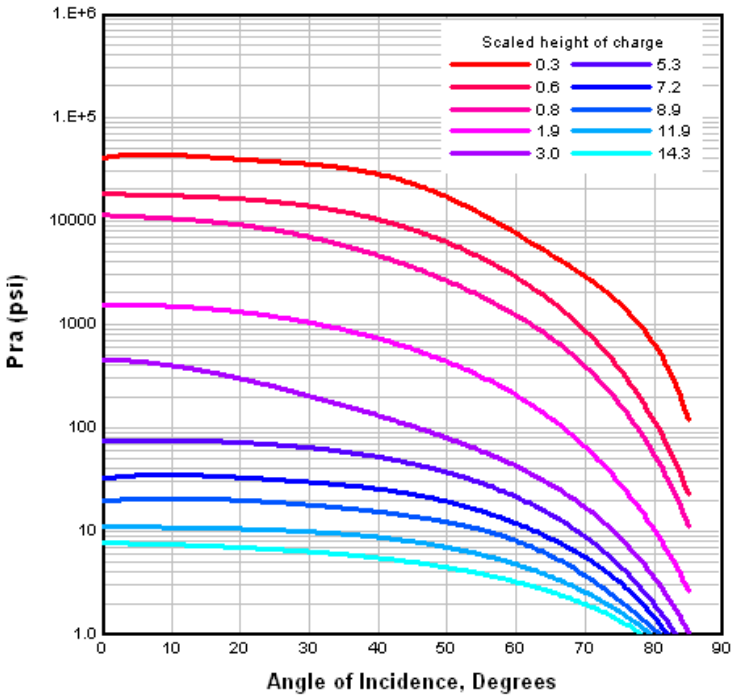

Figure 2.6: Reflected pressure versus angle of incidence (reproduced from [6])

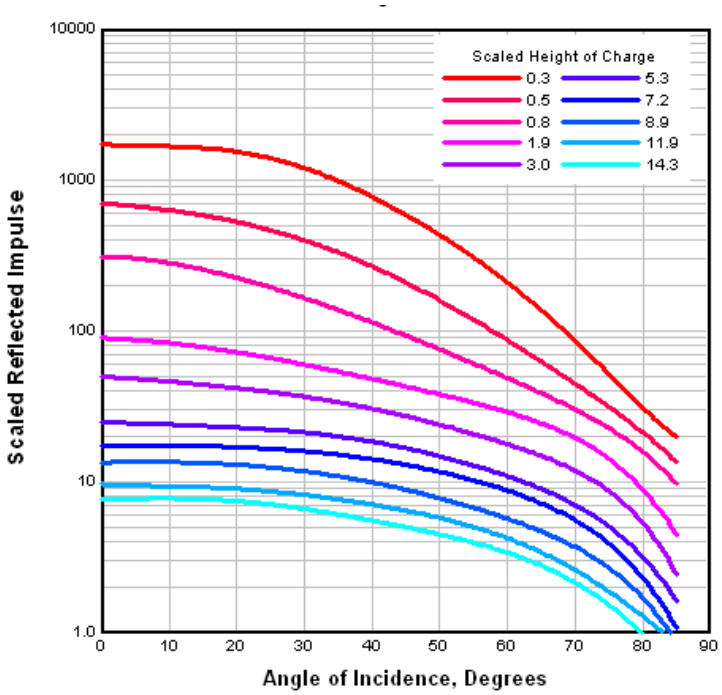

Figure 2.7: Reflected impulse versus angle of incidence (reproduced from [6])

2.2.2 AIR BURSTS EXPLOSIONS

In air burst explosions the detonation occurs at a distance above the ground and away from the structure resulting in a blast wave that reflects off of the ground before the incident wave reaches the structure. A schematic of an air burst configuration is shown in Figure 2.8.

The reflections described in the previous section on free air burst explosions are when the incident angle is equal to 0°. For the case when the incident angle is equal to 90° no reflection will occur and the surface of the structure will be loaded by the side-on pressure pulse. For the range of incident angles between these limits the reflection can be either a regular reflection or a mach reflection. Regular reflections occur at angles of incident that range from 0° and 40°, while mach reflections occur at angles above 40°. Smith and Hetherington [3] describe the Mach reflections as a complex process where the incident wave 'skims' off the reflecting surface instead of 'bouncing' which is observed for regular reflections. The incident wave that is traveling along the surface will catch up to the reflected wave and combine to form a third wave front that is denoted as the Mach front.

The point at which the incident, reflected, and Mach wave fronts intersects is called the triple point. The height of the triple point will increase as the Mach front travels away from the detonations. The pressure profile of the Mach front is similar to the incident wave except the pressures are amplified. When calculating the loads on a structure from an air burst explosion the height of the triple point relative to the height of the building is required to determine the type of loading that will be experienced. For the

case when the triple point is higher than the height of the building it is assumed that the blast wave is planer and the magnitude of the parameters will be uniform along the height. For the case when the triple point is lower than the height of the building the parameters of the blast wave will vary along the height of the building [3]. One approach is to use a uniform reflected pressure up to the triple point and then used the incident pressure above it.

The method set forth by TM 5-1300 to determine the pressure profile parameters for an air burst explosion are as follows [6]:

- Calculate the scaled height and angle of incidences from the configuration where the scaled height is $H_C/W^{1/3}$

- Use Figure 2.6 to determine the reflected pressure, p_{ra}, from the scaled height and the angle of incidence. Do the same to find the reflected impulse, i_{ra} using Figure 2.7

- Determine the scaled distance associated with both the reflected pressure and reflected impulse using p_{ra} in Figure 2.3 for P_{so} and i_{ra} into Figure 2.4 for i_{so}

- Use scaled distance and pressure with Figure 2.3 to determine any parameters associated with the pressure including p_r, p_{so}-, $t_a/W^{1/3}$, U, $L_W/W^{1/3}$, and L_W-$/W^{1/3}$ using.

- Use scaled distance for the impulse to determine any parameters associated with the impulse including i_r,i_s-,i_r-,$t_o/W^{1/3}$, and t_o-$/W^{1/3}$ using Figure 2.4.

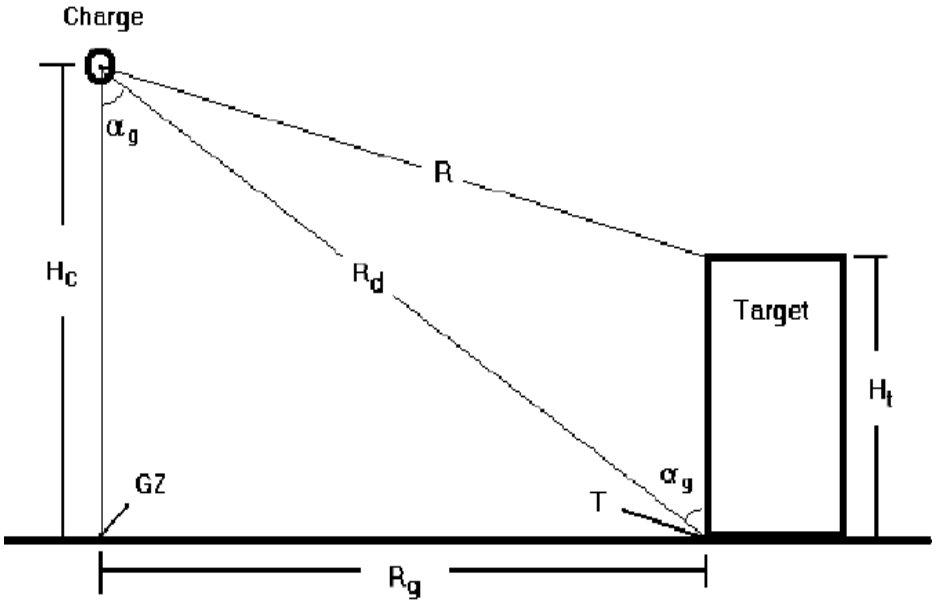

Figure 2.8: Air burst configuration (reproduced from [6])

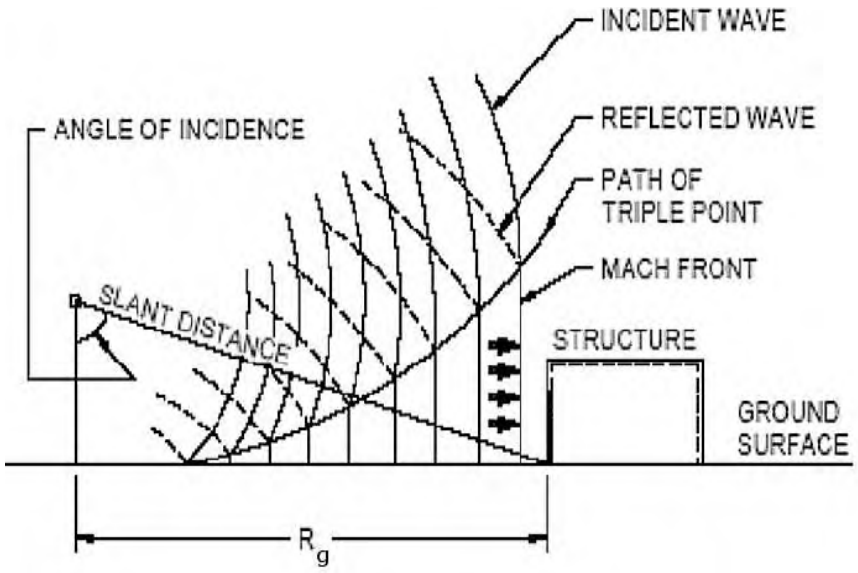

Figure 2.9: Mach wave front (reproduced from [6])

2.2.3 SURFACE BURSTS EXPLOSIONS

In a surface burst, the detonation occurs near the ground and the shock wave that is created is immediately reflected off of the surface. The incident wave will then merge with the reflected wave and a single hemispherical blast wave with travel outward from the source. According to Smith and Hetherington [3] and ASCE [4] the parameters of the blast wave in this situation are determined in a similar fashion as a free air burst except the explosive weight is scaled by an enhancement factor. In the case where the ground is a perfect reflecting surface the blast wave energy is doubled, however in practice an enhancement factor of 1.8 is applied to the explosive weight because some of the energy is dissipated in the formation of craters and ground shock [4]. TM 5-1300 [6] does not adjust the weight of the explosive and instead developed graphs relating the parameters of a ground burst to the scaled distance, *Z*, similar to the one shown in Figure 2.3. The plot for the positive and negative phase parameters from a ground blast are shown in Figure 2.11 and Figure 2.12, respectively.

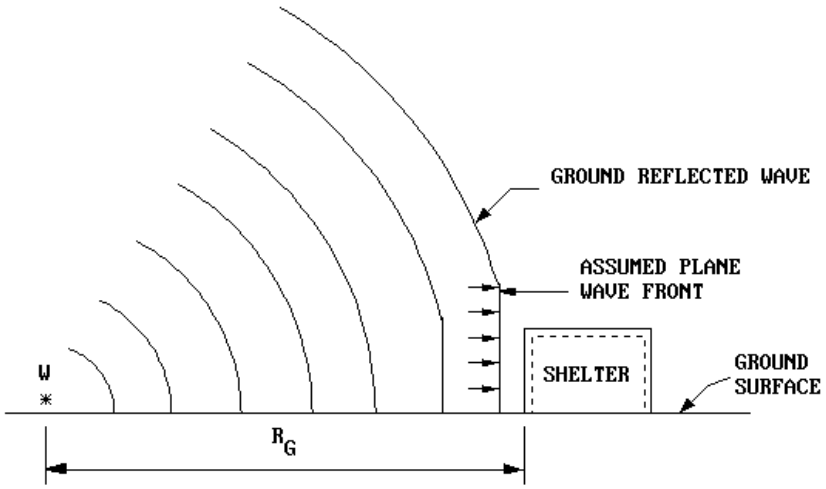

Figure 2.10: Surface burst wave front (reproduced from [6])

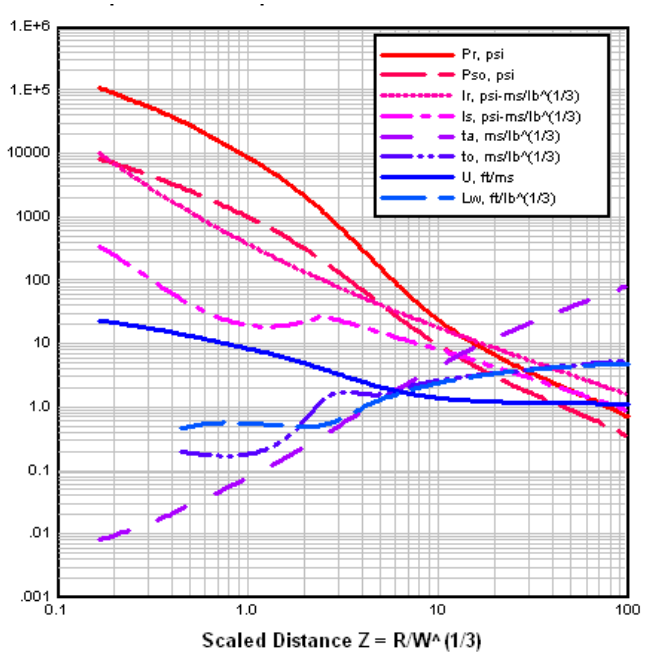

Figure 2.11: Positive phase surface burst blast wave parameters vs. scaled distance (reproduced from [6])

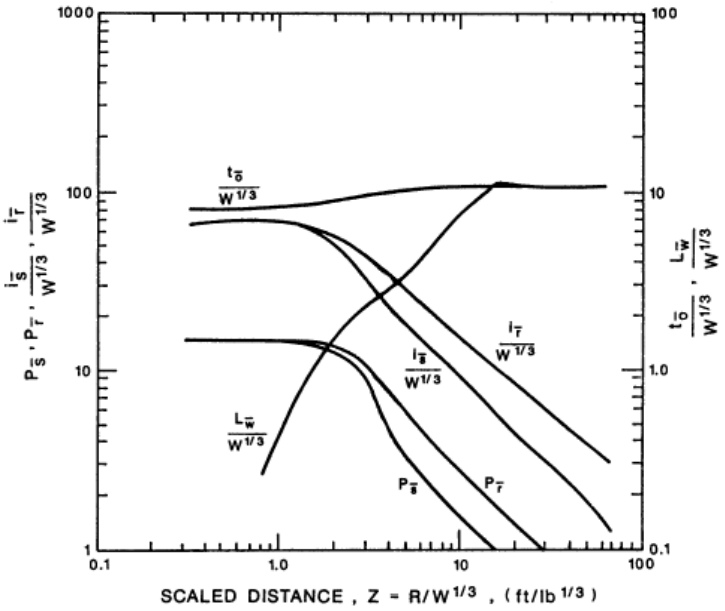

Figure 2.12: Negative phase surface burst blast wave parameters vs. scaled distance (reproduced from [6])

2.3 VCE EXPLOSIONS

A vapor cloud explosion occurs when flammable mixtures containing vapor, gas, aerosol, or mist is ignited and the speed of the flame front reaches a sufficiently large velocity to generate significant overpressure. A typical setting of a VCE is an oil refinery where a large quantity of flammable gas is stored in tanks, transported in containers or piping systems. VCE blast loads can arise from detonation or deflagration where detonation results in a shock pulse while deflagration generates a pressure pulse. The shock pulse is similar to the loads generated in an HE blast that are described in the previous section. The pressure pulse for a VCE is characterized by a slower rise time to peak overpressure and generally the duration of the pulse is longer than a shock pulse. Pressure waves generated by deflagration can develop into a shock wave as the front moves outward. This shock front may not develop until it is a significant distance from the source of the explosion. In some cases the shock front does not form until after the blast wave decays to an acoustic wave.

According to the "Guidelines for Evaluating Process Plant Buildings for External Explosions and Fires" [7] a VCE with a damaging overpressure can occur when:

- The released material is flammable and in the form of a vapor cloud under the ambient conditions.

- There is an ignition source to initiate the explosion; higher energy sources lead to more severe explosions.

- A sufficiently large cloud has formed before it is ignited; ignition of the material as it escapes is most likely cause a large fire, jet flames or a fireball, but VCE is unlikely.

- Turbulence is present to accelerate the flame to velocities associated with VCEs. Turbulence can be caused by interaction between the flame front and obstacles or from material released explosively or via pressure jets. Flame propagation is generally deflagration, but in some instances detonation may occur. Without turbulence only small overpressures are generated and the cloud burns as a flash fire.

- The vapor cloud is confined by obstacles such that pressure during combustion increases rapidly and generates flame speeds that result in significant overpressures.

Three approaches are summarized in [7] to determine the parameters of a blast wave generated by a VCE: the TNT equivalence method, the Netherlands Organization (TNO) Multi-energy method, and the Baker-Strelhlow method. These methods are described herein.

The TNT equivalence method for VCE loads is similar to the method described in an earlier section for HE loads. The mass of the fuel is converted to an equivalent mass of TNT and then the blast wave parameters are determined from the curves in Figure 2.3. The VCE is represented as an equivalent weight of TNT with the following equation:

$$W = \alpha_e \frac{W_f H_f}{H_{TNT}} \tag{2.13}$$

where W_f is the weight of the fuel, H_f is the heat of combustion of the fuel, H_{TNT} is the detonation energy of the TNT, and α_e is the TNT equivalency based on energy.

According to [7] different organizations concerned with VCE blast effects base calculations on the amount of the fuel included, the TNT equivalency, the TNT blast data, and the TNT detonation energy. Typically, only 1%-10% of the released fuel contributes to the energy in the explosion [7].

The TNT equivalence method for determining VCE loads is an advantageous approach because it is easy to use and no estimates on the size of the vapor cloud or the amount of confinement are required. Additionally, a large volume of data describing the blast effects of equivalent TNT on structures exists over a large range of scaled distances. However, despite its advantages a VCE-TNT equivalency is not well defined. The characteristics of a HE blast wave and a VCE blast wave are also different; typically VCE blast waves have a lower overpressure and a longer duration than an HE blast wave with the same amount of energy. The attenuation of the blast waves is also different for HEs and VCEs. The TNT equivalency method overestimates the overpressures near the source and underestimates its further away. This can be corrected with the use of different TNT equivalencies in the near and far fields [7].

As stated, observations of VCE suggest that there is little correlation between the amounts of fuel in a vapor cloud to the blast effects caused by an equivalent weight of TNT. Furthermore, the equivalent TNT method assumes that the source of the blast is

concentrated at one point where in actuality it is not and the strength of the blast varies over the area of the vapor cloud. The Multi-energy method and the Baker-Strehlow method take into account factors such as size, surrounding obstructions, and confinement which contribute to the VCE blast effects. The type of blast described with these methods is called fuel-air charge blasts [7].

According to [7], the Multi-Energy method divides the vapor cloud into different regions based on the level of confinement and obstacles in those regions. Each region is assumed to represent a hemispherical stoichiometric, fuel-air mixture with an explosive strength. The volume of material in each region is given a strength index, ranging from one to ten, that relates the effect of confinement and obstacles on the severity of the blast wave generated. A strength index of one is the least severe condition with little or no obstacles or confinement and ten is the most severe condition. Curves relating scaled overpressure and duration versus scaled distance for strength indices ranging from one to ten are then used to predict the parameters of the blast wave generated by each volume of material. An example of a Multi-Energy method curve relating scaled distance to maximum overpressure for varying strength indices is shown in Figure 2.13 [7].

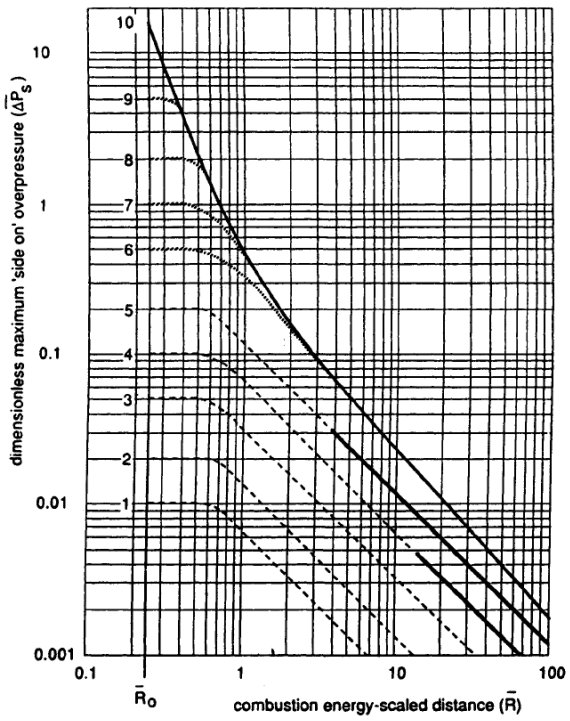

Figure 2.13: Overpressure versus scaled distance for Multi-Energy method (reproduced from [7])

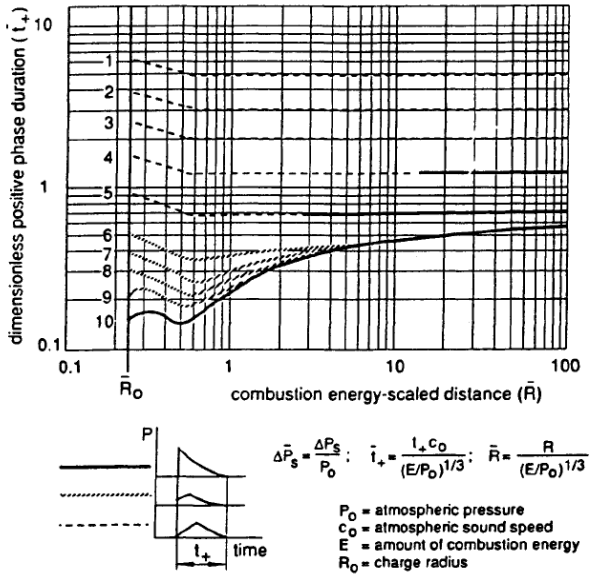

Figure 2.14: Scaled duration versus scaled distance for Multi-Energy method (reproduced from [7])

The Baker-Strehlow method uses numerical and experimental data to determine the parameters of the blast wave generated by a flame that propagates with a constant or increasing flame speed away from the source. The maximum flame speed and the equivalent energy of the explosion are input into curves to determine peak overpressure and positive phase impulse. The maximum flame speed is a function of confinement, obstacles, fuel reactivity, and ignition intensity. The equivalent energy of the explosion is related to the heat released by the volume of the vapor cloud that contributes to the blast wave. Three approaches to determine the energy are suggested [7]:

- Separate the cloud into regions based on confinement and obstacles; each region becomes a individual blast source and the energy is found multiplying the mass of the region by the heat of combustion

- Estimate the total amount of flammable material released in an appropriate amount of time; the mass of this material is then multiplied by the heat of combustions and an efficiency factor

- Estimate the total amount of material within the flammable limits and multiply the mass of this material by the heat of combustion; a dispersion model is used in this approach to determine material in the flammable limit

Research has been conducted over the last 14 years to improve Baker-Strehlow method [8], [9], [10], and [11]. The method was first presented by Baker et al. in 1994 [8]. In this paper the authors provided curves relating scaled overpressure and impulse to a scaled standoff distance for several different flame speeds. Also provided were flame

speed tables with 27 combinations of fuel reactivity, confinement, and obstacle density. Fuel reactivity was classified as low, average and high according to recommendation of Zeeuwen and Wiekema [12]. The confinement of the fuel-air mixture is denoted 3-D (3-dimensional) for a spherical flame front, 2-D for a cylindrical front and 1-D for a planer front. The obstacle density is categorized as low, medium, and high. This parameter of the model, based on a blockage ratio and pitch, is the most difficult to quantify and is the least objective. The blockage ratio is determined by the area blocked by obstacles divided by the total cross-sectional area, while the pitch is the distance between the obstacles. The authors suggest that in situations where the blockage ratio is less than 10% the obstacle density is classified as low. A high density would be for blockage ratios greater than 40% and medium density is anything in between high and low.

Baker et al. [9] made revisions to the original method in 1998 to include a systematic identification of potential explosion sites, selection of confinement level for mixed zones of 2D and 3D confinement, classification of flame expansion when confinement is elevated above the vapor cloud, and predicting blast loads when there are multiple ignition sources within the vapor cloud. The authors presented several revisions to the original methodology based on their experience gained from application of the method to hazard assessment in refineries and chemical plants. First it was stated that potential explosion sites separated by distances greater than 5 meters should be considered individually. In the case when the confinement can possibly be 2-D and 3-D, a 2.5-D confinement flame speed interpolated between 2-D and 3-D may be used. An example would be the case where a frangible barrier provides 2-D confinement early, but

as the flame expands the barrier fails and the flame expansion is 3-D. It was also stated that confinement above 3.2 times the cloud height can be ignored in the analysis. The authors also adopted Le Chatelier's rule to determine fuel reactivity for mixtures. Finally, it is suggested for multiple potential explosion sites that the multiple blast waves be combined into a single pulse with the highest peak pressure and an impulse equal to the sum of all the impulses. The authors suggest designers perform structural analysis of multiple blast waves for the case where sufficient information is available to accurately predict the load histories.

Tang and Baker [10] presented new blast curves in 1999 which were denoted the Baker-Strehlow-Tang curves to improve the prediction of the blast parameters for detonation, supersonic deflagrations, and subsonic flames. As before the curves relate overpressure and impulse to scaled distances for different flame speeds. Additional curves relating negative overpressure, negative impulse, and time of arrival are also included in the paper. The new curves were validated against new VCE data with special consideration for large deflagration experiments. The authors concluded that the validation of the method showed good agreement in the supersonic and subsonic regimes and is conservative in its predictions in the sonic deflagration regime.

Pierorazio et al. [11] presented the most recent updates to the method in a paper published in 2005. The paper discusses a series of full scale experiments that were performed to refine the relation used to determine flame speed from the level of confinement, obstacles, and fuel-air mixture reactivity. A full scale test series was conducted in part because previously published curves were validated against small scale

experiments which may not be applicable to a full scale environment. The result of the study was a new flame speed table for confinement levels of 2D, 2.5D, and 3D; reactivity levels of high, medium and low; and congestions levels of low medium and high. The authors excluded the 1-D level of confinement in the table because maximum flame speed in a true one-dimensional expansion (i.e. a pipe) is a function the length-to-diameter along with the pipe geometer, level of congestion and fuel reactivity. It was stated that many fuels undergo a detonation-to-deflagration transition if the ratio and the level of congestions is high and a single value for flame speed was not applicable to all ratios. The authors suggest that more detailed analysis be used in one-dimensional situations. The authors also recommend that further research be performed on issues such as scale, detonation-to-deflagration limits, modeling of mixed congestion and confinement situation, applicability of reflection factors derived from shock physics, clearing of blast waves, and the effect of frangible confinement.

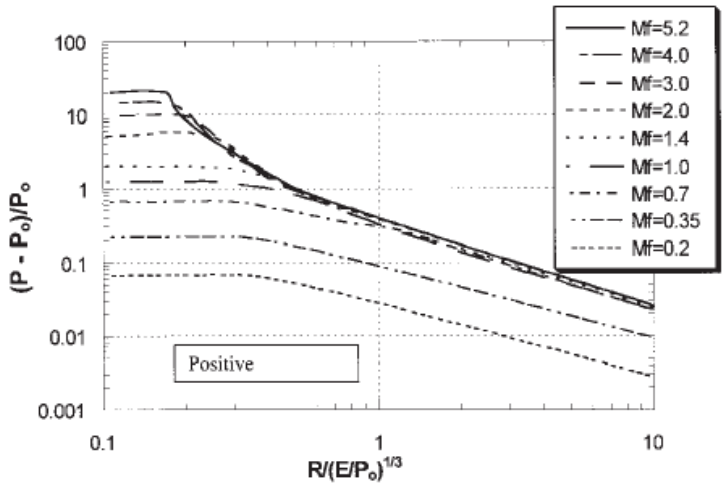

Figure 2.15: Positive overpressure versus distance for various flame speeds (reproduced from [11])

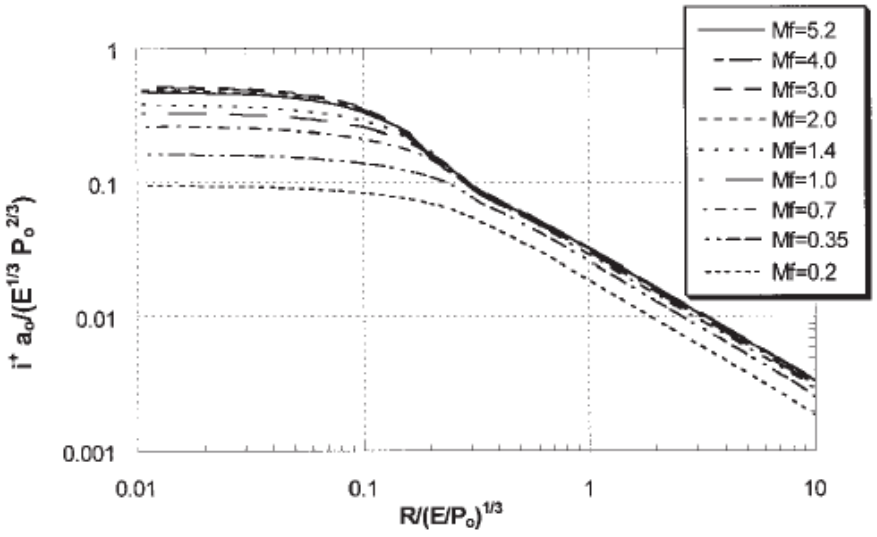

Figure 2.16: Positive impulse versus distance for various flame speeds (reproduced from [11])

2.4 STRUCTURAL LOADS

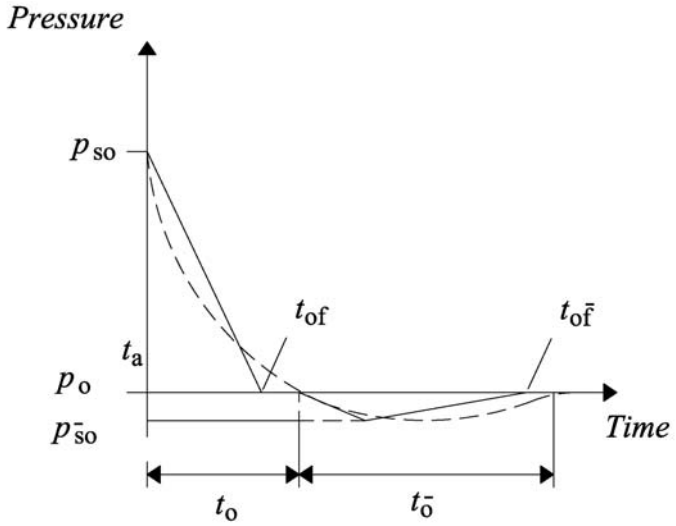

Figure 2.17: Idealized pressure pulse

The previous sections explained the parameters of a pressure pulse generated in unconfined blast created by HE detonations and for a VCE. Included in these sections

are the graphical methods to determine the parameters for each type of load. The pressure loading defined by these parameters can be idealized as shown in Figure 2.17 to simplify the analysis. In the idealization, the pressure has an instantaneous rise time, then it decays back to zero until it continuous to decrease linearly to the peak negative pressure load and finally it returns back to zero. The duration of the idealized positive phase is determined with

$$t_{of} = \frac{2i_s}{p_{so}} \tag{2.14}$$

while the idealized rise time of the negative pressure pulse will equal 0.25 times t_{of}^- which can be found with

$$t_{of}^- = \frac{2i_s^-}{p_{so}^-} \tag{2.15}$$

When designing a structure to resist blast effects, the applied loads arise from free-field incident pressure, dynamic pressure, and reflected pressures. In sections 2.2.1, 2.2.2, and 2.2.3 these pressure pulses were calculated for free air bursts, air bursts, and surface bursts assuming that the surface of the structure interacting with the load was significantly large and normal to the shock front. In situations similar to the illustration in Figure 2.18 the pressure load on the front wall will be dependent on the geometry of the building. The front wall is the section of the wall that will be focused on in this chapter. A plot of load on the front wall is shown in Figure 2.19. As the blast wave hits, the peak reflected pressure will be instantaneously applied to the front face. The pressure

will decay until the blast wave travels over the top and around the sides of the structure. The clearing time, t_c, to relieve the reflected pressure which according to [6] is given by

$$t_c = \frac{4S}{(1+R)C_r} \tag{2.16}$$

where S is the smaller of H_c or $W_c/2$, R is the ratio of S to G (G is the larger of H_c or $W_c/2$), and C_r is the speed of sound in the reflected region (Figure 2.22). Again according to [6], the pressure on the wall after the reflected load has cleared, $_{psc}$, is equal to

$$p_{sc} = p_{so} + C_D q_s \tag{2.17}$$

where C_D is a drag coefficient typically equal to one and q_s is the dynamic pressure that corresponds to the peak incident pressure. A fictitious duration, t_r, can be derived for the reflective pressure based on the assumption that the pulse is triangular shape with

$$t_r = \frac{2i_r}{p_r} \tag{2.18}$$

Once the reflected curve with and without clearing is constructed, as shown in Figure 2.19, the curve that has the smallest impulse is used as the load on the wall.

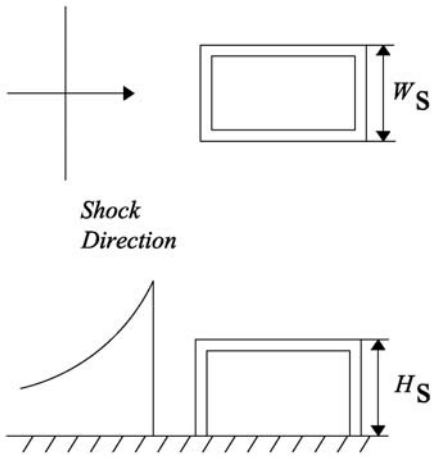

Figure 2.18: Blast loading of a building

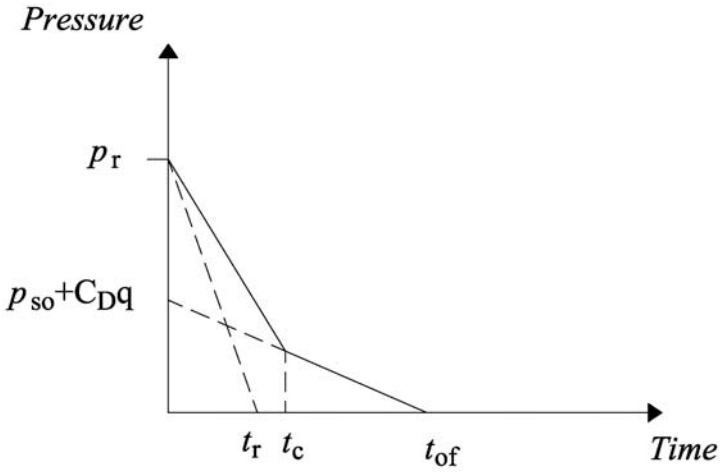

Figure 2.19: Front wall loading

For the case in which the surface of the structure is at an oblique angle to the shock front, as shown in Figure 2.20, the peak reflected pressure can be found via the following equation

$$p_r = C_{r\alpha} p_{so} \tag{2.19}$$

where the coefficient $C_{r\alpha}$ is determined with use of the graph shown in Figure 2.21.

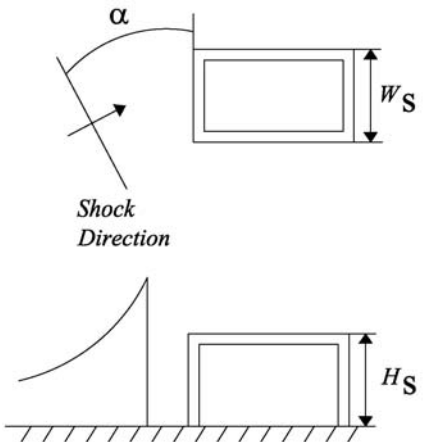

Figure 2.20: Example of oblique reflection of a shock front

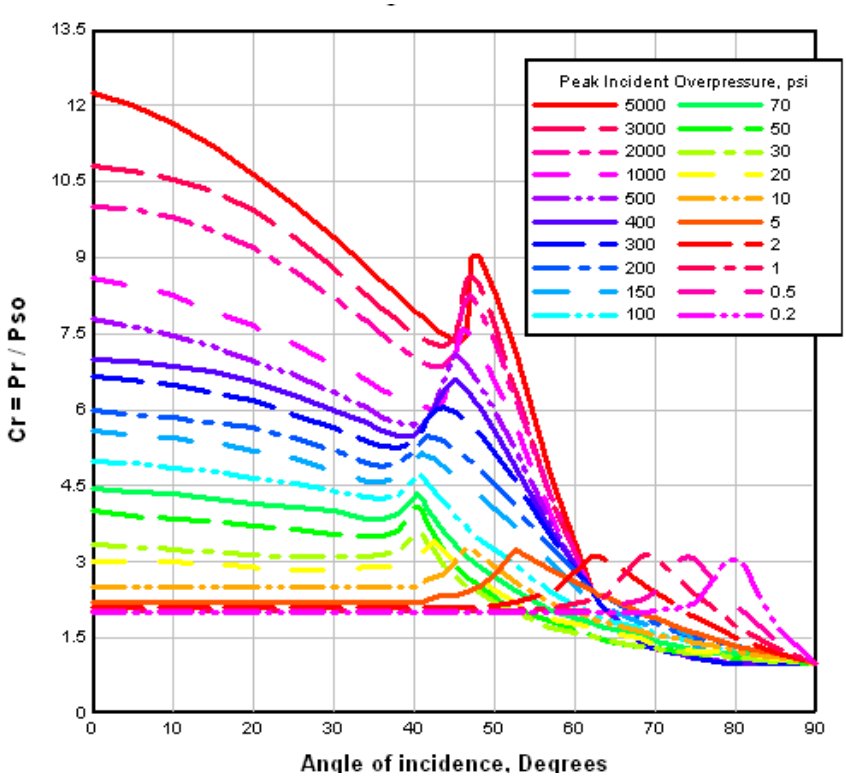

Figure 2.21: Angle of incidence versus reflected pressure coefficient (reproduced from [6])

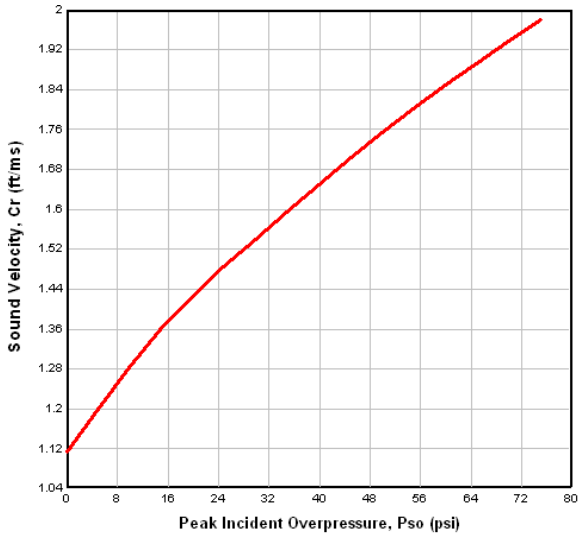

Figure 2.22: Peak incident overpressure versus sound velocity (reproduced from [6])

EXAMPLE: WALL LOADED BY HE BLAST

A wall that is part of a two story building is loaded by a 300 lbs charge of ANFO placed 25 ft away and raised 3 ft off the ground. A schematic of the loading situation for the wall is shown in Figure 2.23. The wall is in the middle bay of a building that has a total height equal to 25 ft and a width equal to 45 feet.

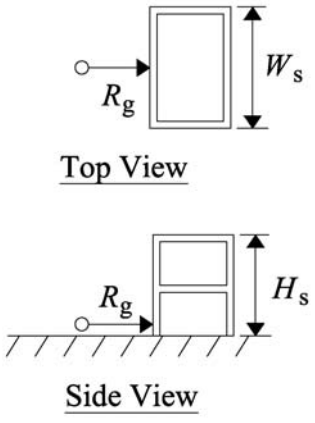

Figure 2.23: Schematic of load configuration for HE blast

The location of the charge is close to the ground relative to the distance to the front of the building; therefore it is assumed that the explosion will be a surface burst. The equivalent weight of TNT is

$$W = 0.82 \cdot 300lb = 246lb \tag{2.20}$$

and the distance from the charge to the wall, R_g, is 25 ft; thus

$$Z = \frac{R_g}{\sqrt[3]{W}} = \frac{25\,ft}{\sqrt[3]{246lb}} = 4.1\frac{ft}{lb^{1/3}} \tag{2.21}$$

This value of Z can be used with Figure 2.11 and Figure 2.12 to find the following parameters of the blast wave:

$$p_{so} = 75\,psi \tag{2.22}$$

$$p_r = 300\,psi \tag{2.23}$$

$$p_r^- = 7\,psi \tag{2.24}$$

$$i_r = 308\,psi - msec \tag{2.25}$$

$$i_r^- = 123\,psi - msec \tag{2.26}$$

$$t_a = 4.92msec \tag{2.27}$$

$$t_o = 9.22msec \tag{2.28}$$

$$t_o^- = 61.5msec \tag{2.29}$$

In the calculation of the clearing time the clear height, H_c, is 25 ft and the clearing width, W_c, is 45 ft; thus for equation (2.16), S is equal to $W_c/2$ which is 22.5 ft and R is equal to

0.9. The sound velocity, C_r, is equal to 2 ft/msec when using Figure 2.22 with a peak incident pressure, P_{so}, equals 75 psi. Therefore the clearing time is found with

$$t_c = \frac{3 \cdot 22.5\, ft}{(1+0.9)2\, ft/m\sec} = 17.8 m\sec \tag{2.30}$$

The fictitious duration for the reflected peak pressure using equation (2.18) is 2.05 msec which is significantly less than the clearing time. Therefore the impulse created by the peak reflected pressure and fictitious duration will be used for the load because the magnitude of this impulse is lower than the impulse calculated with clearing effects. Please note that according to [6] the smaller impulse is selected when calculating the effects of clearing. The idealized pressure pulse is shown in Figure 2.24.

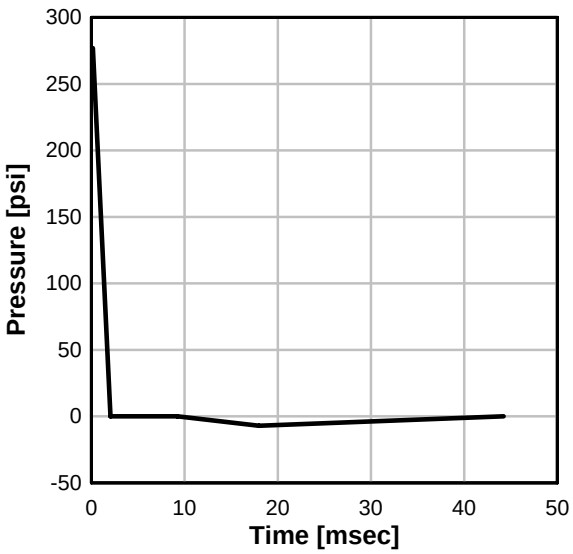

Figure 2.24: HE example- idealized pressure pulse

EXAMPLE: WALL LOADED BY VCE BLAST

This example demonstrates the Baker-Strehlow method to determine the pressure load on a control building at a refinery in a VCE blast. The building is 45 ft wide, 15 ft tall and is located 150 ft away from the source of the blast. The explosion occurs in a high congested area of processing plant where there are several of pipes closely spaced and additional equipment elevated overhead. The source of the explosion is ethylene that leaked into the process area that has a volume equal to 45 ft x 45 ft x 25 ft. The vapor cloud that has been trapped is a near-stoichiometric fuel-air mixture which has a high reactivity. Finally, the shock front generated in the explosion approaches the front surface of the wall at an oblique angle equal to 20 degrees.

The first step to determine the overpressure generated in the blast is to calculated the volume of the vapor cloud

$$Volume = 45\ ft \times 45\ ft \times 25\ ft = 50625\ ft^3 \tag{2.31}$$

Next, the according to table 7.1 in [13] the volumetric combustion energy of ethylene in a stoichiometric mixture with air is

$$H_{ce} = 76012 lb \cdot\ ft\ /\ ft^3 \tag{2.32}$$

Also, atmospheric pressure is

$$p_o = 14.7\ psi \tag{2.33}$$

The scaled distance can now be found with

$$\bar{R} = \frac{R_g}{(E_t / p_o)^{1/3}} = \frac{150\,ft}{((50625\,ft^3 \cdot 76012 lb \cdot ft / ft^3) / (2116\,psf))^{1/3}} = 1.23\,ft \qquad (2.34)$$

where

$$E_t = H_c \cdot volume \qquad (2.35)$$

The most recent flame speed table, Table 2 published in [11], is used to calculate the flame speed. In this example the fuel-air mixture has a high reactivity, the congestion at the source of the explosion is high, and the equipment above the leak creates a 2D confinement condition where the shock will propagate in a cylindrical directions. The flame speed, M_f, for the conditions in this example is

$$M_f = 5.2 \qquad (2.36)$$

Now using this flame speed with the scaled distance and the charts given in [11] and displayed in Figure 2.15 and Figure 2.16 the scaled peak pressure and positive impulse can be found as follows:

$$\bar{p} = \frac{p_{so} - p_o}{p_o} = 0.3 \qquad (2.37)$$

$$\bar{I} = \frac{i_s \cdot a_o}{E_t^{1/3} p_o^{2/3}} = 0.02 \qquad (2.38)$$

where a_o is the sound velocity at ambient conditions and is equal to 1116 ft/sec. The negative phase of this pulse is ignored. From the equations above, the peak overpressure

is 4.4 psi and the impulse is 121 psi-msec. The duration of an idealized pulse created by the VCE can be found with equation (2.14) and is equal to 55 msec.

The final step to calculate the loads on the building is to determine the reflected pressure pulse. The shock front will have an oblique reflection off the building at a 20º angle; thus, using Figure 2.21, the reflection coefficient, $C_{r\alpha}$, is equal to 2. The reflected peak pressure is then

$$p_r = C_{r\alpha} p_{so} = 2 \cdot 4.4\,psi = 8.8\,psi \tag{2.39}$$

The impulse associated with this pressure is equal to 242 psi-msec given duration equal to 55 msec. A plot of the pressure pulse applied to the structure is shown below.

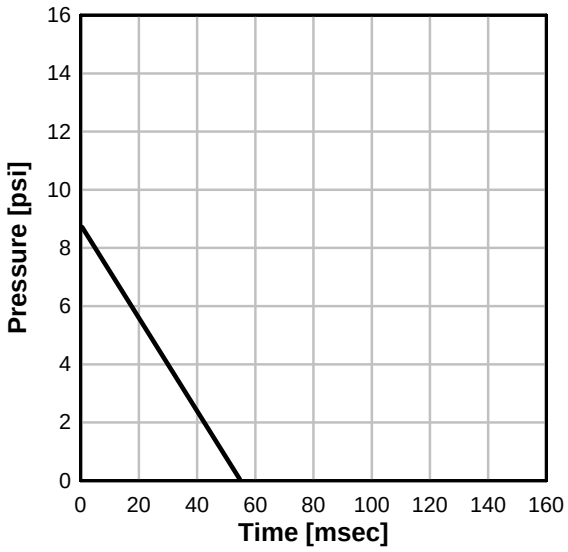

Figure 2.25: VCE example- idealized pressure pulse

2.5 NUMERICAL CODES FOR CALCULATION OF BLAST WAVE PARAMETERS

Computer codes are also available for calculating blast effects on structures. ConWep is a program used to calculate blast effects generated from the detonation of conventional weapons. The calculations performed are based on equations and curves of TM 5-855-1 [14]. The blast effects calculated by the program include airblast loads, fragment penetration, projectile penetration, breach, cratering, and ground shock. The program requires charge size, standoff distance, geometry of target and geometry of the reflective surface. The curves and equations used in the program are similar to those given in TM 5-1300 [6] and discussed in previous sections. The distribution of this program, along with TM 5-855-1 is limited to U.S. government contractors.

BLASTX is a code described in [15] that calculates the effects from the shock wave and the explosive gas pressures that are generated in the detonation of a conventional explosive in a confined space with an option for venting. The program will also calculate the propagation of shocks and gas pressures into adjacent room. The code only models bare, spherical charges of TNT, but can simulate multiple, non-simultaneous explosions in one room. The walls in the simulations are assumed to be rigid, but there are options that allow it to form openings based on failure criteria.

More complex simulations to calculate the blast effects on structures might require a computational fluid dynamics (CFD) code such as CTH [16]. The CTH software was developed by Sandia National Laboratories in Albuquerque. It is an Eulerian code that has several models to simulate plastic material behavior, high explosive detonation, fracture and fragmentation. This program is ideally used in

situations where the curves and equation given by [6] are not applicable such as the case where a loaded building has a complex geometry or for a “close-in” charge.

2.6 SDOF ANALYSIS

2.6.1 EQUATION OF MOTION

Single degree-of-freedom analysis is one method used to estimate the dynamic response of structural components to blast loads. This method takes a uniformly loaded continuous system with infinite-degrees-of-freedom and distributed mass and stiffness and treats it as a rigid mass that is forced by a point load and resisted with a "spring" or resistance function. Herein a brief derivation of the beam equation of motion is presented. The walls studied in the dissertation all deform in a one-way flexural mode which can be described by the derived equation. Similar derivations can be found in [17] and [18].

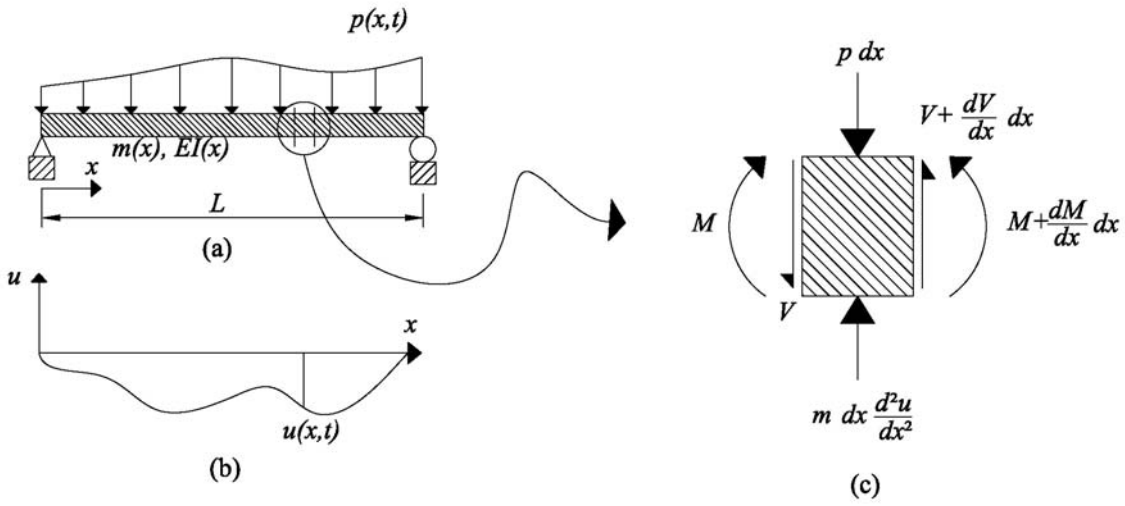

Figure 2.26: Beam with distributed mass and cross sectional properties: (a) beam with applied load; (b) displacement; (c) forces on differential element

Figure 2.26 (a) displays a one-way element with a distributed load, *p(x,t)*, which is a function of time and position from the left support, *x*. The beam has a length, *L*, a

mass per unit length, *m(x)*, and flexibility per unit length, *EI(x)*. Both the flexibility and mass can also vary with position. The displacement of the beam, as shown in Figure 2.26 (b), is a function of position and time. Damping is neglected in this derivation; in the analysis of structural components to blast loads the damping forces are typically small and do not effect the response of the system. The partial differential equation that governs the motion of this system can be derived through the conservation of linear momentum on a differential element cut from a one-way member. Using D'Alembert's principle the product of the element mass and acceleration is applied as an inertial force that acts in the direction opposite that of the accelerations.

A cut of a differential element is shown in Figure 2.26 (c); included are the load, the inertial force, the transverse shear, *V(x,t)*, and the bending moments, *M(x,t)*. Equilibrium of the forces in the direction of the displacement gives

$$\frac{\partial V}{\partial x} = p - m\frac{\partial^2 u}{\partial t^2} \tag{2.40}$$

Summation of the moments in the element about the center, ignoring higher order terms and also ignoring any rotational inertia associated with the angular acceleration of the mass, yields

$$V = \frac{\partial M}{\partial x} \tag{2.41}$$

It can be shown that the bending moment is related to the curvature in the beam, ϕ, by

$$M = \phi EI \tag{2.42}$$

if shear deformations are neglected. The curvature for small deformations is related to the displacement by

$$\phi = \frac{\partial^2 u}{\partial x^2} \tag{2.43}$$

Substitution of equations (2.41), (2.42), and (2.43) into (2.40) gives

$$p(x,t) = m(x)\frac{\partial^2 u}{dt^2} + \frac{\partial^2}{\partial x^2}\left[EI(x)\frac{\partial^2 u}{\partial x^2}\right] \tag{2.44}$$

which is the partial differential equation that describes the motion of a beam, *u(x,t)* to an external load, *p(x,t)*.

2.6.2 GENERALIZED SDOF

The system that is described by the equation of motion derived above is modeled as an equivalent SDOF mass with a point load and a "spring" force or a force provided by a "resistance function." Several references describe the generalization of structural systems as an equivalent SDOF, such as [6], [17] and [18]. In the equivalent SDOF the displacements of a beam are expressed as a combination of a shape function, $\psi(x)$ and a generalized coordinate, $\Delta(t)$, such that

$$u(x,t) = \psi(x)\Delta(t) \tag{2.45}$$

In the case of a simply supported one-way wall Δ corresponds to the midspan displacement. The requirement on the shape function used in the equivalent SDOF is that

it must satisfy the displacement boundary conditions of the element being loaded. The equations of motion of the equivalent SDOF is now given by

$$p_{eq}(t) = m_{eq}\ddot{\Delta} + k_{eq}\Delta \tag{2.46}$$

where $p_{eq}(t)$ is the equivalent applied load on the system, m_{eq} is the equivalent mass, and k_{eq} is the equivalent stiffness. The equation above is for the case when the specimen responds linearly to the load. Often in blast design the loads generated by an explosion cause the specimen to behave nonlinearly due to a combination of inelastic material behavior and geometric effects. In these situations the stiffness term is replaced by a nonlinear resistance function that is dependent on deformation of the specimen. The double dot above z in equation (2.46) denotes the second derivative of z with respect to time. In the following derivation of the equation of motion of the equivalent SDOF system a dot above a variable denotes a time derivative, $\dot{(\bullet)} = \frac{\partial(\bullet)}{\partial t}$, a double dot denotes the second time derivative and so on. Similarly a dash after a variable denotes a derivative with respect to x, such that $(\bullet)' = \frac{\partial(\bullet)}{\partial x}$.

The principle of virtual displacements is one method, which is used by [17, 18], for deriving the equation of motion for the equivalent SDOF. The principle states that if a system in equilibrium is given a virtual displacement $\delta u(x)$, the external work δW_e is equal to the internal work δW_i:

$$\delta W_e = \delta W_i \tag{2.47}$$

The external forces on the system are the load *p(x,t)* and the inertial force that is added using D'Alembert's principle. The external virtual work is then

$$\delta W_e = \int_0^L p(x,t)\delta u dx - \int_0^L m(x)\ddot{u}\delta u dx \tag{2.48}$$

The internal virtual work in the beam arises from the bending moments acting through the curvature corresponding to the virtual displacements:

$$\delta W_i = \int_o^L M(x,t)\delta\phi(x)dx \tag{2.49}$$

and for beam bending when displacements are small and shear deformations are ignored

$$M(x,t) = EI(x)\phi(x) \tag{2.50}$$

where $\phi(x)=u''(x)$ and $\delta\phi(x)=\delta(u''(x))$. Substitution of (2.50) into (2.49) gives

$$\delta W_i = \int_o^L EI(x)u''(x)\delta[u''(x)]dx \tag{2.51}$$

The virtual displacement is consistent with the shape function selected for the deformed element, thus

$$\delta u(x) = \psi(x)\delta\Delta \tag{2.52}$$

and

$$\delta u''(x) = \psi''(x)\delta\Delta \tag{2.53}$$

Substitution of equations (2.52) and (2.53) into equations (2.48) and (2.51) which can then be substituted into (2.47) to give

$$\delta\Delta\left[-\int_0^L p(x,t)\psi(x)dx+\ddot{\Delta}\int_0^L m(x)\psi^2(x)dx+\Delta\int_0^L EI(x)[\psi''(x)]^2dx\right]=0 \qquad (2.54)$$

This equation is valid for all virtual displacements; therefore δz can be dropped and the equation reduces to equation (2.46) where

$$p_{eq}=\int_0^L p(x,t)\psi(x)dx \qquad (2.55)$$

$$m_{eq}=\int_0^L m(x)\psi^2(x)dx \qquad (2.56)$$

$$k_{eq}=\int_0^L EI(x)[\psi''(x)]^2dx \qquad (2.57)$$

For the case when a resistance function is used, equation (2.46) can be replaced with

$$p_{eq}(t)=m_{eq}\ddot{z}+R_{eq}(\Delta) \qquad (2.58)$$

where R_{eq} is the equivalent resistance function that can be derived by the same method that was used to derive the equivalent load:

$$R_{eq}=\int_0^L R(\Delta)\psi(x)dx \qquad (2.59)$$

with $R(\Delta)$ being the resistance function that is dependent on the displacement of the element.

2.6.3 SHAPE FUNCTIONS

The general requirement for a shape function used in an equivalent SDOF analysis is that it satisfies the displacement boundary conditions. The typical method for determining the shape function in blast analysis is to take the first mode deflected shape of the element to a uniform static pressure and normalize it by the maximum displacement. For a wall undergoing one-way bending under uniform load with simply supported boundaries the following shape function can be used:

$$\psi_{ss} = \frac{16}{5L^4}(x^4 - 2Lx^3 + L^3x) \tag{2.60}$$

For the case of a one-way bending wall under uniform load with a pin support on the left and a fixed support on the right the following function is used:

$$\psi_{pf} = \frac{185}{48L^4}(2x^4 - 3Lx^3 + L^3x) \tag{2.61}$$

Finally, for the case of a one-way bending wall under uniform load with a fixed-fixed support the following shape functions can be used:

$$\psi_{ff} = \frac{16}{L^4}(x^4 - 2Lx^3 + L^2x^2) \tag{2.62}$$

The load factor, mass factor, and effective stiffness for these three shape functions can be found with equations (2.63), (2.64), and (2.65), respectively. Table 2.3 lists the

load, mass, and effective stiffness for an elastic one-way member with simple-simple, pin-fixed, and fixed-fixed supports. Also included in the table is the load-mass factor, K_{LM} which is equal to the mass factor divided by the load factor. The load-mass factor is used to scale the mass in the case when a resistance function is used. This is done to simplify the equation of motion and can be proven algebraically to give the same results by dividing through the equation by the load factor.

$$K_L = \int_0^L \psi(x)dx \tag{2.63}$$

$$K_M = \int_0^L \psi(x)^2 dx \tag{2.64}$$

$$K_S = \int_0^L EI(x)[\psi''(x)]^2 dx \tag{2.65}$$

Table 2.3: Load, mass, and effective stiffness for equivalent SDOF

Shape	K_{LM}	K_L	K_M	K_S
ψ_{ss}	0.78	0.64	0.50	$\frac{384EI}{5L^3}$
ψ_{pf}	0.78	0.58	0.45	$185EI$
ψ_{ff}	0.77	0.53	0.41	$384EI$

It is important to note that these shape functions are based on the assumption that the walls undergo deformation in bending. It is possible that loads with very short duration and high pressures will produce shapes in the member where the deformation is localized closer to the supports. For this case the mass of the member experiences a large

amount of inertia, preventing it from bending and producing large shear strains near the ends. This should be considered when using SDOF analysis as it is a limitation of the method. In situations where this type of behavior arises it is suggested that a designer use a more detailed method, such as the finite element analysis.

2.6.4 RESISTANCE FUNCTIONS

The resistance functions for the reinforced concrete and masonry one-way bending walls are calculated by using a moment-curvature relation for a cross section to determine the midspan displacement associated with a level of load, R. The walls are assumed to deform in a flexural mode under uniformly distributed load (Figure 2.27 (a)). First the progression of damage for a simply-supported wall is described. Initially the wall deforms according to elastic beam theory as shown in Figure 2.27 (b). When the yield moment is reached at the midspan the wall forms a plastic hinge and the deformation in the wall will be concentrated in the plastic hinge region Figure 2.27 (c). The wall will finally form a mechanism when the moment at the midspan reaches M_u and the concrete crushes. After the maximum moment is reached there is no resistance to lateral load and the wall is assumed to undergoes perfectly plastic deformation

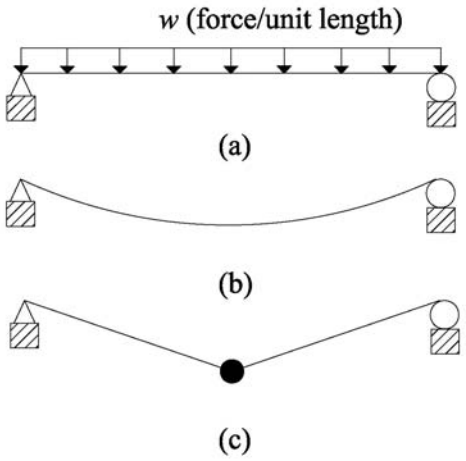

Figure 2.27: Hinge formations in simply-supported slab under uniform loading

The total force, *R*, resisted by a one-way slab under uniform loading is found from the maximum moment by the following equation:

$$R = \frac{8M_u}{L} \tag{2.66}$$

where *L* is the span of the slab. The displacement at which plastic hinge forms, Δ_y, can be found with the following expression:

$$\Delta = \frac{5\phi_u L^2}{48} \tag{2.67}$$

This expression can be derived by substituting $w = \frac{8M}{L^2}$ and $\phi = \frac{M}{EI}$ into the equation for peak midspan displacement of uniformly loaded elastic beam:

$$\Delta = \frac{5wL^4}{384EI} \tag{2.68}$$

It is assumed in the development of the resistance functions that the walls behave elastically up to the crushing of the concrete or concrete masonry. The ultimate moment, M_u, and the ultimate curvature ϕ_u are determined from moment-curvature analysis.

2.6.5 PINNED-FIXED

A resistance function for a fixed-pinned one-way wall can be constructed by solving for the midspan deflection as the loads are incrementally increased and plastic hinges are formed first at the support and then near the midspan. A schematic of the assumed kinematics for the fixed-pin slab is shown in Figure 2.28.

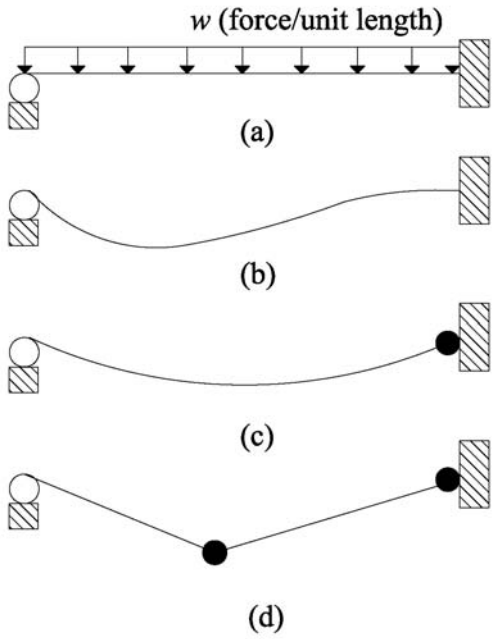

Figure 2.28: Progression of hinge formation in pinned-fixed slab

The first hinge is assumed to form near the fixed support. The moment at the hinge is equal to M_u. The load resisted by the wall at the formation of the first hinge, R_1, can then be found with

$$R_1 = \frac{8M_u}{L} \tag{2.69}$$

The expression in equation (2.69) can be derived by replacing the fixed end moment with M_u and solving for the reactions at the supports under uniform loading. It can also be shown that the moment at the midspan at the formation of the first hinge is equal to $0.5M_u$. The midspan displacement in an elastic fixed-pin wall is related to the curvature by

$$\Delta = \frac{\phi L^2}{24} \tag{2.70}$$

where ϕ is the curvature at the midspan. The deformation in the wall is assumed to be elastic until the first hinge forms, which means that the relation between the curvature and the moment is linear. Therefore, the curvature at the midspan is equal to $0.5\phi_u$ at the formation of the first hinge and the displacement at R_1 is

$$\Delta_1 = \frac{\phi_u L^2}{48} \tag{2.71}$$

Between the formation of the first and second hinge, it is assumed that the wall has a simply-supported displaced shape. The resistance of the wall at this point is approximately

$$R_2 = \frac{12M_u}{L} \tag{2.72}$$

The second hinge forms at the location of the maximum moment, which is actually at $\bar{x} = \frac{7L}{12}$ where $\bar{x}$ is measured from the location of the support with the fixed end. However, for simplicity it is assumed that the hinge forms at the midspan and the displacement at R_2 is

$$\Delta_2 = \frac{5\phi L^2}{48} + \Delta_1 \tag{2.73}$$

where ϕ is the increment of curvature in the wall when the force increases from R_1 to R_2 and $\phi = 0.5\phi_u$. The wall becomes a mechanism after the formation of the second hinge and the force-displacement relation at this point is treated as perfectly-plastic.

An example of the load displacement behavior for the resistance function used in the SDOF analysis is displayed in Figure 2.29. This schematic is of a typical resistance function that has a tri-linear curve. It is assumed in the example that the magnitude of the resistant force is equal in tension and compression. This assumption in an actual wall may not be true. For example, a reinforced concrete wall may have more tension steel than compression steel and the resistance associated with positive bending is greater than the resistance for negative bending; where positive bending is defined as compressive strains at the top of the cross-section and tensile at the bottom. When the wall is initially loading the resistance and deflection will be on the curve shown in the Figure 2.29. When the wall rebounds it will unload linearly with a slope equal to the initial stiffness from the linear-elastic portion of the resistance function as shown in Figure 2.30. Unloading along this slope will continue for a single or several load reversal until the force in the wall element is less than the yield stress in tension or exceeds the yield stress

in compression. An example of a theoretical hysteresis loop for the wall during an analysis is shown in Figure 2.31. In this example the wall element loads in compression according to the initially defined piecewise linear resistance function. Next it unloads linearly with a slope, *K,* until it yields in tension. Upon yield it will loads according to the initial function, but with a displacement offset equal that represents a plastic deformation. The plastic deformation is defined as the displacement at which the force is equal to zero. Finally, the load direction changes again and the force in wall element increases linearly with a slope equal to *K*.

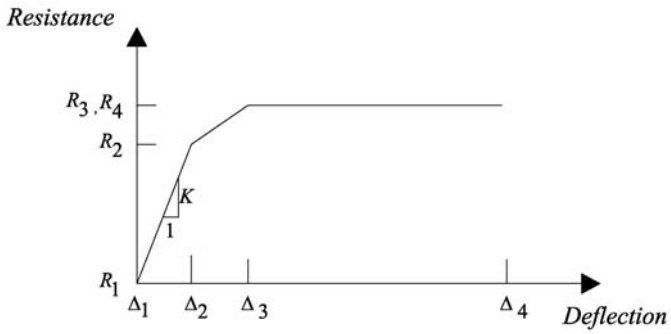

Figure 2.29: Resistance Function

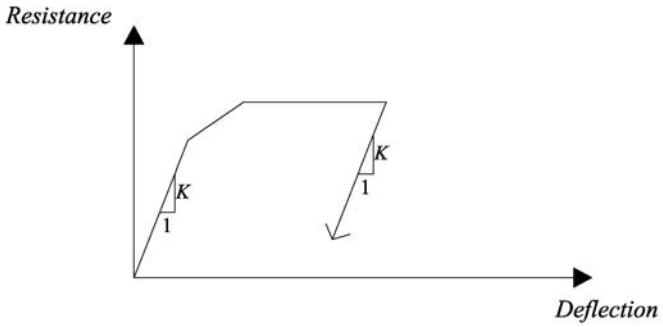

Figure 2.30: Resistance Function-Unloading

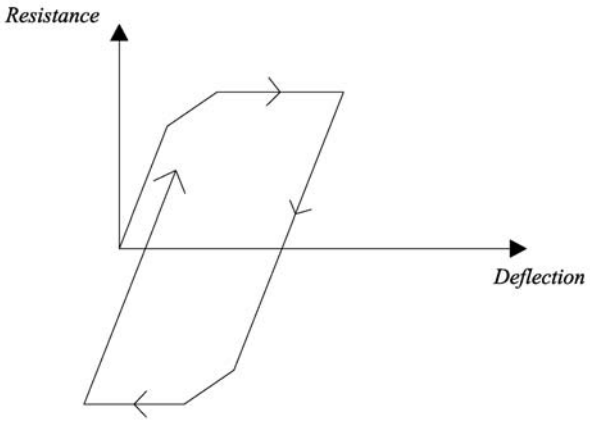

Figure 2.31: Resistance Function-Unloading and Reloading

2.6.6 DYNAMIC REACTION FORCES

The reaction forces in the wall that develop due to the blast loading will not be equal to those which occur when the wall is loaded statically. The difference in the reactions is because of inertia effects which resist the blast loads. The common approach to determine the reactions, as suggest in Biggs [18], TM 5-1300 [6], and Smith and Hetherington [3], is through the use of the following equation:

$$V(t) = \psi_1 R(t) + \psi_2 p(t) + \psi_3 M_u / L \tag{2.74}$$

where *R(t)* is the concrete core resistance, p*(t)* is the blast load, M_u is the moment at which a yield hinge forms, L is the span and ψ_1, ψ_2 and ψ_3 are dynamic reaction coefficients. These coefficients can be determined by satisfying the moment equilibrium equation on the assumed deformed shape of half the span with a load. This analysis requires making a cut at the center line of a deformed beam and replacing the remainder of the beam with a moment and shear force representing the internal forces in the member. A free body diagram for a uniformly loaded, simply supported beam is

displayed in Figure 2.32. Summations of the moments about the point through which the inertia force acts will give the following equations

$$V(t)\bar{x} + p(t)(\frac{L}{4} - \bar{x}) - M(t) = 0 \tag{2.75}$$

where $\bar{x}$ for a simply supported member is equal to 61L/192 and the moment at the midspan is equal to

$$M(t) = \frac{RL}{8} \tag{2.76}$$

Therefore, if the terms of equation (2.75) are rearranged the dynamic support reaction force is equal to the expression in equation (2.74) with ψ_1 equal to 0.38, ψ_2 equal to 0.11 and ψ_3 equal to zero. Table 2.4 lists the coefficients used in equation (2.74) for one-way bending walls with a selection of different boundary conditions and strain states.

Table 2.4: Dynamic Reaction Coefficients

Boundary Conditions	Strain State	Location	ψ_1	ψ_2	ψ_3
Simple-Simple	Elastic	both	0.39	0.11	0
	Plastic	both	0.38	0.12	0
Fixed-Simple	Elastic	simple	0.26	0.12	0
	Elastic	fixed	0.43	0.19	0
	Plastic	simple	0.38	0.11	-1
	Plastic	fixed	0.38	0.11	1

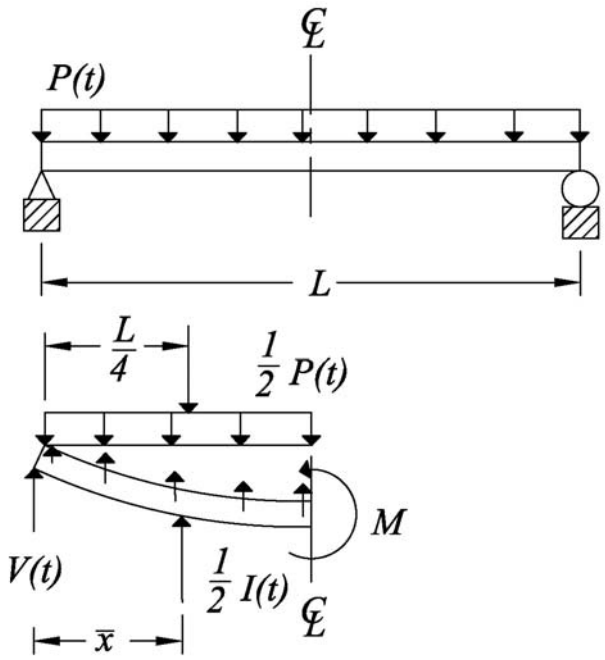

Figure 2.32: Dynamic reactions

2.6.7 NUMERICAL SOLUTION TO EQUATION OF MOTION-EXPLICIT

The solution to the equation of motion for the SDOF can also be found using an explicit type of Newmark's method called the central-difference method. In this method, the integration parameter, β, equals zero and the other parameter, γ, equals one-half. One implementation of this method, predictor-corrector, is described in detail in Hughes [19] and is presented herein. The displacement, u, and the velocity, $\ddot{u}$ at the next time-step can be found with (2.77) and (2.78), respectively.

$$u_{i+1} = u_i + \Delta t \dot{u}_i + \frac{\Delta t^2}{2}[(1-2\beta)\ddot{u}_i + 2\beta\ddot{u}_{i+1}] \tag{2.77}$$

$$\dot{u}_{i+1} = \dot{u}_i + \Delta t[(1-\gamma)\ddot{u}_i + \gamma\ddot{u}_{i+1}] \tag{2.78}$$

In both of the equations above the updated displacement and velocity are based on the previous displacement, velocity and acceleration in addition to the updated acceleration. To solve for the updated accelerations we define a predictor displacement, u_{i+1}^{p} and a predictor velocity, $\dot{u}_{i+1}^{p}$, which are found with:

$$u_{i+1}^{p} = u_i + \Delta t\dot{u}_i + \frac{\Delta t^2}{2}(1-2\beta)\ddot{u}_i \tag{2.79}$$

$$\dot{u}_{i+1}^{p} = \dot{u}_i + (1-\gamma)\Delta t\ddot{u}_i \tag{2.80}$$

The updated acceleration is then found with the load, predictor displacement, and predictor velocity at the updated time.

$$\ddot{u}_{i+1} = \frac{(p_{i+1} - c\dot{u}_{i+1}^{p} - ku_{i+1}^{p})}{(m + \gamma\Delta tc + \beta\Delta t^2 k)} \tag{2.81}$$

When the updated acceleration is known the predictor displacement and velocity can be corrected to give the updated displacement and velocity with the following equations.

$$u_{i+1} = u_{i+1}^{p} + \beta\Delta t^2\ddot{u}_{i+1} \tag{2.82}$$

$$\dot{u}_{i+1} = \dot{u}_{i+1}^{p} + \gamma\Delta t\ddot{u}_{i+1} \tag{2.83}$$

When the central difference method is used β=0 and the predictor displacement is equal to the corrected displacement and the term $\beta\Delta t^2 k$ in equation (2.81) goes to zero. The equations shown above are for the case when there is a mass with a spring and a damper.

For the case when the spring is replaced by a nonlinear resistance function the term ku_{i+1}^{p} in equation (2.81) is replaced with $R_{i+1}(u_{i+1}^{p})$.

2.7 SDOF ANALYSIS PROGRAM

A quasi-SDOF analysis code was written to analyze the response of reinforced concrete and reinforced masonry walls. This code uses the concepts describe in this section to predict displacement and shear forces to pressure pulse created by HE and VCE detonations in addition to those generated by the blast simulator. This program was written in MATLAB and uses the explicit form of the central difference method to solve the equation of motion as described in section 2.6.7. The parameters required by the program are as follows:

- Load
    - Pressure pulse defined using up to 10 points
    - BG velocity which also requires weight, programmer dimensions and programmer type
- Specimen geometry and boundary conditions which are used to calculated mass and shape functions
- Resistance function which is defined by user or calculated automatically using functions that rely on moment curvature analysis

Chapter 3 will discuss an addition to the SDOF model to simulate the impact of the blast generators with a wall. Included in the description is a model of the programmers and was validated with test data. The SDOF program with the blast generators is used in later chapters to validate the models for the different walls.

Automatic generation of the resistance function is described in detail in subsequent chapters. Chapter 4 describes the resistance functions that can be determined for grouted masonry walls and grouted masonry walls with CFRP retrofits. Chapter 5 describes how resistance functions are generated for reinforced concrete walls. Chapter 5 also describe a multi degree-of-freedom model based on standard concepts of SDOF analysis that was developed to predict the response of reinforced concrete walls with blast mitigating frangible panels. In each of these chapters are sections describing the validation of the program with data from blast simulator experiments on the different types of walls.

2.8 BASIC PROPERTIES OF CONCRETE

In this dissertation reinforced concrete and concrete masonry walls subject to simulated blast loads are discussed. This section proved a background on the basic properties of concrete. Figure 2.33 is an illustration of the behavior of concrete under uniaxial compressive stress. Concrete behavior under uniaxial compressive load is linear at strains that range from zero to about 0.001. The modules of elasticity for normal weight concrete, with a density of 145 lbs/ft^3 is given by the empirical formula provided by ACI-318 [20] is

$$E_c = 57,000\sqrt{f'_c} \text{ (psi)} \tag{2.84}$$

where *f'c* is the uniaxial strength of the concrete in psi. After the linear portion of the stress-strain relation the concrete has a hardening behavior up to its peak stress which occurs at a strain of about 0.002. Increased strain after the peak stress results in a decrease of stress until failure which typically occurs at a strain near 0.003. This softening behavior of the concrete is dependent on the axial strength of the concrete; the slope of the softening portion of the curve tends to be flatter than the ascending portion for moderate strength concrete and when the strength increases the slope becomes steeper.

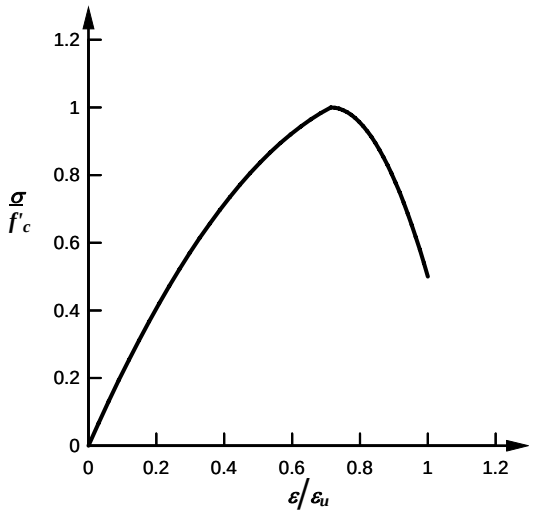

Figure 2.33: Concrete stress-strain relation under uniaxial compressive stress

In uniaxial tension concrete behaves linear up to its peak tensile stress which occurs at a strain equal to about 0.0001. Increased strain from this point result in a decay in stress until cracking. The uniaxial tensile behavior is often displayed by a curve that

plots stress versus crack width. The area under this curve is referred to as the fracture energy, G_f. This is the energy required to create a unit crack.

The tensile strength of concrete is often estimated by the modulus of ruptures, f_r', which is determined from a split-cylinder test. The relation between uniaxial compression strength and modulus of rupture is usually taken as

$$f_r' = 7.5\sqrt{f_c'} \tag{2.85}$$

The walls studied in this dissertation undergo one-way bending which subjects the concrete to a state of biaxial stress for moment-shear interaction. The strength, failure modes, and stress strain relations are all affected by biaxial states of stress. The strength of a concrete specimen will vary when subject to biaxial loading as shown in Figure 2.34. The figure includes the failure modes that occur when concrete is subject to uniaxial compression stress, uniaxial tension stress, and biaxial compression-tension stress. The modes shown in the figure demonstrate that failure occurs when the concrete fractures in tension with the cracked plane in the normal direction of the maximum tensile stress or strain.

The maximum strength of concrete in biaxial compression-compression will increase according to curve *C-D* in Figure 2.34 [21]. In this stress state the maximum tensile strain in the direction opposite of the plane that is loaded will also increase and so will its ductility. In a tension-tension biaxial stress state, shown in the plot by the curve designated *A-B*, the maximum strength will remain about the same as for uniaxial stress. The maximum principle tensile strain will also be similar at 0.0008. In a biaxial

compression-tension state of stress, the compressive strength decreases as the tensile stress increases, this is displayed as curve *B-C* in Figure 2.34. Also in biaxial compression-tension the magnitude of both the principal compressive and tensile strain decreases as the tensile stress increases.

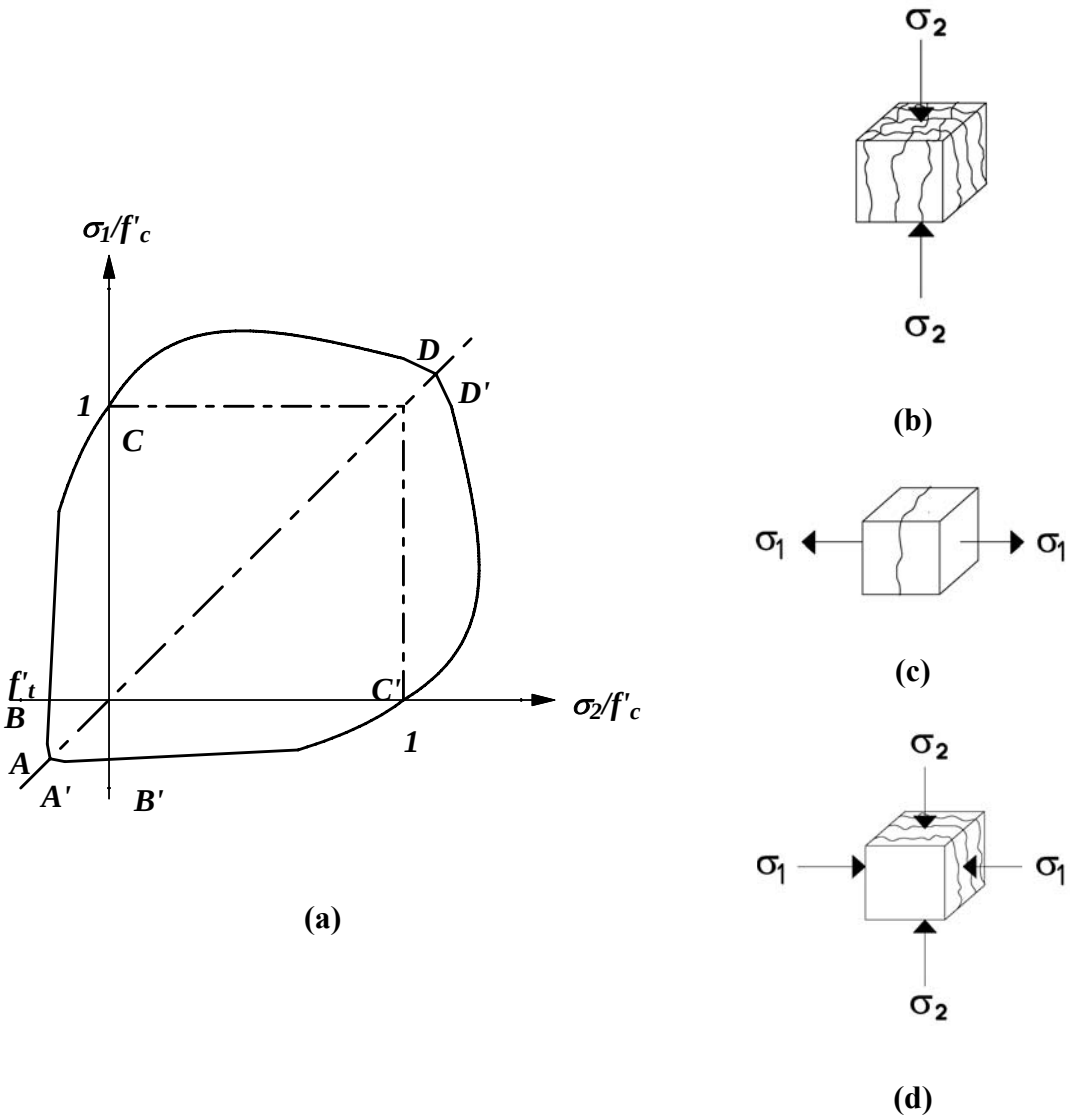

Figure 2.34: Strength and failure modes for concrete load with biaxial stresses; (a) Strength of concrete under biaxial stress; (b) uniaxial compression failure; (c) uniaxial tension failure; (d) biaxial compression failure

Uniaxial and biaxial tests also demonstrate that concrete will increase in volume as the stress reaches its maximum strength. Figure 2.35 is a schematic that shows the volume increase with the increase in stress. In the figure volume reduction corresponds to positive values and volume expansion corresponds to negative values. The increase in volume is called dilatancy and it is attributed to the aggregate interlock where the aggregate pushes the crack apart when the fractured surfaces slide over each other. The limit on dilatancy occurs when the crack width is greater than the thickness of the aggregate in the crack.

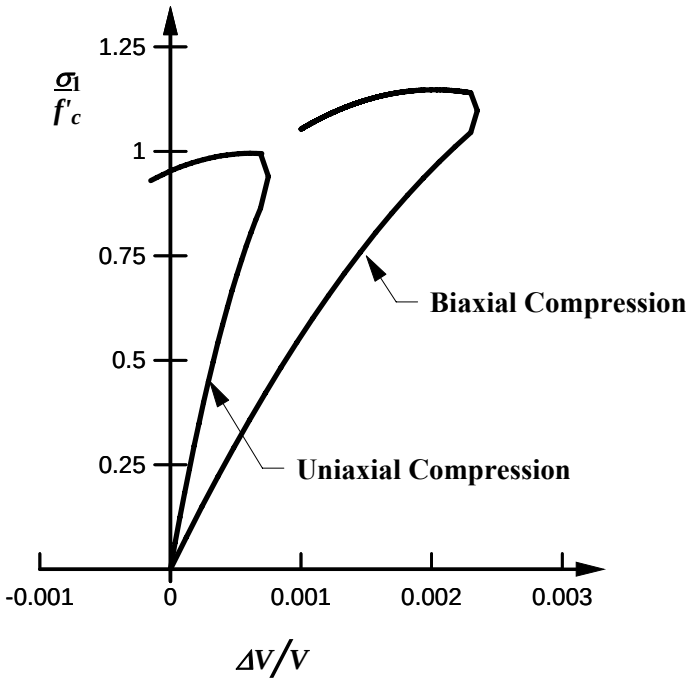

Figure 2.35: Concrete volume change under biaxial compression

Concrete under triaxial compression loading will exhibit increased strength and ductility. The behavior of concrete depending on the amount of confining pressure can

vary from brittle to plastic-hardening. According to Chen [21], the confining pressures reduce bond cracking and shift the failure mode from cleavage to crushing of the cement paste. Stress-strain data taken from [22] was used to construct stress-strain relations for concrete at various levels of confinement that are displayed in Figure 2.36. In this figure, σ_3 corresponds to the radial stress applied to a cylinder. For the levels of confinement considered the increase in strength exceeds five times the unconfined strength and the failure strain increases by more than a factor of eight.

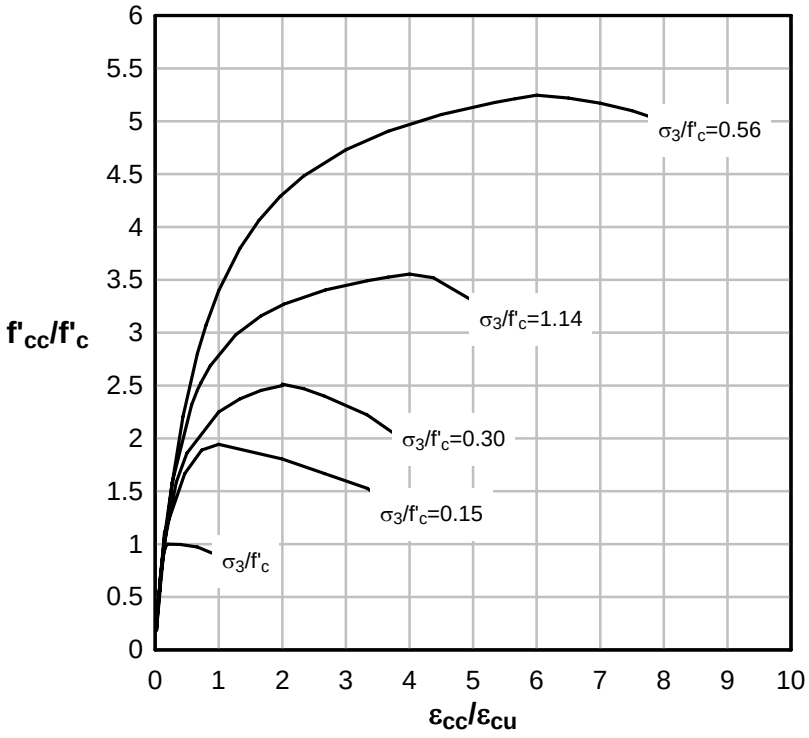

Figure 2.36: Effect of confinement on concrete stress-strain relation

Under pure hydrostatic compression loading the concrete will have a nonlinear behavior as shown in Figure 2.37, which was constructed using data taken from [21]. The concrete will initially load according to the elastic bulk modulus. The curve will

soften when the pores in the material begin to collapse. When all of the pores have consolidated the material will stiffen and slope of the curve will begin to increase. The material will then unload according to an unloading bulk modulus as shown in the figure.

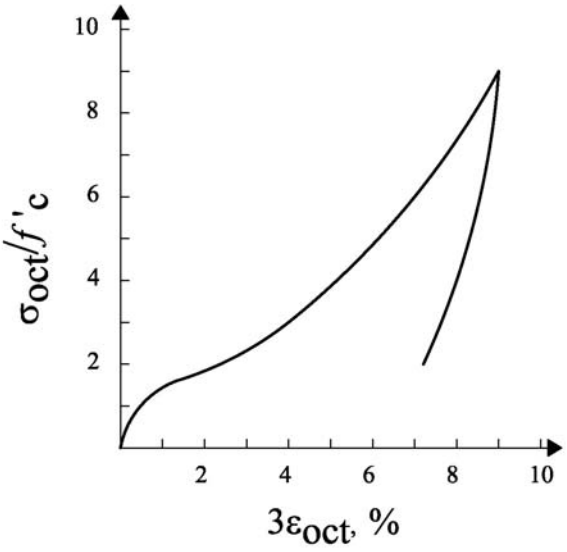

Figure 2.37: Concrete under compressive hydrostatic load

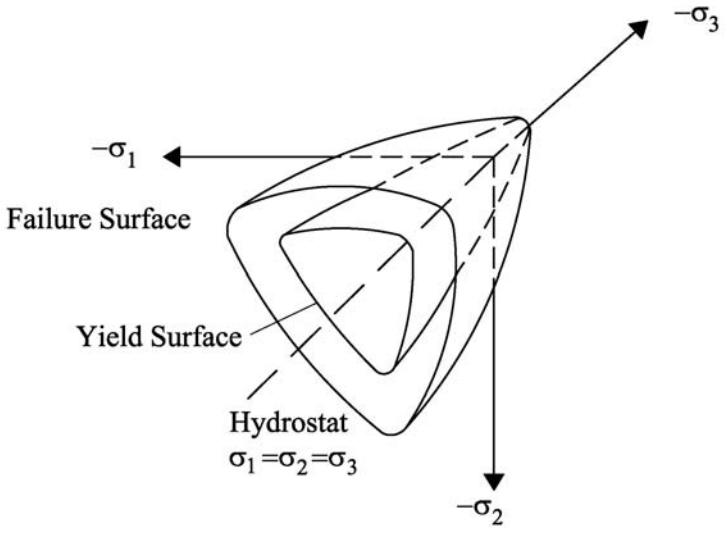

Figure 2.38: Failure Surface in principal stress space

A failure surface for concrete in three dimensional stress space is depicted in Figure 2.38. This failure surface is described in detail in Chen [21] The shape of the surface in the plane of the deviatoric stresses is triangular with convex corners at lower hydrostatic pressures and at higher hydrostatic pressures the shape becomes more circular. The hydrostat is the line in stress space where the three principal stresses are equal. The hydrostatic component of the stress corresponds to pure hydrostatic pressures on the body. The deviatoric components of the stress are the stresses that correspond to shear distortions. When the deviatoric plane intersects the origin, the hydrostatic pressure will be zero and any point in the plane, other that the origin represents a state of pure shear stress.

The William and Warnke [23] concrete model defines the failure surface with the three stress invariants in the form of $f(I_1, J_2, \theta)$. The first invariant of the principle stress, I_1, defines the location of the deviatoric plane along the hydrostat. The second invariant of the deviatoric stress, J_2, is used to determine the distance from the hydrostat to the failure surface. The third invariant called the angle of similarity, θ, is used to define the shape of the failure surface in the deviatoric plane. Figure 2.39 is a schematic of the failure surface in the deviatoric plane.

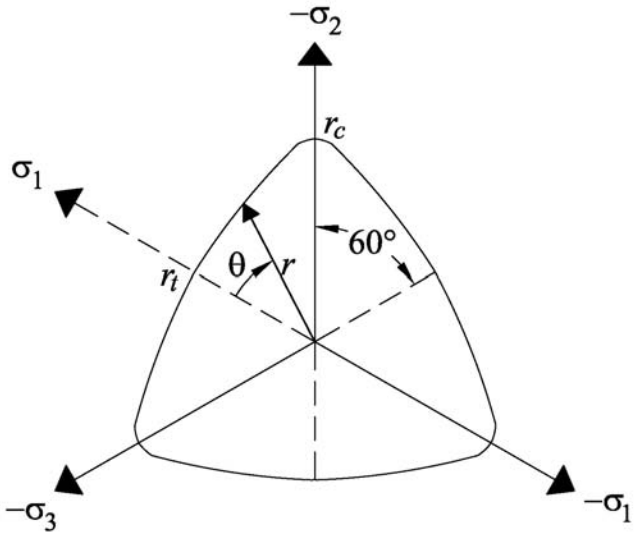

Figure 2.39: Failure surface in deviatoric plane

The angle, θ, can be found from J_2 and J_3 with

$$\cos 3\theta = \frac{3\sqrt{3}}{2}\frac{J_3}{J_2^{3/2}} \tag{2.86}$$

The surface is smooth and convex with a continuous derivative everywhere. The surface in the deviatoric plane is symmetric about three planes and only needs to be defined from $0° \leq \theta \leq 60°$. The shape of the surface in the deviatoric plane is triangular at low hydrostatic pressures and more circular as that pressure increases. The meridians of the failure surface are defined by second order parabolas which are also convex. The parabolic shape of the meridians allows the failure surface to change with increased hydrostatic pressure. The meridian at $\theta = 0°$ is called the compressive meridian and corresponds to a test condition in which a concrete cylinder is loaded with hydrostatic pressure in the radial direction and a smaller force is applied in the axial direction. The

tensile meridian at $\theta = 60°$ is when the hydrostatic pressure is applied in the radial direction and a larger force is applied in the axial direction.

The properties of concrete are also sensitive to strain rate. The strength and strain at failure both increase with an increase in strain rate. The fracture energy, G_f, in tension is also thought to increase with increase in strain rate. The strain rate behavior is attributed to several causes including the limit on the rate of crack propagation, water in the voids and dynamic confinement from lateral inertia. The strain rate effects on concrete strength are different in tension and compression; in compression the strength can more than double, while in tension the strength can increase by more than six times. The modulus of elasticity is not significantly affected by strain rate. This is because the modulus is measured at low stress levels where there is no cracking and as previously stated strain rates are in part due to limits of crack propagation. A reasonable range of strain rates for the levels of blast loading considered in this dissertation is zero to 1000 sec^{-1}.

2.9 CONCRETE MATERIAL MODEL

Finite element (FE) analyses of several concrete and concrete masonry walls were conducted as part of this dissertation. The FE analysis was performed with LS-DYNA [24] and the concrete and masonry was modeled with *MAT_72 release 3, otherwise known as the K&C concrete model. This model was chosen because it includes several features that help it capture the 1D, 2D, and 3D behaviors described above including strain rate effects. The K&C concrete model is a plasticity model that decouples the volumetric and deviatoric parts of the concrete response. The volumetric part is treated

with a tabulated equation of state (EOS) that gives the pressure as a function of volumetric strain. The deviatoric response is then defined by a movable surface that is found between three independent failure surfaces that correspond to the limit of elastic behavior, $\Delta\sigma_y$, the maximum concrete strength, $\Delta\sigma_m$, and the residual concrete strength, $\Delta\sigma_r$. These three failure surfaces are defined by parabolic equations shown below:

$$\Delta\sigma_y = a_{0y} + \frac{p}{a_{1y} + a_{2y}p} \tag{2.87}$$

$$\Delta\sigma_m = a_{0m} + \frac{p}{a_{1m} + a_{2m}p} \tag{2.88}$$

$$\Delta\sigma_r = \frac{p}{a_{1f} + a_{2f}p} \tag{2.89}$$

$$p = -\frac{\sigma_1 + \sigma_2 + \sigma_3}{3} \tag{2.90}$$

where σ_1, σ_2, and σ_3 are the principal stresses and p is the pressure and a_{0y}, a_{1y}, a_{2y}, a_{0m}, a_{1m}, a_{2m}, a_{1f}, and a_{2f} are constants that have been determined with experimental data. The convention used here is that stresses are positive in tension and pressure is positive in compression. The failure surface in the deviatoric plane described in [25] is signified by $\Delta\sigma$ which is related to the second invariant of the deviatoric stress by:

$$\Delta\sigma = \sqrt{3J_2} \tag{2.91}$$

A current failures surface is found by interpolating between the three independent surfaces. When concrete reaches the yield failure surface, $\Delta\sigma_y$, and has not yet reached the maximum failure surface, $\Delta\sigma_m$, the current failure surface is defined by linear interpolations between these two surfaces. The slope of the linear interpolation is governed by a hardening parameter that varies between 0 to 1. Once the maximum surface is reached the failure surface is then interpolated between the maximum and residual surfaces with the slope of the interpolation given by a softening parameter softening parameter that varies between 1 and 0. The failure surfaces are depicted in Figure 2.40 (a) with a uniaxial stress path. This figure demonstrates the path of the current failure surface. Figure 2.40 (b) is a plot of the uniaxial stress-strain behavior of the concrete with different stress points associated with the points along the stress path displayed in Figure 2.40 (a).

The hardening and softening parameters are dependent on the accumulated effective plastic strain parameter as denoted as a damage parameter. This damage parameter is related to the shear strain and determined from an increment of effective plastic strain, $d\bar{\varepsilon}^p$, is defined as

$$d\bar{\varepsilon}^p = \sqrt{(2/3)\varepsilon_{ij}^p \varepsilon_{ij}^p} \tag{2.92}$$

where ε_{ij}^p is the plastic strain tensor.

The concrete model accounts for volumetric damage for the case when the concrete is subject to hydrostatic tensile loads. Without this consideration the pressure

could decrease to the tensile failure strength and the material would not fail because in this state of stress there is no deviatoric component.

The failure surface is also dependent on the third invariant, θ, which allows the failure surface in deviatoric plane to have the triangular shape that was described in earlier sections. This gives the model the capability of simulating the differences in compressive and tensile behavior. The curves given in (2.87), (2.89), and (2.89) define the compressive meridians of the surface and θ would be used to find the tensile meridian of the surface and the surface between the compressive and tensile meridians.

The concrete model has a pressure cutoff that corresponds to the maximum tensile strength determined from triaxial tensile tests. When the cutoff is reached the concrete has cracked and cannot resist any pressure. Upon failure the model reduces the failure surface from the maximum to the residual and resets the cutoff to zero. The reduction rate of the failure surface and the cutoff criteria were calibrated so that the model matches fracture energies found from uniaxial tensile tests and hydrostatic triaxial tensile tests. The fracture energy in the model is normalized by the element size in an attempt to make the model mesh objective. Shear dilation is modeled using a partially associated flow rule. Strain rate effects are accounted for in the model by scaling the surfaces along radial paths in the plane of $\Delta\sigma$ and pressure. Specific equations relating strength to strain rate are given in Chapter 4 for concrete masonry and Chapter 5 for reinforced concrete.

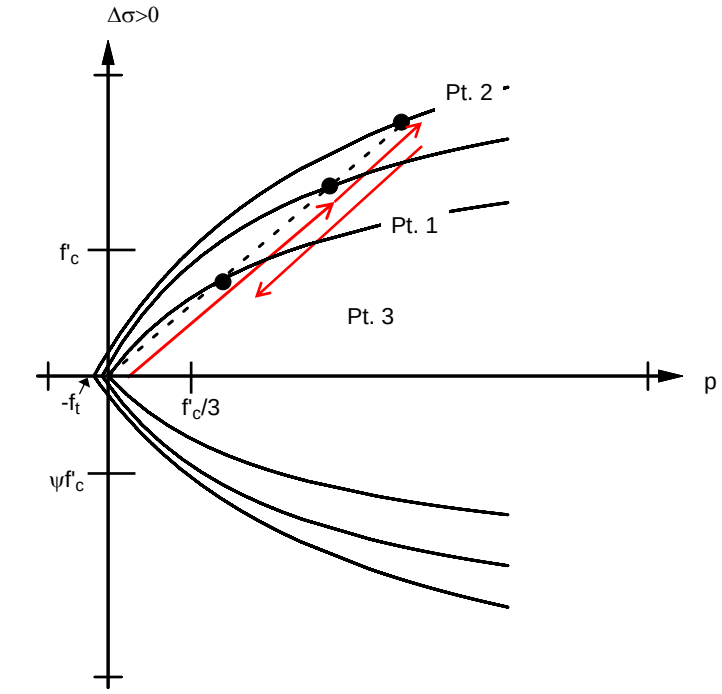

(a)

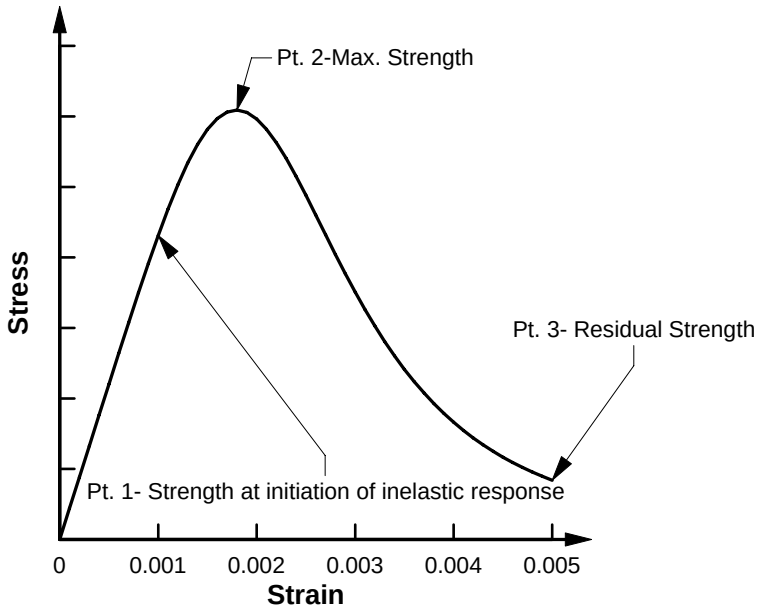

(b)

Figure 2.40: Failure surfaces for concrete model; (a) failure surfaces and uniaxial stress path; (b) uniaxial stress strain response

3 THE BLAST SIMULATOR: EXPERIMENTAL AND NUMERICAL METHODS

3.1 THE BLAST SIMULATOR

The UCSD blast simulator facility incorporates an array of high speed nitrogen/oil driven actuators to apply blast like loads to full scale structural components. Typically in an HE blast event, the loading is in the impulsive regime meaning that all of the energy is deposited into the structures in a short duration of time relative to the time that it takes the structure to respond, i.e. the load imparts an initial velocity to the structure. The blast simulator actuators deliver impulsive loads to the structure through an impact mass that is accelerated to a specified impact velocity. Upon impact the impact mass transfers momentum to the structure which is equivalent to the impulse that would be imparted in an actual blast.

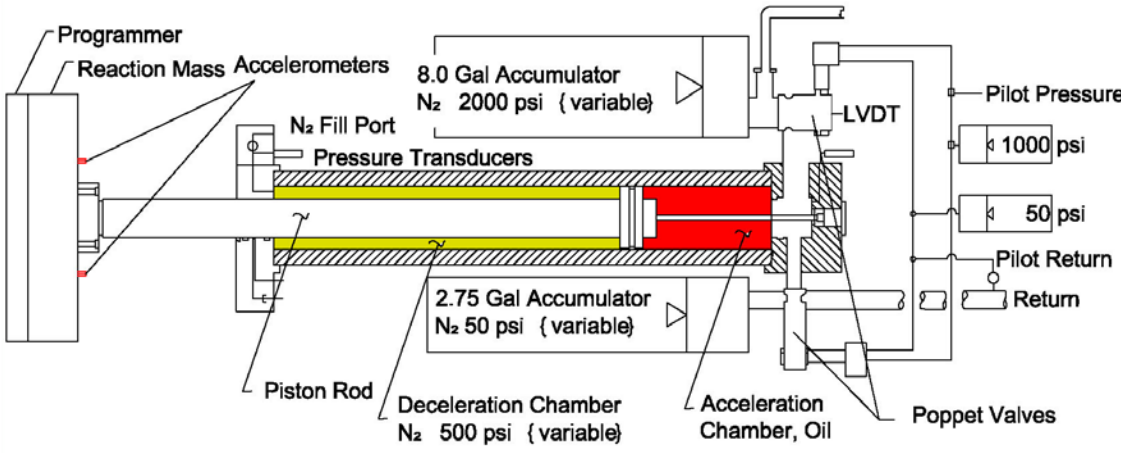

Figure 3.1: BG Schematic

The actuators used to generate the impulsive load are called blast generators (BGs). A schematic of a blast generator is provided in Figure 3.1. The BG consists of

three cylindrical oil/nitrogen accumulators, two servo poppet valves, a piston rod, and an impact module, which includes an instrumentation package, a rectangular reaction mass and a polyurethane programmer. The impact mass used on the BG is attached to the piston rod with “break away” bolts. These bolts have a reduced cross-section that was designed such that the bolts fail in tension before a significant torque from a rotated plate can be transferred to the piston rod, thus preventing it from being damaged. The BG masses are also guided by a support system with guiderails. The BGs and wall impact masses in the support system are shown in Figure 3.2.

Figure 3.2: BGs with wall impact masses and programmers

The BG operates in both closed loop and open loop control. Currently the closed loop control is used to position and exercise the actuators prior to a blast test, which

includes cycling of the impact mass and rod for warm up and tuning and balancing the servo valves. Temposonics® displacement transducers provide the displacement feed back on the location of the impact rod and mass during closed loop control. These transducers run parallel with the actuator and measure the location of the impact mass with a horseshoe shaped magnet which straddles an aluminum tube with a rod in the middle that detects the location of the magnet. The feedback for the servo valves during closed loop control is provided by linear variable displacement transducers (LVDT).

During the actual blast simulator test event the BGs are typically run in open loop control in which a specified impact velocity is achieved through the initial position of the impact mass and rod, the timing and magnitude of the poppet valve openings, and the initial pressures in the different accumulators. There are three accumulators that are used to drive the BGs during a simulated blast event; the supply accumulator, the main actuator, and the return accumulator. The accumulators are cylindrical steel tubes that contain volumes of both nitrogen and oil which are separated by a steel piston. In the main actuator the piston has a steel rod that attaches to the impact module. The flow of oil between the supply accumulator and the main actuator is controlled by the supply valve. In a blast test the supply accumulator is charged with nitrogen to an initial pressure typically ranging from 2000-3000 psi. Hydraulic oil is then pumped into the supply accumulator through the supply line connected to the facility accumulators. At this moment the supply valve to the main actuator is closed preventing flow into that accumulator. The oil pressure is always greater than the initial nitrogen pressure so that the nitrogen is compressed giving it potential energy. Once the command is given, the

supply valve opens to the specified magnitude which creates a pressure differential between the oil in the supply accumulator and the main actuator. The hydraulic oil then is driven into the acceleration chamber of the main accumulator where it applies a pressure on the piston rod accelerating it in the direction of the specimen. The main actuator also has nitrogen on the opposite side of the piston in the deceleration chamber. This pressure works against the oil during the acceleration, but its effect on the velocity of the impact module is small compared to the oil in the acceleration chamber.

Typically, it is desired that the mass and rod reach the maximum velocity and maintain that velocity without accelerating or decelerating immediately prior to impact. Upon impact the impact module delivers an impulse to the specimen where the magnitude is governed by the conservation of linear momentum and conservation of energy. After it delivers the impulse to the specimen the impact module has a residual velocity where the direction is dependent on the effective coefficient of restitution and the ratio of the module mass to the specimen's effective mass. At the time of impact the supply valve begins to close and the valve between the return accumulator and the main actuator begins to open. This allows results in a drop in pressure on the impact rod and the hydraulic oil begins to flow out of the main accumulator. The nitrogen in the deceleration chamber is compressed at impact and it begins to force the rod and impact module away from the specimen when the supply valve shuts and the return valve opens.

The supply valve immediately closes from the full command signal to an anti-cavitation opening at impact. The rate at which the valve closes from the anti-cavitation

opening to fully closed is more gradual and lasts about 100 msec. This is done to prevent cavitation from occurring when the supply valve shuts and the return valve opens.

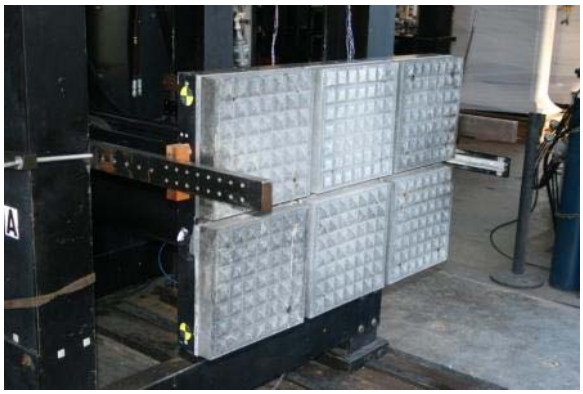

Figure 3.3: Wall programmer

The shape of the pressure pulse applied to the target specimen during the impact with the BG is controlled by polyurethane programmer pads. These pads exhibit both geometric and material nonlinearities. The programmers have a pyramid texture at the impact interface, as shown in Figure 3.3, which are a source of geometric nonlinearity. The programmer is made from a urethane material that exhibits nonlinear viscoelastic behavior. It has been observed in blast simulator experiments that the programmer dissipates energy during the impact which results in a collision that is somewhere between elastic and plastic. A coefficient of restitution equal to unity corresponds to an elastic collision and a coefficient of restitution equal to zero corresponds to a plastic collisions. In an elastic collision the total kinetic energy of two bodies prior to impact is equal to the kinetic energy in the bodies after impact. In an inelastic collision the kinetic energy is not conserved and for a plastic collision the bodies will “stick” together after contact.

Values of the coefficient of restitution observed in blast simulator tests have varied between about 0.6 and 0.2 for the different types of wall specimens. It is assumed that the source of energy dissipation that results in these values is the programmer, but additional sources could be friction at the supports, excitation of the supports, excitation of flexural waves in the impact mass, rigid body rotation of the impact mass associated with the failure of the break away bolts, etc.

Numerical efforts to simulate the blast simulator tests require a model for the programmer. A later section of this chapter will describe a one-dimensional model used in SDOF-type analyses and a multi degree-of-freedom model used with FE analyses. These models have been compared to small scale dynamic test data on the programmer and have been implemented in SDOF and FE analysis to simulate the loads applied by the BGs.

3.2 LABORATORY FACILITY

The blast generators used in the blast simulator tests are only one component of a large infrastructure that comprises the laboratory facility. Figure 3.4 is a three dimensional drawing of the lab with a test setup for CMU walls with CFRP retrofits that are discussed in Chapter 4. The figure illustrates that the BGs are reacted with a fixed reaction wall. The support structure for the BGs is shown in Figure 3.2. This reaction wall is 12 ft 3 in. tall by 5 ft 9 in. deep by 15 ft wide and is post-tensioned to the reaction floor. The reaction floor is 35 ft 6 in. long by 15 ft wide by 4 ft. thick and rests on base isolators that react against a large concrete tube which serves as the foundation. A movable reaction wall that is 18 ft tall by 8 ft deep by 15 ft wide is also post-tensioned to

the reaction floor. The movable reaction wall was match cast and can be disassembled if required for a test program. The specimen in the tests is reacted against the reaction floor and the movable reaction wall. Typically in wall testing the top of the wall is reacted in bearing against a RC slab while the base rests on a footing that is post-tensioned to the floor. Spacer blocks between the footing and the back reaction wall are also used for additional shear resistance.

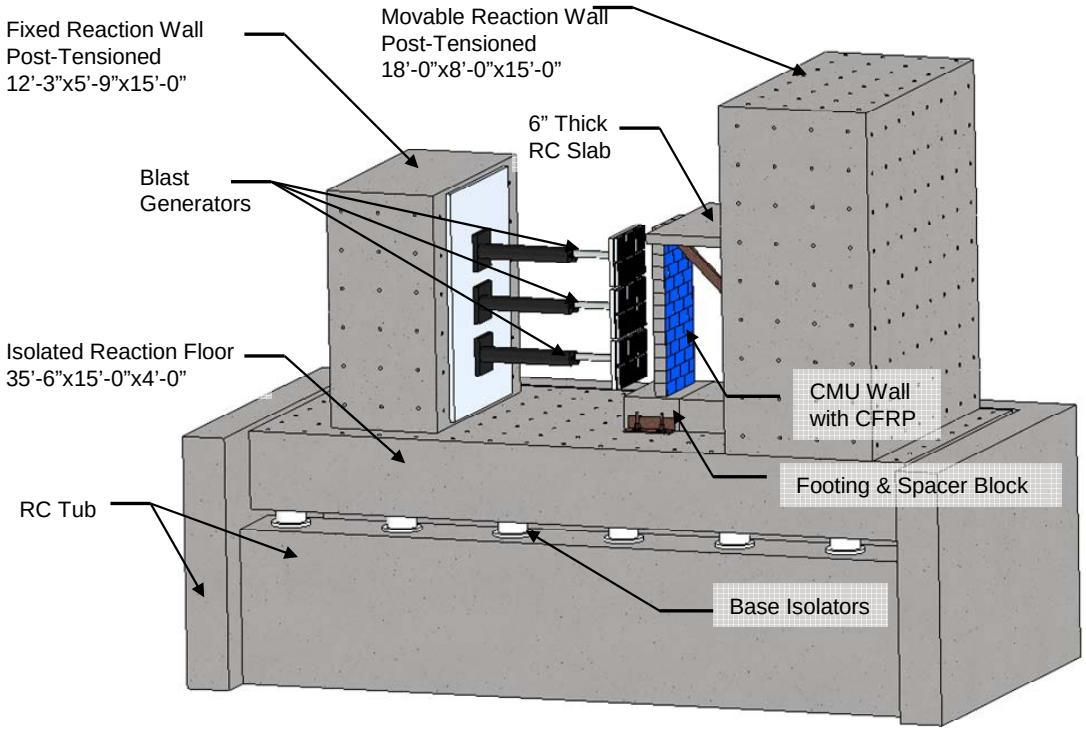

Figure 3.4: Overview of laboratory facility

The schematic shown in Figure 3.4 is for a blast simulator test run on the west side of the fixed reaction wall. The blast lab also has the capability of testing on the south side of the reaction wall. In this configuration the BGs are still reacted against the fixed wall and are isolated from the foundation. The specimen, however, is reacted with a reaction floor that was cast monolithically with the foundation. The specimens tested

off this side need to have a relative low resistance so that large loads that could cause significant damage are not transferred to the foundation. All of the walls tested for the research covered in this dissertation were tested off the west side of the fixed reaction wall.

3.3 IMPULSE CALCULATION

Impulse is the metric that is used in the blast simulator tests to quantify the loads that are applied by the BGs to the specimen. The SDOF and FE simulations require an accurate measure of the impulse in order to validate the numerical models. Therefore, two methods were employed to measure the impulse in each test; the first is to integrate scaled accelerations recorded by the accelerometers on the BG impact masses; the second was to differentiate a scaled displacement time history calculated by tracking software analysis on the video captured by high speed cameras.

The first method integrates scaled acceleration records of the BGs during the impact event. For this purpose an array of accelerometers was placed on each BG and an average of the accelerations signals was used to determine the impulse for each impact module. The records were scaled by the mass and normalized by the impact area to give the impulse in units of psi-msec. It should be noted that the impulse divided by the area is typically called the specific impulse; the units associated with impulse are lb-msec. In the remainder of the dissertation the term impulse will be used to denote the specific impulse. The impact area used to normalize the records was determined using a tributary area of the wall associated with each BG impact. The impulse calculation by the accelerations is given by:

$$i_s = \frac{1}{n_a}\sum_{i=1}^{n_a}\int \frac{m_i a_i(t)}{area_i}dt \tag{3.1}$$

where, n_a is the number of accelerometers, m_i is the tributary mass of the ith accelerometer, $area_i$ is the tributary of the wall, and $a_i(t)$ is the acceleration time history of the ith accelerometer.

Figure 3.5 shows the average acceleration signal for a BG for the test series on the CMU walls with CFRP retrofits. Included on the plot is a time history of the specific impulse. The figure shows that the impulse increases to a peak around 274 psi-msec and then decreases after 34 msec. The decrease in impulse occurs after the impact and is associated with change in the mass velocity due to the deceleration pressures from the accumulator. The BGs are unable to apply a tension load to the specimen.

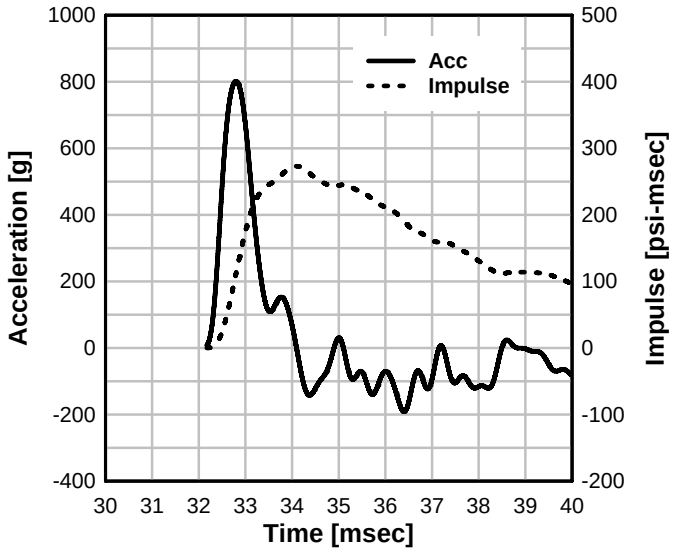

Figure 3.5: Acceleration and impulse time history

The other method used to determine the impulse delivered by the BGs was differentiation of the displacement record generated with the *Track Eye Motion Analysis (TEMA)* software package from Image Systems. The velocity time history was scaled by the mass and impact area to calculate the change in BG velocity during impact. With the change in velocity the specific impulse was calculated with

$$i_s = \frac{m_i \Delta v_i}{area_i} \tag{3.2}$$

where, m_i is the mass of the ith BG, $area_i$ is the tributary area of the ith BG, Δv_i is the change in velocity for the ith BG.

Figure 3.6 is a velocity time history plot of a single BG. Displayed in the plot are two horizontal lines that marked the velocity of the impact module before and after impact. The plot shows the final velocity oscillates near zero velocity before the module decelerates and begins to retract. The final velocity was determined by taking the average velocity over the first two oscillations. This method was used consistently for all tests.

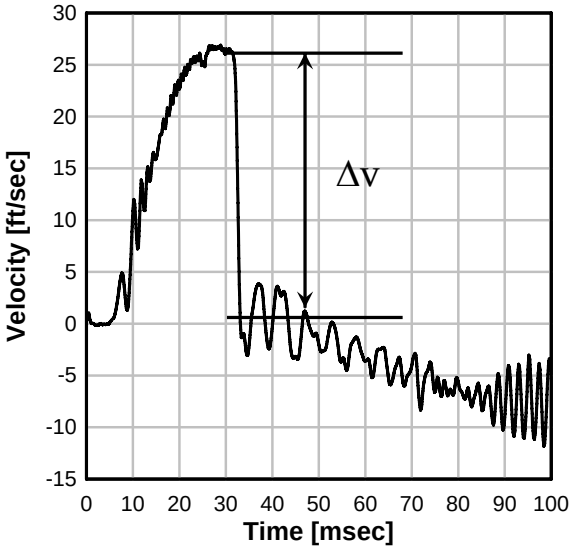

Figure 3.6: Velocity time history of BG at impact

3.4 PROGRAMMER

3.4.1 INTRODUCTION

Ballistic impact tests were carried out with the blast simulator to quantify energy losses in the BG programmer materials that were observed during structural component tests. Two types of programmers, column and wall, were tested in the series. The BG programmer is a polyurethane pad on the impacting face of the BG flyer plate. Its purpose is to soften the initiation of the impact to limit high frequency response. The geometric and material characteristics of the programmer were designed to produce a pressure loading history that had similar period, peak, and impulse to those observed for live explosives. The nonlinearities also resulted in an inelastic collision between the BGs and the specimen. As a result the ballistic impact tests were performed to obtain data on

the coefficient of restitution over a large range of velocities that could be used to validate a model of the programmer. A detailed description of the ballistic impact tests and the results are given in [26].

The data generated in the tests were used by Rodriguez et al. [27] to validate a one-dimensional model for the different programmers which can be implemented into a SDOF analysis. This section of the chapter will briefly summarize the results of the second series of ballistic impact tests of the wall programmer. The results from these tests will then be compared to analyses performed with the proposed material model. This will be followed by a section that demonstrates the ability of the model to predict the impulse delivered in full scale tests through comparisons with the data from all of the wall tests series. The final section will discuss a material model used in FE simulations of the blast simulator tests. This section will include a comparison of FE simulations with the model and the results of the ballistic impact tests.

3.4.2 BALLISTIC IMPACT TESTS

The blast simulator is capable of testing different types of structural components, including columns and walls. These two types of test specimens require different BG impact plates and programmers. The material and geometric properties of programmers that were fabricated for the column and wall impact masses are different and thus dynamic material tests were required to characterize the behavior of each. Two series of tests were performed for each programmer material. In the first series, the impact mass remained attached to the BG piston rod when it collided with a target mass. In the second series, the impact mass was launched by the BG with a push plate; it then collided with

the target mass. Rodriquez et al. [27] only used the results from the second test series to validate the proposed model because in that test configuration the effects of the deceleration pressure on the impact were negated with the flyer plate test setup. Therefore, in this section only a brief discussion of the second test series is included. Furthermore, since this dissertation only pertains to wall testing with the blast simulator, only the wall programmer tests will be discussed. For further information regarding the first ballistic impact test series the reader is directed to [26].

3.4.3 COEFFICIENT OF RESTITUTION CALCULATION

The coefficient of restitution (COR) was calculated in each test of [26] to quantify the amount of energy that is dissipated by the programmer during the impact between the BGs and a specimen. The coefficient of restitution is calculated with the following equation:

$$COR = \frac{v_{22} - v_{12}}{v_{11} - v_{21}} \tag{3.3}$$

where v_{11} is the velocity of the impact mass before the collision, v_{12} is the velocity of the impact mass after the collision, v_{21} is the velocity of the target mass before the collision, v_{22} is the velocity of the target mass after the collision.

3.4.4 TEST SETUP

The dimensions of the wall programmer used in the ballistic impact tests were 14.31 in. by 15.25 in. by 2.37 inches. The programmer had a total of 49 2 in. by 2 in. by 0.37 in. pyramids that function to dampen out high frequency noise during impact. The

programmers were bonded to 0.5 in. thick aluminum backing plates with an epoxy adhesive. This assembly was then bolted to a 3 in. thick steel plate through counter-sunk holes. Figure 3.7 illustrate the wall and the aluminum backing plate.

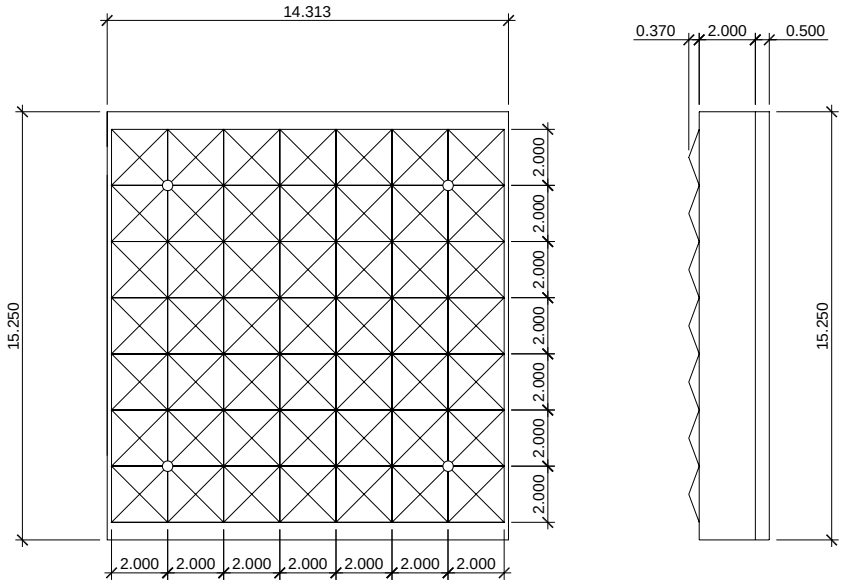

Figure 3.7: Wall Programmer

The ballistic impact test series was designed to produce a two body collision. The test consisted of a push plate, impacting plate and a target mass. The push plate was constructed of a 16 in. by 16 in. by 3/4 in. steel plate that was attached to the BG. The impact mass was a 16 in. by 16 in. by 3 in. steel plate with the programmer attached to the front face. The target mass was also a 16 in. by 16 in. by 3 in. steel plate. The weight of both the impact and target masses was 226.5 lbs.

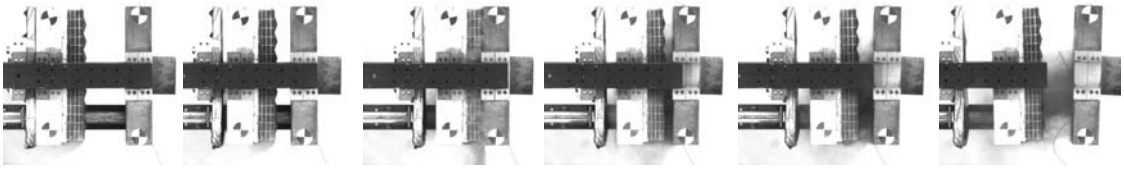

Figure 3.8: Ballistic Impact Tests II- Video Sequence

During the test the impacting plate was placed flush with the push plate at a specified distance away from the target mass. The push plate and impact mass were then accelerated to the desired velocity by the BG. Once the impact mass reached its desired velocity the push plate and BG rod began to decelerate causing the impact mass to separate and travel freely until it eventually collided with the target mass. After impact the target mass and the impacting mass both continued to move off the rail supports. Figure 3.8 shows a test with a sequence of frames taken from a black and white Phantom video. Figure 3.9 and Figure 3.10 illustrate the test setup for the second series of ballistic impact tests.

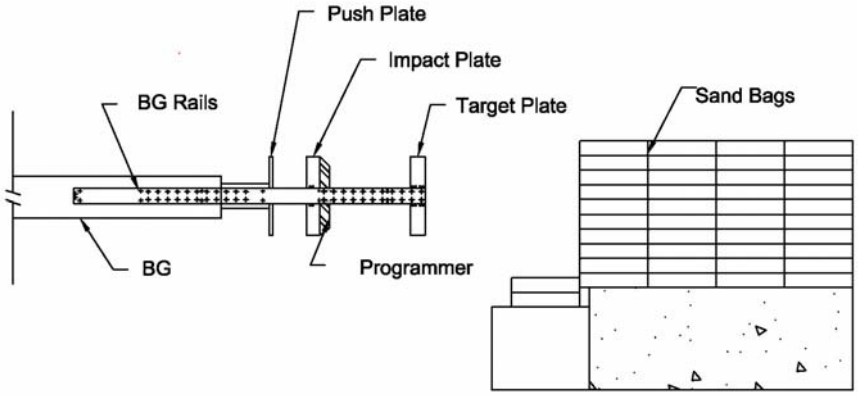

Figure 3.9: Ballistic Impact Test II- North Elevations

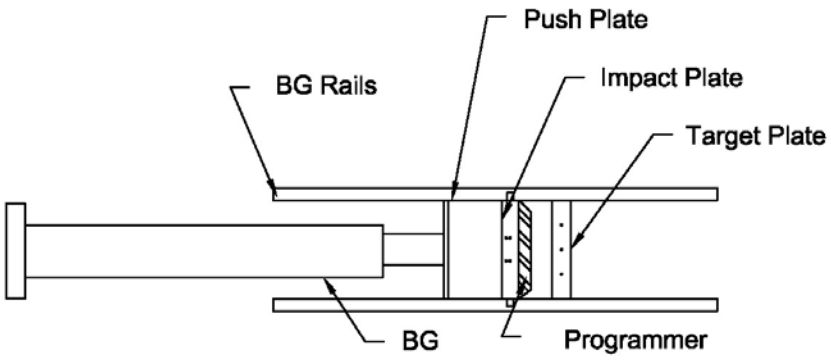

Figure 3.10: Ballistic Impact Test II- Plan View

3.4.5 INSTRUMENTATION

High speed videos were captured for each test with three Phantom cameras. One of the cameras recorded in black and white at a rate of 10000 frames per second at a resolution of 400 x 500. This camera was located on the north side of the testing structure and was equipped with a zoom lens that allows for a close-in view of the impact. The other two cameras recorded in color at a rate of 5000 frames per second at resolution of 400 x 500. One of the color cameras was also equipped with a zoom lens and focused on a close-in view of the impact from above the test using a mirror at an angle. The color other camera recorded an overall shot of the test and was not used to make measurements.

A tracking software package called *TEMA* was used to calculate displacement time histories from the Phantom camera videos. The program also generates velocity time histories through numerical differentiation of the displacement data. Two tracking

targets were placed on the side of the impact mass and target mass that was captured by the camera during the test. Two targets were also placed on the top of each plate. These targets were used with *TEMA* to determine the initial and final velocities of the impact and target plates. These velocities were then used to find the coefficient of restitution for each ballistic impact test using equation (3.3).

3.4.6 RESULTS

The second series of ballistic impact tests consisted of 21 tests on the wall programmers which were conducted from September 27 to October 3rd, 2007. The results of the second series of ballistic impact test performed on the wall programmer are summarized in Table 3.1 which lists the initial velocity of the impact plate, v_{11}, final velocity of the impact plate, v_{12}, final velocity of the target plate, v_{22} and the calculated coefficient of restitution. An example of the velocity time history generated with the Phantom video data from TEMA is plotted in Figure 3.6. Figure 3.12 is a plot of the initial velocity versus the coefficient of restitution for the wall programmer. This plot demonstrates that the coefficient of restitution decreases as the velocity increases. The plot in Figure 3.12 includes a line fit to the data with regression analysis. The correlation coefficient for the line, R^2, equals 0.96 and the average error about the line was 0.024.

Table 3.1: Ballistic Impact Test II- Wall Programmer Data

Test	Date	Target Test Velocity [ft/sec (m/sec)]	v_{11} [ft/sec]	v_{12} [ft/sec]	v_{22} [ft/sec]	COR
1	9/27/2006	32.8 (10)	33.0	7.7	29.0	0.646
2	9/27/2006	32.8 (10)	32.7	7.5	29.3	0.666
3	9/27/2006	32.8 (10)	32.4	7.6	28.1	0.631
4	9/28/2006	19.7 (6)	22.4	4.9	20.0	0.675
5	9/28/2006	19.7 (6)	22.7	5.0	19.9	0.654
6	9/28/2006	26.2 (8)	29.3	7.3	24.7	0.595
7	9/28/2006	26.2 (8)	29.6	6.5	26.1	0.663
8	9/28/2006	49.2 (15)	49.2	13.2	41.2	0.569
9	9/28/2006	49.2 (15)	46.0	11.3	39.5	0.612
10	9/28/2006	39.4 (12)	36.3	8.5	32.1	0.650
11	9/28/2006	39.4 (12)	36.6	8.8	32.1	0.638
12	9/28/2006	26.2 (8)	29.4	7.1	25.6	0.629
13	9/28/2006	39.4 (12)	36.4	9.2	30.8	0.595
14	10/3/2006	13.1 (4)	16.1	3.1	14.8	0.726
15	10/3/2006	13.1 (4)	16.3	3.5	15.1	0.716
16	10/3/2006	13.1 (4)	16.2	3.2	14.7	0.710
17	10/3/2006	19.7 (6)	23.3	4.9	20.8	0.682
18	10/3/2006	65.6 (20)	63.2	16.6	51.6	0.552
19	10/3/2006	65.6 (20)	63.2	16.8	51.4	0.547
20	10/3/2006	98.4 (30)	88.8	30.6	65.5	0.393
21	10/3/2006	98.4 (30)	87.1	27.3	67.0	0.457

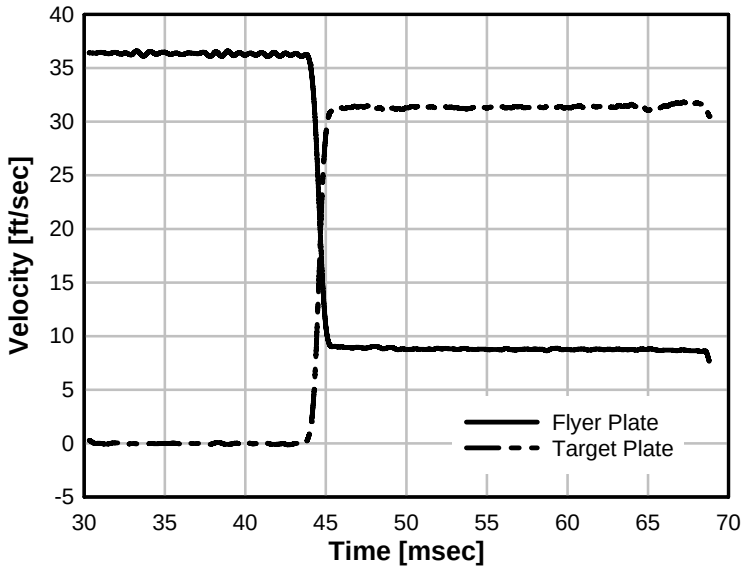

Figure 3.11: Velocity time history for Ballistic Impact Test 11

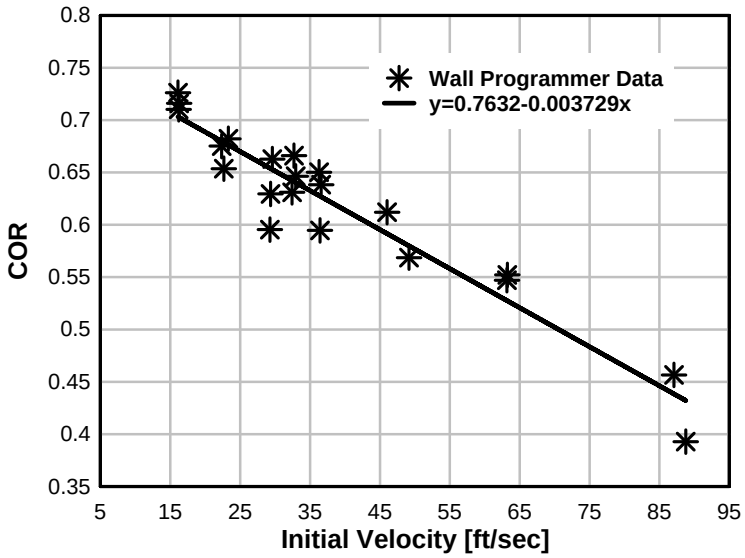

Figure 3.12: Impact velocity vs. COR for wall programmer

3.4.7 SDOF PROGRAMMER MODEL

The behavior of the programmer was simulated [27] with a mathematical model that relates force to deformation and deformation rate. The actual behavior of the programmer is not fully understood and a complete model that fully captures the behavior is outside the scope of the research for this dissertation. Research regarding these topics can be fount in [28], [29], and [30].

Numerical studies in [29] and [30] have shown that programmer behavior is influenced by the material properties of the urethane, geometry of the pads, and the boundary conditions between the programmer and specimen. These effects were lumped together by [27] in a one-dimensional engineering model to simulate the behavior of the programmers.

The backbone of this model was determined by [27] from static tests on a 14 in. by 30 in. column programmer. The data from these tests were fitted with a nonlinear least squares fit to generate a loading curve represented by a power law given below:

$$F_{pb} = 4021\Delta_p^{1.993} \tag{3.4}$$

where F_{pb} is the baseline force of the programmer in kips and Δ_p is the deformation in the programmer with units of inches. The geometry of the test specimen used in the fit of equation (3.4) was accounted for using a shape factor, *s*, which is defined as the area of the loaded face divided by the area of the unloaded face. Figure 3.7 displays the wall programmers that are used in the blast simulator tests. Three impacting masses are shown in the figure and on each mass there are six programmer pads. Each of these pads is referred to as a sub module. For the prismatic shape of the programmer sub module the shape factor is

$$s_n = \frac{b_{sn}h_{sn}}{2(b_{sn}+h_{sn})t_n} \tag{3.5}$$

where b_{sn} is the width of the sub model, h_{sn} is the height of the sub model, and t_n is the thickness of the sub model. The shape factor is then used to modify the backbone loading curve for a programmer pad with

$$F_{pn} = S_N F_{pb} \tag{3.6}$$

where the modification factor S_n is found with

$$S_n = \frac{b_{sn}h_{sn}(k_1 + k_2 s_n^2)}{b_r h_r (k_1 + k_2 s_r^2)} \tag{3.7}$$

where the subscript *r* in equation (3.7) corresponds to the programmer used to derive the backbone curve and the subscript *n* refers to the sub module for which the relation is being calculated. The coefficients k_1 and k_2 were taken from Gent and Lindley [31] are used to relate the modulus of a material with one shape to the modulus of the same material with a different shape. In the model described here k_1 equals 1.0 and k_2 equals 2.2; these are the coefficients used for a square pyramid.

The dynamic behavior is then represented by multiplying the static baseline curve with the shape modification factor by a dynamic modification factor that is a function of deformation rate, $D(\dot{\Delta})$. The equation for the force then becomes

$$F_{pd} = D(\dot{\Delta}) S_n N_n F_{pb}(\Delta_p) \tag{3.8}$$

where N_n is the number of sub modules on the impact mass. The dynamic modification factor is related to the deformation rate in the programmer with the following equation

$$D = 1 + sign(\gamma_p)(c_1 |\gamma_p| + c_2 {\gamma_p}^2 + c_3 |\gamma_p|^3) \tag{3.9}$$

where γ is a non-dimensional form term found by normalizing the deformation rate by the peak impact velocity that was used in the ballistic impact test.

The parameters c_1, c_2, and c_3 were determined using an optimization routine which included numerical simulations of each ballistic impact test. The simulation included an impacting mass at a specified initial velocity and a target mass at rest. The force between the plates is determined with the programmer model and a one-dimensional contact condition that checked if the distance between the two masses was

less than the thickness of the programmer. When it is determined that the plates are in contact the difference between the thickness and the distance between the plates is taken as the deformation in the plate. This deformation and the associated deformation rate are then entered into the function given in (3.8) to determine the corresponding force. This force is then divided by the magnitude of each mass to calculate their accelerations. The analysis then used explicit time integration to compute the time history for each plate. The coefficients determined for the wall programmer with the optimization along with an correlation coefficient for the fit are listed in Table 3.2.

Table 3.2: Dynamic Modification Factors for Wall Programmer

Parameter	Wall Programmer
c_1	5.5937
c_2	-22.3014
c_3	30.3103
R^2	0.9306

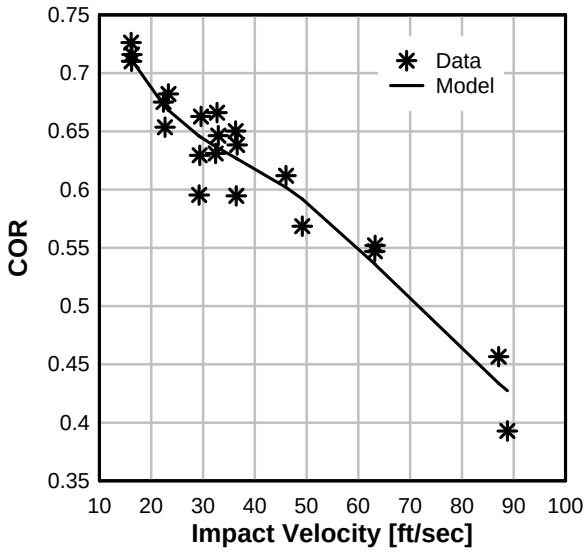

Figure 3.13: Fit of model to ballistic impact tests on wall programmer

The features of the model with the dynamic modification factors given by [27] are:

- It is equal to one at zero deformation rate, it is greater than one for positive deformation rates, and it is less than one for negative deformation rates.
- It is symmetric about the point (0,1) with the following exception.
- It may not be less than zero because the contact surface between the programmer and the specimen cannot develop tension.
- It is nonlinear.

3.4.8 COMPARISON OF PROGRAMMER MODEL TO EXPERIMENTAL RESULTS

In the previous section a one dimensional model developed in [27] was described. The parameters of the model were fit to a static backbone curve and the dynamic results from a series of ballistic impact tests. The next step is to compare the model when implemented into a structural model to the results of full scale wall tests. The programmer model was added to the SDOF analysis described in Chapter 2 to simulate the impact of the BG masses. The addition of the BG impact mass, m_{BG}, added a second degree-of-freedom to the code. In the code the BG is treated as a free flying mass that has the contact condition that was used to simulate the ballistic impact tests. A schematic of this two DOF system is displayed in

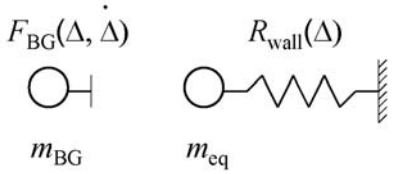

Figure 3.14: Two DOF system with BG impact mass and wall

This model uses the central difference method to perform the time integration of the equation of motion. An explanation of this method for multi degree-of-freedom systems is discussed in further depth in Chapter 5.

Simulations were performed demonstrate the ability of the programmer model to predict the impulse delivered to the specimen. Comparisons between the model and measured results are plotted in Figure 3.15. The test results displayed in the plot include the impulses for the 6 in. thick CMU walls tests discussed in a later section of this chapter, the CMU with CFRP wall tests from Chapter 4, RC wall tests from Chapter 5, and URM wall tests with and without polyurea from Chapter 6. The RC wall tests in which the specimens had frangible panels were not included because a slightly different model, which is discussed in Chapter 5, was used.

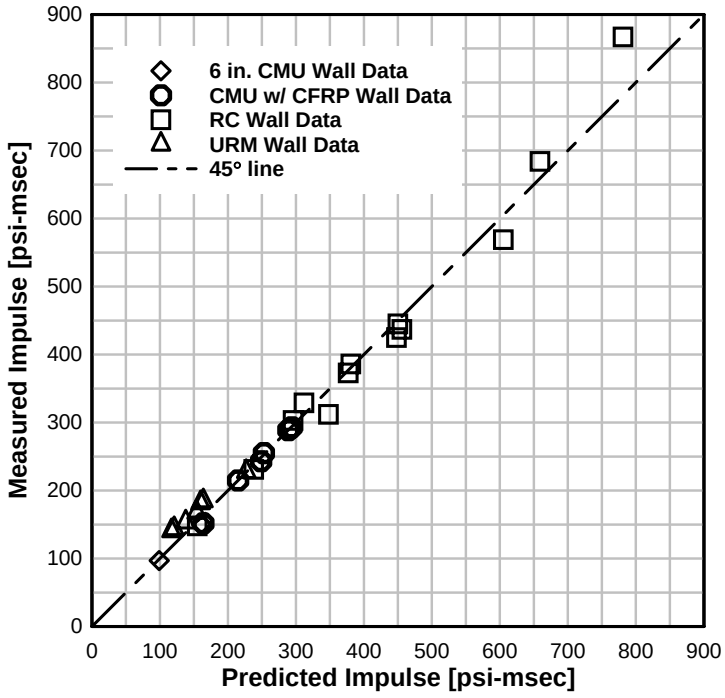

Figure 3.15: Comparison between BG model and test results

Figure 3.15 demonstrates that the impulses predicted by the one-dimensional model are in agreement with the impulses measured in the tests. Included in the plot is a 45º line which represents a perfect fit between the results and the analysis. The plot shows that overall the data is centered about this line indicating that there is a good correlation. Furthermore, the data is close to the line indicating that the error between model and the experiments is low.

It should be noted that the calculation of the impulse for the URM tests only included an effective mass of the wall and did not account for its resistance. Inspection of the data points for these walls reveals that the model under predicted the impulse for six of the seven tests. The lack of the resistance function most likely rendered the wall more compliant; thereby reducing the impulse generated by the BG impacts.

3.4.9 FE PROGRAMMER MODEL

An effort to develop a constitutive model to be used in a finite simulation has been undertaken in a study described in [28]. The objective of this study has been to fully characterize the behavior of the programmers, including the nonlinearities associated with its material, geometry, and boundary conditions. At this time the research has not produced a material model that can be implemented in any of the finite element packages that are suitable for modeling the blast simulator tests. Therefore, an alternative model has been used to simulate the tests on the reinforced concrete and concrete masonry walls studied in this dissertation. By using this material model the impact loads generated by the BGs can be simulated explicitly with a contact surface between the programmers and the front face of the specimen.

The material model used for the programmers is *MAT_057 also called *MAT_LOW_DENSITY_FOAM. This model was selected for the programmer material because of similarities between the stress-strain behavior and the energy dissipation characteristics of compressible foams and the programmer. According to [24] the main applications of the model are for seat cushions and padding for impact dummies used in automotive testing. The behavior of the model under uniaxial loading is assumed not to significantly couple in the transverse direction. In tension a tensile cutoff stress can be defined, but this is not a concern because during loading in a BG impact test, tensile forces cannot be developed.

The model also requires the density and initial modulus of the material which were set equal to 0.03 lb/in. and 2262 psi, respectively. The unloading behavior for the

material is governed by two parameters, HU and SHAPE. In the LS-DYNA keyword manual [24], HU is defined as the hysteretic unloading factor between zero and unity were unity corresponds to no energy dissipation. The parameters SHAPE is the shape factor for unloading. Values of SHAPE less than unity reduce the energy dissipation and those greater than unity increase dissipation.

A loading curve was input into the model to define the stress-strain relation for the programmer. Figure 3.16 displays the stress strain behavior measured for the wall programmer. The curve was obtained with a compression testing machine, which was used to load a 14.37 in. by 15.25 in. programmer pad. It can be observed that there is a significant amount of hysteretic energy that is dissipated by the pad during the test. This energy dissipation is believed to reduce the amount of energy transferred to the specimen during the blast simulator tests. It can also be seen that the material exhibits an unusual behavior as unloading begins. The slope of the curve suggests that the deformation increases as the force is decreasing. In actuality during this portion of the test the displacement was held constant for several seconds before unloading began. The pads exhibited some relaxation which caused the stress to decreases. The increase in displacement during is believed to be an artifact of the controller which was unable to maintain constant displacement.

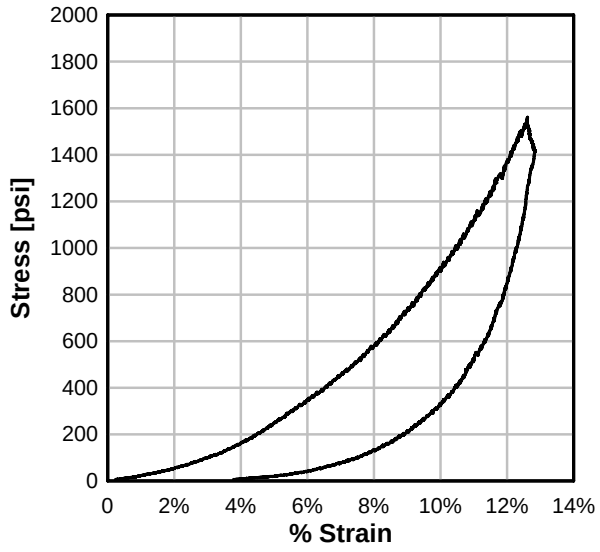

Figure 3.16: Stress-strain curve for wall programmer

The model is also capable of accounting for rate effects by using a linear viscoelastic treatment that effectively is a Maxwell element consisting of a damper and a spring in series. Strain rate effects for the programmer modeled here were not included; therefore, the parameters for this portion of the model were left blank. Validation of a material model that predicts the strain rate behavior of the programmer is outside the scope of this dissertation. This is a recommended area for future research.

In the FE simulations included in this dissertation different parameters of the *MAT_57 were adjusted to match test data a posteriori. The different tests modeled with FE analysis were the CMU walls with CFRP retrofits, RC walls with frangible panels, and URM walls with polyurea catcher systems. In all of these simulations the programmer was modeled with the material model described above. The implementation of this model in the dissertation does not account for strain rate effects on the amount energy dissipated during the impact despite observations of the effect in the ballistic

impact tests and the full scale blast simulator test. The approach in the modeling effort was to select values for the parameters SHAPE and HU that provided the best prediction of impulse delivered by the BG impacts over the full range of load for a test series. Once these two parameters were selected they were held constant for all of the FE simulations in a test series.

The effects of the parameters SHAPE and HU on the coefficient of restitution at various velocities was studied using a FE simulation of the ballistic impact tests. Figure 3.17 illustrates the setup and mesh details for the simulation. The model included the steel impact mass, aluminum backing plate, programmer with pyramids and the steel target mass. In the simulation the impact mass was given an initial velocity and the impact with the target was achieved with the *CONTACT_NODE_TO_SURFACE contact card. Analyses were performed in the study with velocities were set to 15, 40, 65, and 80 ft/sec. The parameter, SHAPE, was set to 2, 5, 10, 50, 100, and 200, while HU was set to 0.01, 0.05, and 0.1. The different combinations of the initial velocity, SHAPE, and HU resulted in 56 runs with the FE model.

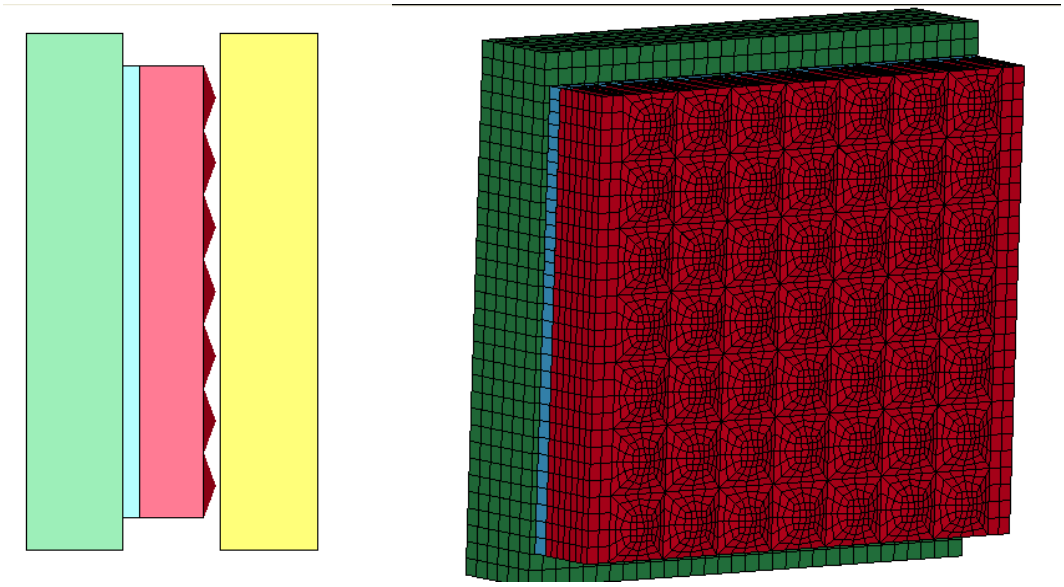

Figure 3.17: FE model for ballistic impact tests

The effect of the parameter SHAPE on the coefficient of restitution for different velocities is displayed in Figure 3.18. In this plot the parameter HU is equal to 0.01 for all curves. It can be observed in the plot that for each value of SHAPE the COR is relatively constant with an increase in velocity. It is also shown that as SHAPE increases the value of COR decreases. The difference in COR between the curves for SHAPE=2 and SHAPE=5 is greater than for the curves corresponding to SHAPE=100 and SHAPE=200; thus the trend between SHAPE and COR is not linear. Finally, the plot demonstrates that the curves for the different values of SHAPE intersect the linear fit of the ballistic impact data. This means that at each velocity a value of SHAPE exists that can be used to reproduce the experimental results.

Figure 3.19 is a plot of velocity versus COR for three different values of the parameter SHAPE and three different values of the parameter HU. This plot demonstrates that for a constant value of SHAPE an increase in HU results in an increase

in COR. As the value of SHAPE increases the effect of HU on COR also increases. The difference between the COR for SHAPE equals 10 for HU equal to 0.01 and 0.1 is smaller than for SHAPE equals 100 and HU equals 0.01 and 0.1.

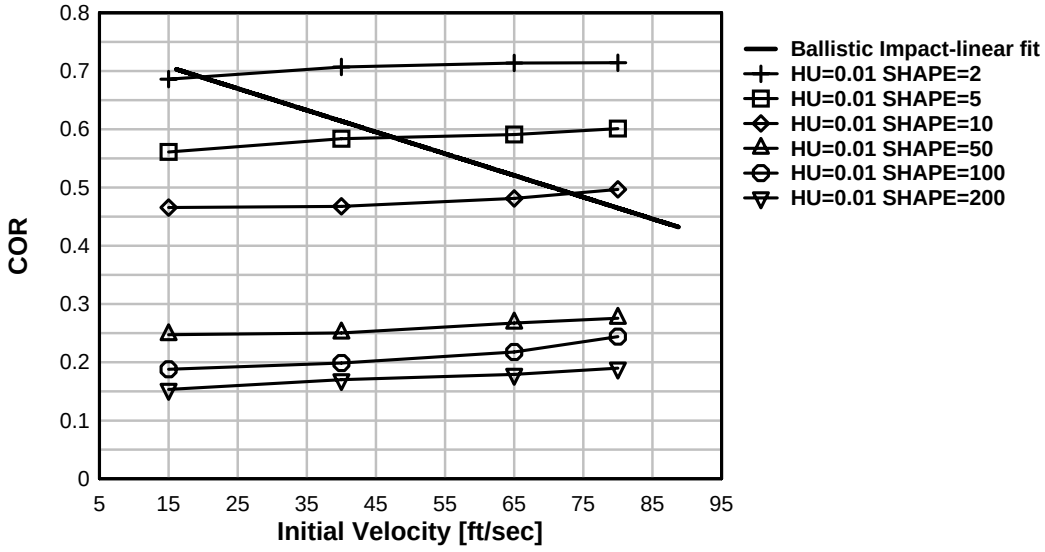

Figure 3.18: Effect of SHAPE on COR vs. velocity plot for programmer model

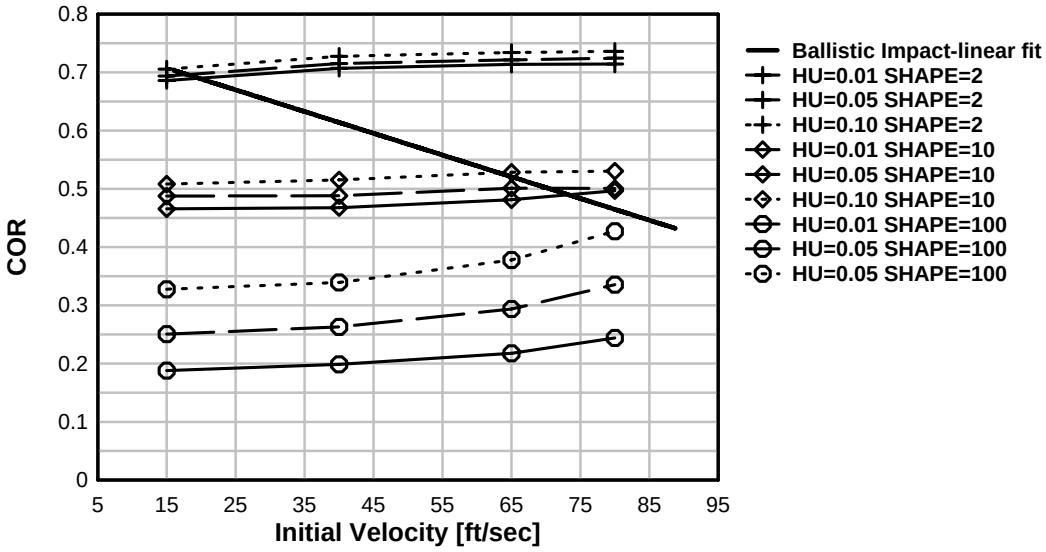

Figure 3.19: Effect of HU on COR vs. velocity plot for programmer model

A comparison between the pressure pulse recoded in Test 18 of the ballistic impact testing and the FE model with parameters that produce a similar COF is displayed below. Figure 3.20 shows the two data points that are compared. Figure 3.21 displays the pressure time history calculated for Test 18 using the accelerometer data with the calculated pressure from the FE simulation. The figure demonstrates the FE analysis is able to predict the general pulse shape well. The pressure recorded in the test has more oscillations which is attributed to flexural waves in the target plate that are excited at impact. The magnitude of the FE model's pressure pulse is also lower than the test data. This, however, is expected because, as Figure 3.20 shows, the impact plate and programmer in the experiment had a slightly higher coefficient of restitution than the simulation which will result in a slightly higher pressure.

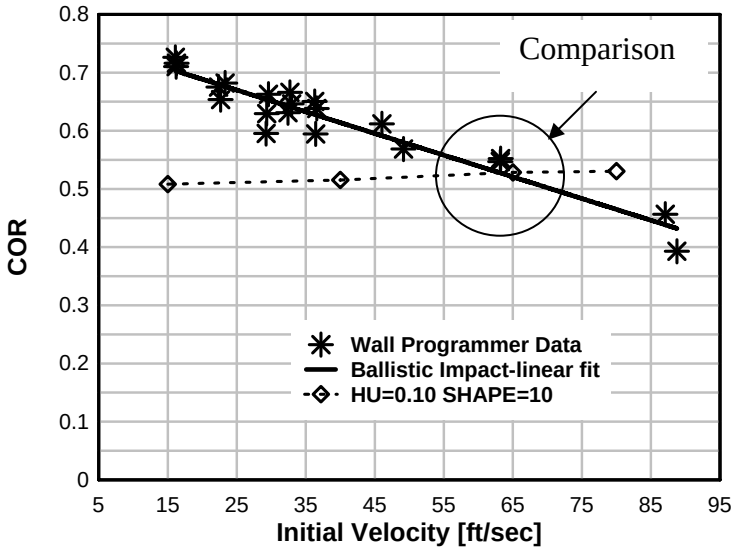

Figure 3.20: Data points for pressure comparison

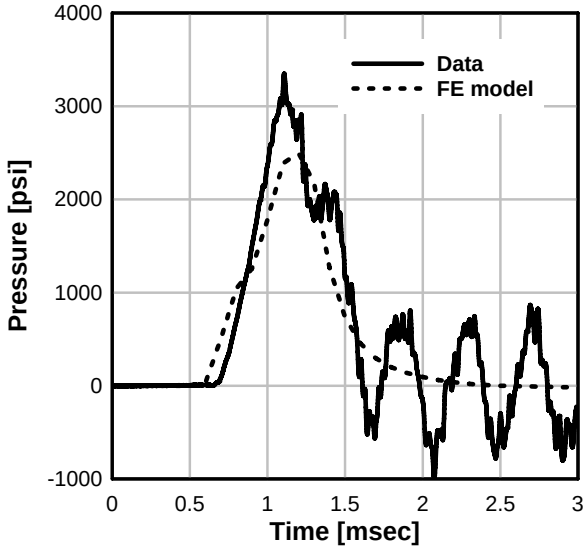

Figure 3.21: Comparisons of pressure pulse from Test 18 and FE analysis

3.5 RECOMMENDATION FOR LOAD PREDICTION IN BLAST SIMULATOR TESTS

In the previous two sections of the dissertation two numerical models, a one-dimensional model for a SDOF-type of analysis and a three dimensional material model for FE analysis, were described. Included in the descriptions were comparisons with experimental data, which demonstrated that the one-dimensional model can predict the impulse generated by the BGs for given input velocity; and the parameters of the FE material model can be adjusted to generate an impulse associated with BG impact velocity if the impulse is known beforehand. These models can now be used with SDOF and FE numerical tools to provide prediction of wall response to blast simulator impacts a priori.

In an SDOF type of calculation the programmer model proposed by [27] can be used together with the effective mass and resistance function for the specimen to determine the impulse. This model has been shown to be accurate for predicting impulses that range from 0 to 900 psi-msec.

For pre-test calculations using FE analysis with the programmer material model the impulse should first be determined using the one-dimensional BG model with the SDOF type of calculation. Once the impulse is predicted, then the parameters SHAPE and HU can be adjusted so that the impulse delivered by the BGs at the specified impact velocity matches it. This will require iteration until the impulse converges. The parametric study conducted in the previous section illustrated that it is best to change the SHAPE parameter when course adjustments are needed and change HU for fine adjustments.

Future research is still needed to develop a fully characterized programmer model that can be implemented into FE analysis code. Additional material testing on the individual programmer types are needed to determine stress-strain curves, viscous coefficients, boundary effects, and strain rate effects.

3.6 BLAST SIMULATOR TESTS ON 6 IN THICK CMU

3.6.1 INTRODUCTION

A commissioning test series was conducted to provide a direct comparison between the walls loaded with the blast simulator and walls loaded by an actual blast. The following section describes the test setup and results for the blast simulator tests.

This is followed by a section that compares the results from the lab with data from the field tests. Finally, a section is included that discusses the effect of the negative phase on masonry wall response.

3.6.2 TEST SPECIMEN

Three 6 in. thick (nominal) reinforced CMU wall specimens were built for the commissioning tests. The overall dimensions of each wall were 5 5/8 in. thick by 8 ft 8 in. tall by 4 ft 8 in. wide. The walls were built with 6 in. x 8 in. x 16 in. concrete blocks. The masonry had a specified strength, f'_m, equal to 1350 psi. All the cells of the blocks were fully grouted with material that had a specified strength equal to 2000 psi. The longitudinal reinforcement consisted of two grade 60 #4 bars. The bars were 8 ft. 6 in. long, spaced at 32 in. on center horizontally. The transverse reinforcement consisted of 9 gauge, 2 strand, ladder-mesh spaced at 16 in. on center vertically. All three walls were built on the casting bed concurrently. The blocks were stacked with the mortar in a running bond as shown in Figure 3.22. The walls were grouted using a pump. Following several days of curing each wall was lifted into the blast simulator test fixtures using a crane and friction lifting device as shown in Figure 3.23.

Figure 3.22: CMU wall construction

Figure 3.23: Placement of wall in test setup

3.6.3 TEST SETUP

The test setup for the CMU walls was designed to simulate a uniformly loaded wall with simple support boundary conditions and one way bending. The test setup for the CMU wall tests is shown in the following Figure 3.24.

Figure 3.24: Setup for 6 in. thick CMU wall tests

The CMU wall tests used three BGs with the 48 in. by 30 in. programmers to impact the specimen. The BGs were aligned so that there was a 1 1/2 in. gap between any two programmer plates. A 1 1/2 in. gap was also set between the bottom BG programmer plate and the footing and between the top BG programmer plate and the bottom of the top support.

A detail of the CMU wall test setup is illustrated in Figure 3.25. The top of the CMU wall was reacted in bearing with a 6 in. thick slab that was connected to the reaction wall. A 1/4 in. bent steel plate was used to prevent rebound at the top of the wall. Neoprene compressible foam was used to provide cushion between the top of the wall and the steel plate. The bottom of the wall was supported in bearing with a steel angle that was fastened to a concrete footing with five 1/2 in. steel anchor bolts. A steel angle was also provided in front of the wall to support it during rebound. Neoprene compressible foam was used to provide cushion between the steel and the bottom of the wall. Shear forces in the slab and the footing were transferred to the large reaction mass that was post-tensioned to the reaction floor. For the footing the forces were transferred through a post tensioned connection and spacer blocks.

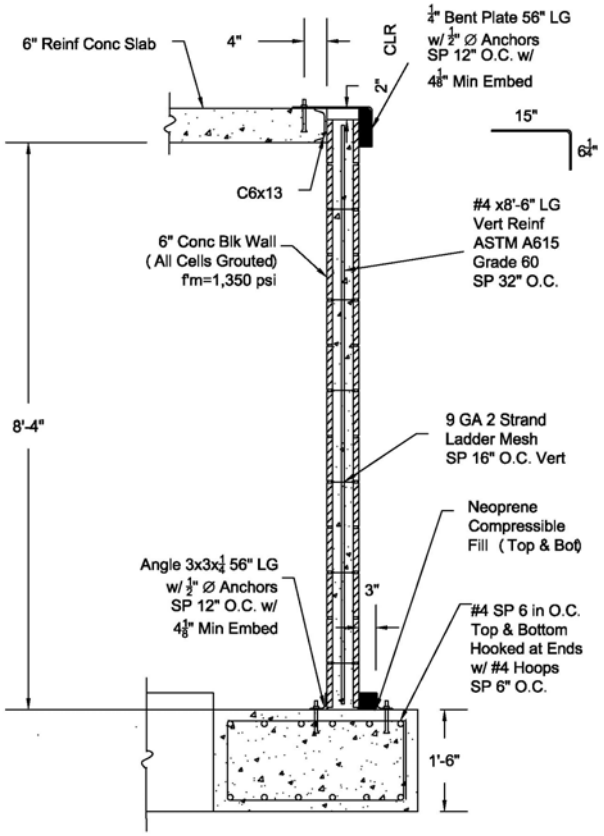

Figure 3.25: Setup details for 6 in. thick CMU wall tests

3.6.4 INSTRUMENTATION

Six strain gages were applied to the vertical reinforcing steel bars in the CMU wall. Three gages per reinforcing bar were located at midspan and at plus or minus 3 in. from the midspan. The locations of the gages are displayed in the following figure.

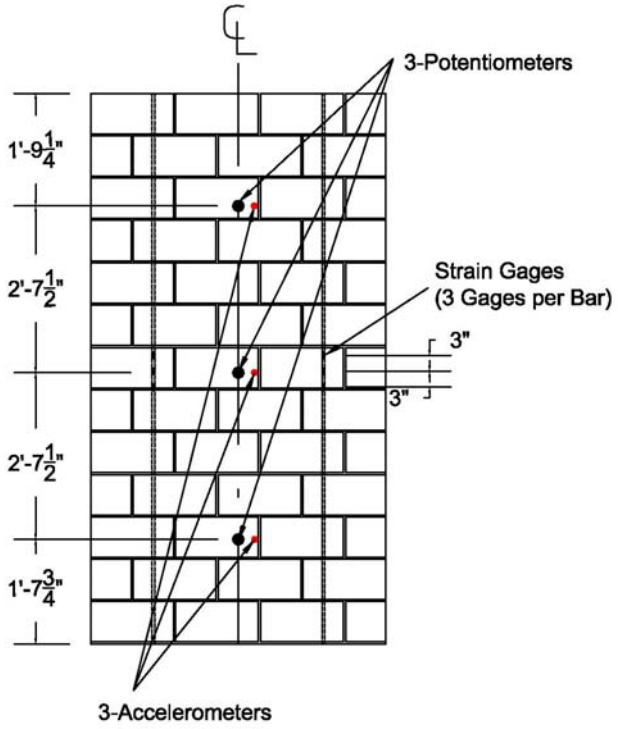

Figure 3.26: Strain gage and accelerometer locations of 6 in. thick CMU wall tests

Three linear potentiometers were used to measure displacements at different vertical locations for CMU walls 1 and 2. The potentiometers were connected to the wall at the horizontal centerline by rods that were anchored into the CMU with epoxy. The location of the potentiometers was set so that no holes were drilled into the mortar joint. Holes for instrumentation were only drilled into the face shell of the masonry blocks. Three accelerometers were used to measure accelerations along the height of CMU walls 1 and 2. The accelerometers were placed at the same vertical locations as the potentiometers, but were offset to the north by about 1". The accelerometers were also set into drilled holes with epoxy.

The third CMU wall that was tested did not have any linear potentiometers or accelerometers. This was done because several instruments were damaged in the previous test.

All of the CMU tests used a single high speed Phantom camera to record the behavior of the specimens to the BG impacts. The camera recorded in black and white at a rate equal to 5000 frames per second. The placement of the Phantom camera is shown in Figure 3.27.

Figure 3.27: Location of phantom camera for 6 in. thick CMU wall tests

3.6.5 MATERIAL DATA

Material test specimens were made to determine compressive strength of the masonry, grout, and mortar used to construct the CMU walls. The specified strength of the masonry was 1.35 ksi. The grout had a specified strength of 2 ksi. The walls all had

the same 7 day and 28 day strength because all were built at the same time with the same batch of materials. The masonry compressive strength was determined by testing masonry prisms according to ASTM E447. The prisms consisted of three blocks with two mortar joints and both cells fully grouted. Figure 3.28 shows the details of the masonry prisms. The grout compressive strength was determined by testing grout prisms according to ASTM C1019. Figure 2 shows a picture of the grout prisms being cast. Mortar compressive strength was found by testing cylinders that were 4 in. long and had a 2 in. diameter. Figure 3 displays the mortar and the test cylinders as they are being made. Twelve test specimens were made for each material. The results from the material tests are presented in Table 1. The table lists the average of three values of compressive strength for the masonry prisms, grout prisms, and mortar cylinders at 7 days, DOT (day of test) 1, DOT 2, and 28 days. The dates for DOT 3 and 28 days coincided with each other, thus they have the same compressive strengths. The yield and ultimate strength of the steel reinforcement was determined according to ASTM A615. The average values of yield and ultimate strength taken from a sample of three test specimens are 69.5 ksi and 112.8 ksi respectively.

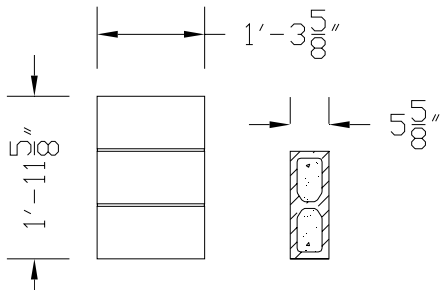

Figure 3.28: Masonry prism test specimens

Figure 3.29: Grout material test specimens

Figure 3.30: Mortar material test specimens

Table 3.3: Material Strengths for 6 in. CMU wall tests

	Masonry Prism [ksi]	**Grout [psi]**	**Mortar [psi]**
7 day	1440	3670	3440
DOT 1	1510	4670	4070
DOT 2	1600	4920	4800
DOT 3	1740	5180	4420

3.6.6 RESULTS

TEST 1

The first CMU wall was tested on June 10, 2005 at a specified target impact velocity of 13.1 ft/sec (4 m/sec). The average of the actual impact velocity for the three BGs in the test was 11.2 ft/sec (3.4 m/sec). The actual average velocity was lower than specified because the middle BG impacted the specimen nearly 7 msec after the top and bottom BGs made contact. Acceleration pulses for each BG are displayed in Figure 3.31-Figure 3.33. The acceleration plot for BG 2 shown in Figure 3.32 suggests that the impact mass did not deliver a significant impulse to the specimen. This is because by the time the impact occurred the deceleration chamber of the actuator had slowed the mass plate significantly. Furthermore, during the impact the nitrogen in the accumulator was doing work against the impact mass thereby reducing the energy it transmitted to the wall. Velocities and impulses determined from the BG accelerometer data and the phantom camera data are listed in Table 3.4. The average impulse delivered to the specimen was 97 psi-msec.

Table 3.4: Test 1- Impact Velocity and Impulse

BG	Impact Velocity [ft/sec (m/sec)]	Impulse [psi-msec]		
		Accelerometers	Camera	Average
3	12.6 (3.8)	138	117	128
2	8.1 (2.5)	20	36	28
1	12.8 (3.9)	137	133	135
Avg	11.2 (3.4)	98	95	97

It can be observed in all three acceleration plots that the impulse increases linearly following the initial impulse associated with the first large acceleration pulse. This

additional impulse is not included in the calculation of the load applied to the wall. The source for the increase is that the deceleration chamber of the actuator which is slowing down the specimen following the impact. This behavior can also be observed in the data for Tests 2 and 3 of this series.

The impulse delivered by the BGs imparted an initial velocity to the wall equal to 10.2 ft/sec. This velocity caused the wall to deform in a one-way bending mode until it reached a peak midspan displacement equal to 4.31 inches. When the wall rebounded and eventually reached static equilibrium it did not did not have significant permanent deformation. A time history plot of displacement recorded are displayed in Figure 3.34. A photo sequence taken from the Phantom camera video displays the response of the wall at several instances following impact.

Most of the damage imparted to the wall involved cracking of the mortar joint near the midspan. Several hairline cracks were also observed on the back face of the wall at almost every horizontal mortar joint. The crack was located at the 6^{th} mortar joint from the bottom was the largest and had a width of 1/16 inch. Hairline cracks were also found along the vertical mortar joints. Some of these cracks propagated through the face shell of the concrete blocks.

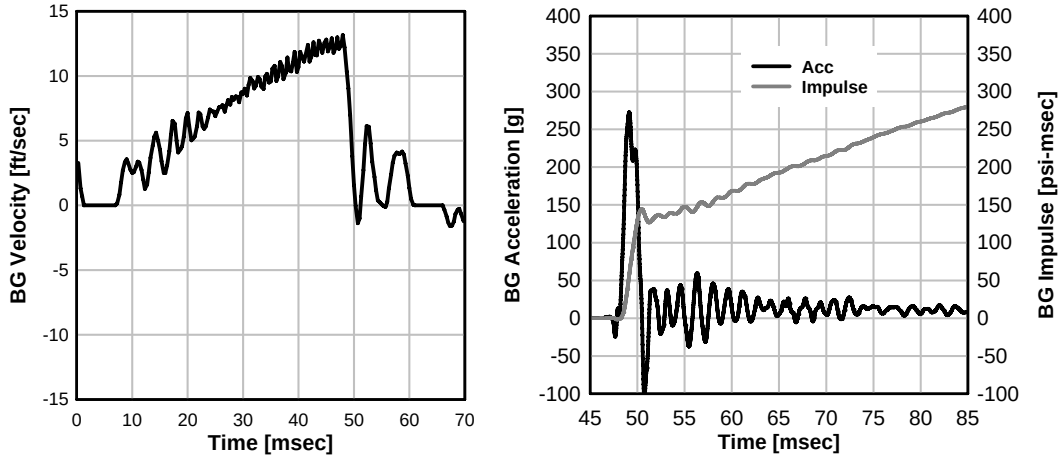

(a) **(b)**

Figure 3.31: Test 1- BG 3 data (a) BG velocity; (b) BG acceleration and impulse

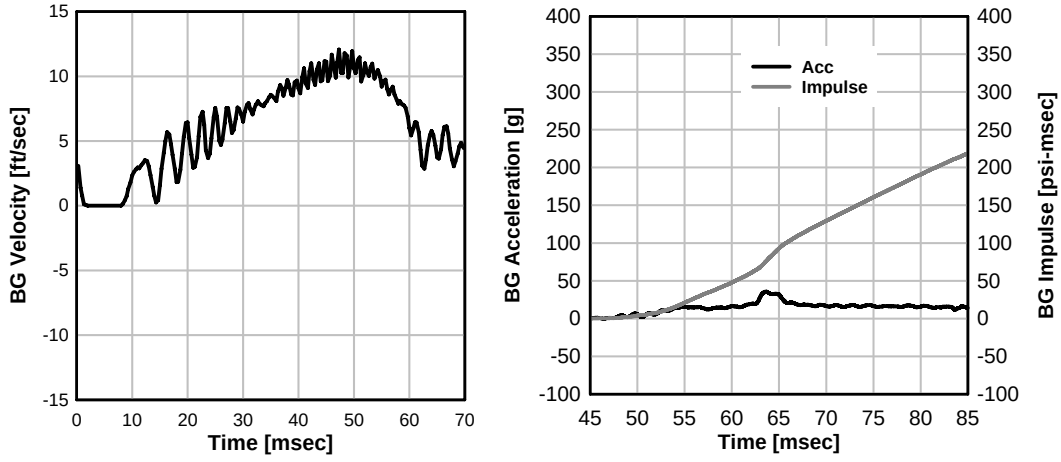

(a) **(b)**

Figure 3.32: Test 1- BG 2 data (a) BG velocity; (b) BG acceleration and impulse

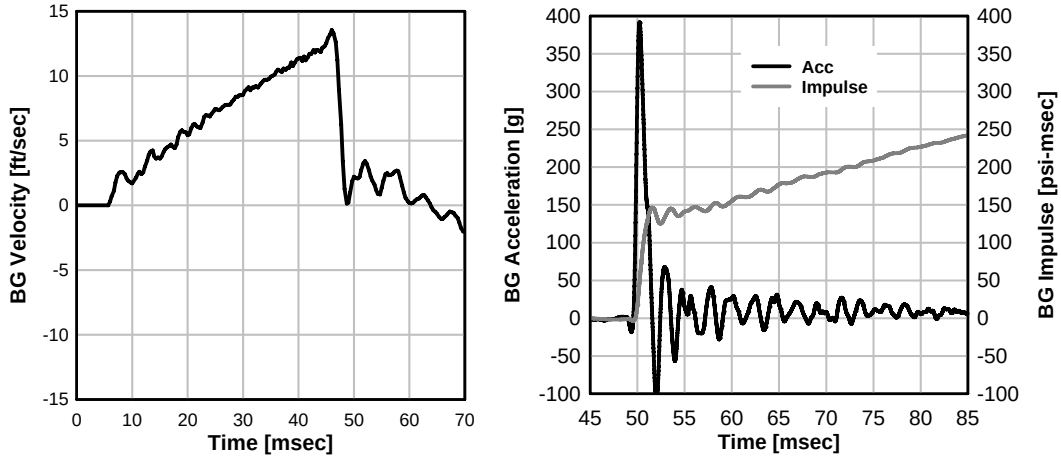

(a) **(b)**

Figure 3.33: Test 1- BG 1 data (a) BG velocity; (b) BG acceleration and impulse

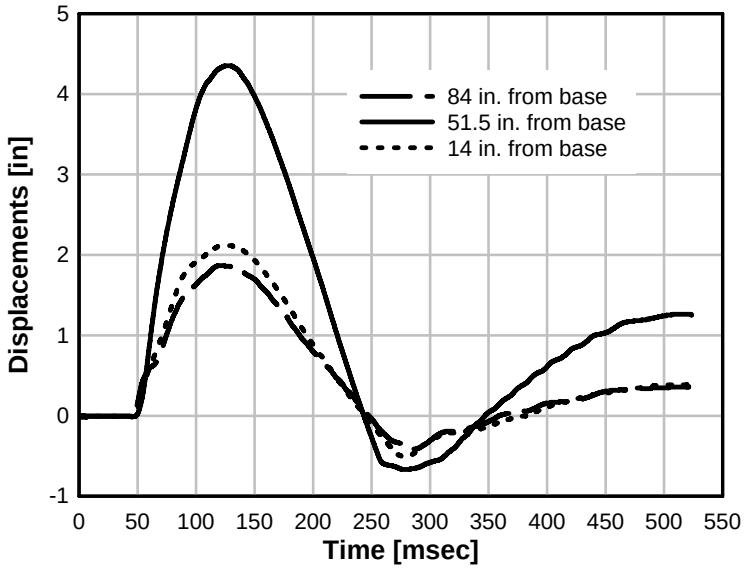

Figure 3.34: Test 1- specimen displacements

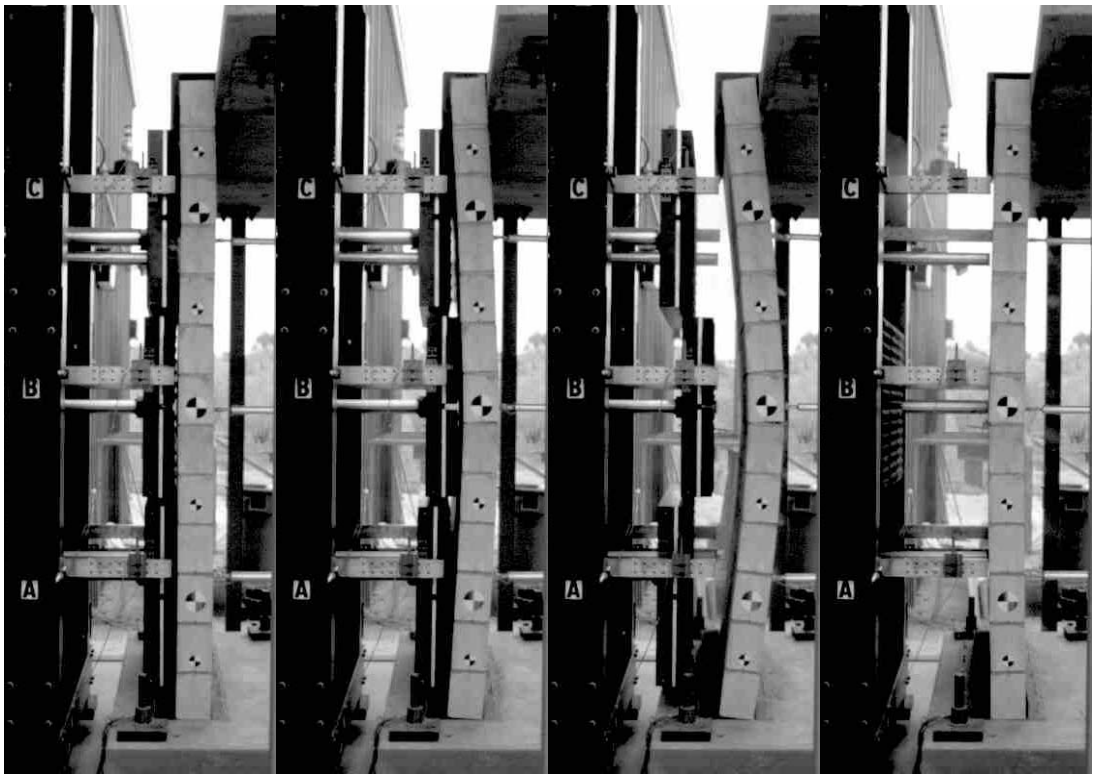

Figure 3.35: Photo sequence from 6 in. CMU Wall Test 1

TEST 2

The second CMU wall was tested on June 15, 2005 at a specified target impact velocity of 19.7 ft/sec (6 m/sec). The average of the actual impact velocity for the three BGs in the test was 18.8 ft/sec (5.7 m/sec). The time spread from when the first and last BG impact was 7 msec. Velocity time history and acceleration pulses for each BG are plotted in Figure 3.36-Figure 3.38. Similar to the results for the first test, the acceleration plot for BG 2 shown in Figure 3.43 suggests that the impact mass did not deliver a significant impulse to the specimen. This again is because by the time the impact occurred the deceleration chamber of the actuator had slowed the mass plate

significantly. Velocities and impulses determined from the BG accelerometer data and the Phantom camera data are listed in Table 3.4. The average impulse delivered to the specimen was 151 psi-msec.

Table 3.5: Test 2- Impact Velocity and Impulse

BG	Impact Velocity [ft/sec (m/sec)]	Impulse [psi-msec]		
		Accelerometers	Camera	Average
3	19.5 (5.9)	200	194	197
2	17.2 (5.2)	65	68	67
1	19.9 (6.1)	192	186	189
Avg	18.9 (5.7)	152	149	151

The BG impulses imparted an initial midspan velocity to the wall equal to 15.7 ft/sec. Initially, the wall had an elastic deformed shape with one-way bending. Then a crack formed at the mortar joint closest to the midspan and additional deformation was concentrated as in this area until a second hinge formed near the top of the wall. The bent steel plate constrained the rotation of the top block creating a negative moment and producing the hinge at the top. As the wall continued to displace a compression failure occurred on the front face of the wall near the midspan. The failure occurred around the 6^{th} mortar joint, centered about the reinforcing steel. The wall continued to deform until it became unstable and collapsed. Specimen displacement time histories are displayed in Figure 3.39, but are incomplete due to the collapse. A photo sequence of the test taken from the Phantom camera video is shown in Figure 3.40. Figure 3.41 shows the collapsed wall following the test.

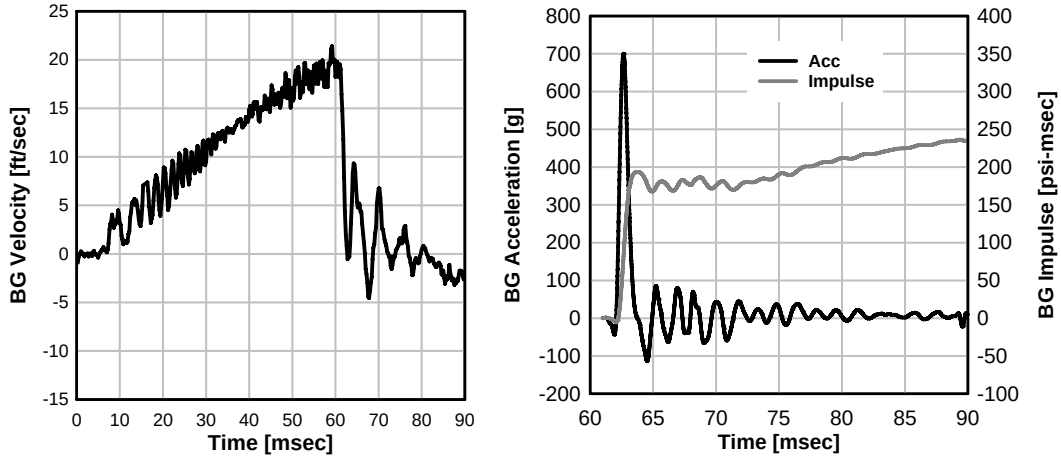

(a) **(b)**

Figure 3.36: Test 2- BG 3 data (a) BG velocity; (b) BG acceleration and impulse

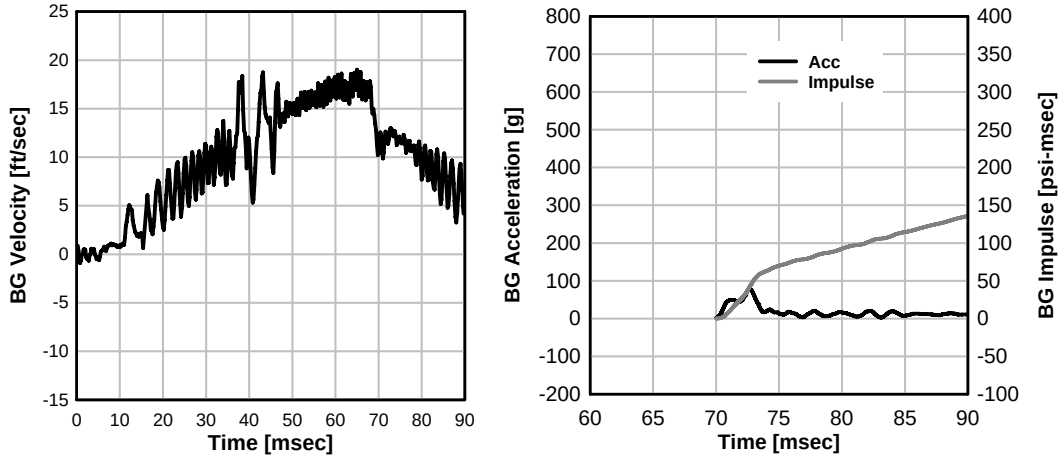

(a) **(b)**

Figure 3.37: Test 2- BG 2 data (a) BG velocity; (b) BG acceleration and impulse

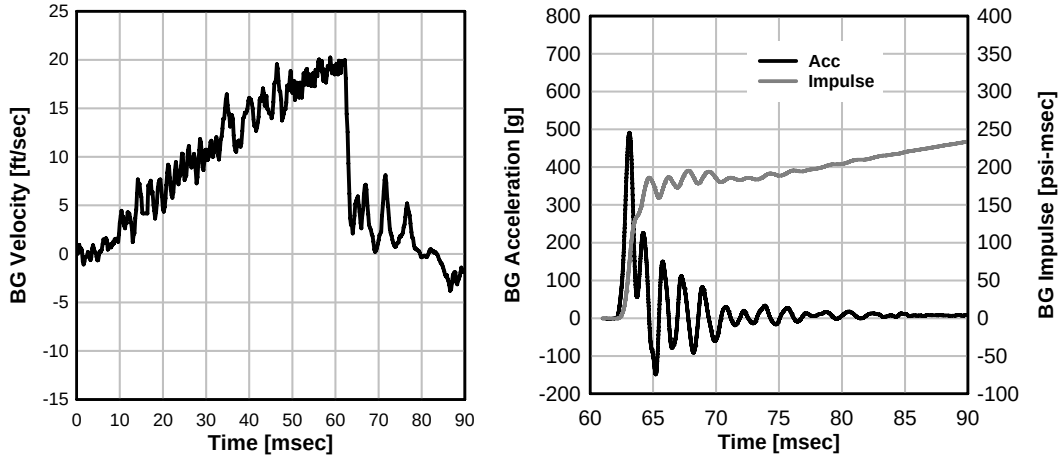

(a) **(b)**

Figure 3.38: Test 2- BG 1 data (a) BG velocity; (b) BG acceleration and impulse

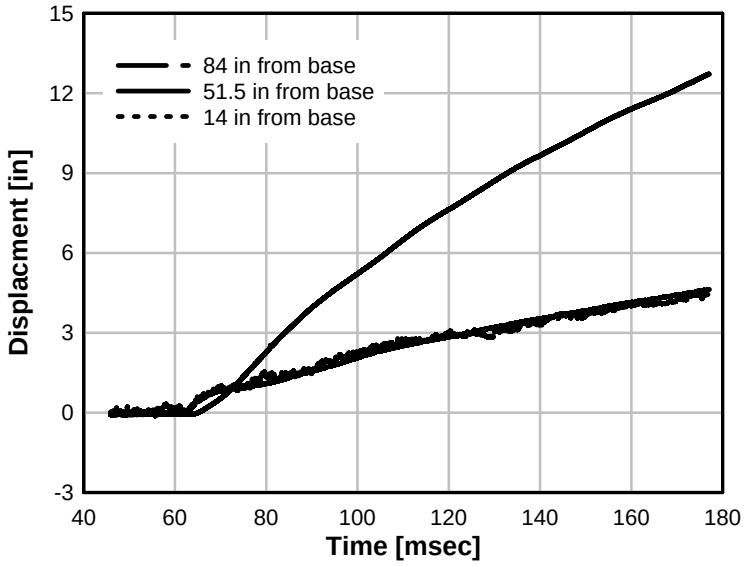

Figure 3.39: Test 2- specimen displacements

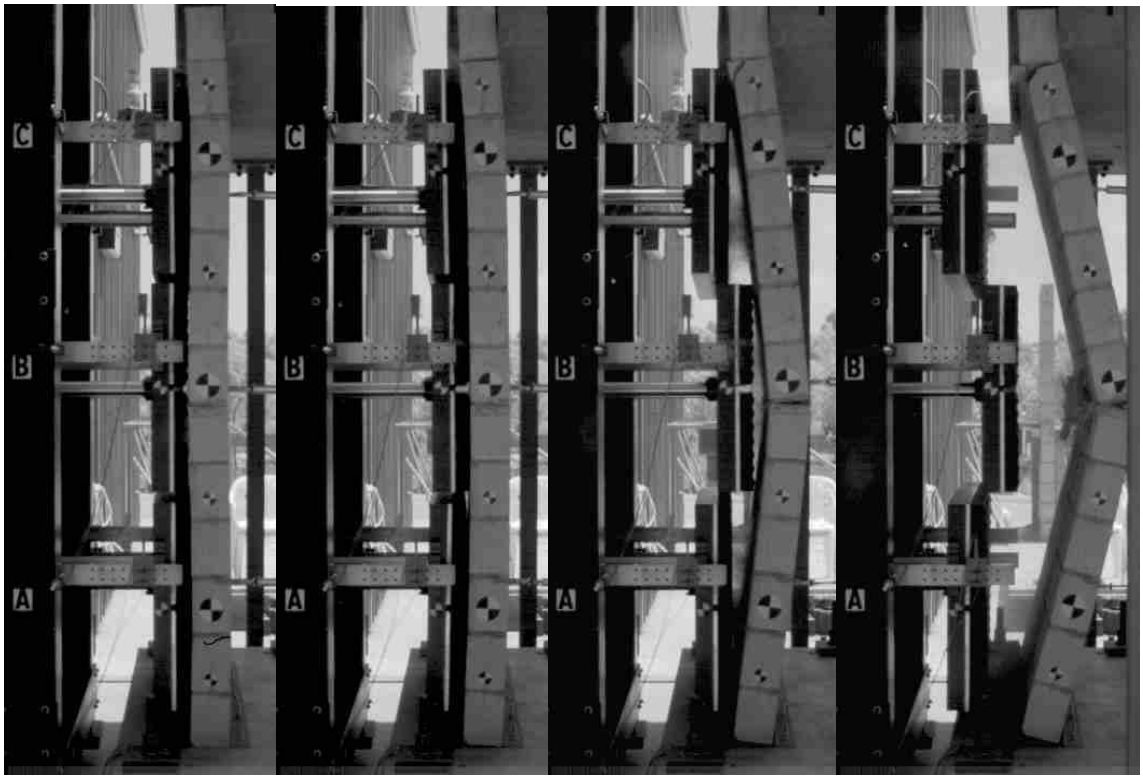

Figure 3.40: Photo sequence from 6 in. CMU Wall Test 2

Figure 3.41: Test 2- post test photo

TEST 3

The final CMU wall test of the series was conducted on June 23, 2005 with a specified target impact velocity equal to 16.4 ft/sec (5 m/sec). The actual average impact velocity was equal to 19.1 ft/sec (5.8 m/sec) and the time spread between the first and last BG impact was approximately 4 msec where BG 2 impacted first followed by BG 3 and BG 1. The actual average velocity was greater than the specified velocity and the velocity of the previous test. The reason for this is that the BGs were re-calibrated to correct timing issues; the re-calibration was unsuccessful and the BG velocities were also increased. The impulse delivered by the BGs in the test was equal to 149 psi-msec. Table 3.6 lists the impact velocity and the impulses determined from the accelerometers and the camera data.

Table 3.6: Test 3- Impact Velocity and Impulse

BG	Impact Velocity [ft/sec (m/sec)]	Impulse [psi-msec]		
		Accelerometers	Camera	Average
3	18.8 (5.7)	164	129	147
2	20.2 (6.1)	191	153	172
1	18.3 (5.6)	133	126	130
Avg	19.1 (5.8)	163	142	149

The BG impacts imparted an initial midspan velocity equal to 16.4 ft/sec to the specimen. This caused the specimen to undergo one-way bending until it reached a peak displacement equal to 11.73 inches. The damage observed in the wall was in the form of flexural cracks around the mortar joints with the largest cracks near the midspan. In addition as the wall approached its peak displacement compression failures were observed near the midspan at the location of the longitudinal rebar. Figure 3.46 is a

photo sequence of the test taken from the Phantom camera video. Figure 3.47 displays the front and back side of the wall following the test.

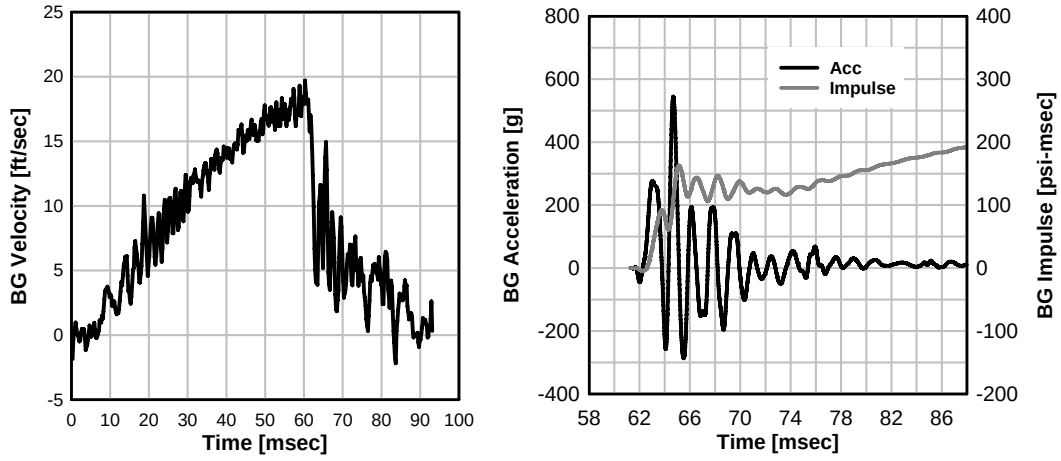

(a) **(b)**

Figure 3.42: Test 3- BG 3 data (a) BG velocity; (b) BG acceleration and impulse

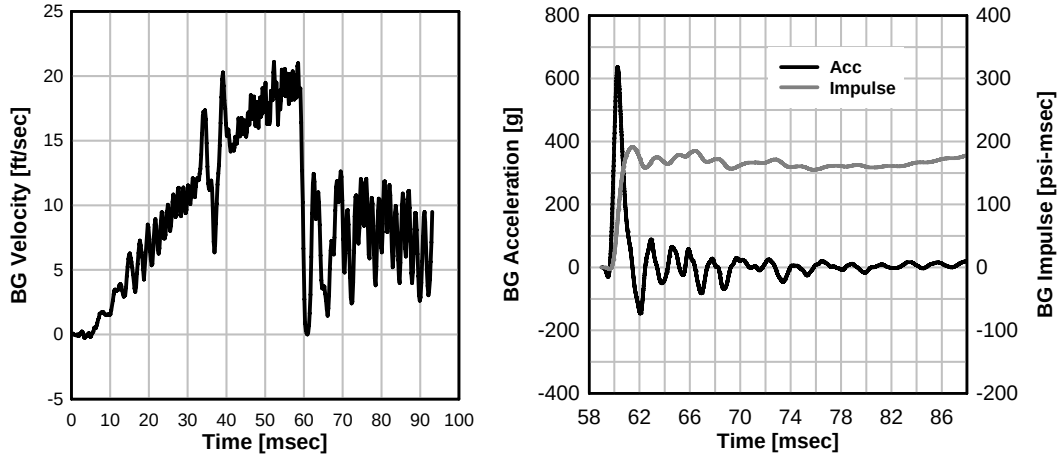

(a) **(b)**

Figure 3.43: Test 3- BG 2 data (a) BG velocity; (b) BG acceleration and impulse

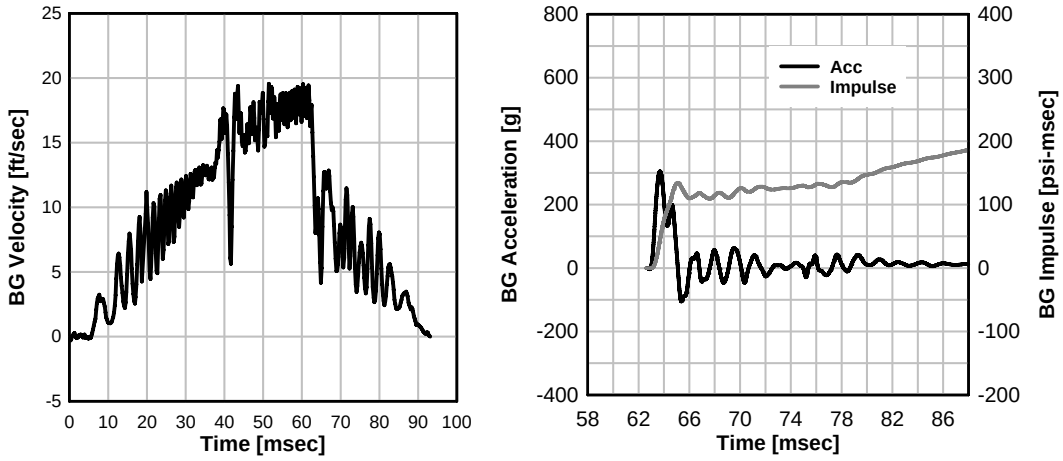

(a) **(b)**

Figure 3.44: Test 3- BG 1 data (a) BG velocity; (b) BG acceleration and impulse

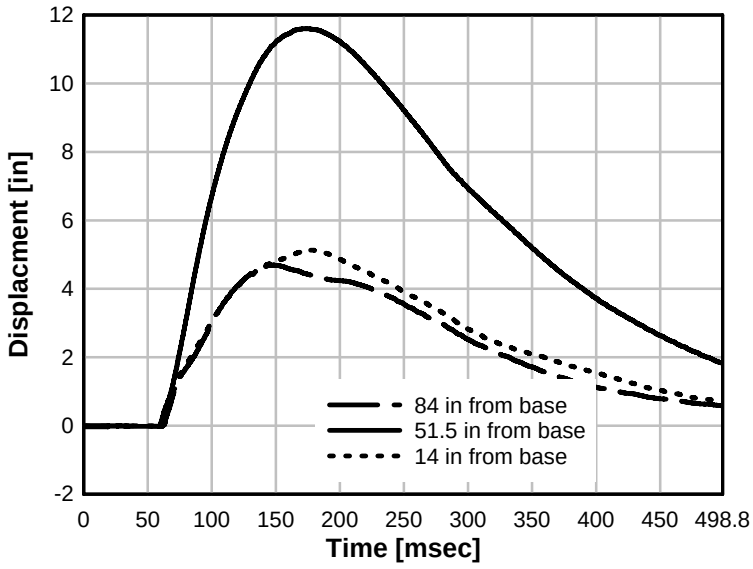

Figure 3.45: Test 3- specimen displacements

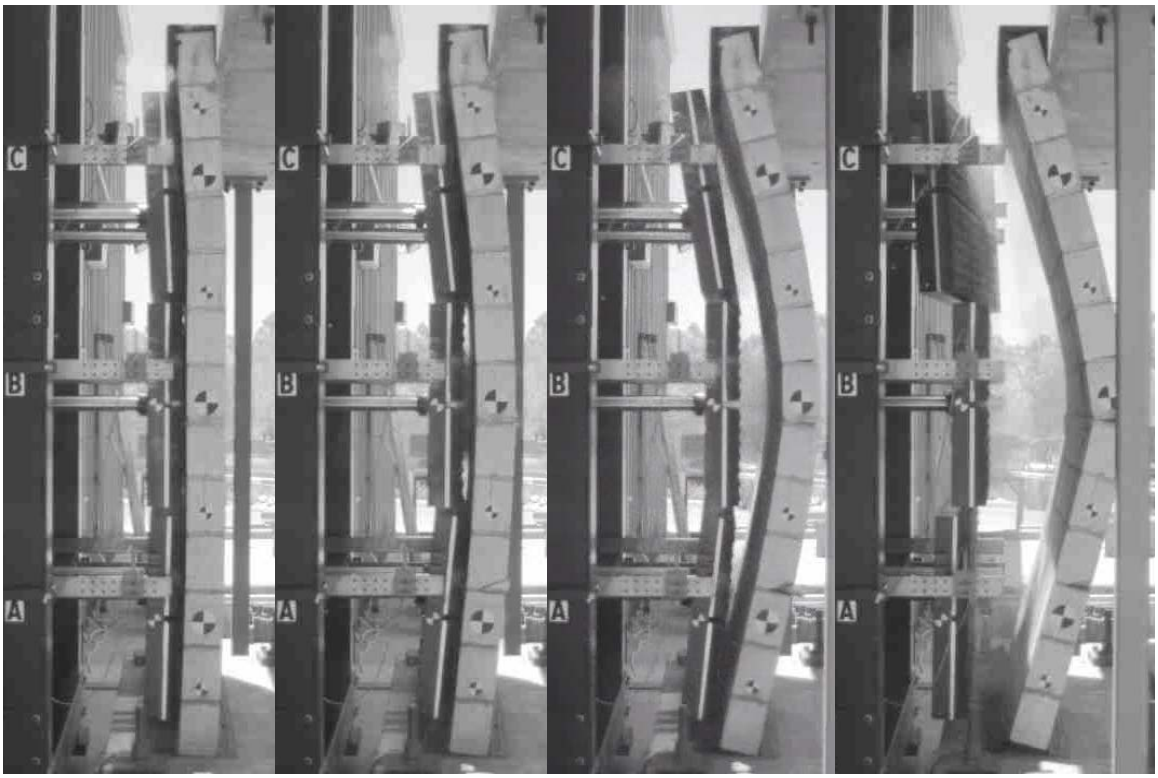

Figure 3.46: Photo sequence from 6 in. CMU Wall Test 3

Figure 3.47: Test 3- post test photos

SUMMARY OF 6 IN. THICK CMU WALL TESTS

Blast simulator tests were conducted on three fully grouted, lightly reinforced 6 in. thick CMU walls. The walls were impacted by the BGs with velocities that ranged from 11.1 to 19 ft/sec (3.4 to 5.8 m/sec). The impulses generated in the tests ranged between 97 and 144 psi-msec and produced responses that varied from 4.3 in. of displacement to total collapse. The walls in the test all responded with one way bending and damage observed was in the form of flexural cracks that initiated at the mortar joints and compression failures near the longitudinal rebar at the midspan.

Table 3.7: Summary of 6 in. thick CMU Wall Tests

Test	BG Velocity [ft/sec (m/sec)]	Impulse [psi-msec]	Displacement [in]
1	11.2 (3.4)	97	4.33
2	18.9 (5.7)	151	collapse
3	19.1 (5.8)	149	11.73

3.7 COMPARISON OF BLAST SIMULATOR AND FIELD TESTS

The test setup used for the CMU wall test was based on field experiments performed by Energetic Materials Research and Testing Center (EMRTC) [32]. EMRTC tested 26 CMU walls subjected to uniform blast overpressures from various masses of C-4 at a standoff distance equal to 30 ft. The walls were 6 in. thick by 8 ft 6 in. tall by 16 ft wide and fully grouted. The walls had zero reinforcement, light reinforcement with one # 4 bar spaced at 32 in., or heavy reinforcement with #4 bars spaced at every 8 inches. The light reinforcing ratio is the same as the ratio used for the blast simulator tests described

above. The boundary conditions used by EMRTC were also replicated for the blast simulator tests.

The damage observed in the CMU wall tests was quantified in [32] on a scale from 1-5, the level of damage associated with each number is defined below.

1. Light Damage: Slight or no damage to wall. Wall can still perform intended structural function. Repairs are required for cosmetic reasons only.
2. Moderate Damage: Wall must be repaired to restore structural integrity.
3. Severe Damage: Wall is damaged beyond repair and may collapse due to typical environmental conditions (e.g. wind).
4. Collapse Damage: Wall has been damaged such that the structural envelope has been breached. Portions of the wall may become debris hazard.
5. Blowout with Significant Residual Velocity: The entire wall panel is breached and CMU blocks are scattered throughout the adjacent room floor.

Table 3.8 lists the results from the lightly reinforced CMU wall tested by EMRTC.

Table 3.8: EMRTC impulse and damage data

Case #	Charge Weight [lb]	Equivalent TNT [lb]	i [psi-msec]	Peak Disp. [in]	Damage
6	45	58	86	2.8	1
13	85	109	151	5.8	2
8	100	128	148	9.8	2
14	100	128	156	7.3	2
10	125	160	178	14.1	2
19	125	160	233	failure	2
9	150	192	261	5.9	3
15	150	192	223	6.3	3
11	165	211	248	9.6	4
20	165	211	282	7.3	4
12	250	320	319	13.2	5
21	250	320	375	failure	5

Table 3.9 lists the level of damage for CMU Walls 1-3 tested with the blast simulator.

Table 3.9: UCSD Damage Data

Specimen	Damage
CMU 1	1
CMU 2	4
CMU 3	3

The blast simulator was successful at producing failure modes in CMU walls that have been observed in field tests by EMRTC. Figure 3.48 (a) display photos that compare the damaged state of blast simulator CMU Wall 1 and Test 6 from EMRTC. The lab wall was impacted by the BGs with an average impact velocity equal to 11.2 ft/sec (3.4 m/sec). The EMRTC wall was subjected to a blast of 58 lbs of C-4 at a standoff of 30 ft. The damage level for both walls is one.

(a) **(b)**

Figure 3.48: Comparison of damage: (a) EMRTC Test 6; (b) CMU Wall Test 1

CMU Wall 2 was impacted by the BGs with an average impact velocity of 18.9 ft/sec (5.7 m/sec) which produced a damage level of four. Figure 3.49 displays a photo of CMU wall 2 post-test along with a photo of EMRTC Test 1 and 20. The Wall 20 tested by EMRTC was subjected to 250 lbs of C-4 at a standoff distance of 30 ft which also produced a damage level of four. Even though the walls had similar levels of damage the EMRTC wall remained standing after the test, while CMU Wall 2 collapsed. Also shown in Figure 3.49 is a photo of EMRTC Test 1 which is an unreinforced CMU wall subjected to 58 lbs of C-4t at 30 ft. This photo is included in the figure to demonstrate how the wall from Test 20 would look if it had become unstable.

(a) **(b)**

(c)

Figure 3.49: Comparison of damage: (a) EMRTC Test 1; (b) CMU Wall Test 2; (c) EMRTC Test 20

Figure 3.50 through Figure 3.52 compare the damage seen in CMU Wall 3 and EMRTC Tests 9 and 15. CMU Wall 3 was impacted by the BGs with an average impact velocity equal to 19.1 ft/sec (5.8 m/sec). The walls in EMRTC Tests 9 and 15 were subjected to 192 lbs of C-4 with a standoff distance of 30 ft. All three of the walls displayed in these figures have a damage level of three. Figure 3.50 compares the back

side of CMU Wall 3 to the back side of EMRTC Test Wall 15. Figure 3.51 and Figure 3.52 compare CMU Wall 3 and EMRTC Test Wall 9 from the side and front, respectively.

(a) **(b)**

Figure 3.50: Comparison of damage: (a) EMRTC Test 15; (b) CMU Wall Test 3

(a) **(b)**

Figure 3.51: Comparison of damage: (a) EMRTC Test 9; (b) CMU Wall Test 3

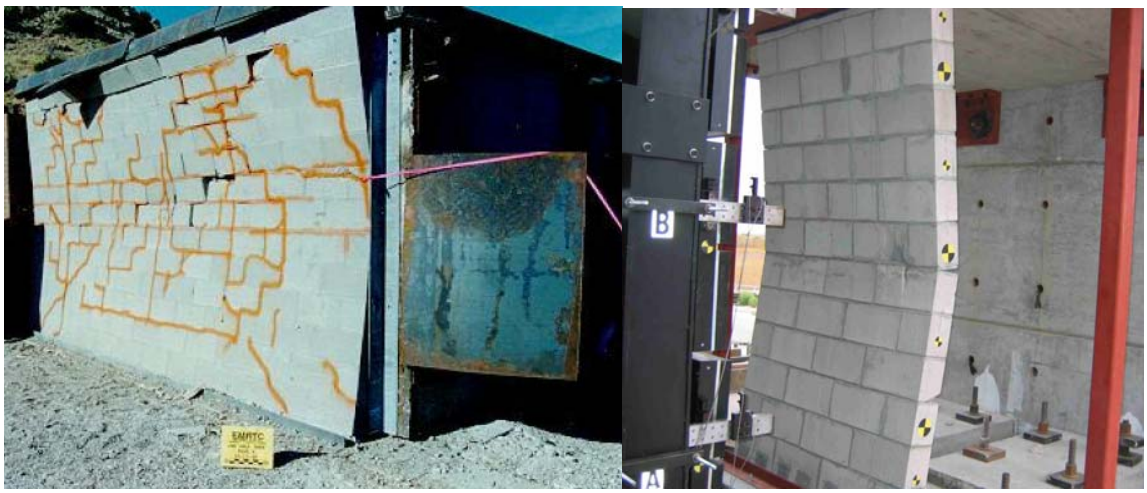

(a) **(b)**

Figure 3.52: Comparison of damage: (a) EMRTC Test 9; (b) CMU Wall Test 3

Figure 3.48 through Figure 3.52 demonstrate that the blast simulator can produce failure modes in CMU walls that are similar to those observed in the field. The blast

simulator tests were able to capture the local damage in the form of cracking and crushing of the CMU block. The blast simulator was also able to generate the global response which was a flexural mode with one-way bending.

Another comparison between the blast simulator data and the field test data from EMRTC is displayed in Figure 3.53 which plots impulse versus peak displacement. It should be noted that the data points which have a peak displacement equal to 30 in. signify tests where the specimen collapsed. There were only three data points generated in the blast simulator tests so it was important to include all three in the plot in order to draw comparisons with the field data. Two observations can be made about the data plotted in Figure 3.54. The first is that for both the lab and field data the relation between impulse and displacement is nonlinear. In both cases there is an impulse at which small increases in load result in large increases in displacement. The second observation is the field tests experienced less displacement for equal levels of impulse.

In blast simulator tests on RC columns with CFRP retrofits Rodriguez-Nikl [33] demonstrated that the displacement produced by a BGs impact could be correlated to a displacement produced by pressure pulses generated in an actual explosion through the impulse. Unfortunately, the comparison shows that for the CMU walls tested one cannot use this type of correlation to relate lab and field data.

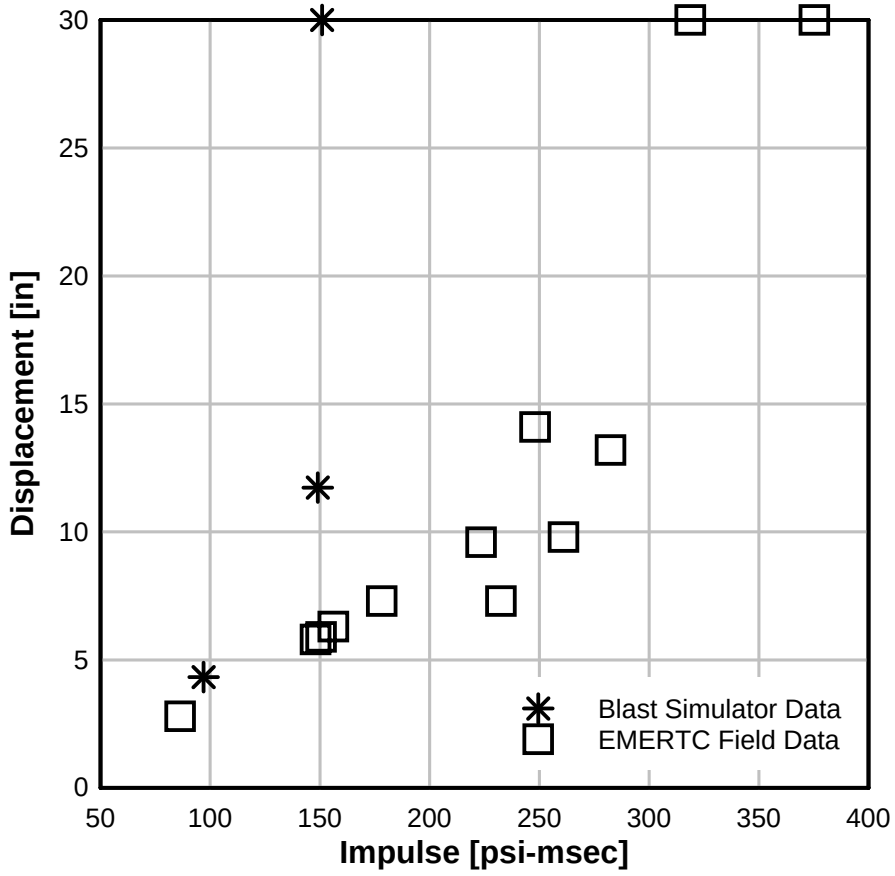

Figure 3.53: Comparison of impulse vs. peak displacement for blast simulator and field data

3.7.1 SDOF MODEL OF 6 IN CMU TESTS

The most likely source of the disparity between the laboratory and field data in Figure 3.53 is the effect of the negative phase on the wall response. In the blast simulator tests the load is delivered in a fraction of the time that it takes the specimen to respond, i.e. the load is impulsive. This type of load generates an initial velocity in the wall and then the wall is free to vibrate without any additional load. In the event of an actual

explosion the pressure time history has a positive phase and a negative phase as described in Chapter 2. For the types of blast loads considered in the EMRTC field tests the duration of the positive phase is short compared to the duration of the negative phase. Also, the magnitude of the peak pressure for the positive phase is significantly larger than the peak negative pressure associated with the negative phase. In this type of loading situation the positive phase will load the structure impulsively and then the negative phase will do work against the structure to decelerate it; thereby reducing the displacement demand.

To investigate the effect of the negative phase on the CMU walls an analysis of the blast simulator tests was run to validate a SDOF model. Next the model was subject to blast loads with and without a negative phase to provide a comparison between the different specimen responses. Finally, a parametric study was run to investigate the effect of the negative phase on walls that vary in strength and mass.

The blast simulator tests were simulated using an SDOF model that incorporates BG impact mass with the one-dimensional programmer model described in an earlier section of this chapter. The BGs in the model were given initial velocities equal to the average impact velocity recorded in the blast simulator tests. The loads generated by the BGs were applied to an SDOF model of the CMU walls with the contact condition describe earlier. The CMU walls were modeled with an effective mass and a resistance function using the analysis code described in Chapter 2. The resistance functions for the lightly reinforced, fully grouted walls were generated with a moment-curvature routine that is described in Chapter 4 for CMU walls with CFRP retrofits. For the 6 in. thick

unretrofitted CMU walls modeled here, the thicknesses of the CFRP laminates required for input was set equal to zero. The resistance functions also considered rate effects in the steel reinforcement and concrete masonry. Table 3.10 lists the peak rebar strains recorded in the three tests. In the moment-curvature analysis a strain rate equal to 0.47 sec^{-1} was used for all of the materials. This rate is one half 0.93 sec^{-1}, which is the average peak strain rate for the three tests. Half of the peak was used because it is assumed that the strain rate varied linearly during the loading; so one half is the average strain rate over the load duration. The ultimate moment and the corresponding curvature for the CMU walls are listed in Table 3.11. Also listed in the table are the peak resistance for and the displacement at which the wall is assumed to behave plastically.

Table 3.10: Peak Rebar Strain Rates

Test	BG Velocity [ft/sec (m/sec)]
1	0.64
2	0.95
3	1.21
AVG	0.93

Table 3.11: Moment-curvature and peak resistance function for 6 in. CMU walls

	M_u [k-ft]	**ϕ_u [10^6/in]**	**R_u [psi]**	**Δ_u [in]**
6 in. thick CMU	7.50	500	1.36	0.42

A comparison of the impulse delivered between the SDOF analysis with the BG impact and the test results is shown in Table 3.12. The table shows that the model is capable of predicting the impulse delivered to the wall at BG velocities that range from 11.2 to 19.1 ft/sec. The largest error was for Test 3 in which the model predicted an impulse that was 8.7% greater than measured. The ability of the model to predict the

impulse is significant because the model assumes that all three BGs impacted the specimen simultaneously, which did not happen. Instead, in all three experiments there was a large time spread between BG impacts. An explanation for why the model is still accurate is that the loads over the time spans observed were still in the impulsive regime; thus the specimen did not have time to respond before all three BGs impacted. An investigation of this behavior is recommended for future research.

Table 3.13 lists the displacements measured in the tests and predicted by the SDOF analysis. In the first test the error was only 6.0% and in the third test the error was even less significant at 3.9%. There is, however, a discrepancy between the model and the results for the second test where the specimen collapsed due to the BG loads. The difference is attributed to the variability in the test specimens especially under loads that generate such highly nonlinear responses. The specimens in Test 2 and Test 3 were subject to similar impulses and the difference between these displacements is significant. At these load levels the specimen is most likely approaching the envelope of catastrophic collapse. This makes it very sensitive to small variations that can significantly affect the response. Despite the noted discrepancy the model has been demonstrated to be in agreement with the test data.

Table 3.12: Comparison of impulse for experiment and SDOF analysis

Test	BG Velocity [ft/sec (m/sec)]	Exp. Impulse [psi-msec]	SDOF Impulse [psi-msec]	% Error
1	11.2 (3.4)	97	99	2.1%
2	18.9 (5.7)	151	161	6.6%
3	19.1 (5.8)	149	162	8.7%

Table 3.13: Comparison of displacement for experiment and SDOF analysis

Test	BG Velocity [ft/sec (m/sec)]	Exp. Disp. [in]	SDOF Disp. [in]	% Error
1	11.2 (3.4)	4.33	4.39	6.0%
2	18.9 (5.7)	collapse	11.1	NA
3	19.1 (5.8)	11.73	11.27	3.9%

The model validated with the blast simulator test results was used to investigate the effect of the negative phase in the comparison of the lab and EMRTC field data. The model can also be validated with respect to its capabilities to simulate the field tests because the EMRTC walls had the same reinforcing ratios, were built using materials with similar strengths, and the test setup had similar boundary conditions. The major difference between the lab and field specimens is the width of the walls. This difference should not affect the model because the resistance and mass of the model is normalized by the loaded area of the wall. The validated model was loaded with pressure time histories associated with seven different charge sizes used in the field tests and listed in Table 3.8. The parameters of the pressure time history were calculated using the methods described in Chapter 2. Table 3.14 lists the parameters.

Table 3.14: Blast Pressure Parameters

Charge Wt. [lbs]	**p_r [psi]**	**i_r [psi-msec]**	**t_{of} [msec]**	**t_o [msec]**	**p_r- [psi]**	**i_r- [psi-msec]**	**t_{of}- [msec]**
45.00	41.80	89.00	4.26	8.50	3.50	71.00	44.60
85.00	74.50	140.00	3.76	8.55	4.70	110.00	49.20
100.00	86.80	158.00	3.64	8.55	5.00	122.00	50.00
125.00	108.00	186.00	3.44	8.75	5.40	139.00	54.80
150.00	129.30	213.00	3.29	9.05	5.70	153.00	57.40
165.00	142.10	229.00	3.22	9.25	5.80	161.00	58.20
250.00	216.20	311.00	2.88	10.65	6.80	211.00	66.20

The SDOF analyses were run using the pressure loads with and without the negative phase. The results of these analyses are displayed in Figure 3.54 which plots impulse versus displacement. Included in the plot are the data from the laboratory and field tests. The figure demonstrates that the negative phase decreases the peak displacement for a given impulse. One can observe that the results from the analyses with the negative phase are in agreement with the field data; and the results from the analyses with only positive phase matches the laboratory data reasonable well. This evidence supports the assumption that the negative phase is the cause for the difference between lab and field data.

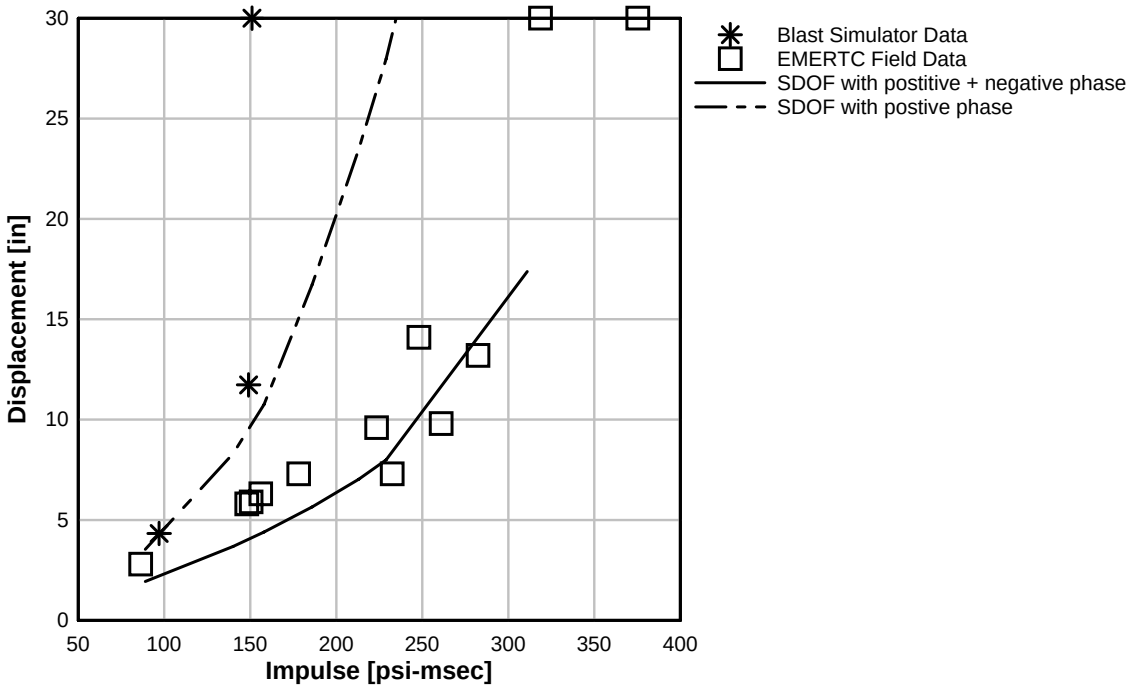

Figure 3.54: Comparison of impulse vs. peak displacement for blast simulator and field data with SDOF analysis

3.7.2 Behavior of Walls Subject to Blast Loading with and without a Negative Phase

A parametric study using a SDOF model was conducted to further investigate the effect of the negative phase on wall response to blast loads. In this study several analysis were run where the blast loads, the wall mass, and the wall peak resistance were varied. The blast loads used in the study are the same loads used in the previous study and the parameters of these loads are listed in Table 3.14. Analyses were run with and without the negative phase. The mass of the walls was varied by considering three different thicknesses, 6 in. nominal and 8 in. nominal, which are typically used in CMU wall design and a third thickness equal to 10 in. nominal, was also considered. This is not a typical CMU block size, but it is included to expand the study. Finally, the resistances at each wall thickness were varied to three levels that correspond to a lightly reinforced wall, moderately reinforced wall and heavily reinforced wall. The peak resistance and yield displacement for each wall are listed in Table 3.15.

Table 3.15: Resistance Functions for Negative Phase Parametric Study

Thickness [in]	R_u [psi]	Δ_y [in]
5.625	1.20	0.44
5.625	6.22	0.56
5.625	23.91	0.39
7.625	1.20	0.44
7.625	6.22	0.56
7.625	23.91	0.39
9.625	1.20	0.44
9.625	6.22	0.56
9.625	23.91	0.39

The results of the study are displayed in Figure 3.55 which plots a non-dimensional form of the impulse, I_{bar}, versus the ductility demand, μ. The non-dimensional impulse was calculated with the following equation:

$$I_{bar} = i\sqrt{\frac{Lg\Delta_y}{K_{LM}K_r w_l M}} \tag{3.10}$$

where L is the span, g is the acceleration of gravity, Δ_y is the yield displacement of the resistance function, K_{LM} is the load-mass factor, K_r is a boundary condition coefficient equal to eight for simple-simple supports, w_l is the weight of the wall normalized by the loaded area, and M is the maximum moment associated with the ultimate resistance. The ductility demand for the wall can be found with:

$$\mu = \frac{\Delta}{\Delta_y} \tag{3.11}$$

Where Δ is the peak displacement recorded for the analysis. The plot of impulse versus ductility demonstrates the effect of the negative phase on the response of the CMU walls with different masses and resistances.

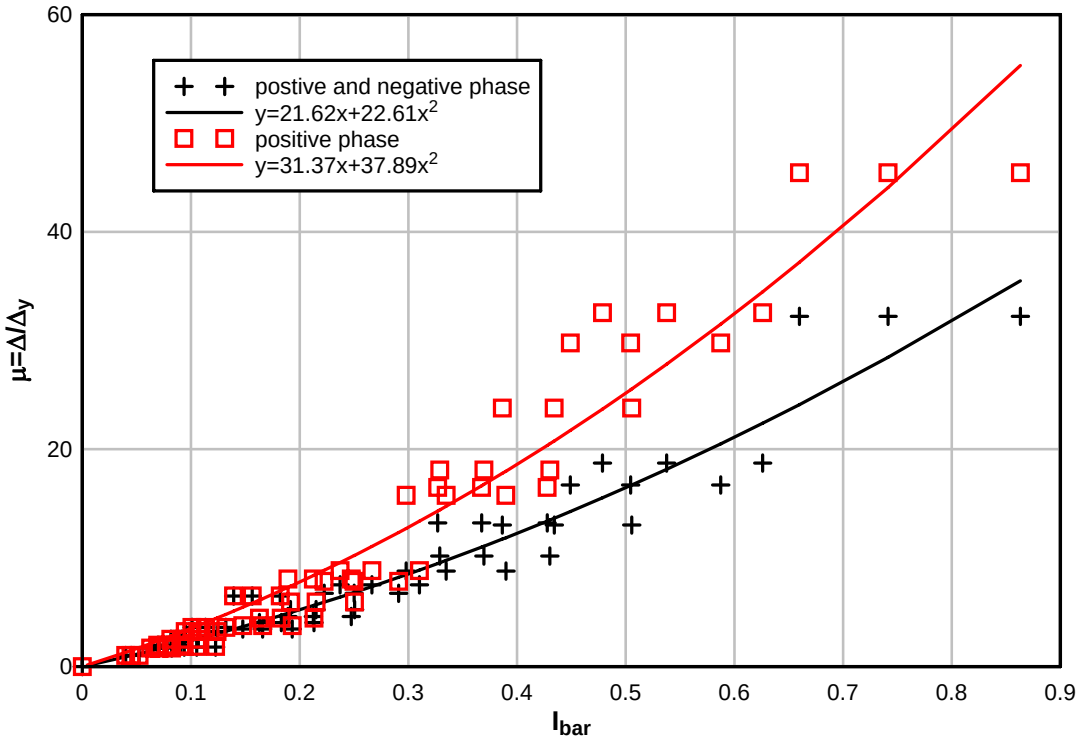

Figure 3.55: Non-dimensional impulse versus ductility demand

Inspection of equation (3.10) reveals that an increase in the mass or an increase in resistance will decrease the non-dimensional impulse because these terms are in the denominator. In the figure it can be observed that for lower values of I_{bar} the analyses with and without the negative phase produce similar ductility demands. As the non-dimensional impulse increases, or the mass and resistance decrease, the ductility demand for the load with only a positive phase is significantly greater than the load with a positive and negative phase. The results for the analyses with both load types were fit with 2nd order polynomial curves that were constrained to pass through the origin. These curves are also plotted in Figure 3.55.

3.7.3 RELATION BETWEEN BLAST LOADING AND BLAST SIMULATOR LOADING

A method that uses SDOF analysis can be used to relate the loads generated in the field due to an explosion to the loads generated in a blast simulator wall test. The main assumption of the method is that the behavior and damage modes suffered by the walls are similar for both loading types. The first step is to define the blast load with negative phase that is applied to the wall. This load is then applied to the wall in a SDOF analysis to measure the peak response. Typically, the peak response considered is the peak displacement or residual displacement because they are used by the design guidelines to estimate levels of damage. Ideally, if field test data exist it has been verified that the SDOF accurately predicts the response. Once the peak response is calculated for the blast load case with the negative phase the wall can then be analyzed using the SDOF-type of analysis that models the BG impacts as described earlier in this chapter. The initial velocity used in the model of the blast simulator test should be selected so that the impulse delivered matches the positive phase impulse of the blast load. Using conservation of linear momentum and the equation of coefficient of reinstitution (equation (3.3) the following expression can be derived to relate BG impact velocity, v11, to the positive phase impulse, i^+:

$$v_{11} = \frac{i^+(m_{bg} + m_{eq})}{(1+COR)m_{bg}m_{eq}} \tag{3.12}$$

where m_{bg} is the mass of the BG impact plates and m_{eq} is the effective mass of the specimen. Equation (3.12) requires a value of COR which can be estimated to be equal to approximately 0.5. Accuracy of the value of COR is not essential in this initial

calculation because the next step requires iteration and uses the programmer model that has been validated for a large range of BG impact velocities in section 3.4.8. The impact velocity determined from equation (3.12) can then be input into the SDOF model that included the BG impacts. The response of the wall calculated by this model can the be compared to the response of the wall with the blast load; if the responses are similar then the BG velocity is used in the experiment; if the responses are not similar the BG velocity is adjusted and the analysis is re-run. This process will be repeated iteratively until the responses from the two types of loads converge.

It is recommended, when using this methodology, to also model the specimen with high fidelity physics based numerical tools. This additional analysis should be performed to verify the assumption that the behavior and damage modes of the wall to the loads in the field and in the laboratory are similar. High fidelity physics based calculations are especially important for situation when the behavior of the specimen is not understood very well. In these situations the basic assumptions used for SDOF-type of analysis may not be applicable.

3.8 SUMMARY

The purpose of this chapter was to introduce the reader to the blast simulator. Included in the chapter was a detailed description of the blast generators and the laboratory infrastructure. The methodology used to calculate the impulse in the blast a simulator test was presented. This methodology uses integration of acceleration and differentiation of displacement data to converge on the impulse delivered by the BGs. Issues regarding the programmers were also discussed and a test program used to

characterize the energy losses in the programmers was described. The data generated in the ballistic impact test was used to validate a one-dimensional model used with SDOF analysis. This SDOF model was demonstrated to have the capability of predicting the loads delivered by the BGs to specimens in full scale tests. The data was also used to validate a 3D material model that can be used in FE simulations of blast simulator tests. This model currently cannot be used to predict impulses delivered by specified BG impact velocities, but the parameters can be adjusted so that the model can match measured impulses a posteriori. Finally, the results of a test series conducted with the blast simulator were presented and compared directly to field data on nearly identical walls. The conclusions drawn from this comparison are:

- The blast simulator can generate damage modes that are similar to those experienced in an actual blast.

- The effect of the negative phase is significant for walls with relatively low mass and/or stiffness. For these types of walls correlation between air blast and blast simulator loads through the positive phase impulse could result in a considerable over-estimation of ductility demand.

4 CMU WALLS WITH CFRP RETROFITS

4.1 INTRODUCTION

A common structural component for frame type buildings is concrete masonry unit walls. These walls typically consist of a combination of the following materials: concrete block, grout, mortar, and rebar. This wall type is frequently used because it is inexpensive and it provides significant axial load capacity. In a blast environment, however, this type of wall is susceptible to failure in the out-of-plane direction at relatively low load levels. Carbon fiber reinforced polymer composites are a suitable retrofit in this situation because they are light weight and can be installed with relative ease in comparison to other retrofits, such as steel backing plates. In this chapter a retrofit solution using a CFRP composite was investigated with the blast simulator to assess its effectiveness in mitigating blast hazard for CMU walls. The data generated in the tests was used to validate an SDOF model and an FE model. The validated FE model was then used to study different design scenarios where the loads and the number of layers of CFRP were varied. The results for these tests have been summarized using PI curves. The chapter concludes with design recommendations based on the parametric studies along with suggestions on future areas of research.

The scope of this chapter includes a summary of experimental work performed on full-scale CMU walls with CFRP retrofits, the validation of SDOF and FE models of the walls with the results, a parametric study of CMU walls with CFRP retrofit where the load parameters and the design of the retrofit are varied, and finally a list of design guidelines for using CFRP to retrofit CMU walls against blast.

The following are the objectives of this chapter:

- Provide information on the response of CMU walls with CFRP retrofits to blast like loads
- Validate both SDOF and FE models that can be used to study behavior of CMU wall types
- Demonstrate that the blast simulator is a viable method for proof-of-concept testing and for validating numerical tools
- Develop PI curves for CMU walls with different CFRP retrofit designs

4.2 PREVIOUS RESEARCH

Experimental work investigating blast resistance of CMU walls with FRP has been conducted over the last several years. Muszynski and Purcell [34] performed several tests on full scale air-entrained concrete masonry walls including one test that directly compared an unprotected wall to a wall with CFRP laminate strips on the back side. The unprotected wall collapsed and the blast loads breached into the occupant space. The retrofitted wall had considerable spalling on the front face and all the mortar joints had suffered damage, but only had 0.12 in. of residual displacement at its midspan.

Carney and Myers [35] investigated small scale un-grouted URM walls uniformly loaded with an air bag. The tests included several different retrofit schemes that used both glass fiber reinforced polymer (GFRP) rods and GFRP laminates strips to strengthen the wall in the out-of-plane direction. The anchorage detail at the top and bottom boundary conditions were paid close attention to and included an epoxy filled groove to

attach the laminate to the termini. A shear retrofit was also investigated, based on similar work of Meyer et al. [36] that identified a shear problem at the base of walls reinforced with FRP. The test setup used in the program was designed to allow for the walls to develop arch action. Results showed that the wall with anchored laminates performed significantly better than the walls with an unanchored laminate. The unanchored walls with laminate, however, still had an increase in strength over the unreinforced walls. For the case of the walls that used GFRP rods, the wall with anchored rods had increased strength over the unreinforced wall, while the wall with unanchored rods had no improvement. None of the walls had shear failures so the effectiveness of the shear retrofit was inconclusive. Photos showing the scatter of debris of the failed wall show that the laminate strips perform slightly better over the rods for containing the blocks.

Myers et al. [37] tested eight full scale ungrouted, URM walls with three different retrofit types including horizontal GFRP rods, vertical GFRP strips, and both horizontal rods and vertical strips. Four of the walls were constructed with 4 in. x 8 in. x 12 in. block and the four other with 8 in. x 8 in. x 16 in. block. The test setup consisted of a steel frame with boundary conditions that were capable of developing arch action. Un-reinforced walls responded impulsively and failed out-of-plane with a tensile failure mode in regions of high flexure. In one series of tests on retrofitted walls with FRP strips the laminate resisted the tensile stress and the masonry only resisted the compressive stress. The elastic energy stored in the FRP was large enough that shear failure occur upon rebound. The capacity of the wall to resist blast was limited by the shear capacity of the masonry because there was no mechanism to transfer the rebound forces to the

boundaries and the FRP retrofit did not add to the shear strength of the wall. The walls would protect the occupants from an initial attack, but will not be functional against an additional attack. The authors concluded that a FRP laminate is still a desirable retrofit even though walls fail because the scatter is more contained and the failure occurs on the rebound away for building occupants whereas the unreinforced walls fail inward in a brittle flexural mode.

Tan [38] conducted static and field blast tests of brick masonry walls with glass and carbon FRP retrofits on the back side. Walls were anchored to the supports and deformed with two-way action. Four failure modes were identified in the static tests: flexural compression due to brick crushing, punching shear at the location of load application, flexural bond failure from FRP delaminating, and tensile failure of the FRP. The results of the static tests were used to develop load resistance relations with failure modes that could be used with simplified methods to predict the dynamic response in the field tests. In the dynamic tests the walls with FRP failed at higher loads than the unreinforced walls. Predictions of wall displacements and FRP strains calculated with FE simulations matched field data well.

Tan and Patoary [39] summarized 30 of the static tests of the previous test series. They investigated the failure modes and the ability of the design equations and tools to capture the response. The walls underwent two-way bending and experienced the four types of failure that are listed above. It was concluded that load capacity increased with increase in laminate thickness. Specimens without an anchorage system failed

prematurely through FRP debonding from the masonry bond interface. Specimens with proper anchorage details failed in punching shear or crushed brick in compression.

Baylot et al. [40] tested 43- quarter-scale walls in the field to produce data that could be used to improve the analysis program *WAC* [41]. Data presented for each test included the level of damage done to the wall by the load and the hazard presented by debris generated by the blast. Several types of walls were tested including: unreinforced, ungrouted walls, partially reinforced and grouted walls, fully grouted, unreinforced walls GFRP retrofitted walls, spray-on polyurea retrofitted walls, and steel backed retrofitted walls. Static tests were conducted to determine resistance functions for each wall type. They found that the debris velocity was directly related to impulse, but they conclude that debris velocity is not a good indicator of hazard level. Also, all of the retrofits were successful in reducing the hazard level inside the structure. In the cases with the steel retrofitted walls the bolts connecting the plate to the support structure failed, which resulted in debris entering the structure for both the ungrouted and partially grouted walls. For the ungrouted walls the FRP and polyurea were successful in preventing the debris from entering the structure, but the connection of the retrofit to the reactions began to debond. Partially grouted walls with FRP and polyurea retrofits were also tested with and without steel clamps to connect the retrofit to the supports. In the tests without the connections both the FRP and the polyurea retrofitted walls debonded at the top and the wall fell into the occupant space The connection for the FRP consisting of steel clamping plates also failed in the tests when the FRP pulled out from underneath the

clamp. The polyurea retrofitted walls the debris was contained and the wall stayed in place, but the polyurea did have significant tears near the steel clamps.

Dennis et al. [42] also discussed testing on the one-way unreinforced, ungrouted quarter scale CMU walls from [40] with the objective of validating numerical simulations used to predict the response the walls to blast loads. The program included one static test loaded uniformly with a water bladder and five dynamic tests with live explosives. The FE model was constructed with DYNA3D and used a concrete model with CMU material properties as the input parameters. In the model every vertical and horizontal mortar joint was modeled with a contact surface with a failure criterion. It was found that the material model used over predicted the static capacity of the wall and also under predicted the displacement response of the wall to the blast loads. The analysis also did not predict the failure modes accurately for the cases where the wall failed and suffered total collapse. The researchers suggest that this is because the model does not accurately simulate the loss of mortar at the horizontal joints that was observed in the experiments. Without modeling the loss of the mortar the wall can still develop friction and membrane forces across the horizontal joints and the wall remains stable. Despite the inability to capture the wall failure observed in the experiments the authors did conclude that the model was capable of accurately predicting the level of hazard to the occupants of the building because the walls failed with no horizontal velocity.

Urgessa et al. [43] conducted one full-scale field test in which four un-reinforced masonry walls retrofitted with four types of reinforcement were subject to a blast load. The objective of the experiment was to develop design guidance for walls retrofitted with

GFRP and shotcrete based on the results. Additionally, the authors wanted to validate their formulation for a simplified non-linear dynamic analysis used to predict response of these wall types to blast loads. All four specimens were retrofitted with E-glass on the outside face of the wall; two different fabric weights were considered (49 oz./yd^2 and 96 oz./yd^2) and two of the walls also had 2 in. of shotcrete on the inside face. Steel angles were used to anchor the FRP to the end supports allowing for membrane action. The walls were loaded from the inside simulating a letter bomb. The authors only reported the results of the wall with shotcrete and the 49 oz./yd^2 E-glass. The GFRP of this specimen remained bonded to the walls and the steel angles used to transfer the loads to the supports. The author notes that the shotcrete adds mass to the wall and suggests that it protects the masonry from the blast effects enabling it to resist flexural deformation. The authors compared the results from the experiment to their SDOF model. The measured deflection was 5 in. and the analysis predicts a deflection of 6.2 inches.

Wesevich and Oswald [44] compiled results of 236 field and shock tube tests on conventional masonry walls with various spans, thicknesses, supports, and reinforcements. In the study they classified damage level in each test as reuse, replace, collapse, and blowout. The empirical data was then used to create non-dimensionalized pressure-impulse damage iso-curves. The study included data from 15 shock tube tests on CMU walls retrofitted with E-glass composites. The CMU wall construction included both unreinforced, ungrouted walls and reinforced, grouted walls. The damage in the walls was correlated to peak end rotation; if the rotation was below 7° the wall would be reusable and above 7° the wall would be replaced.

The authors found that the walls tended to be governed by shear failure modes at the higher levels of damage over flexural modes such as compression crushing or composite debonding. They also noted that TM 5-1300 [6], which was used to calculate the flexural capacity for the non-dimensionalized variable of the PI diagram, does not take into account any shear capacity increase due to strain rate effects or from in-plane confinement provided by longitudinal reinforcement. The authors concluded by showing that the retrofitted walls can delay the onset of wall replacement and collapse. They also state that additional research and testing is needed to validate the impulse sensitive portion of the P-I diagram.

Stanley et al. [45] performed a blast test on 8 in. thick unretrofitted, unreinforced walls with and without an FRP retrofit. The retrofit in the test consisted of multiple layers of bi-directional carbon fiber fabric, glass fiber fabric, and rigid carbon laminate strips in an epoxy resin on the interior and exterior faces of the wall. The results of the test demonstrated that un-retrofitted wall failed catastrophically while the retrofitted wall remained standing albeit a 3 in. permanent outward displacement that occurred upon rebound. Damage to the structure was limited to slight cracking on the exterior face near the support.

In a similar manner Stanley et al. [46] tested two walls, one retrofitted and one unretrofitted. The retrofit consisted of a uni-directional glass fabric with epoxy resin and glass fabric anchors which connected the top and bottom CMU block courses to the supports. Both walls in the test failed from the blast loads. The retrofitted wall was

successful in limiting the generation of debris, but completely collapsed when the composite failed.

In summary, several studies have been conducted on FRP retrofitted CMU walls, which have shown that FRPs are effective for increasing resistance against blast load. The data generated in these test, however, is limited by lack of quantity and in some cases quality. This lack of data was the motivation of the study performed with the UCSD Blast Simulator on fully grouted, reinforced CMU walls with CFRP retrofits.

4.3 EXPERIMENTAL WORK

4.3.1 INTRODUCTION

Laboratory tests simulating the effects of blast wave generated in the detonation of high explosives or from vapor cloud explosions on CMU walls with CFRP retrofits were conducted with the UCSD Blast Simulator between February 6th and April 8th, 2008. The experimental work included six tests on three fully grouted walls each with two #4 longitudinal bars spaced at 42 inches. The walls were built from 8 in. x 8 in. x16 in. CMU blocks and were 4 ft wide and 8 ft 8 in. tall. All three walls were retrofitted on the back side with four layers of CFRP laminate and one wall also had an additional two layers of CFRP on its front side. Table 4.1 is a matrix for the blast simulator tests on the CMU walls. It should be noted that Tests 2, 3, and 5 were performed on specimens that had already been damaged in a previous test. In Test 2 and Test 3 a jack was used to push the base of the wall back to its original position prior to the previous test and the CMU face shell that had spalled was bonded on with an epoxy to provide a plane impact surface. In Test 5 the wall was pushed back into position and the portion CMU face shell that spalled off was replaced by patching material and a portion of the CFRP laminate on the front face was replaced.

Table 4.1: Test Matrix

Test	Date	Specimen	Layers of CFRP		Target Velocity
			Front	Back	
1	02/06/2008	1	--	4	13.1 (4)
2	02/19/2008	1*	--	4	19.7 (6)
3	02/25/2008	1*	--	4	26.2 (8)
4	02/29/2009	2	--	4	23.0 (7)
5	03/21/2008	3	2	4	23.0 (7)
6	04/08/2008	3**	2	4	26.2 (8)

* Specimen was retested with only minor repair work
** Specimen was retested with repair of spalled concrete and replacement of front CFRP

4.3.2 TEST SPECIMENS- CMU WALLS

The three CMU walls tested were built for a NEES sponsored research projected that was conducted on the UCSD LHPOST (large high performance outdoor shake table) at ESEC (Englekirk Structural Engineering Center) [47]. The focus of this test program was connections between brick veneers and infill walls, including CMU. In the tests the brick walls were excited by the inputted ground motion, but the infill walls were braced preventing them from responding. As a result, the infill walls were undamaged after the tests and could be used to investigate retrofit methods with CFRP for walls subject to explosive loads.

The walls were constructed with 8 in. x 8 in. x 16 in. CMU blocks and were 4 ft wide by 8 ft 8 in. tall. In each wall the cells were fully grouted and there were two #4 longitudinal reinforcing bars spaced at 42 in., symmetric about the centerline. The bars spanned from the top to the bottom of the wall where it was connected to a reinforced concrete footing with 24 in. long lap splices. The laps were with #4 starter bars that were embedded 18 in. into the footing and terminated with 90° hooks. In the transverse direction the walls have W1.7 ladder type joint reinforcement that was spaced at 16 in. on center and had cross wires at 16 in. on center. Also in the transverse direction were four # 4 reinforcing bars; one located in the bottom course, one near the midspan, and two in the top course.

The footings at the base of the wall were 3 ft deep, 5 ft long, and 1 ft 8 in. tall with a 1 in. lip that was flush with the front face of the CMU. The RC footing was reinforced with six #6 bars top and bottom and had #4 hoops spaced at 6 in. on center.

There were also PVC ducts embedded in the footing for post-tensioned tie-downs to the shake table. Unfortunately, the hole pattern in the footing did not match the pattern of the isolated slab in the blast lab.

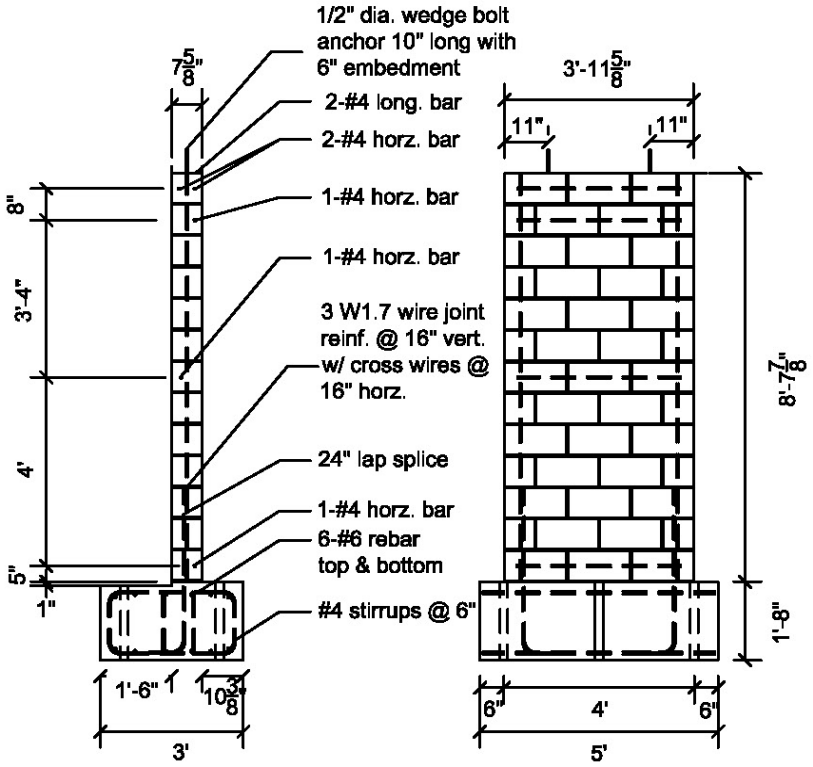

Figure 4.1: Specimen Details

4.3.3 CFRP RETROFIT

All three CMU test specimens were retrofitted on their non-impacted side with four layers of CFRP. The laminate was applied with a wet lay up procedure by Slater Waterproofing, Inc. on January 21st and 22nd, 2008.

The CFRP consisted of unidirectional 18 oz. carbon fabric and a two part epoxy resin provided by Edge Structural Composites, Inc. The carbon fabric used for this retrofit was *VelaCarb 600U* and the epoxy resin was the *Veloxx LR*. The retrofit also

used *Veloxx AP*, a two part two component epoxy paste that is used for bonding and filling voids before the application of the CFRP system.

There were several steps in the wet lay up procedure for applying the CFRP to the CMU walls. The wall was first prepared with a hand grinder to eliminate any irregularities on the surface and to provide a porous substrate for optimum bond strength between the laminate and the wall. The two components of the epoxy resin were then mixed and applied to the freshly prepared surface as a primer coat. Following the application of the primer, a putty paste was spread on the wall to smooth the surface at the locations of the mortar joint. Application of the paste prevents the CFRP laminate from bridging over the joints, which could result in a localization of strain and cause the laminate to fail prematurely.

The carbon fabric was impregnated with epoxy using a drum type resin bath. Each layer of fabric was pulled through the bath once before it was hung on the CMU walls. The saturated fabric was hung on the wall one layer at a time with a short delay after the first two layers to allows them to dry before the last two layers were added. This was done to reduce the weight carried by the uncured laminate, preventing the fabric from sliding down. The fabric was smoothed after application as to provide an evenly distributed bond. The fabric on the sides and the bottom was cut after application to eliminate any laminate hang over the edges.

The third CMU test specimen was also retrofitted with two layers of CFRP on its front face on March 12th, 2008. This specimen had additional retrofit work done following the testing of the first two walls. The CFRP on the front was also applied with

a wet lay up method that was almost identical to the one previously describe. The only difference was that the fabric was not impregnated with a drum type resin bath. Instead the resin was applied by hand with a paint roller and a squeegee.

4.3.4 TEST SETUP

The setup for the retrofit CMU wall test series is illustrated in Figure 4.2 and Figure 4.3, which depict elevations from the south and the east, respectively. The span of the wall was 8 ft 4 inches. The wall was supported at the top and bottom allowing for one-way bending. The top support was simple and the bottom had a fixed boundary condition where the wall was connected to a reinforced concrete footing by lap splices with 24 in. long starter bars. The pattern of the holes for post-tensioned tie downs in the footing did not match the pattern of the reaction slab because it was originally designed for tests on the shake table. Therefore, it was attached to the slab by 8 in. x 8 in. x 1 in. steel angles that were connected to the sides of the footing with 3/4 in. diameter wedge anchors. The angles were each then post-tensioned to the reaction floor with 1 3/8 in. diameter Dywidag bars. The connection is shown in Figure 4.4.

Shear forces at the base were transferred to the moveable reaction wall through reinforced concrete spacer blocks. The top of the wall reacted in bearing against a 6 in. thick RC slab where it was allowed to rotate and to translate in the vertical directions. The bearing support did not provide any mechanism to prevent separation with the top of the wall during rebound. This was prevented with two tie back rods that ran through holes drilled in the wall and attached to an angle that was bolted to the bottom of the 6 in. thick RC slab. Figure 4.5 displays the tieback connection from the front and back of the

wall. The shear forces that developed at the top of the wall were transferred through the slab to the moveable reaction wall. The slab was supported at the wall with steel angles mounted to plates that were post-tensioned to its front face. The other side of the slab nearest the specimen was supported by two struts made from hollow shaped tube section. These struts were welded to a mounting plate that was also post-tensioned to the front face of the movable reaction wall.

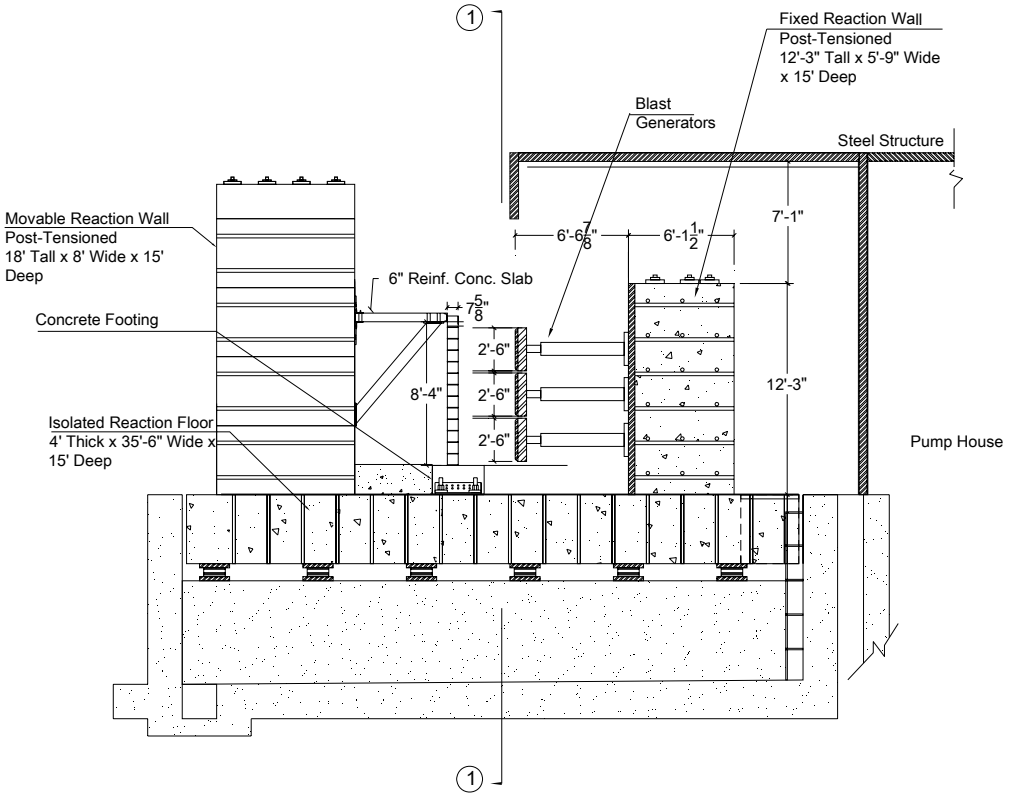

Figure 4.2: Test Setup (South Elevation)

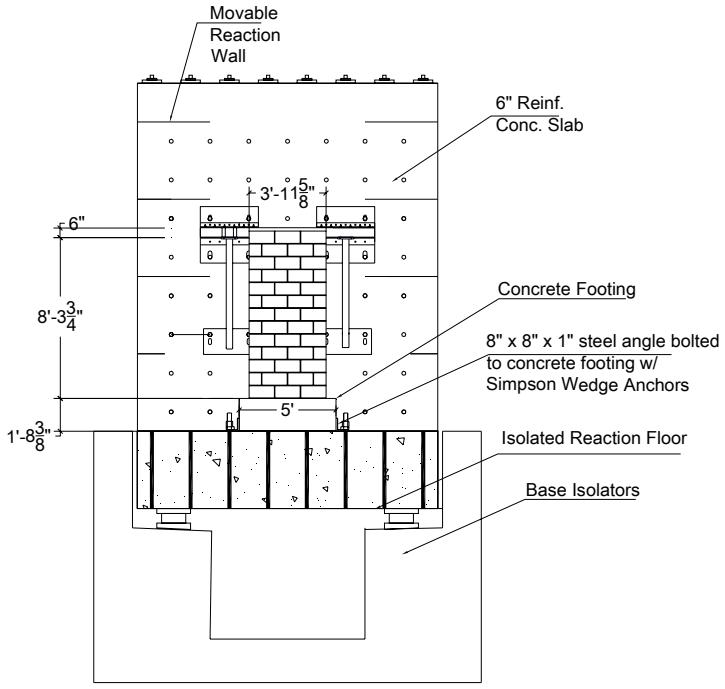

Figure 4.3: Test Setup (East Elevation)

Figure 4.4: Connection of footing to reaction slab

Figure 4.5: Tie back connection at top

An array of three blast generators was used to load the specimens in this test series. The dimensions of the BG impact plates were 30 in. x 48 inches. The plates are accelerated to the desired target impact velocity by a 94 lb (42.6 kg) piston rod, which it is attached with four 3/8 in. diameter breakaway bolts The plates are guided on the north and south side by 1 7/8 in. x 1 5/8 in. steel rails that extend past the impact plane of the wall to prevent the BG plates from coming off of the rails when the break away bolts fail.

The loading protocol used in the blast simulator tests on the CMU wall specimens used all three BGs, which impacted the specimen simultaneously at uniform velocities. The purpose of this type of loading was to produce a response in the wall that is equivalent to what it would experience in an actual explosive event.

The center-to-center spacing of the plates was 31 in., which left a 1 in. gap between the plates. At the top and bottom of the specimen there was a 4 in. gap between edges of the BG plates and the edges of the support. Following the first test a 3 in. x 3 in. angle was added to the bottom behind the wall to provide additional resistance. As a result the gap at the bottom between the top of the angle and the bottom of the BG

decreased to 1 inch. Throughout this chapter the BGs are labeled 1-2-3 from bottom to the top.

4.3.5 INSTRUMENTATION

DATA ACQUISITION SYSTEM

A high speed data acquisition system from *Hi-Techniques* was used. This system samples at 14 bits and 1 MHz. Currently the data acquisition system has a capacity of 52 channels. It is externally triggered from the MTS controller that is used to fire the BGs.

HIGH SPEED VIDEO

High speed video was captured with three Phantom v7.1 (Vision Research) cameras. The first camera recorded in black and white at a rate of 5000 frames per second at a resolution of 400 x 600. The other two cameras recorded in color and also ran at a rate of 5000 frames per second with a resolution of 400 x 600. The cameras were externally triggered from the MTS controller. TEMA software package from Image Systems was used to obtain graphical displacement and velocity measurements from the video capture.

The cameras provide visual evidence of the test that is used to observe specimen behavior under impulsive loading. Phantom camera 1 (black and white) was placed on the north side of the test setup and was used to measure displacements and velocities of the entire wall. The video from this camera was also used to determine the impact velocities of the BGs. Phantom camera 2 (color) was placed behind the wall and recorded the behavior of the CFRP laminate and the connection at the base. Phantom

camera 3 (color) was equipped with a zoom lens and was placed on the north side of the setup to record the behavior of the wall near the top support. A plane view of the test setup with the location of the cameras is shown in Figure 4.6.

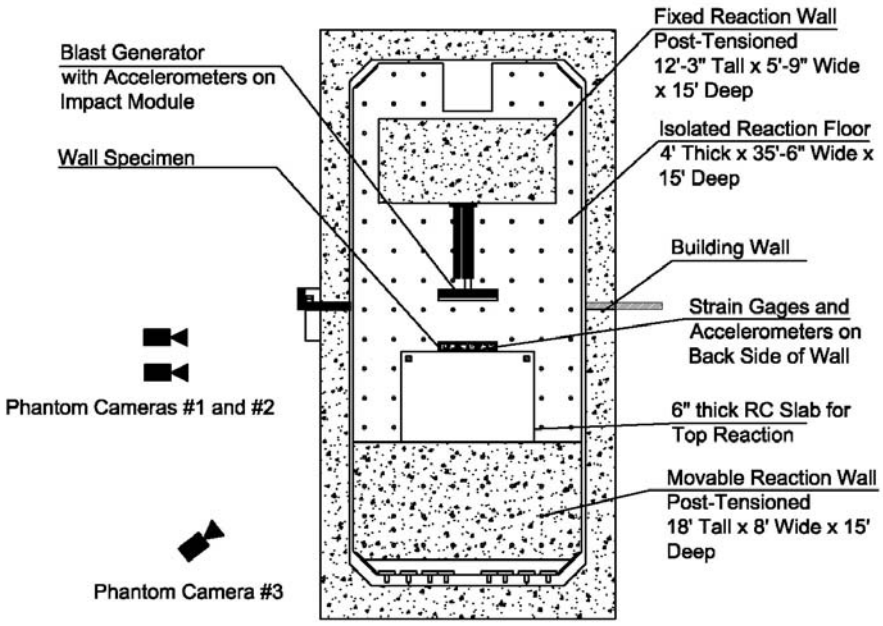

Figure 4.6: Plane view of test setup with camera locations

BG ACCELERATIONS

The accelerations of the BG impact plates during impact were measured with 10K g piezoelectric shock accelerometers. Four gages were mounted on each BG impact plate to ensure accuracy and redundancy. The acceleration signal of four different accelerometers was typically averaged and integrated to measure the impulse delivered to the specimen during the test. The gages were mounted to the back of the plate to the right, left, top and bottom of the center of gravity as shown in Figure 4.7. The cables that transmit the acceleration signal to the data acquisition system were fastened to the BGs to

minimize artificial signals in the data caused by their vibration. The accelerometer configuration for the BGs can be seen in Figure 4.8.

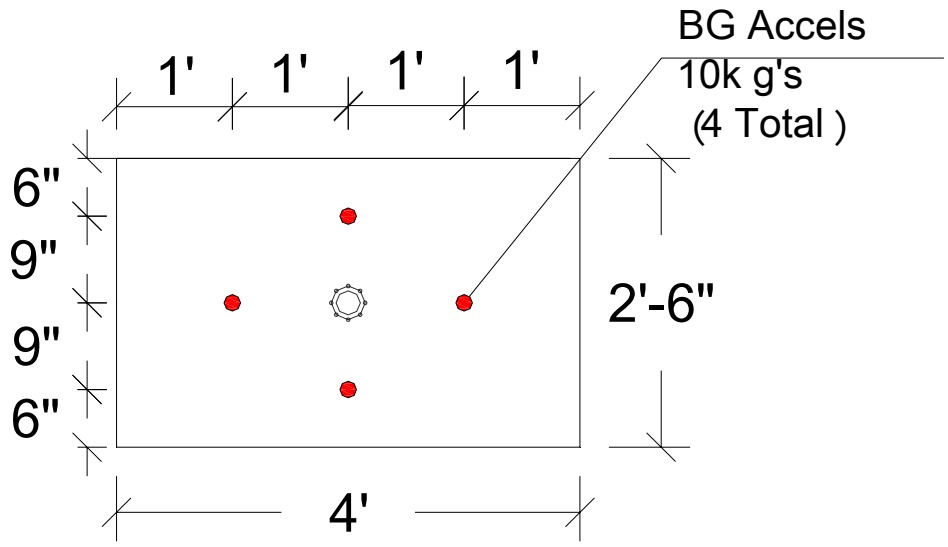

Figure 4.7: BG accelerometer locations

Figure 4.8: BG accelerometers configuration

BG VELOCITIES

The velocity for each BG was determined from the Phantom video record using the TEMA software package. For each BG, a point is selected on the impact mass and the software records its displacement time history. The software then differentiates the

displacement time history using a 7 point numerical differentiation scheme to obtain the velocity time history.

SPECIMEN DISPLACEMENTS

The Phantom camera videos were used in conjunction with the TEMA software to measure specimen displacements at several different locations. The specimen displacements could be differentiated with respect to time to get the specimen velocities time histories. This was done numerically by the TEMA software. Targets were mounted on the wall before the test to assist in tracking the wall displacements (Figure 4.9). The distance from the bottom support to the larger targets used for tracking the specimen displacement are listed Table 4.2.

Figure 4.9: Tracking targets on specimen

Table 4.2: Target locations

Displacement Target	Distance from bottom support [in]
7	100
6	84
5	68
4	52
3	36
2	20
1	4

A linear potentiometer was also used to measure the specimen's midspan displacement. This was done to ensure that measurements made using the Phantom video were accurate and redundant. The free end of the linear potentiometer was bolted to the wall with a threaded rod that was embedded into the concrete with a drop-in anchor. The fixed end was bolted to the BG support tower. The location of the linear potentiometer can be seen in Figure 4.10.

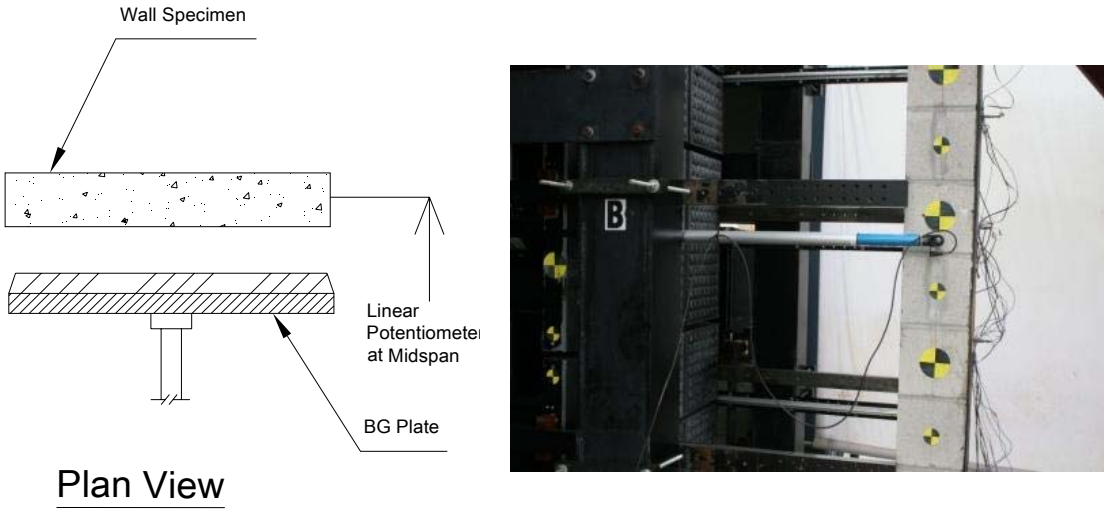

Figure 4.10: Location of linear potentiometer

SPECIMEN ACCELERATIONS

Accelerations in the wall were measured with 5K g piezoelectric shock accelerometers. One of the gages was located on the back of the wall at its midspan. The other 4 gages were mounted on the back of the wall each at the same elevation as a BGs centroid. The accelerometers were fixed to the back of the wall with couplers that were attached to 1/4 in. thread rod that was embedded into the concrete with epoxy. The cables that transmit the acceleration signal to the data acquisition system were connected

to the wall with strain relief to minimize artificial signals in the data due to their vibration. The elevations of the gages are the same as displacement targets 2-6. The locations can be seen in Figure 4.11.

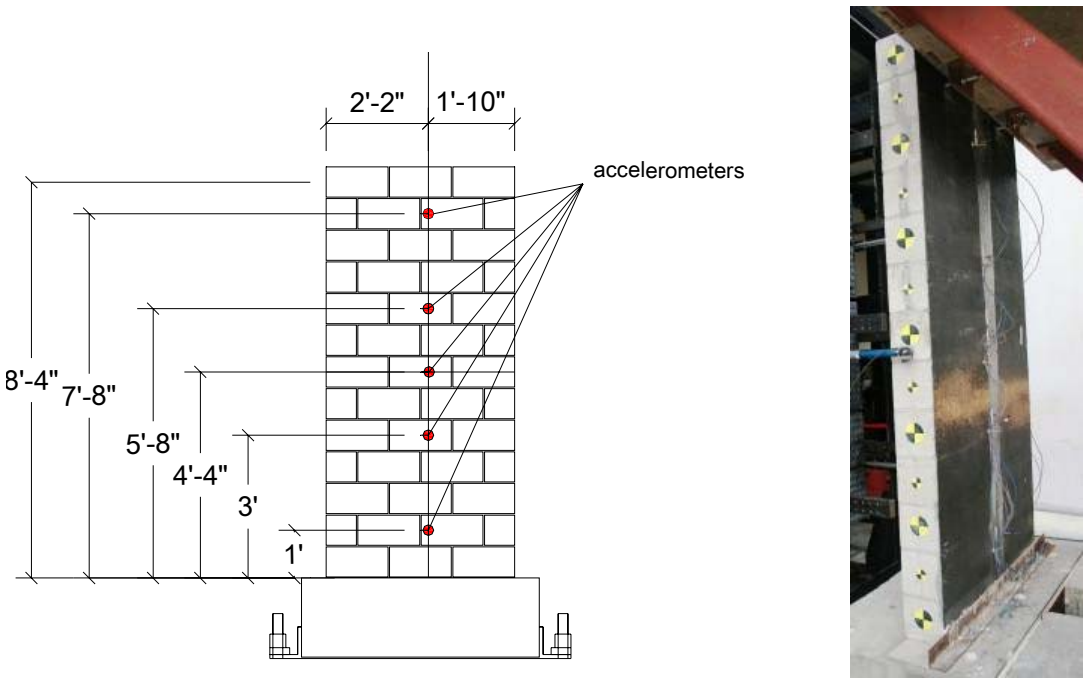

Figure 4.11: Specimen accelerometer locations

REBAR STRAINS

The strains in the reinforcing steel were measured using 5 mm gages (model *TML-FLA-5-11LT*). These are 120 Ω strain gages that have a peak strain capacity of 5%. The gages were installed on the rebar near the midspan during the construction of the walls.

CFRP STRAINS

The strains in the CFRP laminate were measured at the seven locations shown in Figure 4.12. The gages used were mostly model *TML PL-60-11-5LT*, which have a 120

Ω gage resistance, a 60 mm gage length, and the peak strain is 3%. The second and third specimen tested measured strains with the 60 mm gages except at the top and bottom locations where the strain was measured with the model *TML PL-20-11-5LT*, which had a 20 mm gage length. In the results the gages are labeled Strain 1 to Strain 7 from bottom to top.

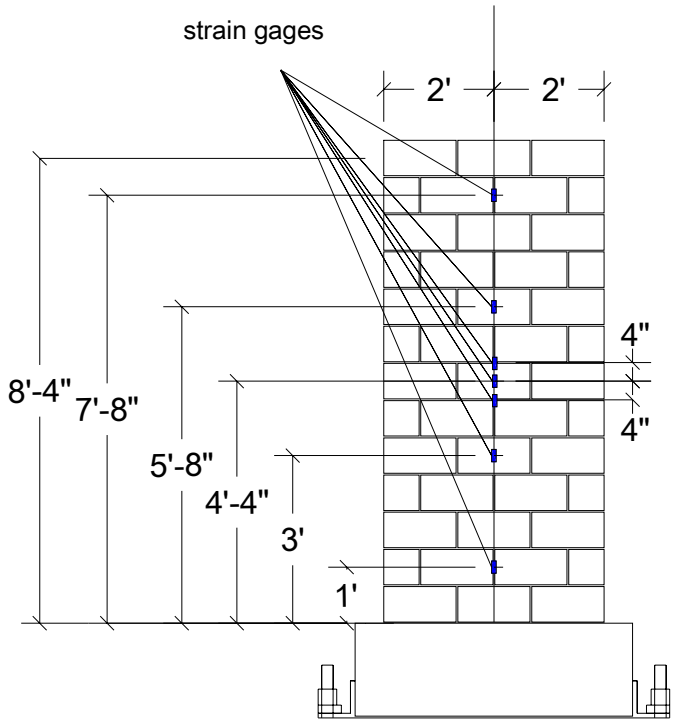

Figure 4.12: CFRP strain gage locations

4.3.6 RESULTS

TEST 1

The first specimen of the CMU wall series was tested on February 6th, 2008 at a specified target velocity equal to 13.1 ft/sec (4 m/sec). The average of the actual impact velocity for the three BGs in this test was 14.2 ft/sec (4.3 m/sec) and there was a 2.3 msec spread between the times of impact. The average impulse was 152 psi-msec. The impact loading of the BGs produced an initial velocity equal to 8.8 ft/sec at the midspan of the specimen, which resulted in a peak displacement equal to 0.64 in. at the midspan. The wall responded primarily in a flexural mode with one-way bending, however due to the larger force demands at the base the wall also had a horizontal translation. The damage in a throughout most of the wall was relatively small; the flexural cracks in the masonry were small and the CFRP was not damaged (Figure 4.13). The wall did, however, have some noticeable damage at the base where it translated. When the wall moved the dowel action of the starter bars cracked the nearby CMU block and grout which caused the front face of CMU to spall off, as shown in Figure 4.14.

Figure 4.13: Test 1- CMU 1 post test

Figure 4.14: Test 1- CMU 1 bottom support post test

TEST 2

The first CMU wall was repaired after the initial test and was impacted by the BGs a second time on February 19th, 2008 at a specified impact velocity equal to 19.7 ft/sec (6 m/sec). The wall had a permanent translation equal to 5/8 in. at its base and in order to bring the wall back to plumb the bottom was forced back to undamaged location with a hydraulic jack. The wall also had two large pieces of CMU and grout that spalled near the base as a result of dowel action of the starter bars. These pieces were re-attached to the wall with epoxy so that the wall had an even surface when the BGs impacted it. A 3 in. x 3 in. x 1/4 in. steel angle was also added to the wall at its base to provide some resistance to the loading because the capacity was significantly due to the level of damage that occurred in the previous test. The BGs impacted the wall with a velocity equal to 19.3 ft/sec (5.9 m/s) and a time spread equal to 1.2 msec. The average impulse from the three impacts was 215 psi-msec. The impact loading of the BGs produced an initial velocity equal to 13.7 ft/sec at the midspan of the specimen which resulted in a peak displacement equal to 1.1 in. also at the midspan. The damage in the wall following this test was similar to the previous test; damage was almost non-existent along the span except at the base were the wall translated and in this test the anchors of the angle exhibited significant plastic deformation. Figure 4.15 displays the wall after the test and Figure 4.16 displays the damage done at the base. Much of the damage done in this test was in the location where the CMU and grout that were rehabbed after the first test. Inspection of the angle revealed that it was not damaged, but that the wedge anchors that were embedded into the footing concrete had been severely deformed.

Figure 4.15: Test 2- CMU 1 post test

Figure 4.16: Test 2- CMU 1 bottom support post test

TEST 3

The first CMU wall was repaired a second time after the second test and was impacted by the BGs a third time on February 25th, 2008 at a specified impact velocity equal to 26.3 ft/sec (8 m/sec). A significant portion of the wall including the top support was undamaged following the previous test, but it did have a permanent translation at its base. It was brought back to plumb again with a hydraulic jack and a 3 in. x 3 in. x 1/4 in. steel angle was also used at its base to provide some resistance to the loading.. The damaged portions in the wall near the base that were rehabbed before the previous test were re-damaged by the impact and were rehabbed a second time, again with epoxy to bond the pieces back together. The average velocity at impact was equal to 26.3 ft/sec (8.0 m/s) and the time spread between the impacts was 0.5 msec. The average impulse from the three impacts was 293 psi-msec. This produced an initial velocity equal to 22.3 ft/sec at the midspan of the specimen.

The initial velocity generated by the impact caused the wall to reach a peak displacement equal to 1.7 in. at the midspan. Shear cracks formed in the CMU near the top and bottom support due to the loads while the front face of the specimen did not exhibit any evidence of crushing due to the bending stresses in the wall. The addition of the CFRP laminate increased the flexural capacity of the wall, but the added stiffness in the wall also increased the level of shear forces that needed to be transferred to the supports. The maximum shear forces were experienced near the supports and this is where the shear cracks formed. Figure 4.17 displays the wall after the test. Figure 4.18 displays the shear crack that formed near the top support. The crack runs along the entire

width of the wall and on the front face some of the CMU face blocks had spalled off. The damage at the base of the wall following this test was similar to the previous test; the base of the wall translated and the anchors of the angle exhibited significant plastic deformation (Figure 4.19).

Figure 4.17: Test 3- CMU 1 post test

Figure 4.18: Test 3- CMU 1 shear failure post test

Figure 4.19: Test 3- CMU 1 bottom post test

TEST 4

The second CMU wall specimen was tested in the UCSD Blast Simulator on February 29th, 2008 at a specified impact velocity equal to 23.0 ft/sec (7 m/sec). The first test had shown that the bond between the mortar and the footing concrete at the bottom joint was weak, most likely as a result from the earthquake loading that was experienced. The weak joint had resulted in a translation of the base which activated dowel action between the starter bars and the CMU/grout that surrounded the reinforcement thereby causing localized damage. Therefore, a 3 in. x 3 in. x ¼ in. steel angle was also added to the wall at its base to provide some increased resistance to the lateral loading. The average velocity at impact equal to 22.1 ft/sec (6.7 m/s) and the time spread between the BG contacts was 0.5 msec. The average impulse from the three impacts was 243 psi-msec. The impact loading of the BGs produced an initial velocity equal to 16.4 ft/sec at the midspan of the specimen which resulted in a peak displacement equal to 1.2 in. also at the midspan. The wall response initially was in a flexural mode with one-way bending mixed with a slight translation at the base. However, when the wall reached about 95% of its peak displacement a shear crack opened up near the top support. At approximately 5 msec after the first crack opened at the top, an additional crack opened near the base. The wall did not have much kinetic energy when the shear cracks opened and there was enough internal energy stored in the CFRP laminate and the rebar that the wall rebounded after reaching its peak deflection. Figure 4.20 displays the wall after the test. Figure 4.21 displays the shear crack that formed near the bottom support. Some of the damage at the base of the wall was similar to the previous test; the base of the wall translated and the

anchors of the angle exhibited significant plastic deformation causing two to fracture. The shear crack at the top can be observed in Figure 4.22. This crack is similar to the one that formed in the third test. The crack runs through the entire with of the wall and caused some of the CMU face blocks to spall off.

Figure 4.20: Test 4- CMU 2 post test

Figure 4.21: Test 4- CMU 2 damage at bottom

Figure 4.22: Test 4- CMU 2 damage at top

TEST 5

The third CMU wall specimen was tested in the UCSD Blast Simulator on March 23rd, 2008 at a specified impact velocity equal to 23.0 ft/sec (7 m/sec). This wall was similar to the previous two walls that were tested, except that it included two layers of CFRP laminate on its front side in addition to the four layers on the back. The first test in the series had shown that the bond between the mortar and the footing concrete at the bottom joint was weak, most likely as a result from the earthquake loading that was experienced in previous experiments. The weak joint had resulted in a translation of the base which activated dowel action between the starter bars and the CMU/grout that surrounded the reinforcement, thereby causing localized damage. Therefore, a 3 in. x 3 in. x 1/4 in. steel angle was also added to the wall at its base to provide some increased resistance to the lateral loading. The average velocity at impact was equal to 22.9 ft/sec (7.0 m/s) and the time spread was 0.1 msec. It appeared in the video that the top two BGs possibly impacted the specimen multiple times. The average impulse from the three impacts before the second hit was 255 psi-msec. The total impulses delivered by BG 2 and BG 3 after the second impacts were equal to 355 psi-msec and 323 psi-msec, respectively; the impulse from BG 1 did not increase after the initial impact. The increase of impulse in both BGs was about 37%. The impact loading of the BGs produced an initial velocity equal to 16.9 ft/sec at the midspan of the specimen which caused the wall to reach a peak midspan displacement equal to 0.98 inches. When the wall began to rebound, the bolts connecting the angle to the footing failed and a shear crack formed near the base causing the bottom of the wall to translate. As the wall

translated, the shear force was transferred between the wall and the footing through dowel action of the starter bars, which ultimately caused the front faces of the CMU blocks near the rebar to spall. Furthermore, the CFRP on the front face was bonded to a lip on the concrete footing and when the base of the wall translated the CFRP delaminated from the block. Figure 4.23 displays the wall after the test. Figure 4.24 displays the shear cracks and spalled face blocks at the bottom support. The top of the wall following the test was relatively undamaged.

Figure 4.23: Test 5- CMU 3 post test

Figure 4.24: Test 5- CMU 3 damage at bottom

TEST 6

The third CMU wall was tested a second time in the UCSD Blast Simulator on April 10th, 2008 at a specified impact velocity equal to 26.2 ft/sec (8 m/sec). Following the first test the wall had two areas of spall caused by sliding at the base and dowel action of the starter bars. There was also a large area of delaminated CFRP across the entire width caused by the spall and the connection conditions of the laminate. The concrete footing had a 1 in. lip that was flush with front of the wall at the bottom. The CFRP extended below the wall and onto this lip. When the wall translated at the base the CFRP remain attached to the lip and the laminate debonded from the CMU blocks.

Figure 4.25: Test 6- CMU 3 removal of CFRP and concrete spall

The wall was repaired by first moving it back to its original position at the base with hydraulic jacks. Next the delaminated CFRP and the concrete spall were removed, as shown in Figure 4.25. The figure shows that the laminate was removed at about 8 in. above the footing along the entire width of the wall. On the north side an additional 12

in. was removed around the spall area. The spall areas were then cleaned patched with SikaTop® 123 Plus as shown in Figure 4.26.

The patching material was allowed to cure for 24 hours before a new layer of CFRP laminate was added to the repaired area. Two layers of CFRP were added to a 2 ft x 4 ft area. The laminate was connected to the existing CFRP lap splice that varied along the width of the wall. Near the north side of the wall the lap was about 6 in. and over the rest of the width the lap was about 18 inches. The repair portion of the wall can be seen in Figure 4.27. Figure 4.28 shows the detail at the 1 in. lip in the footing; the laminate was terminated above the lip to prevent it from delaminating again.

Figure 4.26: Test 6- CMU 3 patched spall areas

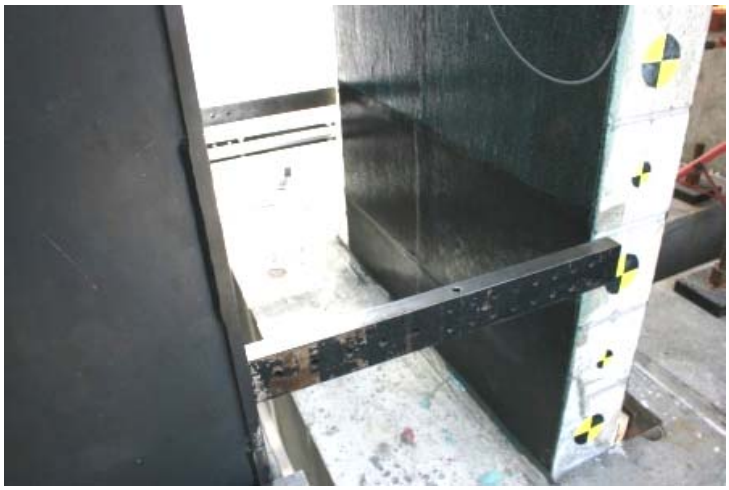

Figure 4.27: Test 6- CMU 3 repaired portion of the wall

Figure 4.28: Test 6- CMU 3 CFRP at footing lip

The final preparation of the wall before the test was to increase the number of bolts used to secure the bottom support angle. Figure 4.29 displays the angle with six bolts. Also shown in the figure are two planks of wood located between the back of the wall and the angle, which were included to soften the impact at this location during the test.

Figure 4.29: Test 6- CMU 3 angle at base

The average velocity at impact equal to 25.9 ft/sec (7.9 m/s) and the time spread between impacts was 0.8 msec. The average impulse from the three impacts was 287 psi-msec. The impact loading of the BGs produced an initial velocity equal to 23.1 ft/sec at the midspan of the specimen which resulted in a peak midspan displacement equal to 1.27 inches. The wall initially deformed in a flexural mode until 50 msec after the trigger when shear cracks formed near the top and bottom support. Following the formation of these cracks the middle portion of the wall began to move more as a rigid body. Some elastic energy was still stored in the wall after it cracked allowing for a slight rebound. The shear cracks that formed spanned across the thickness at an angle of about 30 degrees, measured from the wall's back face. The shear cracks became more vertical at the front face resulting in debonded areas of CFRP laminate. Figure 4.30 displays the wall after the test. Figure 4.31 displays the shear cracks that formed at the bottom support on the north and south side. The shear cracks at the top of the wall from the north side can be observed in Figure 4.32.

Figure 4.30: Test 6- CMU 3 post test

(a) **(b)**

Figure 4.31: Test 6- CMU 3 damage at bottom (a) north view; (c) south view

Figure 4.32: Test 6- CMU 3 damage at top

SUMMARY OF EXPERIMENTAL RESULTS

In all of the tests the retrofitted walls exhibited flexural deformation accompanied by some localized damage. None of the walls failed catastrophically under the applied loads. As non-load bearing walls, they would have protected occupants inside of a building.

Two different types of damage mechanisms were observed in the tests. The first was a translation of the base resulting in spall of the CMU face blocks near the location of the starter bars. For this situation the wall still had additional capacity to resist lateral pressures and is expected to carry gravity loads. The other damage mechanism displayed was the formation of shear cracks near the supports. No failure of the CFRP was observed in any of the tests.

The results of these tests indicate that, for non-load bearing walls; this particular retrofit has the capacity to resist even higher loads than tested. However, for load bearing walls, the shear failure observed at 6.9 m/s and above would indicate that the wall would most likely be unable to resist any significant gravity loads. Nevertheless, even for load bearing walls, this retrofit provides a large increase in lateral capacity compared to the unretrofitted wall. Results for the six tests are listed in Table 4.3.

Table 4.3: Test Results

Test	Specimen	Velocity [ft/sec (m/sec)]	Impulse [psi-msec]	Displacement [in]	Damage
1	1	14.8 (4.5)	151	0.62	Spall of CMU near starter bars
2	1	19.4 (5.9)	215	1.10	Spall of CMU near starter bars
3	1	26.6 (8.1)	293	1.71	Shear failure top and bottom
4	2	22.6 (6.9)	243	1.20	Shear failure top and bottom
5	3	22.6 (6.9)	255	0.98	Spall of CMU near starter bars
6	3	25.9 (7.9)	287	1.26	Shear failure top and bottom

4.4 ANALYSIS

4.4.1 RESISTANCE FUNCTION FOR SDOF ANALYSIS

A nonlinear resistance function has been developed to be used in the SDOF code described in Chapter 2 to predict the response of CMU walls with CFRP retrofits. The resistance function, which is generated semi-automatically with a routine within the SDOF code, is determined with a moment-curvature analysis of the retrofit section, its diagonal shear strength, and the kinematics of the deformed wall. This section will describe the method used to generate the resistance function and then provide a comparison between the model and the experimental data.

MOMENT-CURVATURE RELATION

The procedure described below is for a cross-section of a CMU wall that has CFRP on both the front and back side, but can easily be modified to include cross-sections with CFRP only on one side by setting that CFRP thickness equal to zero. The moment-curvature relation is determined for a CFRP retrofitted CMU section by varying the curvature in the section and then using strain compatibility, the constitutive relations of the materials, and equilibrium of the internal forces to calculated the associated moment. Figure 4.33 is a schematic representing a width of the CFRP section which shows the strain distributions, the associated stresses in the different components, and the internal forces that are found from the stresses. In the actual program the strain at the extreme compression fiber of the masonry is set to a specified strain. The strain in the CFRP, ε_m, is related to the curvature in the section, ϕ, by:

$$\phi = \frac{\varepsilon_m}{c} \tag{1.1}$$

and *c* is the distance from the top to the neutral axis where the strain is equal to zero..

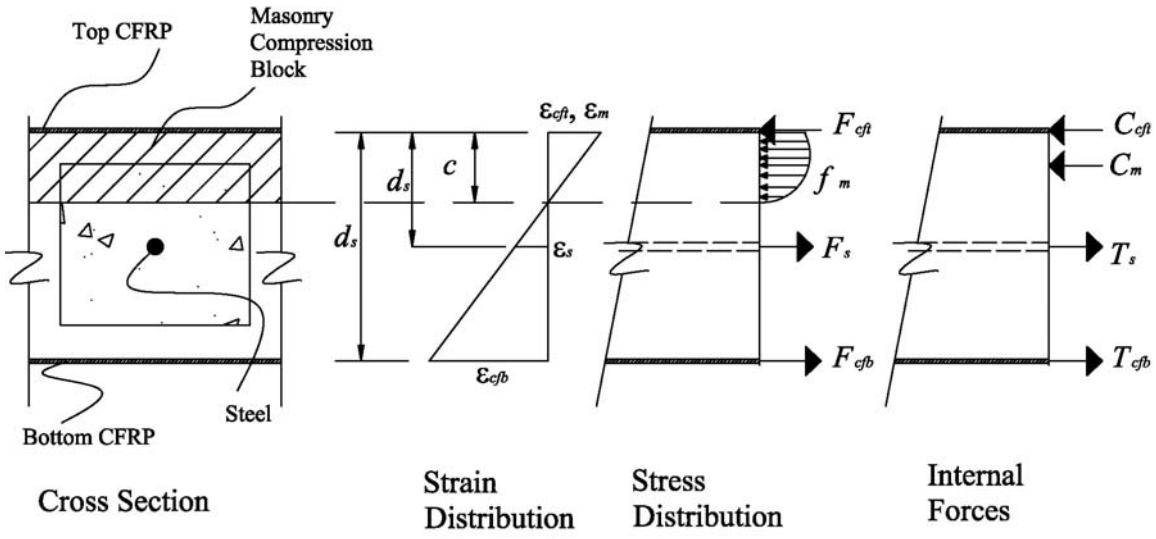

Figure 4.33: Strain distribution, stress distribution, and internal forces in CFRP retrofitted CMU wall cross-section

The strain distribution in the section varies linearly with the assumption that plane strains remain plane. Using this assumption the strain in the steel, ε_s and the strain in the bottom CFRP, ε_{cfb}, can be found with the respective equations:

$$\varepsilon_s = \varepsilon_m \frac{d_s - c}{c} \tag{1.2}$$

$$\varepsilon_{cfb} = \varepsilon_m \frac{d_{cfb} - c}{c} \tag{1.3}$$

where d_s is the distance from the top to the steel and d_{cfb} is the distance from the top of the section to the centroid of the CFRP The strain in the top CFRP is taken to be equal to the strain at the extreme most compression fiber. This is reasonable because the bottom of the laminate is at the same location as the extreme fiber of the masonry and the

thickness of the CFRP is small relative to the thickness of the compression block in the CMU.

The stress distribution in the section is then found from the strain distribution using the constitutive relations for the different materials. The stress-strain relation used for the masonry is one that was proposed by Collins and Porasz [48] to describe the uniaxial behavior of concrete. The difference when describing the behavior of the masonry is that the masonry strength, f'_m, and modulus E_m are substituted for the concrete strength and modulus. The Collins and Porasz concrete model was based on one originally suggested by Thorenfeldt et al. [49] and Popovics [50]; it was modified to account for the behavior observed in high strength concrete. The equation which is a function of the masonry strength is given by

$$f_m = f_m^{'} \frac{\varepsilon_m}{\varepsilon_{mo}} \frac{n_c}{n_c - 1 + (\varepsilon_m / \varepsilon_{mo})^{n_c k_c}} \tag{1.4}$$

where n and k are factors that define the hardening and softening of the curve when it becomes nonlinear and are given by

$$n_c = 0.80 + \frac{f_m^{'}}{2466} \tag{1.5}$$

$$k_c = 0.67 + \frac{f_m^{'}}{8992} \tag{1.6}$$

when the masonry strength, f'_m, is in psi. The model also requires the strain of the masonry at peak stress, ε_{mo}, which is given by

$$\varepsilon_{mo} = \frac{n_c}{n_c - 1} \frac{f_m^{'}}{E_m} \tag{1.7}$$

where E_m is the modulus of elasticity of the masonry is found according to a modified form of the equation given in ACI 318 [20]:

$$E_m = c_e 33 w_m^{1.5} \sqrt{f'_m} (psi) \tag{1.8}$$

where c_e is a factor that is set equal to 0.75.

The masonry also has a tensile strength. This, however, is ignored in the analysis because the tensile strength is small relative to the compressive strength and will not contribute much to the overall moment.

Typically, in addition to rebar, CMU is made from a combination of concrete blocks, grout, and mortar and each have there own stress-strain properties. In this analysis it is assumed that the strength of the whole masonry section, f'_m, can be determined with the strength of the CMU block, f'_{cb}, the strength of the grout, f'_g, and the ratio of net block cross sectional area to the gross block cross sectional area, r_{cb} with the following equation given by Pauley and Priestly [51]:

$$f'_m = (0.59 r_{cb} f'_{cb} + 0.90(1 - r_{cb}) f'_g) \tag{1.9}$$

The properties of masonry are sensitive to strain rate. In the SDOF analysis a strain rate equal to 0.2 sec^{-1} is assumed for the masonry, CFRP, and steel reinforcements. This rate is the average of the strain rates suggested by *TM 5-1300* {} for members responding in flexure to close-in design range and far design range. The strength and

strain at failure both increase with an increase in strain rate. The strain rate behavior is attributed to several factors including the limit on the rate of crack propagation, water in the voids and dynamic confinement from lateral inertia. In the analysis the strain rate effects are accounted for with a dynamic increase factor (DIF) on the masonry strength. The DIFs used for the masonry are based on expression given in Malvar and Crawford [52] for concrete given by

$$DIF = \left(\frac{\dot{\varepsilon}}{\dot{\varepsilon}_s} \right)^{1.026\alpha} \tag{1.10}$$

where the strain rate, $\dot{\varepsilon}$, is in sec^{-1} and $\dot{\varepsilon}_s$ is the static strain rate which is equal to $30x10^{-6}$ sec^{-1}. For concrete the parameter α is given by

$$\alpha_g = \frac{1}{(5 + 9\frac{f_g}{f_{co}})} \tag{1.11}$$

where f'_g is the static compressive stress and f_{co} is equal to 1450 psi. Magallanes et al. [53] adjusted the α value to match a limited amount of experimental data. For the grout this value is the same as the one used for concrete, however for the concrete block the authors suggest the following equation:

$$\alpha_{cb} = \frac{1}{(10 + 9\frac{f_{cb}}{f_{co}})} \tag{1.12}$$

In the moment-curvature analysis the strength of the grout and the concrete block is combined according to equation (1.9) to get an overall strength of the masonry. The

same expression is used with the DIFs calculated with equations (1.10) and (1.12) for the grout and equations (1.10) and (1.12) for the concrete block to calculate an overall DIF for the masonry.

The rebar model used for the analysis is a piecewise linear curve consisting of a linear elastic portion, a yield plateau, and a portion corresponding to strain hardening. Figure 4.34 displays the stress-strain relation. Table 4.4 lists the expected properties for two steel types; A615 Grade 40 and 60 rebar. The stress-strain relations are the same in tension and compression for these steels.

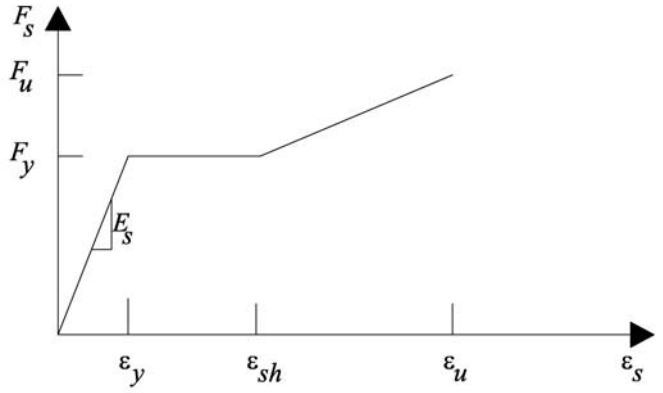

Figure 4.34: Rebar stress-strain relation

Table 4.4: Steel reinforcement properties

Type	E_s [ksi]	F_y [ksi]	F_u [ksi]	ε_{sh}	ε_u
A615 Gr. 40	29 x 10^3	48	81	0.7%	15.5%
A615 Gr. 60	29 x 10^3	69	109	0.7%	12.5%

The reinforcing steel is also sensitive to strain rates; thus DIFs are used to increase yield and ultimate strengths of the steel in the analysis. The DIFs for yield and

ultimate strength of the rebar were found with the following equations provided by Malvar and Crawford [54]

$$DIF = \left(\frac{\dot{\varepsilon}}{10^{-1}} \right)^{\alpha} \tag{1.13}$$

where for the yield stress, $\alpha = \alpha_{fy}$ and

$$\alpha_{fy} = 0.074 - 0.040 \frac{F_y}{60} \tag{1.14}$$

and for the ultimate stress, $\alpha = \alpha_{fu}$ and

$$\alpha_{fu} = 0.019 - 0.009 \frac{F_y}{60} \tag{1.15}$$

where the strain rate, $\dot{\varepsilon}$, is in $\sec^{-1}$ and the yield strength of the bar, $F_{y,}$ is in ksi.

The CFRP laminate in the model is assumed to behave linear elastically up to failure, which is defined by a failure strain. Typically, in the section analysis the masonry will crush or a shear failure will occur prior to the laminate failing. As a result, strain rate effects on the CFRP, which increase strength, but do not change the modulus of elasticity, will be ignored.

The stress in the CFRP and steel, in actuality, is distributed over the thickness of the materials, however in the analysis it is assumed that these stresses are concentrated at the centroid of the material. Once the stress distributions in the materials are known equilibrium is used to write an expression for the internal forces:

$$T_{cfb} + T_s - C_{cft} - C_m = 0 \tag{1.16}$$

where

$$T_{cfb} = A_{cfb} F_{cfb}$$

$$T_s = F_s A_s$$

$$C_{cft} = A_{cft} F_{cft}$$

where A_{cfb} is the area of the bottom layer of CFRP, A_s is the area of steel in the section, and A_{fct} is the area of the top layer of CFRP.

The equivalent force in the masonry, $C_{m,}$ is computed by integrating the stress distribution from the neutral axis to the extreme compression fiber. In the moment-curvature analysis this is accomplished using Gaussian quadrature with five points to approximate the integral. The Gaussian quadrature rule is an approximation of the definite integral of a function, *f(x)*, which uses a weighted sum of the function evaluated at specific points within the bound of integration.

$$\int_{-1}^{1} f(x)dx \approx \sum_{i=1}^{n} w_i f(x_i) \tag{1.17}$$

where w_i are the weighted values that correspond to the evaluation points, x_i. The location of the points and the weights associated with each point are listed in Table 4.5.

Table 4.5: Points and Weights for Gaussian Quadrature

Number of points, n	Points, x_i	Weigths, w_i
1	0	2
2	$\pm\sqrt{1/3}$	1
3	0	$8/9$
	$\pm\sqrt{3/5}$	$5/9$
4	$\pm\sqrt{(3-2\sqrt{6/5})/7}$	$\frac{18+\sqrt{30}}{36}$
	$\pm\sqrt{(3+2\sqrt{6/5})/7}$	$\frac{18-\sqrt{30}}{36}$
5	0	$128/225$
	$\pm\frac{1}{3}\sqrt{(5-2\sqrt{10/7})}$	$\frac{322+13\sqrt{70}}{900}$
	$\pm\frac{1}{3}\sqrt{(5+2\sqrt{10/7})}$	$\frac{322-13\sqrt{70}}{900}$

The unknown variable in equations (1.1), (1.2), (1.3), and (1.16) is, c, the depth from the top of the section to the neutral axis. In the analysis the neutral axis is determined iteratively by satisfying the equilibrium equation. The iterations are governed by the method of bisection. When the neutral axis is determined the internal forces are summed about the top to give the moment, M, with the following expression:

$$M = T_{cfb} d_{cfb} + T_s d_s - C_m \bar{a} \tag{1.18}$$

where $\bar{a}$ is the distance from the top of the section to the centroid of the nonlinear stress profile in the concrete. The equation for computing the centroid of a stress distribution, $\bar{a}$, is:

$$\overline{a} = \frac{\int x\sigma(x)dx}{\int \sigma(x)dx} \tag{1.19}$$

where x is the distance from the extreme compression fiber. The integrals in equation (1.19) were also approximated using Gaussian quadrature.

Another approach to calculate the compressive force contribution from the masonry would be to assume an equivalent constant stress block in the compression zone. For this approach the compressive force can be found with

$$C_{mu} = 0.85 f'_m ab \tag{1.20}$$

where a is the depth of the compression block. The depth of the equivalent compression block is related to the neutral axis by

$$a = \beta_1 c \tag{1.21}$$

where β_1,according to ACI [20] section 10.2.7.3, can be taken as 0.85 for concrete with strengths that range from 2500 to 4000 psi. It is assumed here that value of β_1 is also valid for the analysis of the concrete masonry.

The procedure used to calculate the moment from the curvature is repeated several times for curvatures that range from zero to the curvature at which the CFRP fails governed by a peak strain. At each increment of curvature, the strain at the extreme masonry compressive fiber is checked for spall conditions, which occurs at 0.5%. If the concrete meets this condition the analysis is stopped. A typical moment-curvature curve for a CMU wall with CFRP is plotted in Figure 4.35. The values of moment and

curvature in the plot have been normalized by the peak moment, M_u, and the peak curvature, ϕ_u, respectively.

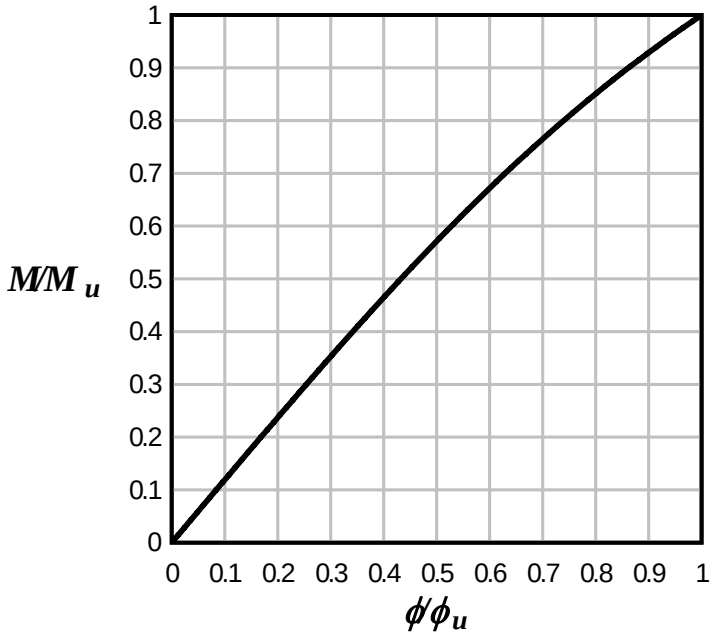

Figure 4.35: Normalized Moment-curvature relation for CMU with CFRP retrofit

RESISTANCE FUNCTION

The generation of a resistance function requires that the moment-curvature relation is idealized with only a few discrete points. The analysis used here assumes that the first point is at the origin and allows for two additional coordinates to define an elastic plastic relation. Typically, the behavior of CMU with CFRP is elastic up to failure and for this case the moment-curvature relation can be represented as a line up the maximum values followed by a plastic portion in which no additional moment occurs with increased curvature.

When the CFRP retrofit design is unbalanced, meaning that the thickness on the front is different than the thickness on the back, the moment-curvature relation for positive bending will differ from the relation for negative bending. Positive bending occurs at the midspan of a uniformly loaded wall with one-way bending and simply supported boundary conditions. When the design is unbalanced a moment-curvature relation needs to be defined for both positive and negative bending. The negative bending relation for a simply supported wall will be used to generate the resistance function used when the wall rebounds.

The peak force, R_u, resisted by a one-way wall in bending under uniform loading is found from the maximum moment, M_u, by the following equation:

$$R_u = \frac{8M_u}{L} \tag{1.22}$$

where L is the span of the wall.

The curvature at failure, ϕ_u, is used to determine the displacement associated with the peak load using the following expression:

$$\Delta = \frac{5\phi_u L^2}{48} \tag{1.23}$$

This expression can be derived by substituting $w = \frac{8M}{L^2}$ and $\phi = \frac{M}{EI}$ into the equation for peak midspan displacement of uniformly loaded elastic beam:

$$\Delta = \frac{5wL^4}{384EI} \tag{1.24}$$

The resistance function after this displacement is reached is assumed to be perfectly plastic meaning that the load remains constant for any additional displacement. The resistance function is defined for both positive and negative bending using the respective moments and curvatures. Once the resistances from flexure are determined the capacity of the wall to resist a diagonal shear failure is checked. The shear capacity of the wall, V_n, is found by

$$V_n = V_m + V_s \tag{1.25}$$

where V_m is the shear capacity of the masonry and V_s is the shear capacity of the web reinforcement. In the walls modeled here the web reinforcement consisted of W1.7 wire ladder mesh in the mortar joints spaced at 16 in. on-center. The contribution to the shear strength of the wall from this reinforcement is small, thus it was ignored in the analysis.

The shear capacity of the masonry specified by *UBC* 2108.2.6.2.8 [55] is

$$V_m = C_v A_e \sqrt{f'_m} \tag{1.26}$$

where A_e is the effective shear area and C_v is interpolated between 1.2 for a moment to shear demand ratio greater than 1.0 and 2.4 for a moment to shear demand ration less than 0.25. The resistance functions for the CMU walls with CFRP retrofits will use C_d equal to 2.0.

Figure 4.36 displays an example of a resistance function that would be calculated for a retrofitted CMU wall where the failure was controlled by its flexural strength. An example of a resistance function where a shear failure is a concern is shown in Figure 4.37. In the SDOF analysis used herein the flexural resistance function will be used.

Following analysis the peak dynamic shear demand will be compared to the shear strength of the wall to check if failure occurred. In the situations where a shear failure does occur it should be noted that the predicted response according to the flexural model is not longer applicable because the original assumptions of the model are no longer valid.

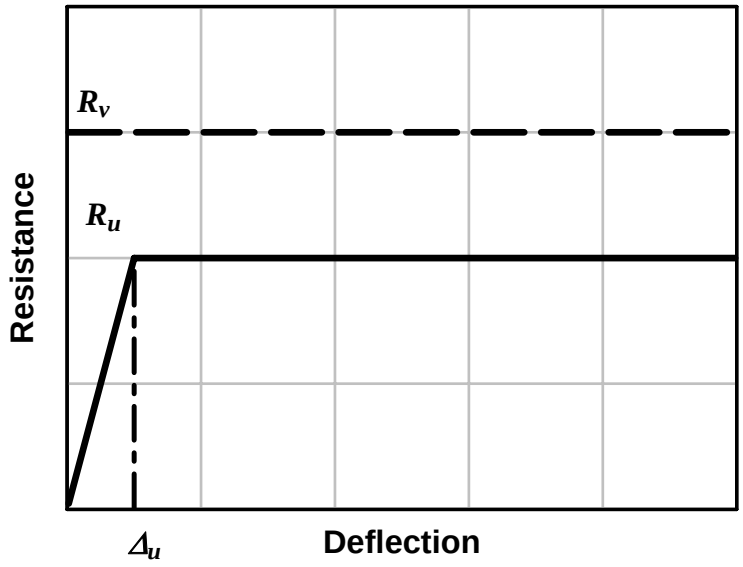

Figure 4.36: Resistance function for wall with flexural failure mode

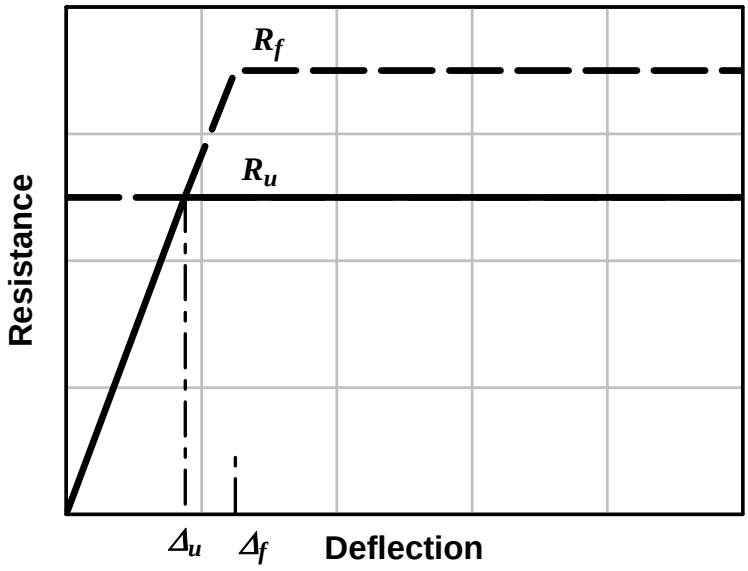

Figure 4.37: Resistance function for shear critical wall

4.4.2 COMPARISON BETWEEN BLAST SIMULATOR DATA AND SDOF MODEL INPUT PARAMETERS

The data generated for the CMU walls with CFRP retrofits was used to validate the SDOF analysis that predicts specimen response to blast like loads. The walls in the analysis were loaded using the BG loading function in the program. This function requires the number of BGs, the velocity at impact, and the programmer type. In the CMU tests three BGs were used with the wall programmer at velocities that ranged from about 14.2 to 26.3 ft/sec (4 to 8 m/sec).

The mass of the specimen was determined by assuming that the CMU wall, including the rebar, has a density equal to 130 lbs/ft^3 while the density of the CFRP laminate is 490 lbs/ft^3. The mass of the walls with four layers of CFRP on the back side

used in the analysis was 7.62 lbs-s^2/in. and the mass used for the walls with the additional two layers of CFRP on the front was 7.94 lbs-s^2/in.

The material properties for the CMU walls were used to validate the program. The grout strength as reported by [47] was equal to 3600 psi. Tests were not performed on the CMU block, thus it was assumed that the strength was equal to 1500 psi. The combinations of the grout and block strength with equation (1.9) gives a static masonry strength equal to 2110 psi. The rebar was ASTM A615 Grade 60 steel and the expected properties as listed in Table 4.4 were used in the model. The CFRP material used in the retrofit were provided by Edge Composites, Inc. and the properties used in the model matched those specified by the manufacturer. The modulus was equal to 10.1 x 10^6 psi and the failure strain was set equal to 1.2%.

As stated earlier strain rate effects are included in the SDOF analysis by multiplying the CMU strength, f'_m, used in the moment-curvature analysis by a scale factor. Strains gages were used to measure strains on the rebar and CFRP laminate on the back side of the wall during the blast simulator tests. The peak strain rates in the CFRP and the rebar were calculated by numerical differentiation of the strain time histories recorded by the gages. The strain rate in the CMU was not measured, but it was assumed to be equal to the same value determined for the CFRP. The assumption that the strain rates are equal is justified because moment-curvature analysis shows that at CMU crushing the neutral axis of the section is equal to half the depth and with the assumption that plane sections remain plane the strains in the CMU and CFRP will be equal. The peak strain rates measured on the CFRP for the six tests are listed in Table 4.6 and the

average was 2.17 sec^{-1}. The analysis for the validation used a strain rate equal one half the average peak, 1.09 sec^{-1} which would be the average strain rate for the wall as it displaced from zero to maximum displacement if it is assumed that the rate varied linearly. According to equations (1.10) through (1.12) the strain rate used in the analysis results in a dynamic increase factor equal to 1.62 for the masonry. As a comparison, a scale factor equal to 1.4 is recommended for the concrete strength at this strain rate in section 4-13.2 of *TM 5-1300* [6].

Peak strain rates measured for the rebar are also listed in Table 4.6, the average peak strain rate was equal to 0.97 sec^{-1}. For the analysis a strain rate equal to 0.49 was used because it is the average rate from zero to maximum deflection assuming that the rate varies linearly. The DIFs for this rate according to equations (1.13), (1.14), and (1.15) are 1.27 for the yield stress and 1.08 for the ultimate stress. In comparison, *TM 5-1300* [6] at these strain rates results in a factor equal to 1.25 for the yield and the ultimate strength in the rebar. It should be noted that in the moment-curvature analysis, the CMU typically will crush before the steel yields, thus the rate effects in the rebar do not affect the stiffness of the wall sections. *TM 5-1300* [6] does not specify the use of a DIF for the shear strength because a shear failure is a brittle mode and omission of a DIF is conservative.

Table 4.6: Strain Rates in CFRP and Rebar

Test	Peak CFRP Strain Rate [1/sec^{-1}]	Peak Rebar Strain Rate [1/sec^{-1}]
1	1.03	0.26
2	1.61	0.79
3	2.05	NR
4	2.66	1.00
5	3.18	1.08
6	2.47	0.84
Average	2.17	0.97

The resistance functions for the retrofitted walls tested with the blast simulator are displayed in Figure 4.38 and Figure 4.39. In the negative direction the resistance function for the wall without any composite on the front face has a minimum strength that has a significantly lower magnitude than in the positive direction. This is because lack of composite on the tension face when the wall undergoes negative bending results in the retrofitted wall behaving effectively as unretrofitted masonry. Upon rebound large negative displacements are expected. For the wall with two layers of composite on the front face the wall resistance function is also non-symmetric. The result is a slightly lesser stiffness in the negative direction; however, the magnitude of the failure resistance is not affected because the design is controlled by a shear failure.

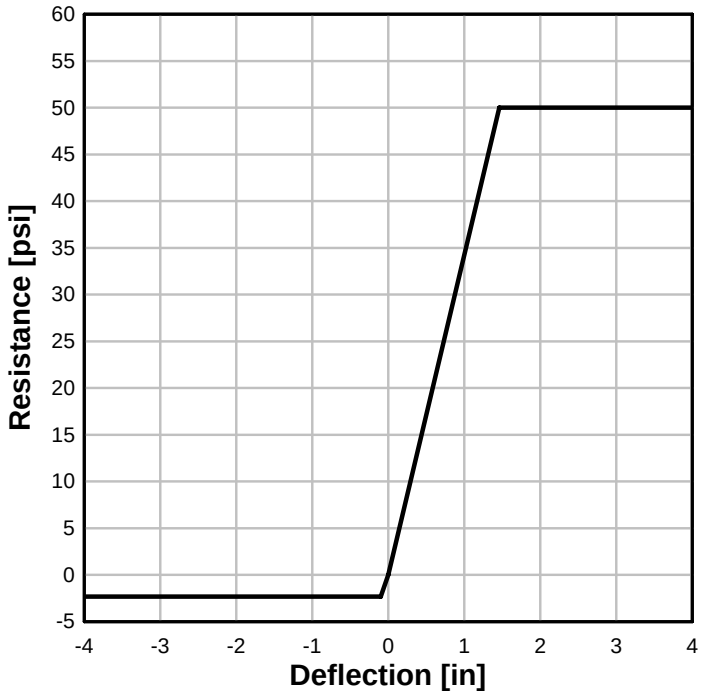

Figure 4.38: Resistance for CMU wall with CFRP retrofit used in Tests 1-4

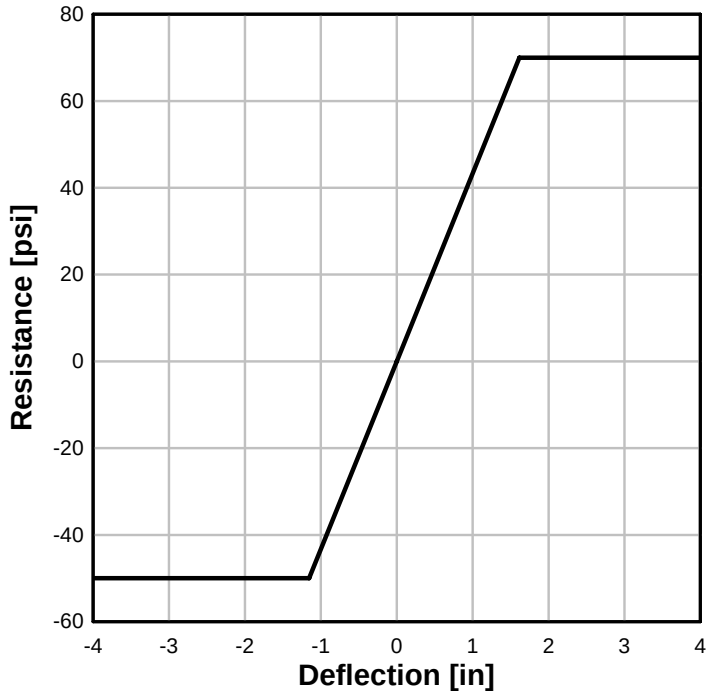

Figure 4.39: Resistance for CMU wall with CFRP retrofit used in Tests 5 and 6

The SDOF wall analysis was loaded using the BG load function that is presented in Chapter 2. The walls were loaded simultaneously by three impact masses with the wall programmers. The average impact velocities and the impulses delivered to the specimens in each test are listed in Table 4.7.

Table 4.7: Load Details

Test	Impact Velocity [ft/sec (m/sec)]	Impulse [psi-msec]
1	14.2 (4.3)	152
2	19.0 (5.8)	215
3	26.3 (8.0)	293
4	22.1 (6.7)	243
5	22.5 (6.8)	255
6	25.6 (7.8)	291

RESULTS

The impulse delivered to the specimen is the best measurement of the load that is applied to the specimens. Table 4.8 lists the impact velocity, measured impulse, predicted impulse, and the percent difference between the two. The largest error between the analysis and the experiment was 7.0% for the first test; the remaining tests all have an error less than 4%. A plot of the predicted impulse versus the measured impulse is shown in Figure 4.40. Included in the plot is a line that forms a 45° with the x-axis which represents a perfect correlation between the model and the experiment. Also included is a line fit to the data using regression analysis. The line has a correlation coefficient equal to 0.99 and a standard error about the line equal to 4.3. The comparison of the predicted impulse and the measured impulse shows that the SDOF model does a good job of simulating the loads applied by the BGs.

Table 4.8: Comparison of impulse for blast simulator and SDOF

Test	Impact Velocity [ft/sec (m/sec)]	Exp. Impulse [psi-msec]	SDOF Impulse [psi-msec]	Error
1	14.2 (4.3)	152	163	7.4%
2	19.0 (5.8)	215	216	0.4%
3	26.3 (8.0)	293	291	0.6%
4	22.1 (6.7)	243	247	1.6%
5	22.5 (6.8)	264	253	3.5%
6	25.6 (7.8)	289	285	0.8%

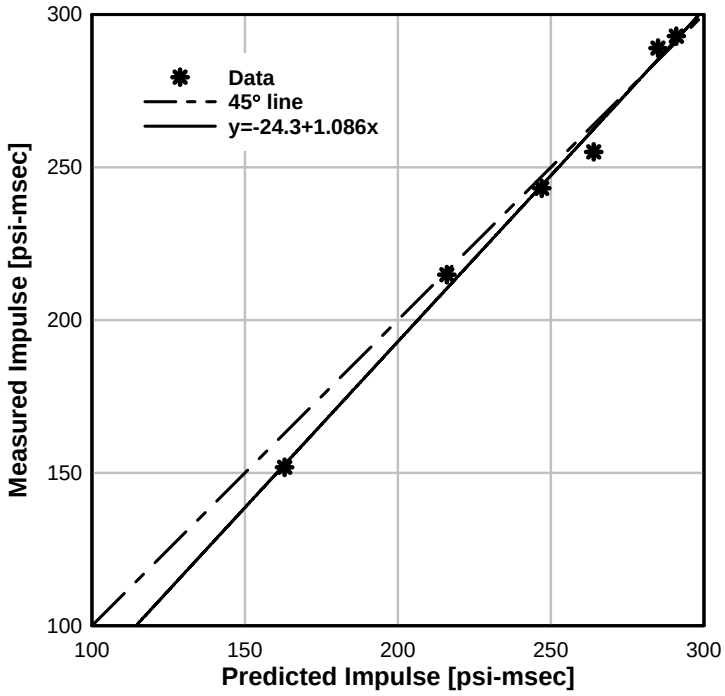

Figure 4.40: Predicted impulse versus measured impulse

Another comparison made between the SDOF model and the blast simulator tests was of the peak midspan displacement. Level of protection in blast design is typically specified to be a function of drift demand; therefore it is important to be able to predict peak midspan displacement. The peak midspan displacement measured and predicted for the BG impacts in the six tests are listed in Table 4.9. The maximum error between the experiments and the analysis was 34.2% for test 5. A plot of predicted displacement versus measured displacement is displayed in Figure 4.41. The plot includes a 45° line and a line fitted to the data with regression analysis. The correlation coefficient of the fitted line is 0.91 and the standard error about the line is 0.15.

Table 4.9: Comparison of displacements for blast simulator and SDOF

Test	Impact Velocity [ft/sec (m/sec)]	Exp. Disp [in]	SDOF Disp [psi-msec]	Error
1	14.2 (4.3)	0.62	0.83	33.9%
2	19.0 (5.8)	1.10	1.13	2.7%
3	26.3 (8.0)	1.71	1.52	11.1%
4	22.1 (6.7)	1.20	1.31	9.2%
5	22.5 (6.8)	0.98	1.12	13.3%
6	25.6 (7.8)	1.26	1.26	0.0%

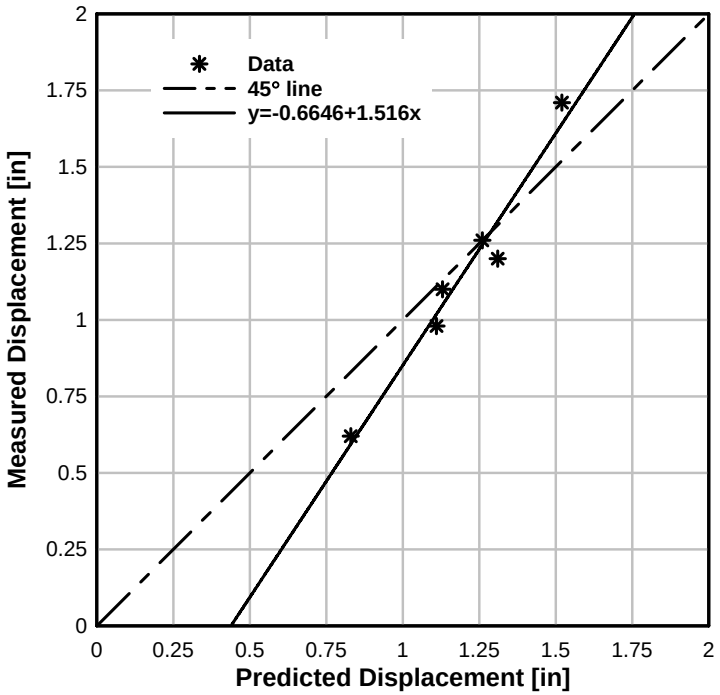

Figure 4.41: Predicted displacement versus measured displacement

The plot in Figure 4.41 shows that the SDOF model does a fairly good job of predicting the displacement recorded in the tests. The largest error, equal to 33.9%, was for Test 1 and in all other tests the error was less than 13%. The additional displacement predicted in Test 1 is probably the result of the higher impulse was delivered in the model which was 7.4% greater than in the experiment. It should be noted that the SDOF model

slightly over predicted the displacements in all of the other tests expect Test 3. Of all the blast simulator experiments, the specimen in this test suffered the largest amount of shear cracking. It is therefore reasonable that the SDOF model under predicts the displacement because the model can not capture the shear failure or corresponding displacements.

According to equation(1.9) the masonry strength of the walls, f'_m is equal to 2815 psi. The shear strength which is determined with equation (1.26) is equal to 38.9 kips, which when normalized by the loaded area of the wall is equal to 8.1 psi. Using this strength the model predicts that all of the walls fail in shear which is conservative because shear failures were only observed in Tests 3, 4, and 6.

Table 4.10: Comparison between blast simulator and SDOF for shear failure

Test	Shear Demand	Shear Capacity [psi]	Failure EXP
1	11.5	8.1	No
2	17.1	8.1	No
3	26.9	8.1	Yes
4	21.0	8.1	Yes
5	21.6	8.1	No
6	26.4	8.1	Yes

Some limitations of the SDOF model have arisen in the comparison with the tests data. The model is limited to flexural behavior and has shown to under predict peak displacements when a shear failure occurs. The errors for these tests are small, which is a result of the low levels of overall displacement; however a more detailed model should be considered when a shear failure is predicted. The model also does not account for dynamic effects in the material strengths when determining the walls shear strength. This approach is conservative, but consideration of dynamic strength increase could lead to

more efficient designs. Finally, the SDOF model used above is not capable of predicting some of the other localized failure modes observed in the tests, such as the failures observed at the base of the test specimen. The connections are often the critical component of a structure; therefore, it is recommended that more detailed analysis methods, such as finite element analysis be used to aid in the design of these details.

4.5 FINITE ELEMENT ANALYSIS

4.5.1 MODEL DESCRIPTIONS

The experiments on the CMU walls with CFRP retrofits were simulated with a finite element (FE) model that was analyzed with the program LS-DYNA [24]. LS-DYNA is a three dimensional explicit, Lagrangian finite element code that uses a central difference time-integration method. This program is commonly used for linear and nonlinear dynamic problems including those that are related to blast and impact loading.

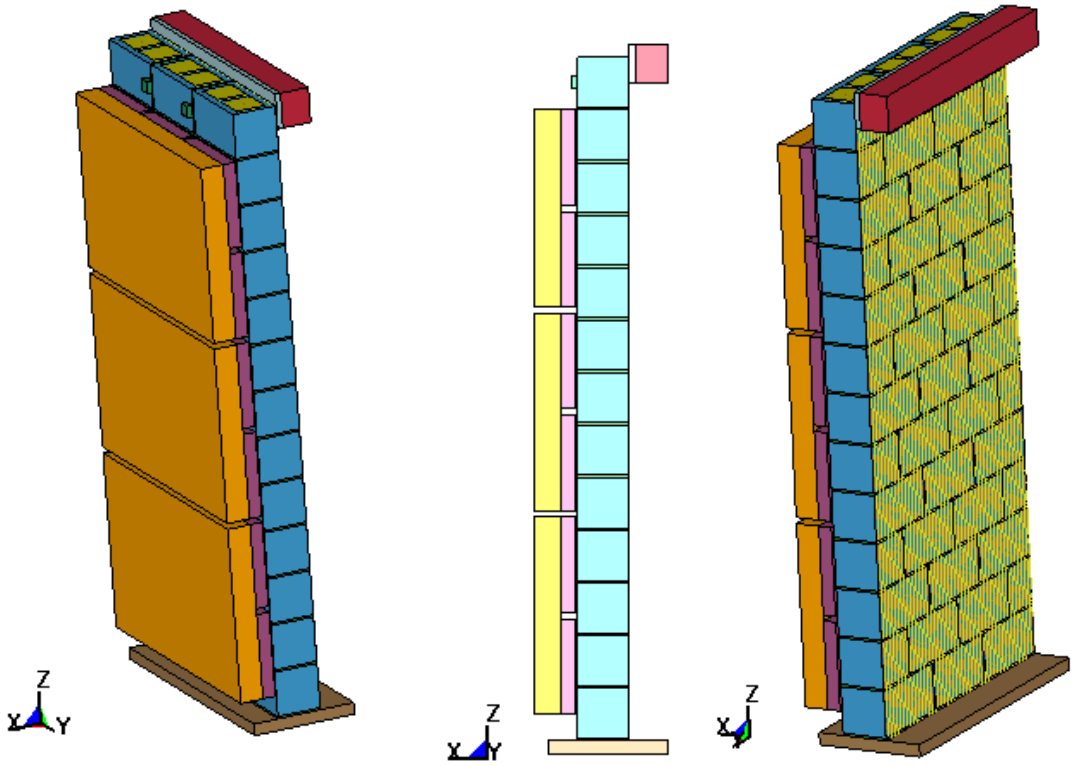

Figure 4.42: FE model of CMU wall with CFRP

The FE model of the blast simulator tests is depicted in Figure 4.42. In the model the impact masses and programmers were given an initial velocity corresponding to the impact velocity recorded in the actual test. Contact surfaces between the BG

programmers and the front face of the CMU wall were used to transfer the forces from the impact modules to the wall when impact occurred.

Eight node brick elements with single integration points were used to model the CMU elements along with the programmers, aluminum BG masses, and concrete supports. The different components of the wall including the CMU blocks, grout, mortar, and steel reinforcement were all modeled separately, but shared coincident nodes between elements which were merged together. Figure 4.43 shows the individual components of the CMU and Figure 4.44 displays the details of the mesh used in the FE model.

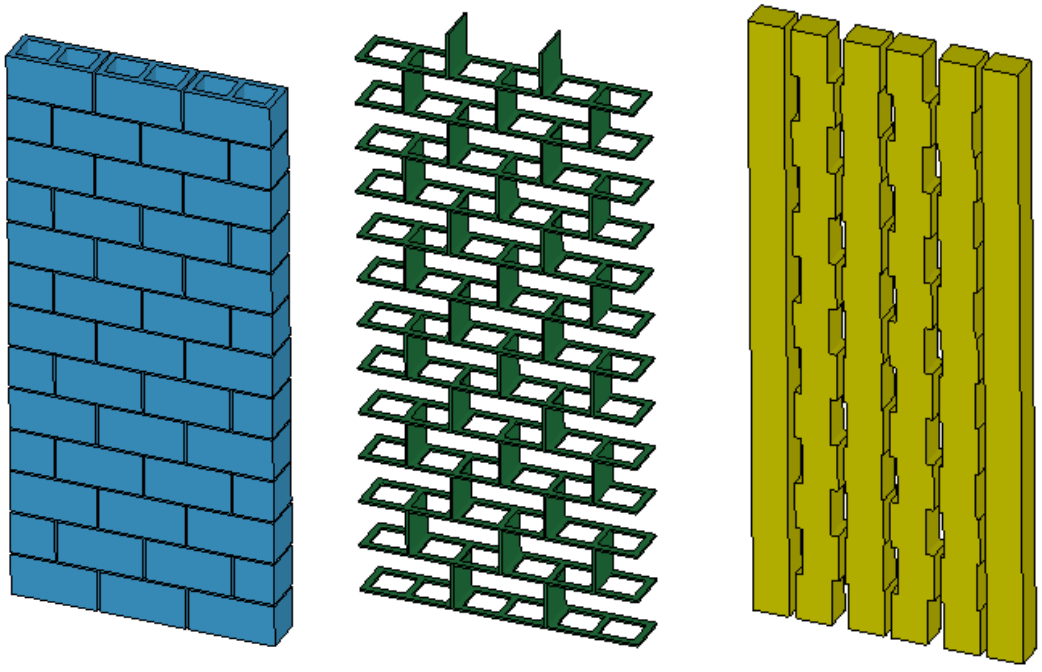

(a) **(b)** **(c)**

Figure 4.43: Individual CMU components: (a) CMU block; (b) mortar; (c) grout

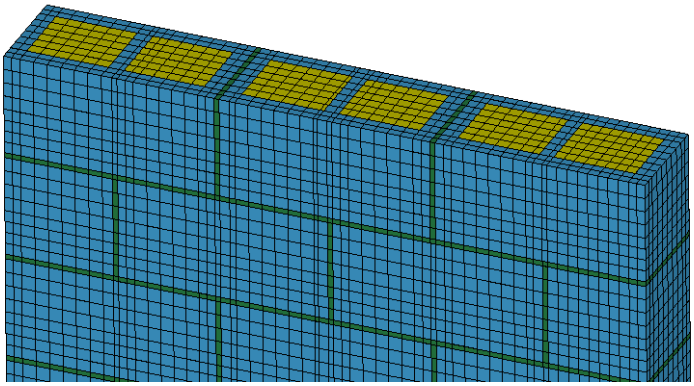

Figure 4.44: CMU Mesh

The Hughes-Liu with cross-sectional integration beam element formulation was used to model the reinforcing steel and the CFRP laminate. The nodes of the rebar beams were merged with the solid elements for the grout and CMU. Figure 4.45 displays the mesh for the steel reinforcement. Beams were also the most suitable element for modeling the CFPR laminate which had fibers oriented only in the vertical direction.

The nodes of the CFRP beams were merged to the shell elements whose nodes were in the same plane as the back face of the CMU wall. The shell elements were included to provide a reliable contact surface for the CFRP laminate. The shells were tied to the CMU elements with a tied contact surface representing a perfect bond between the block and the laminate. The shell elements were only used to provide a contact surface, thus a *MAT_NULL material card was used for those elements. The mesh for the CFRP and the *MAT_NULL shells are displayed in Figure 4.46.

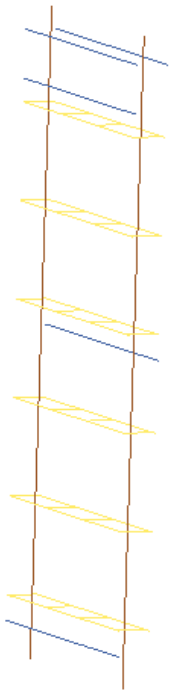

Figure 4.45: Reinforcing steel

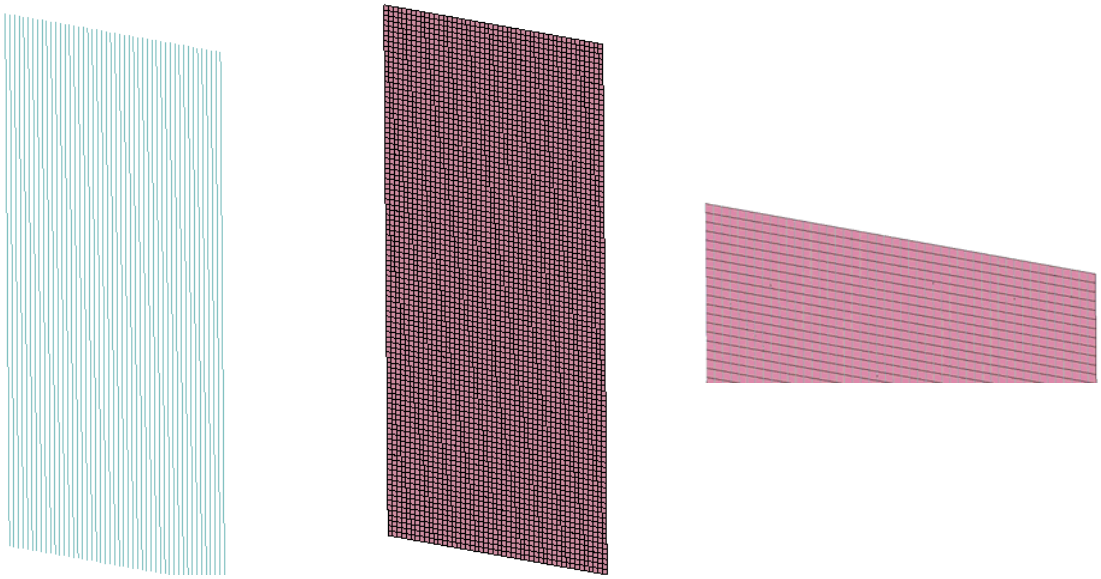

(a) **(b)** **(c)**

Figure 4.46: CFRP Mesh: (a) CFRP Beams; (b) *MAT_NULL shells; (c) beams and shells merged together

The bond strength between the mortar and the CMU block is often the weakest component of the wall during out-of-plane loading. In this model the coincident nodes between the CMU and mortar elements were merged with the assumption that the failure mechanism at the joint can be captured with the failure in the mortar material model. Another option was to use a tiebreak contact surface with failure between the mortar and CMU element. This option, however, was not used because it is more costly to compute the interactions at the tiebreak surface.

The contact used to simulate the impact of the BGs with the wall specimen was the **AUTOMATIC_SURFACE_TO_SURFACE_CONTACT* with the soft option 2, which is a segment-based penalty method. According to the *LS-DYNA Keyword User Manual* [24], the segment-based penalty formulation contact algorithm checks for segment versus segment penetration instead of node versus segment. The algorithm determines if a segment is penetrating and then chooses the master segment which it then applies penalty forces to in the normal direction. The default parameters for option 2 were chosen for these simulations.

After impact, the materials for the programmer and the mass were deleted from the model using the *MAT_EROSION command. This was done to prevent a second hit in the simulation; in the actual experiment the second hit was prevented with the deceleration pressure in the BG accumulator which works against the impact mass to slow it down and push it back to its pre-test position. The use of the erosion card was determined after the first iteration of the impact simulations where the impulse delivered to the specimen in the model was 20%-30% higher than observed in the experiment. The

BG impact masses in the simulations delivered a large impulse in the first 5 msec which was followed by additional pushing with momentum transfer at a slower rate. This second impulse transfer corresponded to the additional 20-30% of impulse that was not recorded in the experiments. In the experiment, after the BGs impact the specimen, the BGs still have velocity in the same direction as the initial velocity. The kinetic energy associated with this velocity and the BG mass is then dissipated by the work done by the nitrogen in the deceleration chamber of the BG.

To account for the fact that the deceleration chamber is not modeled in the FE simulation the elements for the BG masses were eroded after 5 msec. This approach allowed for the simulation to produce the same impulse as recorded for the experiment. One drawback of the approach is that the BGs can possibly catch up to the wall and apply additional pressure after the initial impulse is delivered. The magnitude of this pressure, however, was not measured and is assumed to be insignificant. Another drawback of this approach is that, as the video from the experiments show, the wall impact the BG plates a second time when it rebounds because the actuator did not have enough time to retract the plates out of the way. This second impact happens after the wall has reached a peak displacement and the video shows that if shear cracks form during the test, they form before this second impact. Therefore, it is assumed that the second impact upon rebound does not affect the outcome of the simulation.

The CMU block, mortar, and grout of the wall were modeled using modified versions of *MAT_072 Release 3. It is assumed that the fundamental concepts used to capture the behavior of concrete can be applied to the different components of CMU due

to the similarities in the materials. However, there are differences in density, aggregate size, aggregate strength and porosity in the materials which can result in a different initial modulus, unconfined stress-strain relation, confined stress-strain relation, tensile strength, equation of state, and strain rate effects. Thus the parameters of the material model for normal weight concrete were adjusted by Magallanes et al. [53] to fit available material test data for the different CMU components.

The model calibration [53] included determining new parameters which define the three parabolic failure surfaces associated with yield, maximum and residual strength of the materials. A linear scaling law was also implemented to interpolate the failure surfaces for each material with a different unconfined axial compressive strength. New tabulated equations of state were also defined based on data obtained for CMU block and mortar. The EOS relations were also scaled according to the unconfined axial compressive strength of the materials. The initial modulus and tensile strength were adjusted to better match available data; these adjusted properties are consistent with recommendations from ACI [20] for lightweight concrete which has lower values for both properties. The equation for the modulus in this model was also used in the development of the resistance function for the SDOF analysis (equation (1.8)). The fracture energy coefficient was fit to the CEB model [56] for concrete, but with lower compressive and tensile strengths and smaller aggregate. Finally, the parameters for the strain rate enhancement equations, originally proposed by [52] were adjusted for the mortar and the CMU materials. The enhancement for the grout was assumed to be the same as normal weight concrete.

The input parameters for the modified K&C concrete model are the material type (i.e. CMU, mortar, grout), the density, the aggregate size, and the unconfined axial compressive strength. The only available material test data for the materials used in the CMU walls was the grout which had strength equal to 3,600 psi. This strength was used in the model along with a density equal to 145 lbs/ft^3 and 0.75 in. aggregate. For the other two components of the CMU wall the material strengths were estimated. The strength of the CMU block material was set at 1,500 psi with a density of 110 lbs/ft^3 and 0.25 in. aggregate. The mortar strength was assumed to be 920 psi with a density of 110 lbs/ft^3 and 0.13 in. aggregate. The properties used are slightly lower than expected for Type S mortar. This was done to represent the lower tensile strength at the interface between the mortar and block because the interface was not modeled explicitly.

The CFRP behaved linear elastically in all of the tests. Typically, the CFRP is linear elastic to yield where there is a brief softening before the material fractures. The material model used for the CFRP was *MAT_PLASTIC_KINEMATIC or material type 3 [24]. The properties of the CFPR laminate used in the model matched the specified material properties given by the manufacturer. Young's modulus for this model was equal to 10,100 ksi with a yield stress equal to 130 ksi. The failure strain for the model was set to 1.3%.

The reinforcing steel in the wall was modeled with a piecewise material model that best matched the material properties for ASTM A615 grade 60 rebar, which has a density of 0.28 lbs/in^3, Young's modulus of 29,000 ksi, yield stress of 69 ksi, an ultimate stress of 109 ksi, and a failure strain equal to 0.12. The material model also includes

strain rate effects by scaling the yield and failure stress according to Malvar and Crawford [54].

A linear elastic material model with Young's modulus equal to 10,000 ksi, Poisson's ratio equal to 0.3, and a density of 0.1 lbs/ft^3 was used to capture the response of the aluminum impact masses. The thickness of the plate was increased by 5/8 in. to account for the mass of the rod, which was not modeled explicitly in the simulation.

The programmer material was modeled with *MAT_LOW_DENSITY_FOAM or Material Type 57 [24]. A stress-strain curve was input into the model as a load curve. The stress-strain curve used in the model is a modified curve taken from quasi-static tests on a column programmer described in Rodriquez [33]. The wall programmer is made from slightly stiffer material and a factor of 1.7 was applied to the ordinate of the curve to account for it. The parameters *SHAPE* and *HU* were set at 200 and 0.01 respectively. These parameters describe the unloading behavior of the material and thus control the energy dissipation during the impact. The values were chosen so that the impulse transferred to the specimen in the simulation was similar to the actual experiment for all the tests.

The top slab boundary condition was modeled with a 48 in. x 6 in. x 6 in. block made of brick elements with a *MAT_072 Release 3 material card. The axial compression strength of this boundary condition was equal to 5,000 psi. A contact interface was used between the top of the wall and the front face of the slab. The nodes on the back face of the slab were fully restrained from translating in all three directions.

The bottom footing was modeled with a 48 in. x 18 in. x 2 in. block of brick elements with a *MAT_072 Release 3 material card. The nodes on the bottom of this footing and around its perimeter were fixed against translation in three directions. Several alternatives were used to model the interface between the bottom of the CMU wall and the top of the footing including a tied contact surface, tiebreak contact surface, and a sliding contact surface with friction.

4.5.2 FE Model Validation

Test 1

The first test was on a CMU wall with four layers of CFRP on the back side. In the actual experiment the wall did not have any support at the bottom boundary condition, other than friction and dowel forces between the footing and the first course of blocks. This interaction was modeled in the FE simulation with a surface to surface tiebreak contact in LS-DYNA. The static friction coefficient was set to 0.6, the normal stress failure was to 200 psi, and the shear stress failure was set to 700 psi. The BGs in the simulation were given initial velocities equal to the velocities recorded in the experiment immediately prior to impact. Table 4.11 lists the impact velocity, experimental impulse and the FE analysis impulse for each BG. On average the difference between the overall impulse in the experiment and the analysis was only 4.7%. The small error in the overall comparison satisfied the requirement that the input load in the experiment and the analysis were similar.

Table 4.11: Comparison of impulse for experiment and FE analysis

BG	BG Velocity [ft/sec]	Exp Impulse [psi-msec]	FE Impulse [psi-msec]
3	13.0	110	149
2	14.7	176	132
1	12.8	167	151
Average	13.5	151.0	144.0

A time history plot of the midspan displacement is shown in Figure 4.47 for the experiment and the FE analysis. The plot shows that the analysis provides a good match with the experiment up to the peak displacement. The peak displacement in the analysis was equal to 0.63 in. while the test the displacement measured was 0.62 inches. The difference between these displacements is equal to 1.6%. During rebound the simulation does not match the experiment very well which is a limitation of the concrete model. The model does not simulate the closing of cracks in the concrete with sufficient accuracy.

The displaced shapes for the experiment and the model are displayed in Figure 4.48 at displacements equal to 25%, 50%, and 100% of the maximum displacements. This figure shows that the model does an acceptable job of predicting the displaced shape except at the base where, at 100% of the peak displacement, the simulation exhibits significantly more displacement. This displacement can be reduced by adjusting the contact parameters at the base; however it is important to observe that the model is capable of predicting the damage that occurred at the base. Figure 4.49 compares the results with the analysis for the damage in the overall specimen, while Figure focuses on the damage at the base. Both figures show that the damage is similar for the experiments and the analysis.

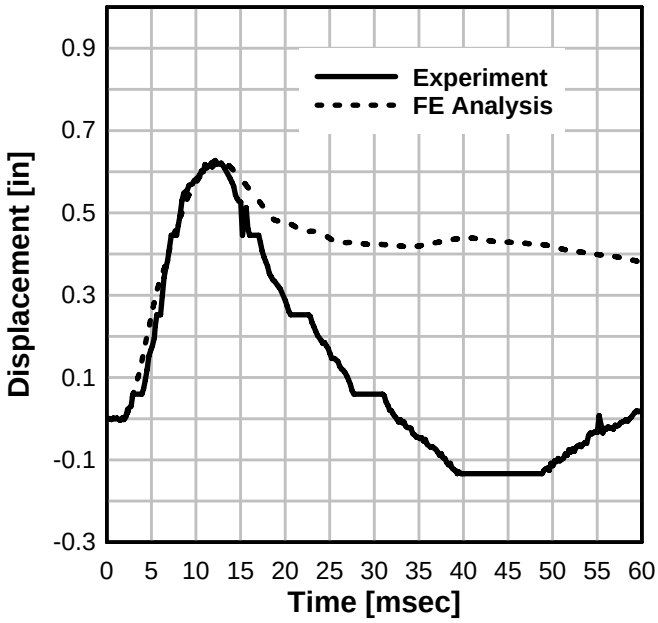

Figure 4.47: Test 1 comparison of midspan displacements

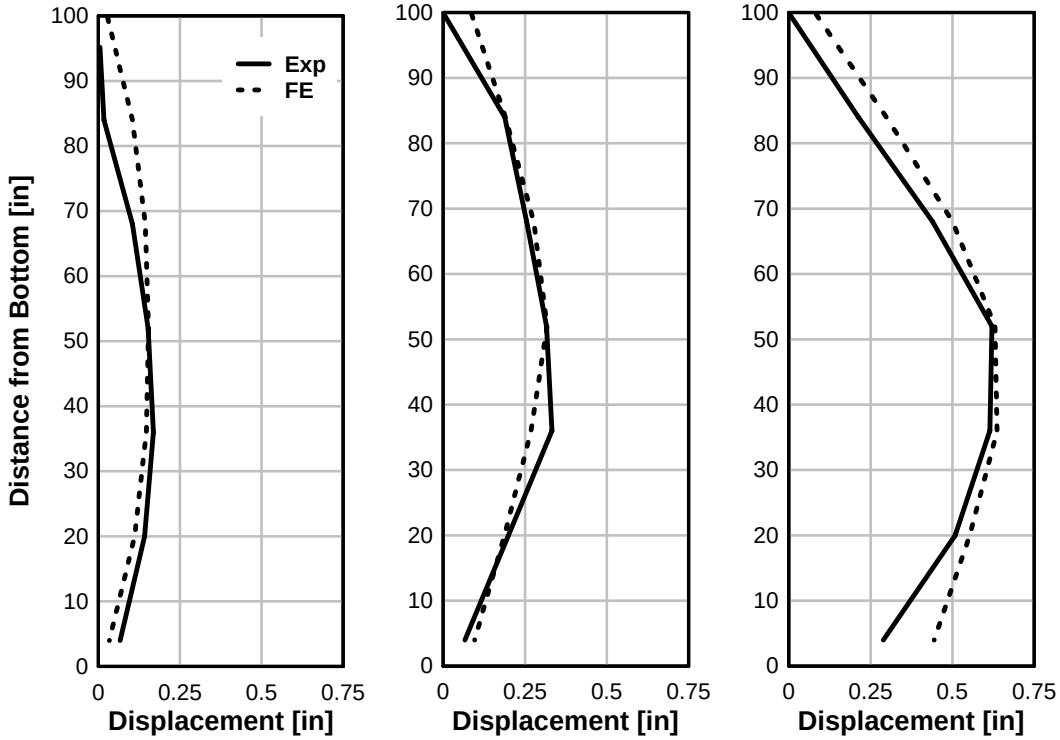

Figure 4.48: Test 1 comparison of displaced shape

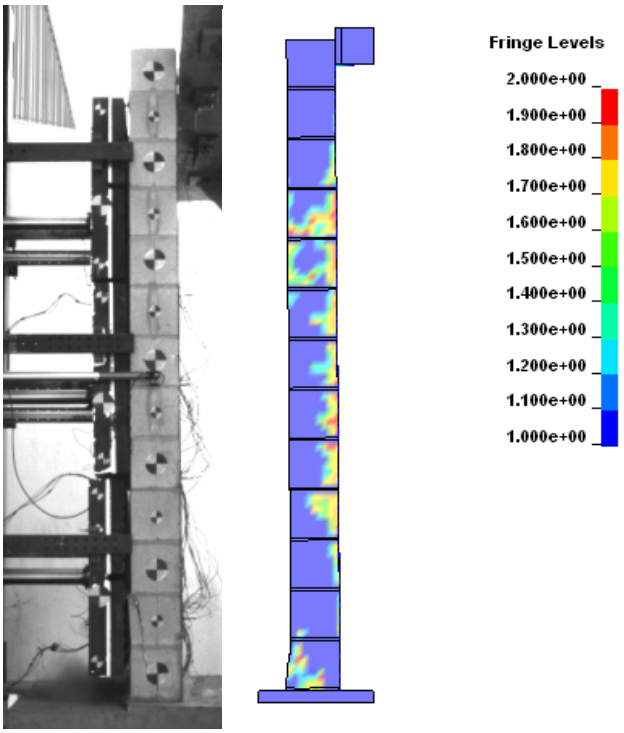

(a) **(b)**

Figure 4.49: Test 1 comparison of damage; (a) Experiment; (b) FE analysis

(a)

Figure 4.50: Test 1 comparison of damage at base; (a) Experiment; (b) FE analysis

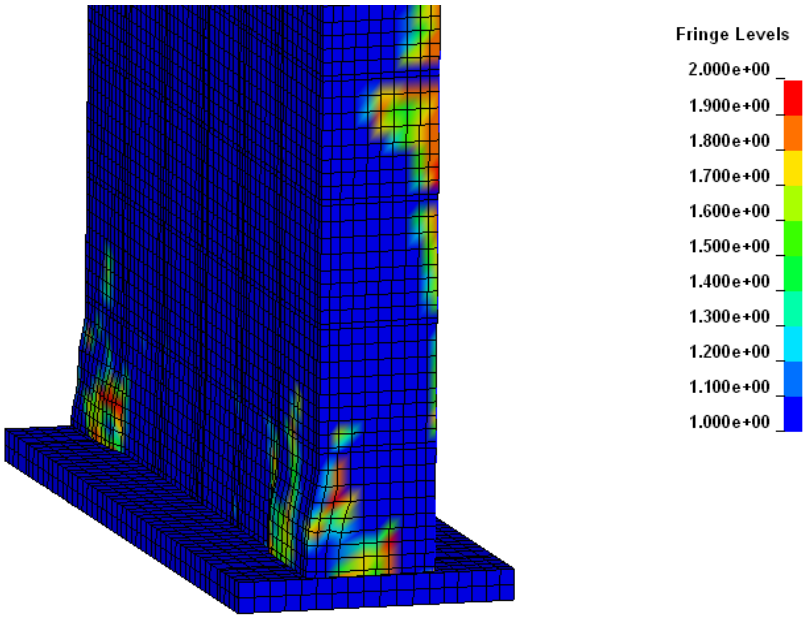

(b)

Figure 4.50 (continued): Test 1 comparison of damage at base; (a) Experiment; (b) FE analysis

TEST 2

The second test was performed on the specimen that was impacted in the previous test. Due to the damage at the base, the wall was rehabbed and an angle was placed behind the wall at the base to simulate the connection to the base. In the FE analysis the angle was modeled with shell elements and the bolts used to connect the angle were modeled with beam elements. In the model the wall was given an initial 1/2 in. gap between the back of the composite on the wall and the vertical leg of the angle as shown in Figure 4.51. This was done because in the actual experiment the steel angle had oversized holes and when the bottom of the wall began to translate due to the load the

angle slide before the bolts came into bearing with the angle. A contact surface was used to model the interface between the first course of block and the footing. This surface allowed the interfaces to slide across each other with a friction coefficient equal to 0.6. Unlike the previous analysis, there was not tiebreak condition because the joint at the interface had been completely ruptured.

The BGs in the analysis were given initial velocities equal to those measured in the experiments. Table 4.12 lists the impact velocity, experimental impulse, and FE impulse for each BG. The table shows that the model did not match the impulse well on the BG level; however overall the experiment had an average velocity equal to 200 psi-msec while the FE average impulse was equal to 214 psi-msec. The difference between the two is equal to 6.4%.

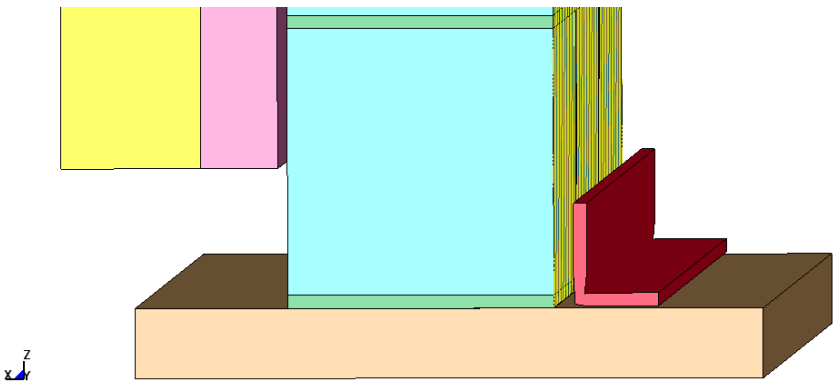

Figure 4.51: Test 2 angle with gap

Table 4.12: Comparison of impulse for experiment and FE analysis

BG	BG Velocity [ft/sec]	Exp Impulse [psi-msec]	FE Impulse [psi-msec]
3	18.1	204	235
2	19.7	229	279
1	19.3	209	186
Average	19.0	214.0	233.3

A time-history displacement is plotted in Figure 4.52 for the experiment and the analysis. The peak displacement in the test was 1.1 in. compared to the analysis where it was 1.0 inches. The difference between the two is equal to 9.1%. The plot again shows that the FE simulation does not match the rebound behavior observed in the experiment.

The displaced shapes at 25, 50, and 100% peak displacement, shown in Figure 4.56, display that the model is able to predict displacements over the entire span reasonably well. At the base the analysis under predicts the displacement when the midspan is at 25 and 50% of its peak, but at 100% of it peak the analysis matches the experiment. Figure 4.54 compares the damage in the experiment and the FE analysis. Similar to Test 1, the model was able to capture the localized damage that occurred near the base where the wall began to translate and the block near the rebar cracked.

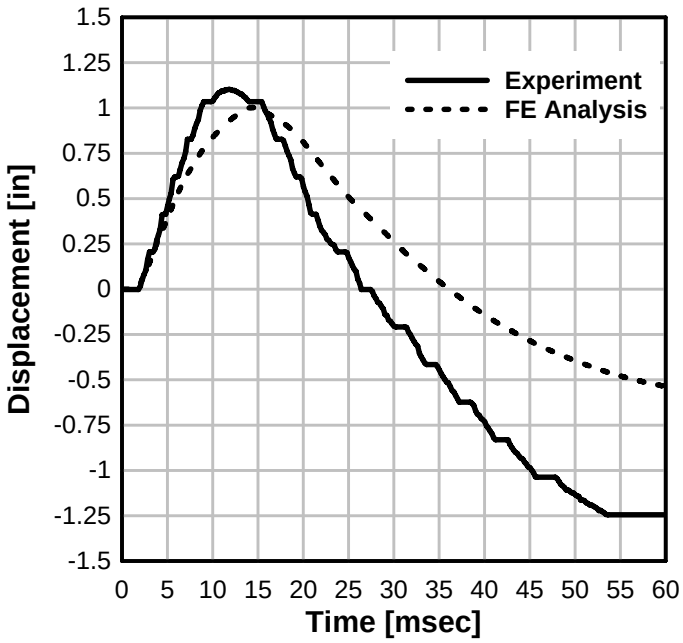

Figure 4.52: Test 2 comparison of midspan displacements

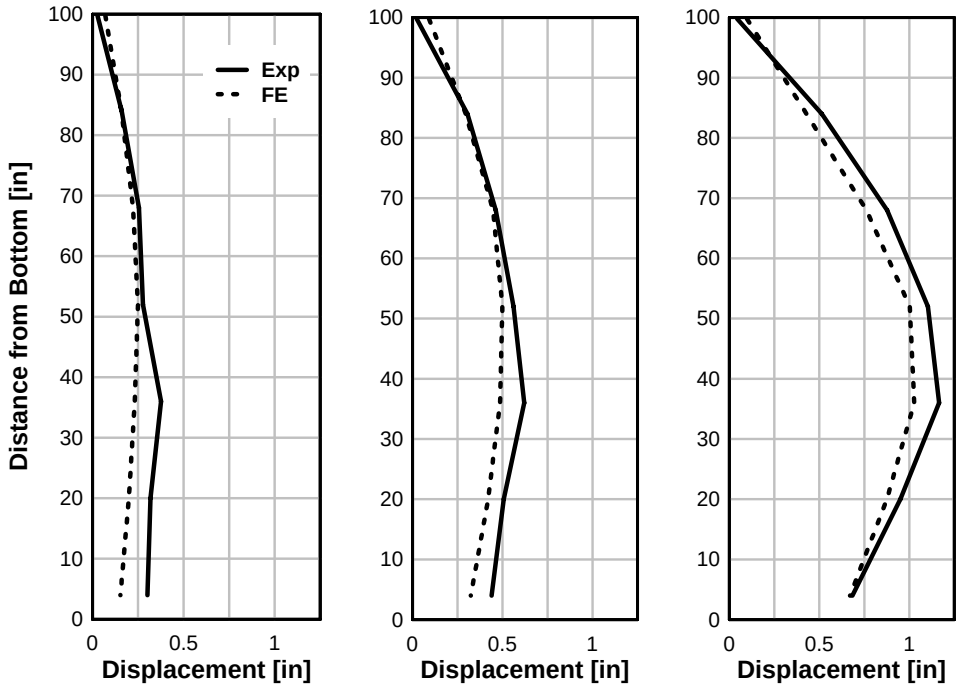

Figure 4.53: Test 2 comparison of displaced shape

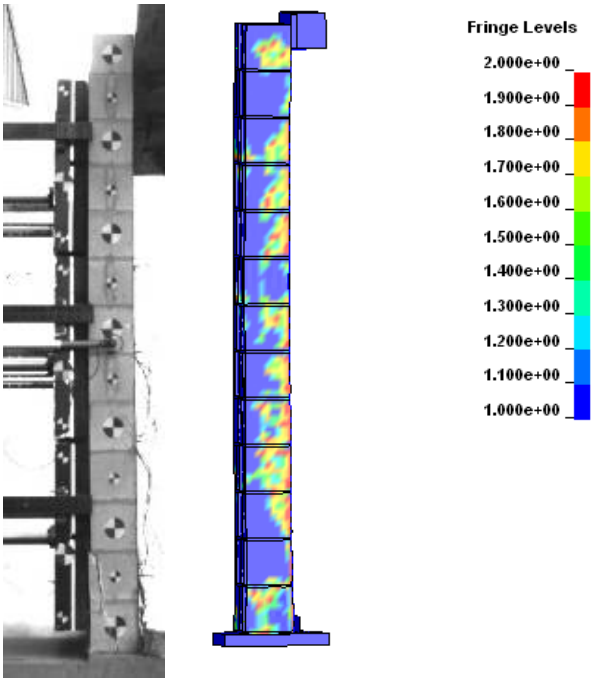

(a) **(b)**

Figure 4.54: Test 2 comparison of damage; (a) Experiment; (b) FE analysis

TEST 3

Test 3 was the third experiment conducted on the first wall specimen. The damage observed in the previous tests was from the wall translating on the footing and concrete cracking near the rebar from dowel action. The FE model used to predict this test was identical to the one used for Test 2. The velocities given to the BGs in the analysis are listed in Table 4.13 along with the impulses measured in the experiment and calculated in the analysis. The average impulse measured in the experiment was equal to 291 psi-msec. In the FE analysis the BGs delivered an impulse equal to 278 psi-msec which is 4.7% less.

Table 4.13: Comparison of impulse for experiment and FE analysis

BG	BG Velocity [ft/sec]	Exp Impulse [psi-msec]	FE Impulse [psi-msec]
3	24.9	277	335
2	27.0	297	238
1	27.0	300	261
Average	26.3	291.3	278.0

Figure 4.55 is a time-history plot of the midspan displacement. This plot shows that the model predicted a displacement equal to 1.73 in. which is 1.2% greater than the 1.71 in. measured in the experiment. The agreement of the peaks is very good, however shape of the curves are significantly different. The wall in the experiment rebounded suddenly, while in the analysis the rebound was softer.

A comparison of the displaced shape experienced in the experiment and the analysis are shown in Figure 4.56. Figure 4.57 shows the damage in the experiment and the analysis. These plots show that the FE analysis was able to model the behavior and

failure mechanism of the wall very well. Overall the analysis was able to predict the peak displacement, matched the displaced shape, and predicted the occurrence and location a shear failure and damage at the base.

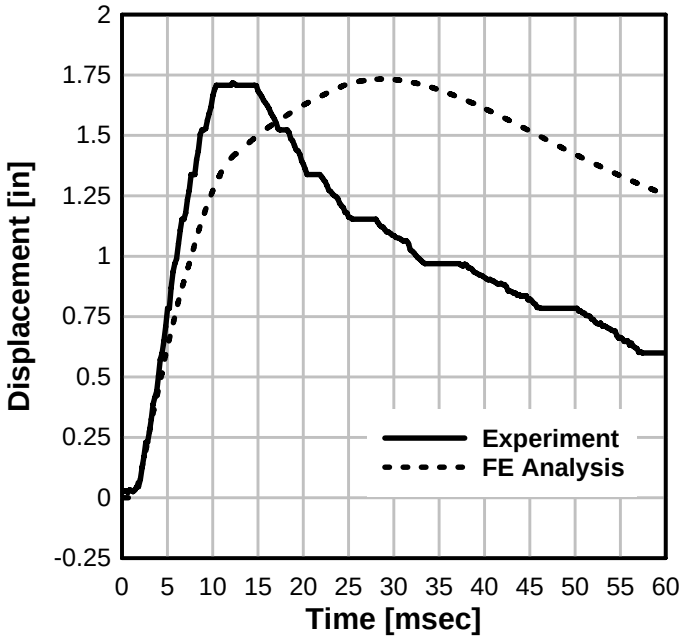

Figure 4.55: Test 3 comparison of midspan displacements

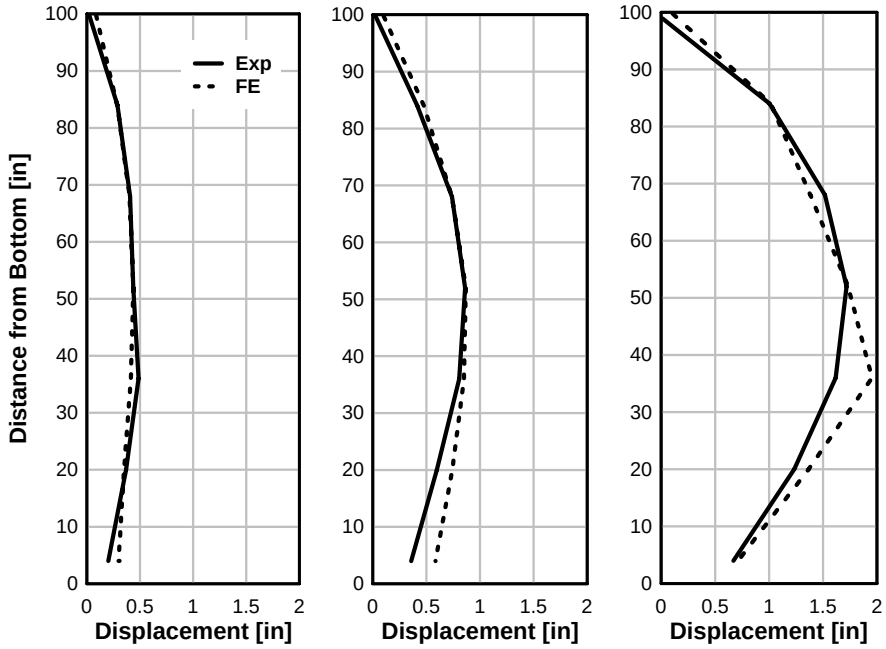

Figure 4.56: Test 3 comparison of displaced shape

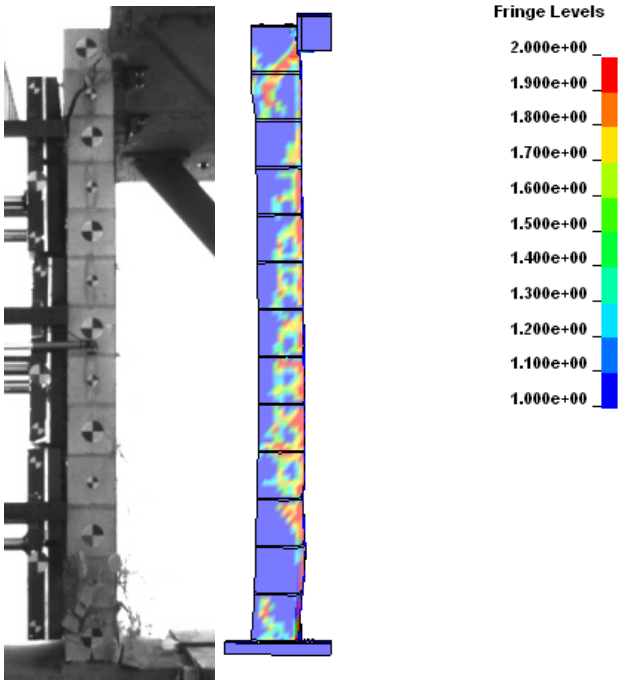

(a) **(b)**

Figure 4.57: Test 3 comparison of damage; (a) Experiment; (b) FE analysis

TEST 4

Test 4 was performed on the second specimen used in the test series. The test setup for the experiment was similar to that of Tests 2 and 3, therefore the model was also similar. The BG impact velocities measured in the tests and used in the analysis are listed in Table 4.14 with the impulses that were measured and predicted. The variation between the experiment and the simulation varied significantly for each BG. Overall, however the average impulse measured equal to 242 psi-msec is only 4.3% greater than the impulse that was predicted.

Table 4.14: Comparison of impulse for experiment and FE analysis

BG	BG Velocity [ft/sec]	Exp Impulse [psi-msec]	FE Impulse [psi-msec]
3	20.2	212	267
2	23.3	272	216
1	22.0	242	212
Average	21.8	242.0	231.7

Comparisons between the displacement time-history, displaced shape, and damage state for the experiment and the FE analysis are shown in Figure 4.58, Figure 4.59, and Figure 4.60, respectively. There is very good agreement displayed in each of these plots. In the time-history the analysis matches the experiments for both inbound and rebound displacements; however, this may be a coincidence because it has been shown for other tests and the concrete model does not simulate the closing of cracks well. The peak midspan displacement in the experiment was equal to 1.2 in. and in the analysis it was 1.18 inches. The difference between the two is equal to 1.7%. In the experiment the wall formed diagonal shear cracks near the top support and near the base. This damage was also predicted in the model.

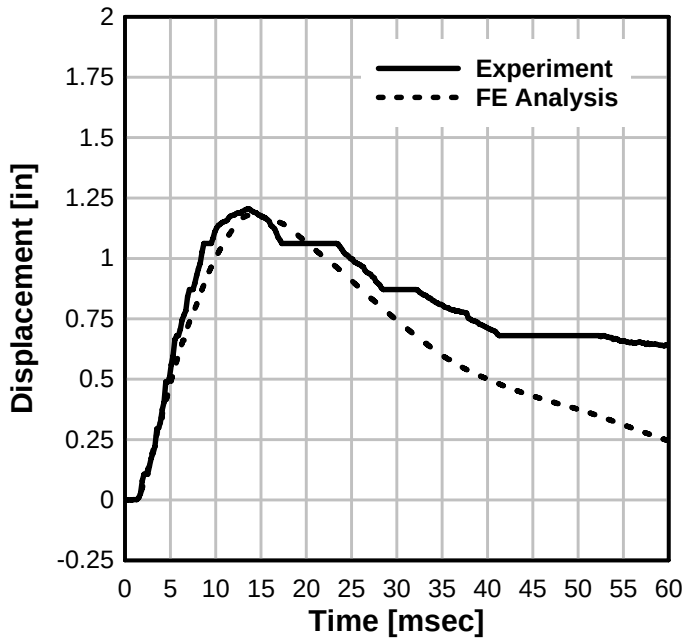

Figure 4.58: Test 4 comparison of midspan displacements

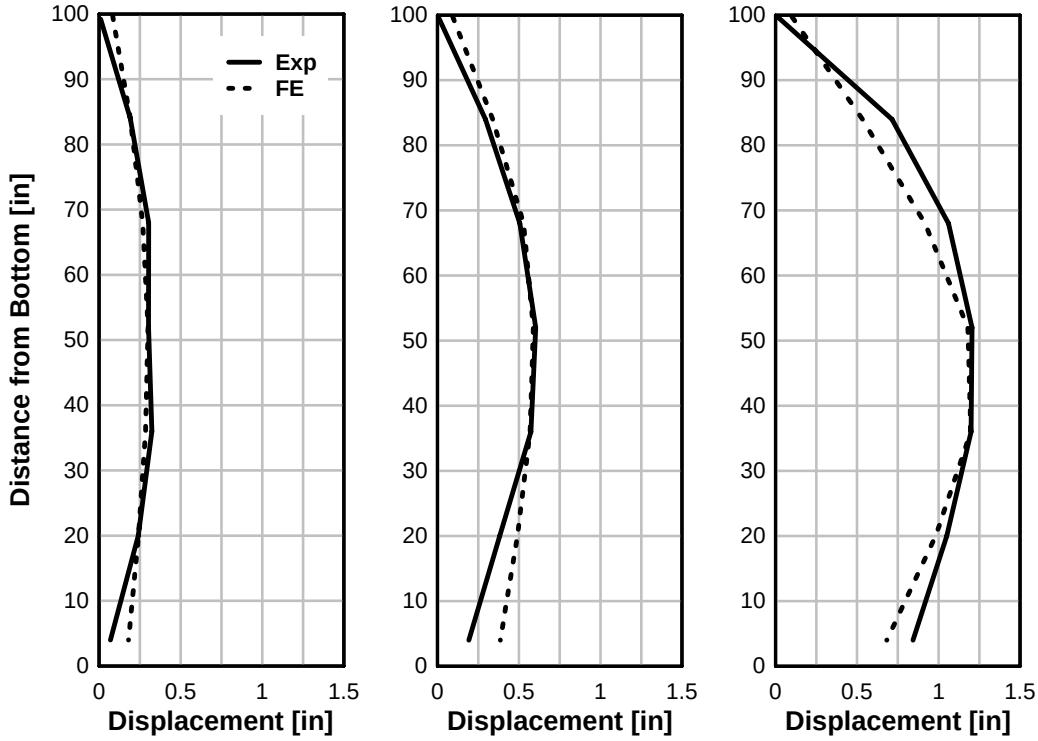

Figure 4.59: Test 4 comparison of displaced shape

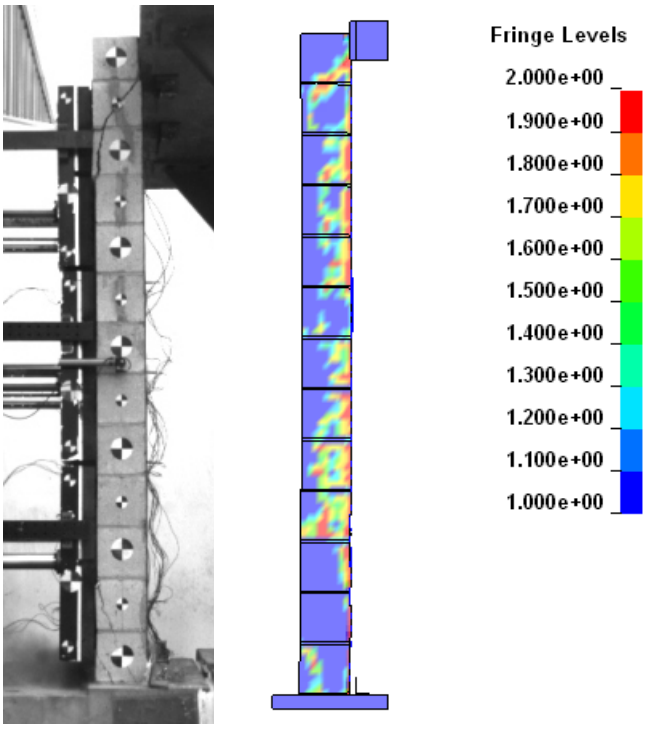

(a) **(b)**

Figure 4.60: Test 4 comparison of damage; (a) Experiment; (b) FE analysis

TEST 5

The fifth test was performed on the third CMU wall specimen that had an additional two layers for CFRP applied to its front side. The wall also had a steel angle similar to the one used in Tests 2-4, attached at the base to provide additional resistance against the reaction forces. In the blast simulator tests the angle bolts fractured immediately after the load was applied and most of the damage done to the wall was due to translation at the base. In the FE model the base condition matched that used to simulate Test 1, which used a contact condition to model the failure between the footing and the first course of blocks. The normal and shear failure stresses used in the model were 200 psi and 700 psi. The static coefficient of friction was equal to 0.6. The model

did not include an angle because it was decided that the resistance provided by the angle in the test was small and could be accounted for with the contact surface.

The BG velocities, the measured impulse, and the predicted impulse are listed in Table 4.15. The table shows that the impulses differ between the individual BGs, but that the average impulse for the analysis is only 3.8% less than the experiment.

Table 4.15: Comparison of impulse for experiment and FE analysis

BG	BG Velocity [ft/sec]	Exp Impulse [psi-msec]	FE Impulse [psi-msec]
3	20.5	243	274
2	23.6	250	217
1	22.2	268	242
Average	22.1	253.7	244.3

Figure 4.61 is a plot of the displacement time-history at the midspan of the specimen. The plot shows that the analysis matches the experiment well up to the peak displacement at 0.98 inches. In fact the displacement predicted at this time is also equal to 0.98 inches. Following this point both curves stay nearly constant out to 60 msec after impact. The rebound is small in both the test and the experiment because of large translation at the base when the angle failed and the masonry near the rebar cracked. The FE analysis predicts that the displacement will increase another 0.25 in. after the initial peak which is 25% higher than what was measured in the experiment. Figure 4.62 displays the displaced shapes for the specimen in the experiment and the FE analysis at 25, 50, and 100% of the initial 0.98 in. peak displacement. The figure shows that the analysis matches the shape very well. In the analysis at 100% of the experimental midspan peak displacement the displacement is greater at the base by about 20%. Figure

4.63 displays the displaced shape at a later time when the FE analysis reaches the second peak. It can be observed in this plot that the shapes are similar; furthermore the difference at the base is now much smaller. Finally, the difference at the midspan can be attributed to the rebound of the wall top in the analysis which reduces the displacement along the span. Figure 4.64 and Figure compare the damage between the model and the experiment for the overall specimen and at the base, respectively. The figures show that the model was able to capture the level of damage observed in the test, especially at the base where most of the damage occurred.

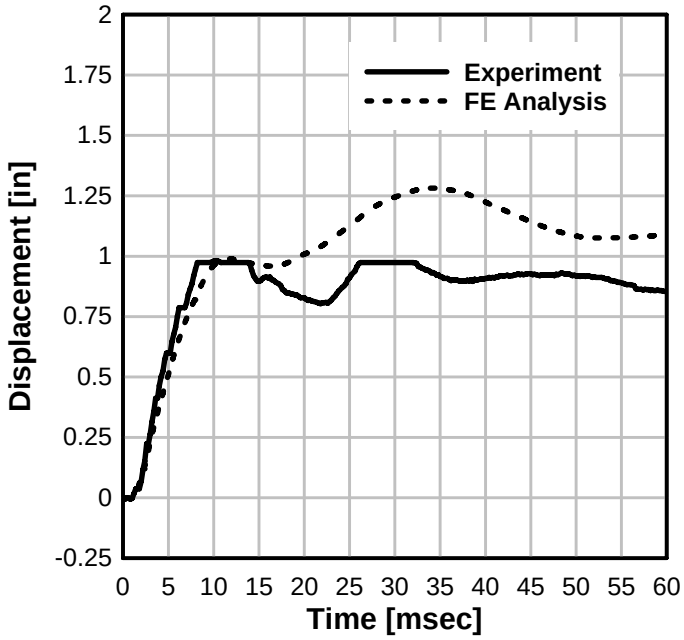

Figure 4.61: Test 5 comparison of midspan displacements

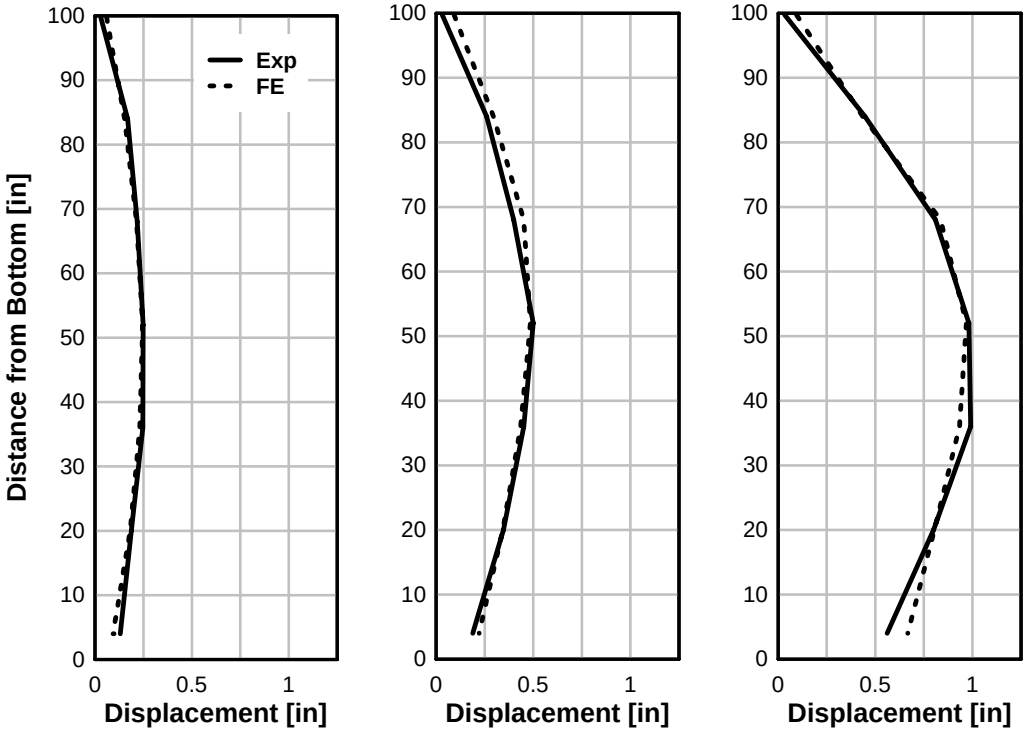

Figure 4.62: Test 5 comparison of displaced shape

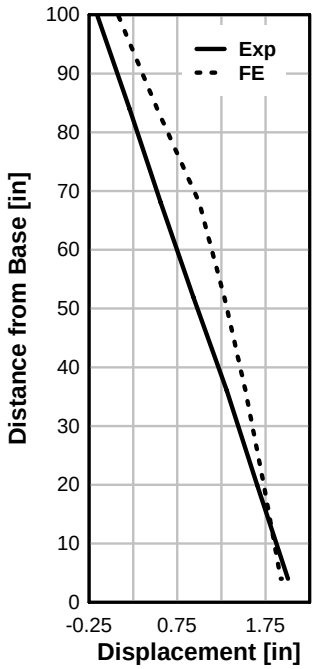

Figure 4.63: Test 5 comparison of displaced shape at later time

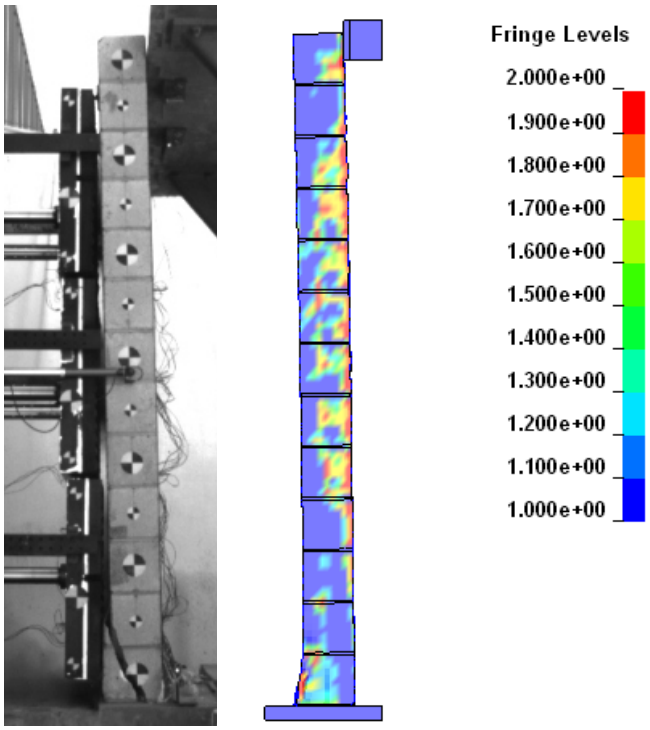

(a) **(b)**

Figure 4.64: Test 5 comparison of damage; (a) Experiment; (b) FE analysis

(a)

Figure 4.65: Test 5 comparison of damage at base; (a) Experiment; (b) FE analysis

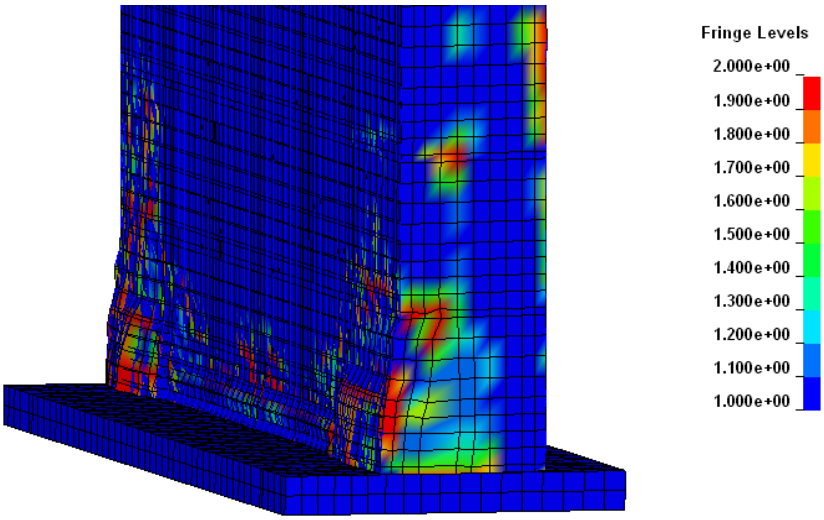

(b)

Figure 4.65: (continued) Test 5 comparison of damage at base; (a) Experiment; (b) FE analysis

TEST 6

The final test was performed on the specimen that has been previously impacted in Test 5. This specimen had been rehabbed to repair the damage that occurred at the base and a larger, stronger angle was used in replacement of the angle that failed in the previous test. The velocity, the impulse measured in the experiment and the impulse predicted in the FE analysis are listed for each BG in Table 4.16. The table shows that the predicted and measured impulses are different, but that the average impulse is similar. The measured average impulse was 286 psi-msec and the predicted impulse was 5.4% greater at 301 psi-msec.

Table 4.16: Comparison of impulse for experiment and FE analysis

BG	BG Velocity [ft/sec]	Exp Impulse [psi-msec]	FE Impulse [psi-msec]
3	24.3	274	347
2	26.3	256	227
1	26.2	327	329
Average	25.6	285.7	301.0

Figure 4.66 is a plot of the displacement time-history at the midspan of the specimen. This plot shows good agreement between the experiment and the analysis. The predicted peak displacement was equal to 1.23 in. which is 2.4% less than the 1.26 in. of displacement measured in the experiment. Figure 4.67 displays the displaced shapes at 25, 50, and 100% of the peak midspan displacement. The figure shows that at lower displacements the analysis matches the experiment very well. At 100% of the peak displacement the shapes differ more significantly. The damage states in the analysis and experiment are compared in Figure 4.68. The figure shows that the model was able to capture some of the damage observed at the base and near the top support. The level of the damage in the analysis, however, looks more distributed along the whole span which differs from the experiment where two significant cracks formed near the reactions.

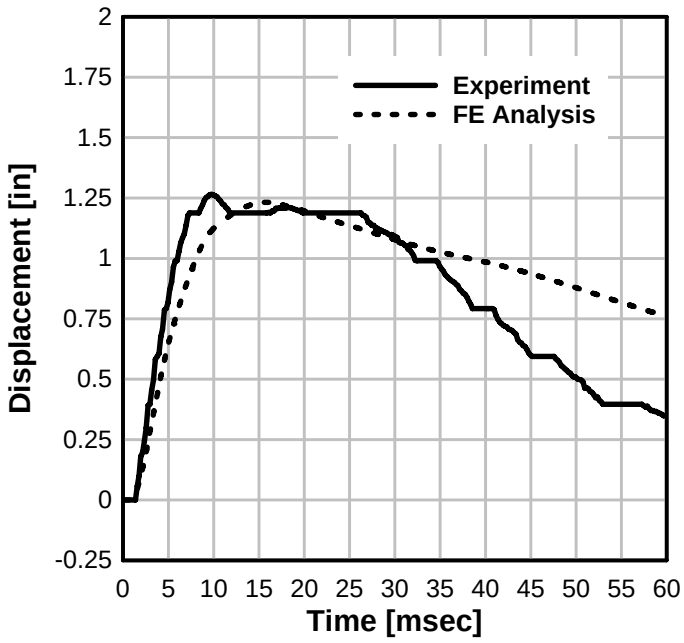

Figure 4.66: Test 6 comparison of midspan displacements

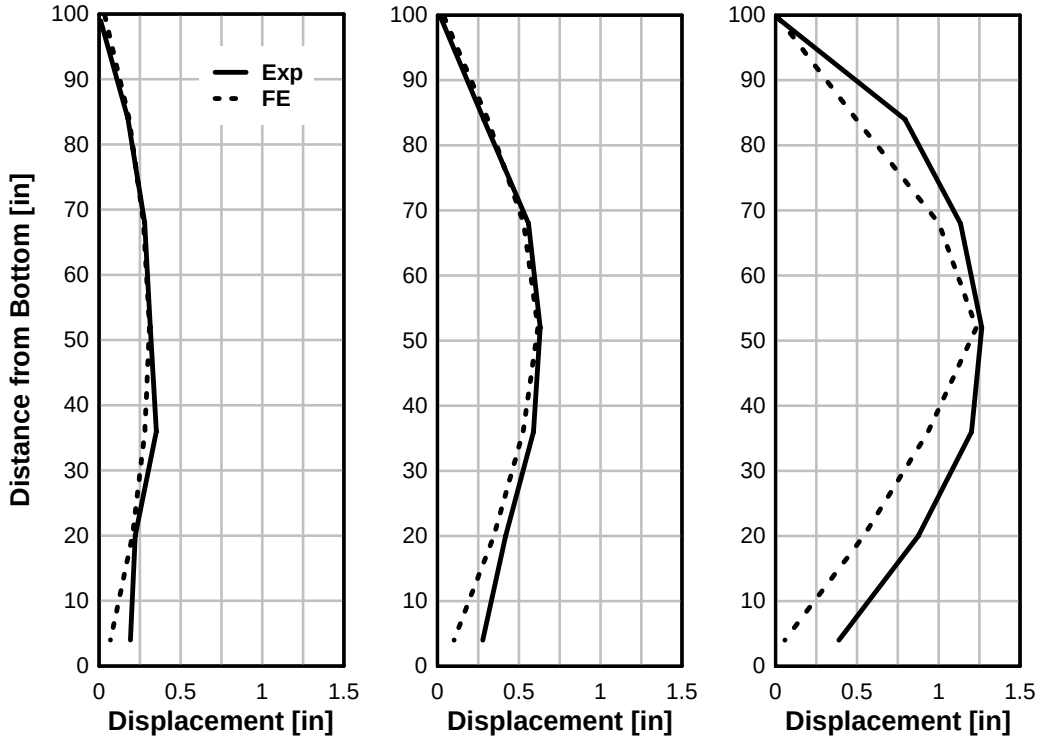

Figure 4.67: Test 6 comparison of displaced shape

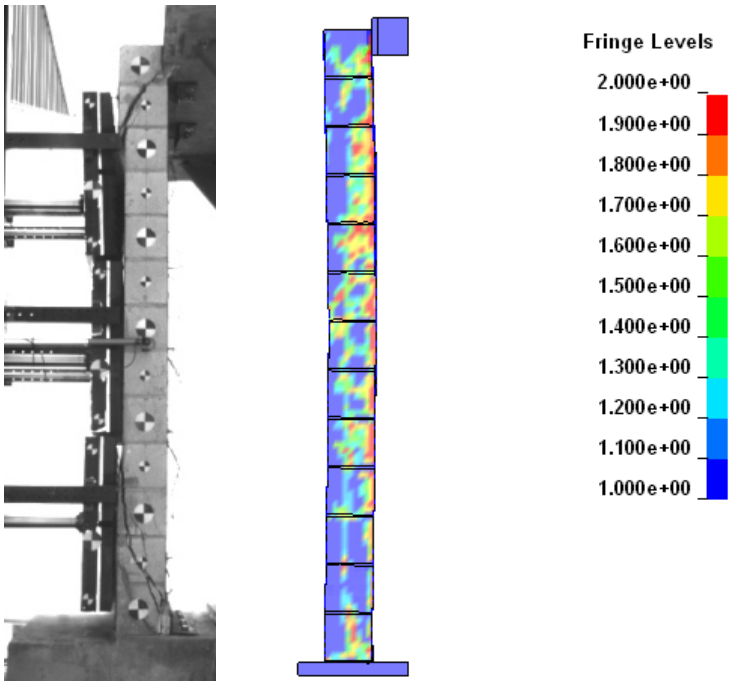

(a) **(b)**

Figure 4.68: Test 6 comparison of damage; (a) Experiment; (b) FE analysis

SUMMARY

The FE analysis of the blast simulator tests on CMU walls with CFRP retrofits provided accurate predictions of impulse, peak displacement, displaced shape, and damage for nearly all of the tests. Figure 4.69 is a plot of the predicted average impulse delivered by the BGs to the specimen versus the measured impulse. Included in the plot are a 45° line which represents a perfect fit of the experimental data and a line fit to the data with a regression analysis. The correlation coefficient for the fitted line is 0.98 and the standard error about the line is 9.78.

The plot shows that the FE model does a good job modeling the loads that are generated by the BGs when they impact the specimen at the specified velocity. In the

previous sections comparisons were made between impulses delivered in the analysis and the experiment for each BG in each test. Significant differences in impulse at the BG level were reported, while the overall impulses were similar. Despite the difference in load distribution, the FE analysis has been found acceptable for delivering the correct load because the displaced shapes for all the analyses matched the experiments reasonable well. This provides confidence that the differences in the load distribution do not significantly affect the behavior of the wall as long as the average load is similar.

Figure 4.70 is a plot of the predicted peak midspan displacement versus the measured peak midspan displacement. This plot includes a 45° line and the data has also been fit with a line determined by regression analysis. The correlation coefficient for the fitted line is 0.99 and the standard error about the line is 0.04. The plot demonstrates that the FE analysis predictions closely match those measured in the blast simulator tests.

Overall, it has been demonstrated in this section that the numerical model used with finite element analysis to simulate the response of CMU walls with CFRP retrofits to blast simulator impact provide accurate results that compare well to the experimental data. Quantitative comparisons between the analysis and the experiments show that the average impulses applied by the BG impacts are all within 6.4%. Furthermore, the predicted displacements are all within 9.1% of the measured displacements. Qualitatively it has been shown that the displaced shapes found with the analysis match the experimental results. The FE analysis was also able to produce the damage observed in the tests which consisted of translation and cracking at the base and/or diagonal shear failures near the top supports.

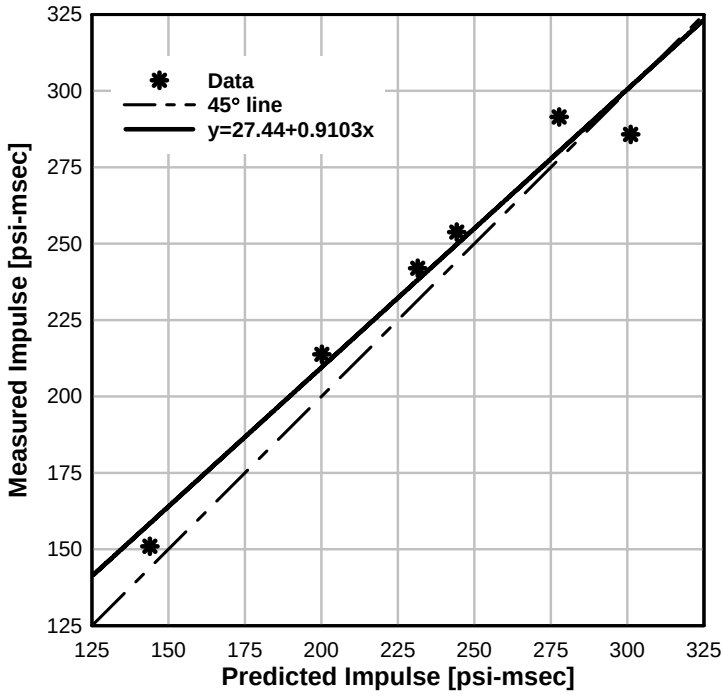

Figure 4.69: Predicted impulse versus measured impulse

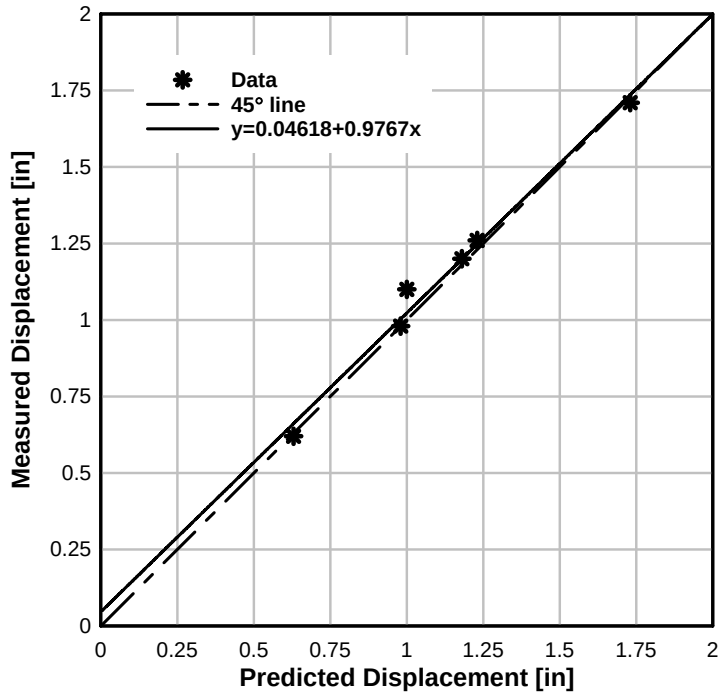

Figure 4.70: Predicted displacement versus measured displacement

4.6 PARAMETRIC STUDY

4.6.1 SPECIMEN AND RETROFIT DETAILS

The FE model described and validated in earlier sections of this chapter was used in a parametric study to investigate the effectiveness of CFRP retrofits on CMU walls subject to explosive load by both HE detonations and VCEs. Several retrofit designs were considered in the study; in all simulations the CFRP laminates were oriented in the longitudinal direction and the number of layers on the front and back were varied. Table 4.17 lists eight different designs that were used with the number of layers on the front and back side of the wall. An un-retrofitted wall was also included in the study to serve as a control.

Table 4.17: Retrofit Details for Parametric Study

Design	No. of Layers on Front	No. of Layers on Back
1	0	1
2	0	2
3	0	4
4	1	1
5	2	2
6	2	4
7	4	4
8	8	8

The details of the CMU wall FE model used in the parametric study match those used to model the blast simulator tests. The wall was 48 in. wide, 7.626 in. thick with a span equal to 8 ft 4 inches. Each wall was loaded in LS-DYNA using the keyword card *LOAD_SEGMENT. The boundary condition at the top uses a surface-to-surface contact with a 6 in. concrete slab and has beam elements used to tie back the wall during

rebound. At the base the wall has a tied contact with the footing and has a fixed 3 in. x 3 in. x 1/2 in. angle behind the wall.

4.6.2 LOAD DETAILS

The study varied the load to investigate the efficacy of the CFRP in mitigating hazards created by both HE and VCE blasts. In all of the simulations the load was applied to the front face of the wall as a pressure pulse that had an instantaneous rise to a peak pressure followed by a linear decrease back to zero. The duration of the load, t_L, is defined as the length of time from the peak pressure, p_{peak}, to zero pressure. It is also important to note that the impulse from this load, i, is equal to the area under the curve and is calculated with

$$i = \frac{1}{2} p_{peak} t_L \tag{1.27}$$

A schematic of the load applied in each analysis is displayed in Figure 4.71.

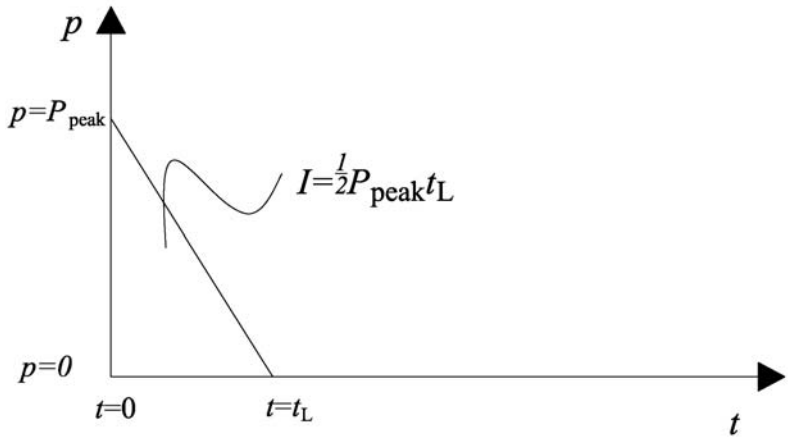

Figure 4.71: Pressure load for parametric study

The performance of the retrofit was assessed using pressure-impulse (PI) diagrams. A PI diagram is a plot of a curve with pressure on the x-axis and impulse on the y-axis. The curve represents a design criteria threshold where all combinations of pressure and impulse below and to the left of that line signify a passing design and all of the combinations above and to the right of the line signify a failure. PI diagrams can be reduced to the three loading regimes for walls; pressure sensitive regime, dynamic regime, and impulse sensitive regime. The pressure sensitive regime is when the duration time of the applied load is greater than the time it takes the specimen to respond. In this regime the response of the wall is a function of the peak pressure. Most CMU wall response to pressure pulses generated in VCE blasts are in this regime. In the impulsive regime the duration of the applied load is small compared to the time it takes the wall to respond. When loaded in this regime the walls will receive an initial velocity. The peak response of the wall in this regime will be a function of the impulse. CMU walls typically respond impulsively to pressure pulses created by HE detonations. Finally, in the dynamic regime the load duration of the pulse is similar to the time it takes the specimen to complete one cycle of free vibration. This regime is a transition from the pressure and impulsive sensitive regions. The walls may respond dynamically to both HE and VCE blast waves.

PI curves were generated by subjecting the FE models to loads in all three regimes. In the pressure sensitive regime the impulse was initially set to 800 psi-msec and then increased to 1200 psi-msec. At each impulse the peak pressure was varied between 0 and 40 psi. The duration of the load in this region was determined with

equation (1.27). In the case of the dynamic loading regime two sets of analyses where performed. In the first the load duration was set equal to 50 msec and the peak pressure was increased from 5 to 35 psi. The impulses was calculated for each pressure with equation (1.27). In the second set the pressure was set equal to 50 psi and the impulse varied from 0 to 750 psi-msec. For the impulsive sensitive regime, the peak pressure was set to 300 psi and then increased to 600 psi. At each level of pressure the impulse was varied between 0 and 450 psi-msec. Again, equation (1.27) was used to determine the duration time for each load. The ranges of loads used in the study are listed in Table 4.18. As an example, Figure 4.72 plots the combinations of pressures and impulses on a log-log scale that were used for the retrofit design using two layers of CFRP on the back side. Each point on the plot represents a single FE analysis. Included in the plot is a curve representing 2 in. of displacement. Every PI combinations above and to the right of the curve produces displacements greater than 2 in. and every combination below and to the left produces displacements less than 2 inches. The pressure and impulse required to give 2 in. of displacement were found through linear interpolations.

Table 4.18: Loading Parameters

Load	p_{peak} [psi]	i [psi-msec]	t_L [msec]
Pressure	0-35	800, 1200	45-200
Dynamic	5-35	5-875	50
Dynamic	50	0-750	0-30
Impulsive	50,300, & 600	0-450	0.58-2.33

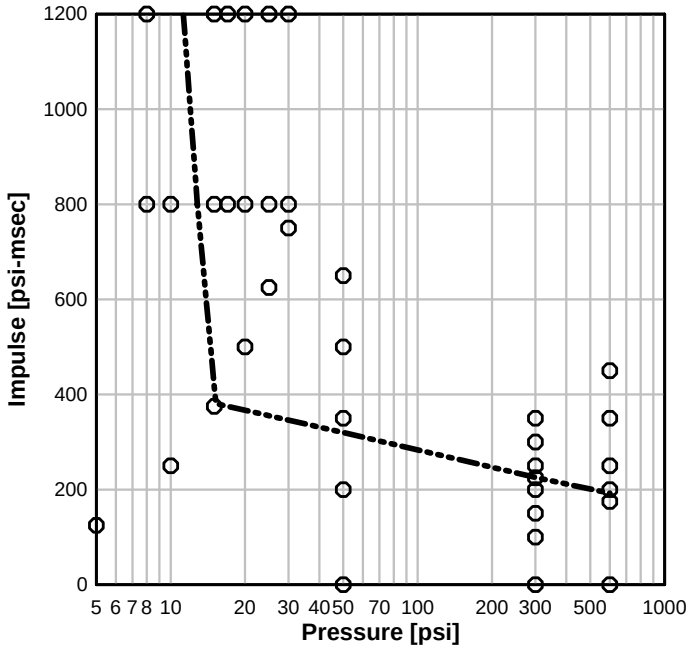

Figure 4.72: Loading combinations for PI curve generation

4.6.3 RESULTS

The results of the parametric study are summarized in the PI diagram illustrated in Figure 4.73. This PI diagram uses maximum support rotation equal to 2º as the design criteria to assess the performance of the walls. This rotation corresponds to a low level of protection as defined by the Unified Facilities Criteria (UFC) guidelines [57]. In a wall with a span equal to 100 in. this rotation occurs for a midspan rotation equal to 1.75 inches.

Figure 4.73 displays the PI curves for eight different CFRP retrofit designs and an as-built design. The plot very clearly shows that the use of CFRP composite can greatly improve the response of reinforced masonry walls. In the pressure sensitive region the retrofit walls meet the design criteria for peak pressures at least four times those required

to fail the un-retrofitted wall. When eight layers of CFRP are used front and back the peak required to meet the design criteria is nearly ten times greater than that for the as-built wall. The loads experienced in this region would be similar to those generated in a VCE detonation. In the case of the loads generated by an HE blast the wall response is in the impulse sensitive regime. The plot shows that the impulse required to fail the lightest retrofit wall with only one layer on the back is about twice that needed to fail the as-built wall. The retrofit with eight layers of composite front and back requires about three times the impulse as the as-built wall to reach the design criteria.

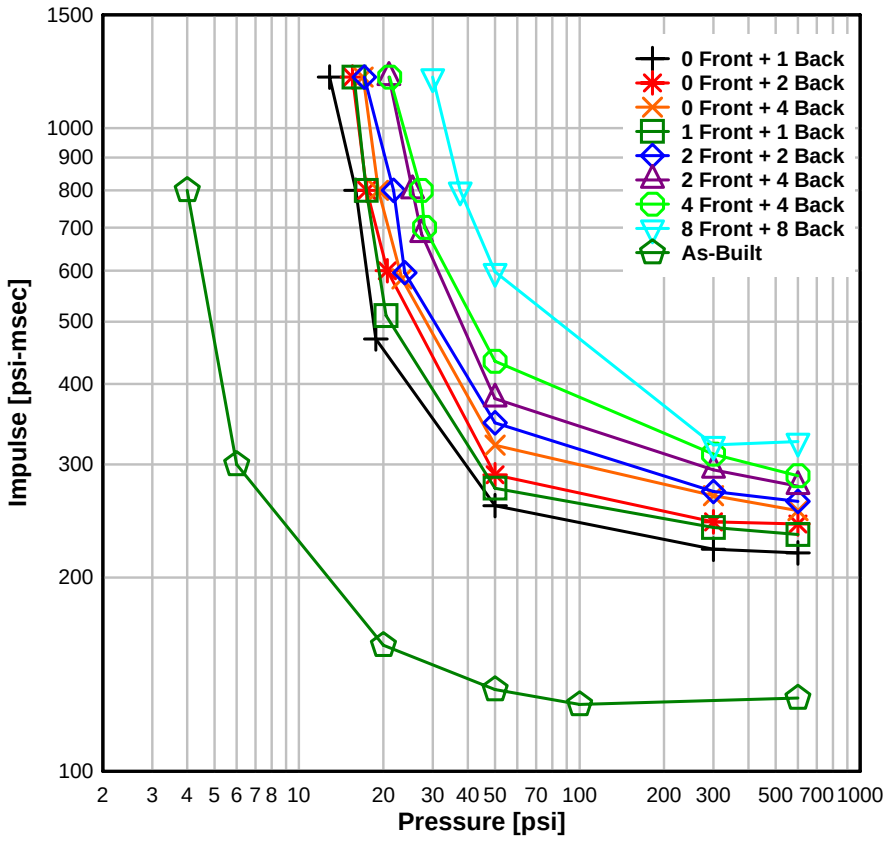

Figure 4.73: Pressure-Impulse diagram

The design criteria used to generate the PI plot above is based only on peak rotation demand and does not consider shear force demand in the wall. As a result the retrofitted walls loaded in the impulsive regime meet the design limit, but suffer a shear failure. It has been demonstrated in the blast simulator tests that a non-load bearing wall with a shear type of failure can still remain intact and will not pose a threat to the occupants of the building. A load bearing wall with a shear failure however, would be susceptible to a progressive collapse conditions and should be avoided.

The failure modes predicted by the FE analysis varied for the different wall types and the different loading regimes. The as-built wall failed in a flexural mode with the formation of a plastic hinge near the midspan. This type of failure occurred for all of the loading regimes. The retrofit walls, on the other hand, experienced two types of failures: the first being a flexural failure near the midspan and due to the masonry crushing and debonding of CFRP from the back face; and the other was a shear failure at the supports, typically near the top slab. The flexural failures were observed for the pressure sensitive and dynamic load regimes and the shear failures were predicted for the impulse sensitive load regime. Figure 4.74 displays examples of the flexural and shear failure modes predicted by the FE analysis for the wall with two layers of CFRP on the back and zero layers on the front. Figure 4.74 (a) illustrates the flexural failure that occurred from a pulse with a peak pressure equal to 25 psi and an impulse equal to 800 psi-msec. The failure is highlighted by crushing of the concrete masonry near the midspan on the impact face. The figure also shows that the CMU elements tied to the CFRP reinforcement have failed due to the large shear stresses being transferred from the composite to the wall. It

appears that this debonding failure occurs near the end supports and near the midspan on the tension side near where the compression failure occurs. The shear failure mode displayed in Figure 4.74 (b) shows the large transverse deformations near the top support. This failure mode occurs suddenly and releases some internal energy upon formation.

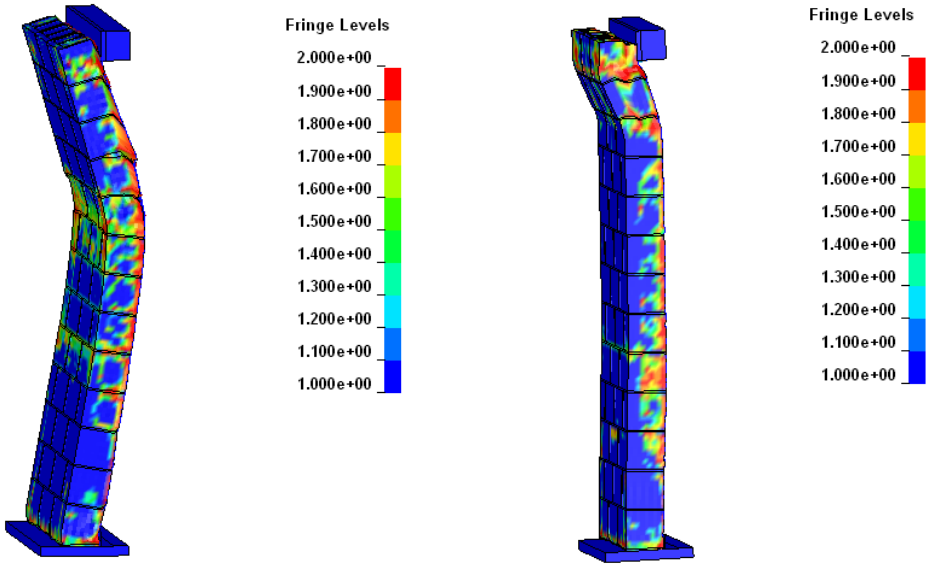

Figure 4.74: Example of failure modes; (a) flexural mode; (b) shear mode

It is interesting that the retrofit causes the walls to fail in shear under impulsive loads and in flexure under dynamic and pressure sensitive loads. This behavior can be explained by understanding the shear forces that are transferred to the reactions. Simple design calculations, as described in Chapter 2, determine the reaction forces that develop at the supports as a function of applied load and resistance force. The relation for the shear force is found by solving an equilibrium equation on a deformed member with uniform load. In the case of an impulsive load, the peak pressure of the applied load can be fairly large and the shear demand is too high. In this situation a large velocity is imparted to the mass of the wall and it does not have time resist in bending before a shear

failure occurs. When the load is in the dynamic or pressure sensitive region the applied load and the peak resistance are both small enough that the inertia and the bending are able to resist the load without a shear failure.

Plots of the shear forces calculated in the FE analysis with section cuts near the top of the wall are shown in Figure 4.75. The shear forces in the figure are from analysis performed on the retrofit wall with two layers of CFRP on the front and two layers on the back. Two curves are shown, the first is for the wall subject to a peak pressure of 300 psi and an impulse of 230 psi-msec; the second is for a load with a peak pressure equal to 20 psi and an impulse of 800 psi-msec. The peak displacement midspan displacement was equal to about 1.30 in. for both cases. Despite equal displacements the impulsively load wall had a shear failure and the wall with the pressure sensitive load only had flexural deformation. The curves of the plot demonstrates that the reaction force for the impulsive load increases rapidly to a peak force that is nearly double the load in the pressure sensitive regime. These plots are typical for the wall loaded in the different regimes for all of the FE analyses performed in the parametric study.

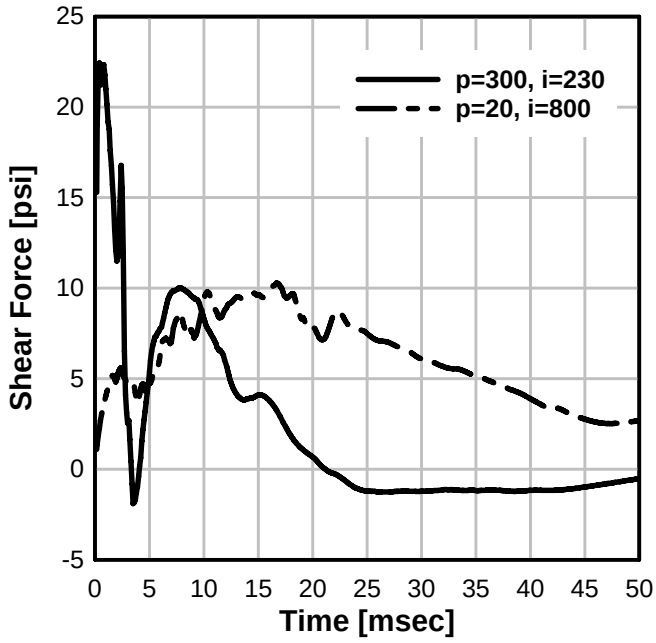

Figure 4.75: Shear force at top of wall

A plot of pressure versus peak shear force at the top of the wall for loads in the pressure sensitive regime is shown in Figure 4.76. The impulse associated with the pressures on the x-axis is constant and equals 800 psi-msec. In the plot are two curves: one is for a wall with zero layers of CFRP on the front and 1 layer on the back; the other is for a wall with eight layers on the front and eight layers on the back. The curves for these retrofit designs are plotted because they are the maximum and minimum CFRP reinforcement ratios used. Figure 4.77 is a similar plot except that shear force is plotted versus impulse for the walls in the impulsive load regime. The pressure associated with the impulses plotted on the x-axis is constant and equal to 300 psi. The two plots are shown to demonstrate that the shear force demand for an impulsively loaded wall is significantly greater than for a load in the pressure sensitive regime.

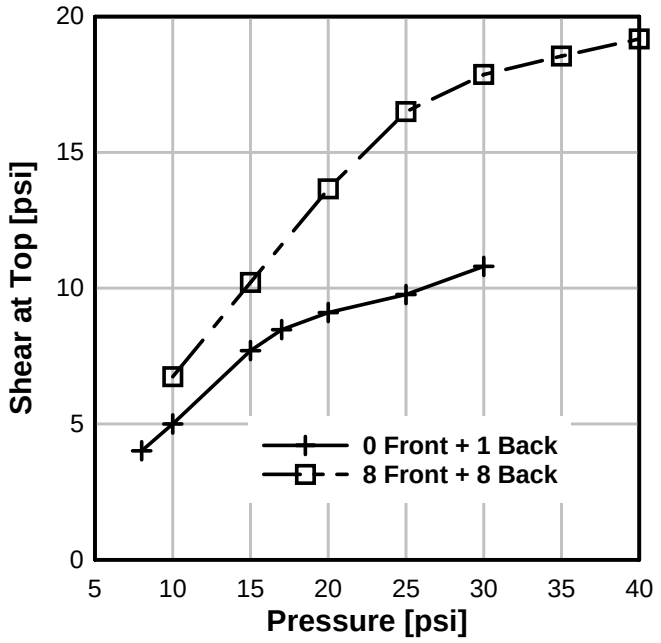

Figure 4.76: Shear force versus pressure in pressure sensitive load regime

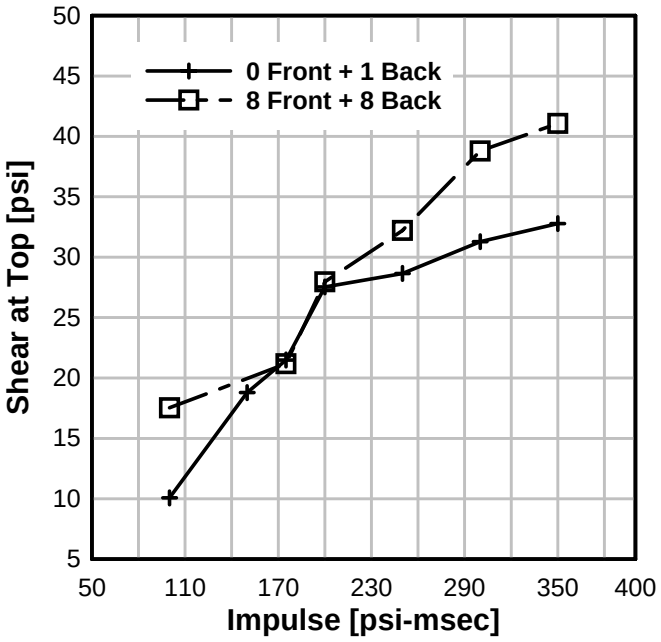

Figure 4.77: Shear force versus impulse in impulse sensitive load regime

All of the shear failures observed in the FE analysis for the impulsively loaded walls with a peak pressure of 300 psi occurred between 200 and 225 psi-msec; one exception was the wall with zero layers on front and four layers on the back failed at 250, although no runs were performed between 200 and 250 psi-msec so a failure could occur at a lower impulse.. The minimum shear force at which a failure occurred was 27.3 psi. It can be seen in Figure 4.76 that when the wall is loaded in the pressure sensitive regime the design most likely to develop a shear failure (8 layers front and back) has a peak shear force demand that is less than 20 psi.

Table 4.19: Peak shear and displacements for impulsive loading

Layers of CFRP on Front	Layers of CFRP on Back	Pressure [psi]	Impulse [psi-msec]	Shear at Top [psi]	Peak Displacement [in]
0	1	300	200	27.5	1.50
0	2	300	225	28.6	1.50
0	4	300	250	28.2	1.35
1	1	300	215	31.5	1.48
2	2	300	215	29.0	1.16
2	4	300	225	27.3	1.00
4	4	300	215	30.9	0.87
8	8	300	200	28.0	0.54

The table above shows that for a wall loaded impulsively an increase in the number of layers of CFRP used will result in a shear failure at a lower displacement. This is because the addition of CFRP makes the wall stiffer; thus the wall will attract larger loads at smaller displacements. This was observed in the FE parametric study where the wall with eight layers front and back developed a shear failure at a midspan displacement of 0.54 in. and the wall with one layer of CFRP developed a shear failure when the displacement was close to 1.5 inches. Figure 4.78 plots the displacement at

which a shear failure was observed in the CMU wall versus the reinforcement ratio of CFRP, ρ_{CFRP}.

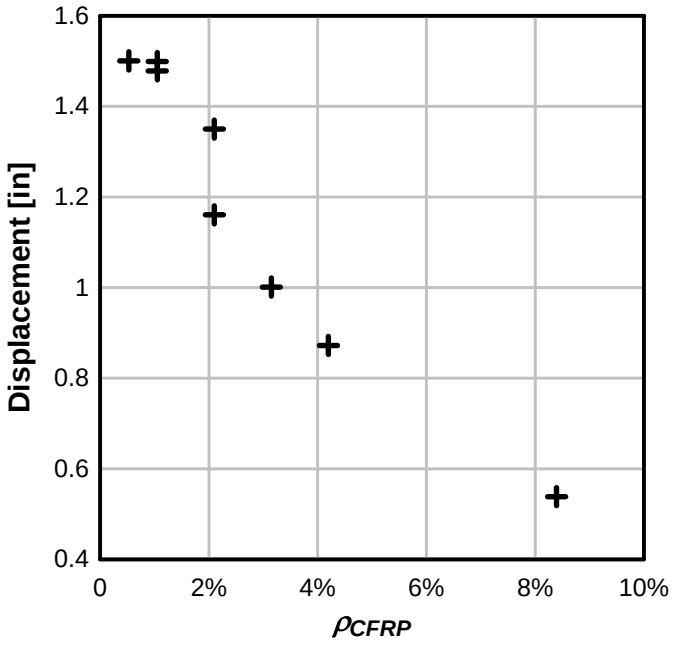

Figure 4.78: Displacement at shear failure versus CFRP reinforcement ratio

In summary, the results of the parametric study have shown that the performance of a CMU wall retrofitted with CFRP can be dramatically improved. However, a designer must take into account the shear force demand that arises from the additional strength and stiffness provided by the retrofit. A shear failure may be acceptable for the situation where the wall is non-load bearing because it has been shown that the CFRP can still contain the failed sections of the wall. However, when the wall is load bearing a shear failure can result in progressive collapse. The analysis has shown that the risk of a shear failure for a CFRP retrofit is highest when the load type is in the impulsive regime, such as the case when a wall is subject to a HE blast. When the wall is loaded by a VCE

blast, however, the shear forces that develop are significantly less, thus an ideal situation for a CFRP retrofit.

The FE analysis in the validation section and parametric study has also shown the importance of the blast simulator as a method for model validation. In SDOF analysis as described by TM 5-1300 [6] dynamic effects on the shear strength are ignored as a conservative measure. In the FE analysis the shear strength of the walls in increased with strain rates through scaling of the failure surfaces. If the assumed strain rate effects used in the FE model over predict dynamic increases on strength, then the analysis could be non conservative. This highlights the importance of validation of material models with the blast simulator. Conducting full scale tests with loads similar to actual blasts provides data that gives designers confidence in the analytical tools used to assess the performance of the structural component or system.

4.7 DESIGN METHODOLOGY

The following is a design procedure for determining the number of CFRP layers in the retrofit of a grouted CMU wall so that it meets the design criteria.

- Calculate the loading time history from the expected threat (HE detonation or VCE load) using methodologies described in Chapter 2.
- Select number of layers of uniaxial CFRP composite for trial retrofit design
- Calculate moment-curvature relation. This can be accomplished using a moment-curvature analysis program as described earlier in this chapter or by solving for moment and curvature at the strain state when the concrete crushes. Strain rate effect should be included for the material properties of the different materials.

For the second method use equations (1.1), (1.2), and (1.3) for the strain distributions; assume equivalent stress block for stress distribution in the masonry using (1.20) and use the stress-strain relations for CFRP and rebar as described in section 4.4.1. Vary the neutral axis until equation (1.16) is satisfied. Once neutral axis is found the moment at crushing can be determined with (1.18) and the curvature is found with (1.1).

- Calculate resistance function based on flexural strength and stiffness (moment-curvature relation). For simply supported wall use equations (1.22) and (1.23)
- Input resistance function and effective mass of the specimen into SDOF
- Run nonlinear SDOF analysis
- Check if design exceeds displacement criteria
- Check to see if loading results in shear failure
- Design details at the supports so that the connection strength exceeds the capacity of the wall. It is also important to design supports so that the boundary conditions used in the analysis are similar to the actual boundary conditions. If the actual boundary conditions vary the dynamic reactions calculated in the analysis may vary. It is suggested that final designs be checked with more advanced analysis methods, such as finite element analysis.

4.7.1 DESIGN EXAMPLE

This design example is included to demonstrate the steps taken to determine the number of layers of CFRP composite that are needed in the retrofit of an insufficient CMU wall. The HE and VCE loads that were calculated in examples for Chapter 2 will be used as the design loads; the HE load had a peak pressure of 300 psi, an impulse equal to 308 psi-msec, and a duration of 2.05 msec; the VCE load had a peak pressure of 8.8 psi, an impulse equal to 242 psi-msec, and a duration equal to 55 msec. The retrofit design will be evaluated for both types of loads.

The CMU wall to be retrofitted under goes one-way bending and is 7.625 in thick and is 15 ft wide by 8 ft 8 in. tall. The wall is grouted and has one layer of #4 longitudinal rebar spaced at 24 in. on-center which gives 0.1 in^2/ft. The bars are located 3.8125 in. from the front face of the wall. The shear reinforcement is minimal and it is assumed that is will not contribute to the shear strength. It is a load bearing wall and the design requirement for a high level of protection by the UFC [57] is that the support rotations must not exceed 1º or 0.8 in. of displacement under the blast load. The trial design for the CFRP will used two layers front and back.

MATERIAL PROPERTIES

The CFRP composite has a modulus of elasticity equal to 10.1×10^6 psi and will fail at 1.2% strain. The thickness of each layer of CFRP composite is equal to 0.08 inches. The reinforcing steel is assumed to have yield strength equal to 69 ksi, an ultimate strength equal to 108 ksi, and a modulus of elasticity equal to 29×10^6 psi. The strength of the concrete block is assumed to by 2000 psi and the grout strength is 4000

psi. The loading is a far range scenario and, according to TM 5-1300 [6], the strain rate in the masonry can be assumed to be 0.1 sec^{-1}. The dynamic increase factors for the concrete block and the grout with:

$$DIF = \left(\frac{\dot{\varepsilon}}{\dot{\varepsilon}_s} \right)^{1.026\alpha} \tag{1.28}$$

For the grout the parameter α is found with

$$\alpha_g = \frac{1}{(5 + 9\frac{f_g}{f_{co}})} = \frac{1}{(5 + 9\frac{4000}{1450})} = 0.033 \tag{1.29}$$

and the DIF is

$$DIF = \left(\frac{0.1}{30x10^{-6}} \right)^{(1.026)\cdot(0.033)} = 1.31 \tag{1.30}$$

The parameter α for the concrete block is found with

$$\alpha_{cb} = \frac{1}{(10 + 9\frac{f_{cb}}{f_{co}})} = \frac{1}{(10 + 9\frac{2000}{1450})} = 0.044 \tag{1.31}$$

and the DIF is

$$DIF = \left(\frac{0.1}{30x10^{-6}} \right)^{(1.026)\cdot(0.044)} = 1.44 \tag{1.32}$$

According to (1.9) the dynamic strength of the masonry is

$$f'_m = (0.59 r_{cb} f'_{cb} + 0.90(1 - r_{cb}) f'_g) = (0.40 \cdot 2000\,psi + 0.61 \cdot 4000\,psi) = 3240\,psi \tag{1.33}$$

where r_{cb}, the ratio of CMU block area to grout area equals 0.48.

MOMENT-CURVATURE RELATION

The moment and curvature at the strain when the concrete begins to crush will be used to develop the resistance function for the wall. It is assumed that the concrete will begin to crush at a strain equal to 0.003. The wall is one-way bending so the moment-curvature relation is only determined for a 12 in. strip.

To begin assume a neutral axis depth, c, equal to 2.47 inches and solve for strain in steel and bottom CFRP; strain in the top CFRP is equal to 0.003.

$$\varepsilon_s = \varepsilon_m \frac{d_s - c}{c} = 0.003 \cdot \frac{3.8125 \cdot in - 2.47 \cdot in}{2.47 \cdot in} = 0.00163 \tag{1.34}$$

$$\varepsilon_{cfb} = \varepsilon_m \frac{d_{cfb} - c}{c} = 0.003 \cdot \frac{7.625 \cdot in - 2.47 \cdot in}{2.47 \cdot in} = 0.00626 \tag{1.35}$$

The strains in the steel and CFRP are all below yield, therefore the stresses are related through the modulus of elasticity for the material. The tensile force in the CFRP on the bottom is equal to

$$T_{cfb} = E_{cf} \varepsilon_{cfb} A_{cfb} = (10.1x10^6 \cdot psi) \cdot (0.00626) \cdot (0.16 \cdot in \cdot 12 \cdot in) = 121.4 \cdot kip \tag{1.36}$$

The compressive force in the CFRP at the top is equal to

$$C_{cft} = E_{cf} \varepsilon_{cft} A_{cft} = (10.1x10^6 \cdot psi) \cdot (0.003) \cdot (0.16 \cdot in \cdot 12 \cdot in) = 58.2 \cdot kip \tag{1.37}$$

The tensile force in the rebar is equal to

$$T_s = E_s \varepsilon_s A_s = (29x10^6 \cdot psi) \cdot (0.00163) \cdot (0.1 \cdot in^2) = 4.7 \cdot kip \quad (1.38)$$

The compressive force in the masonry found with an equivalent stress block is

$$C_{mu} = 0.85 f'_m ab = 0.85 \cdot (3240 \cdot psi) \cdot (0.85 \cdot 2.47 \cdot in) \cdot (12 \cdot in) = 69.4 \cdot kip \quad (1.39)$$

Summation of the forces gives

$$121.4 \cdot kip + 4.7 \cdot kip - 69.4 \cdot kip - 58.2 \cdot kip = -1.5 \cdot kip \quad (1.40)$$

Equation (1.40) is close to satisfying equilibrium; therefore, the distance from the top of the section to the neutral axis is equal to 2.47 inches. If the summation of the forces was not equal to or near zero the neutral axis would be adjusted and the process would be repeated until equilibrium was reached. The moment at crushing can be found with

$$M = T_{cfb} d_{cfb} + T_s d_s - C_m \frac{a}{2} \quad (1.41)$$

$$M = 121.4 \cdot kip \cdot 7.625 \cdot in + 34.7 \cdot kip \cdot 3.8125 \cdot in - 69.4 \cdot kip \cdot \frac{2.47 \cdot in}{2} = 972 \cdot k - in \quad (1.42)$$

The curvature at crushing is

$$\phi = \frac{\varepsilon_m}{c} = \frac{0.003}{2.47 \cdot in} = 1215x10^{-6} \cdot \frac{1}{in} \quad (1.43)$$

RESISTANCE FUNCTION

The resistance function is determined with the moment-curvature with the equations that correspond to the resistance and midspan deflection when the concrete

crushes. The span of the wall is equal to 96 in. which is the total height 104 in. minus the support lengths top and bottom which are 4 in. each. The peak force will be

$$R_u = \frac{8M_u}{L} = \frac{8 \cdot 749 \cdot kip \cdot in}{96 \cdot in} = 77.3 \cdot kip \tag{1.44}$$

For blast design the resistance is typically normalize by the loaded area; thus the resistance is equal to

$$\frac{R_u}{bL} = \frac{77.3 \cdot kip}{12 \cdot in \cdot 96 \cdot in} = 67 \cdot psi \tag{1.45}$$

The deflection associated with concrete crushing is found with

$$\Delta = \frac{5\phi_u L^2}{48} = \frac{5 \cdot 1215x10^{-6} \cdot \frac{1}{in} \cdot 96^2 \cdot in^2}{48} = 1.16 \cdot in \tag{1.46}$$

The resistance function is elastic-perfectly plastic; the force displacement relation will be linear-elastic up to the 1.16 in. of displacement. If the displacement demand exceeds 1.16 in. the force will be limited to 67 psi. The CFRP retrofit design is symmetric so the resistance function will be symmetric for positive and negative bending.

SDOF ANALYSIS INPUT

The input parameters of the SDOF analysis are the resistance function, the load, and the mass. The mass of the specimen can be determined from its volume and the density of the masonry and the composite. The density of the masonry is assumed to be 130 lb/ft^3=0.075lb/in^3. The density of the CFRP composite is 0.28 lb/in^3. Therefore, the mass of the section is

$$m = \frac{8784 \cdot in^3 \cdot 0.075 \cdot lb/in^3 + 369 \cdot in^3 \cdot 0.28 \cdot lb/in^3}{386.2 \cdot \frac{in}{s^2}} = 1.99 \cdot lb \cdot \frac{s^2}{in} \qquad (1.47)$$

An effective mass equal to 0.78*m* is used when the wall responds elastically and is equal to 0.66*m* when the wall forms a hinge at the midspan and deforms plastically.

SDOF OUTPUT

The peak displacement output by the SDOF program for the VCE load case was 0.25 in. and the peak dynamic shear is 6.7 psi. The shear capacity of the wall is calculated with the static strength of the masonry as recommended by [6]. The static grout strength is 4000 psi and the static concrete block strength is 2000 psi which gives

$$f'_m = (0.59 r_{cb} f'_{cb} + 0.90(1 - r_{cb}) f'_g) = (0.28 \cdot 2000\,psi + 0.47 \cdot 4000\,psi) = 2440\,psi \qquad (1.48)$$

The shear strength is then equal to

$$V_m = 2\sqrt{f'_m}\, t_w b_w = 2\sqrt{2440}\,psi\,(7.625 \cdot in)(12 \cdot in) = 9.04 \cdot kip \qquad (1.49)$$

When normalized by the loaded area the shear strength is 7.84 psi. Therefore, the shear capacity exceeds the shear demand and the design is adequate for the VCE loads. It should be noted that the shear calculation here does not account for rate effects which can increase the overall strength. Increase factors may be suitable to design more efficient wall retrofits. It is recommended, however, that the models that use rate effects to predict strength are validated with test data.

The peak displacement output in for the HE load case is 1.10 in. and the peak shear is 31.25 psi. In this situation the additional layers of reinforcement are needed to reduce the displacement. However, the dynamic shear demand has already exceeds the shear capacity and additional layers will only increase the shear demand. In the situation where this is a non-load bearing wall a shear failure may be acceptable because tests have shown that the CFRP will contain the wall after failure. FE analysis should be performed to simulate the shear deformations that are not accounted for in the SDOF model. Load bearing walls subject to the defined blast load will require additional design considerations if CFRP composite retrofits are used. A method for shear strengthening is required otherwise the wall may fail and lead to progressive collapse. Test data for load bearing CMU with CFRP retrofits is needed to investigate their failure modes. Additional strength may be added through compression membrane action; however this is difficult to model without quality test data.

4.8 CONCLUSIONS

A series of six experimental tests were conducted on CMU walls with CFRP retrofits using the simulated blast loads. The tests demonstrated that the retrofits can add strength to the walls and that diagonal shear cracking is the predominant failure mode. The data from the tests was used to validate both a SDOF model and a FE analysis model. These models were then used to perform parametric studies on several different CFRP retrofit designs under a range of loads representing both HE and VCE blasts. The following conclusions have been drawn from the work described in this chapter:

- CMU walls with CFRP retrofits have increased strength against blast loads and will likely fail due to diagonal shear cracking to impulsive loads. Despite the cracking the retrofits contained the wall post failure preventing occupants of the building from being injured
- High fidelity data and high resolution visuals generated in the blast simulator tests can be used to validate both SDOF and finite element models. These models that incorporate both simple and complex material behaviors which include rate effects are useful tools that can aid engineers in designing efficient blast hardened structures. Validation of these models is important to provide engineers confidence in their design.
- A parametric study of several different CFRP retrofit designs subject to a range of different load types demonstrated that the system can be effective against load generated in HE and VCE blasts. In the case of HE blast the wall were susceptible to shear failures which should be avoided especially when the walls

are load bearing. The CFRP retrofit was very beneficial for walls subject to VCE blasts. The failure mode observed in this case was a flexural one, which is desired.

- A design methodology was also presented with examples of walls loaded by HE and VCE blasts. An example using this methodology demonstrated that CFRP retrofitted walls can be designed to resist VCE blast loads. These types of retrofit were not successful in the design against impulsive loads as experience in HE blast due to a shear failure. Additional strategies might be required to increase shear strength of the wall

4.9 RECOMMENDATIONS FOR FUTURE RESEARCH

The data available for CMU walls with FRP retrofits subject to blasts loads are limited to a small number of tests. The blast simulator has been demonstrated in this chapter to be a valuable tool which can be used to study specimen behavior including failure modes. The following is a list of recommendations for future research on CMU walls that could be performed with the blast simulator or by another testing method:

- Grouted CMU walls with CFRP subject to simulated VCE loads. This could be done with the blast simulator with a modification of the BG programmer
- Investigation of FRP debonding under blast type loads. This is a typical failure mode observed in static testing and is possible under blast loads
- Investigation of composite strips. This could reduce the reinforcement ratio enough so that the wall is strengthened, but shear failures are prevented
- Investigation of anchorage systems with CFRP composites

5 REINFORCED CONCRETE WITH FRANGIBLE BLAST PANELS

5.1 INTRODUCTION

A system that uses frangible panels on the exterior of reinforced concrete walls has been identified as a solution to reduce the hazard created in a HE blast. The panels used in the system are constructed from a mixture of cement, water, and wood chips that are pressed together to form a solid piece of material. When loaded by a blast the panels undergo crushing which is intended to dissipate energy and alleviate the hazardous effects of the load.

Multiple test series were performed with the UCSD Blast Simulator on RC walls with frangible panels to characterize the behavior of the protection system and to evaluate its efficacy in comparison to plain RC walls. The data generated from the experiments has been used to validate a simple one-dimensional model and a more detailed FE numerical model. The one-dimensional model provides a fast method for estimating the peak midspan displacement of RC walls with frangible panels and fixed-pin or simple-simple boundary conditions. The one-dimensional model was used to perform parametric studies on RC walls with frangible panels. The objective of the parametric study is to evaluate the situations when the use of frangible panels on RC walls is beneficial. The scope of this chapter includes:

- Summary of blast simulator testing on RC walls with and without frangible panels
- Description and validation of one-dimensional model for RC walls with frangible panels

- Description and validation of FE model for RC walls with frangible panels
- Comparison of one-dimensional model and FE model to air blast
- Results of parametric study with one-dimensional model
- Conclusions and recommendations for future research

5.2 PREVIOUS RESEARCH

The frangible panels investigated in this chapter are used in a specific system that has not been studied previously in any detail. However, several researchers have investigated other materials and systems with similar behavior as potential blast mitigation devices. These research programs have included experimental material testing, small scale laboratory testing, and full scale field testing and numerical modeling. Descriptions of some of the past work are described herein.

Reid and Peng [58] studied the dynamic crushing of wood under uniaxial load. In the study the authors tested several species of wood at multiple grain orientation under quasi-static loads to determine initial crush stress and locking strain. Specimens were then tested with uniaxial dynamic loads with impact velocities up to 300 m/sec. These tests demonstrated a significant strength enhancement of the initial crushing strengths of the specimens under dynamic loads. The author also present a simple shock model basted on a rate-independent, rigid-perfectly-plastic-locking (r-p-p-l) stress-strain relation for the wood. This model has been used in several following studies to determine the effectiveness of exterior panels to alleviate damage from blast loading. The authors

concluded that this model was successful in predicting the dynamic enhancement of the crushing strength of the specimen when loaded across that grain. When loaded along the grain the model was less successful.

Harragin et al. [59] used the r-p-p-l shock wave propagation theory to model the dynamic crushing of honeycomb aluminum foam under uniaxial impact loading. The curve is governed by the crushing strength and the locking strain of the foam. The authors concluded from the experiments on the foam that the crushing stress of a cellular material is sensitive to the impact velocity. At larger impact velocities the crushing mechanism of the cells is altered resulting in an enhancement of initial crushing stress and plateau stress. The plateau stress is well-predicted by the simple r-p-p-l shock model, but the initial crushing stress is governed by uniaxial plastic wave effects not included in the model.

Hanssen et al. [60] used full scale field tests to study the behaviour of aluminum foam panels to blast loads. Charges were detonated near a foam panel at selected standoff distances and the energy absorption or enhancement provided by the panel was measured with a ballistic pendulum that was attached to it. The experiments included some tests in which an aluminum cover plate was attached to the foam. The results of the experimental work demonstrated that the foam panels actually enhanced the energy created by the blast. This was not expected and is explained by the authors to be due to surface effects when the front panel of the foam was deformed by the blast wave. The deformed shape of the front panel is assumed to cause higher reflected pressures.

The authors of [60] also presented an analytical solution to describe the deformation behavior of an aluminum foam bar subject to a linearly decaying blast load. They used the one-dimensional shock model from [58] with the r-p-p-l stress-strain relation in the foam material. A FE model using LS-DYNA was used to verify the accuracy of the analytical model. Both models were used to demonstrate that the foam can decreased the magnitude of the stress wave as it travels from one end to the other. The magnitude of the pressure wave decreases from the peak pressure of the pulse the crushing strength of the material. The authors state that this reduction can provide protection to the structure at the local level. However, due to conservation of momentum, the duration of the pressure pulse is increased proportional to the reduction of the peak and the impulse does not change. The load pulse after traveling through the foam will most likely still be in the impulsive regime for the structure; thus since the impulse does not change the global response will not change.

There have been a few research programs to investigate the use of aluminum foam panels as a blast hazard mitigation strategy for small scale and full scale reinforced concrete structures. As part of a structural component test series Sadot et al. [61] of the Protective Research & Development Center at Ben-Gurion University of Negev in Israel used three different testing techniques to determining the dynamic mechanical properties of the aluminum foam: dynamic test with a Instron compression testing machine, impact testing with a 400 kg pendulum, and shock-wave impact tests using a shock tube. The respective methods provided data for low, medium, and high strain rates of loading. The density of the aluminum foam was also studied to determine its effect on energy

absorption. It was observed that the stress-strain curves at quasi-static rates and at strain rate associated with the impact loading were similar; however for the high strain rates observed in the shock tube tests the stresses where greater than the quasi-static tests when under equal strain. The authors concluded from the study that aluminum foam with greater density can absorb more energy at comparable levels of strain. They also stated that the amount of energy absorbed by a given foam increases as the compression rate increases.

Researchers at Ben-Gurion University also investigated on aluminum foam as a blast mitigation strategy for reinforced concrete structural components [62]. In [62] the authors present the results of experimental and numerical studies on the effect of aluminum foam panels on the response of RC beams and plates. The experimental portion of the study included impact pendulum testing on RC beams and plates with a mass that varied from 250 to 1000 kg. Two full-scale high explosive tests were also conducted on RC plates with and without the aluminum panels. The results of the pendulum test on the RC beam showed that less dense, thicker foam was able lengthen the load pulse duration; thereby reducing the peak dynamic load and the maximum strain in the rebar when compared to the plain RC beam. The denser, thinner foam produced results very similar to the plain RC beam. Similar results were observed for the pendulum tests on the RC plates.

The results of the pendulum experiments were then used to validate a numerical model using FE analysis. A partially validated FE model was also used to demonstrate that the beam with foam lengthened the load pulse duration which prevented the impactor

from rebounding and striking the beam additional times. In the simulation and experiment on the RC beam several load pulses were delivered to the specimen because the impactor rebounded and the struck again. The authors state that the foam decreased the impulse delivered to the specimen. They came to this conclusion by comparing the data of the test where only one impact occurred in the foam-protected wall to the data for the plain RC beam that was impacted repeatedly by the rebounding impactor. This however, may not be a fair comparison because in an airblast the load is applied only once. Most likely the foam protected structure will have a similar impulse as the plain structure due to conservation of momentum. The final portion of the study was to perform a field test with actual explosives on two walls; one with aluminum panels and one without. The authors concluded from these tests that the wall with the panels performed better because it had less cracking, lower peak rebar strains and lower peak accelerations at the midspan.

Additional full scale field tests on RC plates with aluminum foam panels carried out by Ben-Gurion University are discussed in [63]. The purpose of these tests was to generate data that could be used to verify and validate the computer codes used to model this system and to study the efficacy of aluminum foams to mitigate blast effects. Two tests were performed on four specimens. The two specimens in the first test were reinforced with conventional rebar; one with aluminum foam and one without. The two specimens in the second test had fiber reinforcement in addition to rebar. According to the authors the results of the tests on the concrete with fiber reinforcement demonstrated that the wall with aluminum panels had less cracking on its back side and thus less

damage. The protected wall also had a significantly reduced acceleration, velocity, and displacement at the midspan. Similar results were observed for the RC walls with conventional reinforcement; the specimen with aluminum panels had less cracking and smaller peak acceleration, velocity, and displacement at the midspan. The results of the experiments were then compared to hydro-code simulations which showed good agreement between the two. The authors conclude that the aluminum foam is capable of modifying the response of the slab; however, they are unable to make a definitive conclusion as to the efficacy of the foam for practical purposes.

Zou et al. [64] simulated the crushing of 2D hexagonal-cell honeycomb using finite element analysis to explore the dynamic response of cellular materials and to investigate the assumptions used to derive the one-dimensional shock theory used in [58]. In this one-dimensional model the material had a r-p-p-l stress-strain relation. The authors concluded from the study that at a critical crushing speed the cells collapse in a shock-like manner. This critical velocity was determined to vary with the density of the material. They also found that the shock front thickness is equal to about one cell dimension and is independent of shock velocity and relative density. With the FE model they were also able to demonstrate that the crush strength of the material and the energy dissipation increase with increased crush velocity. Finally, it was found that the one-dimensional model based on the r-p-p-l curve tends to over estimate the crushing stress and energy absorption.

In another study Ye and Ma [65]-[66] modified the one-dimensional shock model for foam cladding originally presented in [58] by including the interaction between the

load, cladding, and structure. The model was used in a parametric study to investigate when the cladding improves the response of the structure. The authors concluded in the study that the foam panels are most effective when the force needed to crush the panel is similar to the plastic resistance of the structure assuming an elastic perfectly plastic load deformation response. They also state that the thickness and density need to be selected so that the foam does not become fully compacted prior to the total load being transferred. The optimum design is for the foam to reach total compaction at the instance when the walls reached its peak midspan displacement. The authors concluded that the addition of foam cladding can increase the blast capacity of the structure, but needs to be designed appropriately with consideration of the crush strength, density, and thickness relative the mass and resistance of the structure.

Li and Meng [67] investigated the characteristics of compressive shock wave propagation in cellular materials using a one-dimensional mass-spring model. The model used a nonlinear spring for the stress-strain relation of the cellular material. The nonlinear force deformation was elastic perfectly-plastic with a densification region. Following a description of the numerical model the authors demonstrate the wave propagation that is simulated in the analysis. The results of the simulations demonstrate that shock enhancement in the cellular material will occur. The authors state that when a protected structural component is sensitive to pressure intensity more than impulse, the addition of cellular material may cause unexpected results.

5.3 SERIES I BLAST SIMULATOR EXPERIMENTS

5.3.1 SERIES I INTRODUCTION

Two test series were conducted on full scale reinforced concrete walls with frangible panels. The first test series consisted of seven quasi-static tests on six specimens and nine blast simulator tests on an equal number of walls. These tests consisted of simply-supported specimens with one way bending at different thickness with and without frangible panels subject to a range of blast simulator loads. A second test series was conducted to expand the understanding of the same frangible panels. This series was performed with 12 additional walls; six with frangible panels and six without. These specimens had a fixed-pinned boundary condition with one way bending and were used to provide direct comparisons between RC walls with and without the panels.

There were fifteen walls built as part of the first wall test series with frangible panels. Six of the fifteen walls were tested quasi-statically and nine of the walls were tested dynamically with the blast simulator. Three of the six walls that were tested quasi-statically were built with frangible panels and the other three were constructed with only reinforced concrete. In the nine dynamic tests there were six walls that were built with frangible panels and the remaining three walls made of reinforced concrete.

Each of the wall specimens was labeled X(X)-Y-ZZ (-2) where

X(X): RC= reinforced concrete; FP = frangible panel

Y: D = Dynamic; S = Static

ZZ: Wall thickness in cm

2: Second wall of this type

5.3.2 SERIES I WALL SPECIMEN DETAILS

All the walls are 137.8 in. (350 cm) tall and 4 in. (122 cm) wide. The reinforcing steel for the walls is Grade 40 and the concrete has specified 28 day strength of 4351 psi (30 MPa). The frangible panels are 1.57 in. (4 cm) thick. Therefore, the 20 cm, 25 cm, and 30 cm thick overall frangible panel walls have core thickness of 4.72 in. (12 cm), 6.69 in. (17 cm), and 22 cm (8.66 in.). The 20 cm and 25 cm frangible panel and RC walls had seven 8 mm longitudinal bars with 90° hooks at the both ends spaced at 7.87 in. (20 cm) for the front layer of reinforcing. The back layer of longitudinal reinforcing consisted of 12-8 mm bars with 90° hooks at the both ends spaced at 3.94 in. (10 cm). The transverse reinforcement consisted of 8 mm stirrups spaced at 7.87 in. (20 cm) on the front face and 3.94 in. (10 cm) on the back face. The layout of the reinforcement for the 30 cm thick frangible panel and RC walls is similar to the of the 20 and 25 cm walls except that the seven longitudinal bars in the front layer and 12 bars in the back layer are 10 mm. The stirrups for the 30 cm frangible panel and RC walls are also 10 mm and have the same spacing as the 20 and 25 cm walls.

5.3.3 SERIES I QUASI-STATIC TEST SETUP

Six specimens were tested quasi-statically to characterize wall behavior. The data from this test will be used to develop the resistance function for the frangible panel walls. The span for each wall was 129.75 inches. Four 50 kips actuators applied a uniform load to the full span of the walls to produce one-way bending. The walls were loaded until

they failed. Failure was be determine by the condition of the concrete and the reinforcing steel during the test. The walls were simply supported by half round roller supports mounted on concrete abutments. The actuators were mounted on a W14x109 beam, which was connected to two steel frames that were post-tensioned to the reaction floor with 1-3/8 in. diameter Dywidag rods. The load was transferred between the actuators and the specimen by a steel load spreader. The load spreader was built-up by ¾ in. plates. It is 8 in. tall and has a footprint of 27 in. x 48 inches. At the interface between the load spreader and the specimen was a 2 in. thick rubber pad that was used to apply the uniform load more efficiently. East and south elevation views of the quasi-static test can be seen in Figure 5.1 and Figure 5.2. A plan view of the test setup can be seen in Figure 5.3.

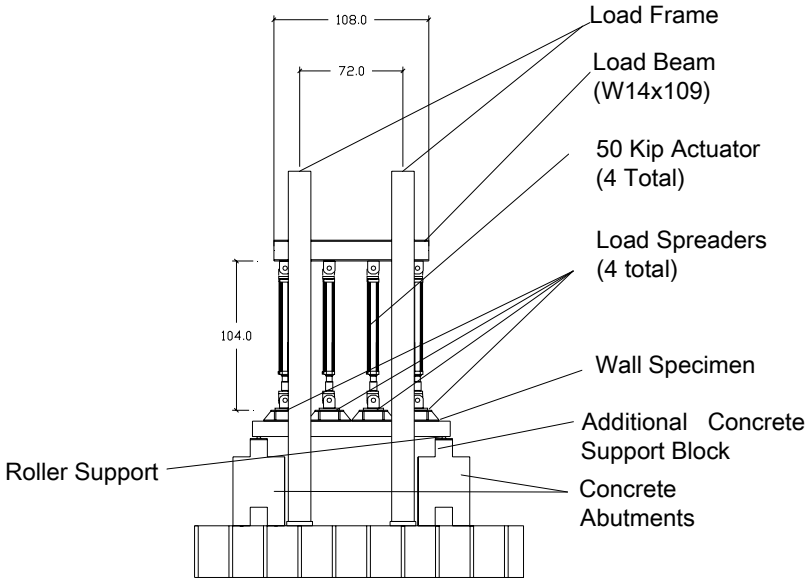

Figure 5.1: Quasi-static test- East elevation

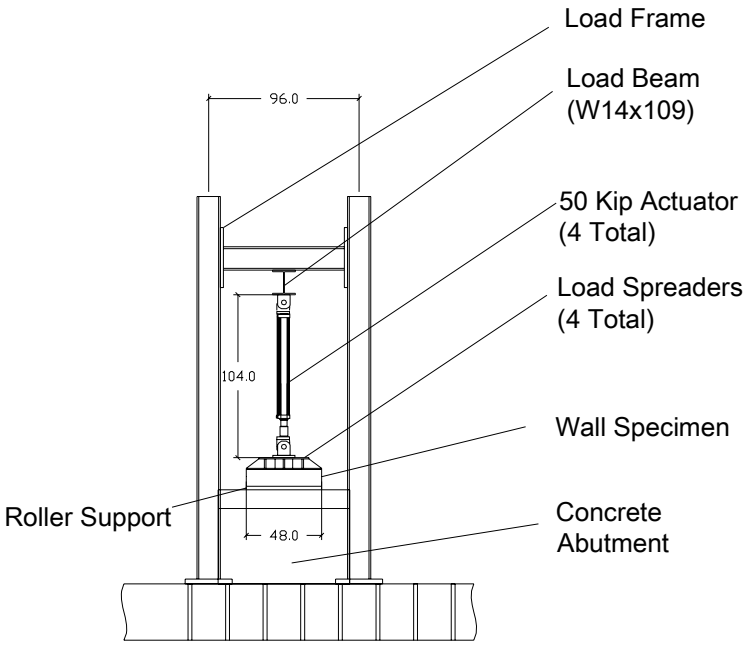

Figure 5.2: Quasi-static test- South elevation

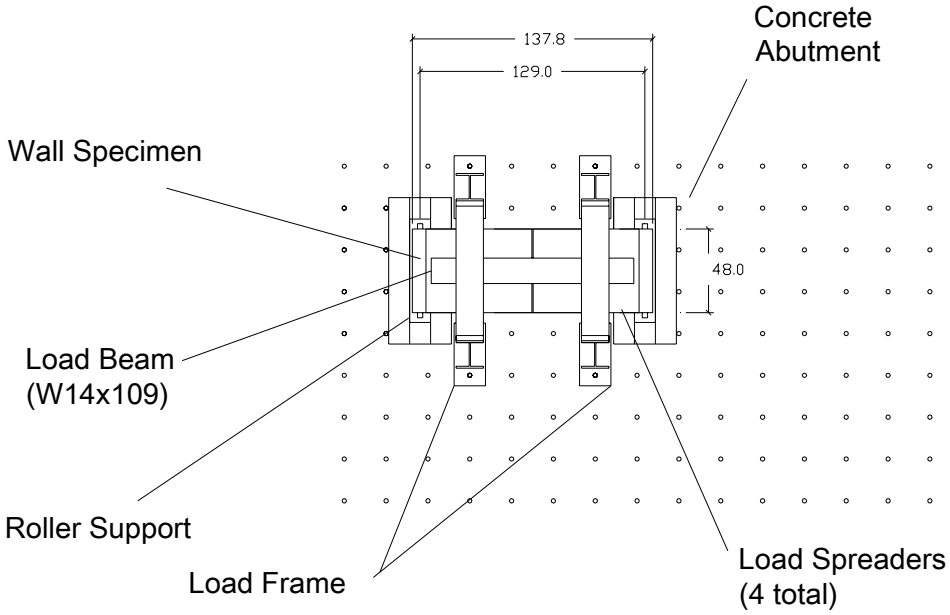

Figure 5.3: Quasi-static test- plan view

5.3.4 SERIES I DYNAMIC TEST SETUP

Nine specimens were tested in the blast simulator. The purpose of these tests was to study the behavior of the frangible panel walls at loading rates equivalent to those seen during blast loading. The setup for the dynamic tests is illustrated in Figure 5.4 which is an elevations of the test from the east. The span of each wall was 129.75 in. (329.6 cm), which was the same as the span for the quasi-static tests. The wall was simply supported at the top and bottom to allow one-way bending. At the top support, 4 in. of the wall reacted against a 6 in. reinforced concrete slab that was tied into the back reaction wall. The wall rests on a stepped concrete footing and reacts against a 4 in.x4 in. angle that was embedded in the concrete. The shear forces were transferred by the footing through a concrete spacer block to the back reaction wall. At the top supports two 12 in. long 1/4 in. thick bent steel plates are used to catch the edge of the wall when it rebounded. The bottom of the wall was restrained during rebound by two 12 in. long section of 4 in. x 4 in. x 1/4 in. steel angle. Neoprene foam pads, 4 in. thick, were placed between the steel rebound restraints and the walls to allow the top and bottom of the specimen to rotate freely without crushing the corners (Figure 5.5 and Figure 5.6).

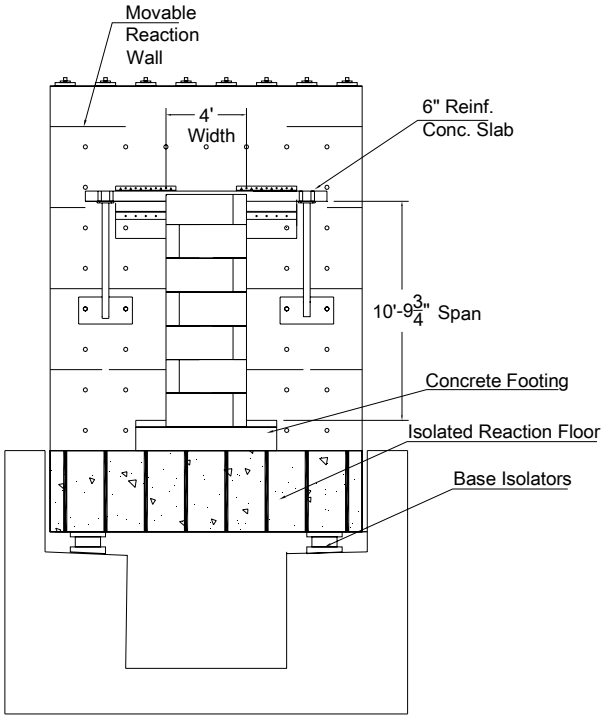

Figure 5.4: Series I dynamic test setup- East elevation

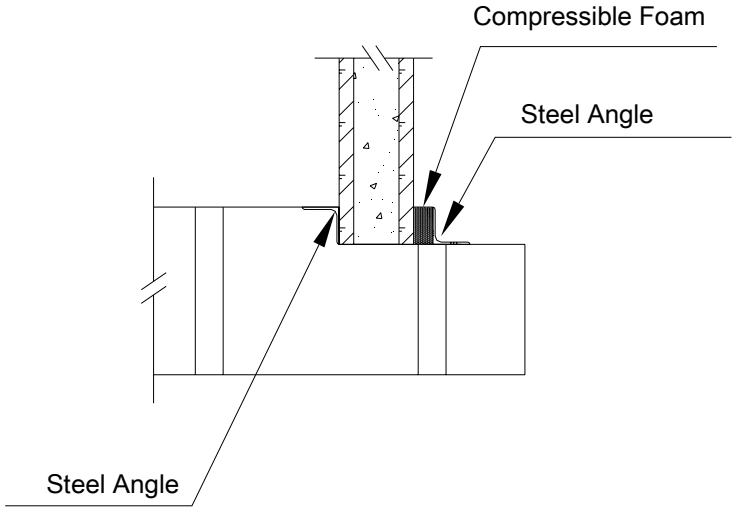

Figure 5.5: Series I dynamic test setup- bottom support conditions

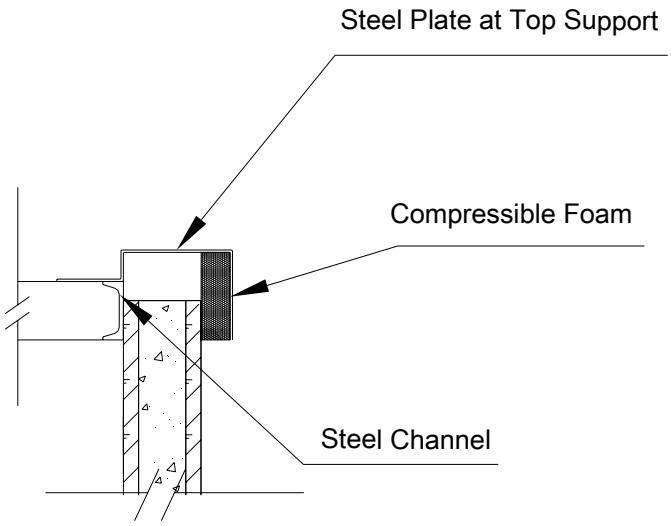

Figure 5.6: Series I dynamic test setup- top support conditions

The specimens were loaded by four BGs that impacted it at a uniform velocity. The dimensions of each BG impact plate are 30 in. x 48 inches. The weight of each BG impact plate is 668 lbs (303 kg). The center-to-center spacing on the plates was 30.75 in., which leaves a 0.75 in. gap between the plates. At the top and bottom of the specimen there was a 3.75 in. gap between edges of the BG plates and the edges of the support.

Each wall specimen was subjected to a simulated blast load that correlated to a charge weight of TNT at a specific standoff distance. The impulse delivered to the specimen by the BGs matched the load from this explosive charge.

5.3.5 SERIES I QUASI-STATIC TEST INSTRUMENTATION

The displacements of the walls during loading were measured using 19 linear potentiometers located at seven different locations that were equally spaced along its span. Figure 5.7 shows a plan view of the wall test with the locations of the potentiometers.

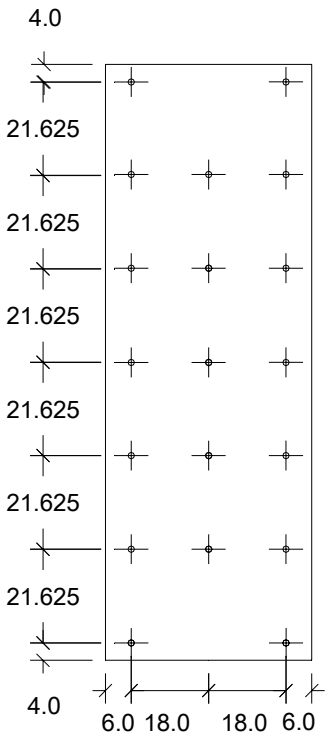

Figure 5.7: Location of linear potentiometers

The specimen rotations along the span of the wall were measured during each test with ±45° inclinometers. The first test used 10 inclinometers to measure the specimen rotation. Five inclinometers were used on each side of the wall. The first pair of meters was located at the south support and the fifth pair was located at the north support. The other three pairs were distributed along the length of the specimen with even spacing equal to 32.44 inches. Following the first test the resolution of the inclinometers was increased and the redundancy was decreased. The second test used nine inclinometers that were mounted on the west side of the wall and distributed between the north and south support with a spacing of 16.22 inches. The final four tests used 10 inclinometers to measure the rotation along the length of the specimen. The meters were distributed

evenly between the north and south support on the west side of the wall with spacing equal to 14.42 inches.

The load applied to the walls during testing was measured by internal loads cells located in the actuators. Four actuators were used to load the wall and their loads were summed to determine the total load on the specimen. The displacement of each actuator piston was also recorded during each test.

The strain in the reinforcing steel was measured rebar gages that were installed at the midspan of the reinforcing steel before the walls were built. There were four gages per wall in the frangible panel walls and two gages per wall in the RC walls. The locations of the gages in the frangible panel and RC walls can be seen in the figures below.

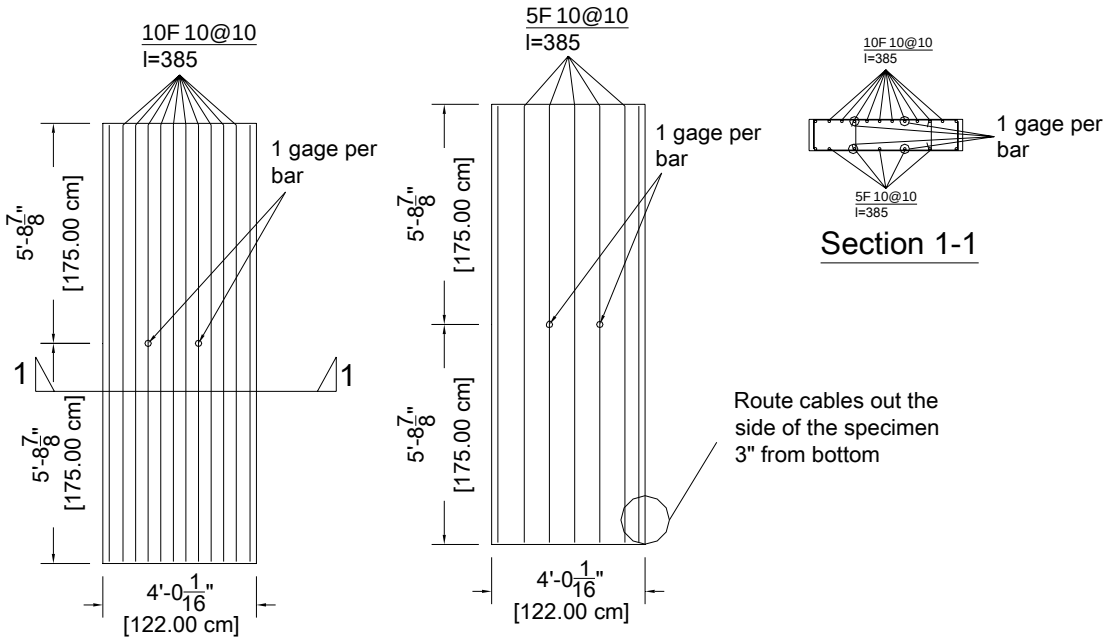

Figure 5.8: Location of strain gages in frangible panel walls

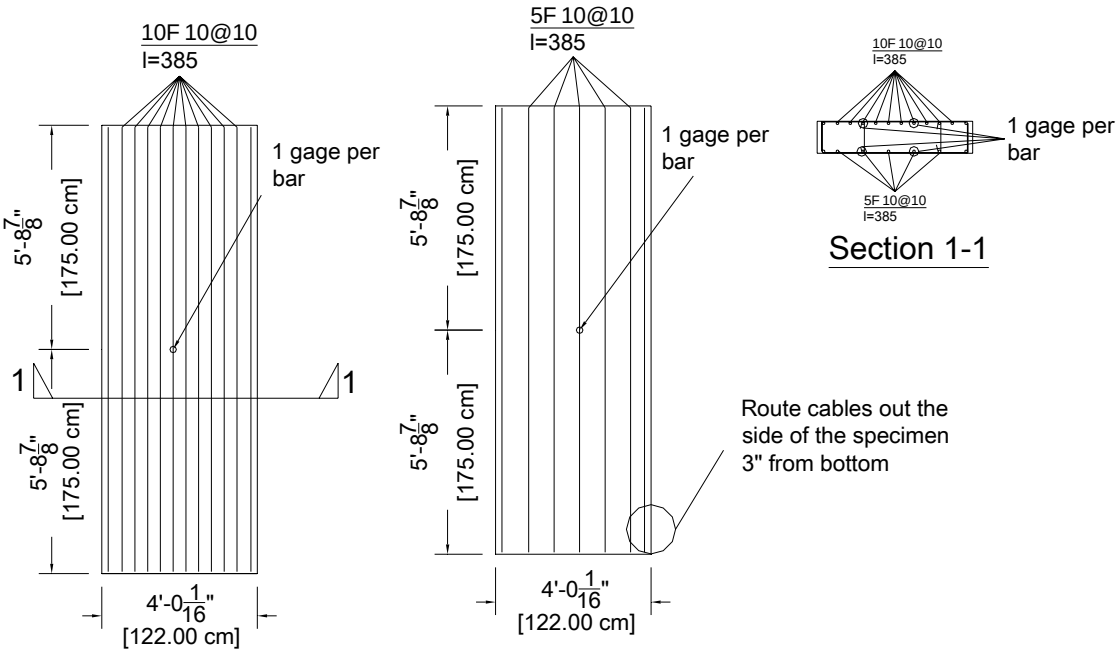

Figure 5.9: Location of strain gages in reinforce concrete walls

5.3.6 SERIES I DYNAMIC TEST INSTRUMENTATION

A high speed data acquisition system was used in the blast simulator tests. This system samples at 14 bits and 1 MHz. The data acquisition system has a capacity of 52 channels and is externally triggered from the MTS controller that is used to fire the BGs.

High speed video was captured with three Phantom v7.1 (Vision Research) cameras. The first camera recorded in black and white at a rate of 5000 frames per second at a resolution of 400 x 600. The other two cameras recorded in color and also ran at a rate of 5000 frames per second with a resolution of 400 x 600. The cameras are capable of different frame rates at different resolutions. The cameras were externally triggered from the MTS controller. TEMA was used to obtain graphical displacement

and velocity measurements from the video capture. Figure 5.10 displays the sections of the wall that were filmed in each test. Phantom camera 1 (black and white) was used to measure displacements and velocities of the entire wall. Phantom cameras 2 and 3 were equipped with zoom lenses and recorded videos in color. These cameras were used to zoom in and measure the top and bottom portion of the wall during the tests. These videos provide impact velocities of the BGs and visuals of the wall behavior under impulsive loading.

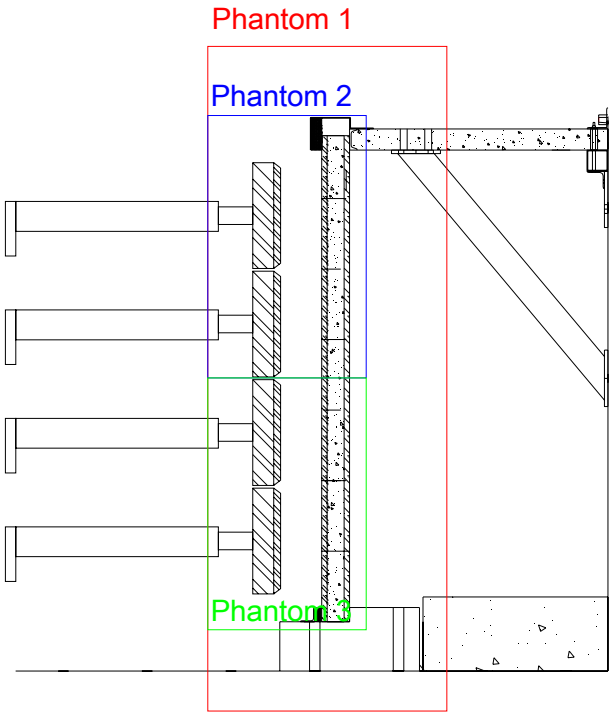

Figure 5.10: Phantom Camera Views

The accelerations of the BG impact plates during impact were measured with 10K g piezoelectric shock accelerometers. Three gages were mounted on each BG impact plate to ensure accuracy and redundancy. They were attached to the back of the plate 12

in. to the right, left, and top of the centroid. The cables that transmit the acceleration signal to the data acquisition system were fastened to the BGs to minimize artificial signals in the data caused by their vibration. Figure 5.11 shows the locations of the accelerometers on the back of the BG plates.

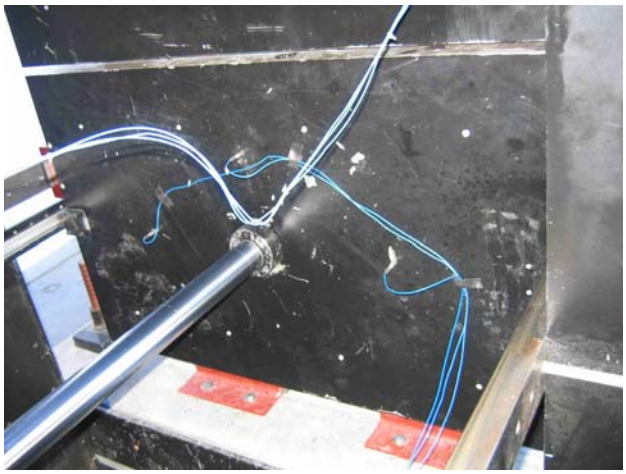

Figure 5.11: Location of BG accelerometers

The velocity for each BG was determined from the Phantom video record using the TEMA software package. The software then differentiates the displacement time history using a seven point numerical differentiation scheme to obtain the velocity time history. The Phantom camera videos were also used in conjunction with the TEMA software to measure specimen displacements at several different locations. Targets were mounted on the wall before the test to assist in tracking the wall displacements. The locations of the targets used to track displacements in the specimen are listed in Table 5.1.

A linear potentiometer was also used to measure the specimen's midspan displacement. This was done to ensure that measurements made using the Phantom video

are accurate and redundant. The free end of the linear potentiometer was bolted to the wall with a threaded rod that was embedded into the concrete with epoxy. The fixed end was bolted to the BG support tower. The location of the linear potentiometer can be seen in Figure 5.12. Accelerations in the wall were measured by 5K g piezoelectric shock accelerometers. The locations of the gages can be seen in Figure 5.7.

The strain in the reinforcing steel was measured using 5mm rebar gages. The gages were installed at the midspan of the reinforcing steel before the walls were built. There were four gages per wall in the frangible panel walls and two gages per wall in the RC walls. The locations of the gages in the frangible panel and RC walls are shown In the figures below.

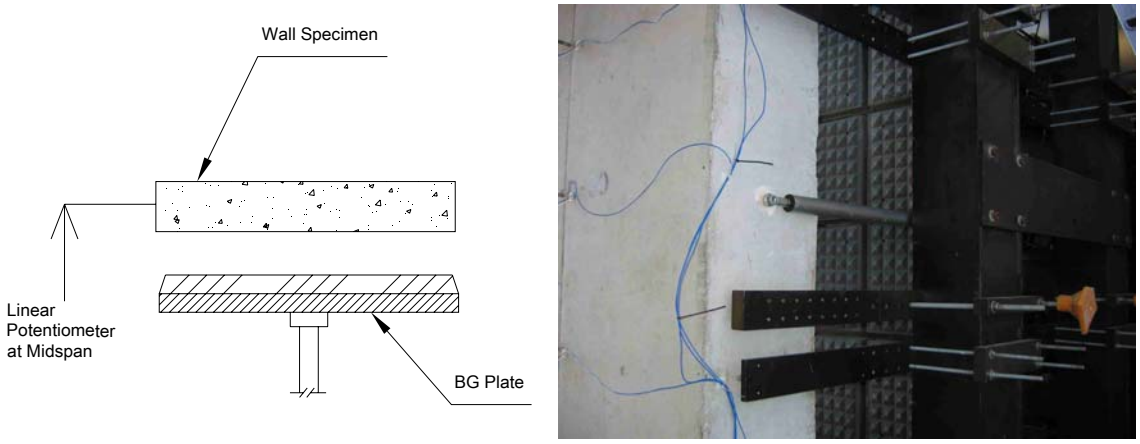

Figure 5.12: Location of linear potentiometer

Table 5.1: Target Locations

Displacement Target	Distance from bottom support [in]
7	129.75
6	108.125
5	86.5
4	64.875
3	43.25
2	21.625
1	0

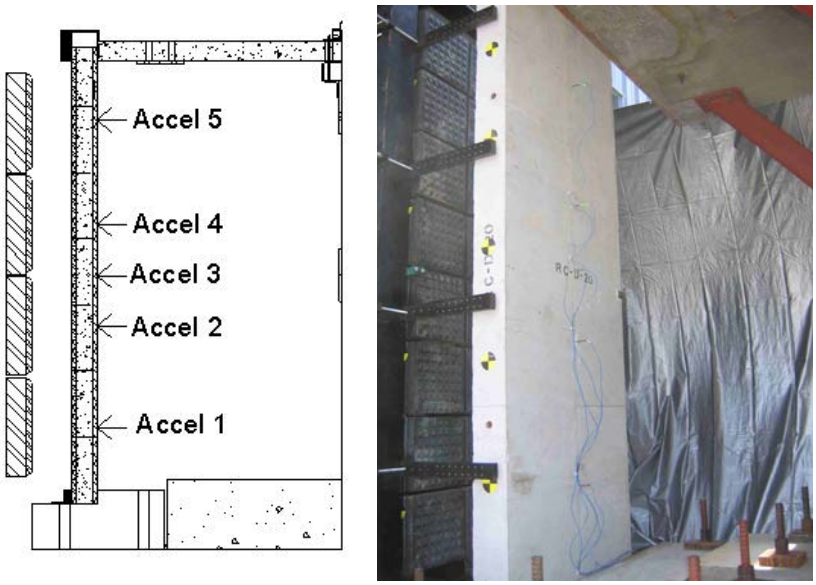

Figure 5.13: Location of accelerometers

SERIES I: STATIC TEST RESULTS

Seven static tests performed on six test specimens as part of the first test series were conducted between August 8th and September 5th, 2006. Tests 1 and 4 were both performed on the reinforced concrete specimen labeled RC-S-20. The specimen was tested twice because the first test was stopped before failure and it was decided afterwards to test all specimens until a significant failure occurred. Failure was defined as when crushing of concrete or fracture of rebar caused a sudden loss of lateral strength in the wall. All walls were loaded monotonically with four actuators to produce a uniform distributed load. The load applied through force control up to the point when yield occurred and then displacement control was used until failure was observed.

The typical wall response was to deform with one-way bending where the displaced shape up to the yield displacement matched the shape that would be predicted by linear elastic beam theory. Following yield the walls demonstrated additional strength with increased load. For this portion of the response cracking in the concrete became more localized near the midspan at the theoretic locations of the maximum moment. An example of the cracking that occurred is displayed in Figure 5.14.

At failure the rebar on the tension side fractured due to the large strain demands in the section. In Test 5 on RC-S-30 the concrete on the compression side of the wall began to crush as shown in Figure 5.15. As the walls neared failure only one or two predominate cracks continued to get wider which indicates that at the large displacement the strain distribution in the rebar is concentrated over a small distance.

It should be noted that for Test 6 on FP-S-30 the specimen was mislabeled and was tested upside down; meaning that there were seven reinforcing bars on the tension side and 12 reinforcing bars on the compression side. It should also be noted that in Test 7 the wall could not be tested all the way to failure due to its large displacement capacity. The bearing plates attached to the wall were nearly in contact with plates that attach the rollers to the abutments (Figure 5.16). Additional displacement would have caused these plates to come into contact, thus changing the boundary conditions. Furthermore, the significant amount of deformation in the wall risked causing damage to the actuators.

Figure 5.14: Series I Static Test 1- RC-S-20 wall cracks

Figure 5.15: Series I Static Test 5- RC-S-30 concrete crushes

Figure 5.16: Static Test 7- FP-D-20-2 Support at 16 in. of displacement

A typical load displacement plot for the static wall tests is shown in Figure 5.17. This plot is for the specimen labeled RC-S-25. The plot shows that specimen has a maximum resistance of 36 kips and reached a displacement of about 8.25 inches. In the plot it can be observed that the wall was unloaded at about 1 in., 3 in., and 6 in. of displacement. This was done to measure the stiffness of the wall at different displacement levels. Table 5.2 summarizes the results for all of the tests. The table lists the peak load and the maximum displacement for each wall along with the energy dissipated during the test. Load displacement plots for each specimen can be seen in Appendix C.

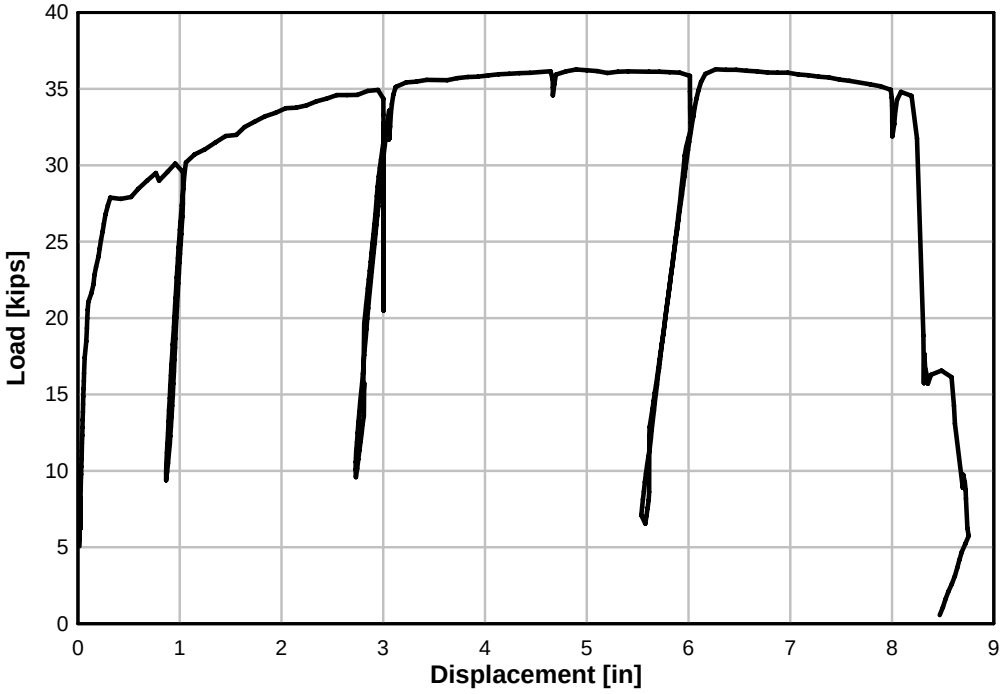

Figure 5.17: Static Test 3- RC-S-25 load vs. displacement at midspan

Table 5.2: Summary of Series I Static Tests

Specimen	Pmax [kips]	Δfail [in]	Energy Dissipated [lb-ft]
RC-S-20	26.5	10.1	20398
FP-D-20-2	13.1	15.5*	15289
RC-S-25	36.3	8.3	24028
FP-S-25	23.3	14.5	27074
RC-S-30	68.2	7.5	40397
FP-S-30**	32.6	9.0	20946

*Specimen did not reach failure. The boundary conditions precluded the specimen from being tested to failure.
**Specimen was tested upside down. The reinforcement steel was not symmetrical.

5.3.7 SERIES I: DYNAMIC TEST RESULTS

The dynamic tests on the specimens of the first series were conducted from August 2nd to September 6th of 2006. The walls were all loaded by four blast generators with a specified simultaneous impact. The test number, test specimen, test date, target impact velocities, actual impact velocities, and time spread for each test are listed in Table 5.3. The time spread was calculated as the time span from when the first impact occurs to when the last impact occurs. The impact velocities reported are the average of the four BGs.

Table 5.3: Series I- BG Impact velocities

Test	Specimen	Date	Target Velocity [ft/sec (m/sec)]	Measured Velocity [ft/sec (m/sec)]	Time Spread [msec]
1	RCD20	8/2/2006	29.5 (9)	28.4 (8.7)	1.3
2	FPD25	8/14/2006	32.8 (10)	33.2 (10.1	0.8
3	FPD30	8/16/2006	29.5 (9)	44.6 (13.6)	1.0
4	RCD25	8/21/2006	32.8 (10)	33.8 (10.3)	0.5
5	FPD20	8/23/2006	32.8 (10)	34.4 (10.5)	1.1
6	RCD30	8/25/2006	36.1 (11)	48.0 (14.6)	0.7
7	FPD30-2	8/29/2006	45.9 (14)	53.8 (16.4)	1.3
8	FPD25-2	8/31/2006	42.7 (13)	39.1 (11.9)	1.0
9	FPD20-2	9/6/2006	49.2 (15)	32.8 (10.0)	0.3

The impulse delivered by the BGs to the specimen is an important measure of the load applied during the test. The methods for calculating the impulse using the accelerometer data and camera velocity data, as described in Chapter 3, were used here. Table 5.4 lists the impulse calculated from the accelerometers and the video for each BG in every test. Also listed in the plot is the average impulse for each test. The impulses due to the BG impacts ranged from 317 to 636 psi-msec. Time history plots for the BG

velocities from the videos and the BG accelerations from the accelerometers are displayed in Appendix C for each test.

Table 5.4: Series I- BG Impulses

Test	BG 4 [psi-msec]		BG 3 [psi-msec]		BG 2 [psi-msec]		BG 1 [psi-msec]		Avg Impulse [psi-msec]
	Accel	Camera	Accel	Camera	Accel	Camera	Accel	Camera	
1	324	273	343	285	323	337	298	363	318
2	348	284	375	319	310	411	395	249	336
3	519	447	544	498	510	466	530	518	504
4	449	406	422	442	421	391	452	443	428
5	372	333	354	318	309	323	406	357	346
6	705	593	617	530	707	594	612	731	636
7	603	554	532	469	598	640	553	591	567
8	414	481	423	381	413	379	396	381	409
9	323	300	304	316	311	358	348	277	317

The wall response to the BG impact loads was similar in all nine tests. The impulses imparted an initial velocity to each specimen causing them to deform in a flexural one-way mode. The early response of the walls consisted of an elastic deformed shape until flexural cracks formed near the midspan. When the peak displacement exceeded 0.5 to 1 in. the deformation in the wall was more concentrated near the midspan in a plastic hinge region. During this phase of the response the reinforced concrete sections near the supports did not undergo significant deformation, but instead experienced rigid body rotations. In several of the specimens the large deformations caused the some of the longitudinal rebar to fracture. In Test 5 the initial velocity caused the wall to deform until all of the rebar fractured and the wall lost stability resulting in a catastrophic collapse. The initial velocity, peak midspan displacement, and number of fractured rebar are listed in Table 5.5. Appendix B displays the midspan displacement for each test specimen along with displaced shapes at different points in time. Also

included in Appendix B are photo sequences taken from the Phantom cameras which display the response of each wall.

Table 5.5: Series I- Specimen Response

Test	Initial Velocity [ft/sec]	Peak Displacement [in]	Permanent Displacement [in]	Failed Rebar
1	17.6	7.6	6	--
2	22.2	14.3	12.5	9
3	24.1	9.8	8.3	--
4	22.8	8.5	7.8	3
5	25.8	collapse	--	12
6	27.4	7.9	6.9	--
7	26.8	11.4	8.9	--
8	24.2	15.3	11.5	--
9	25.5	21.9	19.6	9

An example of the typical damage in the form of flexural cracks that occurred in the walls with the panels is displayed in Figure 5.18, which is a post impact photo from Test 2. When the walls with the panels were impacted the BG programmers left permanent indentations from the pyramids in the material. These indentations, typically 0.3-0.4 in. deep are displayed in Figure 5.19, which is a post test photo from Test 7. A post test photo of Test 5, where the specimen collapsed due to the BG loads is shown in Figure 5.20. An example of the damage that was observed in the RC walls is displayed in Figure 5.21. This figure shows the distribution of cracking observed on the tension face of the wall and the crushing that initiated on the front face. Typically for both plain and retrofitted walls the rebar fractured before for the concrete began to spall due to large strains on the compression face. In Tests 6 and 7, however, portions of concrete on the compression side began to crush in Figure 5.22, which is a post impact shot from Test 6. The compression face for Test 7 is shown in Figure 5.19.

Figure 5.18: Series I Test 2- Post test damage

Figure 5.19: Series I Test 7- Permanent indentations in panels

Figure 5.20: Series I Test 5- Post test damage

Figure 5.21: Series I Test 4- Post test damage

Figure 5.22: Series I Test 6- Damage to compression concrete

SERIES I TEST SUMMARY

In both the quasi-static and dynamic wall tests the test specimens primarily had a flexural mode of failure, which consisted of a yield hinge forming near the midspan. The failure was highlighted by the tension longitudinal steel fracturing and occasionally concrete crushing in the region of high compressive stresses. It is questionable that the frangible panels improved the response of the walls for these test conditions. A more likely conclusion is that the differences in the steel reinforcing ratio and layout caused the frangible panel walls and RC walls to respond differently to the quasi-static and dynamic loads.

A comparison of frangible panel walls and RC walls with the same concrete core is required to properly assess the effectiveness of the panels to improve the response of reinforced concrete walls to blast loads. In addition, the panel material may make a more important contribution in situations where the predominate failure mode is caused by significant concrete spall which, in turn, leads to a reduction of the effective structural cross section. Such a case can occur when the wall has a fixed boundary condition (e.g., a free-standing blast wall) allowing it to withstand higher impulse loads where spall would be observed. Therefore, an additional series of tests was conducted to supplement the results from program described here.

5.4 SERIES II BLAST SIMULATOR EXPERIMENTS

5.4.1 SERIES II INTRODUCTION

Twelve reinforced concrete wall specimens were constructed for the second frangible panel wall test series. The original plan for this test series called for eight of the walls to be tested dynamically in the Blast Simulator and the other four walls to be tested statically at the UCSD Powell Labs. This plan was modified midway through the wall construction when it was decided that the four static tests would be eliminated and replaced with dynamic specimens that included a lap splice detail at the base.

The 12 walls built for the test series included six plain reinforced concrete specimens and six reinforced concrete specimens with frangible panels on the front and back sides. The nominal concrete core thickness of six specimens was 8 in. and the thickness of the other six was 12 inches. There were three specimens for each wall type at each thickness; two of those specimens had a continuous longitudinal rebar detail while the other had a lap splice detail at its base. Each of the wall specimens was labeled

XX-YY-Z

Where

XX: Wall Type; RC=reinforced concrete and FP=Frangible

YY: Nominal Wall Thickness (in inches);

ZZ: Specimen Number; 1 & 2 had continuous rebar and 3 had a lap splice

5.4.2 SERIES II SPECIMEN DETAILS

Details of the test specimens with the continuous rebar detail are shown in Figure 5.23 and Figure 5.24. The walls have a width of 48 in. (122 cm) and an overall height of 11ft -5 3/4 in. (350 cm). The Frangible panels are 1.57 in. (4 cm) thick giving the 8 in. (20.3 cm) and 12 in. (30.5 cm) Frangible walls an overall thickness of 11.14 in. (28.3 cm) and 15.14 in. (38.5 cm), respectively. Grade 60 steel was specified for all of the rebar. The specified concrete strength was 5000 psi. The longitudinal reinforcing steel in the wall consists of 24-#3 bars, 12 bars on the front side and 12 bars on the back side. The longitudinal rebar runs from the top of the wall and down 16 in. (40.6 cm) into the footing where it terminates with a 90° hook and a 10 in. (25.4 cm) tail. The transverse reinforcing steel consists of 38-#3 U-shaped stirrups on the front and back side (76 total) spaced at 4 in. (10.1 cm). The transverse steel is located on the outside of the longitudinal rebar cage and the specified concrete cover was 1.5 in. (3.8).

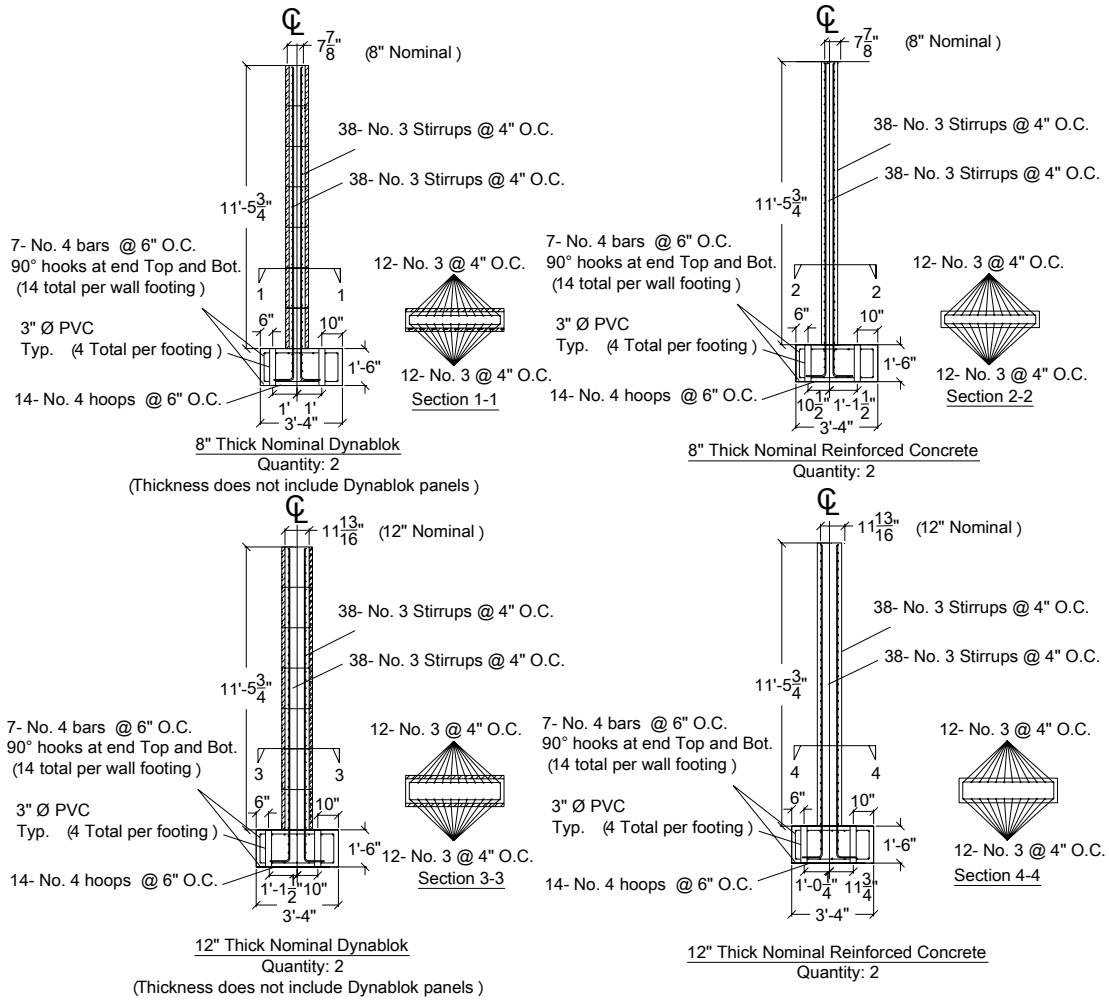

Figure 5.23: Series II Specimen details with continuous rebar

The walls were cast on reinforced concrete footings that were 3ft -4 in. (101.6 cm) x 7 ft -0 in. (2.1 m) x 18 in. (45.7 cm). The position of the walls on the footing vary according to the walls overall thickness to allow for a fixed location of the top reaction slab during testing.

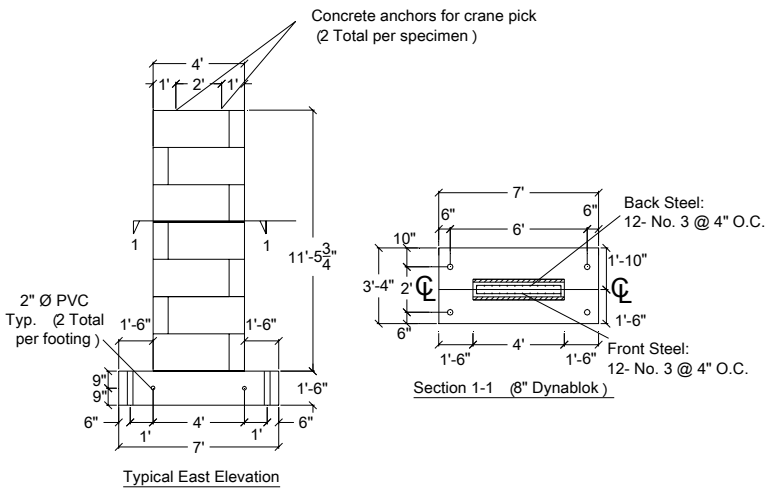

Figure 5.24: Series II Specimen details-East elevation

The wall dimensions of the lap splice specimens are the same as the specimens with continuous rebar. The lap splice specimens also have Grade 60 rebar and concrete with a specified strength equal to 5000 psi. The differences between the two wall types include the lap splice detail and the footing details. The details for these walls are displayed in Figure 5.25 and Figure 5.26. The size and number of the longitudinal bars is the same as before, except that now they run from the top of the wall to the top of the footing. The bars are spliced with a 32 in. (81.2 cm) long lap at the bottom of the wall to the footing with an equal number of #3 starter bars. The starter bars are hooked 16 in. deep into the footing with 10 in. (25.4 cm) tails and extend into the wall.

The dimensions of the footings for the lap splice specimen are 3 ft -0 in. (101.6 cm) x 7 ft -0 in. (2.1 m) x 18 in. (45.7 cm), which is slightly different than for the other specimens. The walls with the lap splice were also cast with their centerlines aligned with the centerlines of the footings, which is not the case for the continuous rebar specimens. The footings are different for the two types of specimen because originally

the lap spliced walls were designed to be tested statically which required a slightly different footing layout.

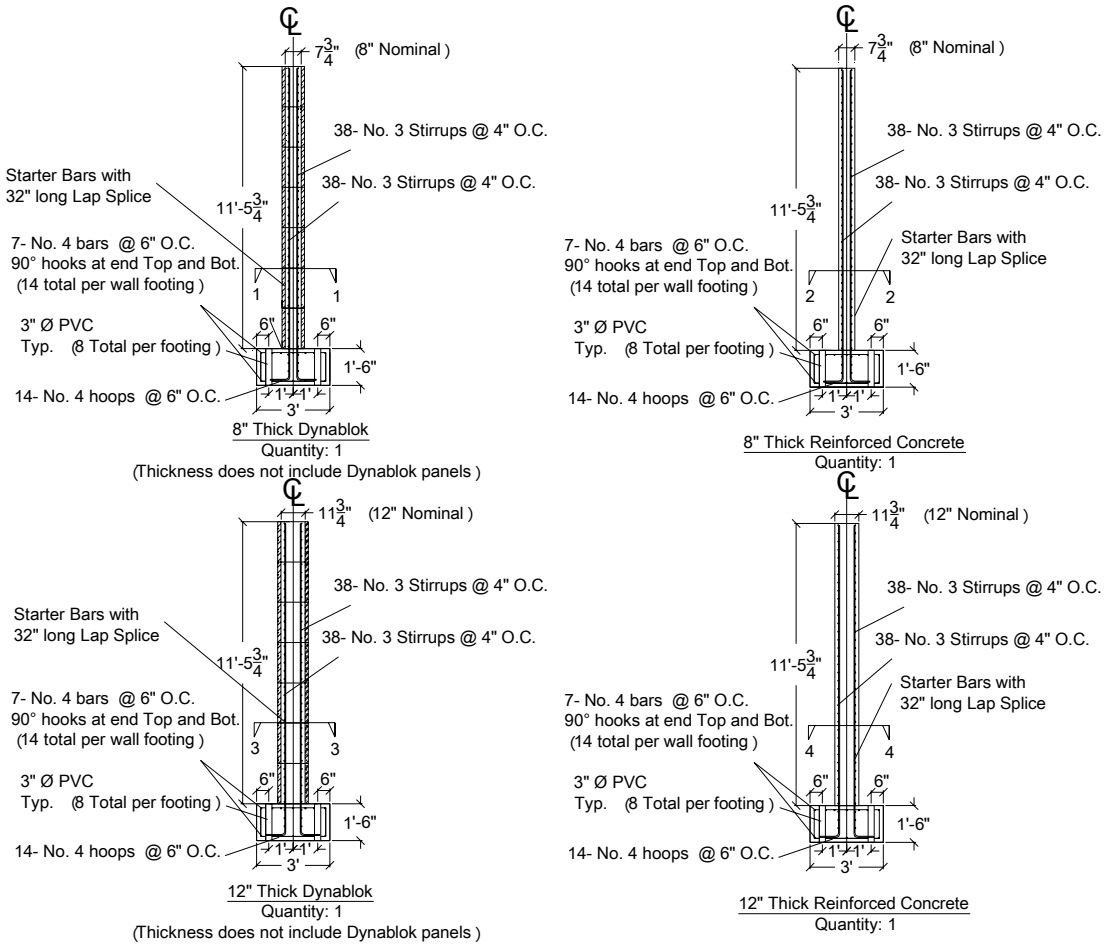

Figure 5.25: Series II Specimen details with lap splices

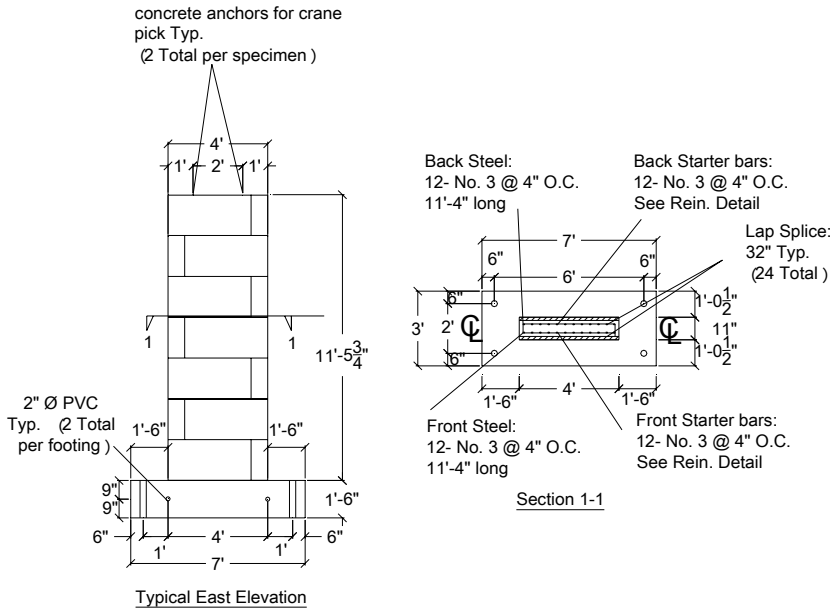

Figure 5.26: Series II Specimen details with lap splices-East elevation

5.4.3 SERIES II SPECIMEN CONSTRUCTION

The walls were built at the Englekirk Structural Engineering Center starting on July 2nd, 2007. Four lifts of concrete were used to cast all 12 walls on August 15th, 2007. The original construction plan called for the frangible panel walls to be cast in 3 ft -3 in. (1 m) lifts with at least 75 min interval between each placement. The time delay between lifts was required to allow the concrete set, preventing the next lift from blowing out the frangible panels from excessive hydrostatic pressures.

Figure 5.27 displays a schematic of the specified frangible panel construction sequence. Although the Frangible panels are meant to serve as stay-in-place forms, additional formwork including bracing, bulkheads, and scaffolding was required to build

the test pieces (Figure 5.28). The RC walls were cast with only two lifts because the formwork for these specimens was built to resist larger hydrostatic forces.

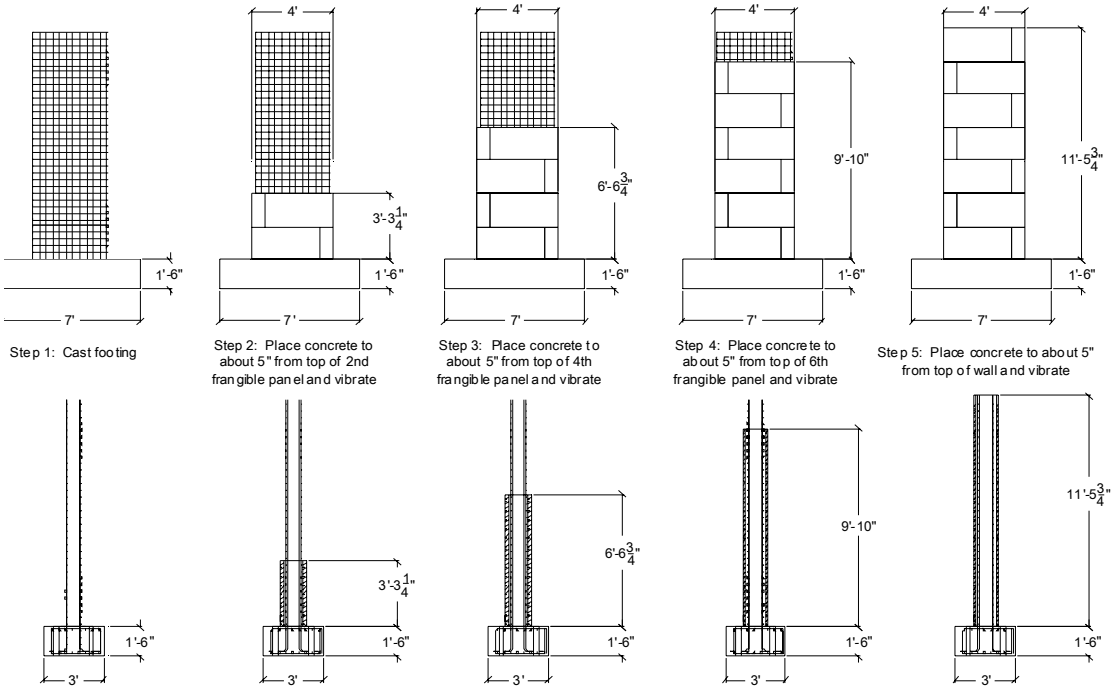

Figure 5.27: Frangible panel wall construction sequence

Figure 5.28: Bracing, bulkheads, and scaffolding for frangible panel specimens

The panels were quickly abandoned as stay-in-place forms when some of them blew out in one of the walls as the first lift of concrete was being vibrated (Figure 5.29). To prevent any additional blow outs the panels were braced with 2 in. x 4 in. lumber at several elevations along the height of the walls. The extensive bracing system can be seen in Figure 5.30. The construction of this system was labor intensive and required significant amounts of lumber per area of each wall.

Figure 5.29: Blow out of frangible panel

Figure 5.30: Bracing of frangible panels following blow out

5.4.4 SERIES II TEST SETUP

The setup for the Frangible II test series is illustrated in Figure 4.2 and Figure 4.3, which depict elevations from the south and the east, respectively. The span of the wall was 10 ft -9 3/4 in. (330 cm). The walls were supported at the top and bottom allowing for one-way bending. The top support was simple and the bottom had a fixed boundary condition where the wall was cast monolithically with a footing which that was post tensioned to the reaction floor at four corners with 1 3/8 in. (3.5 cm) diameter Dywidag bars.

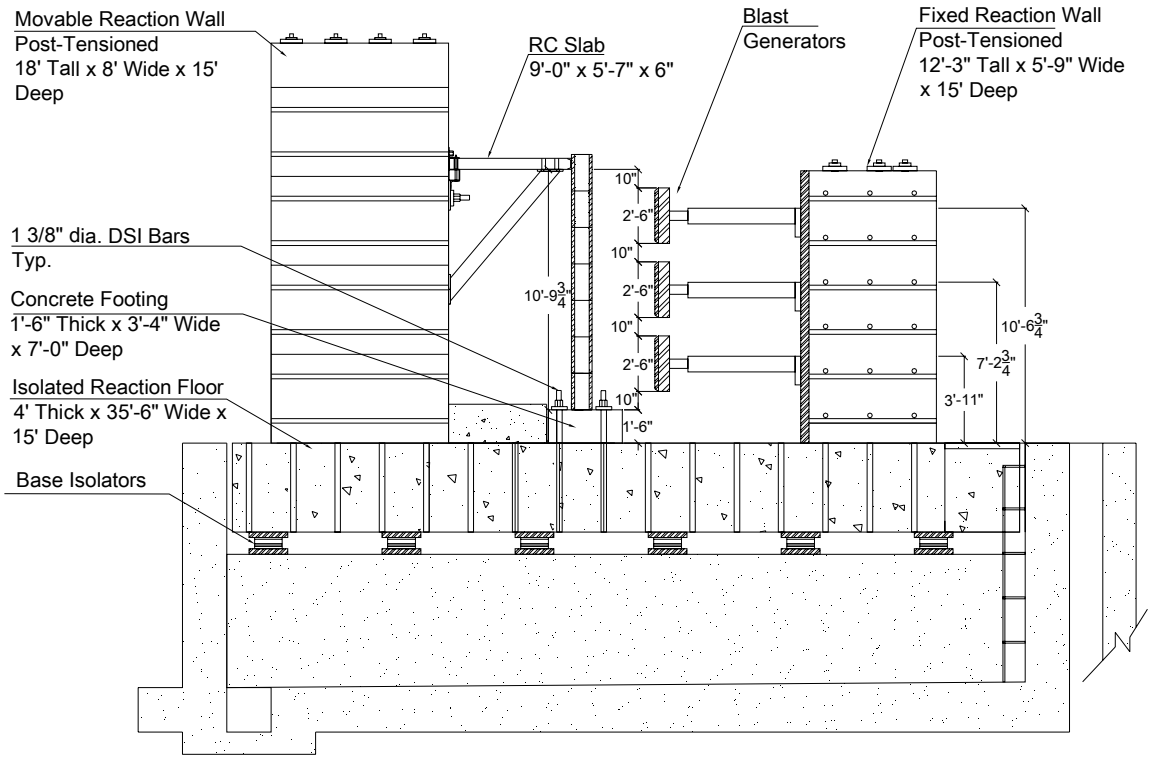

Figure 5.31: Series II test setup (South elevation)

In the first two tests that are described in later sections of this report the reinforcing steel near the midspan and at the joint between the wall and the base

fractured. Following the fracture the wall continued to deform until it lost stability and collapsed. The tests that followed had an additional 4 in. x 4 in. angle at the base to provide some additional lateral resistance at the base.

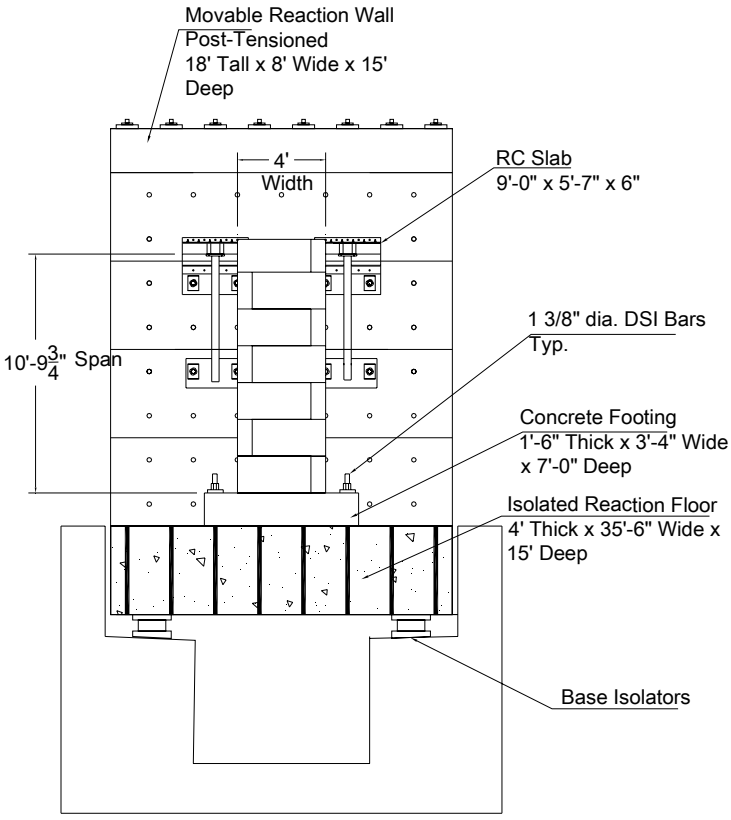

Figure 5.32: Series II test setup (East elevation)

LOADING PROCEDURES

An array of three Blast Generators was used to load the specimens in this test series. The dimensions of the BG impact plates were 30 in. x48 in. (76.2 cm x 121.9 cm). The center-to-center spacing of the plates was 39.94 in. (101.4 cm), which left a

9.94 in. (25.2 cm) gap between the plates. At the top and bottom of the specimen there is a 9.94 in. (25.2 cm) gap between edges of the BG plates and the edges of the support. Figure 4.2 displays the elevations for the BGs measured from the isolated slab to the top of the mounting plate. The BGs are labeled 1-2-3 from bottom to the top.

Two loading protocols were used in the blast simulator tests on the walls specimens in the Test Series II. The first used all three BGs which impacted the specimen simultaneously at uniform velocities. The purpose of this type of loading was to produce a response in the wall that is equivalent to what it would experience in an actual blast event.

The second protocol used BG 1 to impact the wall near its base with a target velocity two to three times larger than the velocities used in the other tests with three BGs. The purpose of this test was to produce a localized damage mechanism without failing the wall. This type of failure is important to understanding the behavior of the lap splice detail. This test was always run on a specimen that had previously been tested at least once with 3 BGs. In most cases the amount of deformation in the specimen before the single BG hit was small.

5.4.5 SERIES II INSTRUMENTATION

High speed video was captured with three Phantom v7.1 (Vision Research) cameras. The first camera recorded in black and white at a rate of 5000 frames per second at a resolution of 400x600. The other two cameras recorded in color and also ran at a rate of 5000 frames per second with a resolution of 400x600. The cameras are capable of different frame rates at different resolutions. The cameras were externally triggered from the MTS controller. The cameras provide visual evidence of the test that is used to observe specimen behavior under impulsive loading. Figure 5.33 displays the sections of the wall that were filmed in the test that used three BGs. Phantom camera 1 (black and white) was used to measure displacements and velocities of the entire wall. Phantom cameras 2 and 3 were equipped with zoom lenses and recorded videos in color. These cameras were used to zoom in and measure the top and bottom portion of the wall during the tests. The camera views for the single BG tests were the same except Phantom camera 2 was placed behind the wall at an angle. This camera location provided a view of the walls back side during the test. The other two cameras were used to determine the velocity of the BG and the displacement and velocity of the wall.

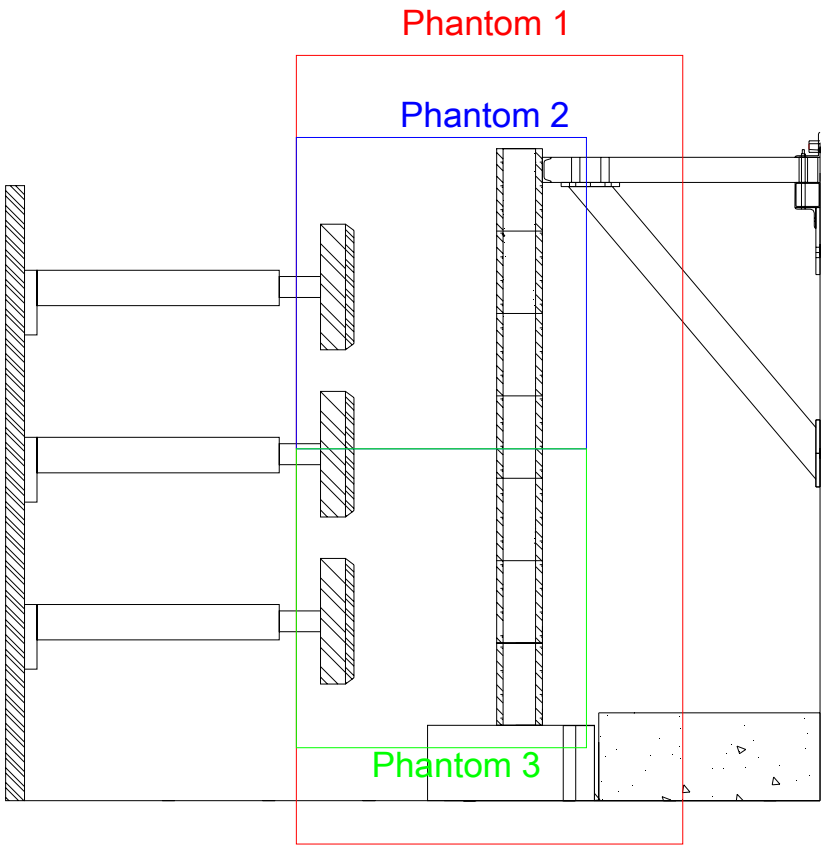

Figure 5.33: Phantom camera view

The accelerations of the BG impact plates during impact were measured with 10K g piezoelectric shock accelerometers. The acceleration signal of four different accelerometers was typically averaged and integrated to measure the impulse delivered to the specimen during the test. Four gages were mounted on each BG impact plate to ensure accuracy and redundancy. The gages were mounted to the back of the plate to the right, left, top and bottom of the center of gravity as shown in Figure 4.7. The cables that transmit the acceleration signal to the data acquisition system were fastened to the BGs to minimize artificial signals in the data caused by their vibration.

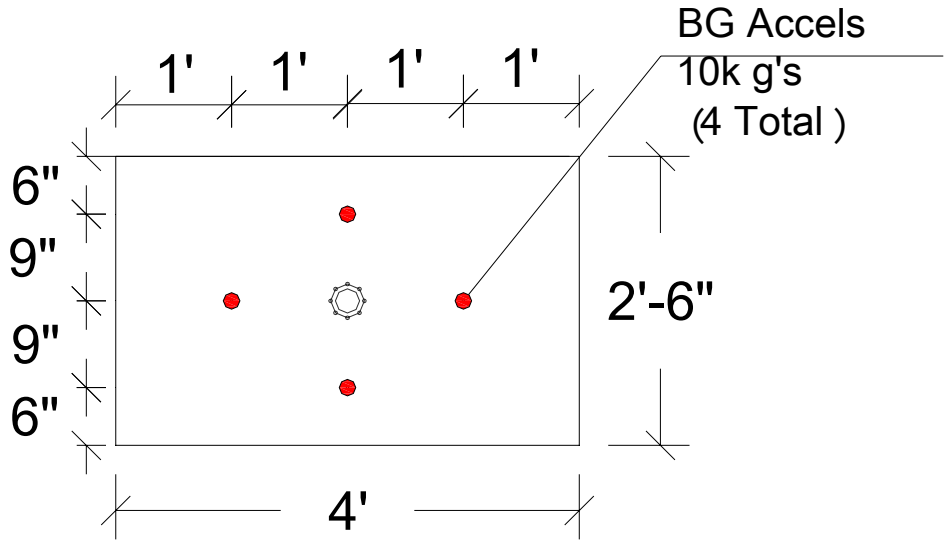

Figure 5.34: BG accelerometer locations

The velocity for each BG was determined from the Phantom video record using the TEMA software package. For each BG, a point is selected on the impact mass and the software records its displacement time history. The software then differentiates the displacement time history using a seven point numerical differentiation scheme to obtain the velocity time history. The Phantom camera videos were used in conjunction with the TEMA software to measure specimen displacements at several different locations. Targets were mounted on the wall before the test to assist in tracking the wall displacements (Figure 4.9). The distance from the bottom support to the targets used for tracking the specimen displacement are listed Table 4.2. A linear potentiometer was also used to measure the specimen's midspan displacement. This was done to ensure that measurements made using the Phantom video are accurate and redundant. The location of the linear potentiometer along with the method used to connect it to the wall can be seen in Figure 5.36.

Figure 5.35: Tracking targets on specimen

Table 5.6: Target locations

Displacement Target	Distance from bottom support [in. (cm)]
7	129.75 (330)
6	119.75 (302)
5	91.25 (232)
4	64.875 (165)
3	32.5 (83)
2	12 (30)
1	1.125 (3)

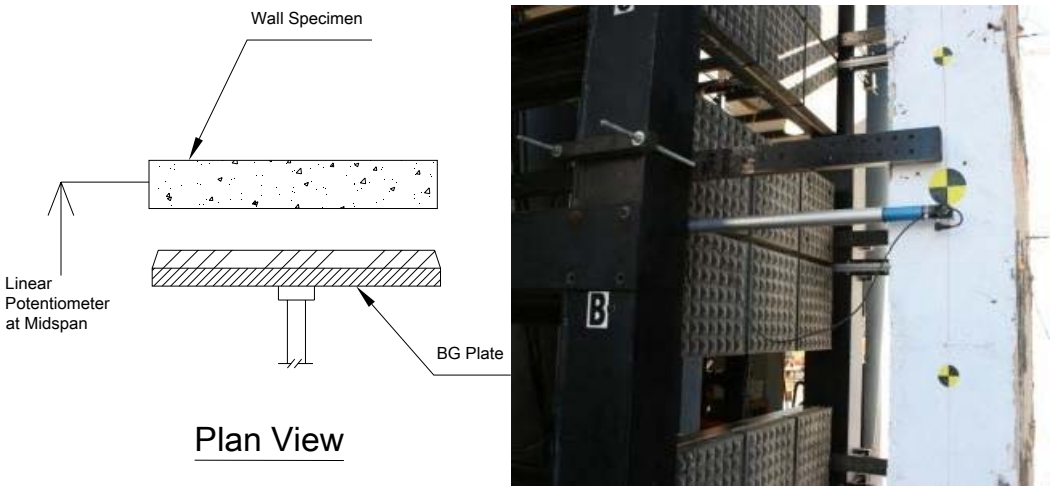

Figure 5.36: Location of linear potentiometer

Accelerations in the wall were measured by 5K g piezoelectric shock accelerometers. The accelerometers were fixed to the back of the wall with couplers that were attached to 1/4 in. thread rod that was embedded into the concrete with epoxy. The cables that transmit the acceleration signal to the data acquisition system were connected to the wall with strain relief in the cables to minimize artificial signals in the data due to their vibration. The locations can be seen in Figure 5.37.

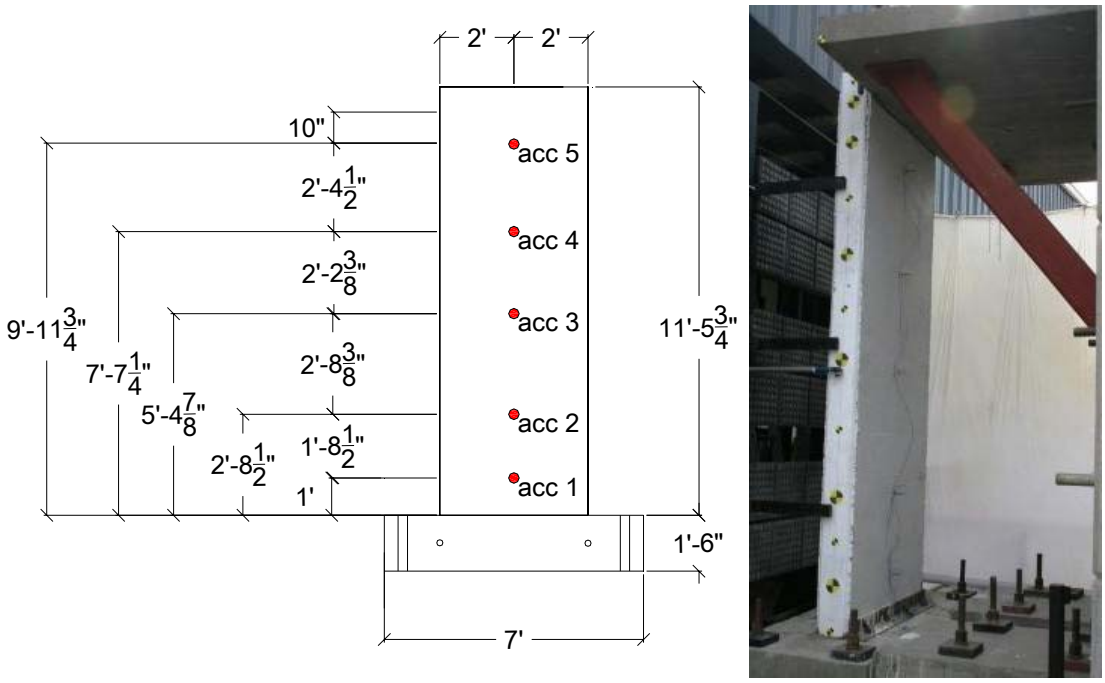

Figure 5.37: Specimen accelerometer locations

The strain in the reinforcing steel was measured using 5mm rebar gages. The gages were installed on the rebar during the construction of the walls. The walls with continuous rebar have four gages total with two a front bar and two on a back bar at elevations of 6 in. and 76 inches. These locations were chosen because they are the theoretical regions that will form plastic hinges. The walls with the lap splice detain had 10 gages total with six gages on the starter bars and four gages on the longitudinal bars.

As with the continuous rebar specimens, half of the gages are on bars in the front layer of steel and the other half are in the back layer. The elevations of the gages were at 3 in., 6 in., 9 in., and 76 in. with two gages at each height, except at 6 in. where there was four gages.

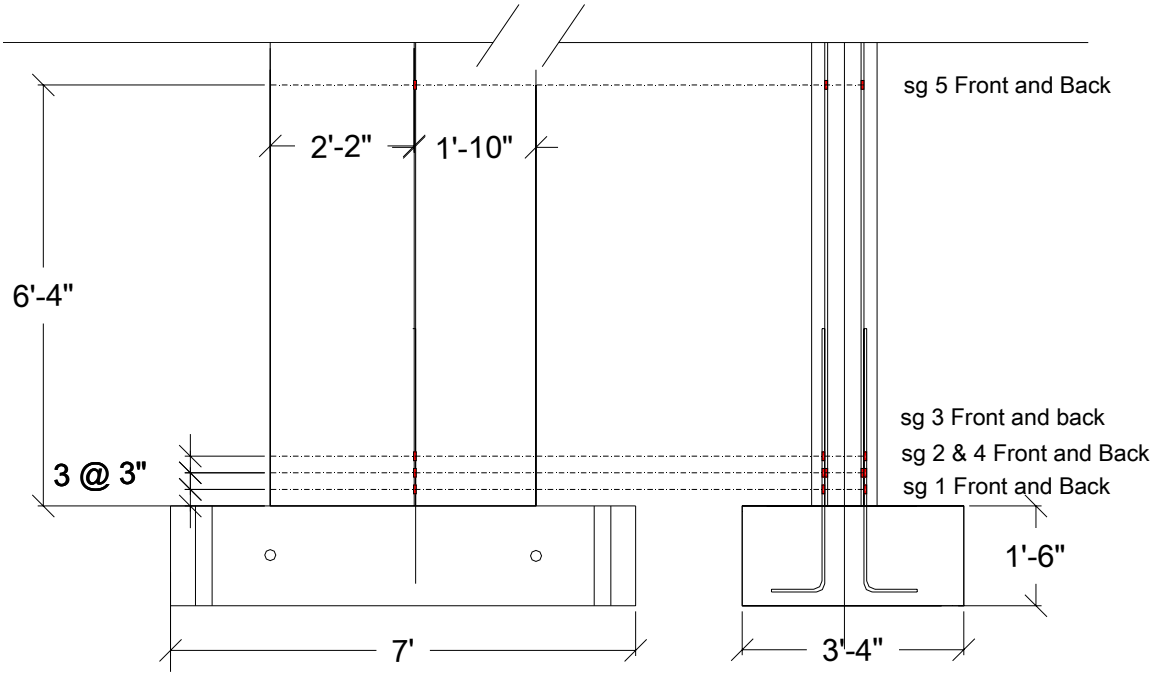

Figure 5.38: Rebar strain gage locations

5.4.6 SERIES II DYNAMIC TEST RESULTS

MULTIPLE BG IMPACT TESTS

Series II blast simulator tests were performed between August 28th, 2007 and January 8th, 2008. The program included 22 Blast Simulator tests on 12 wall specimens. The main objective of the test series was to provide a direct comparison of reinforced concrete walls and the frangible panel walls with the same concrete core thicknesses subject to equal levels of impulsive load. This was motivated by the results of the previous frangible panel wall test series, which were inconclusive because the RC walls used as the control specimens had the same total thickness, but different concrete core thicknesses due to the 1.57" frangible panels on the front and back. The different core thicknesses result in different cross sectional properties, which affect the response of the walls to both static and dynamic loads. Therefore, direct comparison could not be made from these tests.

An additional objective of the test program was to investigate a lap splice detail at the connection between a wall and a footing. In extreme loading situations this connection detail can fail because the concrete, which is the mechanism for transferring the loads between the lapped bars, will spall. Therefore, an RC and frangible panel specimen at each thickness was built with a lap splice.

The data generated from these experimental tests was used to develop and validate numerical tools including simple single degree-of-freedom models and more complex high fidelity physics based simulations. The test setup and procedures

developed for this series were selected with the intent of performing controlled and repeatable experiments.

The target velocities for each test were chosen to provide a direct comparison between RC and frangible panel specimens and between specimens with and without lap splices at the base. A summary of the target velocities used in each test along with the average measured velocity and the time spread between the first and the last BG impact are listed in Table 5.7. The data shown in the table are for the tests in which the specimens were impacted simultaneously by three BGs at uniform velocity. A test number that is followed by the letter "a" signifies that the specimen was re-tested; the re-test is designated by the test number followed by the letter "b".

Table 5.7: Series II- BG Impact Velocities for Tests with Multiple BGs

Test	Specimen	Date	Target Velocity [ft/sec (m/sec)]	Measured Velocity [ft/sec (m/sec)]	Time Spread [msec]
1	RC-12-1	08/28/2007	71.2 (21.7)	74.8 (22.8)	0.7
2	FP-12-1	08/31/2007	71.2 (21.7)	75.5 (23.0)	0.5
3a	RC-12-2	09/21/2007	21.3 (6.5)	21.2 (6.5)	2.3
3b	RC-12-2	09/21/2007	42.7 (13.0)	40.3 (12.3)	1.7
4a	FP-12-2	09/27/2007	21.3 (6.5)	22.2 (6.8)	2.5
4b	FP-12-2	09/27/2007	42.7 (13.0)	40.3 (12.3)	1.1
5a	RC-8-1	10/04/2007	14.8 (4.5)	15.0 (4.6)	0.7
5b	RC-8-1	10/04/2007	29.5 (9)	29.3 (8.9)	0.9
6a	FP-8-1	10/11/2007	14.8 (4.5)	15.6 (4.7)	0.9
6b	FP-8-1	10/11/2007	29.5 (9)	29.8 (9.1)	0.4
7	RC-8-2	10/18/2007	39.4 (12)	36.9 (11.2)	0.5
8	FP-8-2	11/06/2007	39.4 (12)	37.5 (11.4)	0.7
9	FP-8-3	11/14/2007	39.4 (12)	38.9 (11.9)	0.4
10	RC-8-3	11/28/2007	39.4 (12)	38.1 (11.6)	0.8
11	RC-12-3	12/12/2007	42.7 (13.0)	40.9 (12.5)	1.0
12	FP-12-3	12/20/2007	42.7 (13.0)	41.3 (12.6)	0.3

The impulses delivered by the BGs to the specimens were calculated with the accelerometer data and camera velocity data, as described in Chapter 3. Table 5.8 lists

the impulse calculated from the accelerometers and the video for each BG in every test. Also listed in the plot is the average impulse for each test. The impulses due to the BG impacts ranged from 152 to 867 psi-msec. Time history plots for the BG velocities from the videos and the BG accelerations from the accelerometers are displayed in Appendix C for each test.

Table 5.8: Series II- BG Impulses for Tests with Multiple BGs

Test	BG 3 [psi-msec		BG 2 [psi-msec		BG 1 [psi-msec		Avg Impulse [psi-msec]
	Accel	Camera	Accel	Camera	Accel	Camera	
1	787	810	834	973	821	978	867
2	748	792	699	671	736	832	746
3a	273	204	285	216	199	211	231
3b	470	430	453	436	461	417	445
4a	182	210	227	228	240	261	225
4b	408	367	362	407	409	454	401
5a	124	125	156	164	156	166	149
5b	297	259	299	363	282	319	303
6a	154	152	147	138	157	166	152
6b	259	297	264	289	266	296	279
7	410	316	374	401	371	368	373
8	357	336	371	355	353	343	353
9	328	358	356	343	407	383	363
10	390	353	423	415	349	391	387
11	414	412	470	481	469	379	438
12	433	446	406	366	429	474	426

In all of the tests the BG impact loading imparted an initial velocity to the specimens, which deformed in a one-way flexural mode. Typically, the initial deformed shape was similar to the shape of an elastic beam subjected to a static uniform load. As the rebar in the specimen began to yield plastic hinges formed near the base and slightly above the midspan; these locations match predicted hinge locations from the maximum moments. Since the walls were not tied to the top support, during rebound the top of the wall separated from the concrete slab and rotated about the base of the wall. The lack of

a rebound restraint in the setup makes it more difficult to measure a permanent displacement that correlates to damage due to the rigid body rotation about the base; however the measurement of the peak displacement is not affected. Table 5.9 lists the initial velocity and peak midspan displacement for each test.

Table 5.9: Series II- Specimen Response for Tests with Multiple BGs

Test	Initial Velocity [ft/sec]	Peak Displacement [in]
1	32.1	collapse
2	26.8	collapse
3a	8.6	0.89
3b	20.3	3.15
4a	9.9	0.76
4b	15.5	2.32
5a	9.1	1.00
5b	17.7	3.30
6a	7.0	0.90
6b	12.6	2.70
7	24.1	4.52
8	17.9	3.27
9	19.4	3.75
10	20.4	4.67
11	17.5	3.02
12	15.2	1.90

The specimens in Test 1 and Test 2 were subject to significantly higher loads than the other 10 specimens which resulted in different results. When impacted by the BGs they suffered significant damage and collapsed. In both tests the initial velocity of the wall drove it to form a hinge at the base and slightly above the midspan on the wall. At the base the hinge opened up at the joint where the wall was cast on the footing; nearly all of the deformation at the base was localized at the joint (Figure 5.41). Near the midspan the hinge occurred near the theoretical location of maximum moment for a fixed-pinned beam. There were a few cracks distributed around the midspan hinge until the tension

side rebar fractured upon which all of the deformation was localized at the midspan. The tension rebar at the base fractured at about the same time as the midspan rebar. Without any rebar on the tension side in these two locations the wall lost all resistance to lateral motion and the wall collapsed.

The response of the frangible panel wall in Test 2 was similar to the response of the RC wall in Test 1. The initial velocity of the wall drove it to form a hinge at the base and slightly above the midspan on the wall. At the base a cracked formed at the joint where the wall was cast on the footing; nearly all of the deformation at the base was localized at the joint. At 76 in. from the base, about 12 in. above the midspan, a large crack opened. The location of the crack was near the theoretical location of maximum moment for a fixed-pinned beam. There were a few cracks distributed around the midspan hinge until the tension side rebar fractured upon which all of the deformation was localized at one spot. The tension rebar at the base fractured at about the same time as the midspan rebar. Without any rebar on the tension side in these two locations the wall lost all resistance to lateral motion and the wall collapsed. This is shown in Figure 5.40 and Figure 5.40 for Tests 1 and 2, respectively. Following the test it was observed that there was very limited cracking near the base, except at the joint. This is demonstrated in Figure 5.41 which shows the base for Test 1. Upon further inspection it was also observed that the cracks that formed above the midspan were at a construction joint in both walls. Figure 5.42 displays the joint for Test 2. The concrete in the walls were cast at one meter lifts and a clean crack opened up at the top of the second lift. Following the first two tests it was decided that an angle at the base could possibly

increase the walls resistance and prevent it from collapsing at large displacements. Therefore, all subsequent tests in the series had an angle, shown in Figure 5.43, added to the base behind the wall.

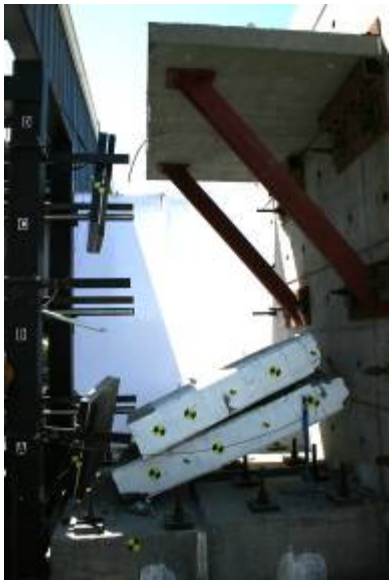

Figure 5.39: Series II- Test 1 post impact

Figure 5.40: Series II Test 2 post test

Figure 5.41: Series II Test 1 base of wall

Figure 5.42: Series II Test 2 midspan failure

Figure 5.43: Series II angle detail

The typical damage and cracking patterns observed in the specimen after BG loading is shown in Figure 5.44 for the 12 in. thick specimens and Figure 5.45 for the 8 in. thick specimen. For the specimens tested multiple times with three BGs, the first impact resulted in insignificant cracking and small permanent deformations. The second impact for these specimens was set to produce more significant peak midspan displacements.

Figure 5.44: Series II 12 in. RC wall, typical damage

Figure 5.45: Series II frangible panel wall, typical damage

COMPARISON BETWEEN WALLS WITH 8" THICK RC CORES

The BG impact velocities are plotted versus specific impulse for all the walls with 8 in. thick concrete cores in Figure 5.46. The plot shows that the BGs deliver slightly smaller impulses to the frangible panel walls in comparison to the RC walls. The difference between the two wall types also becomes larger as the impact velocity increases. Linear trend lines were added to this plot to aid in the comparisons of the data. The trend lines can be used to show that the average decrease in specific impulse when impacting walls with frangible panels instead of plain reinforced concrete at velocities that range between 15 ft/sec and 38 ft/sec is 5.4%.

Figure 5.47 plots the specific impulse delivered to the specimen by the BG impact versus the peak displacement at the midspan for all walls with 8 in. thick concrete cores.

The plot shows that the walls with the frangible panels had slightly smaller peak displacements when loaded by equal levels of impulse as the RC walls. Linear trend lines were fitted to the data to aid in the quantitative comparison of the two wall types. The trend lines can be used to show that the average decrease in peak displacement by using frangible panels instead of plain reinforced concrete is 11.6% for impulses ranging from 150 psi-msec to 360 psi-msec

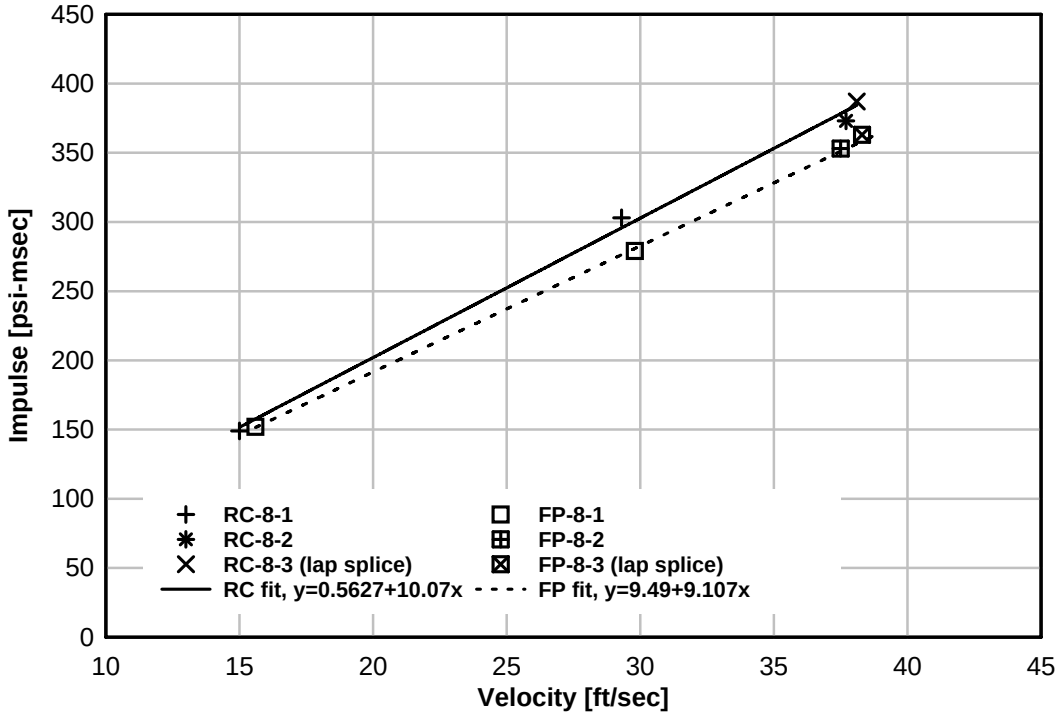

Figure 5.46: Velocity versus impulse for walls with 8 in. thick concrete cores

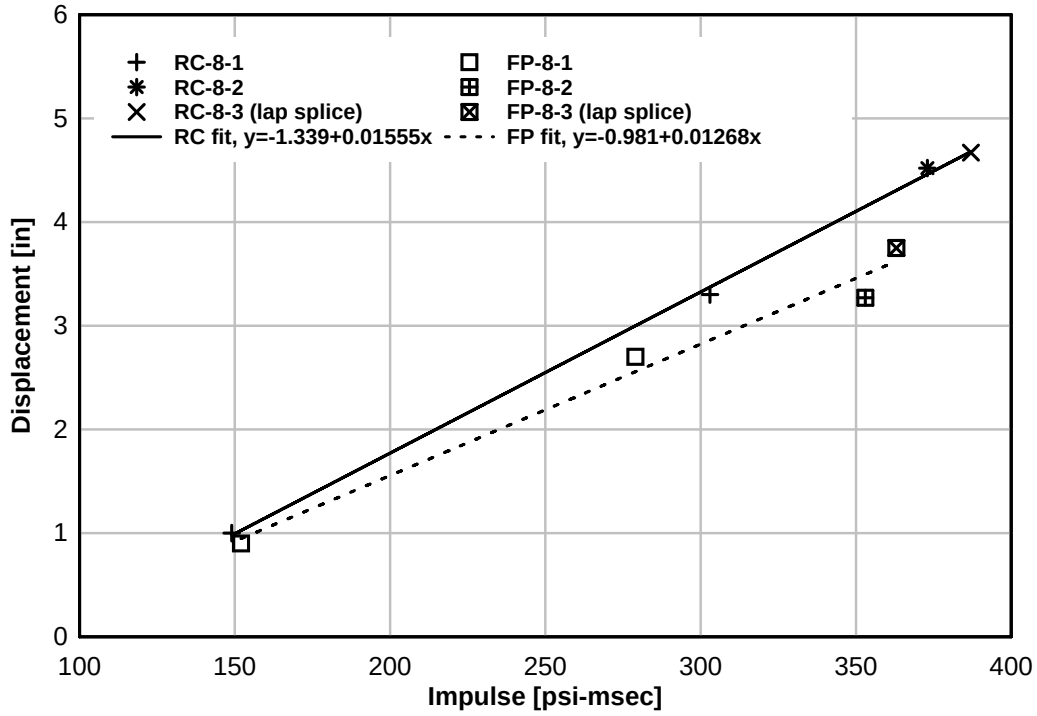

Figure 5.47: Impulse versus displacement for walls with 8 in. thick concrete cores

COMPARISON BETWEEN WALLS WITH 12 IN. THICK CONCRETE CORES

The BG impact velocities are plotted versus specific impulse for all the walls with 12 in. thick concrete cores in Figure 5.48. The plot shows that the BGs delivered smaller impulses to the frangible panel walls in comparison to the RC walls. The difference in impulse between the two wall types slightly increases as the impact velocity increases. Linear trend lines were added to this plot to aid in the comparisons of the data. The trend lines can be used to show that the average decrease in specific impulse when impacting walls with frangible panels instead of plain reinforced concrete at velocities that range between 22 ft/sec and 75 ft/sec is 8.3%.

Figure 5.49 plots the specific impulse delivered to the specimen by the BG impact versus the peak displacement o at the midspan for all walls with 12 in. thick concrete cores. The plot shows that the walls with the frangible panels had similar peak displacements as the RC walls when loaded with similar impulses. Linear trend lines were fitted to the data to aid in the quantitative comparison of the two wall types. The trend lines can be used to show that there is actually an 18% decrease in peak displacement between impulses ranging from 250 psi-msec to 425 psi-msec when using frangible panels instead of plain reinforced concrete.

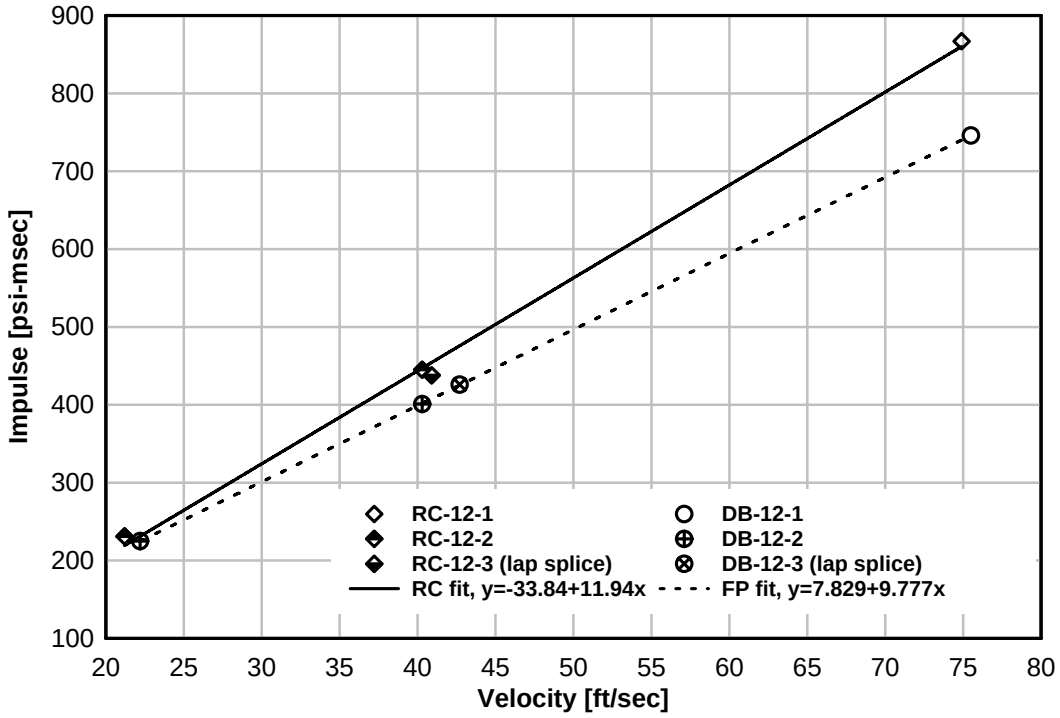

Figure 5.48: Velocity versus impulse for walls with 12 in. thick concrete cores

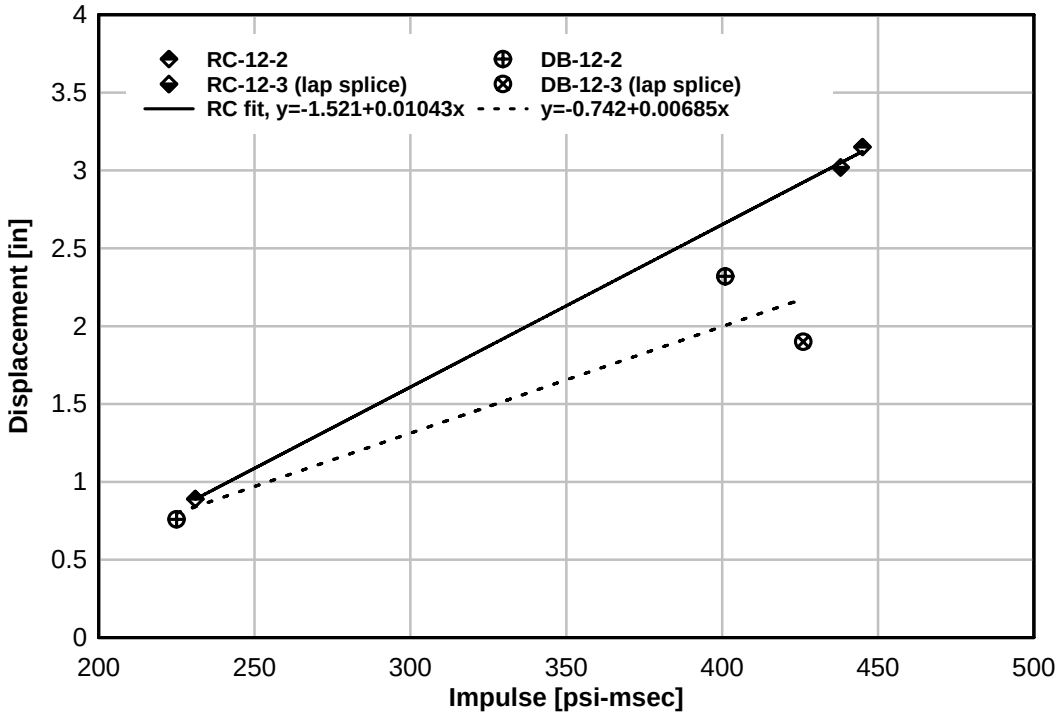

Figure 5.49: Impulse versus displacement for walls with 12 in. thick concrete cores

SINGLE BG IMPACT TESTS

Four of the 8 in. thick specimens were also subject to impact test using a single BG: RC-8-3, FP-8-1, FP-8-2, and FP-8-3. The first test was run on FP-8-2 with a target impact velocity equal to 65.6 ft/sec. The actual velocity at impact was 68.9 ft/sec (21 m/sec), which created an impulse equal to 599 psi-msec. No localized damage was observed in the wall as a result of the load. Following the first test all of the specimens were impacted with a target velocity equal to 82 ft/sec. The actual impact velocities recorded in the tests on RC-8-3, FP-8-1, and FP-8-3 where 76.42, 85.6, and 88.3 ft/sec, respectively. The local impulses generated in the tests were 1023, 1003, and 1093 psi-

msec for RC-8-3, FP-8-1, and FP-8-3, respectively. Spall was observed in the tests on the walls with lap splices, but no localized damage was seen for the specimen with continuous rebar.

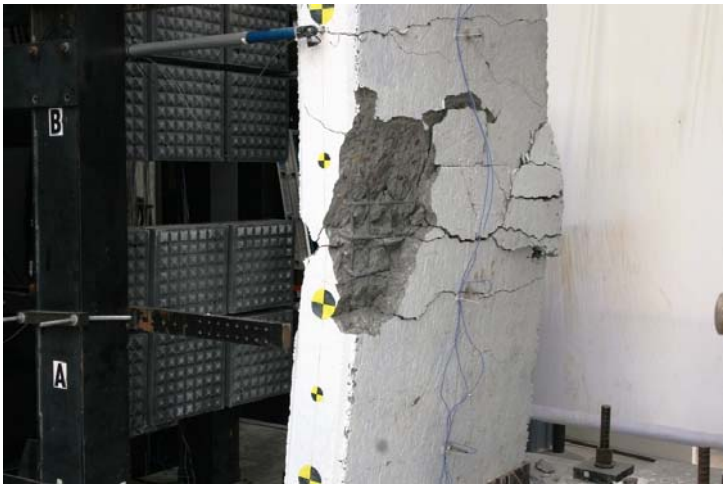

Figure 5.50: RC-8-3 (lap splice) post single BG impact

(a) **(b)**

Figure 5.51: Single BG impact tests; (a) FP-8-1 (lap splice); (b) FP-8-3 (cont. rebar)

The RC wall, RC-8-3, had a greater area of concrete spall when compared to the frangible panel wall, FP-8-3. Furthermore, the RC wall had spall on both the front and back faces, while the frangible panel wall only spalled on the back face. One possible cause for the slightly varied response might be attributed to the fact that frangible panels modify the waveform of the pressure pulse applied by the BG impact. Another possibility is that the frangible panel steel ties that hold the panels in place during construction provided additional strength and confinement to the wall which reduced the extent of concrete spall.

The specimens labeled RC-12-3 and FP-12-3 were subject to impact tests using one BG at a target impact velocity equal to 68.9 ft/sec (25 m/sec). The specimens tested contained longitudinal rebar that had 32 in. long lap splices with starter bars that ran into the footing and terminated with 90° hooks. The actual velocities recorded for the tests on RC-12-3 and FP-12-3 were 87.2 ft/sec and 82.5 ft/sec, respectively. The BG impact produced an impulse equal to 1296 psi-msec in RC-12-3 and 1178 psi-msec in FP-12-3. The impulse caused the walls to reach peak displacements equal to 1.35in. and 0.9 in. at the location of the potentiometer for the RC and the frangible panel walls, respectively. The loading increased the amount of damage observed in the wall, but no spall or localized damage occurred.

SERIES II TEST SUMMARY

In the second test series on walls with frangible panels, performance comparisons were made between reinforced concrete and frangible panel walls with similar concrete core thicknesses. The program also included a comparison between walls with

continuous rebar and spliced rebar at the connection to the footing. The following results were obtained from a series of blast simulator tests:

- The frangible panel walls experienced less impulse when impacted with a velocity similar to those used in the tests on the corresponding RC walls. This effect was more significant for the walls with 12 in. concrete cores where, on average, the total impulse experienced by the frangible panel walls was 8.3% less than the RC walls. For the walls with 8 in. thick concrete cores, the average decrease in impulse was 5.4%.

- The decrease in peak displacement for the 12 in. frangible panel walls when loaded by the same loading protocol as the RC walls was 18.1%. For the 8 in. thick frangible panel walls, the decrease in peak displacement was 11.6%.

- Differences in the level of cracking between the two wall types were insignificant when loaded with the same loading protocol.

- The programmer pyramids made permanent indentations in the frangible panels, ranging in depth from 0.25 in. to 0.4 in., which is evidence of energy dissipation during the impact loading.

- Low reinforcement ratios resulted in localized yield hinges and brittle failure of the rebar at the joint between the wall and the footing. The bars in the test were #3, which exhibit good bond characteristics with the concrete, and experience little bond slip. This behavior was most evident in the walls that had a 12 in. concrete core and a reinforcement ratio equal to 0.23%. The minimum allowable reinforcement ratio specified by ACI 318 is 0.33% [20]. The behavior was slightly improved for the walls with an 8 in. concrete core and reinforcement ratios of 0.34%.

- Lap spliced walls had similar responses as walls with continuous rebar when subject to the same loading protocols using three BGs.

- Loading protocols with one BG on the 8 in. RC and frangible panel lap spliced walls produced concrete spalling in the region where the starter bars were terminated. A similar test on an 8 in. frangible panel wall with continuous rebar did not produce spalling.

5.5 MDOF MODEL

5.5.1 OVERVIEW

A fast running model called Frangible Panel Wall Analysis (FPWA), that was developed to simulate the response of reinforced concrete walls with frangible panels to the effects of pressure pulses created from the detonations of high explosives is described herein. The RC wall and the frangible panels are models with a series of one-dimensional masses and nonlinear resistance functions that relate deformation in the panels and the wall to resisting forces. The model has been validated with experimental data generated from two tests series that were conducted with the blast simulator. Included in this section are a description of the theory that was used to develop the model and validation of the model through comparison with experimental data.

5.5.2 GENERAL MODEL DESCRIPTION

In the test series the frangible panels added mass to the RC walls and possibly dissipated energy during blast simulator loading through crushing of the material. These two effects were considered in the development of the FPWA code. The backbone of FPWA is a generalized single-degree-of-freedom model that is presented in Biggs [24]. A typical SDOF model consists of a mass and a spring or a mass and a nonlinear resistance function that relates wall displacement to a resistant force. The FPWA expands these concepts to a multi-degree-of-freedom (MDOF) model that incorporates a SDOF model to capture the response of the RC core in conjunction with additional masses and resistance functions that simulate the response of the frangible panels. A

schematic of the MDOF model for *N* number of masses and resistance functions is shown in Figure 5.52; it should be noted that in the figure the nonlinear resistance functions for the frangible panels and the RC core are represented with spring elements despite not actually being springs. In the current version of FPWA the frangible panel elements are used to model the panels on the front side of the RC core.

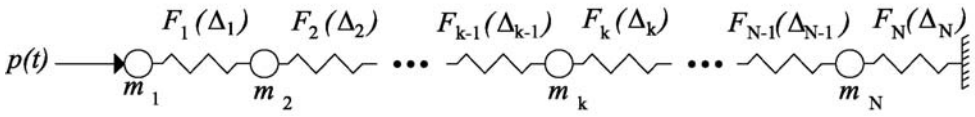

Figure 5.52: Schematic of FPWA

5.5.3 DYNAMIC ANALYSIS

The equation of motion for the MDOF system which contains *k* masses and elements is

$$\mathbf{M}\ddot{\mathbf{u}}(t) + \mathbf{C}\dot{\mathbf{u}}(t) + \mathbf{F}(\boldsymbol{\Delta}(t)) = \mathbf{P}(t) \tag{5.1}$$

where **M** is a mass matrix, **C** is the damping matrix, **F** is a array of the resistance forces on each mass which are functions of the deformation in the adjacent elements, **P** is an array of external loads from the blast pressure, $\ddot{\mathbf{u}}$ and $\dot{\mathbf{u}}$ are arrays containing acceleration and velocity of each mass and $\boldsymbol{\Delta}$ is the deformation in each element. The solution to this equation used for the analysis is an explicit form of Newmark's method called the central-difference method. This method was previously described in Chapter 2 for SDOF analysis. Similar to Chapter 2 the FPWA uses an implementation of this

method called, predictor-corrector, which is described in detail in [19] and is presented herein. The displacement, u, and the velocity, $\dot{u}$ for each mass at the current time-step, $t=i+1$, can be found with equations (5.2) and(5.3), respectively.

$$u_{i+1} = u_i + \Delta t \dot{u}_i + \frac{\Delta t^2}{2}[(1-2\beta)\ddot{u}_i + 2\beta\ddot{u}_{i+1}] \tag{5.2}$$

$$\dot{u}_{i+1} = \dot{u}_i + \Delta t[(1-\gamma)\ddot{u}_i + \gamma\ddot{u}_{i+1}] \tag{5.3}$$

In both of the equations above the updated displacement and velocity are based on the previous displacement, velocity and acceleration in addition to the updated acceleration. At this point the updated accelerations is unknown and to solve for it a predictor displacement, u_{i+1}^p and a predictor velocity, $\dot{u}_{i+1}^p$, are defined as

$$u_{i+1}^p = u_i + \Delta t \dot{u}_i + \frac{\Delta t^2}{2}(1-2\beta)\ddot{u}_i \tag{5.4}$$

$$\dot{u}_{i+1}^p = \dot{u}_i + (1-\gamma)\Delta t\ddot{u}_i \tag{5.5}$$

The equations show that the predictor displacement and velocities are only dependent on the previous displacement, velocity, and acceleration. The predictor displacements are used to determine the deformation of each element, which is then used in the resistance function to calculate a resisting force on each mass. The predictor velocities are used to calculate a damping force at each mass. In order to solve the MDOF system of equations explicitly mass proportional damping is used.

The forces that are applied to the masses of the MDOF at t=i+1 are shown in Figure 5.53. In general each mass is loaded by resistance forces, $F_{k\text{-}1}$ and F_k from the elements k-1 and k and a damping force that is determined with the deformation rate, $\dot{\Delta}$, in the adjacent elements.

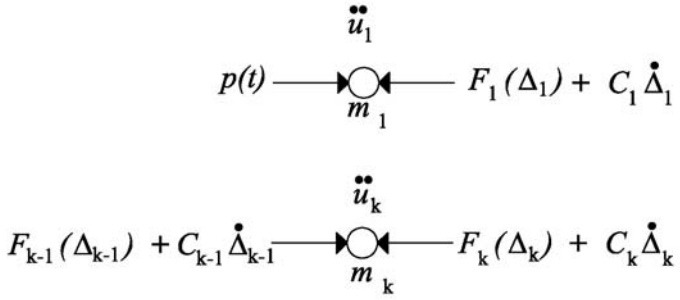

Figure 5.53: Forces on MDOF masses at t=i+1

Once the forces on each mass are resolved the updated acceleration can be found for each mass with:

$$\ddot{u}(t)_k = \frac{F_{k-1}(\Delta_{k-1}) + C_{k-1}\dot{\Delta}_{k-1} - F_k(\Delta_k) - C_k\dot{\Delta}_k}{m_k} \tag{5.6}$$

where in $F_{k\text{-}1}$ is equal to $p(t)$ if k is equal to 1. Also, when k=N the resistance $F_N(\Delta_N)$ is given by the resistance function for the reinforced concrete core, otherwise $F_k(\Delta_k)$ is determined by the stress-strain relation for the frangible panels.

When the updated acceleration is known the predictor displacement and velocity are corrected to give the updated displacement and velocity with the following equations.

$$u_{i+1} = u_{i+1}^p + \beta\Delta t^2\ddot{u}_{i+1} \tag{5.7}$$

$$\dot{u}_{i+1} = \dot{u}^{p}_{i+1} + \gamma \Delta t \ddot{u}_{i+1} \tag{5.8}$$

Finally, when an explicit central difference method is used β=0 and the predictor displacement is equal to the corrected displacement.

5.5.4 LOAD AND MASS FACTORS

In FPWA the mass, external load, and resistance of each element are also scaled by load and mass factors in the equation of motion. The factors are added because the model only consists of point masses and resisting forces while in the actual structure there is distributed mass and elasticity. The load and mass factors can be derived for a structural component using the principal of virtual work as shown in Chapter 2. For the frangible panel elements the equivalent mass and resisting force equals the actual mass and resistance because deformation in the element is assumed to be uniform axial compression which leads to factors equal to one. The reinforced concrete core, however, will undergo one-way bending; thus the displaced shape will vary along the length. The effective load and mass coefficients for the concrete core can be found in Table 2.3 of Chapter 2.

5.5.5 MATERIAL MODELS

CONCRETE- STATIC STRESS-STRAIN RELATION

A model that defines the stress-strain relation for concrete is required to determine a moment-curvature relation for the reinforced concrete core which is then used to develop a resistance function for this part of the model. The concrete model used in

FPWA is the same model that was used to determine the moment-curvature relations for masonry in Chapter 4. This model was proposed by [48], which is a modified version of models suggested by Thorenfeldt et al. [49] and Popovics [50] that accounts for the behavior observed in high strength concrete. The model is defined for a concrete strength equal to f'_c by the following equation

$$f_c = f_c' \frac{\varepsilon_c}{\varepsilon_{oc}} \frac{n_c}{n_c - 1 + (\varepsilon_c / \varepsilon_{oc})^{n_c k_c}} \tag{5.9}$$

where n_c and k_c are factors that define the hardening and softening of the curve when it becomes nonlinear and are given by

$$n = 0.80 + \frac{f_c'}{2466} \tag{5.10}$$

$$k = 0.67 + \frac{f_c'}{8992} \tag{5.11}$$

when f'_c is in psi. The model also requires the strain of the concrete at peak stress, ε_{co}, which is given

$$\varepsilon_{co} = \frac{n_c}{n_c - 1} \frac{f_c'}{E_c} \tag{5.12}$$

where E_c is the modulus of elasticity of the concrete and according to ACI 318 [20] can be determined by

$$E_{\cdot c} = 57{,}000\sqrt{f_c'}(psi) \tag{5.13}$$

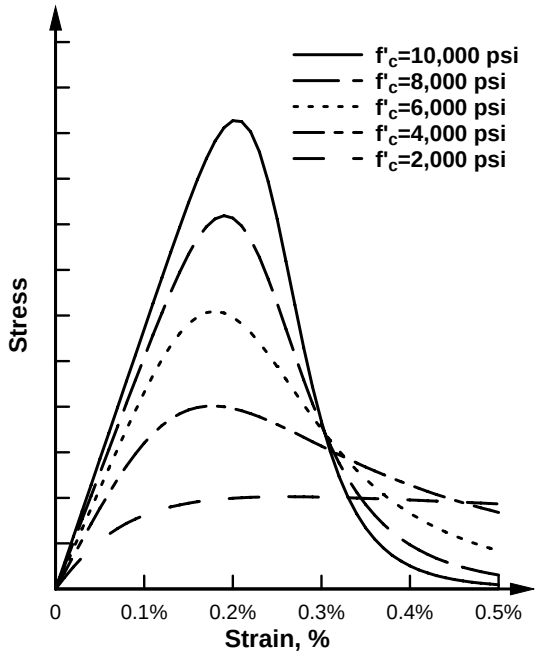

Figure 5.54: Compressive stress-strain curves for concrete at various strengths

Figure 5.54 displays the stress strain relation for concrete with several different compressive strengths. The plot shows that as the compressive strength increases the ascending and descending slopes of the curves in the nonlinear region increase.

CONCRETE- DYNAMIC INCREASE FACTOR

The properties of concrete are sensitive to strain rate. In FPWA a strain rate equal to 0.2 sec^{-1} is assumed for the concrete and steel reinforcements. This rate is the average of the strain rates suggested by TM 5-1300 [6] for members responding in flexure to close-in design range and far design range. The strength and strain at failure both increase with an increase in strain rate. The strain rate behavior is attributed to several factors including the limit on the rate of crack propagation, water in the voids and dynamic confinement from lateral inertia. In FPWA the strain rate effects are accounted

for with a dynamic increase factor on the concrete strength. The DIFs used in the code were found using an expression given in Malvar and Crawford [52]. These equations are given in Chapter 4.

REBAR- STATIC STRESS-STRAIN RELATION

The rebar model used for the analysis is a piecewise linear curve consisting of a linear elastic portion, a yield plateau, and a portion corresponding to strain hardening. This model was also used in Chapter 4 in the determination of moment-curvature relations for masonry walls. FPWA gives the option to use either Grade 40 or Grade 60 ASTM A615 rebar in the automatic resistance function generation option. The properties for these steel types are given in Table 4.4 in Chapter 4.

The reinforcing steel is also sensitive to strain rates; thus DIFs are used to increase yield and ultimate strengths of the steel in FPWA. The DIFs for yield and ultimate strength of the rebar were found with the following equations provided by Malvar [68]. These equations are also provided in Chapter 4.

FRANGIBLE PANEL BEHAVIOR

The resistance function used for the frangible panel elements was determined through compression testing on cylindrical samples taken from unused panels. Three different sample sizes were used. The samples were approximately 1.57 in. thick with diameters equal to 3 in., 6 in., or 15 inches. When the panels on the wall are loaded by a blast or impact pulse the loaded area is much greater than the thickness of the specimen resulting in state of uniaxial compressive strain. The objective of the material testing was

to determine the stress-strain relation under a similar state of strain. Another objective of the material testing was to measure the stress-strain relation over a large range of strains, thus being able to capture the portion of the behavior where the material begins to consolidate. In the FPWA model the consolidation behavior of the frangible panel material is important because it can result in load amplification instead of load reduction when a wall is subject to a blast or impact. The original dimension selected for the uniaxial strain specimens has 15 in. diameter. This specimen has a diameter to thickness ratio equal to about 10 which is suitable for uniaxial strain conditions. These specimens were tested with a 600 kip capacity compression testing machine. The test did show some of the stress-strain relation for the material, but unfortunately the machine did not have the precision to capture the behavior at lower strains and the capacity was not sufficient to measure a significant amount of the consolidation behavior.

A second set of material tests were performed on specimens with 6 in. diameters. The diameter to thickness ratio for these specimens was almost equal to four. The specimens were loaded with a 22 kip capacity load machine. This machine had more precision and the behavior captured at the lower strains was more detailed. Unfortunately, significant consolidation of the material was not measured during the tests because the machine lacked sufficient capacity. The stress-strain relations obtained in these tests did however, roughly matched those obtained in the first set. This suggests that the second set of tests put the specimen in a similar state of stress as the first set despite the smaller diameter.

A final set of tests was performed with specimens that had 3 in. diameters. These specimens were also loaded with a 22 kip capacity load machine. These tests provided a complete picture of the stress-strain relation from zero strain up to and through the strain where consolidation occurs. The behavior of the material in this test is different than the behaviors measured in the first two sets of tests. Therefore, it could not be used exclusively for the frangible panel resistance function.

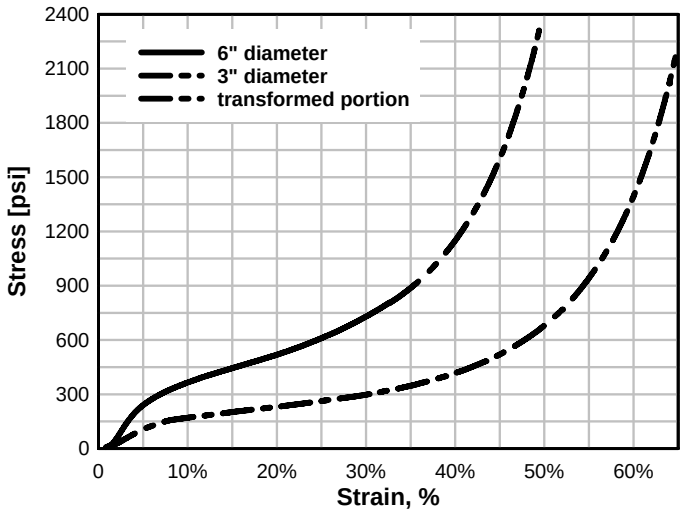

Figure 5.55: Frangible panel stress-strain relation for uniaxial compressive strain

The stress-strain behavior for the frangible panel material in FPWA uses a combination of the stress-strain curves obtained from the second and third sets of material tests. As previously reasoned the stress-strain relation for the 6 in. diameter specimen is in a state of uniaxial compression strain. Unfortunately, the data from these tests does not capture consolidation of the material and to include this behavior data from the 3 in. diameter specimens is used at the higher levels of strain. This was accomplished by offsetting the 3 in. curve from strains of 35% so that a continuous function was

formed with the 6 in. curve. Figure 5.55 shows the relation used in FPWA with the 6 in. diameter tests, shown as a solid line, combined with the consolidation curve from the 3 in. tests, shown as a dashed line. In the FPWA this combined data was fit with a 5th order polynomial equation shown below:

$$\sigma_d = 7594\varepsilon_d - 60026\varepsilon_d^2 + 277294\varepsilon_d^3 - 615202\varepsilon_d^4 + 563665\varepsilon_d^5 \qquad (5.14)$$

where σ_d is the stress (psi) in the frangible panel and ε_d is the strain. Equation (5.14) is then used in the model to relate compressive stress with strain. The correlation coefficient for the polynomial in (5.14) used to fit the data is equal to 0.99.

In the FPWA model the frangible panel elements respond dynamically to compressive stresses which vary with time and may include several load reversals. The hysteresis of the frangible panel to the anticipated scenario of load conditions is displayed in Figure. The behaviors of the frangible panel material model for each load condition shown in the figure are described below:

- **Point A-** The frangible panel is loaded in compression, as shown in Figure (a), according to Eq. (5.14).
- **Point B**- The load is reversed and the frangible panel in FPWA begins to unload along a line with a modulus equal to 330,340 psi as shown in Figure (b).
- **Point C**- Unloading continues linearly until the tensile yield stress is reached, Figure (c). Once the yield plateau is reached the tensile stress will remain constant at 50 psi until the frangible panel begins to reload or the tensile cutoff strain is reached. If the loading changes direction before the tensile yield stress is reached, than the stress-strain relation is still

defined by the linear curve until the original load curve in Eq. (5.14) is reached or the load changes direction again. The cutoff strain when the stress is on the yield plateau is equal to 5%. When the cutoff is reached the stress will drop to zero signifying a tensile failure in the material.

- **Point D**- Another option for the material when the stress is on the yield plateau is to reload. In this situation he material will load according to the same modulus used for unloading as long as the stress does not exceed the original loading curve. The reloading of the frangible panel is shown with Figure (d).

- **Point E**- Upon reloading if the stress does exceed the original compressive load curve, than the stress-strain relation will again be defined by Eq. (5.14), as shown in Figure (e).

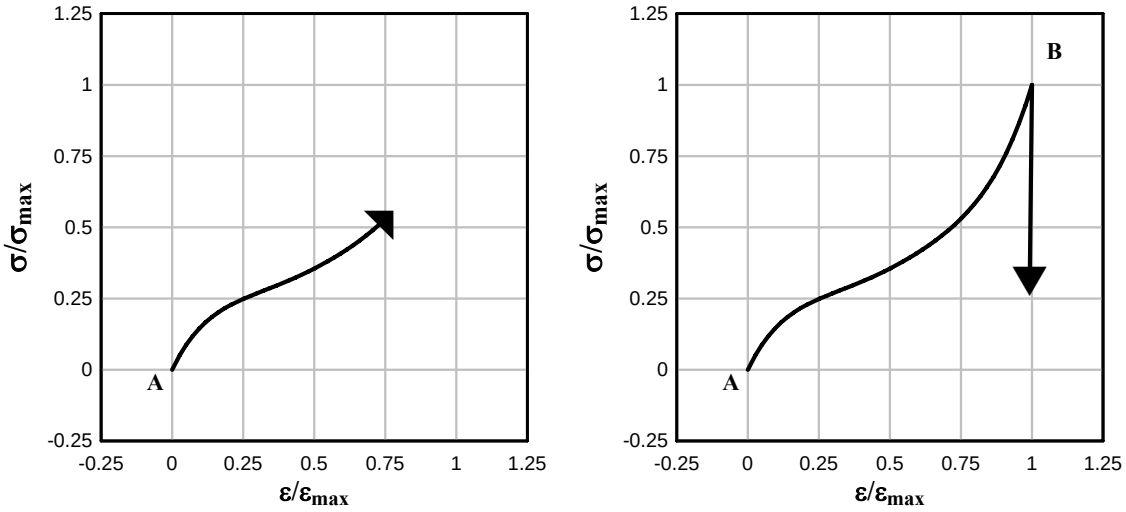

(a) **(b)**

Figure 5.56: Loading sequence for frangible panel material; (a) Loading; (b) Unloading; (c) Yield Plateau; (d) Reloading; (e) Reloading on original curve

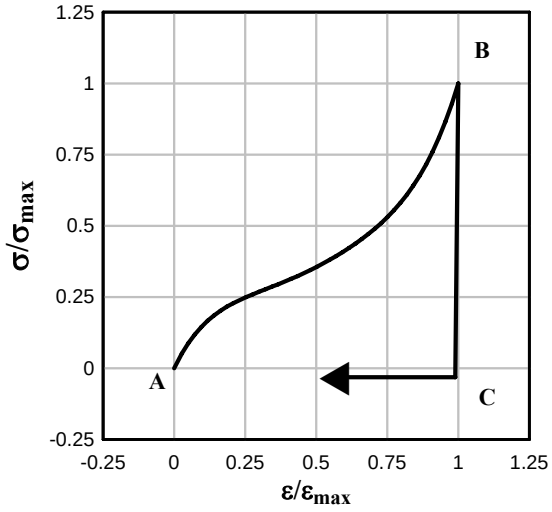

(c)

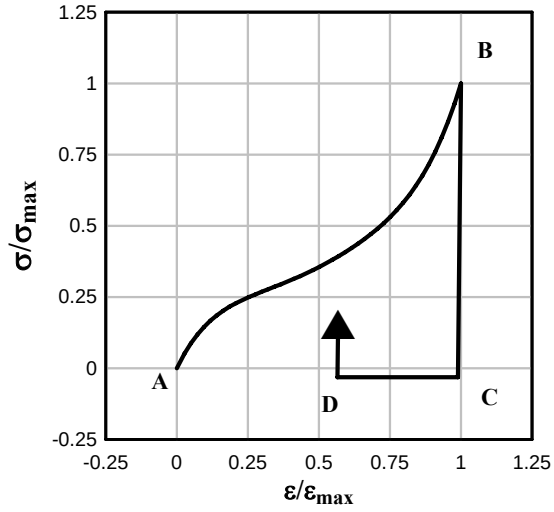

(d)

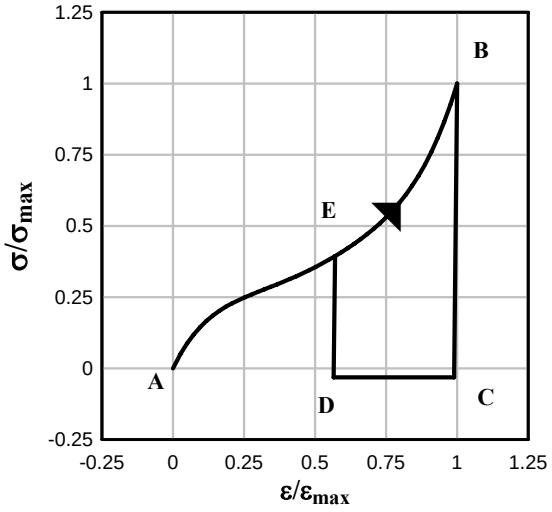

(e)

Figure5.56 (continued): Loading sequence for frangible panel material; (a) Loading; (b) Unloading; (c) Yield Plateau; (d) Reloading; (e) Reloading on original curve

5.5.6 MOMENT CURVATURE ANALYSIS

The observed mode of response in all of the frangible panel experiments was flexural deformation with the formation of plastic hinges at the location of maximum moment. In FPWA a resistance function can be generated automatically with several input parameters that describe the cross-section of the RC core. The first step taken by FPWA to generate the resistance function is to compute a moment-curvature relation for the section. In the analysis the moments and corresponding curvatures for the section are determined at three critical strain states for RC cores that define its inelastic behavior: yielding of the longitudinal steel, maximum stress in the concrete at the extreme compression fiber, and ultimate strain in the concrete at the extreme compression fiber.

An additional strain state that FPWA does not use during automatic generation of resistance functions, but is helpful for demonstrating the mechanics of reinforced concrete walls is the strain at which the concrete cracks. Prior to cracking the section is assumed to behave linear elastically with the strain varying linearly through the depth of the section and the stress related to strain by

$$\sigma = E\varepsilon \tag{5.15}$$

where σ is stress, E is the modulus of elasticity, and ε is the strain. Furthermore an expression for the elastic bending equation can be written:

$$\sigma = \frac{My}{I_s} \tag{5.16}$$

where M is the moment in the cross section, y is the distance from the neutral axis, and I is the moment of inertia of the cross section.

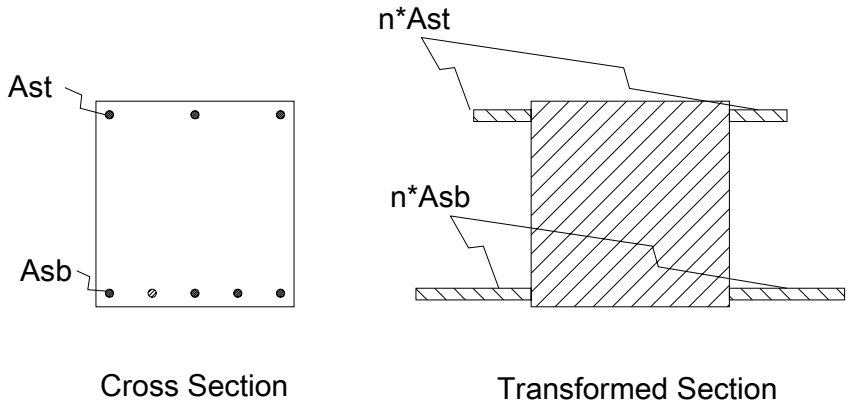

Figure 5.57: Transformed cross section of reinforced concrete

In the case of reinforced concrete the stiffness varies between the concrete and the steel, which results in more stress in one material at an equal strain. Use of the beam equation in this situation requires that the area of one material be transformed so that both materials have the same stiffness, AE. This is done by replacing the area of steel, A_s, with an area of concrete, A_c, using $A_c=n_rA_s$ and $n_r=E_s/E_c$ where E_s is Young's modulus for steel and E_c is Young's modulus for concrete. An example of a transformed cross section is shown in Figure 5.57.

A typical concrete strength is about 5000 psi, which results in a modulus equal to 4031 ksi and modular ratio, n_r, is equal to 7.2. For concrete at this strength the area of the replacement concrete will be 7.2 times greater than the area of the steel. The moment of inertia and the location of the neutral axis then can be calculated from the transformed section and used to determine the cracking moment with the following equation

$$M_{cr} = \frac{f_r I_t}{y_t} \tag{5.17}$$

where the modulus of rupture $f_r = 7.5\sqrt{f'_c}\,(psi)$, I_t is the transformed moment of inertia and y_t is the distance from the neutral axis to the extreme fiber in tension. Equation (5.17) is derived directly from equation (5.16) by substitution of the modulus of rupture for σ and solving for M_{cr}.

The curvature in the section is equal to the angle change over a given length and can be computed by

$$\phi = \frac{\varepsilon}{y} \tag{5.18}$$

where ε is the strain at a distance y from the neutral axis. In an un-cracked beam the curvature is linearly proportional to the moment when the beam behaves elastically. The relation between the curvature at cracking, ϕ_{cr}, and the cracking moment is

$$\phi_{cr} = \frac{M_{cr}}{E_c I_t} \tag{5.19}$$

Following cracking of the concrete the assumption that the section is linear elastic is not valid and the beam equations can no longer be applied. Instead the moment curvature relation is determined using constitutive properties of each material, along with strain compatibility assuming plan sections remain plane strain, and equilibrium of the internal forces.

The first strain state of interest is when determining a moment-curvature relation in FPWA is when the steel yields. A schematic of the typical stress and the strain in a cross section at this strain state is displayed in Figure 5.58. The wall shown in the figure is a representative 12 in. wide cut of the typical wall specimen tested in the program.

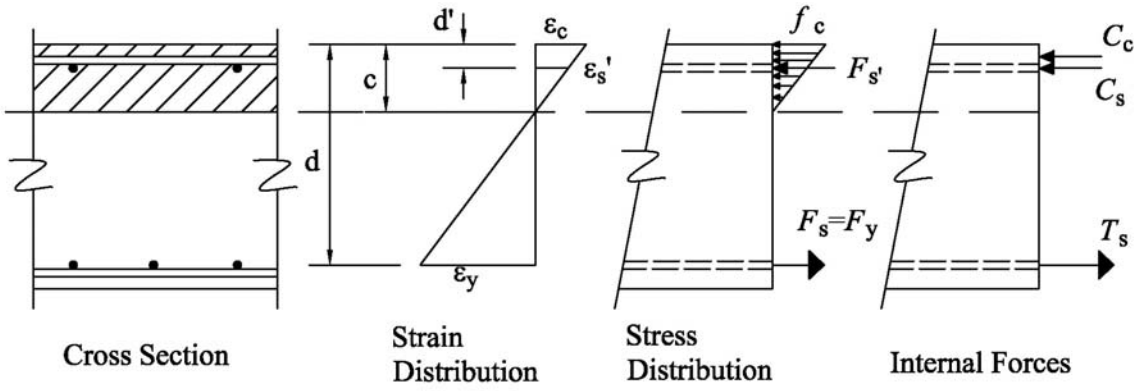

Figure 5.58: Cross section strain, stress, and internal forces at first yield of steel

The figure shows that the strain is assumed to vary linearly throughout the depth of the concrete. The strain in the bottom rebar is set to its yield strain, which can be found by

$$\varepsilon_y = \frac{F_y}{E_s} \tag{5.20}$$

where F_y is the yield stress of the bar. The strains in the top rebar, ε'_s and at the extreme compression fiber, ε_c, are then found using similar triangles:

$$\varepsilon'_s = \varepsilon_y \frac{(c-d')}{(d-c)} \tag{5.21}$$

$$\varepsilon_c = \varepsilon_y \frac{c}{(d-c)} \tag{5.22}$$

where c is the depth of the neutral axis, d is the depth of the bottom reinforcement, and d' is the depth of the top reinforcement.

In FPWA the relation between the stress and strain in the concrete is determined with Equation (5.9). Typically, for under-reinforced concrete sections the steel will yield prior to the concrete crushing and usually the strain at the maximum fiber is about half the strain at the maximum stress, which corresponds to linear-elastic behavior. It should be noted that although this is the behavior displayed in Figure 5.58, FPWA is not limited to linear-elastic stress-strain relation in the concrete at steel yield.

At the neutral axis the stress in the concrete is equal to zero and at the extreme compression fiber the stress can by found with $f_c=E_c\varepsilon_c$ given that the concrete strains are within the linear elastic region; otherwise Eq. (5.9) should be used for the stress distribution. The section analysis at this strain state does not account for any contribution of tensile stress from the concrete.

The stress contribution from the reinforcement steel is concentrated at the location of the bars. In the bottom layer of reinforcement the steel has yielded and, therefore, the stress is equal to F_y. In the top layer of steel the stress in the rebar, F'_s, is less than yield and is found by $F'_s=E_s\varepsilon'_s$. Once the stress distribution is known, an expression for the internal forces and moment can be written:

$$T_s - C_c - C_s = 0 \tag{5.23}$$

where T_s is the force in the bottom steel, C_c is the force in the concrete, and C_s is the force in the top steel. The forces in the steel can be found with:

$$T_s = A_s F_y \tag{5.24}$$

$$C_s = F'_s A'_s \tag{5.25}$$

where A_s is the area of the bottom steel and A'_s is the area of the top steel. The force in the concrete is computed by integrating the stress distribution from the neutral axis to the extreme compression fiber. In FPWA this is accomplished using Gaussian quadrature with five points to approximate the integral. The Gaussian quadrature rule is an approximation of the definite integral of a function, *f(x)*, which uses a weighted sum of the function evaluated at specific points within the bound of integration. The location of the points and the weights associated with each point are listed in Table 4.5 in Chapter 4.

For the case where the concrete strains are within the linear elastic region, which is probable for the current strain state, the integral will be equal to

$$C_c = 0.5 f_c c b \tag{5.26}$$

where *b* is the section width.

The unknown value in equations (5.21) and (5.22) is the depth of the neutral axis, *c*, which can be determined by satisfying equation (5.23). In FPWA this is done iteratively with the method of bisection where *c* is initially set equal to half of the thickness. Once the neutral axis is found the moments due to the internal forces are then summed to give

$$M_y = T_s d - C_c a - C_s d' \tag{5.27}$$

where M_y is the moment at steel yield and a is the distance from the extreme compression fiber to the centroid of the stress distribution in the concrete. The equation for computing the centroid of a stress distribution, a, is:

$$a = \frac{\int x\sigma(x)dx}{\int \sigma(x)dx} \tag{5.28}$$

where x is the distance from the extreme compression fiber. The integrals in Eq. (5.28) where also approximated using Gaussian quadrature. The curvature in the beam at yield, ϕ_y, can then be found by setting $\varepsilon=\varepsilon_y$ and y=(*d-c)* in equation (5.18).

The next strain state considered by FPWA in the moment-curvature analysis is when the concrete at the extreme fiber reaches a maximum stress, ε_{co}. According to the concrete model used in the analysis this strain is a function of the modulus of elasticity and concrete strength and can be found with equation (5.12). A typical cross-section with the strain distribution, stress distribution, and internal forces at this strain state are displayed in Figure 5.59.

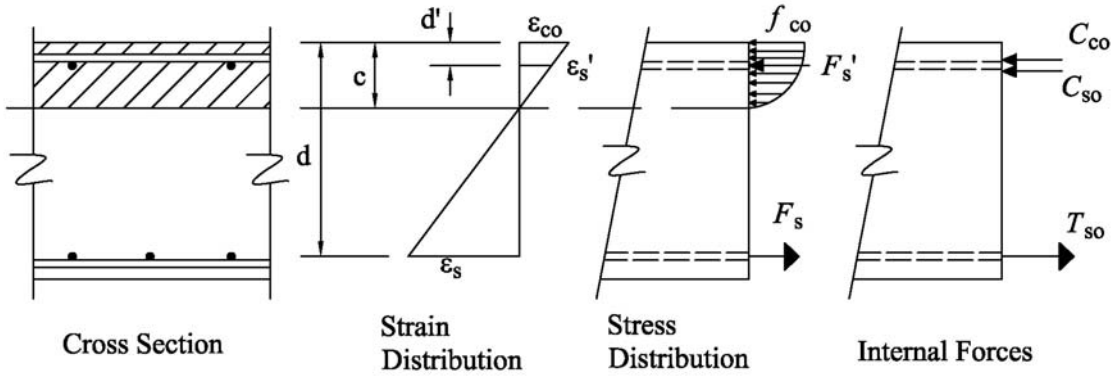

Figure 5.59: Cross section strain and stress distribution at maximum stress

The assumption that plane strains remain plane is still valid at this state; therefore the strain will vary linearly through the depth. The strains in the steel rebar at the top and bottom can be determined using similar triangles and the concrete strain, ε_{co}, as shown below:

$$\varepsilon_s = \varepsilon_{co} \frac{(d-c)}{c} \tag{5.29}$$

$$\varepsilon'_s = \varepsilon_{co} \frac{c-d'}{c} \tag{5.30}$$

where c is the new depth to the neutral axis. When the strain in the top and bottom steel is known, the stresses F'_{su} and F_{su} are determined by the nonlinear constitutive relations provided in a previous section. The strains in bottom layer of reinforcement is beyond the yield at this state therefore, the relation, $F_s=E_s\varepsilon_s$, was no longer applicable. As done for the previous strain state, equilibrium is used to write an expression for the internal forces:

$$T_{so} - C_{co} - C_{so} = 0 \tag{5.31}$$

where the forces in the steel can be found with

$$T_{so} = F_s A_s$$

$$C_{so} = F'_s A'_s$$

The force due to the compressive stress in the concrete can be found by integrating the stress profile from the neutral axis to the top of the section. It is still

assumed that the concrete does not contribute any stress due to tensile strains. FPWA also integrates the stress for this strain rate with an approximate Gauss quadrature rule using five points.

The unknown variable in the equations above is the depth of the neutral axis. In the analysis of the wall sections in this report the neutral axis was solved for by iteration until equation (14) was satisfied. When the neutral axis was determined the moments from the internal forces were summed to give the maximum moment, M_{co} with the following expression:

$$M_{co} = T_{so}d - C_{co}a - C_{so}d' \tag{5.32}$$

where a is the distance from the top of the section to the centroid of the nonlinear stress profile in the concrete. The method for determining the centroid is the same at this strain state as at steel yield. The curvature at maximum stress, ϕ_{co}, is calculated using equation (5.18) by setting $\varepsilon=\varepsilon_{co}$ and $y=.c$.

The final strain state considered by FPWA in the moment-curvature analysis is when the concrete crushes at ε_{cu}=0.003. The stress and strain distribution in the section at this state is shown in Figure 5.60. Again the assumption that plane strains remain plane is held. The assumption that the concrete does not contribute any tensile stress is also carried over from the previous sections. The mechanics in the section at concrete crushing are similar to those at maximum stress; therefore the procedure at the previous state using equations (5.29) through (5.32) is repeated to find the moment and curvature at the current state.

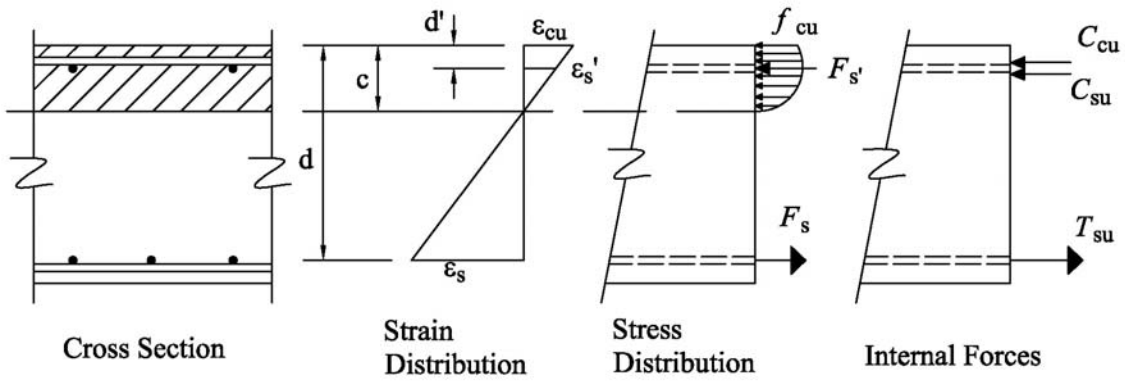

Figure 5.60: Cross section strain and stress distribution at concrete crushing

The moment-curvature analysis using the three strain states will produce a tri-linear curve starting at zero and ending at the ultimate moment and curvature. FPWA simplifies the tri-linear curve as an elastic-plastic relation which is then used to generate the resistance functions. The program sets the plastic moment and curvature such that the internal energy calculated from the area under the curve equals that of the tri-linear curve. Figure 5.61 displays the tri-linear relation from the moment-curvature analysis along with an equivalent elastic plastic curve.

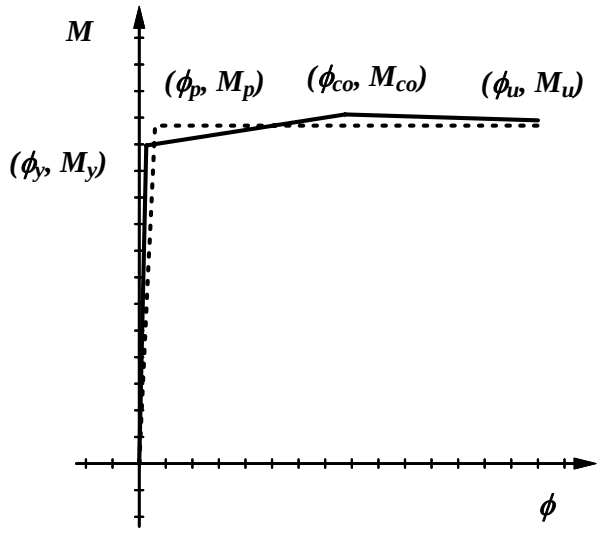

Figure 5.61: Moment-curvature with equivalent EPP curve

5.5.7 RESISTANCE FUNCTIONS

In FPWA a resistance function for the RC core of the frangible panel walls is used to calculate its internal force due to a midspan deflection. A schematic of a typical resistance function that has a tri-linear curve is shown in Figure 2.29 of Chapter 2. Figure 2.30 and Figure 2.31 demonstrate the unloading and re-loading behavior of the resistance function used in FPWA.

The resistance functions used in FPWA to relate load to deflection for the reinforced concrete core are calculated using the moment-curvature relation for the cross section and the kinematics of the displaced wall. The methods for determining the resistance function for a RC wall with simple-simple or pinned-fixed boundary conditions are presented in Chapter 2.

5.5.8 SUPPORT REACTIONS

The FPWA analysis also calculates dynamic support reactions for the wall when loaded by the blast. Chapter 2 describes the method for determining the reactions forces for an SDOF model. The same method is used in FPWA.

5.5.9 MODEL VALIDATION

The FPWA code was validated through comparison with the test data recorded in frangible panel Test Series I and II. The two response features that were used in the comparison are impulse and peak midspan displacement. An observation made in the experiments was that the walls with frangible panels had slightly lower impulses as the plain RC walls; therefore impulse was chosen as a feature of comparison to assess the models ability to accurately simulate this effect. The other feature, displacement, was selected for comparison because, in blast design, peak midspan displacement is often related to limit states used as design criteria.

BG LOADING IN FRANGIBLE PANEL WALL ANALYSIS

The numerical simulation of the blast simulator experiments used a loading option in FPWA that includes the blast generator impact masses instead of a pressure pulse. The BGs are ultrafast high pressure hydraulic oil/nitrogen driven actuators that are used to apply the loads during blast simulator tests. The BGs accelerate an impact module to a specified impact velocity at which it strikes the test specimen. The impact modules includes a piston rod, impact mass, instrumentation package, and “programmer” pads.

The purpose of the programmer pads is to tailor the load pulse delivered to the specimen to match characteristics of an actual blast.

The BGs are included in the model as a mass with a resistance function that is dependent on a contact condition with the first frangible panel wall mass in the MDOF. The contact condition checks the distance between the first frangible panel mass and the BG mass; if this distance is less than the thickness of the programmer a resistance force will be added to the equation of motion between the two masses; if the distance is greater than the programmer thickness then no force is applied. Physically, when the programmer is unloading there is no mechanism to apply a tensile load. In the model tensile loads are prevented with the contact condition. The resistance function for the BG, developed by [27], is dependent on the deformation and deformation rate in the programmer. It was fit to impact test data for the programmer to simulate the energy dissipation that has been observed in previous tests. This model is described in more detail in Chapter 3. A schematic of the MDOF with the BG mass is displayed in Figure 5.62.

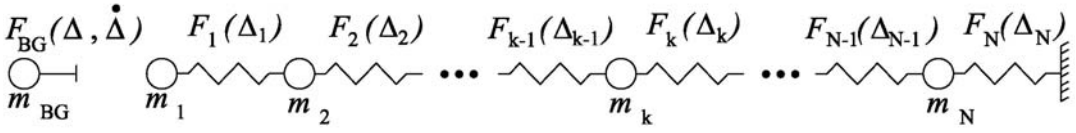

Figure 5.62: MDOF with BG mass

SECTION PROPERTIES

All of the walls in both test series were 48 in. wide and had a length equal to 129.75 in. The concrete used in these was normal weight concrete with a weight density equal to 150 pcf. The walls tested in Frangible Panel Test Series I underwent one-way bending with a simple-simple boundary condition. The walls tested in Frangible Panel Test Series II also underwent one-way bending, but had a fixed-simple boundary condition. The other geometric parameters that varied for the different test specimens were the thickness of the RC core, the area of steel in the top and bottom layers, and the thickness of the cover concrete. Table 5.10 and Table 5.11 list these properties from the first and second test series, respectively.

Table 5.10: Section Properties for Frangible Panel I Tests Specimens

Specimen	Core Thickness [in]	A_{st} [in^2]	A_{sc} [in^2]	Cover [in]
RC-D-20	7.9	0.935	0.545	0.98
RC-D-25	9.8	0.935	0.545	0.98
RC-D-30	11.8	1.461	0.852	0.98
FP-D-20	4.7	0.935	0.545	0.59
FP-D-25	6.7	0.935	0.545	0.59
FP-D-30	8.7	1.461	0.852	0.59

Table 5.11: Section Properties for Frangible Panel II Tests Specimens

Specimen	Core Thickness [in]	A_{st} [in^2]	A_{sc} [in^2]	Cover [in]
RC8/FP8	8	1.325	1.325	1.50
RC12/FP12	12	1.325	1.325	1.50

MATERIAL PROPERTIES

The concrete and steel reinforcement varied for the different walls tested in the two test series. In the first test series the concrete strength was measured at three

different dates. The values for each material test date are listed in Table 5.12. For the analysis of the walls in FPWA, an average of the strengths at the two later dates, equal to 8250 psi, was used for the concrete. The walls tested in the second frangible panel test series were cast with four separate lifts of concrete. The concrete strengths of the four lifts at 7-, 14-, 28-, and 56-days are listed in a table below. In the analysis using FPWA the average of the four lifts at 56-day, equal to 5112 psi, was used for the concrete strength.

In the first test series the walls with overall thicknesses equal to 11.8 in. (30 cm) used bars that had a diameter equal to 0.39 in. (10 mm). The other walls in this test series had bars with a diameter equal to 0.32 in. (8 mm). Tension tests according to ASTM A615 were performed to measure the properties of these bars. The properties are listed in the tables below. In the second test series A615 Grade 60 rebar was used the properties of this type of rebar, shown in Table 5.15.

Table 5.12: Series I Concrete Compressive Strengths

Date Cast	Strength (ksi)		
	28-Day	Strength on 8-23-06	Strength on 8-31-06
4-11-06	5.51	6.14 (135 days)	7.18 (143 days)
4-17-06	5.73	7.80 (129 days)	8.70 (137 days)

Table 5.13: Series II Concrete Compressive Strengths

Lift	Strength (ksi)			
	7-Day	14-Day	28-Day	56-Day
1	3.60	3.96	4.41	4.71
2	3.70	4.49	4.93	5.74
3	3.27	3.72	4.21	4.76
4	3.51	4.26	4.80	5.24

Table 5.14: Series I Steel Properties

Bar Size	F_y [ksi]	ε_y	ε_{sh}	F_u [ksi]	ε_u
8 mm	46	0.21%	1.46%	68	12.1%
10 mm	40	0.24%	1.01%	63	13.3%

Table 5.15: Series II Steel Properties

F_y [ksi]	ε_y	ε_{sh}	F_u [ksi]	ε_u
69	0.21%	0.7%	109	12.5%

In the blast simulator tests it was observed that the pyramids on the front face of the programmer caused permanent indentations in the frangible panel as shown in Figure 5.63. The penetration of the pyramids into the frangible panel softens its initial response resulting in lower stresses during impact compared to a uniform load.

Figure 5.63: Permanent indentations in frangible panel

This was investigated using the FE code LS-DYNA [24] to model a portion of the frangible panel loaded by a flat plate and a plate with pyramids similar in geometry to those on the programmer. The material model used for the frangible panel in the FE

simulation was constructed using the same data for the curve in FPWA. Figure 5.64 displays an illustration from the FE simulation that shows the pyramids prior to loading the frangible panel. A comparison of the stress-strain relations for frangible panel FE simulations with a uniform load and with a load with the pyramids is displayed in Figure 5.65. The plot shows that when loading with pyramids the stress is lower at any given strain. To account for the pyramidal effect in FPWA the stress strain relation given by equation (5.14) was reduced with a scale factor (SF) equal to 0.6. The scaled relation is also shown in Figure 5.65

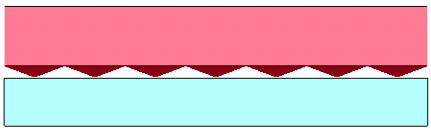

Figure 5.64: FE simulation of loading with pyramids

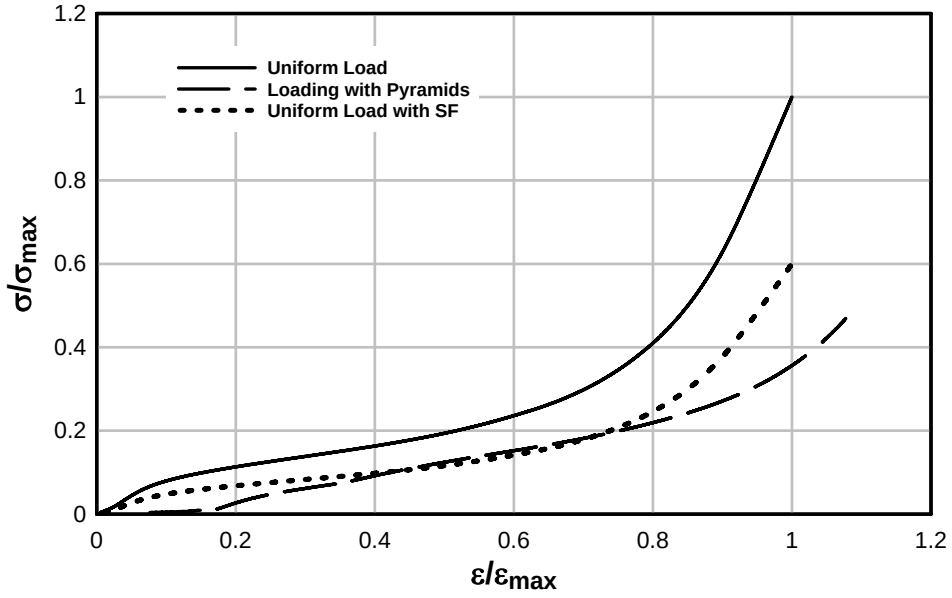

Figure 5.65: Comparison between loading with and without pyramids

DYNAMIC INCREASE FACTORS

Strain rates in the reinforced concrete were measured during Series I and II blast simulator tests with strain gages located in the top and bottom layers rebar near the regions of maximum moment. Values of maximum strain rates observed in these tests are listed in Table 5.16 and Table 5.18 for the first and second series, respectively. These strain rates are greater than the assumed strain rates in FPWA. To validate the model the measured strain rates were used over the assumed ones. In the analysis of these walls with FPWA one half of the average maximum strain rate for the tension rebar was used to calculate the DIF for the steel. One half of the \ average maximum compression strain rate measured on the top rebar was used to calculate the DIF for the concrete. The assumption made for the concrete is that the strain rate during compression is similar to that of the top rebar, which is reasonable considering that the strain varies linearly through the depth and the top steel is located near the extreme compression fiber in the concrete. One half of the maximum was used with the assumption that the strain rate varies linearly when the wall is loaded and one half would be the average strain rate during this time period.

Table 5.16: Series I Observed Strain Rates

Test	Specimen	Compression Rebar		Tension Rebar	
		# of Gages	$\dot{\varepsilon}_{com}$ [sec^{-1}]	# of Gages	$\dot{\varepsilon}_{ten}$ [sec^{-1}]
1	RC-D-20	1	0.41	1	2.7
2	FP-D-25	2	3.8	2	6.7
3	FP-D-30	2	1.0	2	3.5
4	RC-D-25	1	0.65	1	4.8
5	FP-D-20	2	1.8	2	2.7
6	RC-D-30	1	0.4	1	3.4
7	FP-D-30-2	1	2.1	1	3.9
8	FP-D-25-2	2	1.1	2	4.9
9	FP-D-20-2	2	1.7	2	3.8
		Average	1.5	**Average**	4.0

Table 5.17: Series I DIFs

	F_y	Steel Yield	Steel Ultimate	Concrete
Malvar and Crawford	40 ksi	1.65	1.15	1.24
	46 ksi	1.58	1.14	

Table 5.18: Series II Observed Strain Rates

Test	Specimen	Compression Rebar		Tension Rebar	
		# of Gages	$\dot{\varepsilon}_{com}$ [sec^{-1}]	# of Gages	$\dot{\varepsilon}_{ten}$ [sec^{-1}]
1	RC-12-1	0	--	0	--
2	FP-12-1	2	1.67	2	7.33
3a	RC-12-2	1	0.27	2	0.81
3b	RC-12-2	2	0.99	1	0.65
4a	FP-12-2	2	0.13	2	1.27
4b	FP-12-2	1	0.28	2	2.66
5a	RC-8-1	1	0.42	2	1.78
5b	RC-8-1	2	1.02	2	4.05
6a	FP-8-1	2	0.15	2	1.73
6b	FP-8-1	2	0.52	2	2.32
7	RC-8-2	2	1.13	2	5.24
8	FP-8-2	1	0.32	2	2.89
9	FP-8-3	5	0.75	5	1.18
10	RC-8-3	5	1.57	4	1.77
11	RC-12-3	4	0.37	5	0.95
12	FP-12-3	5	0.59	5	1.27
		Average	0.74	**Average**	2.48

Table 5.19: Series II DIFs

	F_y	Steel Yield	Steel Ultimate	Concrete
Malvar and Crawford	69 ksi	1.32	1.09	1.35

MOMENT-CURVATURE RELATIONS

The moment-curvature relations for each test specimen were generated using the previously defined section and material properties. The relations given by FPWA are listed in Table 5.20 and

Table 5.21, respectively.

Table 5.20: Moment-Curvature Properties for Series I Tests Specimens

Specimen	M_y [k-ft]	ϕ_y [10^6/in]	M_{co} [k-ft]	ϕ_{co} [10^6/in]	M_u [k-ft]	ϕ_u [10^6/in]	M_p [k-ft]	ϕ_p [10^6/in]
RC-D-20	36.1	417	40.8	5997	41.0	8478	39.1	417
RC-D-25	46.3	321	51.7	5973	52.2	8430	49.8	321
RC-D-30	79.8	241	88.6	4329	89.7	5937	85.5	241
FP-D-20	21.2	734	23.3	6760	23.5	8908	22.5	734
FP-D-25	31.8	475	34.7	6738	35.0	8875	33.6	475
FP-D-30	59.5	328	64.6	5363	65.2	7177	62.7	328

Table 5.21: Moment-Curvature Properties for Series II Tests Specimens

Specimen	M_y [k-ft]	ϕ_y [10^6/in]	M_{mco} [k-ft]	ϕ_{co} [10^6/in]	M_u [k-ft]	ϕ_u [10^6/in]	M_p [k-ft]	ϕ_p [10^6/in]
RC8/FP8	60.3	602	67.9	2299	69.6	3309	65.3	602
RC12/FP12	98.2	353	110.5	2278	113.7	3275	106.5	353

RESISTANCE FUNCTIONS

The moment-curvature relations for each wall were simplified as elastic-plastic curves which were then used along with the kinematics of the one-way bending walls to

calculate resistance functions. The resistance functions are displayed in Table 5.22 and Table 5.23, respectively. The functions for the first series of tests are bi-linear, while for the second series of tests the functions are tri-linear. In FPWA force remains constant for increasing displacements after the final displacement listed in the tables is reached.

Table 5.22: Resistances Functions for Series I Tests Specimens

Specimen	R_1 [psi]	Δ_1 [in]	R_2 [psi]	Δ_2 [in]
RC-D-20	0	0	4.65	0.73
RC-D-25	0	0	5.92	0.56
RC-D-30	0	0	10.20	0.42
FP-D-20	0	0	2.67	1.29
FP-D-25	0	0	3.99	0.83
FP-D-30	0	0	7.45	0.57

Table 5.23: Resistances Functions for Series II Tests Specimens

Specimen	R_1 [psi]	Δ_1 [in]	R_2 [psi]	Δ_2 [in]	R_3 [psi]	Δ_3 [in]
RC8/FP8	0	0	7.76	0.21	11.63	0.74
RC12/FP12	0	0	12.65	0.12	18.98	0.43

INITIAL PLASTIC DEFORMATION

In the second test series the specimens labeled RC-12-2, FP-12-2, RC-8-2, and FP-8-2 were impact multiple times. Initial comparisons between the experiment and the FPWA analysis for the tests in which these specimens had already been impacted showed that the analysis under predicted the peak midspan displacements. The damage from the previous test was then accounted for by giving the specimen and initial displacement and an initial plastic deformation. The plastic deformations used were based on the final displacements observed in the previous analysis. The test numbers and the plastic deformations applied to the specimens in FPWA are listed in Table 5.24.

Table 5.24: Plastic Deformations

Test	Specimen	Δ_p [in]
3b	RC-12-2	0.78
4b	FP-12-2	0.68
5b	RC-8-1	0.79
6b	FP-8-1	0.69

5.5.10 COMPARISONS OF EXPERIMENTS AND SDOF ANALYSIS

The walls tested in the first and second series were subject to impact loads by the BGs in FPWA at the velocities that were measured in the experiments. The BG velocity, impulse delivered to the specimen, and peak midspan displacement for the experiment and the FPWA analysis are listed in Table 5.25. The table also lists the errors for the predicted impulses and displacements. The table shows that the maximum impulse error was 11.7% for Test 1 in Series 1. The maximum displacement error was 17.3% in Test 7 of series I. In Test 5 of Series I and Tests 1 and 2 of Series II the specimen collapsed after being impacted. In all of these tests the rebar at the plastic hinge fracture. In the FPWA the specimen failure by collapse and rebar fracture is not currently modeled; therefore care needs to be taken when modeling walls where large displacements are recorded.

The FPWA model is also compared to the experimental results in Figure 5.66 and Figure 5.67. The first figure plots the impulse predicted by FPWA versus the impulse observed in the blast simulator tests. The second figure plots predicted displacement versus measured displacement. The data from the test where the walls collapsed are not

included in the plot because there is no displacement associated with collapse. Included in the plots are a linear regression fit and a 45-degree line that represents perfect correlation between the predicted and measured results.

Table 5.25: Comparisons of Experimental and FPWA Response

Series-Test	Specimen	BG Velocity [in/sec]	Exp Impulse [psi-msec]	Exp Disp. [in]	FPWA Impulse [psi-msec]	Impulse Error	FPWA Disp. [in]	Disp Error
I-1	RC-D-20	340	312	7.6	348	11.7%	8.2	8.0%
I-2	FP-D-25	398	338	14.3	366	8.2%	11.1	22.7%
I-3	FP-D-30	535	505	9.8	511	1.2%	9.2	6.1%
I-4	RC-D-25	406	425	8.5	448	5.5%	8.6	0.6%
I-5	FP-D-20	413	347	collapse	331	4.7%	18.2	NA
I-6	RC-D-30	575	684	7.9	659	3.6%	9.0	13.9%
I-7	FP-D-30-2	645	569	11.4	605	6.3%	12.8	12.3%
I-8	FP-D-25-2	469	409	15.3	421	2.8%	14.4	5.9%
I-9	FP-S-20	389	329	21.9	312	5.0%	16.3	25.6%
II-1	RC-12-1	899	867	collapse	781	10.0%	6.8	NA
II-2	FP-12-1	906	746	collapse	738	1.2%	5.8	NA
II-3a	RC-12-2	254	231	0.9	238	3.3%	0.9	4.5%
II-3b	RC-12-2	484	445	3.2	450	1.1%	3.2	1.9%
II-4a	FP-12-2	266	225	0.8	234	4.1%	0.8	3.9%
II-4b	FP-12-2	484	401	2.3	396	1.4%	2.5	9.5%
II-5a	RC-8-1	180	148	1.0	155	4.6%	1.0	2.0%
II-5b	RC-8-1	352	303	3.3	296	2.3%	3.5	4.5%
II-6a	FP-8-1	187	152	0.9	159	4.7%	0.9	4.4%
II-6b	FP-8-1	358	278	2.7	282	1.4%	3.0	9.6%
II-7	RC-8-2	452	373	4.5	377	1.0%	4.1	9.7%
II-8	FP-8-2	450	352	3.3	343	2.6%	3.2	2.1%
II-9	FP-8-3	467	361	3.8	354	1.8%	3.4	9.9%
II-10	RC-8-3	457	386	4.7	381	1.2%	4.2	10.9%
II-11	RC-12-3	491	437	3.0	456	4.3%	2.5	17.5%
II-12	FP-12-3	512	426	1.9	417	2.1%	2.0	7.4%

It can be observed visually in Figure 5.66 that the correlation between the impulse data is strong. This strong correlation along with the low level of error listed in Table 5.25 gives confidence that the frangible panels have been modeled accurately and will adequately predict impulses, in a range from 0 to 800 psi-msec delivered by a dynamic load such as those generated in a blast or by an impact.

Figure 5.67 shows that there is also good correlation between the FPWA model and the experimental peak midspan displacements. It can be observed in the plot that as the displacement increases the correlation becomes weaker with the predicted displacement less than the measured. This is most likely because the assumptions used to develop the resistance function break down at larger displacements where the behavior is highly nonlinear. Furthermore, the resistance function does not account for the self weight of the structure which could affect its stability. Despite this trend, the correlation between the data is good and the relatively small errors listed in Table 5.25 provide confidence that FPWA can predict the displacement of frangible panel walls to blast or impact loads for peak displacements that range between 0 and 15 inches.

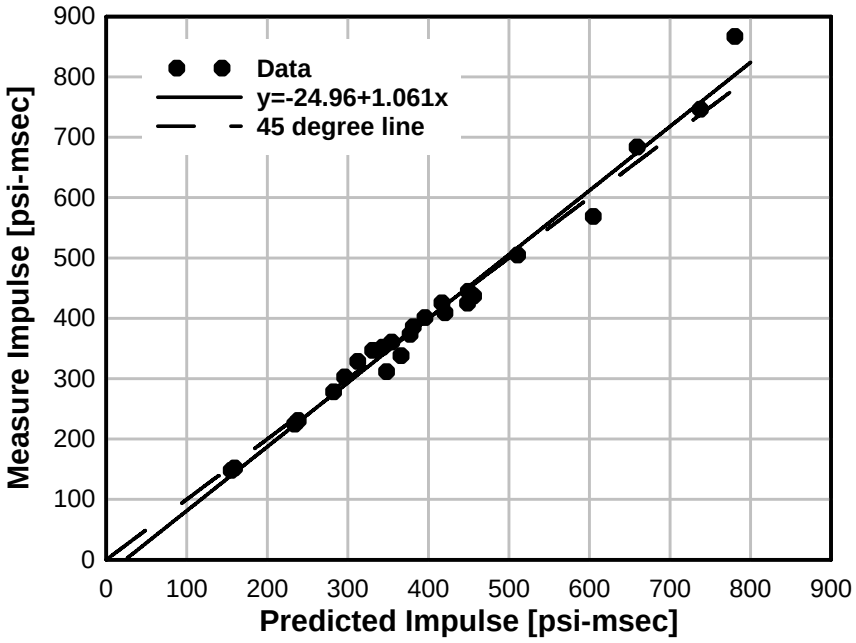

Figure 5.66: Predicted impulse versus measured impulse

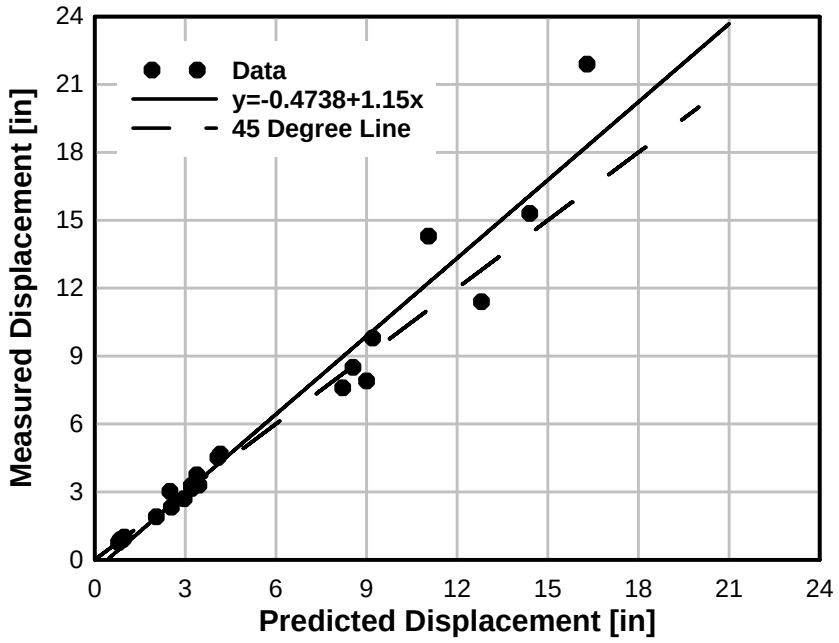

Figure 5.67: Predicted displacement versus measured displacement

5.6 FE MODELS

5.6.1 MESH DETAILS

Finite element models were run using LS-DYNA to simulate the response of the walls impacted by the blast simulator. As described in Chapter 4, LS-DYNA is a three dimensional explicit, Lagrangian finite element code that uses a central difference time-integration method. This program is commonly used for linear and nonlinear dynamic problems including those that are related to blast and impact loading.

The models for the frangible panel wall tests used three dimensional solid elements to represent the concrete, frangible panels, supports, programmers, and BG masses. These elements were eight node bricks with single point integration. Hughes-Liu beam elements with cross-sectional integration formulation were used to model the reinforcing steel. In the analysis for each wall the BGs were given initial velocities equal to the measured impact velocities and the programmer material parameters were set so that the predicted impulse matched the measured impulse.

Model details of the Series I blast simulator tests are shown in Figure 5.68. The figure shows the wall specimen being impacted by four BGs. These BGs transfer load to the specimen with a *AUTOMATIC_SURFACE_TO_SURFACE contact. The elements representing the frangible panels (colored red) are eight node solids that have been attached to the concrete solid elements (colored yellow) with a tied contact surface. The actual frangible panels used in the test specimen had dimensions equal to 19.7 in. x 39.4 in. x 1.57 in. (50 cm x 100 cm x 4 cm) which meant that there were seven rows of panels

along the height (137.8 in.) and about 1.22 panels in each row. The model of the panels included the horizontal joints that existed between each panel to prevent continuity for transferring load that would not be present in the actual specimen. The horizontal joints can be seen in Figure 5.68. The vertical joints that existed in the test specimen were ignored, which is reasonable because the members only underwent one-way bending.

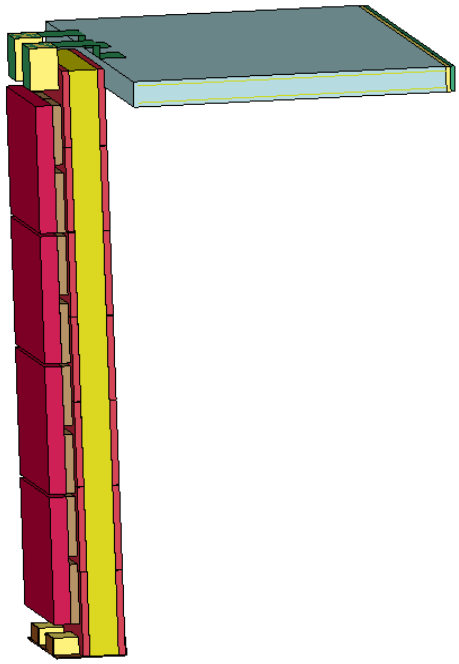

Figure 5.68: FE model for Series I blast simulator tests

The top and boundary conditions for the FE model of the Series I tests are shown in Figure 5.69. The bottom boundary was modeled at a channel with solid elements that was fixed from translating in three directions. Angles and neoprene pads were also modeled at the base with the same dimensions as used in the tests. The reinforced concrete slab at the top boundary condition was modeled with solid elements for the

concrete and beam elements for the reinforcing steel. The bent steel plates and neoprene foam that were used to restrain the top of the wall during rebound were also included in the model. At all boundary conditions in the model *AUTOMATIC_SURFACE_TO_-SURACE contacts were used.

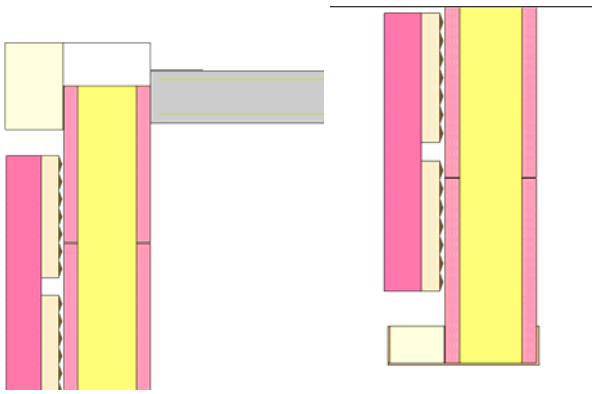

Figure 5.69: Series I top and bottom supports in FE model

The details of the mesh used for the FE model are displayed in Figure 5.70. For each wall sizes there were at least ten elements through the thickness of the concrete core. This is shown in the figure for the specimen labeled FP-D-25. The figure shows that frangible panels had four elements through the thickness. Also included in the figure is the rebar layout used in the FE model which includes the longitudinal bars, stirrups, and a few transverse bars that run through the thickness. The mesh displayed is specific for FP-D-25, but only the section properties, the location of the bars, and the length of the legs on the stirrups vary in the other specimens. The nodes of the rebar were merged to those of the concrete elements representing a perfect bond between the two.

Figure 5.71 shows the mesh details for the programmer used to load the walls in the simulation. In Chapter 4 the programmer was modeled as a flat plate, ignoring the

pyramids, and the results of the analysis matched the experiments within acceptable limits. In the simulations of the wall tests with the frangible panels, however, the interaction between the pyramids and the panels created localized indentations as reported in the results section of this chapter. Therefore, it was important to explicitly model the pyramids, as shown in Figure 5.71, in order to match the test results. During the simulation, in order to prevent a second hit the BG masses and the programmers were deleted from the calculation at 20 msec with *MAT_EROSION card. Also it should be noted that the mass of the BG rods was added to the BG masses by increasing their thickness.

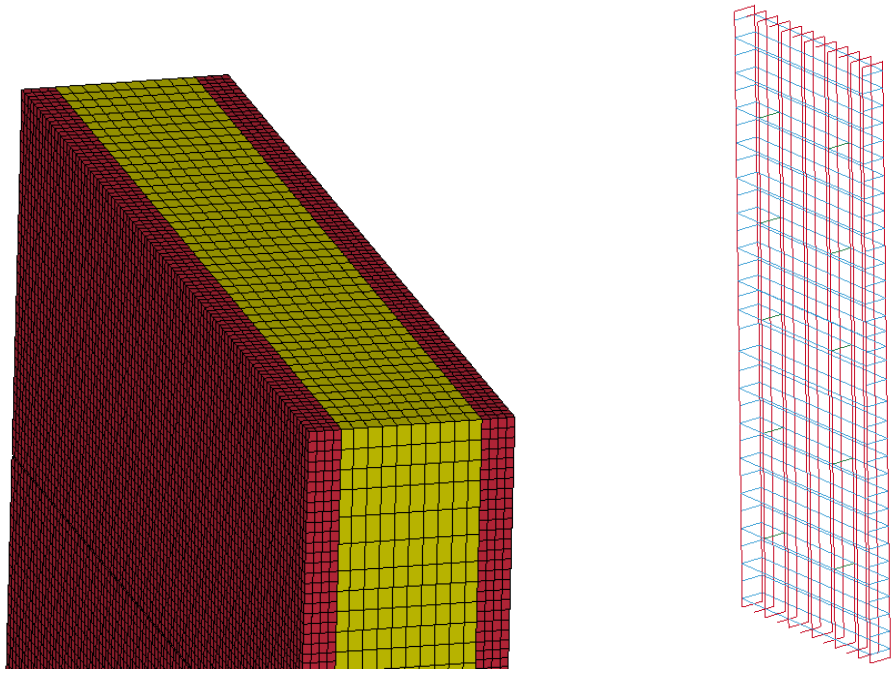

Figure 5.70: Series I mesh

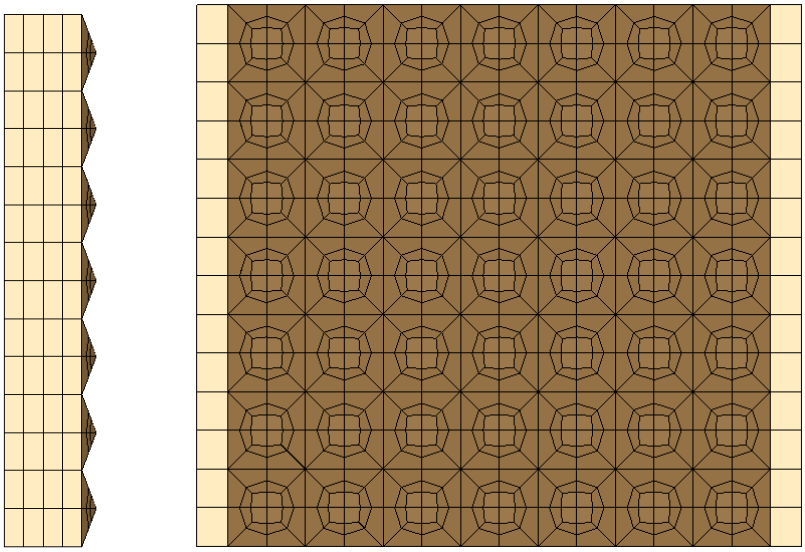

Figure 5.71: Programmer mesh

The FE model for the second test series was similar to that described above for the first. In these models the load from the BGs was also transferred to the specimen with the *AUTOMATIC_SURFACE_TO_SURFACE contact. The BG masses, programmers, concrete, frangible panels, top slab and bottom footing were modeled using eight node brick elements with single point integration. The Hughes-Liu beam element formulation with cross-sectional integration was also used to model the reinforcing steel. An example of the FE model used to simulate a test on a 12 in. thick wall with panels is displayed in Figure 5.72. The reinforced concrete models are similar to the model, except that they do not have the panels on front and back.

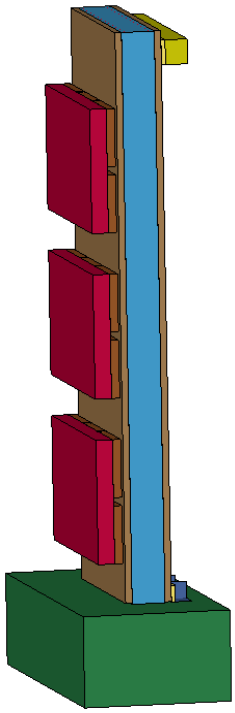

Figure 5.72: FE model for Series II blast simulator tests

The top and bottom boundary conditions are displayed in Figure 5.73. At the top the only support is the concrete slab. In the experiments Hydrostone was used in between the walls and the RC slab to provide an even impact surface at the support. It can be seen that the Hydrostone was included in the model with a layer of solid elements. The Hydrostone is also included at the bottom between the wall and a steel angle. This angle was not present in Tests 1 and 2, but was there for all subsequent tests. It was modeled with shell elements. The base RC footing of the test specimen was also modeled with solid elements. The wall elements were not merged to this footing, but instead used an *AUTOMATIC_SURFACE_TO_SURFACE contact with friction. The static and dynamic friction coefficients were both set to 0.3. The elements were not merged because it was observed in the experiments that a large crack would open at the joint for

all of the specimens. Therefore, the contact surface was added to replicate this behavior. An additional detail to produce this behavior was to debond the rebar at the very bottom of the wall. If this was not done the beams at the nodes coincident with the footing nodes would be merged and the joint strength at the interface would be too large.

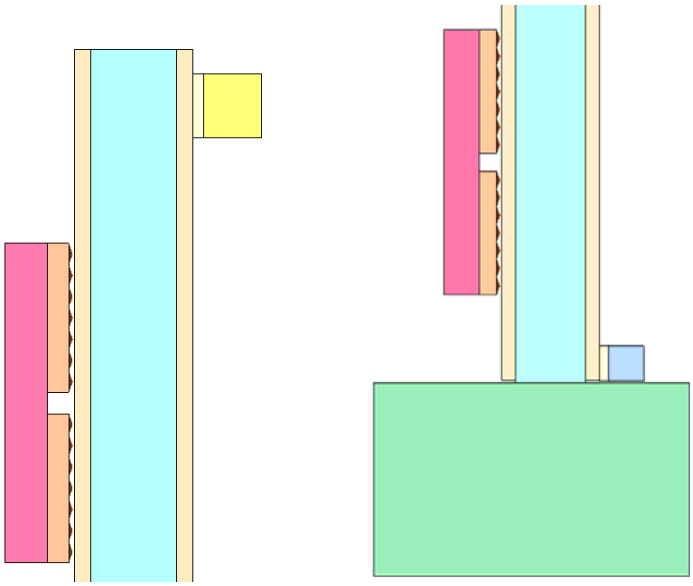

Figure 5.73: FE model for Series II blast simulator tests

The mesh details for the wall and the rebar layout are displayed in Figure 5.74. The frangible panels had four elements through the thickness, while the RC core had at least 10 elements through the thickness. The beams used for the reinforcing steel were in both longitudinal and transverse directions. The nodes of the beams were merged to those of the concrete elements representing a perfect bond between the two.

Only three BGs were used in the simulation of the Series II tests. It was still important to model the pyramids explicitly for this analysis, so the programmer mesh is the same as displayed in Figure 5.71. Also similar to the analysis of the other series, the

BG masses and programmers are deleted after 20 msec and the mass of the BG piston rod is accounted for with additional thickness in the mass plates.

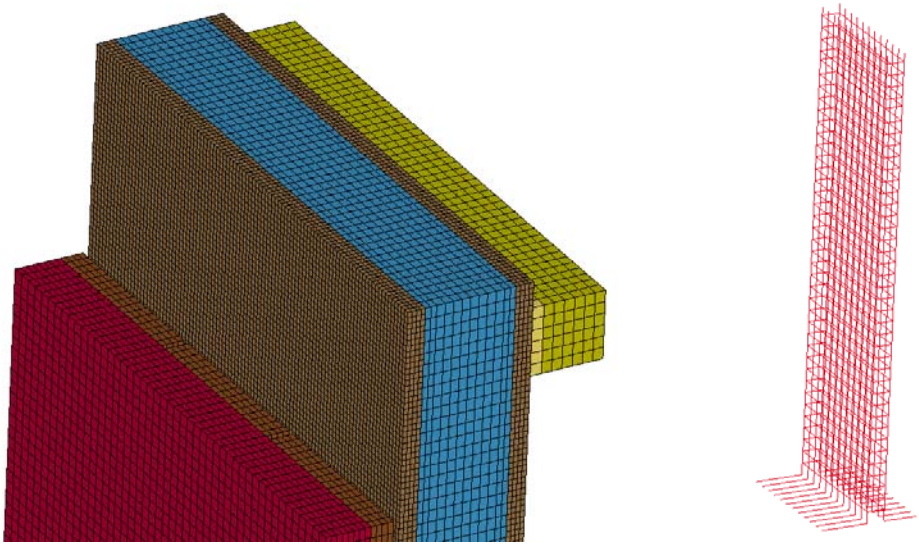

Figure 5.74: FE model for Series II blast simulator tests

5.6.2 MATERIAL MODELS

The concrete in the wall and the reaction structures was modeled with the K&C Concrete Model, *MAT_072 Release 3 [24]. The input parameters for this model are the density and uniaxial compressive strength of the concrete. The remaining parameters of the model, except for the strain rate effects, are determined from these two values. For the simulation of the Series I tests the concrete strength was set to 8000 psi and a density equal to 145 lb/ft^2 was used. In Series II the concrete strength was set to 5000 psi and the density was also equal to 145 lb/ft^2. The factors to account for strain rate effects were inputted into the model using a curve definition with strain rates ranging from -30x10^4 to

$30x10^4$. The increase factor at each strain rate was determined with the equations in Chapter 4.

The material model used for the reinforcing steel was *MAT_PIECEWISE_-LINEAR_PLASTICITY or *MAT_24 [24]. The strength properties used in the model steel are equal to those used for the moment-curvature analysis described in Section 5.5 of this chapter. This material model also accounts for strain rate effects by scaling the yield and ultimate strength of the steel. The strain rate relations are entered into the model with tables using the relations between strength and strain rate given in Chapter 2.

The frangible panels were modeled with *MAT_CRUSHABLE_FOAM or *MAT_63. The parameters inputted into this mode are density, modulus, Poisson's ratio, tensile cutoff, a damping coefficient, and finally a load curve relating yield stress to volumetric strain. The parameters used in that analysis were chosen to best match the data that was recorded and plotted in Figure 5.55. A comparison of the FE model and the material test data is shown in Figure 5.75. The FE analysis on the material was taken to a larger strain than in the actual test before the material was unloaded until zeros strain was reached. The results of the FE analysis show that the predicted material behavior matches the measured behavior of the frangible panels. The results also show the tensile cutoff for the frangible panels. The material behaves plastically when the tensile force in the frangible panel element reaches the cutoff value.

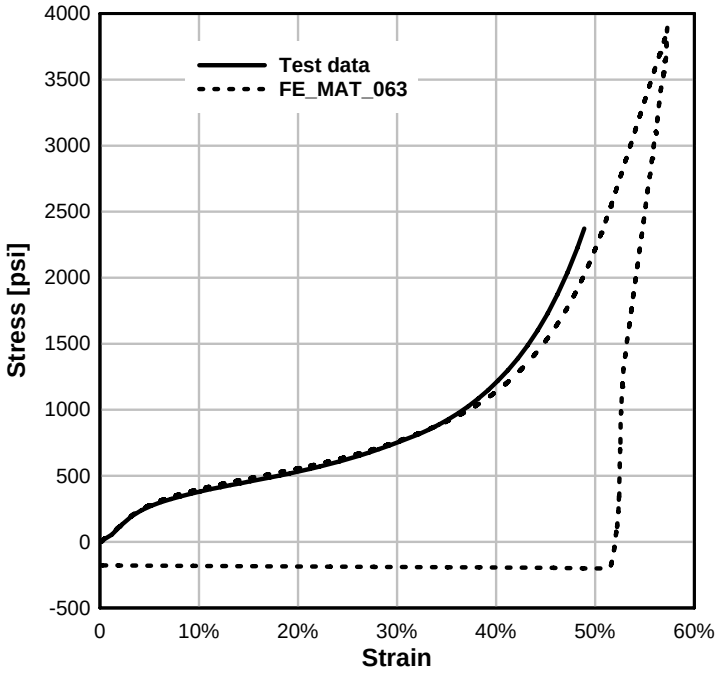

Figure 5.75: Frangible panel material test data versus FE simulation

The model for the programmer in the simulator of the frangible panel tests was similar to the FE analysis in Chapter 4; the programmer material was modeled with *MAT_LOW_DENSITY_FOAM or MAT_57 [24]. A stress-strain curve was input into the model as a load curve. The stress-strain curve used in the model is a modified curve taken from quasi-static tests on a column programmer described in Rodriquez [33]. The wall programmer is made from slightly stiffer material and a factor of 1.7 was applied to the ordinate of the curve to account for it. The parameters *SHAPE* and *HU* were set at 300 and 0.1 respectively for Test Series I. In Test Series II the parameters *SHAPE* and *HU* were set at 20 and 0.1, respectively. These parameters describe the unloading behavior of the material and thus control the energy dissipation during the impact. The values were chosen so that the impulse transferred to the specimen in the simulation was similar to the actual experiment for all the tests.

No data was available for the neoprene pads or the Hydrostone used at the support conditions. It was assumed in the model that both of these materials would have foam like properties under the observed loading conditions; thus they were both simulated using the same material model used for the frangible panels.

The aluminum used for the BG plates and the steel fixtures (i.e. steel angles, bent steel plates) were modeled with *MAT_ELASTIC or *MAT_1. The parameters for this model are the density, modulus of elasticity and Poisson's ratio; which for aluminum are 161 lb/ft3, $10x10^3$ ksi, and 0.33, respectively; for steel they are 484 lb/ft3, $29x10^3$ ksi, and 0.30.

5.6.3 COMPARISON OF FE MODEL AND EXPERIMENTAL RESULTS

Finite element simulations of the 25 blast simulator tests conducted in the two tests series were run with the model described in the previous sections. A comparison of the results from the FE analysis with the experimental data is given in Table 5.26. The table lists the series number, test number, BG velocity used in the analysis, experimental impulse, experimental peak midspan displacement, calculated impulse from the FE analysis, and calculated peak midspan displacement from the FE analysis. The BG velocity listed is the average of the four or three BGs used to impact the specimen; in the simulation each BG was given a different velocity equal to the velocity measured in the tests. Included in the table are measures of the percent error between the experiment and the FE analysis. The error in the prediction of the impulse was relatively small with the largest equal to 7.8% from Test 7 in the second test series. The largest error for the displacements was nearly 43% for Test 3 in Series I. This difference is significant;

however, it appears to be an outlier when the rest of the data is considered. The next largest error is 19.9% for Test 9 in Series I. It should be also noted that in the second test series several walls were tested more than one time. In the analysis simulating a second hit on a wall the model did not account for damage that occurred in the first test. As a result, the analysis under predicted the response of the wall for the re-tests. This can be seen for Tests 3b, 4b, 5b and 6b. Despite the omission of damage in the model before the second impact the predicted results still was fairly accurate compared to the experiment.

Table 5.26: Comparison of FE Analysis on Walls with Frangible Panels to Experimental Results

Series -Test	Specimen	BG Velocity [in/sec]	Exp Impulse [psi-msec]	Exp Disp. [in]	FE Impulse [psi-msec]	Impulse Error	FE Disp. [in]	Disp Error
I-1	RC-D-20	340	312	7.6	316	1.0%	8.1	6.6%
I-2	FP-D-25	398	338	14.3	355	5.1%	12.0	16.1%
I-3	FP-D-30	535	505	9.8	500	1.1%	14.0	42.9%
I-4	RC-D-25	406	425	8.5	404	5.8%	8.3	1.9%
I-5	FP-D-20	413	347	collapse	334	3.7%	20.4	NA
I-6	RC-D-30	575	684	7.9	603	5.2%	8.8	11.5%
I-7	FP-D-30-2	645	569	11.4	606	6.5%	collapse	NA
I-8	FP-D-25-2	469	409	15.3	412	0.9%	15.6	2.0%
I-9	FP-S-20	389	329	21.9	313	5.0%	17.7	19.2%
II-1	RC-12-1	899	867	collapse	814	6.1%	10.5	NA
II-2	FP-12-1	906	746	collapse	728	2.5%	6.2	NA
II-3a	RC-12-2	254	231	0.9	231	0.1%	0.8	10.1%
II-3b	RC-12-2	484	445	3.2	437	1.7%	2.6	17.5%
II-4a	FP-12-2	266	225	0.8	233	3.6%	0.8	2.6%
II-4b	FP-12-2	484	401	2.3	402	0.2%	2.0	13.8%
II-5a	RC-8-1	180	148	1.0	146	1.5%	0.9	8.0%
II-5b	RC-8-1	352	303	3.3	286	5.7%	2.9	10.9%
II-6a	FP-8-1	187	152	0.9	152	0.4%	0.9	1.1%
II-6b	FP-8-1	358	278	2.7	283	1.7%	2.5	6.3%
II-7	RC-8-2	452	373	4.5	356	7.8%	4.4	1.8%
II-8	FP-8-2	450	352	3.3	346	1.8%	3.7	12.2%
II-9	FP-8-3	467	361	3.8	357	1.0%	3.9	3.5%
II-10	RC-8-3	457	386	4.7	363	6.0%	4.5	4.1%
II-11	RC-12-3	491	437	3.0	443	1.5%	2.8	8.9%
II-12	FP-12-3	512	426	1.9	412	3.2%	2.1	11.1%

The correlation between the FE model and the experimental results can be visualized in Figure 5.76 and Figure 5.77 which plot the predicted impulse versus the measured impulse and the predicted midspan displacement versus the measured displacement. A 45º degree line is also plotted in each figure, which represents a perfect correlation between the predicted and measured data. Also included in each plot is a line fit to the data by linear regression.

The comparison of the impulse shows that there is very good correlation between the FE analysis and the experimental results over a range of 150 psi-msec to nearly 850 psi-msec. The data is also very close to the 45º degree line which means that the error between the model and the experiment is small (also shown in Table 5.26). Therefore, the model is capable of accurately loading the specimen when the BG impact velocity is used as the input.

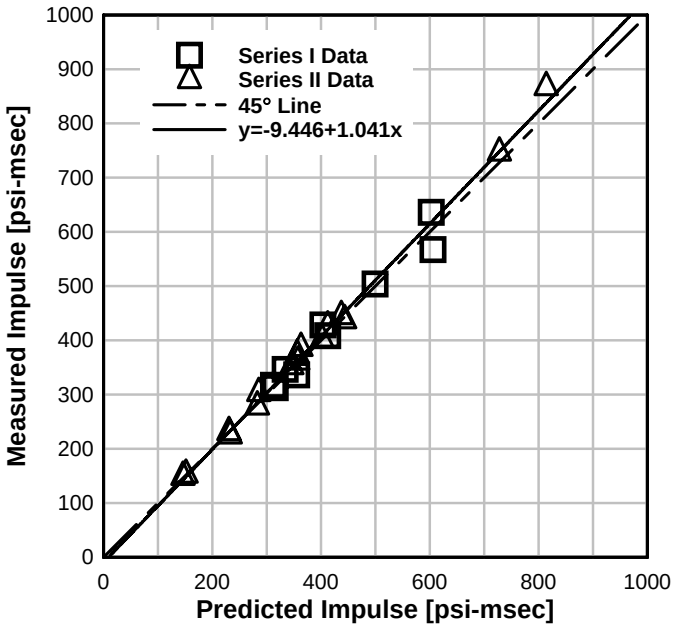

Figure 5.76: Comparison of FE and experimental impulses for frangible panel tests

A comparison of peak midspan displacements for the FE analysis and experiments is shown in Figure 5.77. The plot shows that there is a strong correlation between the predicted and measured displacements especially for displacements smaller than 10 inches. As the peak midspan displacement exceeds 10 in. the correlation is less significant and the error between the two becomes significantly greater. The increase in the error is reasonable considering the high degree of nonlinearity of the wall at these displacements. The inaccurate predictions of the FE analysis at this level of are also may not be important because, according to the UFC design manuals [57] for structural members controlled by flexure, a wall with a rotation greater that 6º will not meet the criteria for low level of protection and a wall with a rotation greater than 4º will not meet the medium to high level of protection. For the walls studied here, with spans equal to about 130 in., these rotations correspond to peak midspan displacements equal to 6.8 and 4.5 inches.

The data associated with the large displacement are all from the first test series. In the second test series the displacements were all under 6 in. of displacement except for Tests 1 and 2 where the specimen collapsed. In hind site it would have been better to include tests on theses walls at lower velocities to generate data over a large range of response.

It should be noted that the plot does not include the data from Tests 5 and 7 from Series I and Tests 1 and 2 from Series II because the wall failed in the experiment or the FE analysis; thus leaving no quantity to plot. In Test 5-Series I the wall collapsed in the experiment and the FE analysis predicted 20.4 inches of displacement which is a very

large displacement signifying that the wall is near a collapse. In Test 7-Series I the wall collapsed in the FE analysis and had a displacement equal to 11.4 in. in the experiment which would have been considered a failure in a design situation. Tests 1 and 2 of the second tests series both resulted in collapse. In the FE analysis Test 1 had 10 in. of displacement which would have been classified as a failure in a design scenario. Test 6 only had a peak displacement of 6 in. and suffered a shear type of failure. The displacement is low and the failure mode is incorrect, but the model did predict a failure that would prevent an engineer from proceeding with this wall as an acceptable design. This behavior of the model needs to be considered when using it to predict the response of these wall types. Overall, these three of the four sets of data from the comparison of displacements between FE analysis and the experimental results qualitatively affirm that the FE model is capable of predicting the response of these wall types in design situations.

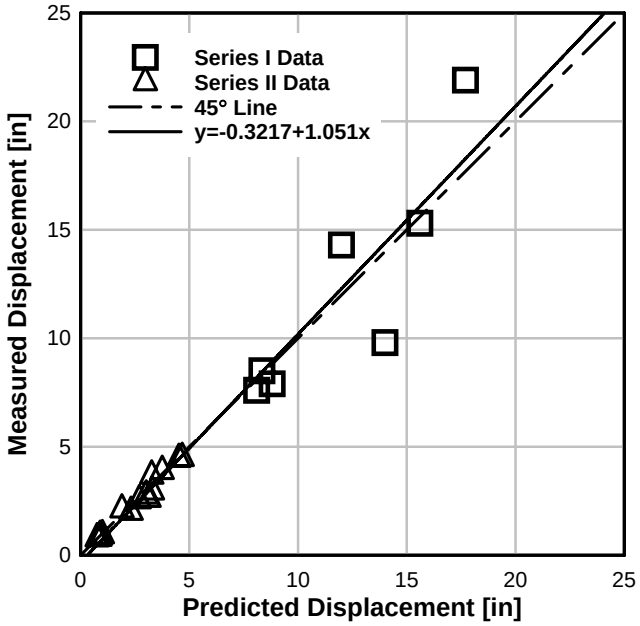

Figure 5.77: Comparison of FE and experimental displacements for frangible panel tests

The results from individual blast simulator tests in the first frangible panel series are compared to the FE simulations in Figure 5.76 through Figure 5.86, which plot midspan displacement time histories and displaced shapes for Test 1, Test 8, and Test 2, respectively. The displacement time history for Test 1 (Figure 5.76) and the plot of displaced shape (Figure 5.77) demonstrates that the FE model is capable of predicting the displacement response and matches the deformation mode of a RC wall. Both the predicted and measured responses show that the wall has an initial elastic displaced shape followed by a plastic shape with significant deformation near the midspan. The ability of the FE model to capture damage in the specimen is demonstrated with Figure 5.80 which displays the model with colored fringes that are associated with the damage state of the concrete. The scale of damage in the figure is from one to two where one is associated

with the maximum failure surface of the concrete and two corresponds to the residual failure surface. The model shown in the figure has damage that is spaced with a similar distribution as the cracking on the tension side of the wall.

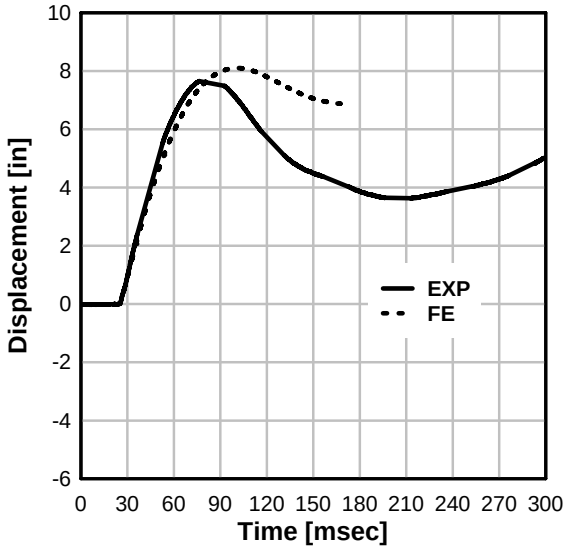

Figure 5.78: Comparison of displacement time history for Series I Test 1

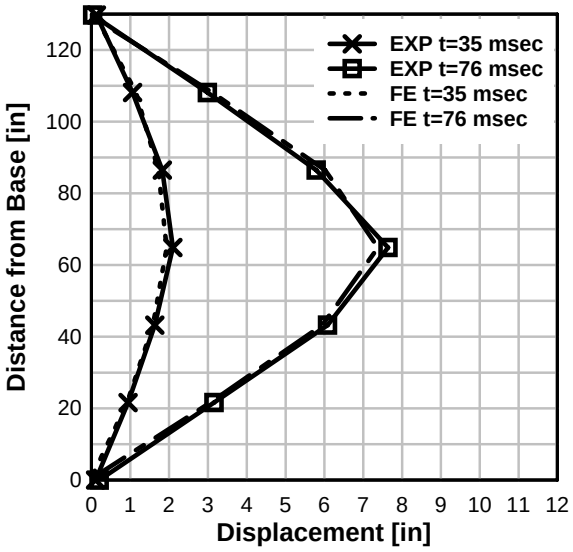

Figure 5.79: Comparison of displaced shape for Series I Test 1

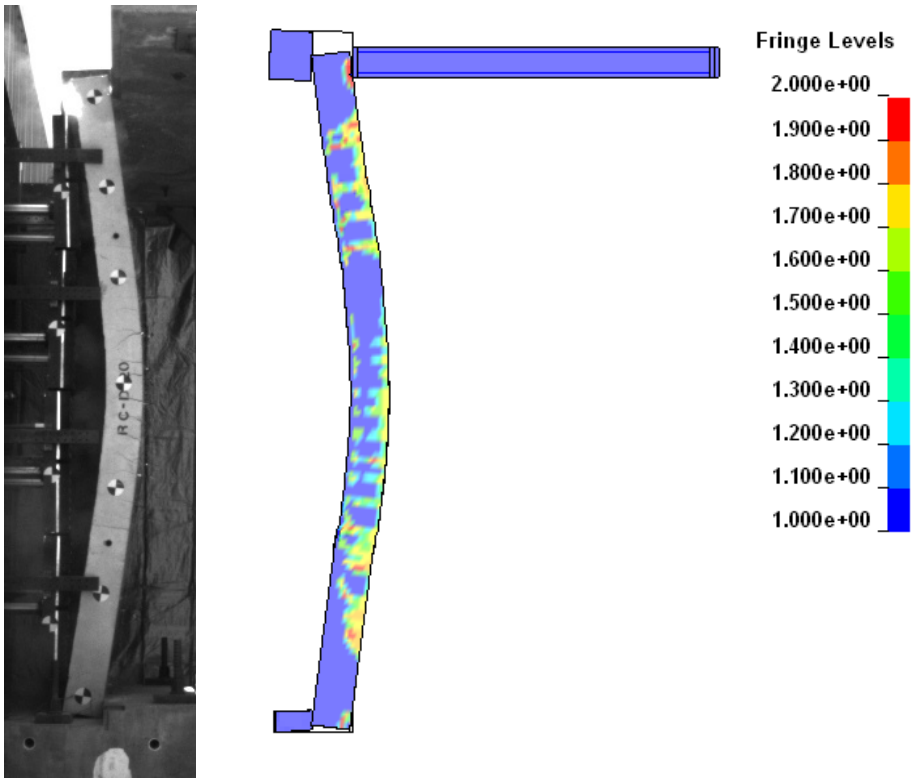

Figure 5.80: Comparison of Damage for Series I Test 1

Comparisons of the FE model and the experimental result for a wall with frangible panels are plotted in Figure 5.81, Figure 5.82, and Figure 5.83. The plot displays a comparison of midspan displacements demonstrating that the FE simulation matches the results of the experiments. The plot of the displaced shapes illustrates that the FE and experimental results are similar. This plot also shows that the wall has an initial elastic displaced shape and then at higher displacements has a plastic shape. The damage fringes for the FE simulation, shown in Figure 5.83, demonstrate that the FE model adequately predicts the level of damage in the wall with the frangible panels. Figure 5.84 further demonstrated the ability of the FE model to simulate the damage in the wall with frangible panels by showing that the model predicts the indentation caused by the programmer pyramids.

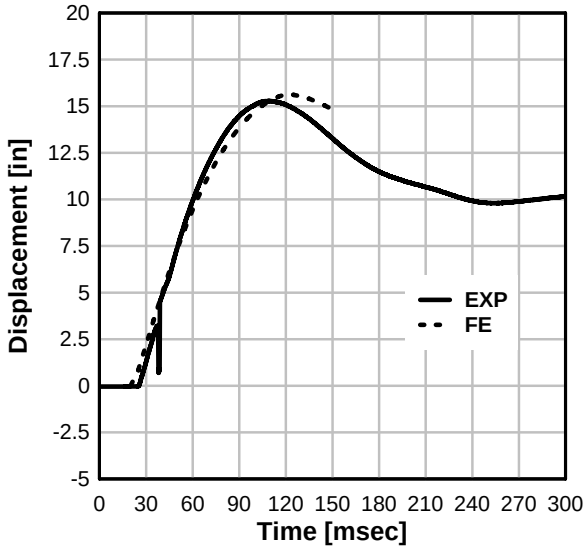

Figure 5.81: Comparison of displacement time history for Series I Test 8

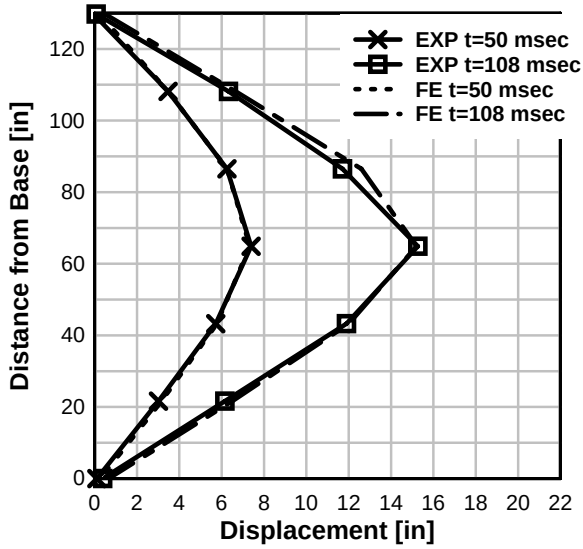

Figure 5.82: Comparison of displaced shape for Series I Test 8

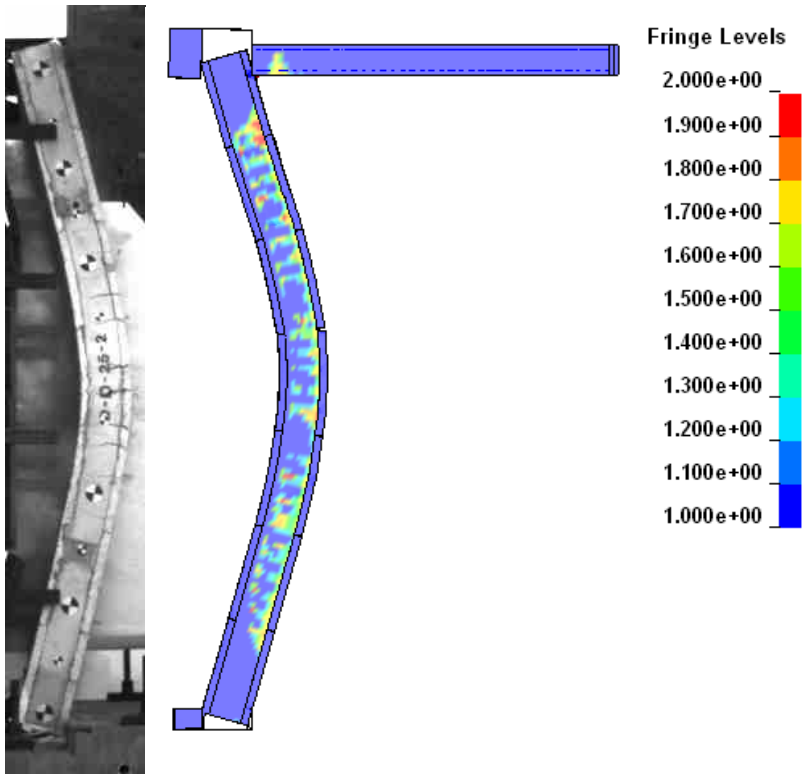

Figure 5.83: Comparison of damaged state for Series I Test 8

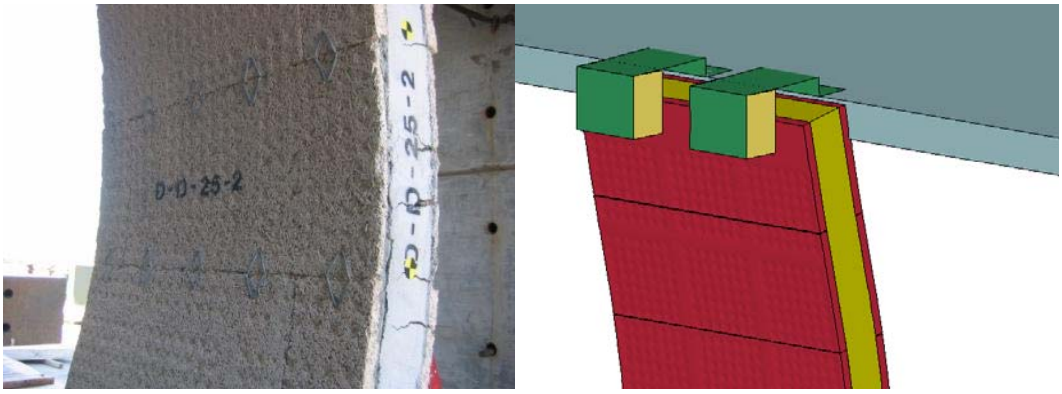

Figure 5.84: Comparison of damaged in front panels for Series I Test 8

Additional plots comparing the results from Series I Test 1 FE analysis and experiment are displayed in Figure 5.86, Figure 5.87, and Figure 5.88. Figure 5.86 shows that the model has the same initial velocity as the experiment, but under-predicts the peak displacement. It can also be observed that the time it takes to teach the peak

displacement is nearly double for the experiment. This is because when the wall in the experiment reaches the larger displacements it accumulates more damage and it softens. The lack of accuracy in the model for this test is not significant because the model still predicts a displacement equal to 12 in. of displacement which causes a support rotation equal to 10.7º. According to [20] this support rotation would not meet the low level of protection deformation criteria. Therefore, the model is able to predict the failure of the wall. Furthermore, Figure 5.87 shows that the model adequately matches displaced shapes in the elastic and plastic range and Figure 5.88 demonstrates that the model does a adequately predicts the level of damage in the wall.

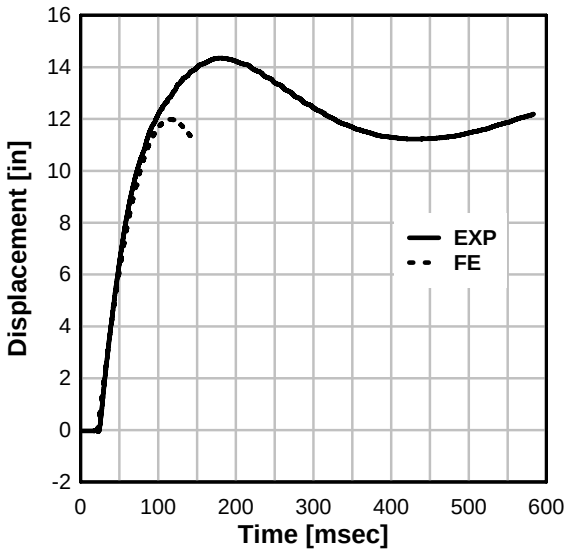

Figure 5.85: Comparison of displacement time history for Series I Test 2

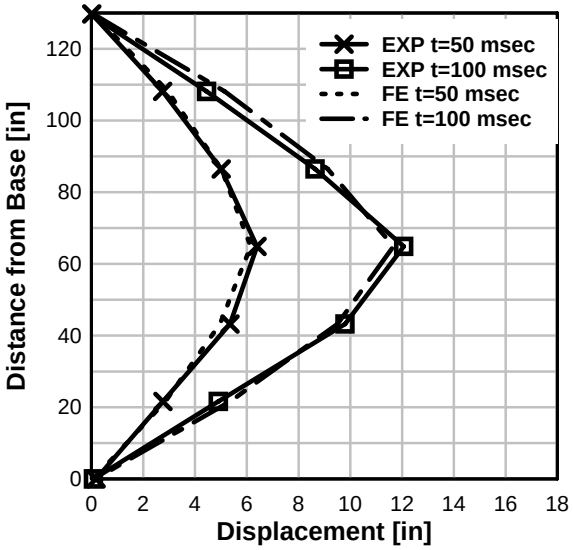

Figure 5.86: Comparison of displaced shape for Series I Test 2

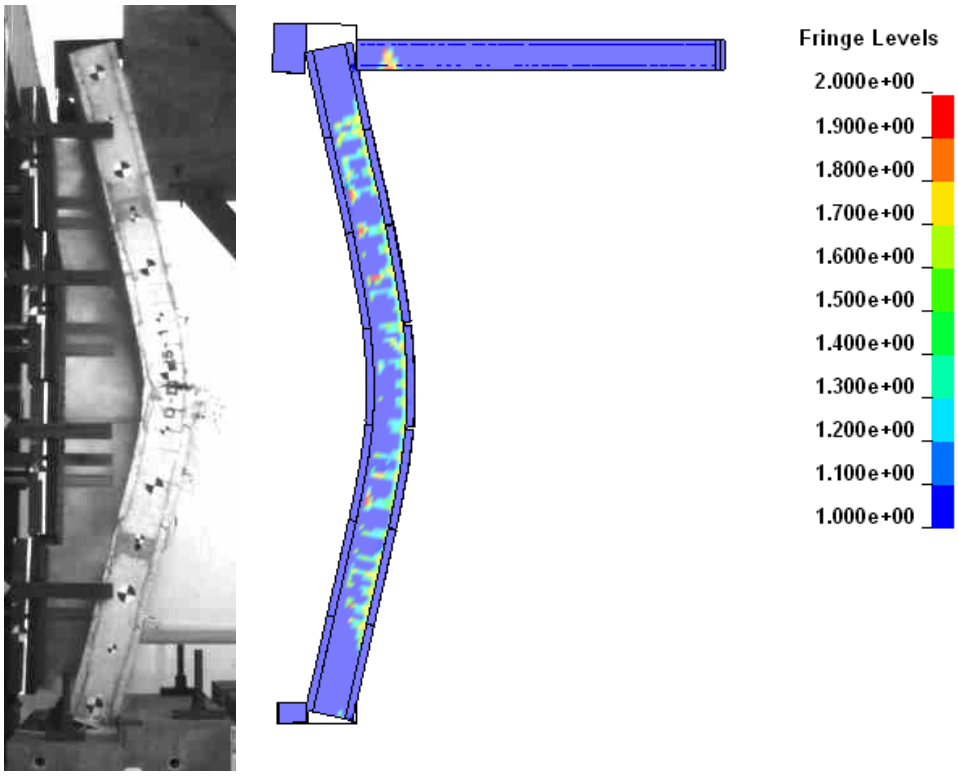

Figure 5.87: Comparison of displaced shape for Series I Test 2

Comparisons for Test 7 of the second series are shown in Figure 5.88, Figure 5.89, and Figure 5.90. Figure 5.88 displays a time history plot which shows that the midspan displacement predicted by the FE analysis matches the experimental results for a RC wall without frangible panels. The displaced shapes predict by the FE model and the measured in the experiment are shown in Figure 5.89. This plot shows that the model matches the experiment in both the elastic and plastic ranges of behavior. Finally, Figure 5.90 displays the damaged state of the wall at the time of peak displacement which demonstrates that the model captures and possibly over-predicts the level of damage and the distribution of cracking.

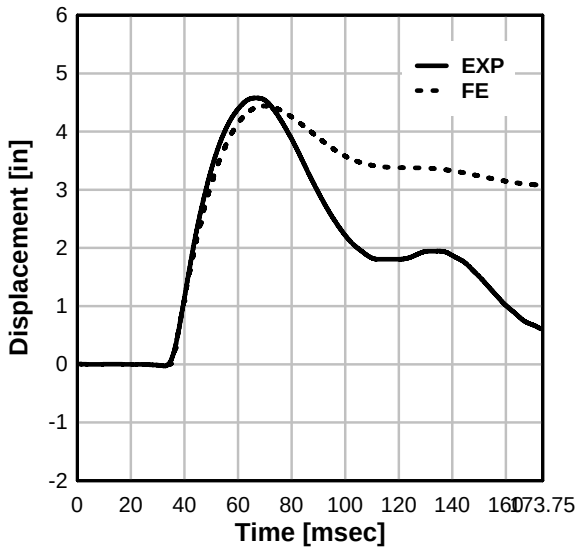

Figure 5.88: Comparison of displacement time history for Series II Test 7

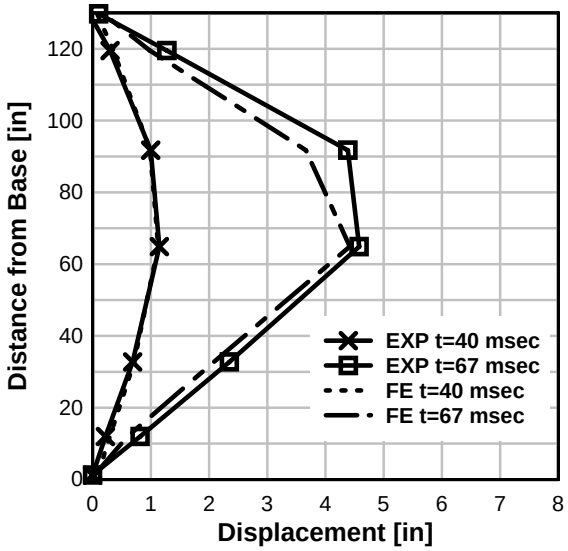

Figure 5.89: Comparison of displaced shape for Series II Test 7

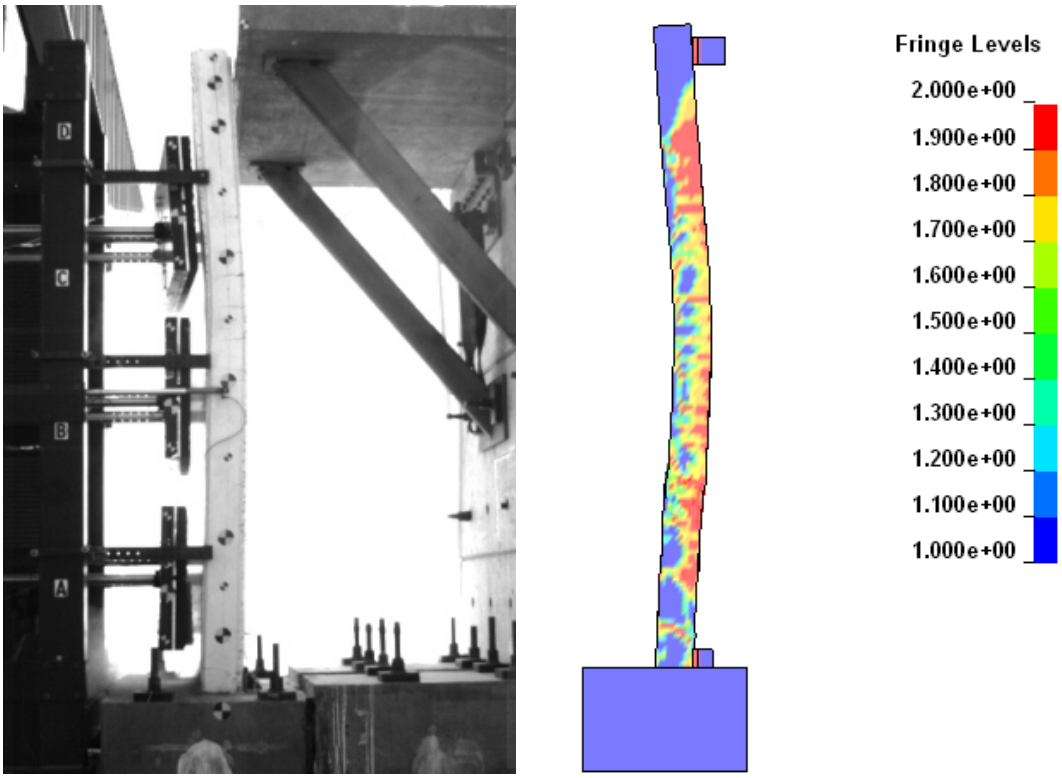

Figure 5.90: Comparison of damaged state for Series II Test7

Comparisons for Test 12 of the second series are shown in Figure 5.91, Figure 5.92, and Figure 5.93. The time history plot displayed in Figure 5.91 demonstrates that the midspan displacement predicted by the FE analysis matches the experimental results for a RC wall with frangible panels. The displaced shapes in the elastic region and plastic region of behavior are shown in Figure 5.92. This plot shows that the FE model has similar displaced shapes as the experiment in both regions. Figure 5.93 displays the damaged state of the wall at the time of peak displacement for the experiment and the FE analysis. This figure shows that the model captures the damage observed in the experiments which was in the form of cracking located around the midspan and near the base.

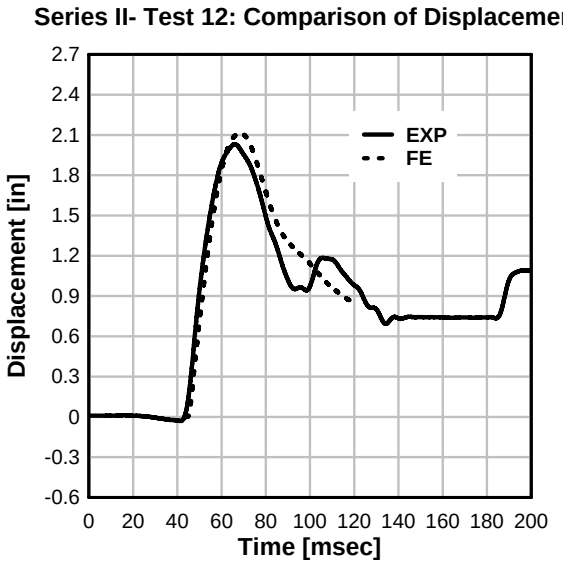

Figure 5.91: Comparison of displacement time history for Series II Test 12

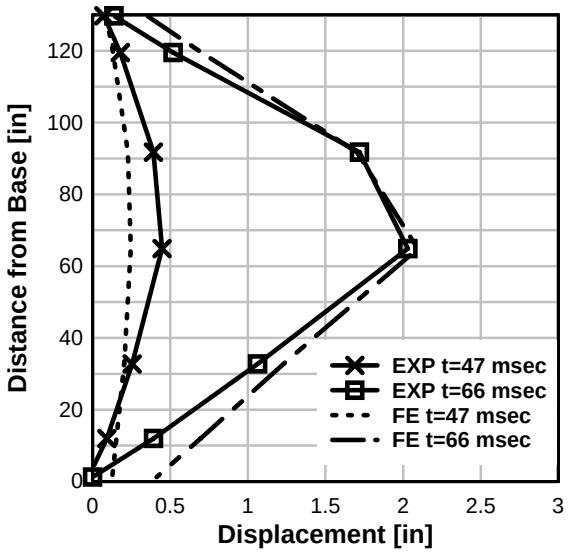

Figure 5.92: Comparison of displaced shape for Series II Test 12

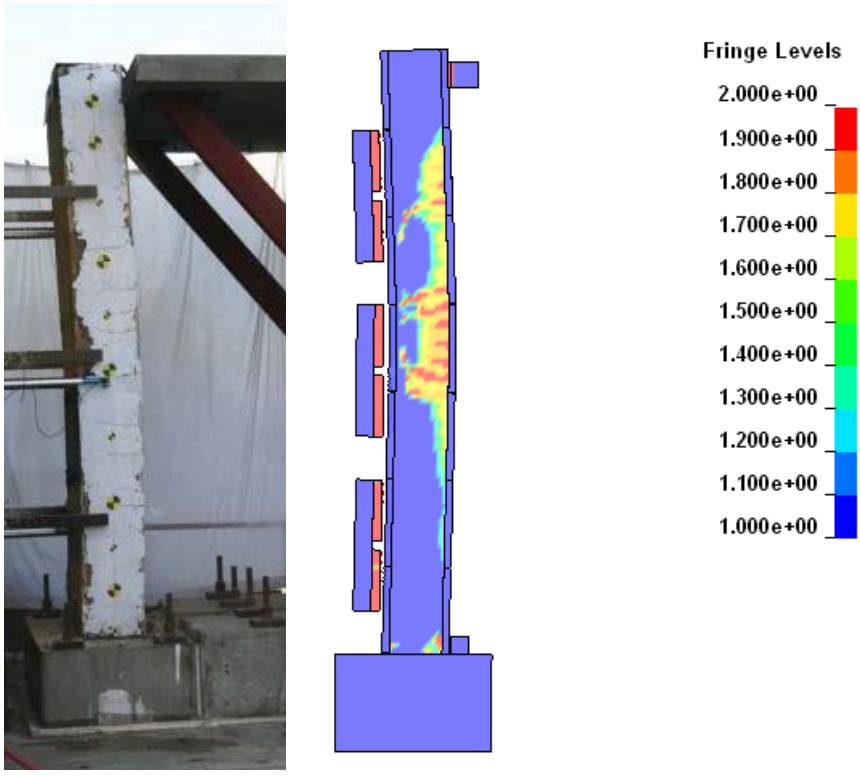

Figure 5.93: Comparison of damaged state for Series II

5.7 COMPARISON OF FPWA AND FE FOR AIRBLAST LOADS

Analyses were performed to compare the predicted response of the frangible panel wall model and the finite element model for the reinforced concrete walls with frangible panels. In this comparative study a 10 in. thick reinforced concrete wall with a 10 ft 9 in. span was subject to air blast loads with the FPWA and the FE model that was validated in a previous section. The details of the reinforcement for the concrete wall are similar to those used in the experimental tests for the specimen labeled RC-D-25. The wall was loaded by a triangular pressure pulse that represents an air blast from an HE detonation. The pressure pulse had an instantaneous rise time and a linear decay back to zero with no negative phase. The parameters of the air blast were determined using methods described in Chapter 2 of this dissertation. The charge used to determine the loads was 200 lbs of TNT and each load listed in the Table 5.27 is associated with a different standoff distance.

Table 5.27: Loads for Comparative Study between FPWA and FE Models

Load	Pressure [psi]	Impulse [psi-msec]	Duration [msec]
1	23	103	9.12
2	63	164	5.19
3	145	232	3.19
4	496	386	1.55

The thickness of the frangible panel on the loaded face of the wall was also varied to three different values: 1.57 in., 3.14 in., and 6.28 in., which correspond to one, two, and four times the thickness of the manufactured panels. Also included in the study was a plain RC wall with no panels on the front or back side. With the different combinations

of load and thickness of the frangible panels a total of 32 analyses were run: 16 with the FE model and 16 with FPWA model.

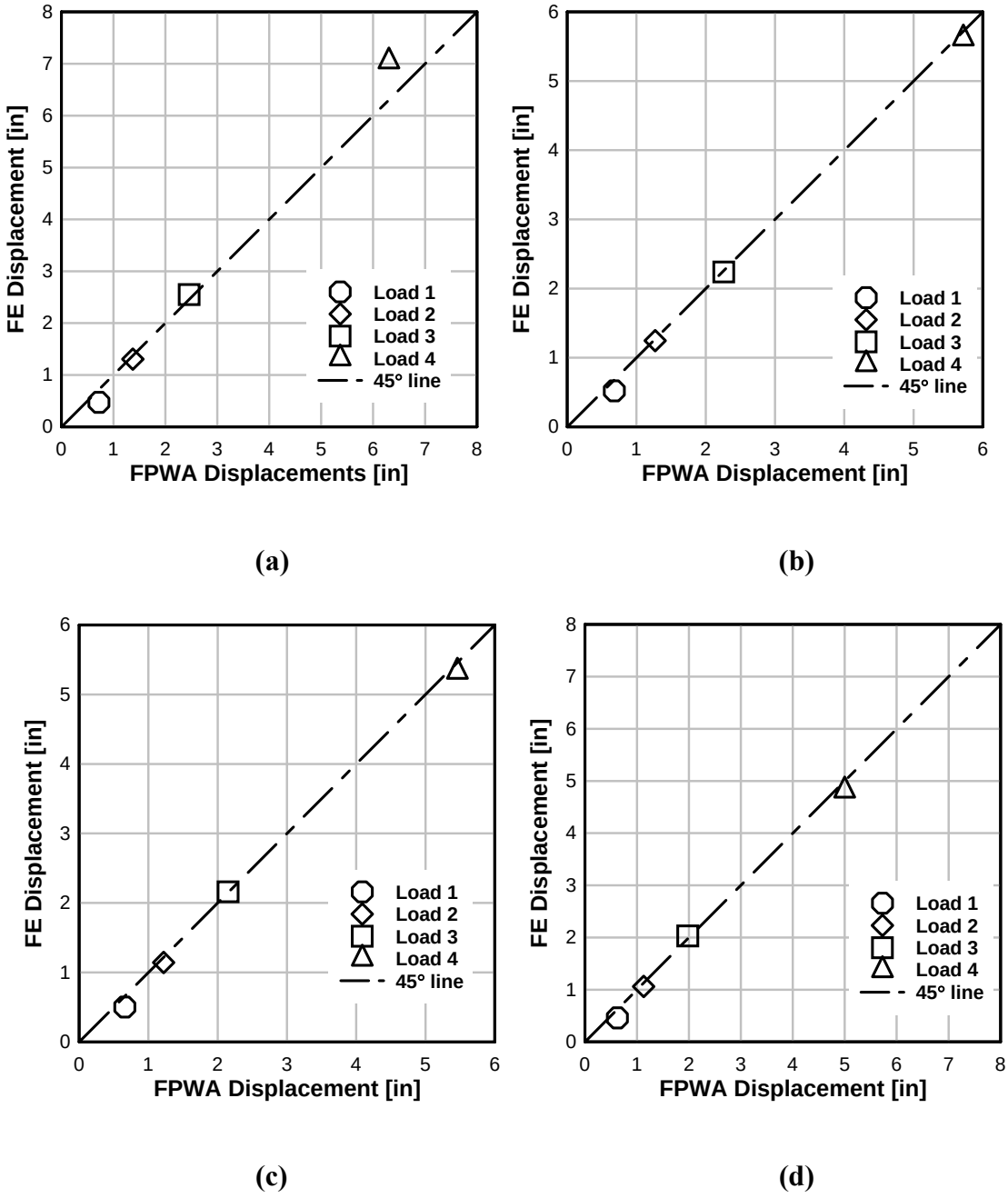

Figure 5.94: Comparison of peak displacement between FPWA and FE models to air blast loads on walls with different thicknesses of frangible panels- (a) plain RC; (b) 1.57 in. thick panels; (c) 3.14 in. thick panels; (d) 6.28 in. thick panels

The results of the study are summarized in Figure 5.94 and Figure 5.95. Figure 5.94 displays the peak midspan displacements predicted by the FPWA model and the FE model for the walls with the different panel thickness. The figure clearly demonstrates that the two models give very similar results for the range of loads used. These range of loads produced displacements that varied from 0.47 to 7.1 inches. Included in each of these plots is a 45º line which represents a perfect fit. The agreement between the peak displacements for the two models is important because displacement is often used as a failure criterion in design.

Comparisons of the load applied to the front face of the RC core after the stress wave has propagated through the frangible panel are plotted in Figure 5.95 for a wall with 1.57 in. thick panels. Similar results were observed for walls with panels that had different thicknesses. The plots show that for the range of loads applied the FPWA model and the FE model give similar peak pressures. Furthermore, for all four scenarios, both models produce load histories that follow a similar trend. The noticeable differences between the models are that the FE model has a lower frequency and attenuates faster.

A final observation made in the comparative study was that both models predicted decreases in peak midspan displacement with increased panel thickness. Figure 5.96 plots panel thickness versus the decrease in displacement relative to the displacement of the wall with no panels. The plot which is for Load 3 shows that as the thickness increases from 1.57 in. to 6.28 in. the displacement decrease increases from 8% to 20%. The effect of the panels on the peak displacement is studied further in the following section.

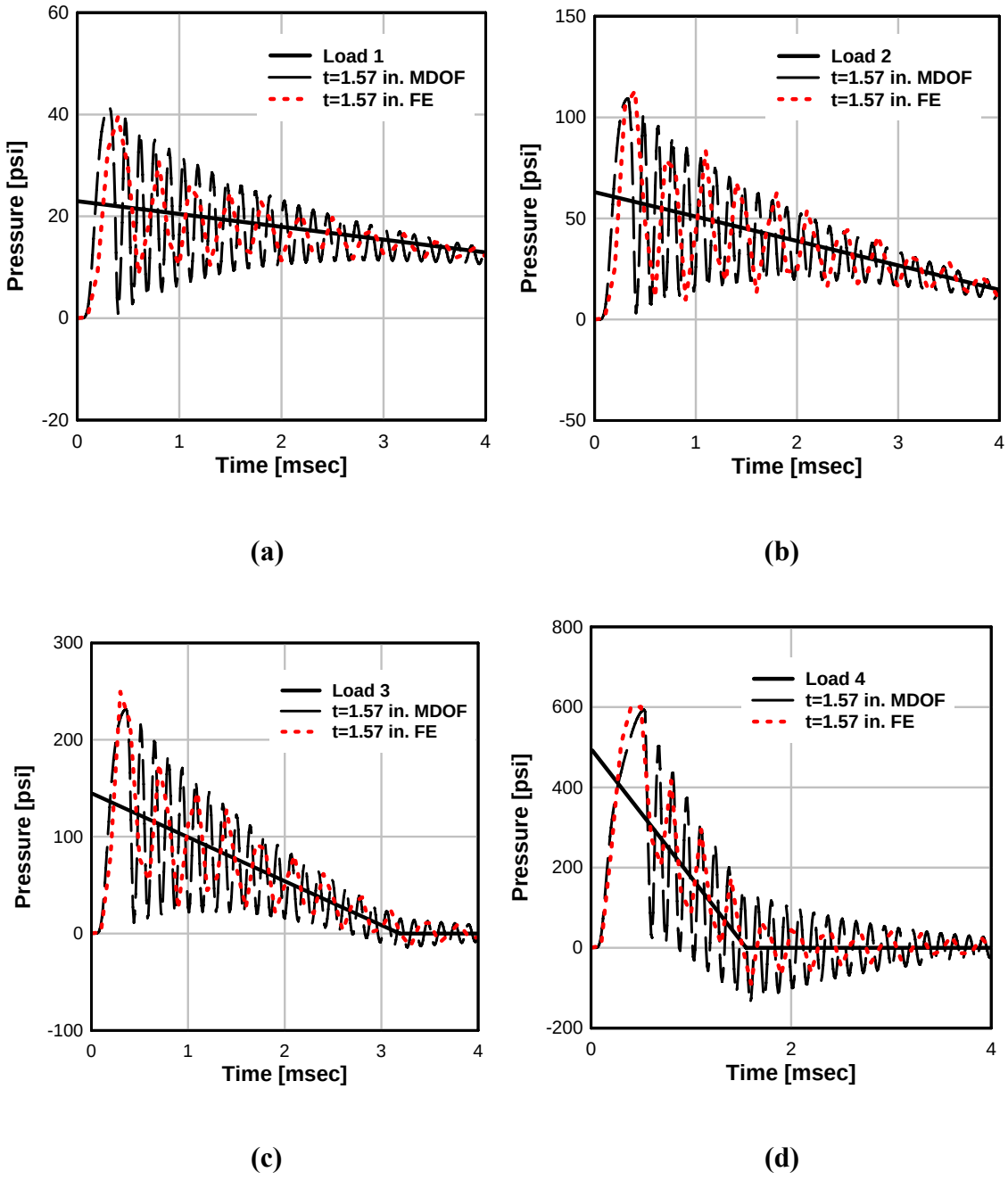

Figure 5.95: Comparison of applied load between FPWA and FE models to air blast loads on walls with 1.57 in. thick frangible panels (a) Load 1; (b) Load 2; (c) Load 3; (d) Load 4

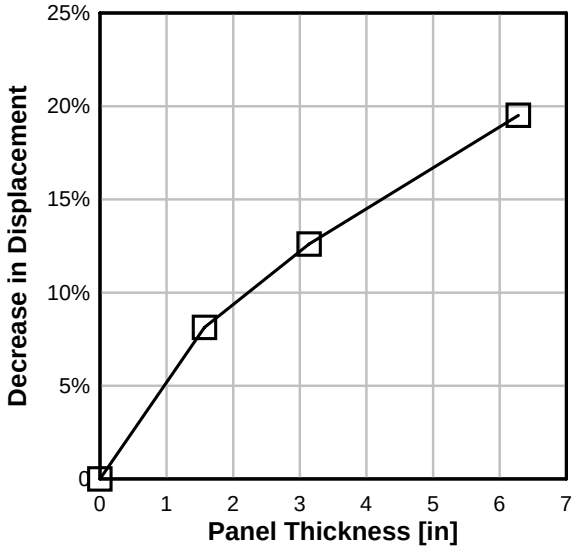

Figure 5.96: Panel thickness versus percent decrease in peak displacement

5.8 FRANGIBLE PANEL PARAMETRIC STUDY

A study was performed to investigate the efficacy of the frangible panels as a blast mitigation strategy for one-way bending of reinforced concrete walls. Analyses were conducted using the FPWA code for one foot wide walls that had variable thickness, reinforcing ratio, frangible panel thickness, and load.

Table 5.28: Frangible Panel Parametric Study Specimens

Thickness [in]	$\rho_{st}= A_s/bd$	A_s [in]	R_u [psi]	Δ_y [in]
6	0.00354	0.21	4.3	1.09
6	0.01255	0.75	13.3	1.28
6	0.02510	1.51	25.2	1.44
10	0.00354	0.38	13.5	0.60
10	0.01255	1.36	44.3	0.69
10	0.02510	1.71	86.0	0.77
14	0.00354	0.55	28.3	0.41
14	0.01255	1.96	94.4	0.47
14	0.02510	3.92	184.3	0.52

The wall thickness was varied between three thicknesses, 6, 10, and 14 in. to determine a relation between mass and panel effectiveness. The thicknesses chosen for the study represent the bound for a realistic reinforced concrete wall design. The walls reinforcement ratio was also varied to three different values equal to the minimum ratio, one-half the maximum ratio, and the maximum ratio which is defined as 0.75 ρ_b where ρ_b is the steel ratio for a balanced condition. A balanced condition is when the steel yields at a strain state that causes the concrete to crush.

Different steel ratios were used to study the relation between the effectiveness of the frangible panels and wall strength. The resistance functions used for the analysis were elastic perfectly-plastic. Table 5.28 lists the different wall thicknesses, reinforcement ratios, ρ_{st}, areas of tension steel, A_s, maximum resistance, R_u, and yield deformation, Δ_y, for the walls analyzed in the study.

Another variable that was included in the parametric study was the thickness of the frangible panel on the front face of the wall. In the experimental portion of this chapter the walls were tested with frangible panels that are 1.57 in. thick. In the parametric study walls the thickness of the panels were varied to equal 1.57, 3.14, and 6.28 inches. This was done to determine if additional thickness would affect the response. In addition to the walls with panels, analyses were also run for reinforced walls with no panels.

Table 5.29: Loads for Frangible Panel Parametric Study

Load	Pressure [psi]	Impulse [psi-msec]	Duration [msec]
1	16	87	10.69
2	23	103	9.12
3	63	164	5.19
4	145	232	3.19
5	496	386	1.55
6	1127	563	0.99
7	2004	764	0.76
8	3065	988	0.64
9	3846	1150	0.60
10	4887	1367	0.56
11	6313	1670	0.52

The final parameter varied in the study was the load which was applied as a pressure with an "instantaneous" rise followed by a linear decay. The peak pressure and the duration of the pulse were varied resulting in a load with several different impulses. The values of pressure and duration were calculated for a 200 lb charge of TNT at several different ranges using methods described in Chapter 2. The parameters for the loads are listed in Table 5.29. Not all of the walls were subject to all of the pressure loads listed in the table: the 6 in. thick walls were analyzed with loads 1 through 5; the 10 in. thick walls were analyzed with loads 1 through 7; and the 14 in. walls were analyzed with loads 1 through 11. The 6 in. and 10 in. thick walls were not subject to all eleven loads because these loads created very large displacements in the specimens which were not realistic.

The results of the parametric study performed with the FPWA wall analysis code are summarized in Figure 5.97 through Figure 5.105. In each figure impulse is plotted versus peak midspan displacement calculated for a wall with panel thicknesses equal to 0,

1.57, 3.14, and 6.28 inches. The nine plots shown are for the nine combinations of wall thickness and reinforcement ratio considered.

The trends displayed in the plots are consistent for all of the tests. The first trend that can be observed is that peak midspan displacement increases strongly with increased impulse. The reason is that, once the response of the specimen is in the plastic range small increases in impulse can produce large differences in peak displacement because the resistance is constant. It can be also observed at each impulse level that the peak midspan displacement decreased with increased panel thickness. The difference between the displacements for the varied panel thicknesses increase with increased impulse. Finally, the displacement demand for the walls at a given impulse decrease with increased reinforcement ratio and increased thickness.

It is understood that the frangible panels add mass to the wall which is a fundamental method used to improve a structures response to an impulsive load. It is unknown, however, if the frangible panels are dissipating energy when loaded, thereby reducing the kinetic energy transferred to the wall. This effect of the frangible panels has been evaluated by plotting a non-dimensional impulse term versus ductility. These non-dimensional terms are used to display all of the results from the analyses with the different masses and resistances on one graph, which can be used to summarize the behavior for all cases.

A non-dimensional plot for all of the analyses performed in the parametric study is shown in Figure 5.106. Additional plots shown in Figure 5.107, Figure 5.108, and Figure 5.109 are also provided to display trends observed for individual wall thicknesses

over a smaller range of impulse. The non-dimensional impulse term, I_{bar}, in these plots was calculated with an equation given below:

$$I_{bar} = i\sqrt{\frac{Lg}{K_{LM}K_r w_{pc} M}} \tag{5.33}$$

Where i is the impulse, L is the length of the span, g is the gravity constant, K_{LM} is a load-mass factor, K_r is a boundary condition term equal to eight for a simple-supported, one-way bending wall, M is the peak moment resisted by the wall, and w_{pc} is the weight wall normalized by the cross-sectional area of the concrete core. The displacement ductility demand, μ, for each analysis was determined by

$$\mu = \frac{\Delta}{\Delta_y} \tag{5.34}$$

The non-dimensional results displayed in Figure 5.106 demonstrate that the relation between the impulse and ductility can be fit by a single equation for all variations that were included in the study. This is especially true for I_{bar} that range from 0 to 0.15. For values of I_{bar} larger than 0.15 the results still follow a trend, but are more scattered. Since the results were normalized with an expression that accounted for wall mass and wall resistance and not frangible panel thickness, it can be concluded that *the panels did not have any additional effect other than adding mass to the wall*. The plots shown in Figure 5.107, Figure 5.108, and Figure 5.109 which focus separately on the walls with 6 in., 10 in., and 14 in. thickness, respectively demonstrate that I_{bar} decreases with increased panel thickness. This trend is highlighted in all three plots by drawing a circle around four points that correspond to walls with the same thickness and reinforcing ratio,

subject to the same input pressure-pulse. The only variable in the set of circled data is the panel thickness. The data circled in Figure 5.107 is for a 6 in. thick wall with a 0.354% reinforcement ratio subject to a load pulse with a peak pressure equal to 63 psi and an impulse equal to 164 psi-msec. In Figure 5.108 the circled data is for a 10 in. thick wall with 2.510% reinforcement ratio subject to a load pulse with a peak pressure equal to 3065 psi and 981 psi-msec. Finally, in Figure 5.109 the walls are 14 in. thick with a 0.354% reinforcement ratio and are subject to a load with a peak pressure equal to 496 psi and 384 psi-msec. All three plots show that an increase in frangible panel thickness decreases the ductility demand, but also decreases the non-dimensional impulse. Furthermore, the trend between I_{bar} and ductility for the cases when the panel thickness is increased generally follows the trend for all of the data that is plotted. Therefore, from the results of the parametric study it can be concluded that the effect of the frangible panels is added mass to the structure.

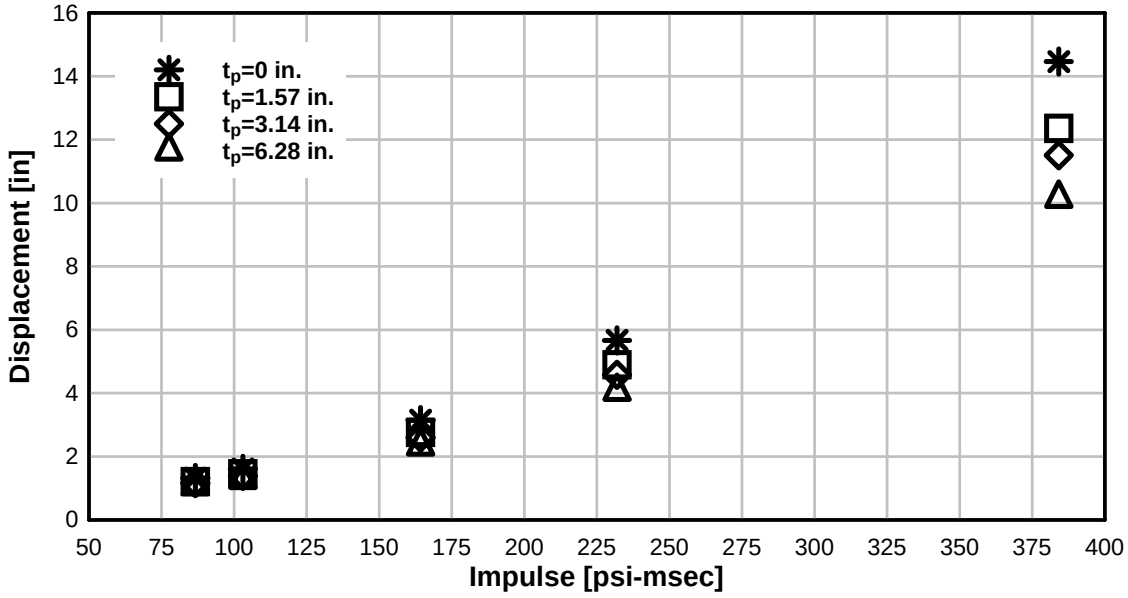

Figure 5.97: Impulse versus displacement for 6 in. thick wall and ρ=0.354%

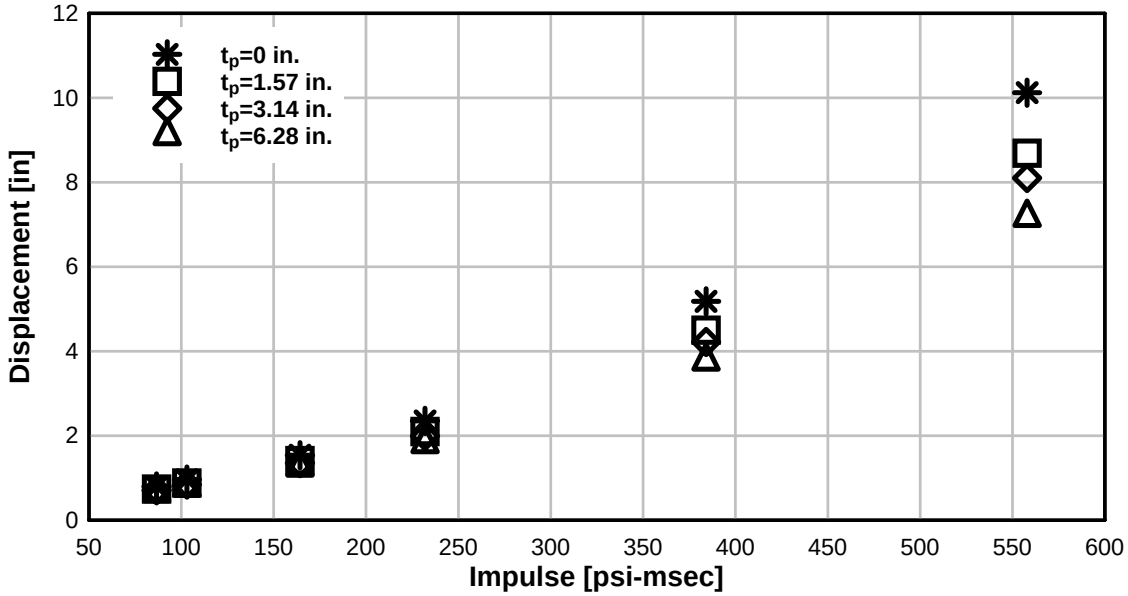

Figure 5.98: Impulse versus displacement for 6 in. thick wall and ρ=1.255%

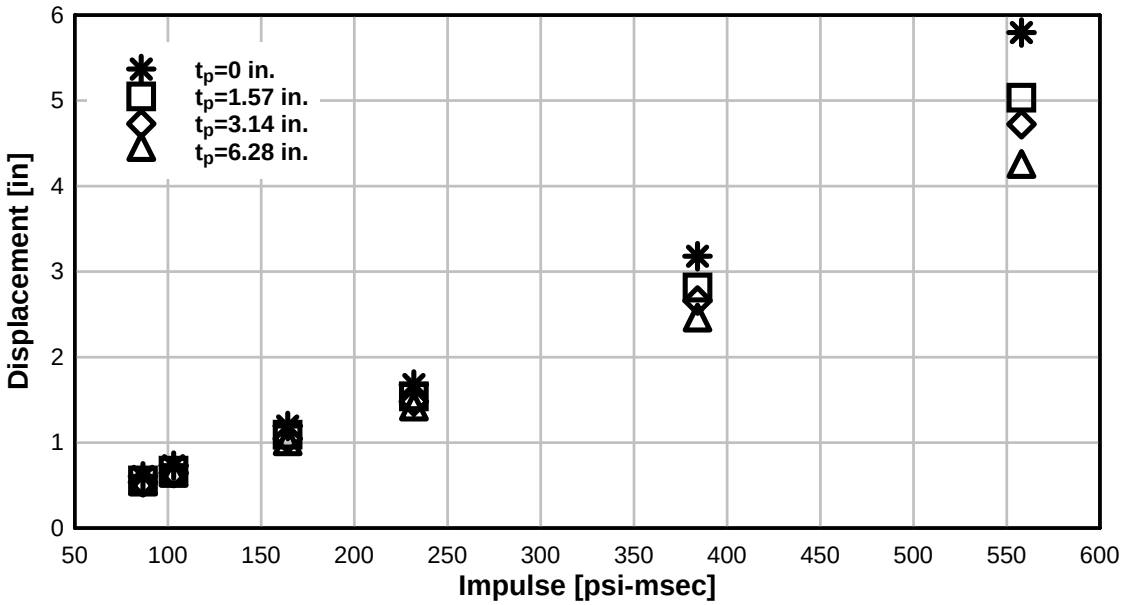

Figure 5.99: Impulse versus displacement for 6 in. thick wall and ρ=2.510%

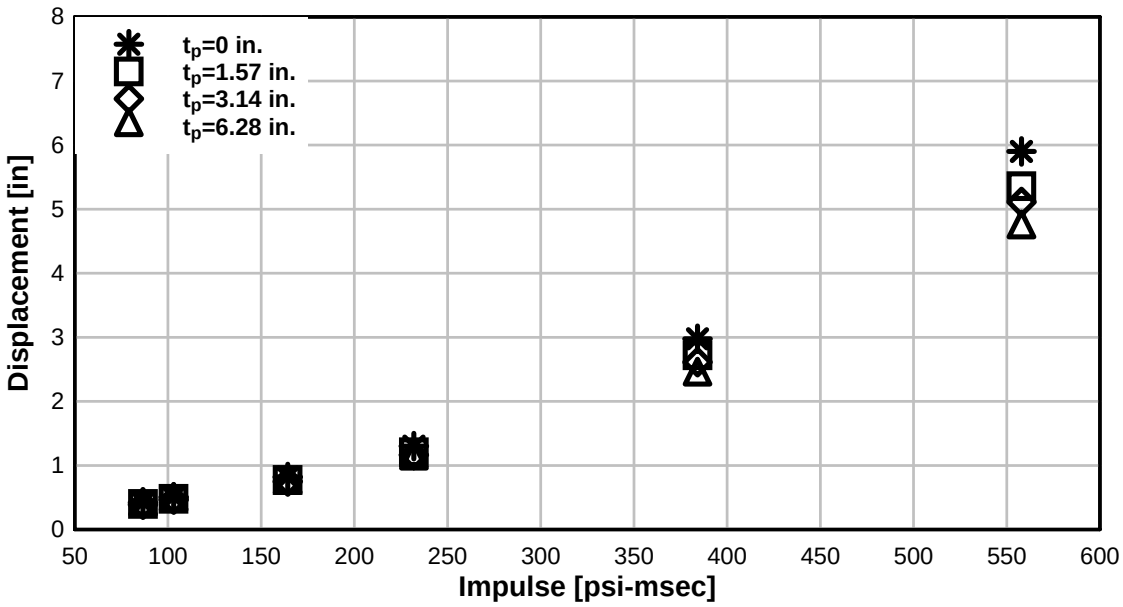

Figure 5.100: Impulse versus displacement for 10 in. thick wall and ρ=0.354%

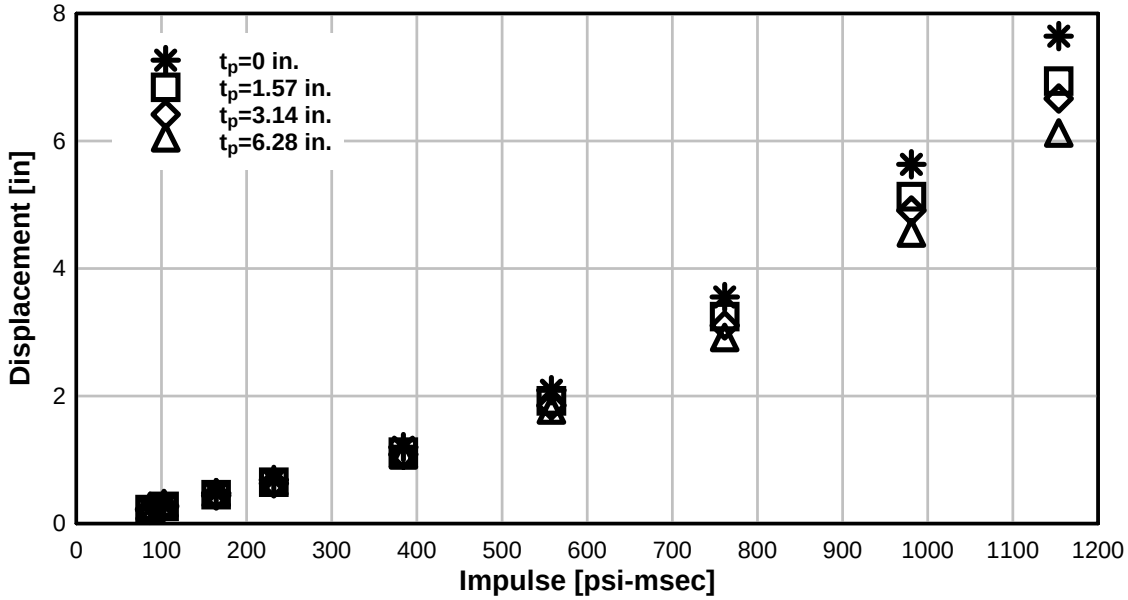

Figure 5.101: Impulse versus displacement for 10 in. thick wall and ρ=1.255%

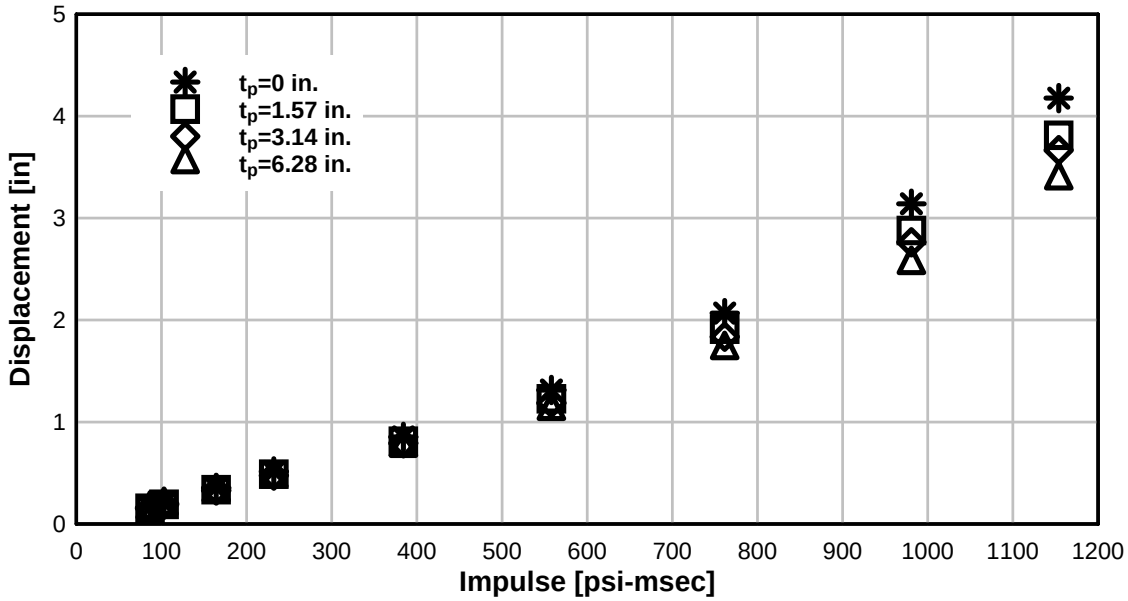

Figure 5.102: Impulse versus displacement for 10 in. thick wall and ρ=2.510%

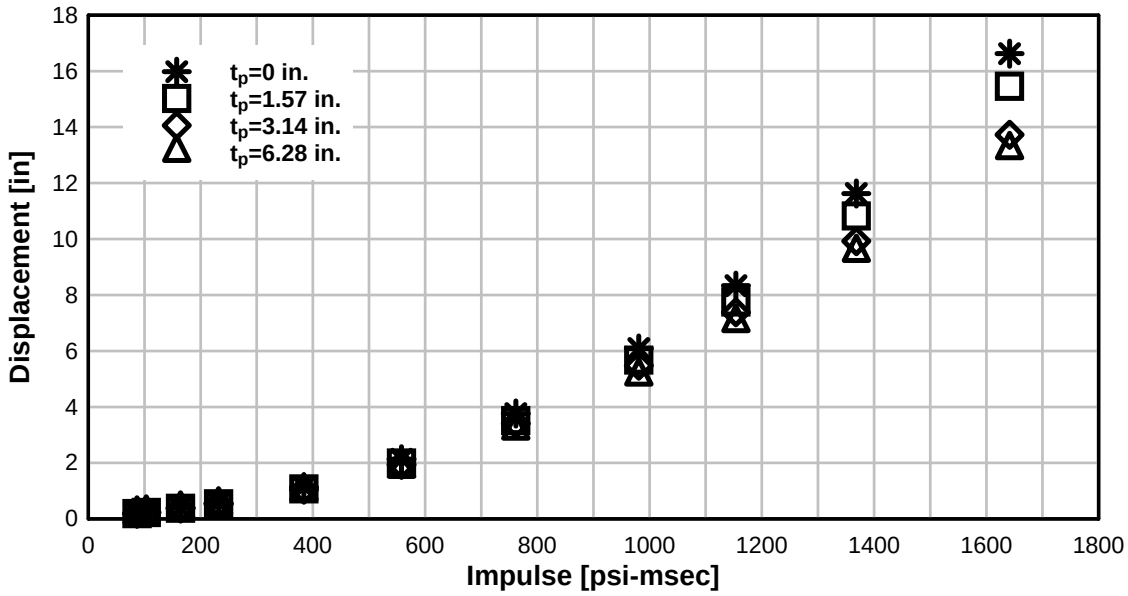

Figure 5.103: Impulse versus displacement for 14 in. thick wall and ρ=0.354%

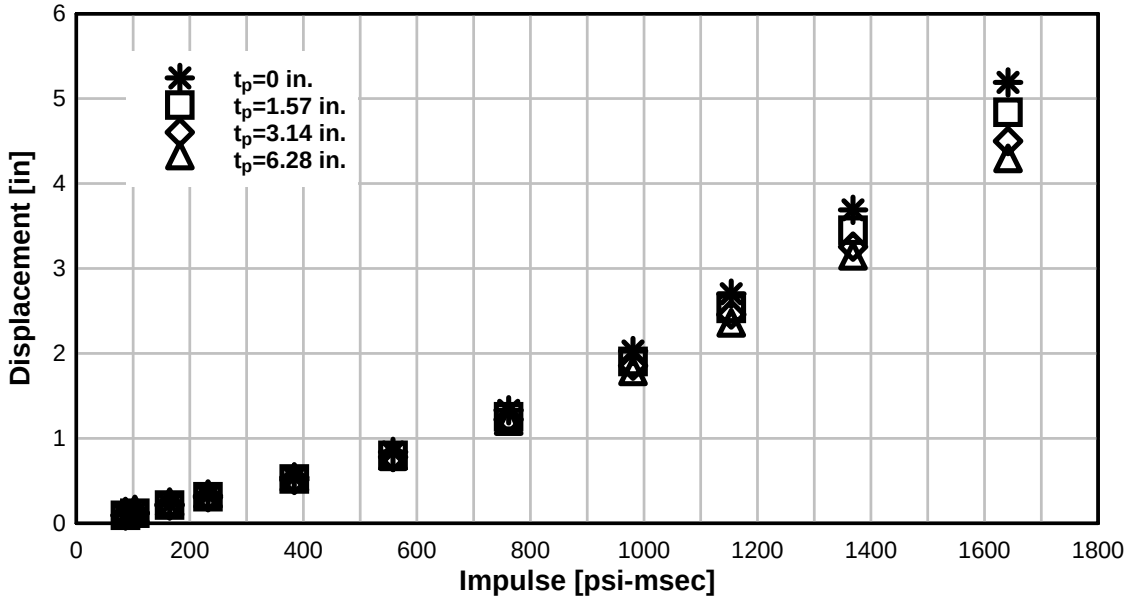

Figure 5.104: Impulse versus displacement for 14 in. thick wall and ρ=1.255%

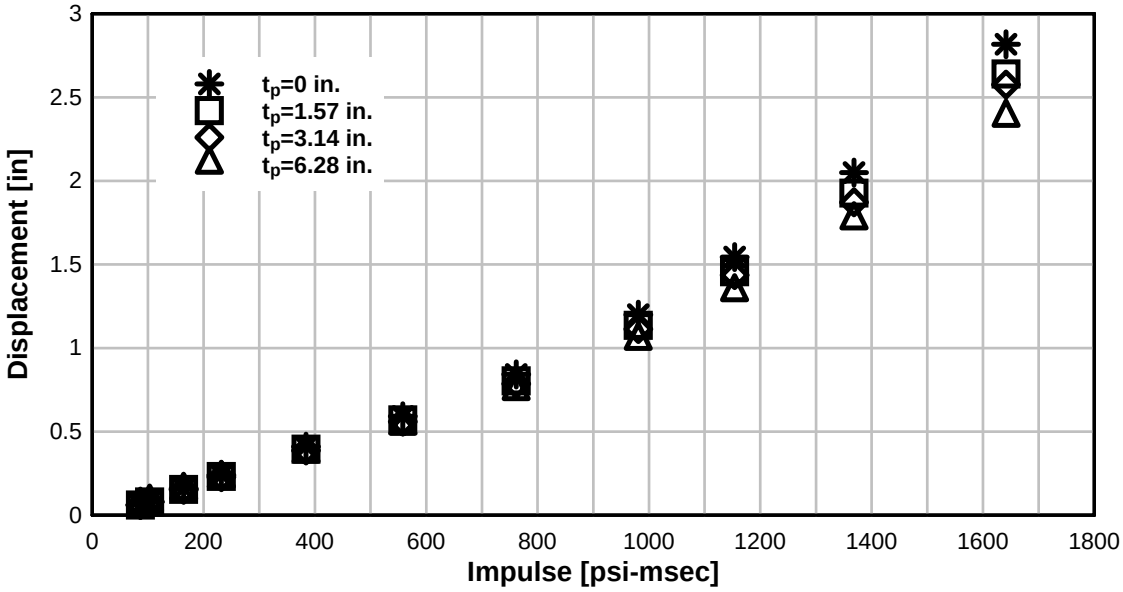

Figure 5.105: Impulse versus displacement for 14 in. thick wall and ρ=2.510%

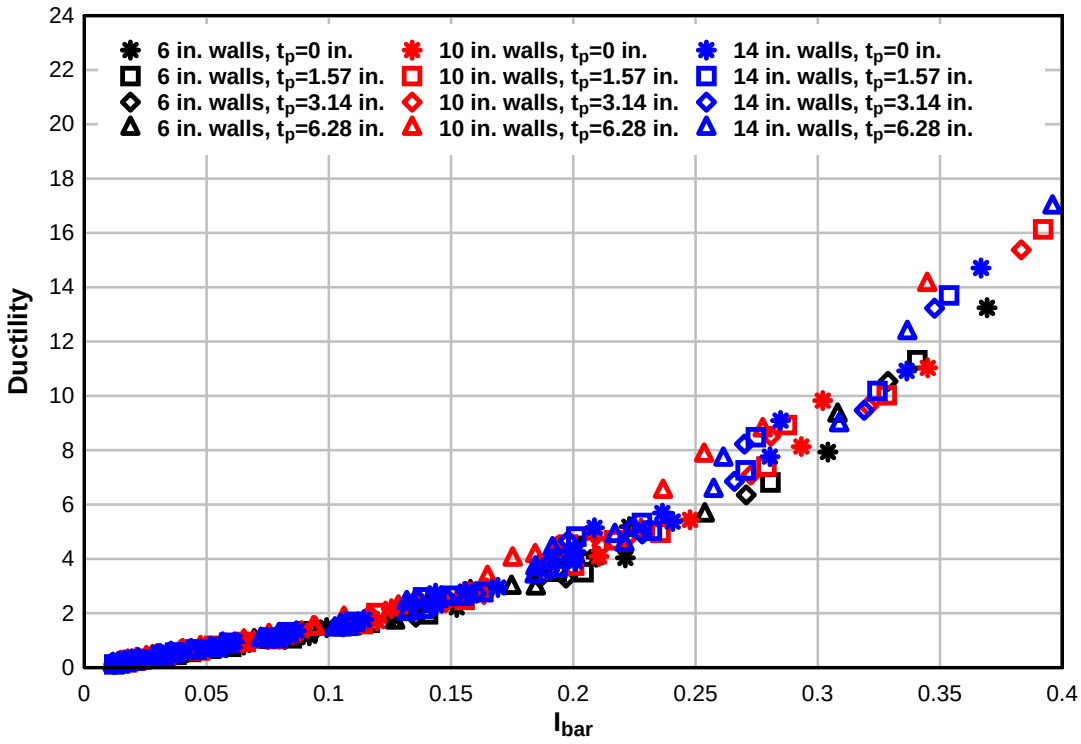

Figure 5.106: Non-dimensional impulse versus ductility demand

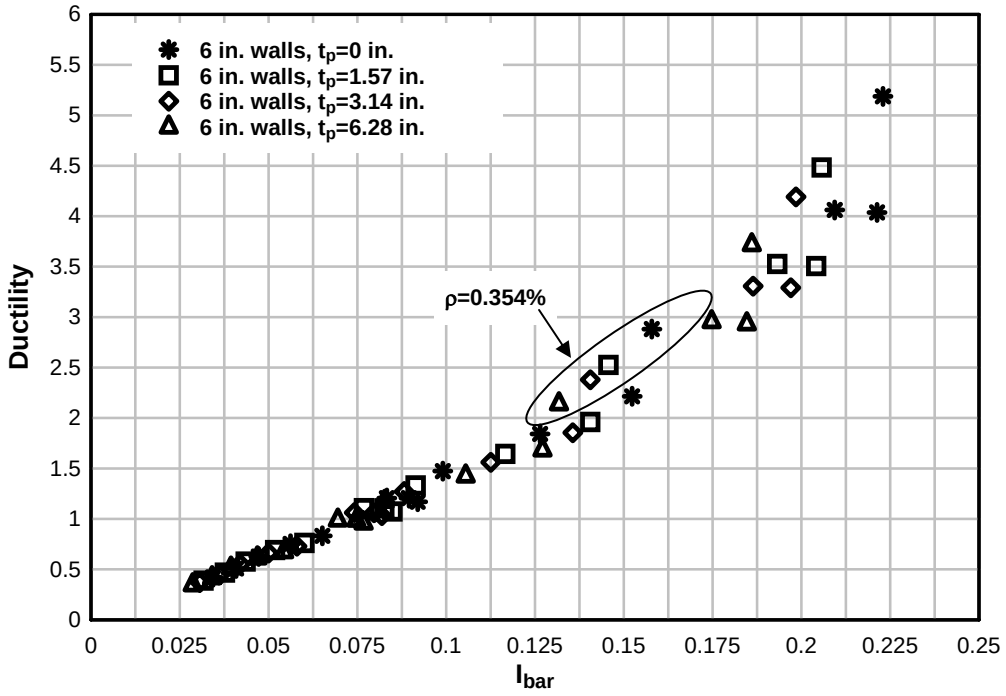

Figure 5.107: Non-dimensional impulse versus ductility demand for 6 in. walls

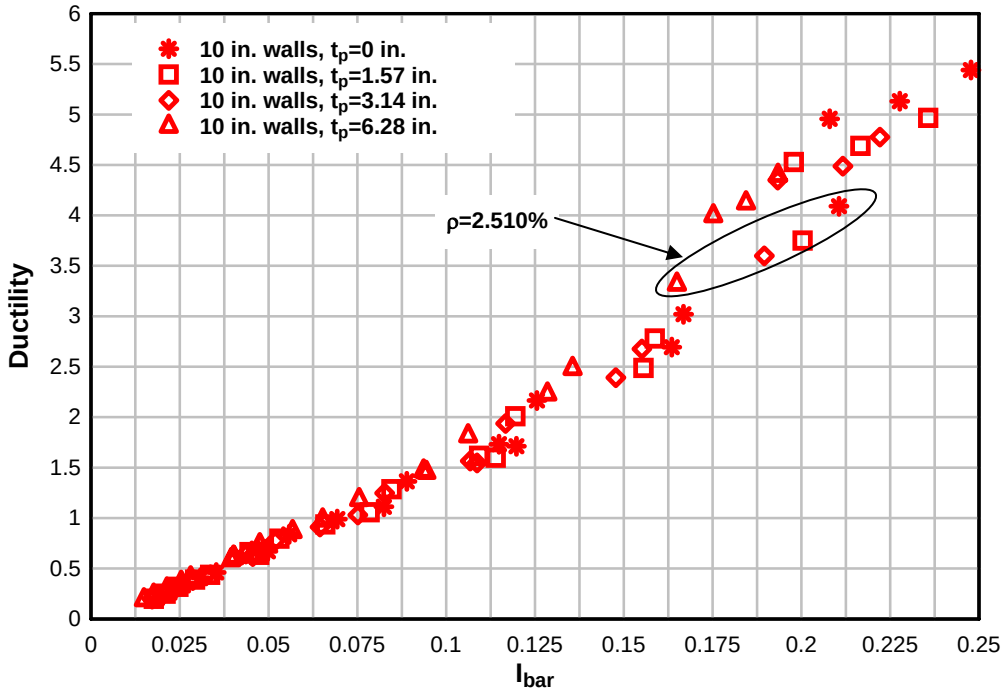

Figure 5.108: Non-dimensional impulse versus ductility demand for 10 in. walls

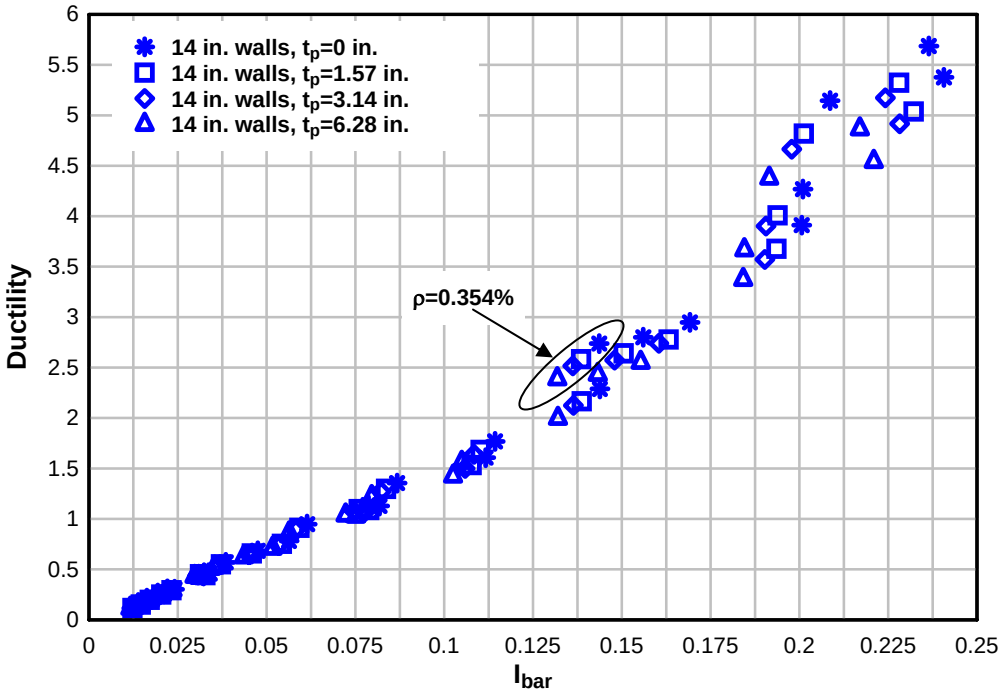

Figure 5.109: Non-dimensional impulse versus ductility demand for 14 in. walls

5.9 CONCLUSIONS AND RECOMMENDATIONS FOR FUTURE WORK

A study investigating the effect of frangible panels as a blast mitigation system for reinforced concrete walls was presented in this chapter. Included was a summary of two experimental test programs, description of the development and validation of a fast running numerical model called FPWA, description of the details and validation of a finite element model, and the results of a parametric study using the FPWA.

The results of the first experimental test program were inconclusive because direct comparisons could not be made between the RC walls with and without frangible

panels. The results from the second experimental test program led to the following conclusions:

- Construction of reinforced concrete walls with frangible panels proved to be difficult and expensive. Panel flexural strength was not sufficient to withstand the hydrostatic load of the concrete during placement. Therefore, an extensive system of formwork was required.

- The frangible panels dissipate some energy during impact loading, which lowers the total impulse experienced by the specimen. The tests have demonstrated that this effect is dependent on the ratio of the frangible panel thickness to overall wall thickness; as the ratio increases the amount of energy dissipation decreases.

- The difference in deformation between the frangible panel walls and RC walls with similar concreter core thicknesses subject to the same loading protocol is also a function of the ratio of panel thickness to overall wall thickness. As the ratio increases, the reduction in peak displacement decreases.

- The reinforcement ratio of the wall should be greater than the specified minimum to prevent brittle failure modes. The 8 in. concrete core walls exhibited fewer failures than the 12 in. concrete core walls because the rebar to concrete ratio is higher in the thinner 8 in. walls than in the thicker 12 in. walls. In addition, low reinforcement ratios with small diameter rebar can cause localized failures, which can result in reduced ductility of the wall.

- Single BG impact tests illustrated the vulnerabilities of the lap splice detail for both RC and frangible panel walls. The lap spliced specimens produced spalling when they were subject to intense localized loads, due in part to a sudden drop in moment capacity at the point where the starter bars were terminated. No concrete spalling was observed in the comparison test with continuous reinforcement.

Data generated in both of the test series was used to validate FPWA model and the FE models made in LS-DYNA. When subjected to an airblast both of these models generated similar results; which demonstrates that both models are fairly accurate for impact and blast problems. The accuracy of both models decreases with large displacements. This, however, is not a significant concern since large errors in the predicted response are for regions of behavior beyond the design limits set by [57].

The FPWA model was used in a parametric study to investigate the efficacy of frangible panels for reducing hazards created from blast loads over a large range of design scenarios. The results of the study suggest that when used with RC walls, the panels add mass to the structure, which has beneficial effects, but no additional energy or momentum dissipation was evident.

There are several topics for additional research on frangible panels as a blast mitigation system for RC walls. One recommendation for future research is to perform a parametric study similar to the one performed here, except with the use of the validated FE model. Additional parameters that could also be included are panel strength, densification strain of panels, and panel density. Another recommendation is for an experimental program using the blast simulator to investigate spall resistance of RC

panels with and without frangible panels. This study would include blast simulator testing with panels impacted by a single BG. The test setup for this program needs to be designed carefully in order to produce spall during the impact loading. To achieve spall, it is suggested to use two-way bending boundary conditions and include axial load. These two measures will increased the panels overall resistance which could drive it to a more localized failure mode.

6 UNREINFORCED CONCRETE MASONRY WALLS WITH POLYUREA CATCHER SYSTEMS

6.1 INTRODUCTION

Unreinforced masonry is often used in the construction of infill walls for low to medium rise buildings. This type of wall is highly susceptible to blast effects due to low flexural strength and brittle failure mode. The fragments of concrete block generated when the wall fails in a brittle manner become projectiles which pose a threat to the occupants of the building. The occupants can also be subjected to the blast pressures directly when a wall fails and collapses. Catcher systems are one mitigation strategy for these types of walls. The objective of the catcher system is to contain the fragments of the failed wall. An effective catcher system requires sufficient ductility to support the large deformation demands of the blast load and an adequate connection design that is capable of transferring the membrane forces in the material to the supports. Polyurea is a polymer material that is ideal for this type of wall retrofit due to its relatively large ductility capacity. Uniaxial tests on polyurea demonstrate that the material can reach elongations equal to nearly 100%. It is also a good candidate due to its ease of application which can be done with a spray device.

This chapter will present the results from a study of URM walls that was conducted with the UCSD Blast Simulator to investigate the effectiveness of polyurea catcher systems. Included in the study were tests on as-built walls, walls with a polyurea lining and a proposed anchor system, and walls with a polyurea lining and no additional

anchorage system. This chapter will also present numerical analyses that were performed and compared with selected test results. Finally, design guidelines to estimate an upper bound peak displacement of the system due to blast loads are presented. Design equations to determine the strength of the polyurea anchorage system are also purposed. Included in this proposal are recommendations for future research to further characterize the behavior and failure modes of the connection.

6.2 PREVIOUS RESEARCH

The concept of polymer lining as catcher systems for unreinforced masonry walls subject to blast loads was first investigated in the late 1990's. An early study on the behavior of unreinforced masonry walls with unreinforced polymers was conducted by Knox et al. [69]. In this study the authors investigated the affect of polyurethane and polyurea. The results of the study showed that the fragments produced in the failure of the wall by the blast load could be contained by the polymer retrofits. The retrofits also demonstrated very large ductility capacities.

Davidson et al. [70] investigated spray-on polymers for unreinforced masonry walls based on initial tests by Knox et al. [69]. The spray-on polymers tests had relatively low strength, but high ductility which enabled deform large enough to contain fragments created during the blast. Several polymers were selected for the tests and the application varied from lining only on the interior face to lining on both the interior and exterior face. The researchers found that the application procedure is not overly burdensome and that the retrofitted walls resisted peak pressures nearly 12 times greater than the unreinforced masonry walls. However, the efficacy of the polymers was

dependent on the peak pressure and duration of the load and the failure mechanisms were affected by the support conditions. One conclusion by the authors was that that spray-on polymer on both sides of the wall will increase the strength and reduce the hazard to the building occupants, but not significant enough to make it cost effective. A second conclusion was that dynamic FE models are needed to accurately simulate unretrofitted and retrofitted URM structures to blast loads. They also called for the development of non-explosive laboratory test procedures that can predict the energy absorbing effectiveness of a given retrofit material candidate. Finally, they concluded that performance criteria for elastomeric coatings for blast reinforcement is required along with innovative hybrid walls system designs and the development of engineering tools and guidelines for this retrofit solution.

A study on 43 1/4-scale walls that was conducted by Baylot et al. [40], as reviewed in Chapter 4, included test specimens that had been retrofitted with a spray-on polymer. The results of the study demonstrated that the retrofit was successful in reducing the hazard level inside the structure. For the ungrouted walls the polyurea was successful in preventing the debris from entering the structure, but the connection of the retrofit to the reactions began to debond. For the partially grouted walls the polyurea retrofits were tested with and without steel clamps to connect the retrofit to the supports. In the tests without the connections the polyurea retrofitted walls debonded at the top and the wall fell into the occupant space. The connection considered to remedy this failure consisting of steel clamping plates. When tested the polyurea retrofitted wall contained

the debris and the wall stayed in place, but the polyurea did have significant tears near the steel clamps.

Davidson et al. [71] investigated the failure modes of ungrouted CMU walls with polymer retrofits. The behavior of these walls to blast loads was characterized by a stress wave that propagates through the wall and potentially fractures its weaker parts. Front face shells of some of the CMU blocks were fractured in the first few milliseconds after the wall is loaded by the blast wave. High localized stresses in the mortar and CMU nearest the supports were identified as a potential cause of tearing in the polymer coating. Fracture of the front face shell of the CMU blocks could also result from compressive stress caused by arch action during flexural deformations. Tensile failure of polymer reinforcement, tearing and debonding of polymer at the supports were also identified as failure modes that could result in global collapse. It was concluded from the experiments that only 6 in. of spray overlap is required to transfer the loads to the support conditions. The experimental portion of the program also showed that the strength of the mortar bond between the blocks will affect whether or not arch action develops. Furthermore, failure of this bond in a direct shear mode can cause a localization of stresses in the polymer resulting in tearing. Finally, the bond between the masonry and the polymer allows composite action in the system. A case study with an un-bonded polymer coating, catcher system, resulted in larger peak displacements.

The research program also included finite element analyses to provide more insight into the behavior of the system in regards to the distribution of strain over the response time interval with intent to better understand the failure mechanisms. The finite

element study was also used to complement the data from the limited number of experiments with a parametric study involving a large range of variables. Finally, the FE study was used to develop analysis methods for investigation of other retrofit concepts for masonry. The studied used a simple crushable foam material to model the CMU block because the authors reasoned that it best captured the fracture observed in the tests. The polymer was modeled with piecewise linear plasticity model with strain rate effects. The bond strength between the block and the polymer was also modeled with a contact interface that employed a tied-node failure rule.

The analysis was able to match the experimental results. Strain rates due to the flexural response were moderate, less than 100 /s. The polymers only reached peak strains of about 20% and these occurred at the mortar lines where the opening between the blocks caused localized strain in the polymer that bridged the joint. Initial modulus and yield stress were found to not have a significant effect on maximum displacement; the later was more affected by ability to absorb energy which is dependent on thickness and elongation capacity.

Several field tests performed by Stanley et al. [72], [73], and [74] who explored several different polymers as retrofit solutions for URM walls. In [72] a test on a wall with a spray-on polyurea that was applied with a 1/4 in. thick layer on both the front and back side, and the wall was subject to a blast load. The connection detail for this wall only consisted of an 18-in layer overlap at the interior floor-to-wall and ceiling-to-wall horizontal interfaces. An 8 in. overlap of the material was also applied on both sides of the wall where it interfaced with the interior walls of the test reaction structure. In this

test the retrofitted wall was tested in the field beside a control URM wall with an actual explosive. The results of the test showed that the control URM wall completely failed while the retrofitted URM wall survived and the CMU block fragments were fully contained by the interior and exterior polyurea layers. Inspection of the interior layer of polyurea revealed insignificant tearing of the lining. The wall had a residual displacement and removal of the exterior polymer revealed that the CMU block had undergone some cracking during loading. The peak displacement of the wall was not reported by the authors.

Stanley et al. also conducted a field test on a wall with a spray-on urethane coating [73]. The retrofit used a 1/2 in. thick lining of the material on the exterior face of the wall and 1/4 in. thick lining on the interior face. The test was conducted with a retrofit and a control wall. The control wall failed catastrophically while the wall retrofit contained the concrete block and remained upright following the test. Upon removal of the exterior polyurethane lining significant damage to the CMU blocks were observed. Furthermore, inspection of the interior face revealed several tears at the mortar lines in the polyurea. Overall, however, the wall did not fail and was able to reach a peak inward deflection approximately equal to12 inches.

The test conducted in [74] was similar to the test Stanley et al. performed in [72] and [73] except the polyurea retrofit used was only applied to the interior face of the all. The lining was connected to the support structure with overlap sections similar to [72]. The results of the test demonstrated that the control wall completely failed while the wall retrofit prevented concrete block fragments from entering the occupant space. Most of

the concrete blocks for the retrofit wall were cracked by the blast pressures around their web portions resulting in smaller fragment. There were no signs of tearing or other damage to the polyurea. The peak inward deflection reported for the retrofit wall was 9 inches.

Reinforced polyurea has also been the topic of some research projects. Hutchinson et al [75] is one example of a study that investigated brick wall specimens with aramid fiber mesh that was coated in polyurea. These tests were performed quasi-statically with the objective of generating data that could be used to derive quasi-static resistance functions.

In addition to tests described in [72]-[74] Stanley et al. [75] also investigated a system that used a spray-on two-part polyurea with an embedded aramid weaved fabric that was applied to the back side of a full scale URM wall. The wall was tested in the field with actual explosive charge next to a control wall that did not have any reinforcement. This retrofit was successful for preventing the formation of wall debris and limited peak deflections in the wall to 9 inches while the control wall was completely destroyed by the blast. Following the blast it was observed that the concrete blocks of the retrofitted URM wall had all been split through the web by the blast wave. This resulted in block fragments falling to the ground in front of the wall when the polyurea rebounded and possibly from the negative phase of the blast wave.

A similar test was conducted using a retrofit that consisted of a nonwoven layer of polypropylene geotextile fabric that was placed between two layers of sprayed-on polyurethane [76]. The retrofit was applied to the front and back face of the wall. In the

test both the control and the retrofitted wall failed. The retrofit did contain some of the block, but a large portion of the wall failed in a punching shear mode and ended up on the inside of the structure due to the blast.

Moradi et al. [77] provided the formulation of the resistance of membrane-retrofit concrete masonry walls to lateral uniform pressure. The authors provided resistance functions for unreinforced concrete masonry walls with and without a membrane retrofit. Also included was the case where the unreinforced masonry walls experienced arch action. These formulations where all based on the assumption that the walls did not suffer any local damage that would reduce the effective mass or stiffness. Recommendations made by the authors for future research include a study on the adherence of polyurea and polymer to concrete masonry and an investigation on connection details and strength.

In [78] Moradi et al. used the methodology presented in [77] to model unreinforced masonry walls with membrane retrofits to blast loads with SDOF analysis. The numerical results were compared to test results from [70], [40], [79], and [80]. The comparisons demonstrated large discrepancies between the SDOF model and the experimental results. One possible explanation is that author's model does not consider local effects from the blast pressures on the integrity of the CMU block in the formulation of the resistance functions. The author's recommendation for future were the same as previously stated in [77].

6.3 EXPERIMENTAL WORK

6.3.1 INTRODUCTION

The previous research conducted on unreinforced masonry walls with polymer catcher systems has included several field tests that have used one-to-one comparisons with as-built walls to demonstrate the effectiveness of different types of polymers. While the results from the direct comparisons are indisputable, the data generated in these types of tests is generally of low quality or incomplete which makes model validation difficult. This was one of the motivations for a series of tests with the blast simulator. Blast simulator tests generate high fidelity data and produce visual data on the behavior of the system with high speed camera video that is not obstructed by a fire ball from the detonation or a large reaction structure.

Another motivation for the blast simulator test series was to investigate an anchorage design used to connect the polyurea catcher to the supports. In both [70] and [77] the different authors recommend connection detail design as an area for future research. The previous research studies reviewed in this chapter have paid little attention to this detail in the experiments: in [40] the connection design used a 6 in. overlap and it worked; in [71] the connection included a steel clamping plate and it failed; in [72]-[74] and [75]- [76] the specimens all had different connection details that typically consisted of large areas of overlap on to the top, bottom, and side supports which in all cases worked. The experimental work presented in this chapter demonstrates that a connection that only relies on an overlap of the polyurea is susceptible to catastrophic failure due to poor bonding conditions which may vary from one application to the next.

The experimental work presented herein included seven blast simulator tests including two as-built specimens, one retrofit wall with a typical overlap connection, two retrofit walls with an anchorage system, and two retrofit walls with an overlap that used a primer to increase adhesion properties. A matrix for the test series is shown in Table 6.1.

Table 6.1: Test Matrix

Test	Date	Target Velocity [ft/sec (m/sec)]	Specimen Details
1	1/24/2006	26.2 (8)	As-Built
2	2/6/2006	19.7 (6)	As-Built
3	2/13/2006	19.7 (6)	Retrofit with 18 in. overlaps
4	3/27/2006	13.1 (4)	Retrofit with anchors
5	4/11/2006	19.7 (6)	Retrofit with anchors
6	4/24/2006	13.1 (4)	Retrofit with 18 in. overlaps + primer
7	5/15/2006	16.4 (5)	Retrofit with 18 in. overlaps + primer

6.3.2 TEST SPECIMENS

Seven ungrouted unreinforced masonry walls were built for this test series. The walls were built from 8 in. x 8 in. x 16 in. (nominal) and 8 in. x 8 in. x 8 in. concrete masonry unit blocks. The mortar used in the wall was Type-S mortar. The overall dimensions of the walls were 8 5/8 in. thick by 4 ft wide by 12 ft-4 in. tall, except for the first wall that was tested, which was 4 ft-8 in. wide. The wall was originally designed to be 4 ft 8 in. wide because it was felt that a wider wall specimen would be more representative of a real wall. However, the results of the first test showed that the load transferred from the 48 in. wide BG was not uniformly distributed across the entire width of the wall. Therefore, the succeeding tests had a wall width equal to the width of the BG programmer.

The walls were built one-by-one in the location of the test (Figure 6.1). This procedure was followed because ungrouted URM walls are relatively fragile making them difficult to move after being built. The date that each wall was constructed is listed in Table 6.2.

Figure 6.1: Wall construction

Table 6.2: Wall construction and retrofit date

Test	Specimen	Construction Date	Retrofit Date
URM 1	As-Built	1/19/2006	NA
URM 2	As-Built	1/24/2006	NA
URM 3	Retro 1	1/31/2006	2/1/2006
URM 4	Retro 2	3/13/2006	3/17/2006
URM 5	Retro 3	3/29/2006	3/30/2006
URM 6	Retro 4	4/13/2006	4/14/2006
URM 7	Retro 5	4/26/2006	5/2/2006

6.3.3 POLYUREA CATCHER SYSTEM

Five of the seven URM walls tested were retrofitted with a spray-on polyurea lining called BUC XS-350 from Line-X. The retrofit design specified a ¼ in. layer of polyurea on the inside face of the URM walls. No lining was applied to the exterior face. The polyurea serves as a ductile membrane that catches the fragments of URM wall preventing them from injuring occupants inside the building.

The polyurea was typically applied 10 days prior to testing. The applicator of the polyurea required protective gloves and suit, along with a fresh air breathing system with a face shield and air-breathing respirator hose to protect him from airborne particulates (Figure 6.2). A high pressured, heated system is used to mix and dispense the "A" and "B" components (Figure 6.3) that form the polyurea coating when allowed to set. Figure 6.2 shows the polyurea being applied to the URM wall with a pressurized spray gun.

Figure 6.2: Application of polyurea

(a) **(b)**

Figure 6.3: Two-Part Polyurea: (a) Component A; (b) Component B

Two different retrofit details were implemented at the connections between the polyurea and support structure. The detail used for the first retrofit URM provided an 18 in. overlap of the polyurea lining on the top and bottom support. Wire tape was used to cut the polyurea so that the area of the section bonded to the concrete was 48 in. x 18 in. (Figure 6.4). Figure 6.5 shows the overlapped layer of polyurea at the top support. The load is transferred from the polyurea to the supports through its adhesion with the concrete. The surfaces of these concrete supports were prepared using a diamond tipped grinder and cleaned with a vacuum and air hose before the polyurea was applied. This was done to provide a clean and rough surface to increase the bond characteristics. After the polyurea was applied it was observed that a small portion of the overlapped lining had de-bonded at the lower support where the wire tape was pulled.

Figure 6.4: Wire tape before surface polyurea applied

Figure 6.5: Top polyurea connection with 18 in. overlap

Simpson Strong-Tie A88 angles were used to increase the strength of the connection for two of the retrofit URM wall tests. The proposed anchor detailed described here is based on an anchorage design CMU walls with FRP retrofits that was originally proposed in [81]. The angles are 2 in. wide with 8 in. legs and have a thickness of about 0.1 inches. Eight angles spaced at 6 in. on center were used at each support

(total of 16 angles per wall). Each angle was bolted to a 1-5/8 in. diameter Simpson Strong-Tie Wedge that was installed about 6 in. behind the wall. The following procedure was used to install the angles for the connection detail:

- Insert Simpson Strong-Tie Wedge Anchors into top and bottom supports
- Roughen concrete surfaces with diamond tipped grinder
- Clean surface with vacuum and air hose (Figure 6.6)
- Protect threads of anchors with duct tape and plastic tubing (Figure 6.7)
- Spray 1/8 in. layer of polyurea lining over prepared surface and lower half of URM wall
- Remove duct tape and plastic tubing from anchors
- Bolt A88 angles to concrete surface with wedge anchors (Figure 6.8)
- Coat angles and surface with an additional 1/8 in. layer of polyurea lining (Figure 6.9)

The bottom connection was sprayed first, then the lining was applied to the middle portion of the wall, and finally the procedure above was followed for the top connection. A schematic of the connection detail used is shown in Figure 6.10.

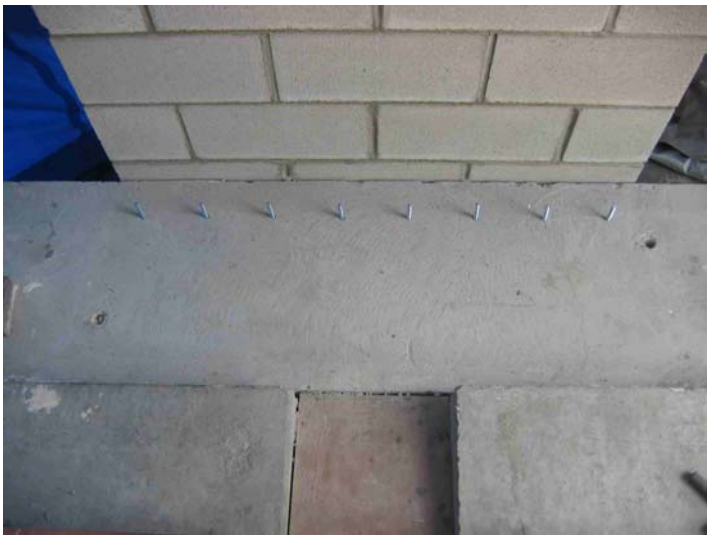

Figure 6.6: Wedge anchors at bottom support

Figure 6.7: Cleaned concrete surface with covered anchors

Figure 6.8: Angles attached to support over first layer of polyurea

Figure 6.9: Angles coated with second layer of polyurea

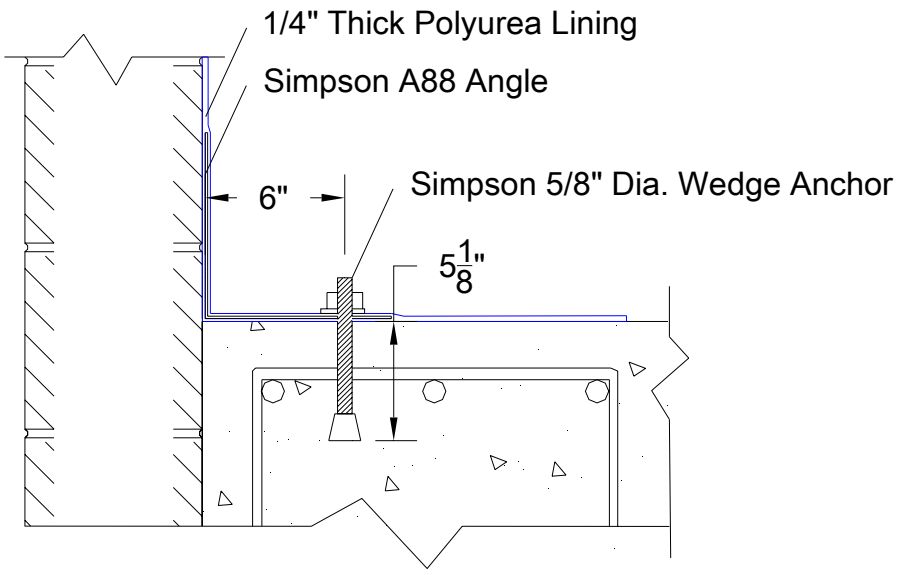

(a)

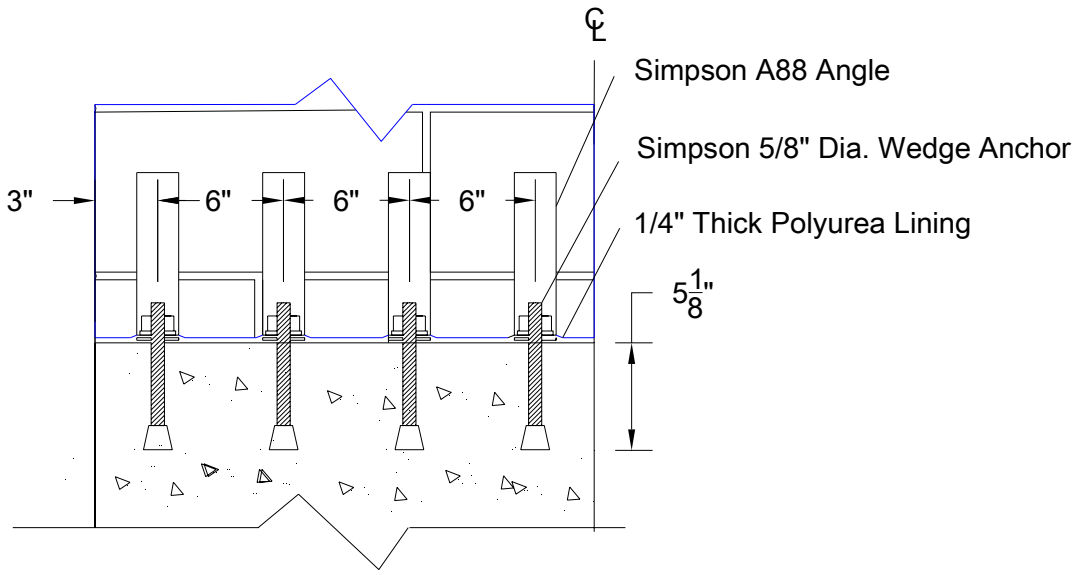

(b)

Figure 6.10: Schematic of connection detail; (a) north elevations; (b) west elevation

The final two retrofit wall tests were performed without Simpson A88 angles at the connections. The connection was the same at the first retrofit wall except that the concrete surface and the wall surface were prepared with a two component primer called XPM Urethane Primer. XPM was suggested by Line-X as the appropriate primer for enhancement of adhesion between concrete and polyurea. The procedure for this primer required a 12 hour dry time after application followed by a 12 hour window in which the polyurea was to be applied. Figure 6.11 shows the wall after application of the primer. Figure 6.12 and Figure 6.13 shows the connection of the polyurea to the top and bottom support after its application. In the picture it can be seen that the edges of the polyurea were not cut with the wire tape. Instead the thickness of the polyurea tapers off as it approaches the edges. This was done to prevent any de-bonding that may occur when the wire tape was used to cut through the polyurea lining.

Figure 6.11: XPM Urethane Primer before polyurea application

Figure 6.12: Top connection for polyurea with primer

Figure 6.13: Bottom connection for polyurea with primer

6.3.4 TEST SETUP

The setup for the URM wall tests was designed to simulate uniform blast loading on a wall with one-way bending and simple-support boundary conditions. The span of the walls during test was 10 ft 7 inches. The walls were loaded with four BGs that are 48

in. wide by 30 in. tall. The BGs were realigned so that a 1 1/4 in. gap was left between any two programmer plates. A 1 3/4 in. gap was also set between the bottom BG programmer plate and the footing; while a 1 1/2 in. was left between the top BG programmer plate and the bottom of the top support.

The top of the URM wall was reacted through bearing with a 6 in. thick reinforced concrete slab that was connected to the reaction wall. The slab was supported by the movable reaction wall on its west edge. The southeast corner was supported by a tubular column. The northeast corner was originally supported by a tubular column, but was replaced by cables that tie into the movable wall. This was done to provide a clear shot for the Phantom cameras used to film the tests. Two posts support the slab at its midspan to provide stiffness to the slab and reduce the moment demands during tests caused by tension membrane forces from the polyurea lining. Figure 6.14 shows the test setup.

Figure 6.14: Test setup for URM walls

6.3.5 INSTRUMENTATION

DATA ACQUISITION SYSTEM

A high speed data acquisition system from *Hi-Techniques* was used. This system samples at 14 bits and 1 MHz. Currently the data acquisition system has a capacity of 52 channels. It is externally triggered from the MTS controller that is used to fire the BGs.

HIGH SPEED VIDEO

High speed video was captured with two Phantom v7.1 (Vision Research) cameras. The first camera records in black and white at a rate 3000 frames per second at a resolution of 800x400 or 5000 frames per second at 704x400. The second camera records in color and runs at a rate of 5000 frames per second at a resolution of 800x400. The cameras are capable of different frame rates at different resolutions. The cameras were externally triggered from the MTS controller. TEMA was used to obtain graphical displacement and velocity measurements from the video capture.

In all tests the black and white camera was placed on the right (north) side of the column, centered on the front edge of the walls at a height of about 6 ft. The color camera was placed north and west of the wall in order to capture its behavior from the back side. Targets were placed on the wall to aid in graphical displacement measurements. Figure 6.15 shows the locations of the cameras for the tests.

Figure 6.15: Phantom camera locations

SHOCK ACCELEROMETERS

The accelerations of the BG impact plates during impact were measured with 10K g piezoelectric shock accelerometers mounted on their back side. Two accelerometers were used per mass plate. The accelerometers were located mid height approximately 7 in. to the left and right of the centroid. The acceleration signal of two different accelerometers was typically averaged and integrated to measure the impulse delivered to the specimen during the test.

BG VELOCITIES

The velocity for each BG was determined from the Phantom video record using the TEMA software package. For each BG, a point is selected on the impact mass and the software records its displacement time history. The software then differentiates the

displacement time history using a 7 point numerical differentiation scheme to obtain the velocity time history.

SPECIMEN DISPLACEMENTS

The Phantom camera videos were used in conjunction with the TEMA software to measure specimen displacements at several different locations. The specimen displacements could be differentiated with respect to time to get the specimen velocities time histories. This was done numerically by the TEMA software. Targets were mounted on the side wall before the test to assist in tracking the wall displacements. One target was place on each CMU block in between the top and bottom horizontal mortar joint. The targets can be seen in Figure 6.14.

Displacements were also measured using a linear potentiometer for tests 3-7 and with a string potentiometer for test 6 and 7. The BG support structure was used a reference point for one end of the linear potentiometer. The other end was connected to the wall via the steel angle that was also used to connect the accelerometer. Figure 6.16 and Figure 6.17 show the connections for tests 3-5 and for test 6 and 7 respectively. In tests 6 and 7 a string potentiometer was also attached to the BG support tower with its string attached to the wall's midspan at the back face on the north side (Figure 6.18). The end of string pot was anchored into the polyurea lining in order to maintain a connection throughout the test.

Figure 6.16: Connection of accelerometer and linear potentiometer, Tests 3-5

Figure 6.17: Connection of accelerometer and linear potentiometer, Tests 6 and 7

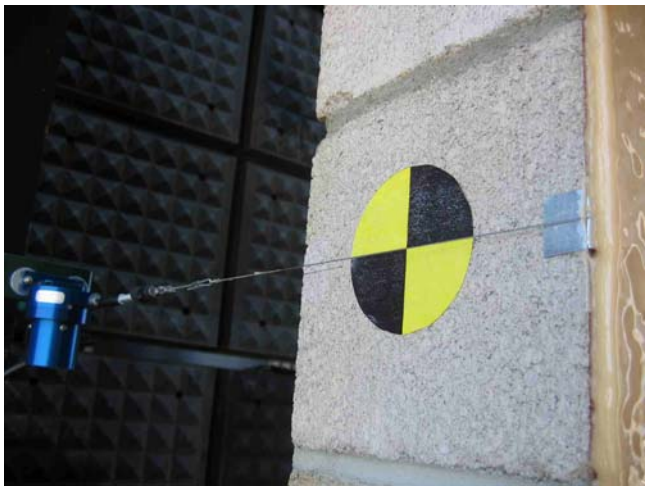

Figure 6.18: String potentiometer at walls midspan, Tests 7 and 8

SPECIMEN ACCELERATIONS

Accelerations on the retrofit URM walls were measured using one 10k g unit at the midspan. The accelerometers were attached to a steel angle that was mounted to the wall. In tests 3-5 one leg of the angle was bolted to a threaded rod that was anchored into a concrete block on the south side with epoxy. The other leg was bonded to the back of the wall with an epoxy joint in between the steel and the polyurea lining (Figure 6.16). During testing the mounting remained attached to the wall until it began to rebound, once it was disconnected the accelerometer moved free from the wall and in most cases broke the cables attaching it to the data acquisition system. In test 6 and 7 one leg of the angle was attached to threaded rod anchored into the wall and the other leg was sandwiched between the polyurea lining and the back side of the block wall (Figure 6.17). This constrained the accelerometer to the back of the wall for the entirety of the test.

POLYUREA STRAINS

Strain was measured in the polyurea lining for each of the retrofit tests. All strain gages were from *TML* and have a guaranteed upper limit of 15-20% strain. In tests 3-5 strain was measured with 20 mm gages (model *YFLA-20-5LT*). In tests 6 and 7 the gauges used were 10 mm (model *YFLA-10-5LT*). Typically five gages were used per test with one gage at the midspan, one gage across the mortar joint above and below the midspan, and one gage in the middle of the block on the course above and below the course at midspan. The gages were placed near the centerline of the wall in the longitudinal direction.

The smoothness and hardness of the polyurea surface made it difficult to bond the gages to it using the manufacturers recommended adhesive. As an alternative the gages were sprayed with a thin coat of polyurea to embed them in the lining (Figure 6.19). The strain gage wires were arranged as shown in Figure 6.19to provide tension relief during the blast test.

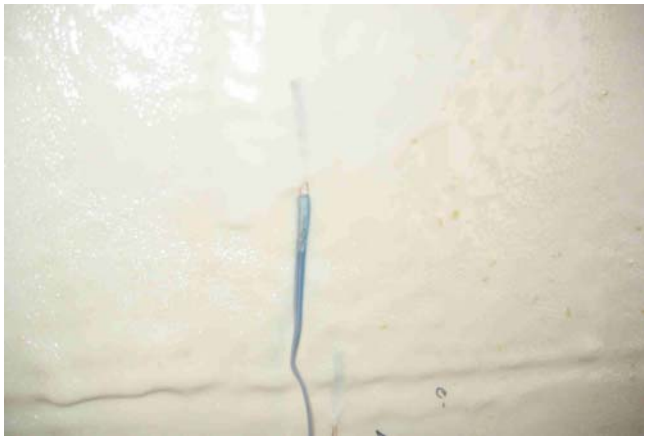

Figure 6.19: Strain gages embedded in polyurea lining

Figure 6.20: Stain gage wires

6.3.6 MATERIAL TESTING

Type-S mortar was used to construct the wall. The compressive strength of the mortar was determined by testing 2 in. diameter cylinders that were 4 in. tall according to UBC [55] Standard 21-19. The cylinders were tested on the day of the blast test or shortly afterwards. Typically the mortar is allowed to cure for 28 days before testing, however due to accelerated test schedule the mortar only cured for about 10-15 days. At least three mortar cylinders were tested to obtain an average compressive strength. The average mortar compressive strength for each wall on or near the day of test is listed in Table 6.3.

Table 6.3: Mortar Compressive Strengths

Test	Date of Test	Average Compressive Strength [psi]
URM 1	1/21/2006	--
URM 2	1/27/2006	3550
URM 3	2/13/2006	4030
URM 4	3/27/2006	4718
URM 5	4/11/2006	4105
URM 6	4/24/2006	3177
URM 7	5/15/2006	3957

MASONRY PRISMS

The masonry compressive strength was determined by testing ungrouted prisms according to ASTM E447. The prisms consisted of three ungrouted, unreinforced, 8 in. x 8 in. x 16 in. concrete blocks with two mortar joints (Figure 6.21).

Figure 6.21: Masonry Prism

Three masonry prisms were made for each URM wall that was tested. The prisms were tested at or near the day of the blast test. Typically, the prism are given 28 days to

cure before testing, however the schedule for the URM walls called for the walls to be tested after only 10-15 days after cure. Therefore, the prisms were typically tested 10-15 days after they were built in order to get masonry compressive strengths for the day of the blast test. Table 6.4 lists the masonry compressive strengths for each test. The strength for test three is noticeably lower than the other tests because the specimens were exposed to rain and became saturated with water.

Table 6.4: Masonry Prism Compressive Strengths

Test	Date of Test	Average Compressive Strength [psi]
URM 1	1/24/2006	1441
URM 2	2/6/2006	1421
URM 3	2/13/2006	1560
URM 4	3/27/2006	1640
URM 5	4/11/2006	1130
URM 6	4/24/2006	1432
URM 7	5/15/2006	1440

CMU BLOCK

The compressive strengths of the CMU blocks used to build the ungrouted URM walls are determined ASTM C 140. The mean compressive strength for three 8”x8”x16” blocks was 2.215 ksi. The tension strength of the CMU block was determined using ASTM C 1006. Three CMU blocks were tested and the mean tensile strength from these tests was 143 psi.

POLYUREA

The tensile strength and modulus of elasticity of the polyurea lining was determined by following the procedures of ASTM D638. Samples of the polyurea were

made by Line-X after the application of the polyurea to the URM walls. Test coupons were then machined out of the samples to the specified dimensions. At least three coupons were tested in tension at 5, 7, and 15 days. The polyurea was tested on different days after it was sprayed to determine how cure time affects strength and stiffness. Table 6.5 lists the mean and standard deviation of the tension strength and modulus of elasticity for the polyurea at 5, 7, and 15 days.

Table 6.5: Polyurea Tensile Properties

Cure Time	Tensile Strength		Modulus of Elasticity	
	Mean [psi]	Standard Dev [psi]	Mean [psi]	Standard Dev [psi]
5 days	1812	17	42570	5263
7 days	1964	10	46797	929
15 days	1975	26	47603	3577

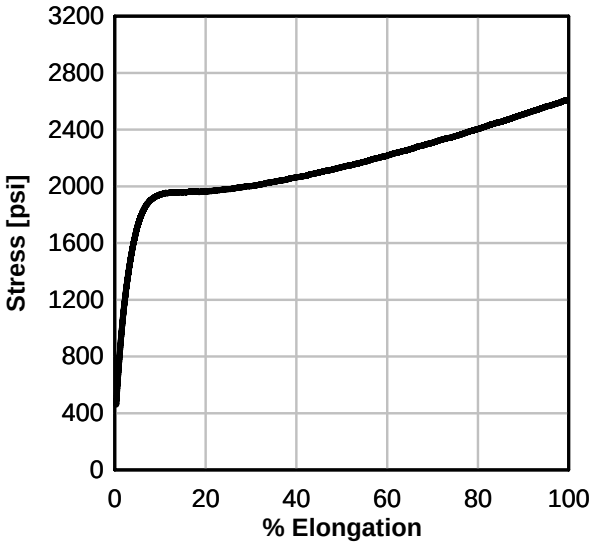

Figure 6.22: Polyurea uniaxial tension test stress versus percent elongation

6.3.7 RESULTS

TEST 1

Figure 6.23: Test 1- prior to impact

The first test of the URM test series was conducted on an as-built on January 19th, 2006. This test specimen served as a control sample for comparison with retrofit tests and it was predicted that the wall would be completely destroyed by the blast simulator loads. The specimen is shown prior to impact in Figure 6.23. The target impact velocity for all four BGs was set to 26.2 ft/sec (8 m/sec) and the actual average impact velocity for the BGs was 26.5 ft/sec (8.1 m/sec). The time spread between initial and final impact was about 0.55 msec. The average impulses delivered to the specimen by the BGs was 216 psi-msec. The wall was completely destroyed by the blast test. The impact caused projectiles of the concrete blocks to intrude into the occupant space behind the wall at high velocities. The Phantom camera shows that the BGs punched through the wall

instead of transferring the load to its entire width (Figure 6.24). This behavior is undesirable, therefore to produce uniform loading on the front face of the URM walls the width of the test specimen in future tests was reduced from 56 in. to 48 in., which is the same width as the BG programmer plates. Figure 6.25 displays the wall following the test.

Figure 6.24: Test 1- BGs punch through wall

Figure 6.25: Test 1- after test

TEST 2

Figure 6.26: Test 2- prior to impact

Test 2 of the URM test series was conducted on an as-built wall on January 27th, 2006. This test specimen served as a second control sample to use for comparison with the retrofit tests. The target impact velocity for all four BGs was set to 19.7 ft/sec (6 m/sec). The only instrumentation provided was accelerometers on the BG plates. Additional instrumentation was omitted from the test because it was predicted that the wall would suffer catastrophic damage from the BG impact. The specimen is shown just prior to impact in Figure 6.26. The actual average impact velocity was equal to 20.0 ft/sec (6.1 m/sec) and the time spread between initial and final BG impact was equal to 0.43 msec. The impulse delivered to the specimen was equal to 152 psi-msec.

The impulse from the BGs imparted an initial velocity of 17.5 ft/sec (5.33 m/sec) to the specimen. The wall under this load failed the blocks near the supports and

translated with a constant velocity until it impacted the support columns behind it. Figure 6.27 displays the remnants of the wall following the test.

Figure 6.27: Test 2- post test

TEST 3

The first retrofit of the URM wall was tested on February 13th, 2006. The wall had a 1/4 in. thick layer of polyurea to the back side of the wall on February 1st, 2006 which was allowed to cure for 12 days before the wall was tested. The target impact velocity for all four BGs was set to 19.7 ft/sec (6 m/sec). The specimen is shown prior to impact in Figure 6.28.

Figure 6.28: Test 3- prior to test

The polyurea lining was connected to the supports by an 18 in. overlap that relied on the adhesion between the concrete and the polyurea. It was observed prior to the test that a portion of the polyurea overlap shown in Figure 6.29 debonded from the concrete. This was caused by the wire tape that was used to cut the polyurea overlap to the 48 in. x 18 in. dimensions as can be seen in the figure.

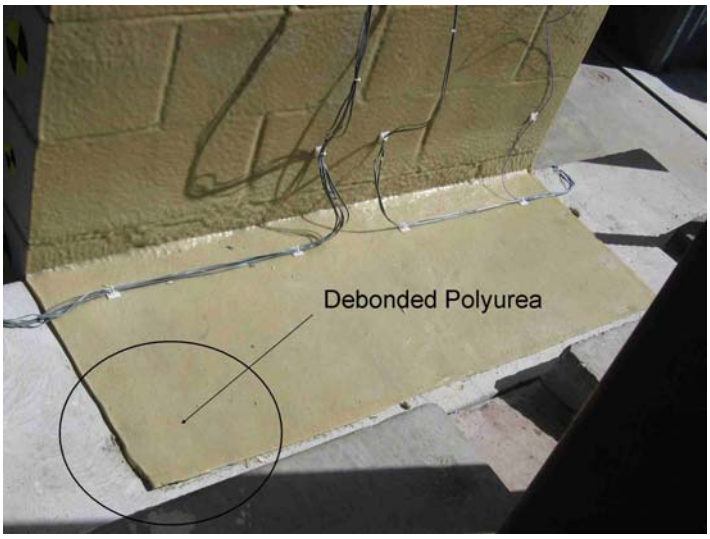

Figure 6.29: Test 3- Debonded polyurea

The actual average impact velocity was equal to 19.9 ft/sec (6.1 m/sec) and the time spread between initial and final BG impact was equal to 0.71 msec. The BG loading delivered an impulse equal to 163 psi-msec to the wall. According to the integrated accelerometers the initial velocity in the wall from the BG impact was equal to 26.4 ft/sec (8.05 m/sec). A sequence of frames taken from the video which display the progression of damage in wall can be found in Appendix C. The video show that a crack forms along the height of the wall about 3 msec after contact. This crack separates the front face of the concrete blocks from the rest of the wall. At the same time the bottom connection between the polyurea and the concrete block began to de-bond. The polyurea overlap at the bottom support began to de-bond shortly after the BGs impact the specimen. The overlap is complete debonded at about 50 msec after the first impact. This allows the bottom of the wall moves freely, which eventually causes the top polyurea overlap to peel off from the top slab. This connection failure caused the specimen to travel into the occupant space and eventually collapse. This test showed that a stronger connection

detail is needed to prevent this failure. Figure 6.30 shows the specimen following the test. It can be observed that, even though the wall collapsed, the polyurea held most of the fragments of the concrete block together and stopped them traveling further behind the wall.

Figure 6.30: Test 3 post test

The most likely cause of the debonding at the bottom support was the use of wire tape to cut the edges of the freshly sprayed polyurea lining. The wire tape was used to provide a neat perimeter along the area of the overlap, however when the tape was pulled it pulled up a portion of the bonded polyurea and initiated the connection failure. All of the retrofit tests following this first one discontinued the use of the wire tap. Instead, the perimeter of the overlapped polyurea was tapered.

Following the test calipers were used to measure the thickness of the polyurea lining at six different locations. The average thickness of the polyurea lining is 0.250 inches. The standard deviation of the thickness is 0.053 inches.

TEST 4

The fourth specimen of the URM wall test series was tested with the blast simulator on March 27th, 2006. A 1/4 in. coating of polyurea was sprayed on to the back side of the wall on March 17th, 2006. It cured for 10 days before it was tested. This test also used Simpson Strong-Tie A88 angles to connect the retrofitted wall to the supports. The target impact velocity for this test was 13.1 ft/sec (4 m/sec). Figure 6.31 shows the wall prior to the test.

Figure 6.31: Test 4 prior to test

The actual average impact velocity recorded for the test was equal to 13.6 ft/sec (4.2 m/sec) and the time spread between initial and final contact of the BGs was equal to 1.3 msec. The BGs delivered an impulse equal to 130 psi-msec to the specimen which resulted in an initial velocity at the midspan of the wall equal to 20.2 ft/sec. The initial velocity in the wall resulted in a peak midspan displacement equal 4.6 inches.

The response of the wall is illustrated frames from the high speed camera video which are displayed in Appendix C. Shortly after impact a crack formed near the bottom support and began to propagate up the height of the wall. When the wall reached its maximum displacement and began to rebound the cracking subsided. Figure 6.32 show clips from the black and white and color Phantom camera at peak displacement. Post test observations found that this crack removed the front faces from the concrete blocks at the lower half of the wall. The crack also appear to initiate at the outer edges along the width of the wall and move in towards it centerline (Figure 6.33).

The connection detail was successful in transferring the loads in the polyurea to the supports. Following the tests it was observed that the Simpson Strong-Tie angles remained relatively undeformed throughout the blast test. The undamaged state of the angles suggests that the wall could undergo higher levels of loading before the connections fail.

Following the test calipers were used to measure the thickness of the polyurea lining at five different locations. The average thickness of the polyurea lining is 0.334 in.. The standard deviation of the thickness is 0.052 inches.

(a) **(b)**

Figure 6.32: Test 4 at peak displacement; (a) black and white camera; (b) color camera

Figure 6.33: Test 4 front face post test

TEST 5

The fifth specimen of the URM test series was impacted with the blast simulator on April 11th, 2006. The wall had a 1/4 in. coating of polyurea on its back side which was applied on April 1st, 2006. The polyurea was allowed to cure for 10 days before it was tested. This specimen also had Simpson Strong-Tie A88 angles to connect the polyurea to the supports. The detail for this connection was the same as for Test 4. The target impact velocity of the BG was equal to 19.7 ft/sec (6 m/sec). Figure 6.34 shows the wall prior to the test.

Figure 6.34: Test 5- prior to impact

The actual average impact velocity for Test 5 was equal to 20.1 ft/sec (6.1 m/sec) and the time spread between initial and final contact was equal to 0.86 msec. The BG

impacts delivered an impulse to the specimen equal to 169 psi-msec. Data from an accelerometer mounted at the walls midspan was integrated to calculate an initial velocity at the wall midspan equal to 21.5 ft/sec (6.55 m/sec). The TEMA tracking software was also used to differentiate the tracked displacements to find an initial wall velocity of 23 ft/sec (7.01 m/sec). This initial velocity resulted in a peak midspan displacement equal to 25.2 inches. Figure 6.35 shows the wall from two different perspectives at the time when it reached peak displacement.

The behavior of the wall during the test was captured with the high speed camera video. Frames from this video displaying the progression of failure in the specimen are displayed in Appendix C. The polyurea responded as a tension membrane with the concrete blocks providing mass to the system, but little or no stiffness. The video showed that a crack formed on the north face of the wall along its height immediately after impact. As the wall deformed this crack widened and it was observed that the front faces of the concrete blocks separated from the rest of the wall. At about 50 msec after impact the polyurea at the bottom connection began to peel off. The peeling can be observed in Figure 6.35. This means that the Simpson Strong-Tie angles had also undergoing significant plastic deformation. The polyurea at the top connection also began to peel at about 145 msec after contact. The polyurea rebounded after it reached the peak displacement. When it rebounded it threw the broken pieces of the wall back in front of the wall. Post test inspection of the wall found that the connection at the top and bottom performed well during the test. The Simpson Strong-Tie angles underwent large plastic rotations without failing and they maintained the connection of the polyurea to the

wall and the supports. Figure 6.36 (a) displays the back of the specimen following the test. In Figure 6.36 (b) it can be observed that only the back faces of the concrete block remain attached to the polyurea. Following the test calipers were used to measure the thickness of the polyurea lining at five different locations. The average thickness of the polyurea lining is 0.277 inches. The standard deviation of the thickness is 0.050 inches.

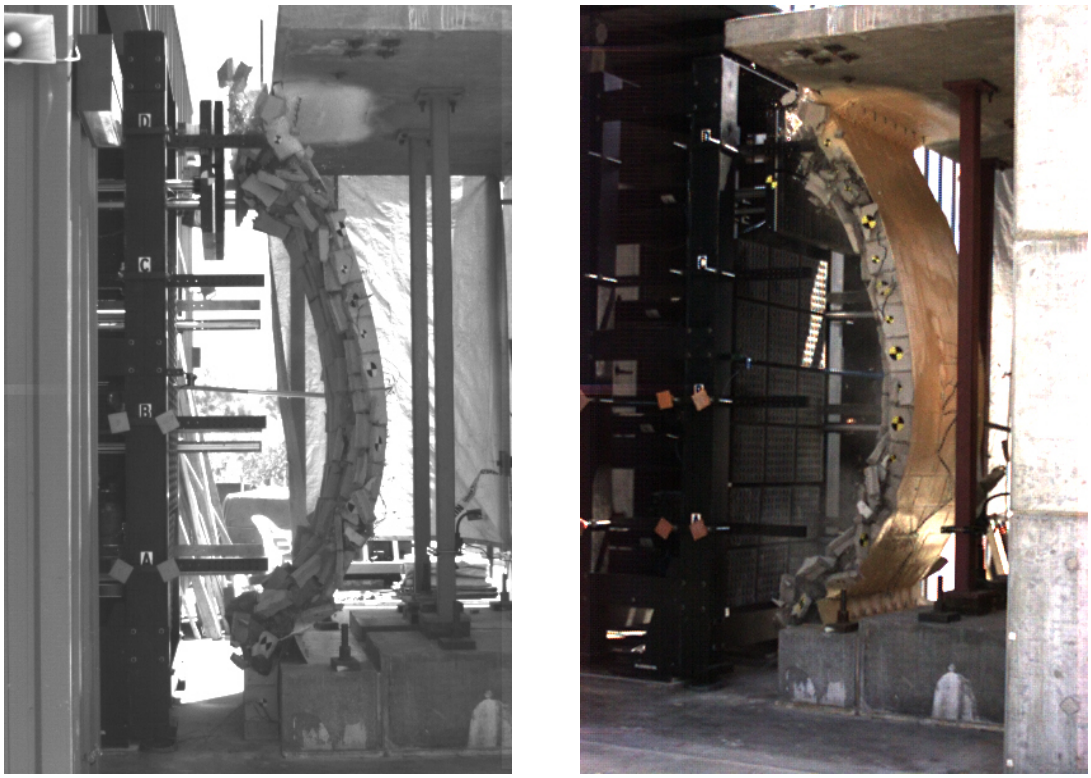

(a) **(b)**

Figure 6.35: Test 5 peak displacement; (a) black and white; (b) color

(a) **(b)**

Figure 6.36: Test 5 post test; (a) back side; (b) front side

TEST 6

The sixth test of the URM test series was conducted with the blast simulator on April 24th, 2006. The test specimen was retrofitted with 1/4 in. coating of polyurea to the back side of the wall on April 14th, 2006. The polyurea was connected to the supports by an overlapping with dimensions equal to about 18 in. x 48 inches. The connection detail for this specimen was different from Test 3, which also only used an overlap, because it did not use wire tape to cut the overspray on the supports. Another difference was that a primer was used to increase the bond strength between the concrete and the polyurea. The primer required a 12 to 24 hour drying time before the wall was sprayed. The polyurea was allowed to cure for 10 days before it was tested. The target impact velocity for the test was equal to 13.1 ft/sec (4 m/sec). Figure 6.37 shows the wall prior to the test.

Figure 6.37: Test 6- prior to test

The actual average impact velocity was equal to 12.7 ft/sec (3.9 m/sec) and the time spread between initial and final BG impact was 0.64 msec. The impulse delivered to the specimen by the BG impacts was equal to 119 psi-msec. This impulse imparted an initial midspan velocity equal to 15.2 ft/sec according to the differentiated displacement data. The peak midspan displacement of the wall due to this velocity was equal to 14.2 inches. The wall at peak displacement is shown in frames taken from the black and white camera and color camera in Figure 6.38.

The behavior of the wall to the BG loads was recorded with the high speed cameras. Frames from the video are given for this test in Appendix C. These frames illustrate the response of the wall and the damage it suffered from the BG impacts. The polyurea responded as a one-way membrane with the concrete blocks providing mass to the system, but little or no stiffness. The video shows that two crack forms on the north face of the wall along its height immediately after impact. These cracks initiate at the top and bottom of the wall and propagate toward the walls midspan. As the wall deforms this crack widens and it can be observed that the front faces of the concrete blocks separate from the rest of the wall. The polyurea connection with the primer was successful keeping the wall attached to the supports. However, at about 170 msec after impact the bottom connection began to peel; a small portion of the polyurea debonded from the concrete as shown in Figure 6.39. The polyurea rebounded after it reached its maximum displacement and pushed the fragments of the crushed concrete blocks towards the front of the wall. No fragments of the wall were allowed to impede into the occupant space behind the wall. Figure 6.40 (a) shows the rubble from the destroyed concrete blocks.

Figure 6.40(b) shows the polyurea lining after the test. Post test inspection of the polyurea found no tears or signs of tensile failure in the lining.

Following the test calipers were used to measure the thickness of the polyurea lining at five different locations. The average thickness of the polyurea lining is 0.286 inches. The standard deviation of the thickness is 0.037 inches.

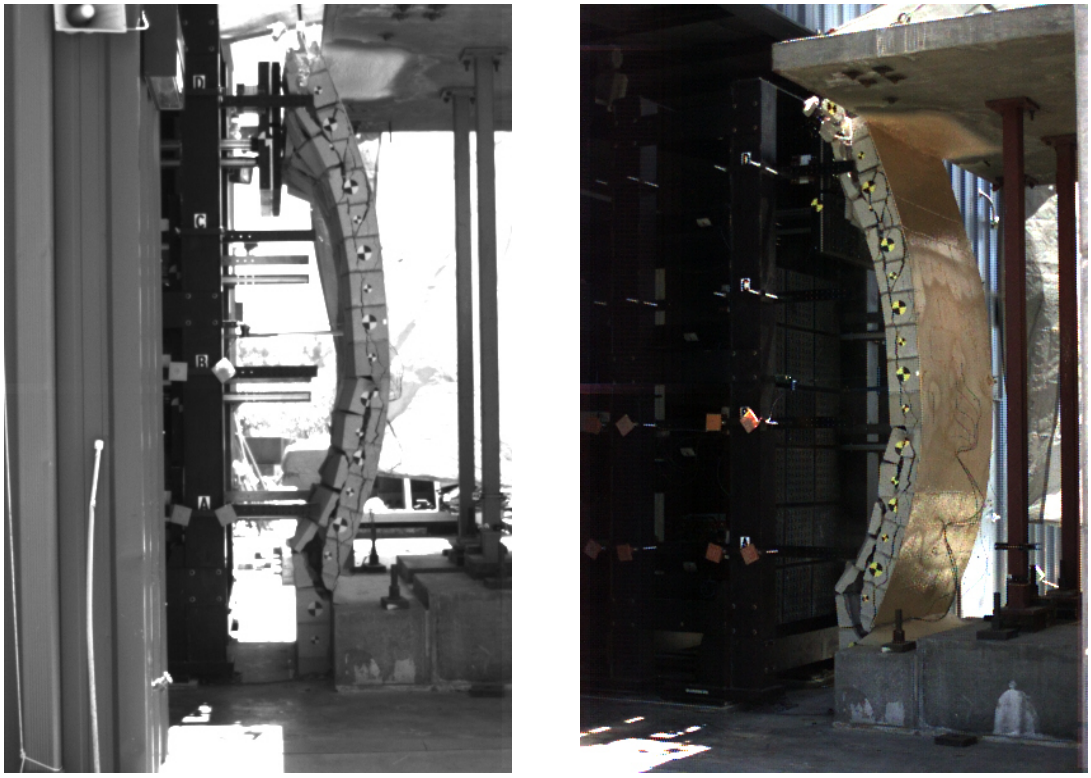

(a) **(b)**

Figure 6.38: Test 6 peak displacement; (a) black and white; (b) color

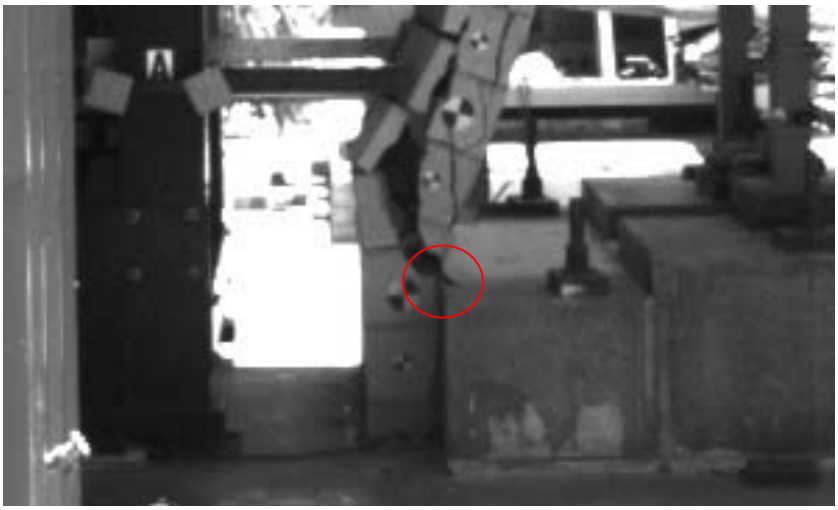

Figure 6.39: Test 6 peeling at bottom support after impact

(a) **(b)**

Figure 6.40: Test 6 post test; (a) base; (b) front of wall

TEST 7

The seventh and final URM wall test was performed on May 15th, 2006. This wall was retrofitted with a 1/4 in. layer of polyurea on its back side on May 3rd, 2006. Before the wall was sprayed the concrete supports and the concrete blocks were coated with the same primer that was used in Test 6. The primer required a 12 to 24 hour drying time before the wall was sprayed. The polyurea was allowed to cure for 12 days before it was tested. The purpose for this test was to evaluate the effectiveness of the polyurea retrofit near the capacity of the connection detail. The detail for the connection in this test was the same as Test 7. The target impact velocity of the BGs was 16.4 ft/sec (5 m/sec). Figure 6.41 shows the wall before the blast test.

Figure 6.41: Test 7 prior to impact

The actual average impact velocity for the test was equal to 17.6 ft/sec (5.4 m/sec) and the time spread between initial BG impact and final BG impact was equal to 1.50 msec. The BGs in the test delivered an impulse to the specimen equal to 142 psi-msec.

This impulse caused the specimen to have an initial velocity at the midspan equal to 17.9 ft/sec which resulted in a peak midspan displacement equal to 25.7 msec. Figure 6.42 displays the wall when it reached its peak velocity from two different perspectives.

The behavior of the wall due to the impacts is illustrated with frames from the high speed videos in Appendix C. The video shows cracks on the north face of the wall that initiated at the top and bottom of the wall. These cracks exist through the entire width of the wall and cause the front face of the concrete blocks separate from the rest of the wall. The polyurea behaved primarily as a tension membrane with the concrete blocks adding mass and little or no stiffness. The connection detail was successful in keeping the wall and polyurea attached to the top and bottom support. However, peeling did initiate at the bottom support around 75 msec after the initial contact. This peeling continued until the wall reached its maximum displacement and began to rebound. Post inspection of the specimen found that 9-12 in. of the polyurea overlap peeled off the footing before the wall began to rebound. The peeled overlap can be seen in Figure 6.43. The top overlap area of polyurea remained connected to the support throughout the entire test. Following the test it was observed that the fragments of the destroyed wall were pushed in front of the wall as shown in Figure 6.44. All fragments were prevented by the polyurea from entering the occupant area behind the wall. Figure 6.44 also displays the polyurea lining after the test; no tears or signs of failure were observed. Only the back faces of the concrete blocks remained attached to the wall except for one block.

Following the test calipers were used to measure the thickness of the polyurea lining at five different locations. The average thickness of the polyurea lining is 0.303 inches. The standard deviation of the thickness is 0.010 in..

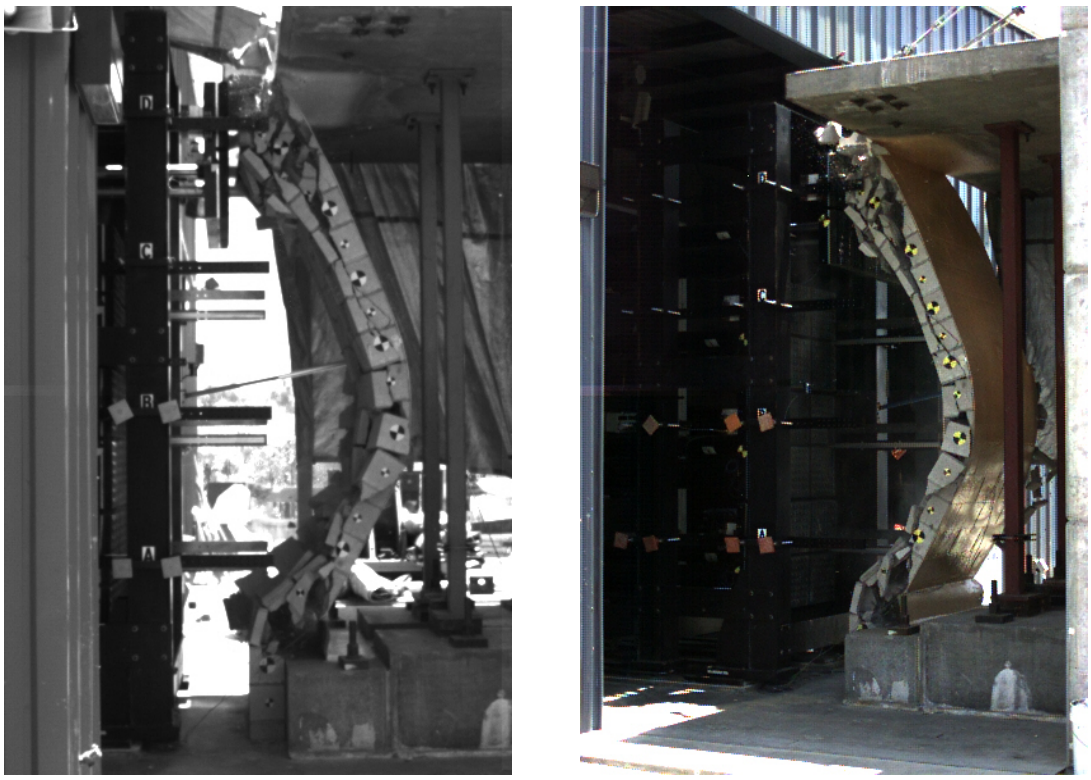

(a) **(b)**

Figure 6.42: Test 7 peak displacement; (a) black and white camera; (b) color camera

Figure 6.43: Test 7 peeling overlap at bottom support

Figure 6.44: Test 7 wall post test

SUMMARY OF EXPERIMENTAL RESULTS

Table 6.6.6 summarizes the results from the blast simulator tests on the URM walls with and without polyurea lining. The table lists the average impact velocity, impulse delivered by the BGs to the specimen, the peak midspan displacement and the details of the wall and its connection to the supports.

Table 6.6.6: Summary of URM Test Results

Test	Average Impact Velocity [ft/sec (m/sec)]	Impulse [psi-msec]	Peak Displacement [in]	Details
1	26.5 (8.08)	216	collapse	as-built, 56 in. wide
2	20.0 (6.11)	152	collapse	as-built, 48 in. wide
3	19.9 (6.08)	163	collapse	retro, 48 in wide, no anchors, without primer
4	13.6 (4.15)	130	4.6	retro, anchors
5	20.1 (6.11)	169	25.2	retro, anchors
6	12.7 (3.87)	119	14.2	retro, 48 in wide, no anchors, with primer
7	17.6 (5.39)	142	25.7	retro, 48 in wide, no anchors, with primer

The results from Test 1 demonstrated that the width of the specimen should be equal to the width of the impact masses. Test 2 was used for comparison with an unretrofitted wall. This as-built URM wall was subjected to an impulse of 152 psi-ms which resulted in complete failure with an extensive debris field. In Test 3, a URM wall with a 1/4 in. thick polyurea overlay was subjected to a 163 psi-ms impulse which resulted in a ‘peeling’ failure of the connection between the polyurea and the supports. Test 4 addressed the connection detail by strengthening it using Simpson Strong-Tie angles. This specimen was subjected to an impulse of 130 psi-ms which resulted in a maximum wall displacement of 4.6 in. with no debris field beyond this value. In Test 5,

with use of the connection detail of Test 4, the loading was increased to 169 psi-ms which resulted in a maximum wall displacement of 25.2 inches. There was no debris field beyond the maximum value of displacement; however occupants should avoid placing desks or chairs within this range of displacement to avoid injury. For Test 6, the specimen supports were coated with a primer prior to being sprayed with the polyurea. This was done to increase the strength of the connections without adding any invasive hardware to the supports. The impulse load here was 119 psi-ms which resulted in a maximum wall displacement of 14.2 in. with no debris field beyond their value. A small amount of the polyurea overlap peeled away from the supports during test. In Test 7, the impulse to the Test 6 configuration was increased to 142 psi-ms; this resulted in a maximum wall displacement of 25.7 inches. Significant peeling of the overlaps at the supports was observed, but did not lead to a catastrophic collapse. There was no debris field beyond the maximum value of displacement; however occupants should avoid placing desks or chairs within this range of displacement to avoid injury.

6.4 FE ANALYSIS

6.4.1 MODEL DESCRIPTIONS

Three dimensional finite element simulations were performed with LS-DYNA to model the blast simulator tests on selected experiments in the URM test series. The FE analysis modeled the BG impacts on the specimen by giving the impact masses an initial velocity and using contact surfaces to transfer the momentum from the plates to the specimen. Figure 6.45 illustrates the FE simulation for an as-built URM wall. The figure displays the wall being impacted by the BG plates along with the reactions at the top and bottom. The slab at the top was modeled with a contact surface between the CMU elements and concrete elements that were fixed to prevent translation in all three directions. The base footing was also modeled with solid elements that had their three translational degrees-of-freedom fixed. The first three CMU blocks at the base reacted to the footing with a tied contact surface.

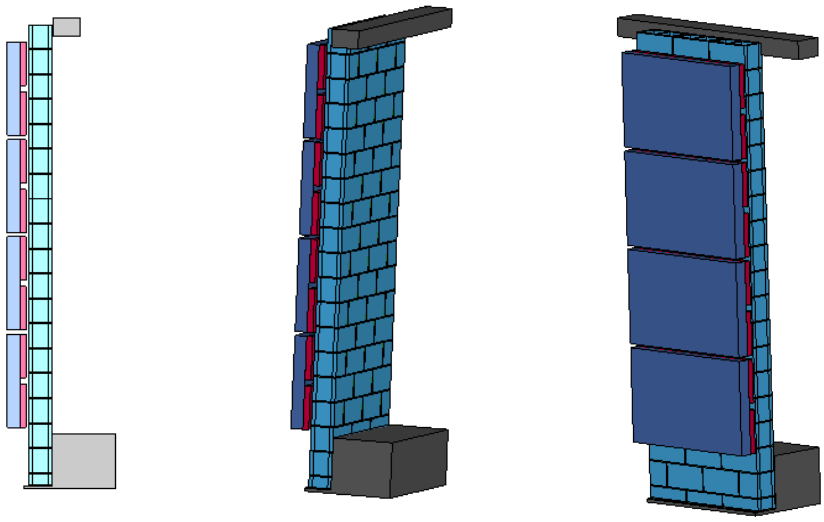

Figure 6.45: FE model of as-built URM wall

The BG impact masses were modeled in the FE analysis as rectangular plates with the programmer pads on the impact face. The programmer model included the pyramidal texture as shown in Figure 6.46. The impact was modeled with *AUTOMATIC-SURFACE-TO_SURFACE contact using the SOFT option number 1. The material model for the programmers was the *MAT_057 which was used in Chapters 3, 4, and 5. The SHAPE parameters of this model in the analysis here was set equal to five and HU was set equal to 0.05. The aluminum impact masses were modeled with a linear elastic material model. The BG rods which contribute mass to the total momentum delivered to the specimen were included in the model by increasing the thickness of the aluminum plates.

Unreinforced masonry block walls are constructed from concrete blocks and mortar. Figure 6.47 illustrates the walls that were studied in the experiments; included in the figure are labels for the different components of the block and the mortar. Each block has a front face shell, three webs, and a back face shell. In the as-built wall model the interface between each of these components was modeled with a tiebreak contact surface. This was done to simulate the brittle failure that occurs when the wall is load. Tiebreak contact surfaces were also included between the CMU blocks and the vertical and horizontal mortar joints. The failure criteria for the interface between the mortar joints and the block were equal to 200 psi in the normal direction and 350 psi in the shear direction. The interface between the face shells and the webs of the block had failure criteria equal to 75 psi in the normal direction and 75 psi in the shear direction. The failure criteria equation calculates the square shear stress divided by the shear strength

plus the square of normal stress divided by the normal strength and if the value is greater or equal to unity the tied surface is released and becomes a surface to surface contact.

The material model used for the CMU blocks and the mortar in the as-built and retrofit FE models is the modified version of *MAT_72_R3 that was used in Chapter 4. The strength of the CMU block and the mortar for each test are equal to the strengths listed in Table 6.3 and Table 6.4. The weight density used for the CMU blocks was about 130 lb/ft^3 and for the mortar it was equal to 110 lb/ft^3.

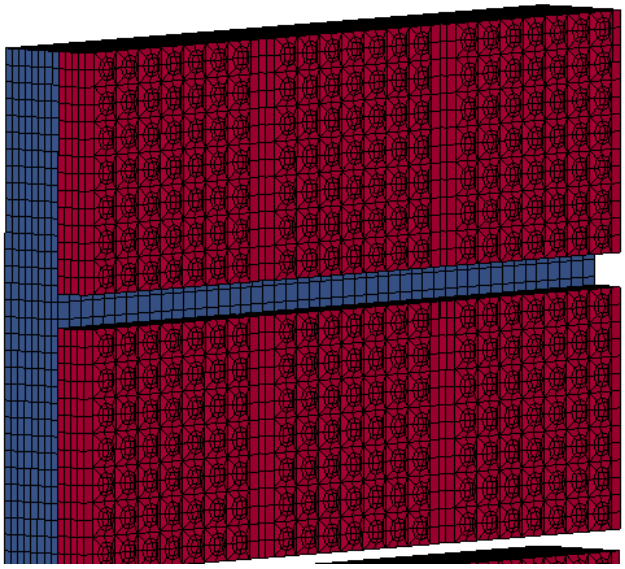

Figure 6.46: FE model of BG mass and programmer

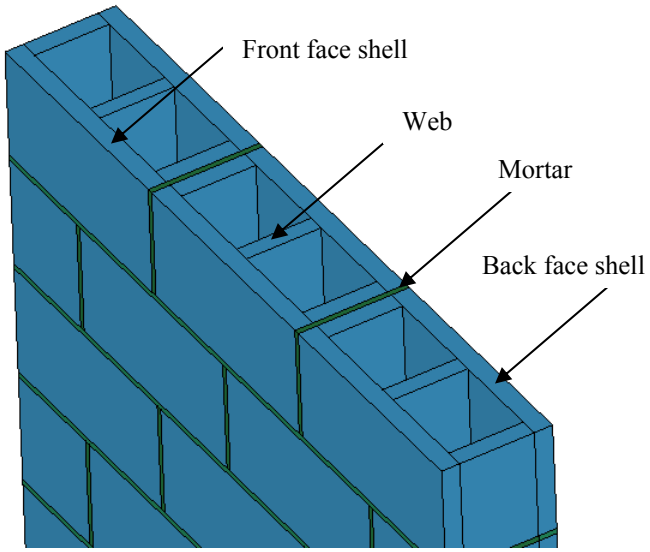

Figure 6.47: URM wall block terminology

One analysis was run to compare the FE model to the results from Test 4. For Test 5 three different analyses were run. This was done to determine the most appropriate method for modeling the contact condition between the polyurea and the supports. An illustration of the model used to simulate the BG impacts on retrofit walls in Test 4 and Test 5 is displayed in Figure 6.48. This figure shows that the boundary conditions for the simulations are similar to the FE model for the as-built walls. In Test 4 and the first simulation for Test 5 the full slab was modeled including the rebar. In the second and third simulation for Test 5 the top slab was replaced with a smaller boundary condition to reduce the time of the simulation.

The polyurea used in the simulation of Test 4 and the first and second simulation of Test 5 was modeled with membrane elements that were tied to the back side of the CMU blocks. In the third simulation of Test 5 the polyurea was modeled with shell elements. The individual components of the model are shown in Figure 6.49. The

polyurea shells were modeled with *MAT_PIECEWISE_PLASTICITY. The density of the polyurea used in the model was equal to 0.04 lb/in^3 and the modulus of elasticity was 47,600 psi. The yield strength was set to 1975 psi, the tangent modulus was 834 psi and a failure strain equal to 96% was also input. These parameters were set to match the material test data measured in the experimental portion of this chapter.

The Simpson Strong-Tie angles were also modeled in the FE simulation. displays the shell elements associated with the angles in the color green. The material model used for these angles was linear elastic. The thickness of the angles used was about 0.08 in. and the polyurea was bout 0.25-0.3 in. thick. In order to model shells of the different materials with equal thicknesses the modulus of elasticity of the steel angles was reduced to give an equivalent axial stiffness as the actual angle. Therefore, the angle was modeled with a thickness equal to 0.30 in. and a modulus equal to 9666 ksi.

The connection of the polyurea to the supports in the modeled for Test 4 was assumed to be fully fixed. Therefore the nodes of the shell elements were tied to the concrete elements. In the simulation for Test 5 three different models were used to simulate the connection to the supports: the first was the same as Test 4 where the nodes were tied to the supports; the second was to use a surface to surface tiebreak with shell elements; the third was to use a surface to surface tiebreak with membrane elements. In the case when the tiebreak contact surfaces were used the tiebreak was defined only from the back of the wall to 6 in. behind the wall at the location of the anchors. The anchors were not modeled explicitly, but were accounted for by assuming that the polyurea and

angles at their location and in the direction away from the wall were tied to the concrete with a surface that was unable to fail.

The mesh details for the walls with the retrofit are shown inFigure 6.50. This mesh demonstrates that there are two elements through each face shell thickness and 10 elements through the thickness of the wall. This mesh without the polyurea is similar for the simulation of the as-built wall from Test 2.

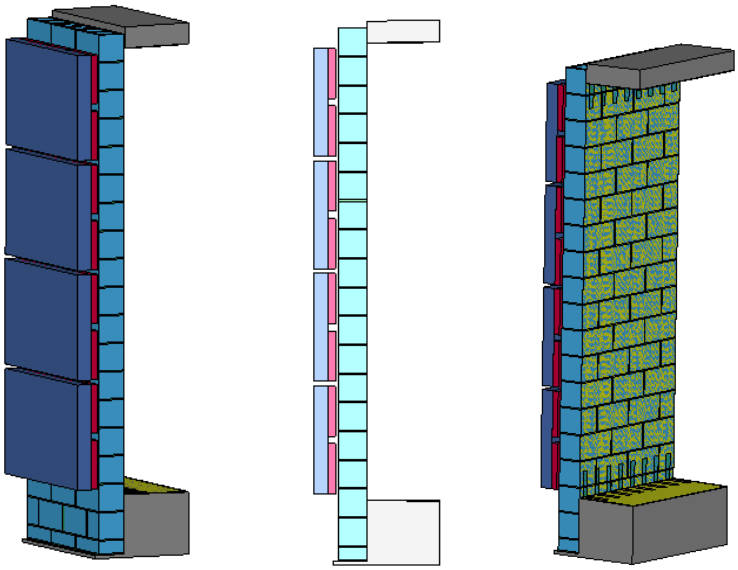

Figure 6.48: FE model of URM wall with polyurea

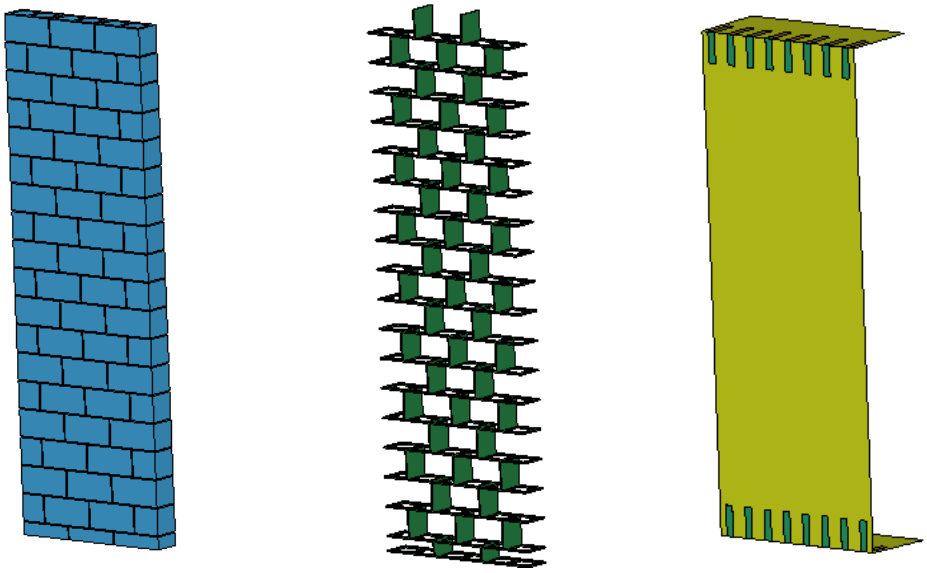

(a) (b) (c)

Figure 6.49: Individual CMU components: (a) CMU block; (b) mortar; (c) polyurea

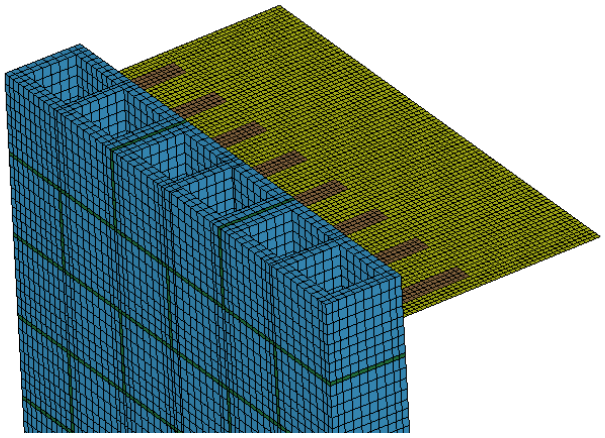

Figure 6.50: CMU Mesh

6.4.2 COMPARISON OF FE ANALYSIS AND TEST 2

The FE simulation of the as-built wall is compared to the results from the second test of the URM test series. The FE model for the as-built wall used contact surfaces to

simulate the failures at the mortar joints and between the web and face shell elements for the CMU block. Table 6.7 lists the impulses delivered by the BGs for the experiment and the analysis. It demonstrates that the overall average impulse predicted by the model using the selected programmer material parameters is within 3.6% of the test results. Another comparison made between the model and the results was for the initial velocity after impact. It is not practical to compare displacements for this test because the walls failed; therefore the velocities were chosen instead. Figure 6.51 compares the velocity time histories for both the model and the experiment. The plot shows that the model slightly over predicts the initial velocity by about 10%.

The damage observed in the test is compared to the damage predicted in the model in Figure 6.52 and Figure 6.53. In these figures the model is plotted with damage fringes that range between 0 and 2 where a value greater than zero corresponds to the onset of inelastic response in the masonry a value equal to unity corresponds to peak strength in the masonry and a value of two corresponds to the residual strength in the material Figure 6.52 demonstrates that the model is able to capture the initial cracking that was captured by the high speed video immediately following impact by the BGs. Figure 6.53 demonstrates that the model is capable of predicting the failure at the mortar joints and the damage near the supports. The model, however, was not capable of predicting the fragmentation of the CMU blocks at the interface between the webs and the face shells.

Table 6.7: Comparison of impulse for Test 2 and FE analysis

BG	BG Velocity [ft/sec]	Exp Impulse [psi-msec]	FE Impulse [psi-msec]
4	19.8	155	162
3	20.6	138	153
2	20.0	141	145
1	19.8	175	171
Average	20.1	152.3	157.8

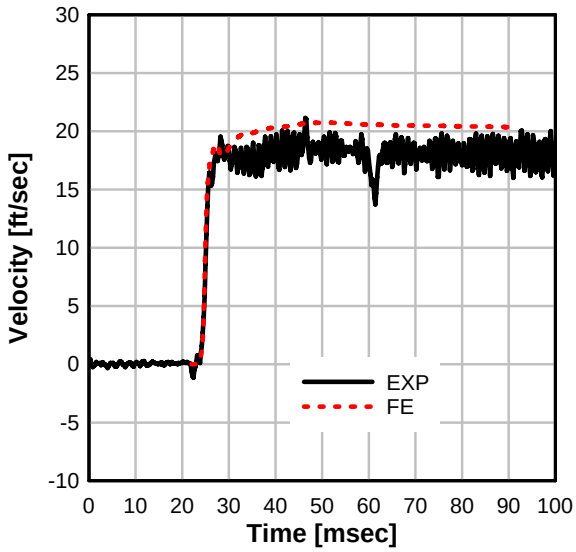

Figure 6.51: Comparison of velocity Test 2 and FE analysis

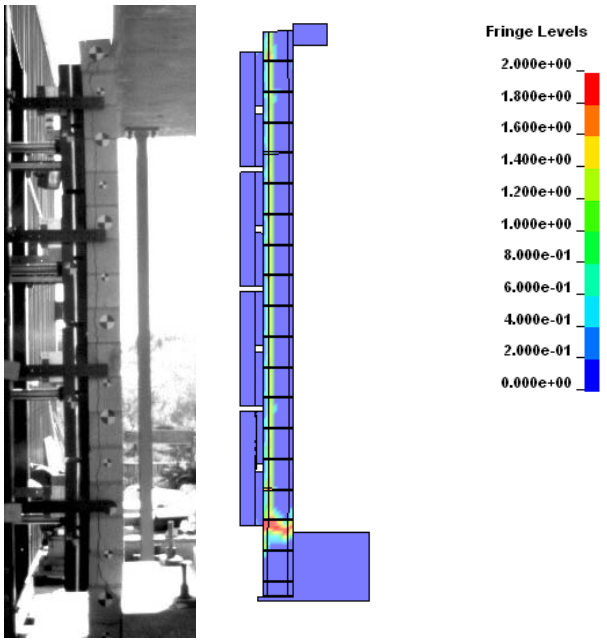

(a) **(b)**

Figure 6.52: Damage for Test 2 after impact (a) Experiment; (b) FEA

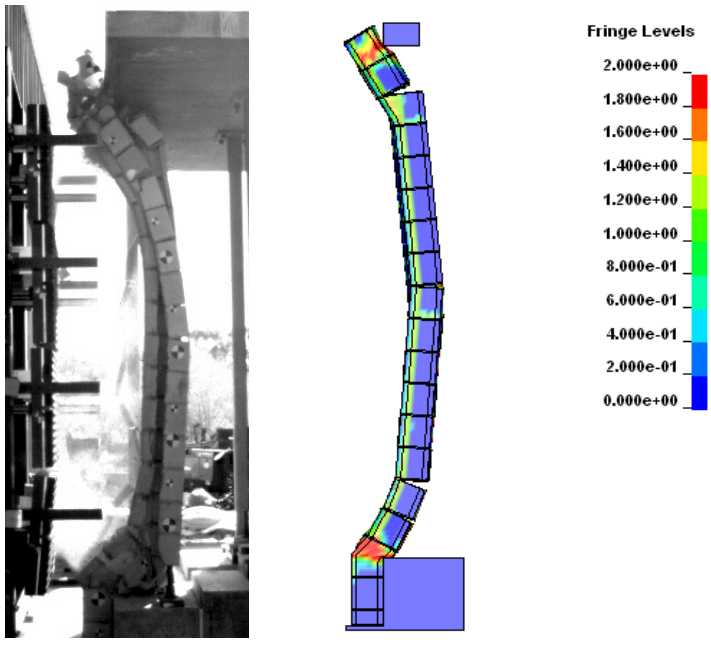

(a) **(b)**

Figure 6.53: Damage for Test 2 at peak displacement (a) Experiment; (b) FEA

6.4.3 COMPARISON OF FE ANALYSIS AND TEST 4

The FE analysis of Test 4 was performed using a model that used solid elements to represent the CMU block and mortar and membrane elements for the polyurea. Unlike the simulation of Test 2, no tiebreak surfaces were used to model failure at the mortar joints or interface between the block face shells and webs. Instead the CMU block elements and the mortar elements were merged and it was assumed that the failure at the joints is modeled sufficiently by the material behavior. The membrane elements used to model the catcher system were fixed at the top and bottom support based on the assumption that the anchorage system prevented any peeling behavior. The impulse delivered in the analysis is compared to the experiments in Table 6.8 which shows that the model was with in 7% of the results. A plot of the initial velocity at the midspan after impact for the analysis and the experiment is displayed in Figure 6.54 and a comparison of displacement time histories is shown in Figure 6.55. These plots demonstrate that response predicted by the model was in good agreement with the results. The peak displacements were within 8% of each other. The peak initial velocity of the FE analysis was reasonably greater than the test result, but over time the velocities matched well.

Comparison of damage shown in Figure 6.56 demonstrates that the model was able to predict the localized damage near the supports. In the experiment it was observed that the initial cracking after impact did not propagate along the whole height of the wall. Figure 6.56 illustrates that the FE model also predicts that this crack will not propagate along the entire height.

Table 6.8: Comparison of impulse for Test 4 and FE analysis

BG	BG Velocity [ft/sec]	Exp Impulse [psi-msec]	FE Impulse [psi-msec]
4	13.1	141	110
3	14.4	117	126
2	13.1	86	96
1	13.9	175	151
Average	13.6	129.8	120.8

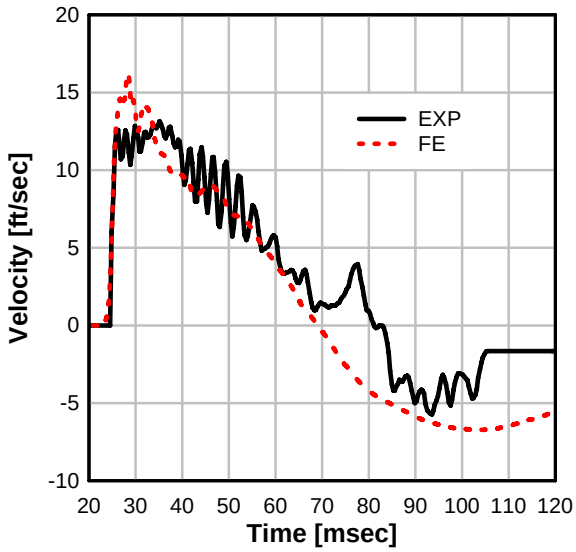

Figure 6.54: Comparison of velocity Test 4 and FE analysis

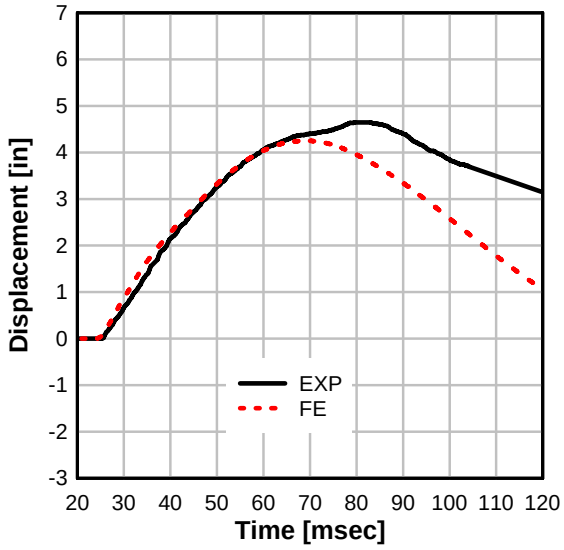

Figure 6.55: Comparison of displacement Test 4 and FE analysis

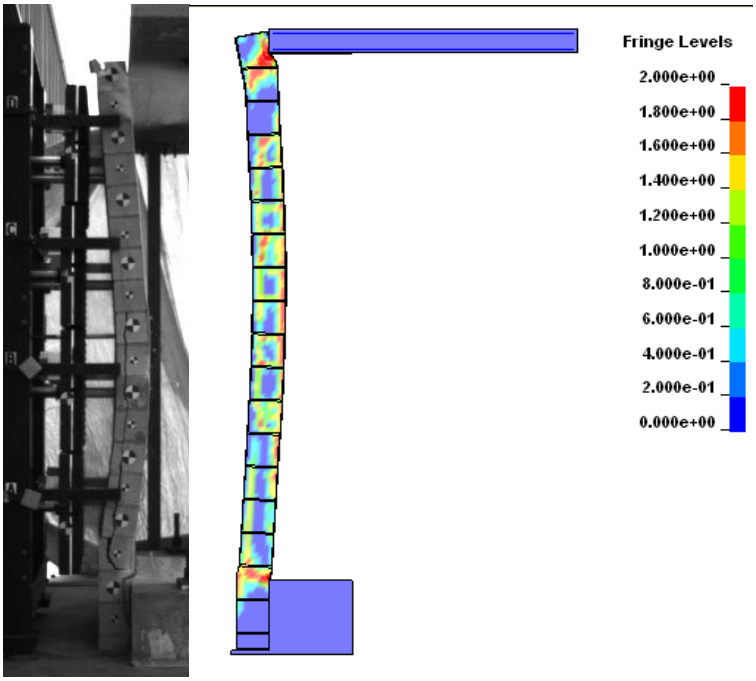

(a) **(b)**

Figure 6.56: Comparison of damage for Test 4; (a) experiment; (b) FE analysis

6.4.4 COMPARISON OF FE ANALYSIS AND TEST 5

Finite element analysis was also performed on models that simulate the response of the wall in Test 5 to the BG impact loads. Three different models were run and compared to this Test 5. Initially, the model used was similar to the model for Test 4 where the polyurea used membrane elements which were fixed to the supports. The results of this analysis matched the impulse delivered to the specimen by the BGs as shown in Table 6.9. The initial midspan velocity calculated by the model also matched the results of the test (Figure 6.57). There is, however, a significant discrepancy between the peak displacement of the model and the experiment. Figure 6.58 displays a comparison of the displacement time history which shows that the model under-predicts the displacement.

Comparisons of damage in Figure 6.59 and Figure 6.60 show that the model matches the experiment at early times, but as the displacement increases the experiment had significant amounts of fragmentation that is not included in the model. The inability of the model to generate CMU block fragments could be one reason that the model under-predicts displacement because in the actual experiments when the blocks undergo a brittle failure they do not contribute any additional stiffness to the system. Whereas when the elements fail in the FE analysis they are still merged to neighboring elements and may constrain the mesh resulting in some residual stiffness. Another cause for the lower displacements in the model is that peeling at the supports was not considered. The anchors are located 6 in. behind the wall. This offset can result in an extra 12 in. length

of polyurea during membrane action. Also when the wall shears at the supports the wall can translate an additional 6 in. before tension membrane behavior is engaged.

The results from the first analysis led to two additional models that were run and compared to the results from Test 5. In both models the length of polyurea between the back of the wall and the locations of the anchors was connected to the supporting member with the *AUTOMATIC_SURFACE_TO_SURFACE_TIEBREAK that is available in LS_DYNA. The anchors were not modeled explicitly, but instead all of the nodes of the polyurea elements at the location of the anchors and in the direction away from the back of the wall were fixed so that they could not translate. The difference between the second and third model that was analyzed was that the second one used membrane elements for the polyurea, while the third model used shell elements.

Table 6.9: Comparison of impulse for Test 5 and FE analysis

BG	BG Velocity [ft/sec]	Exp Impulse [psi-msec]	FE Impulse [psi-msec]
4	18.2	136	151
3	20.3	188	162
2	20.6	128	153
1	21.3	226	193
Average	20.1	169.5	164.8

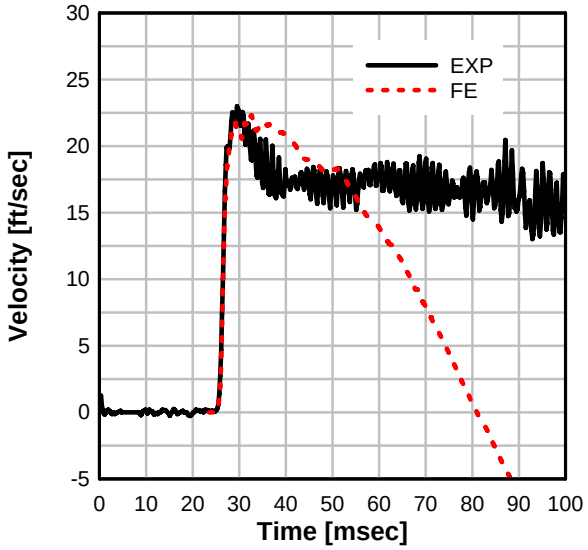

Figure 6.57: Comparison of velocity Test 5 and FEA 1

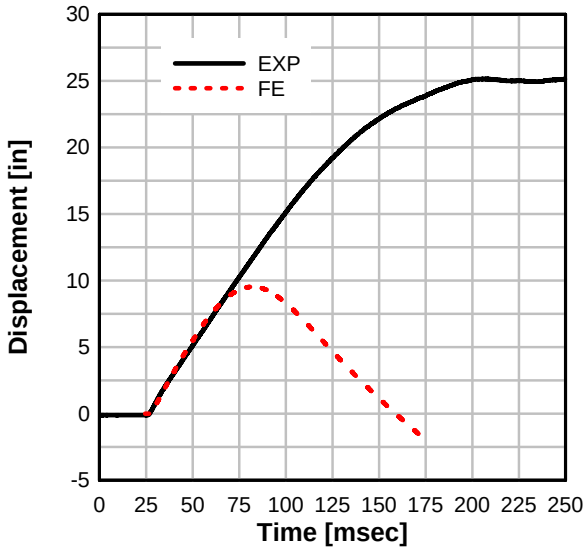

Figure 6.58: Comparison of displacement for Test 5 and FEA 1

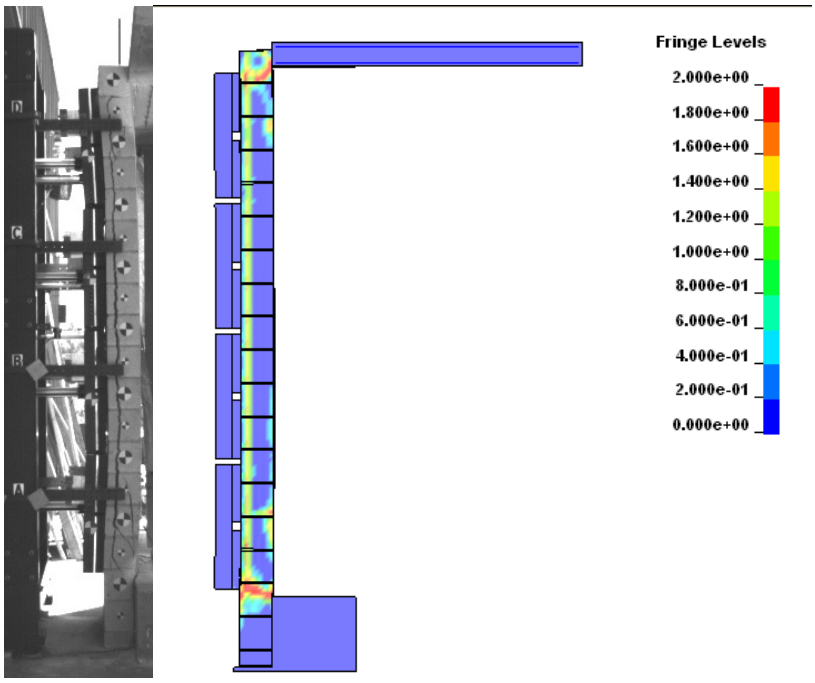

(a) **(b)**

Figure 6.59: Damage for Test 5 after impact (a) experiment; (b) FEA 1

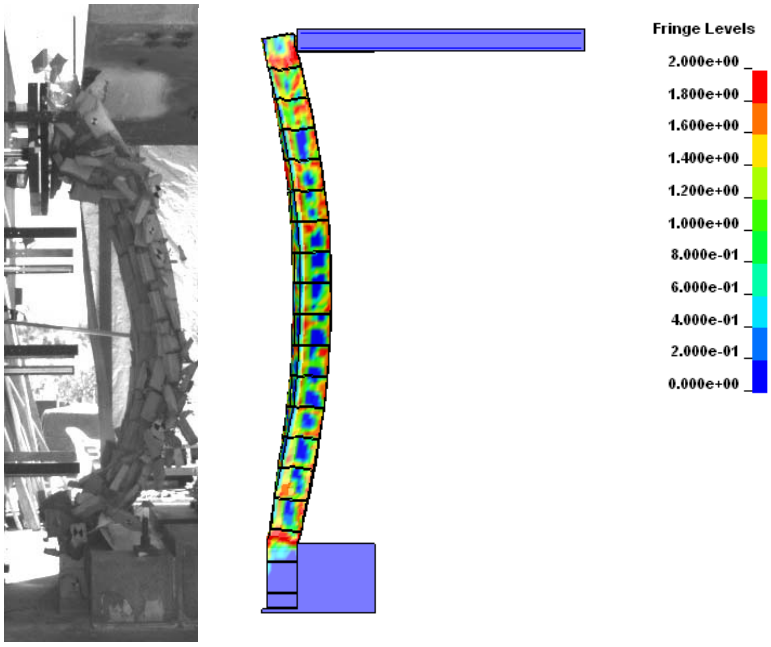

(a) **(b)**

Figure 6.60: Damage for Test 5 at peak displacement (a) experiment; (b) FEA 1

Velocity time histories and displacement time histories for the second model and Test 5 are displayed in Figure 6.61 and Figure 6.62, respectively. It can be observed that the initial velocity prediction is in good agreement with the experiment, but the peak displacement is still much smaller. The displacement, however, is more than double the displacement predicted by the first model with fixed connections. The damage predicted by the second model as shown in Figure 6.63 is very similar to the damage for the first model except in the second model the elements near the supports are severely distorted. The large distortions are now present because the polyurea is peeling. A comparison of the peeling at the top support for the model and the experiment are displayed in Figure 6.64. This figure shows that the membrane elements in the model do exhibit peeling, but are also very irregular looking. Review of the analysis showed that the irregular behavior of the membrane elements occurred when the tiebreak criteria failed and the nodes pulled away from the concrete supports. When this occurred the membranes were initially given a compressive force which caused them to “wrinkle”. As the wall continued to translate in the direction of the displacement the distorted membrane elements exhibited a behavior that can best be described as “looping” through each other. These behaviors were not observed in the Tests and are non-physical. Therefore an analysis with shell elements was also run.

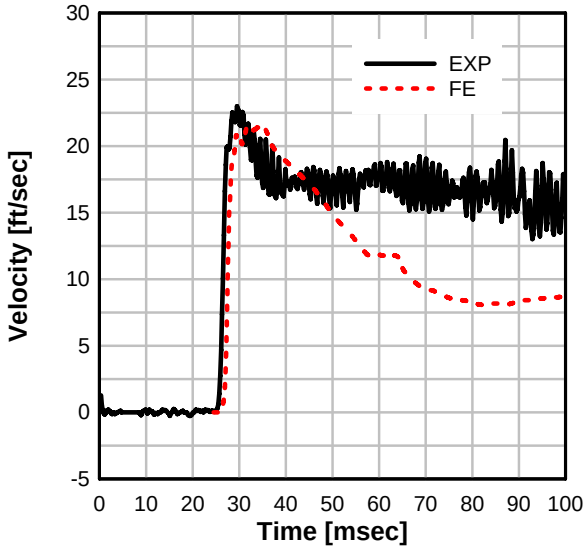

Figure 6.61: Comparison of velocity for Test 5 with FEA 2

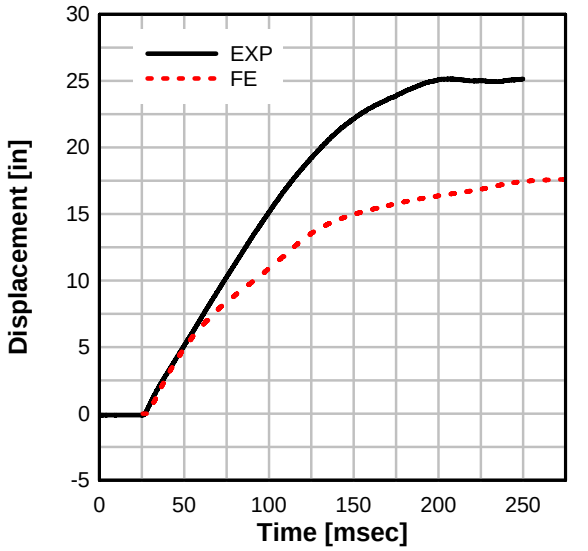

Figure 6.62: Comparison of displacement for Test 5 and FEA 2

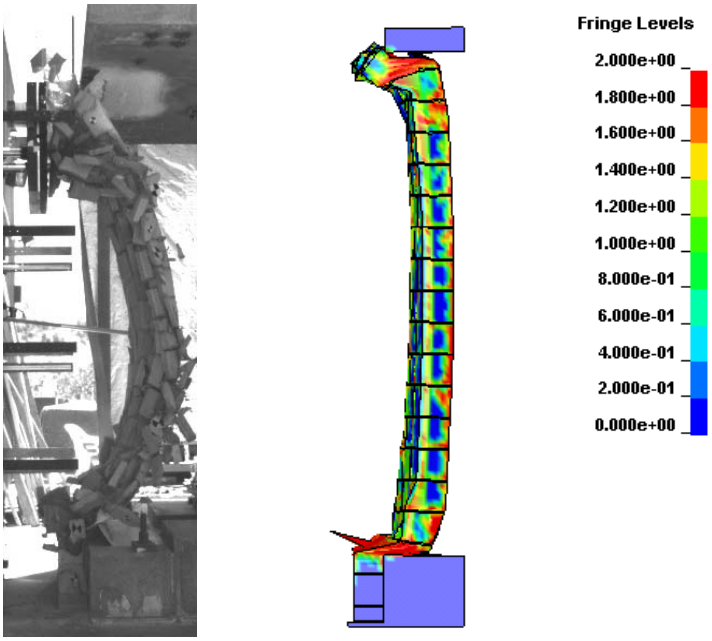

(a) **(b)**

Figure 6.63: Damage for Test 5 at peak displacement; (a) experiment; (b) FEA 2

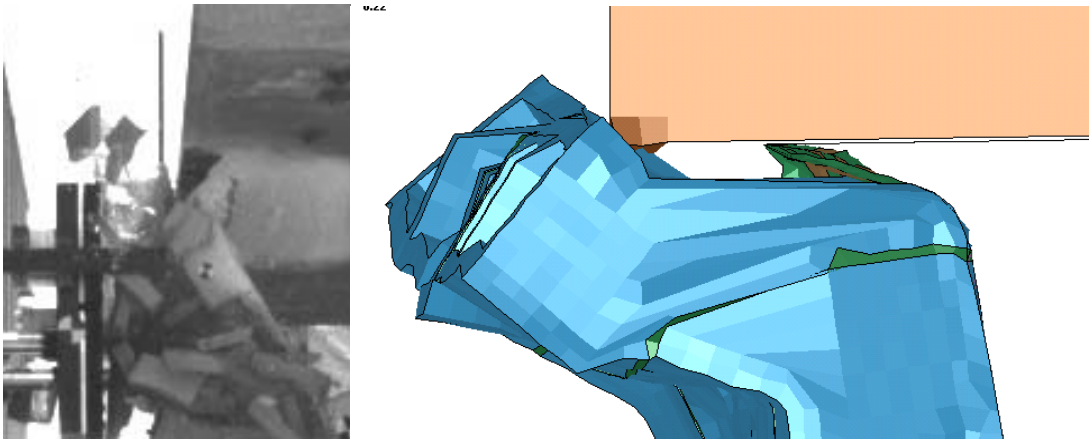

(a) **(b)**

Figure 6.64: Damage for Test 5- peeling at top; (a) experiment; (b) FEA 2

A comparison of the third FE model, which had a tiebreak contact surface at the supports and used shell elements for the polyurea, with the test results is displayed for velocity in Figure 6.65. Midspan displacement time histories are shown for the model

and the experiment in Figure 6.66. The comparison is similar to the other two models where the initial velocity of the wall in the simulation matches the results of the experiment while the peak displacement is significantly under-predicted. The peak displacement for the third model is 13.6 in. which is lower than the second model and greater than the first model. The damage predicted by the model is compared to the results in Figure 6.67 and the peeling behavior seen in the mode and the experiment is illustrated in Figure 6.68. In the third model the peeling is initiated, but as shown in Figure 6.68, the corner where the polyurea on the wall meets the polyurea overlap is an area that may be overly stiff. In the experiments this corner maintained its shape throughout much of the wall response, but eventually it began to "straighten" out. The inability of the model to capture the "straightening" behavior may be a cause for lower predicted displacement.

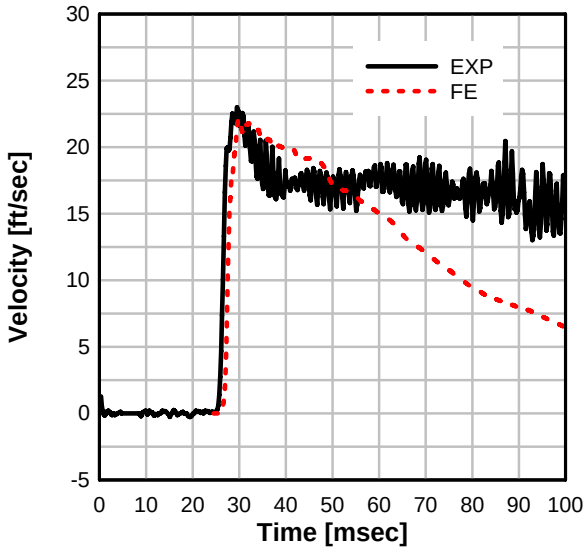

Figure 6.65: Comparison of velocity for Test 5 and FEA 3

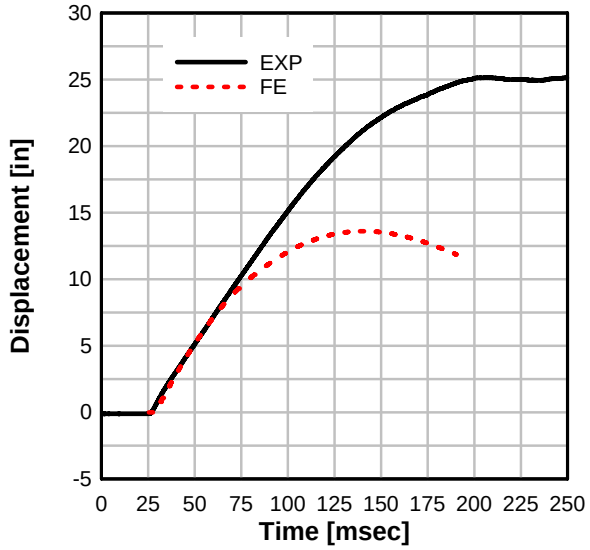

Figure 6.66: Comparison of displacement for Test 5 and FEA 3

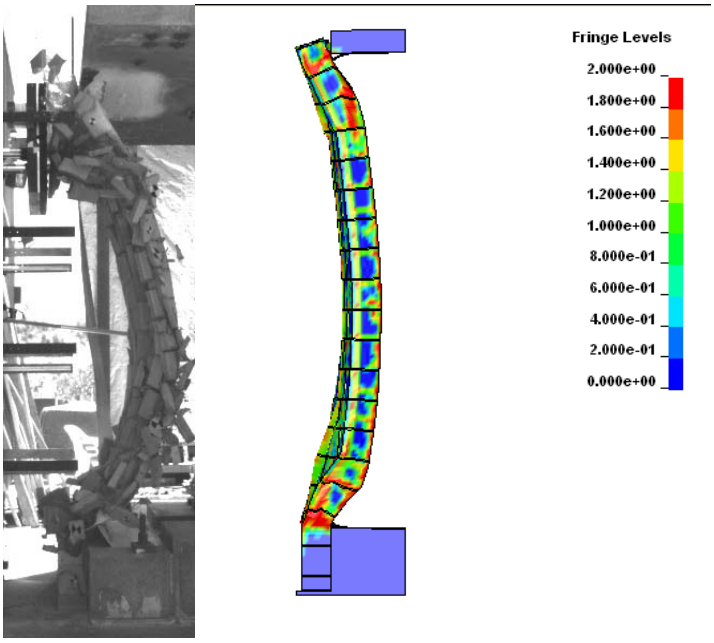

(a) **(b)**

Figure 6.67: Damage for Test 5 at peak displacement; (a) experiment; (b) FEA 2

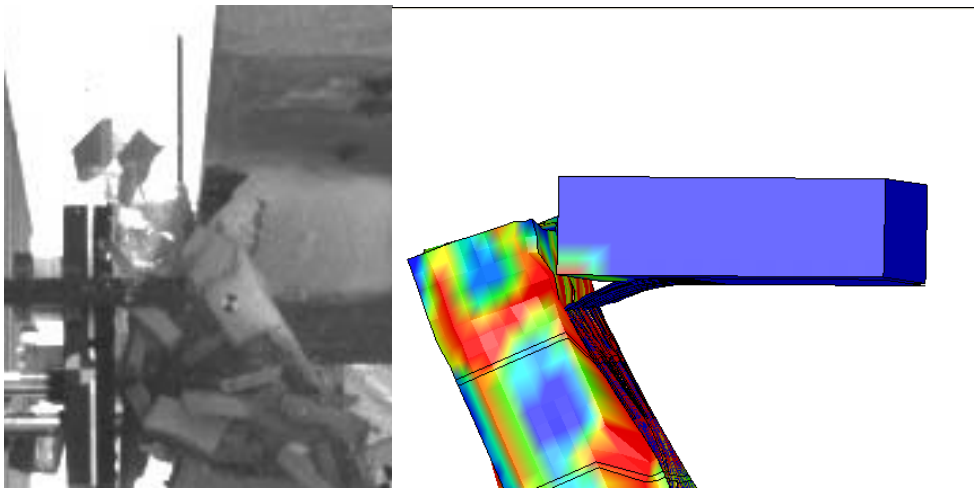

Figure 6.68: Damage for Test 5- peeling at top; (a) experiment; (b) FEA 2

6.4.5 SUMMARY OF FE ANALYSIS

Finite element analyses were performed to simulate the results from Test 2, Test 4, and Test 5. The results from the analysis demonstrate that the numerical tools used can accurately predict the response of the URM walls with and without polyurea lining to blast simulator impact loads given that the wall is not completely destroyed in the test. The case of a wall retrofitted with polyurea that suffered catastrophic damage was simulated using three different models. The results of these analyses illustrated several issues associated with the modeling of complex behaviors; in this case brittle failure and peeling. It is recommended that further research be conducted to study these problems.

The other tests in the URM test program that were not modeled in the section also exhibited brittle fracture and peeling at the supports. In these cases there were no anchors present to arrest the peeling before catastrophic failure. The data from these tests could

also be used to develop a model that could predict when complete loss of adhesion between polyurea and concrete occurs. Based on the numerical work performed thus far it is likely that any model that characterizes the peeling behavior will be sensitive to uncertain parameters that govern the behavior. These parameters may also be highly variable depending on the degree of surface preparation prior to application of the polymer.

6.5 DESIGN OF URM WALLS WITH POLYUREA CATCHER SYSTEMS

Simple methods are required by engineers to design polyurea catcher systems for URM walls subject to blast. The experimental work conducted with the blast simulator along with the supporting finite element analysis demonstrated that the behavior of URM walls with polyurea catchers is difficult to characterize with simple analysis methods. One reason for this is that response of the wall is highly dependent on local behavior of the CMU blocks during initial loading. In some instances the pressure pulse that propagates through the wall when the blast wave arrives can produce a brittle failure in the blocks and the wall loses any capacity to resist the blast in bending. For this case the polyurea catcher will resist the entire load with tension membrane action. In other loading situations the blocks do not crack from the initial pressure pulse and the wall contributes to the resistance of the blast load through composite action between the block and the polyurea. These different behaviors depend not only on the loading parameters, but also the material properties, which may vary significantly. This results in a response that is very difficult to predict.

Another behavior that makes it difficult to develop simple models for URM with polyurea catchers is peeling at the supports. This behavior is nonlinear and requires accurate estimates of the adhesion properties of the polyurea to the concrete. The experimental work with the blast simulator demonstrated that these properties are dependent on surface preparation of the concrete, which requires a level of quality control that may be difficult to implement in real life applications. These difficulties will be considered in a method presented herein for the design of a polyurea catcher system.

In the design of the polyurea catcher system the engineer requires the peak displacement, the tensile force that develops in the polyurea, and an estimate of the connections strength. An energy method is presented here to estimate the peak displacement demand required by the tension membrane to resist the blast load. This method assumes that the URM wall is loaded impulsively, meaning that the mass of the wall is given an initial velocity and is then allowed to respond without any further external load. The negative phase of the blast load is ignored which is conservative because it will most likely do work against the mass before it reaches the peak displacement. When the wall rebounds the negative phase could fail the front face of the block, but this is not a concern because this type of failure will occur in the direction away from the building occupants. The energy method assumes that the retrofitted URM wall is estimated as an SDOF system. The method equates the kinetic energy delivered to an equivalent mass from the blast to the strain energy in the tension membrane, which is determined with a resistance function for the polyurea tension membrane. The method assumes that the wall does not contribute to the resistance function and only adds mass to

the system. The method also does not account for any energy dissipation that occurs when the CMU blocks fail due to the initial pressure pulse propagating through the wall. The energy dissipated due to peeling of the polyurea from the concrete supports is also ignored. These sources of energy dissipation are dependent on material properties that can vary significantly, therefore they were not considered. Ignoring these sources of energy dissipation is conservative because they all reduce the internal energy demand on the tension membrane which would result in a smaller peak displacement.

The energy method requires that the kinetic energy produced in the wall from the load is equal to the internal work done by the polyurea catcher system satisfying the following equation:

$$KE + W_{\text{int}} = 0 \tag{6.1}$$

The kinetic energy deposited in the URM wall from the blast loading is found with

$$KE = \frac{i_s}{2m_{eq}} \tag{6.2}$$

where i_s is the impulse of the blast and m_{eq} is the equivalent mass of the system. The internal work done by the polyurea catcher is found by integrating the resistance function with respect to the displacement as shown in the following equation:

$$W_{\text{int}} = \int_0^{\Delta} R(\Delta) d\Delta \tag{6.3}$$

where Δ in the limits of the integral is equal to the peak displacement. The suggested method for calculating the peak displacement is to first integrate the resistance function

numerically to produce a plot relating internal work to peak displacement. Then the peak displacement for energy balance can then be found graphically.

6.5.1 RESISTANCE FUNCTION

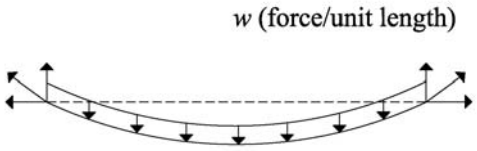

Figure 6.69: Polyurea tension membrane

The resistance function used in the energy balance is derived for a tension membrane element which has a free body diagram displayed in Figure 6.69. The assumed deformed shape for the tension membrane is defined by the following quadratic equation:

$$u = \Delta(1 - 4(\frac{x}{L})^2) \tag{6.4}$$

where the origin of the equation is taken at the midspan of the wall. The slope of the membrane along its length at a distance x is

$$\frac{du}{dx} = \frac{8\Delta x}{L^2} \tag{6.5}$$

Figure 6.70 is a free body diagram of a differential section of the tension membrane. By satisfying equilibrium for the system shown in the figure equations (6.6), (6.7), and (6.8) can be derived.

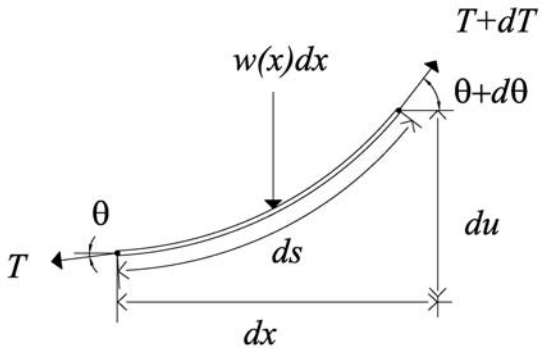

Figure 6.70: Free-body diagram of differential section

$$T\cos\theta = T_0 \tag{6.6}$$

$$T\sin\theta = w(x)x \tag{6.7}$$

$$\frac{du}{dx} = \tan\theta \tag{6.8}$$

In the formulation of the resistance function a small angle approximation is used where $\sin\theta$ and $\tan\theta$ are equal to θ. This means that $\frac{du}{dx}$ equals θ according to equation (6.8). Substitution of $\frac{du}{dx}$ into equation (6.7) for $\sin\theta$ gives a function that relates the load to the tension force in the membrane and the peak displacement. The tensile force associated with the resisted load is assumed to be constant along the length of the membrane. The tensile force can be written as stress, σ, multiplied by cross-sectional area, A, with equation (6.9). This equation can also be substituted into equation (6.7).

$$T = \sigma A \tag{6.9}$$

The final modification of equation (6.7) made by dividing both sides by the wall width, *b*. This puts the resisted load in terms of pressure. The result is the expression given by equation (6.10) which relates the pressure resisted by the tension membrane, *R*, and the displacement of the membrane, Δ.

$$R = \frac{8F_p t_{pl}}{L}\Delta \tag{6.10}$$

where F_p is the current stress in the membrane, t_{pl} is the thickness of the membrane, and L is the initial length of the membrane.

In equation (6.10) the stress in the membrane is related to the strain in the membrane with a constitutive relation for the polyurea material. Figure 6.71 is a plot which shows a bi-linear approximation of the stress-strain relation for polyurea under uniaxial tension stress.

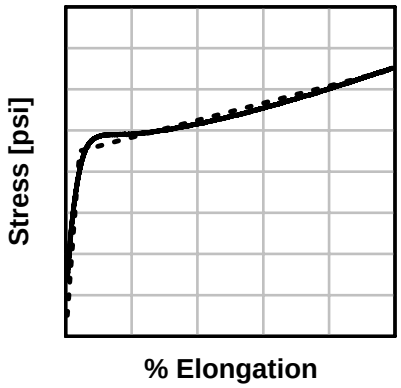

Figure 6.71: Constitutive relation of polyurea in uniaxial tension

The strain in the membrane is related to the displacement based on a compatibility equation where strain is found with:

$$\varepsilon_p = \frac{\Delta L}{L_o} \tag{6.11}$$

where L_o is the distance between the supports. The change in length, ΔL, can be found with:

$$\Delta L = s - L_o \tag{6.12}$$

The arc length of the membrane is determined from equation (6.13) given below

$$s = 2\int_0^{L/2} \sqrt{1 + \left(\frac{du}{dx}\right)^2}\, dx \tag{6.13}$$

which when evaluated with the assumed displaced shape gives

$$s = \frac{L}{2}\sqrt{1 + \frac{16\Delta^2}{L^2}} + \frac{L^2}{8\Delta}\ln\left[\frac{4\Delta}{L} + \sqrt{1 + \frac{16\Delta^2}{L^2}}\right] \tag{6.14}$$

The recommended steps required to calculate the membrane resistance function are given below:

- Choose displacement
- Calculate change in length with equation (6.14)
- Calculate strain from change in length assuming uniform strain and using equation (6.11)
- Determine stress from strain using constitutive relation, see Figure 6.71

- Determine resistance from displacement and stress with equation (6.10)
- Repeat with increased displacement

An additional recommendation for the design of polyurea catcher systems is to limit the displacement so that the polyurea does not reach its yield strain. The yield strain is approximately 5 percent, which typically results in a displacement near 15 to 20 inches. In the blast simulator tests the polyurea linings were not strained significantly past this point; therefore it is difficult to predict what the response of the system would be once the polyurea yields.

6.5.2 RESISTANCE FUNCTION WITH PEELING

For the case when the polyurea peels away from the supports, as shown in Figure 6.72, the displacement at the midspan is increased due to a translation of the support and from an increase in the total length of the membrane. This is accounted for in the energy calculation by shifting the resistance function in the direction of the positive displacement. The translation in the supports is included with a rigid body displacement, Δ_R, which is equal to the distance from the back of the wall to the location where the peeling is arrested. In a design situation this distance should be set equal to the distance to the mechanical anchors. The resistance function will also be shifted in the positive direction by a "slack" displacement Δ_s. When the length of the polyurea is increased due to the peeling the membrane will be "slack" until it reaches the displacement, denoted Δ_S, at which it begins to load. This displacement can be found by solving equation (6.14) for Δ where s_o is equal to

$$s_o = L_0 + 2\Delta_R \tag{6.15}$$

and L_o is the distance between the supports. The initial arc length, s_o, from equation (6.15) is used as the initial length in equation (6.11) when calculating the loading curve that begins when there is no more slack membrane. A depiction of a resistance function for a membrane that experiences peeling is displayed in Figure 6.73.

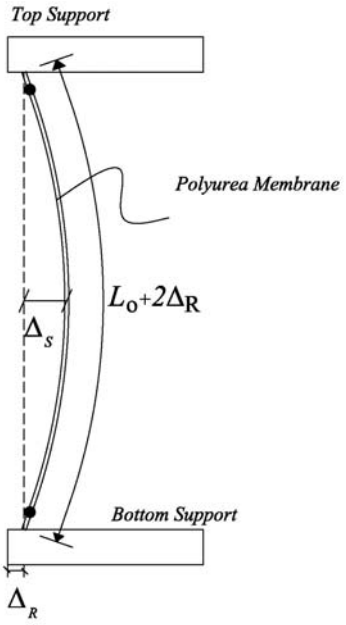

Figure 6.72: Polyurea membrane with peeling

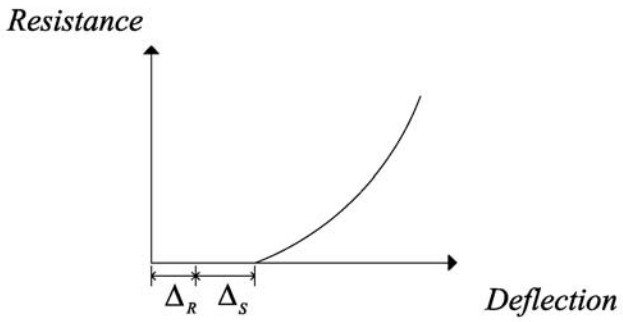

Figure 6.73: Resistance function for polyurea membrane with peeling

The recommended steps required to calculate the membrane resistance function for the case when peeling occurs are given below:

- Determine Δ_R which is equal to the back of the wall to the center line of the connector anchor bolts
- Calculate slack length, so from equation (6.15)
- Determine slack displacement equation (6.14)
- Slightly increase displacement beyond rigid displacement and slack displacement
- Calculate change in length with equation (6.14) using s_o for L_o
- Calculate strain from change in length assuming uniform strain and using equation (6.11) with s_o for L_o
- Determine stress from strain using constitutive relation, see Figure 6.71
- Calculate resistance for displacement and stress with equation (6.10)
- Repeat steps 4 through 8 with increased displacement

6.5.3 COMPARISON OF ENERGY METHOD AND TEST RESULTS

The walls tested with the blast simulator had varying degrees of damage to the CMU blocks and peeling of polyurea at the supports. The method described in the previous section was used to calculate resistance functions for each test and then the energy method was used to predict the peak displacement of the walls. The resistance

function for Test 4 is displayed in Figure 6.74. The wall in this test did not exhibit peeling. A resistance function for both Test 5 and 7 is shown in Figure 6.75. It was assumed in the calculation of this resistance function that the rigid displacement was equal to 3 inches. Finally the resistance function for Test 6 is displayed in Figure 6.76 where it was assumed that the polyurea had one inch of peeling at the supports. It should be noted that in the resistance function curves there is a displacement when the response softens. This softening is associated with inelastic behavior in the polyurea and displacements beyond the initiation of this softening should be avoided. Also included in the resistance function plots are curves representing the internal work in the membrane. These curves can be used quickly to estimate the peak displacement produced by the kinetic energy imparted to the system by the blast load.

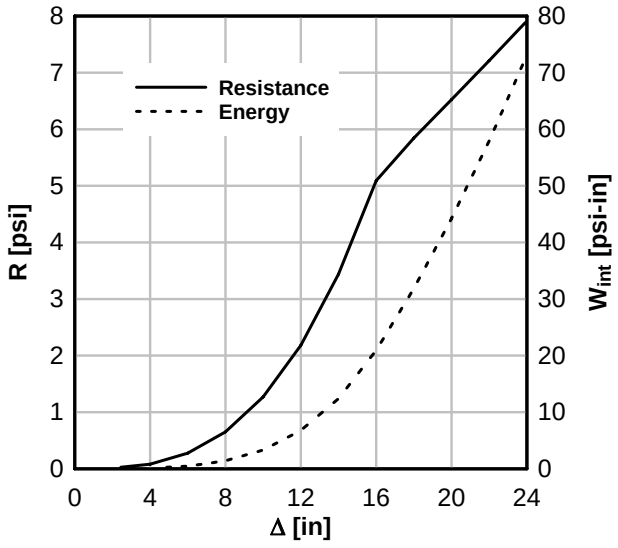

Figure 6.74: Test 4 resistance function

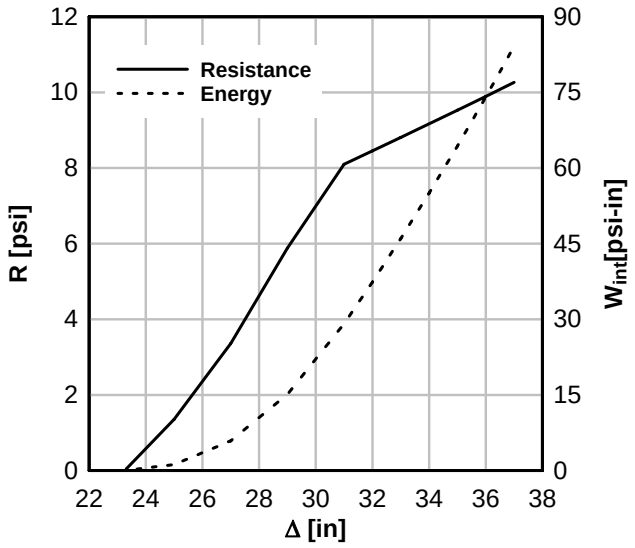

Figure 6.75: Test 5 and 7 resistance function

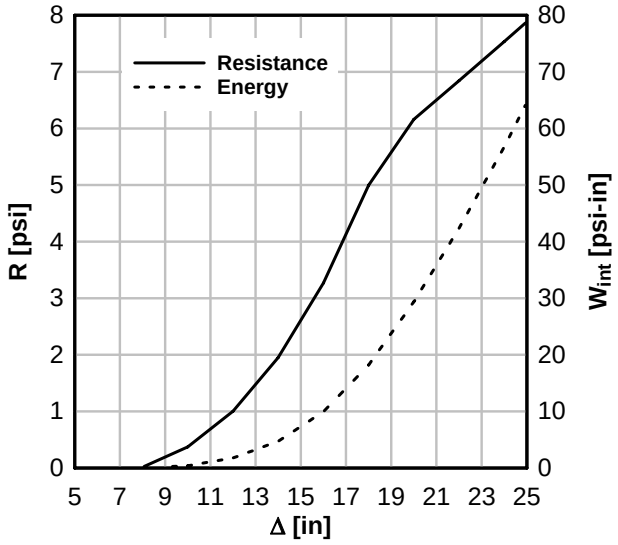

Figure 6.76: Test 6 resistance function

The results from the energy analysis and the blast simulator tests are compared in Table 6.10. The table lists that the method was in good agreement with the experiments for all the tests except for Test 1 where the method significantly over-predicted the peak displacement. A possible reason for this is that in Test 1 the BG impact did not produce

significant damage in the CMU blocks and the wall resisted some of the load. It should be noted that the responses of the individual walls varied greatly for loads that were similar. A comparison of Tests 4 and 7 reveals that the impulse of Test 7 was lower and resulted in a larger displacement. The variability in the responses promotes using a method that is conservative and the table shows that the energy method was conservative for all cases.

Table 6.10: Comparison of Energy Method and Test Data for URM Walls

Test	i_s [psi-msec]	m_{eq} [psi-msec^2/in]	KE [psi-in]	Δ_R [in]	Δ_S [in]	Disp [in]	Exp. Disp [in]
4	130	569	14.9	0	0	14.6	4.6
5	169	569	25.1	3	17.3	30.4	25.2
6	119	569	12.4	1	6.9	16.6	14.2
7	142	569	17.7	3	17.3	29.5	25.7

6.5.4 CONNECTION DESIGN

The blast simulator test program on URM walls with polyurea retrofits demonstrated the need for an adequate connection detail to transfer the tension membrane forced developed in the polyurea catcher system to the supports structure. Test 3 of the series clearly demonstrated that a poor surface bond between a polyurea overlap and concrete can result in catastrophic collapse. Tests 6 and 7 showed that when that even when special attention is paid to the surface preparation a 'peeling' type of de-bonding can still occur. Tests 4 and 5 illustrated that an effective solution for the problem of de-bonding polyurea is to use ductile connectors with mechanical anchors.

In this section of the chapter a set of design equations is proposed to determine the strength of this connection detail. These equations assume several different failure

modes for the different components of the connection detail. Several parameters used in the equation are unknown and need to be determined experimentally. Following the conclusions of this chapter, recommendations for future experiments to determine the different unknown parameters in the design equations are given.

The connections of the polyurea to the support must have sufficient strength resist the tensile forces developed in the membrane. The tensile force associated with the peak displacement in the membrane is found with equation (6.16).

$$T = \frac{wL}{2\sin\theta} \tag{6.16}$$

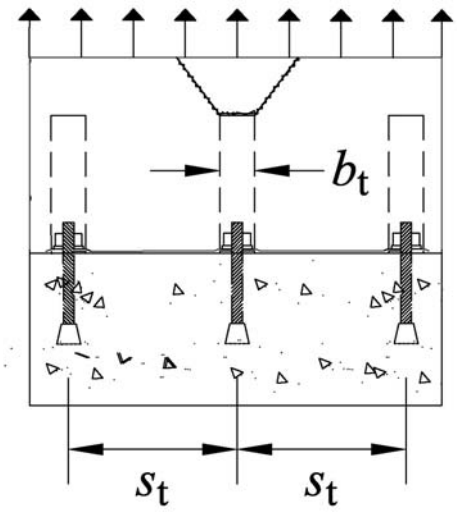

Figure 6.77: Failure of ductile polyurea connection

Finite element analysis was performed to predict the stress distribution in the polyurea and to identify the predominate failure mode at the connection of the polyurea to the steel ties. The model used in the analysis simulated the response with solid element. The mesh of the polyurea lining had nine elements through the thickness. The

properties for the polyurea and steel material models matched those used in the FE analysis from earlier sections of this chapter. The analysis was run with a fixed boundary condition at the bottom. The top of the specimen was given a displacement that increased linear with time until failure. A plot of maximum principle stress in the polyurea-steel tie connection is displayed in Figure 6.78.

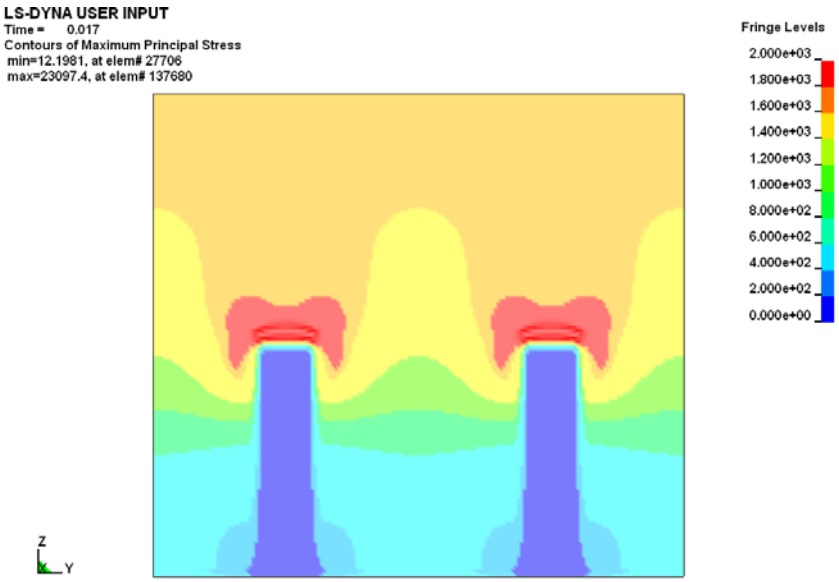

Figure 6.78: Stress distribution in polyurea to steel tie connection

The model suggests that failure of the connection will initiate near the interface between the polyurea and the top of the steel tie due to the discontinuity that exists at this location because of the mismatch in material compliances and from the geometry of the tie. A schematic of the assumed failure mode is illustrated in Figure 6.77. The strength of the connection to resist this type of failure will govern the design of the rest of the connection. The proposed design equation to calculate the strength, R_{PC}, is given below:

$$R_{pc} = F_{yp} t_{pl} b_{eff} \tag{6.17}$$

where F_{yp} is the yield strength of the polyurea, t_{pl} is the polyurea thickness, b_{eff} is the effective width of the polyurea. The effective width of the polyurea is assumed to correspond to the ratio of the tie width to the tie spacing. For the case when the tie spacing is small the ratio will equal one and the effective area of the connection will equal the width of the lining. For the case when the ties are spread far apart the ratio equals zero and the effective width is assumed to be equal to the width of the tie. An equation for the effective width that accounts for these behaviors is

$$b_{eff} = b_t + \alpha_p s_t \tag{6.18}$$

where b_t is the width of the steel tie, s_t is the spacing of the steel ties, α_p is a coefficient that is a function of the tie width to the tie spacing ratio. This coefficient needs to be determined experimentally.

Following the calculation of the connection capacity due to the failure mode described above, the capacity of the anchor bolts and the bond between the ties and polyurea need to be checked. It was demonstrated experimentally in Tests 4 and 5 that the anchorage system proposed has sufficient ductility to accommodate the large deformation demands required for tension membrane action to develop in the catcher system. The next step is to verify that the strength of the bolted connection exceeds the capacity of the polyurea-tie connection.

The strength of the bolt-tie connection can be determined with equations (6.19) and (6.20). These equations assume that the bolt-tie connection is put into a state of pure tension from the membrane forces in the polyurea. This is a reasonable assumption when

the catcher system undergoes large deformations. These deformations cause the angle in the tie to increase from 90º to an angle near 180º. Prior to this state of pure tensile stress the lining may transfer a shear force to the bolts. This force is most likely small, however, because the adhesion between the polyurea overlap and the concrete should be able to resist this force. When the tie-bolt connection is in the assumed state of pure tension it is also assumed that the peel resistance of the polyurea overlaps do not contribute any strength to the connection. This assumption is a conservative one. The strength of the bolts in tension, R_b, can be found with

$$R_b = \beta_p F_{yb} A_b \tag{6.19}$$

where F_{yb} is the yield stress of the bolt, A_b is the cross-sectional area, and β_p. is a knockdown coefficient that accounts for prying forces on the bolt. The strength of the steel ties in tension is found with

$$R_t = F_{yt} A_{t,net} \tag{6.20}$$

where F_{yt} is the yield strength of the tie and $A_{t,net}$ is the net area of the steel tie that accounts for the bolt hole. It can be found with

$$A_{t,net} = t_t (b_t - d_h) \tag{6.21}$$

where t_t is the thickness of the tie, b_t is the tie width and d_h is the diameter of the bolt hole in the tie.

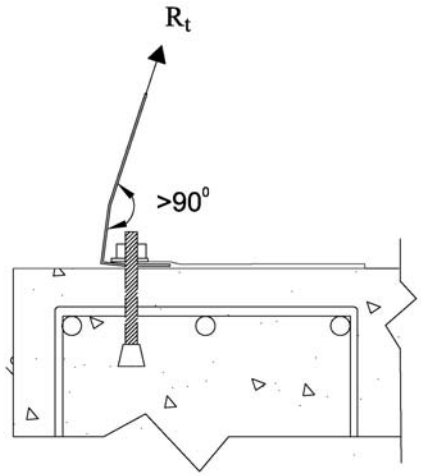

Figure 6.79: Steel ties in tension

The final step in the design of the ductile anchorage system is to ensure that the length of the bonded area between the ties and the angles is sufficient to develop the full strength of the steel ties. The development length of the bond can be determined with

$$l_{dtp} = C_{dl} \frac{F_{yt}}{t_t} \leq l_{cr} \tag{6.22}$$

where C_{dl} is an experimentally determined coefficient and l_{cr} is a critical length beyond which no additional adhesion strength can be gained.

The design equations proposed here are all based on assumed behavior and failure for the polyurea connection. Detailed analysis and additional experiments are needed to fully characterize the behavior of the connections.

6.6 CONCLUSIONS

A series of seven experimental tests were conducted on URM walls to investigate the effectiveness of polyurea catcher systems to mitigate hazards generated in a blast.

The tests demonstrated that the polyurea was able to contain the fragments of concrete block generated by the BG impacts and prevent them from entering a space where they could injury occupants. The experiments also illustrated the need for proper connection details to attach the polyurea lining to the supports. A mechanical anchorage system is proposed that had sufficient strength and ductility capacity to meet the force and deformation demands of the lining. This type of connection is preferred over one that relies only on adhesion between concrete and the polymer. Tests demonstrated that an adhesion connection is susceptible to peeling.

The data generated in the blast simulator tests was used to validate a finite element model of URM walls with and without polyurea. Comparisons of the model and the test data showed good agreement for an as-built wall and a retrofit wall that had a peak displacement less than 5 inches. For larger loads, however, the model was unable to match the test results. It was concluded from the numerical study that the reason for the disagreement was inaccurate modeling of the peel behavior and the inability to fully capture the brittle failure of the concrete blocks.

A design methodology was also presented in this chapter to determine the peak displacement in a retrofitted wall and to determine the number and size of steel ties required to connect the polyurea lining to the supports. The method to determine peak displacement is based on an energy balance where all of the kinetic energy is resisted by internal energy in the polyurea generated with tension membrane action. Equations are also present to determine the number of bolts and steel ties needed to connect the polyurea to the supports. These equations are all based on assumed failure modes that

were not observed in the experiments. Additional research is recommended to investigate these failure modes and validate the design equations that have been given

6.7 RECOMMENDATIONS FOR FUTURE RESEARCH

The experimental work performed on the walls in this chapter only used a polyurea lining thickness equal to 0.25 inches. Additional testing is needed to assess the performance of the catcher system when the thickness is increased. Additional blast simulator testing on URM walls is also recommended to study reinforcement strategies to increase the strength and stiffness of the polyurea lining. Aramid and steel mesh are two materials that could be embedded in the polyurea. These properties may provide interesting effects as they are stiff "brittle" reinforcement in a weak ductile matrix.

The design equations for the ductile were developed based on several assumptions for the failure modes of the system. A research program to investigate these assumptions is needed to validate the design equations. It is recommended that a research study begins with a detailed finite element study to model the full connection detail as well as the individual components, including the anchor bolts, steel angles, and polyurea adhesion. These models can be used to determine which unknown parameters are important for modeling the response of the connection.

An experimental study is also recommended in the research study. Quasi-static testing should be conducted on the tie-bolt component to determine whether or not it will fail in a pure tensile mode. The deformation of the ties under this type of load might

introduce a prying effect on the bolts which could put it into a stress state that included a shear component.

The pullout strength of the ties from the polyurea should also be investigated. In equation (6.22) a coefficient is included that relates the length required to fully develop the tensile capacity of the tie to its yield stress and thickness. This coefficient is not defined because there is no experimental data to support it. Pullout tests to determine this coefficient are recommended.

Peel testing to investigate the adhesion between the polyurea and the concrete supports should also be conducted. These tests should consider the angles at which the peeling may initiate. They should also include dynamic effects on the peel behavior. The data from these tests would be useful for validating simulations similar to the ones described earlier in this chapter.

Component tests on a section of the full connection should also be investigated experimentally. These types of test could be conducted at dynamic rates using the blast simulator. In the setup a membrane would be connected to supports at the top and bottom with the ductile anchor detail. The midspan of the membrane would be connected to a target mass which would be impacted by the BGs similar to the ballistic impact tests. After impact the target mass would have an initial velocity which would put the lining in to membrane action and thereby load the connections in a similar manner as in a URM wall test. These component tests would not include the URM wall, but would be used to validate the assumptions used to develop the proposed design equations. This experiment should be designed to determine a relationship, if one exists, between connection

strength, tie width, and tie spacing. The test would also provide data for validation of numerical models of the connection. After the design equations are validated with the data from these tests larger blast simulator tests with full scale retrofit URM walls could be conducted as ‘proof’ tests for different connection designs.

7 BLAST SIMULATOR WALL TEST PROTOCOL

7.1 INTRODUCTION

This chapter presents a protocol that is recommended to generate design guidelines and methodologies for reinforced concrete and concrete masonry walls with hardening/protective strategies using the blast simulator. A flow chart of the protocol is displayed in Figure 7.1. The protocol begins with an initial concept and a load based on an assumed threat. The specimen design, supporting structure, BG velocity, and instrumentation are all then determined using a predictive model. This process is an iterative process in which the test setup is modified based on comparisons between specimen response to BG impacts and air blast loads with the model. The process requires a validate model that simulates the behavior of the BG programmer pads. A method to accomplish this is discussed in Chapter 3. Any additional data that may exist regarding the walls response to blast loads may be useful in the development of the predictive model.

When test setup is finalized, the protocol calls for the testing of the wall with the blast simulator. The data generated in the test will be reduced and then used to make comparisons between the predictive model and the experiment. Any discrepancies between the two will lead to model modifications which will require that the previously defined threat is adjusted to account for the difference between the model pre and post test.

Models validated with the test data can be used in numerical parametric studies to investigate the effect of different design variables on the response of the walls. These studies should be arranged to answer specific design questions. The results of the study will lead to design guidelines and methodologies.

Direct comparisons between several different tests can also be made with the reduced test data. These comparisons can be made when there is a control specimen and variable specimens that incorporate different design parameters. These comparisons can lead directly to design guidelines or methodologies in certain situations.

The blast simulator can also serve as a means for "proof" testing a design concept. In this situation the objective may be only to observe if the concept passes a certain design criteria. When the criteria are met, the concept can then be implemented in a field test. If the concept does not meet the criteria the wall can be re-tested with a modified design. When the strategy is further refined methods and guideline are required by engineers to design them in real life situations.

The testing protocol presented provides a fast and inexpensive means to investigate different hardening/protective strategies. Implementation of this protocol will assure that different strategies are evaluated in a consistent and objective manner. The protocol, however, is flexible to account for different responses arising from the fact that the BG loads are affected by specimen mass and resistance.

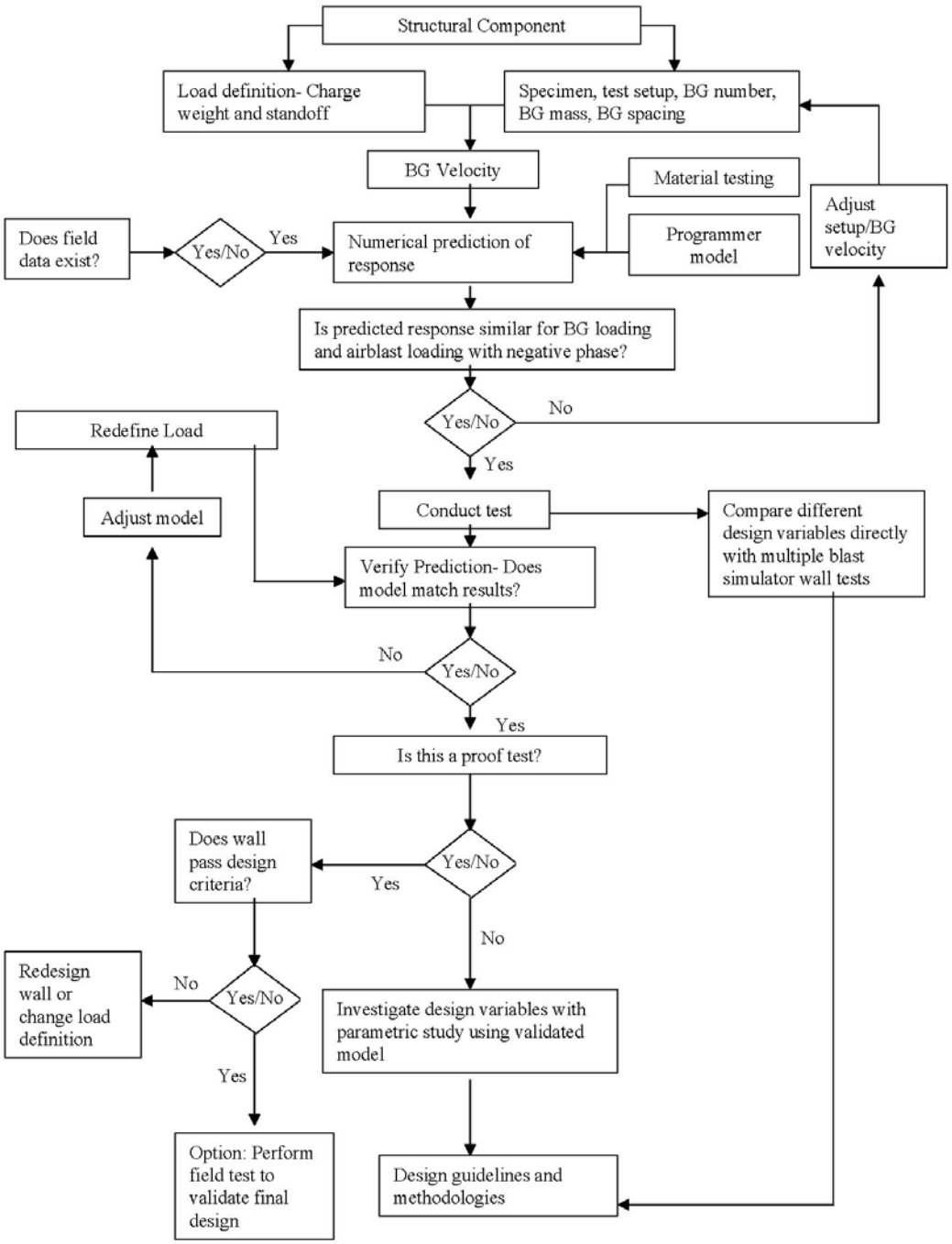

Figure 7.1: Flow chart for test protocol

The presented protocol is for blast simulator tests on wall specimens with the current lab facility. Testing methods for walls using lab configurations that were not

used in this dissertation are not considered. However, the methods described in this dissertation can easily be modified so that they are applicable to different situations. In the following sections recommendations are given to aid researchers in the design of blast simulator experiments.

7.2 SPECIMEN DESIGN

Specimens should be designed to represent behavior of the structural component to the blast load. The walls tested as part of this dissertation were walls subject to uniform loading while exhibiting one-way bending. It is recommended that the width of the wall is set equal to the width of the BG impact mass which is 48 in. wide. Designing the width of the specimen to be equal to the width of the programmer prevents the BG impact from producing localized effects during loading as observed in Test 1 of the URM Test Series. In this test the impact had a "punching" shear effect where the mass of the wall on the outer edges of the BG impactor remained stationary while the remainder of the wall that was impacted had an initial velocity. This is an unlikely failure mode for a one-way bending wall to a uniform blast pressure. An additional concern for wall specimens that extend beyond the width of the BG mass is that wall will impact the support rails of the mass plate during rebound. An impact between the actuator support structure needs to be avoided because it can produce unrealistic damage in the specimen and it can damage the blast simulator equipment.

7.3 BOUNDARY CONDITIONS

Currently the blast simulator laboratory facility has fixtures to provide simple-simple or fixed-simple boundary conditions for a one-way bending wall. The top boundary condition is provided by a 6 in. thick reinforced concrete slab. The bottom boundary condition for a simple case is provided by an angle mounted on a concrete block or a stepped reinforced concrete footing. The forces that are transferred to the bottom support are typically transferred to the reaction structure with post-tensioned connections and with spacer blocks. A method to restrain the wall during rebound is recommended for walls that undergo flexural behavior. Two methods to accomplish this have been used. The first method uses a bent steel plate that is bolted to the top side of the top concrete slab. It is recommended that urethane foam pads be placed between the wall and the steel plate to prevent local damage to the concrete or concrete masonry during rebound and to allow the wall to rotate at the support. The other method uses tie back rods. These rods are connected to the bottom side of the slab and pass through holes that are cored or drilled through the thickness of the wall near its top. The connection uses bearing plates on the front face of the wall to transfer tension forces in the rods during rebound to the wall. For cast-in-place type of test specimens it is recommended that the tie-back holes are made using PVC sleeves in the formwork.

7.4 BGS: NUMBER, SPACING, AND MASS

The number and spacing of the BGs used for a test series is partially based on the geometry the test specimen. The walls tested in this dissertation had span lengths

approximately equal to 8 ft 8 in. or 10 ft 9 inches. The maximum number of impacting masses that can be used for the former span is three. The maximum number of impacting masses for the latter span is four. Ideally, the impacting masses will be spaced so that there is only a 0.5 to 1.0 in. gap between the plates. This will produce a nearly uniform load while preventing the plates from colliding with each other in the case where they are given a rotation during the impact. The space between the BGs and the supports should be set equal to about 0.5 to 1.0 times the depth of the test specimen. This is done to assure that the boundary conditions, which are hard points, do not attract unrealistic loads to the specimen. Finite element analysis on a specimen subject to an airblast load and BG impacts can be performed to determine an ideal distance between the BGs and the supports. The objective of the calculations is to determine a space where the reaction forces in the specimen under BG loads match the reactions when the specimen is loaded by the airblast.

The number of BGs used to test the wall is also based on the ratio of BG mass to specimen mass. This ratio needs to be balanced such that the BGs have a relatively small velocity following impact. In the situation where the impact mass is heavy relative to the specimen the impact mass will have a significant residual velocity in the direction of the wall after the initial impact. The deceleration pressure in the BG might not be sufficient to slow the mass which could result in a multiple impacts. For the other situation where the impact mass is light relative to the specimen the mass will have a significant velocity in the opposite direction of the wall. This situation is more desirable than the previous because there is little chance of a second impact, however there is a large change in

velocity for the impact mass which might result in the failure of the break away bolts. Bolt failure could result in damage to the blast simulator equipment if the mass falls from the supports. The velocity of the BG mass following impact can be estimated using the 1D programmer model in conjunction with the SDOF type of analysis that was validated in Chapter 3. Another method is to simulate the impact with a finite element model using the programmer material model described in Chapter 3 where the unloading parameters of the model are selected with the method described in Section 3.5. This method first estimates the impulse using the 1D model and then adjusts the parameters of the FE material model to produce a similar impulse in the 3D simulation. The current masses of the BG used in the lab are well suited for testing reinforced concrete and concrete masonry walls. Walls made of lighter materials may require lighter impact masses to meet the recommendations given here.

7.5 BLAST LOAD SPECIFICATION

The specified load for the blast can be defined as a charge size and a standoff distance. The parameters of the blast wave associated with the charge can be determined with the methods presented in Chapter 2. Shock physics codes, such as CTH, can also be used to define the loads to be simulated in the experiment. This type of calculation should be used for situations when the methods used in Chapter 2 are no longer applicable.

7.6 BG MODEL INPUT PARAMETERS

The impact velocity specified for a test is attained using software that models they hydraulic oil/nitrogen system used to drive the BGs. A detailed description of this model is given in [27]. To accurately predict the impact velocity for a given set of input parameters this software requires the mass of the impact modules (including the mass of the piston rod), mass of the wall specimen, and distance from the tip of the programmer pyramids to the front face of the wall specimen when the BG masses are in their fully retracted position.

The distance to the front face of the specimen should be measured for each BG that is used to impact the wall. The recommended method is to measure the distance at the four corners of the BG mass and use an average. The measurement may demonstrate that the distance varies for the different BG impact masses. For this case the initial starting point used in the test can be varied so that the BGs impact the specimen simultaneously. The measurement can also be used to assess whether or not the specimen is plumb and square. For the case when the specimen is found to be out of plumb or not square it should be realigned. It is ideal to check the specimen prior to the post-tensioning of any supports. It is also possible that during construction the specimen is built such that it has initial imperfections or that the front face is not entirely flat. During installation these imperfections should be considered so that differences in the distance from the BG to the specimen at the four corners of the impact mass are minimized.

An additional consideration that a researcher should make when determining the input parameters used to generate an impact velocity are the peak pressure produced in the deceleration chamber and cavitation in the main oil chamber. The maximum design deceleration pressure is 8000 psi and cavitation should be avoided. These values are dependent on initial oil and nitrogen pressure along with timing of the valves. They are also highly dependent on final velocity of the BG mass following impact as described in an earlier section. It emphasized here that the ratio of impact mass to specimen mass must be selected to produce a favorable response in the BGs. The most favorable response occurs when the final velocity of the BG is near zero.

7.7 SPECIFIED BG IMPACT VELOCITY

A BG velocity is selected to produce the same damage and peak response that is measured when the protected structure subject to the blast pressure pulse. The correlation between the charge and the BG velocity must account for the negative phase. A method to connect charge size and standoff distance to BG velocity is given in Section 3.7.3. Estimation of the response of the wall to blast and BG loads are calculated with numerical models such as SDOF or FE analysis. The loads generated in a BG impact are predicted using the validated 1D model described in Chapter 3. When FE analysis is used the parameters of the programmer material model need to be selected such that the impulse delivered in the simulation match the impulse predicted by the 1D model. This can be accomplished using the methodology given in section 3.5. The data and the visuals produced in the blast simulator test are used to verify and validate the numerical models used to connect the charge to the BG velocity. If the observed failure mode is not

represented in the numerical model modifications are required and the analysis used to connect the charge to the BG velocity is redone with adjusted model.

7.8 BG Instrumentation and Load Determination

The loads generated by the BG impact with the specimen are determined through integration of scaled acceleration and differentiation of scaled displacement of the impact plates during the impact. The accelerations of the BG impactor are measured over the time of the test with accelerometers that are mounted on the impact masses. It is recommended that a minimum of three accelerometers are used on each impact mass. Multiple accelerations data on a single impact mass is useful for determining if the plate impacted the specimen at a skewed angle and for redundancy of the measurement. The displacements of the BG impact mass are measured at the location of targets mounted on the plates with tracking software which analyses the high speed video of the test. It is recommended that multiple targets are mounted on the impact mass. This will ensure the ability to measure displacements in case one of the targets falls off. It will also provide a means of measuring rotational momentum delivered to the BG during an impact.

Steps to calculate the impulse from the acceleration and displacement of the BGs are given in Section 3.3. These loads can be predicted by the 1D programmer model. The 3D finite element model has been demonstrated to reproduce the loads when appropriate unloading parameters are selected for the material model. The loads recorded in the experiments can be applied to finite element models using two methods. The first is to calculate a pressure time history from the acceleration data by multiplying it by the impact mass and dividing by the tributary area of the impact plate. The second method is

to model the BG impact with the specimen using a contact surface and a material model for the BG programmers. The first method requires less computation time, but might be less accurate because it does not include any of the interactions that might occur between the BG masses and the specimen which could result in localized effects.

7.9 SPECIMEN INSTRUMENTATION

Specimen behavior during the tests is measured with an array of instrumentation including linear potentiometers, accelerometers, strain gages, load cells, and high speed camera video. The most valuable measurements of the specimen response are found with the high speed camera video. The video can be used to track targets to give displacement and velocity time histories of the specimen and the BG masses. The camera video also provides visuals that are invaluable for determining specimen behavior and identifying failure modes. Three high speed cameras are currently available for testing. These cameras should be positioned around the specimen to capture as much of its behavior as possible. However, since the cameras also are used to determine BG velocities it is recommended that they are positioned to make accurate measurements.

The accuracy of the measurement of BG velocities is based on the scale which is defined as pixels per inch. An ideal scale for the measurement of BG velocities is about 0.125 pixels per inch. When the scale is increased beyond this the signal to noise ratio can make it difficult to accurately measure the impact velocity and determine the impulse. When the span of the wall is around 8 ft a single camera can most likely be used to measure the velocities. For walls with 10 ft. plus spans two cameras might be required to capture the velocities of the BG plates; one camera recording the top two BGs

and one camera recording the bottom two BGs. Several tracking targets should be placed on the specimen to measure displacement and velocity time histories at several locations along the span. This will provide information on the displaced shape of the wall in addition to peak displacement and peak velocity. Prior to testing measurement of the distance between the targets should be made and recorded. These measurements are used to determine the scale used by the tracking software.

Linear potentiometers are also recommended for measuring the displacement of the specimen due to the BG loads. The measurements from these instruments can be used to verify the displacements calculated by the tracking software. Mounting of the linear potentiometers requires care because improper mounting can result in poor data. Ideally, the potentiometers should be mounted so that they extend when the wall is loaded, for this case the potentiometers will be attached to the side of the wall. The typical method of connection is with threaded rod that is embedded in the wall with epoxy. The span of the threaded rod should be minimized to prevent any high order vibrations in the recorded signal during the wall response. This thread rod is a cantilever and it will be excited by the impact causing it to oscillate which can cause error in the displacement measurement Accelerometers should be mounted on the specimens to measure accelerations in the wall at several locations.

Strain gages should be used to measure strains in the wall materials during the tests (i.e. rebar, FRP composites). These measurements can be used to determine internal forces of the specimen during the test and to determine strain rates in the wall materials. It is important to note that the strain rates measured in a material may be dependant on

the length of the strain gage. When selecting strain gage lengths considerations should be made as to how the data will be used in the validation of numerical models. Instrumentation of the supporting structure that provides boundary conditions for the specimen might also be considered. During impact loading the BGs may excite a response in the supports which might need to be accounted for in the validation of numerical models. Reaction loads were not measured in any of the tests included in this dissertation. However, measurement of these loads is useful in the validation of numerical models. When applicable, load cells should be employed at one or both of the boundary conditions to measure the forces that are transferred to the supports.

7.10 MODEL VALIDATION

Validation of numerical models should be performed using the data from the blast simulator tests. It should be verified that the model accurately predicts the loads that are delivered to the wall and the response of the wall due to those loads. The blast simulator is simulating blast effects on structural components with a load that has a similar impulse as an actual explosion. Therefore, it is important to match the impulse in the numerical model of the test. The description and validation of a one dimensional and three dimensional model for the BG programmers used for the wall tests is given in Chapter 3.

The response of the wall is often described by its displacement time history. Peak displacement demand is often related to the level of protection provided by a wall. Therefore the models should accurately predict displacement in the wall. The damage modes observed in the wall during the test should also be used to compare the model to the experiment. A qualitative comparison can be made when using *MAT_72_R3 in LS-

DYNA by plotting damage fringes. These fringes illustrate the location and extent of cracking in the concrete model which can be used to predict damage mechanisms. The damage predicted in the model should be similar to the damage observed in the experiments. A comparison of displaced shapes of the wall in the test and in the numerical simulation can also be used to assess the accuracy of the model. These types of plots can be used to determine the behavior of the wall which might be elastic, elastic-plastic, elastic-plastic with a diagonal shear failure, etc.

8 CONCLUSIONS

8.1 SUMMARY AND CONCLUSIONS

The previous chapters of this dissertation presented research that has been conducted with the UCSD Blast Simulator on reinforced concrete and concrete masonry walls. The objective of the dissertation was to generate design guidelines and methodologies for protective/hardening strategies used to mitigate blast hazards in reinforced concrete and concrete masonry walls. The objective of the dissertation was achieved through a succession of tasks that included; the development of a test protocol, validation and implementation of numerical models to predict loads delivered to specimens during blast simulator tests, development of a method to correlate blast simulator loads to air blast loads, generation of high quality data on specimens with mitigation strategies for validation of numerical models to predict response of hardened/protected reinforced concrete and concrete masonry walls, and investigation of design variables with parametric studies.

Summaries for each individual chapter along with conclusions based on principle findings are also given here. Chapter 2 provided background reference material on estimation of blast loads, simple analysis of structures to blast loads, and information on concrete behavior and modeling.

Chapter 3 presented research conducted on the experimental and numerical methods associated with blast simulator testing. The work described in the chapter demonstrated that the behavior of the programmer pads on the BG impact plates can be modeled accurately with a simple one-dimensional model and with a more detailed FE

model. It was also illustrated in the chapter that the negative phase of a blast load can have a significant effect on the peak response of a wall with low mass and/or low stiffness. It was demonstrated that the negative phase is the cause of the difference between laboratory and field data on lightly reinforced CMU walls.

Chapter 4 of the dissertation describes experimental and numerical work that was conducted on CMU walls with CFRP retrofits. The experimental work demonstrated that the walls had sufficient strength to resist impulses up to about 300 psi-msec. The walls however, did exhibit a shear failure that could lead to a progressive collapse situation if they are load bearing. The data generated in the experiments was used to validate a SDOF and FE model. The FE model was capable of capturing the peak displacements and the localized damage due to translations at the base and shear cracking. The validated FE model was used in a parametric study that varied the CFRP design and the load characteristics to assess the performance to HE-type and VCE-type of conditions. In the case of HE blasts, the wall were susceptible to shear failures which should be avoided especially when the walls are load bearing. The CFRP retrofit was very beneficial for walls subject to VCE blasts. The failure mode observed in this case was a flexural failure, which is desired over a shear failure because it is a more ductile failure. A design methodology was also presented with examples of walls loaded by HE and VCE blasts. An example using this methodology demonstrated that CFRP retrofitted walls can be designed to resist VCE blast loads. These types of retrofit were not successful in the design against impulsive loads as experience in HE blast due to a shear failure. Additional strategies might be required to increase shear strength of the wall.

Chapter 5 presents the investigation of frangible panels used as a blast mitigation system for reinforced concrete walls. The research conducted on this topic included several blast simulator tests and a numerical parametric study with a one-dimensional model validated with the test results. The results of the first experimental test program were inconclusive because direct comparisons could not be made between the RC walls with and without frangible panels. In the second series it was observed that construction of reinforced concrete walls with frangible panels proved to be difficult and expensive. Comparisons of BG impact velocity versus impulse in the second test series demonstrated that the frangible panels dissipate some energy during BG impact loading, which lowers the total impulse experienced by the specimen. The reinforcement ratio of the wall should be greater than the specified minimum to prevent brittle failure modes. Low reinforcement ratios with small diameter rebar can cause localized failures, which can result in reduced ductility of the wall. Single BG impact tests illustrated the vulnerabilities of the lap splice detail for both RC and frangible panel walls. The lap spliced specimens produced spalling when they were subject to intense localized loads, while no concrete spalling was observed in the comparison test with continuous reinforcement.

Data generated in both of the test series described in Chapter 5 was used to validate a one-dimensional model called FPWA and finite element models simulated in LS-DYNA. The FPWA model was used in a parametric study to investigate the efficacy of frangible panels for reducing hazards created from blast loads over a large range of design scenarios. The results of the study suggest that when used with RC walls, the

panels add mass to the structure, which has beneficial effects, but no additional energy or momentum dissipation was evident.

In Chapter 6 a series of blast simulator tests were conducted on URM walls to investigate the effectiveness of polyurea catcher systems in mitigation of blast hazards. The tests demonstrated that the polyurea was able to contain the fragments of concrete block generated by the BG impacts and prevent them from entering a space where they could injury occupants. The experiments also illustrated the need for proper connection details to attach the polyurea lining to the supports. A mechanical anchorage system is proposed that has sufficient strength and ductility capacity to meet the force and deformation demands of the lining. The tests also demonstrated that a connection that relies solely on adhesion is less ideal because it is susceptible to peeling. A design method based on energy balance was presented to estimate the peak displacement of the catcher system to a blast load. The method was verified with the experimental data and it was shown that the peak displacements found were conservative. A methodology with proposed equations was also presented in this chapter to design the connection of the polyurea lining to the supports with the anchorage system. These equations are all based on assumed failure modes that were not observed in the experiments.

Chapter 7 presents a protocol for testing a blast hazard mitigation strategy with the blast simulator. This protocol provides steps to take a protective or hardening system for a wall component from initial concept to design guidelines and methodologies. The chapter also provides necessary information required by researchers to execute the protocol. This protocol has been demonstrated to be an effective means of It is

recommended that the presented protocol be used in future blast simulator testing on mitigation strategies of reinforced concrete and concrete masonry walls.

8.2 RECOMMENDATIONS FOR FUTURE WORK

Chapter 3 demonstrated that a material model for finite element analysis with the programmer is able to reproduce the loads delivered by the BGs in a blast simulator test, but is unable to predict the loads without some prior knowledge. It is recommended that the research effort to fully characterize the programmer and to implement a suitable material model in LS-DYNA be continued.

In Chapter 4 the blast simulator has been demonstrated to be a valuable tool which can be used to study specimen behavior including failure modes. The following is a list of recommendations for future research on CMU walls that could be performed with the blast simulator or by another testing method:

- Grouted CMU walls with CFRP subject to simulated VCE loads. This could be done with the blast simulator with a modification of the BG programmer.
- Investigation of FRP debonding under blast type loads. This is a typical failure mode observed in static testing and is possible under blast loads, but has not been studied.
- Investigation of composite strips. This could reduce the amount of FRP material used so that the wall is strengthened, but shear failures are prevented.
- Investigation of anchorage systems with CFRP composites.

In Chapter 5 it was concluded with a parametric study using a one-dimensional model that the most significant contribution made by the frangible panels was increased mass. Some topics for additional research on frangible panels as a blast mitigation system for RC walls are:

- Perform a parametric study using validated FE model
- Investigate the effect of additional parameters such as panel strength, densification strain of panels, and panel density.
- Conduct experimental study using the blast simulator to investigate spall resistance of RC panels with and without frangible panels.

In Chapter 6 design equations for the ductile connectors were developed based on several assumptions for the failure modes of the system. A research program to investigate these assumptions is needed to validate the design equations. It is recommended that the following are included in any studies:

- Pullout strength of the ties from the polyurea lining.
- Failure mode of the tie-bolt connection in tension. Considerations regarding prying effects on bolt strength should be included.
- Peel strength for the adhesion between the polyurea and the concrete supports.
- Component level tests on the full connection assembly are needed to verify assumed failure modes.

APPENDIX A

This appendix contains test data from the blast simulator test series on CMU walls with CFRP retrofits that is described in Chapter 4. The plots included for each test are velocity time histories for BGs 1-3, acceleration/impulse time histories for BGs 1-3, displacement time history at the specimen midspan, and specimen displaced shapes at times when the peak displacement is equal to 25, 50, and 100 percent of the peak midspan displacement. Also included for each test is a sequence of photos captured in the high speed camera video.

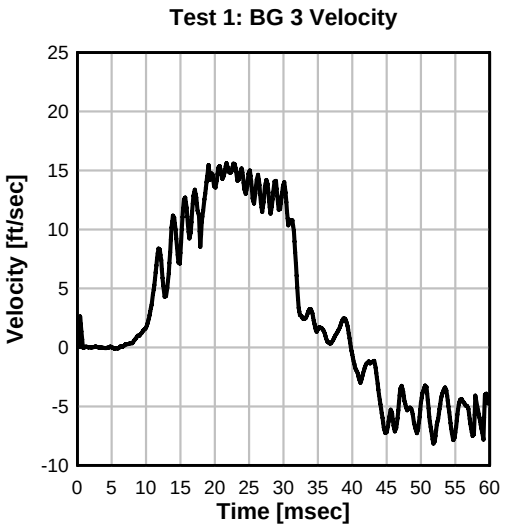
Test 1: BG 3 Velocity
Velocity [ft/sec]
Time [msec]

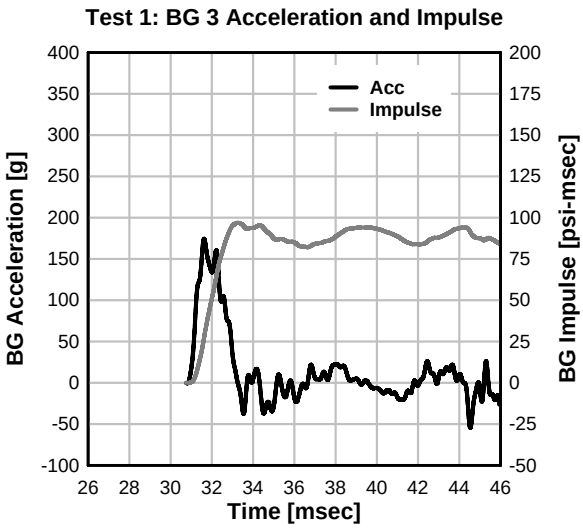
Test 1: BG 3 Acceleration and Impulse
Acc
Impulse
BG Acceleration [g]
BG Impulse [psi-msec]
Time [msec]

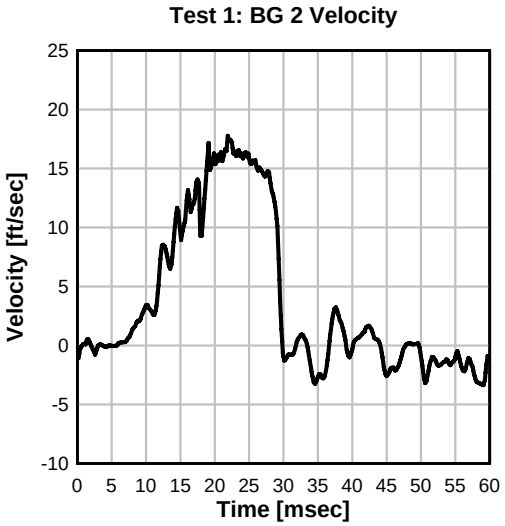
Test 1: BG 2 Velocity
Velocity [ft/sec]
Time [msec]

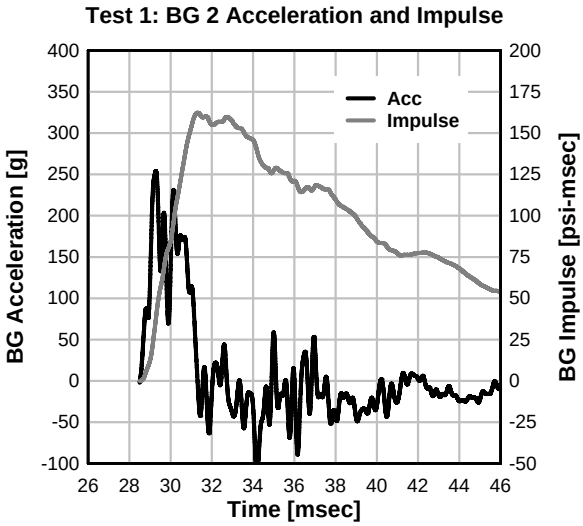
Test 1: BG 2 Acceleration and Impulse
Acc
Impulse
BG Acceleration [g]
BG Impulse [psi-msec]
Time [msec]

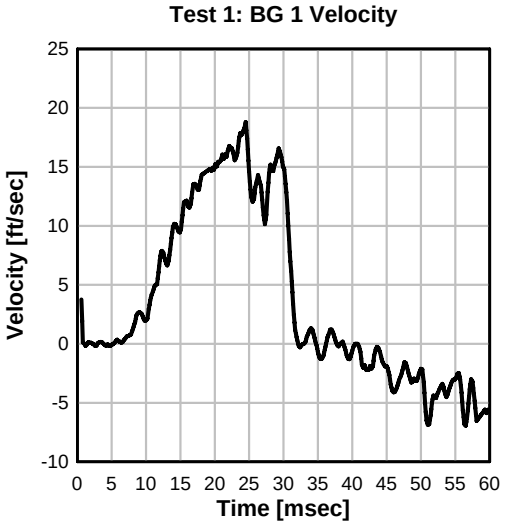
Test 1: BG 1 Velocity
Velocity [ft/sec]
Time [msec]

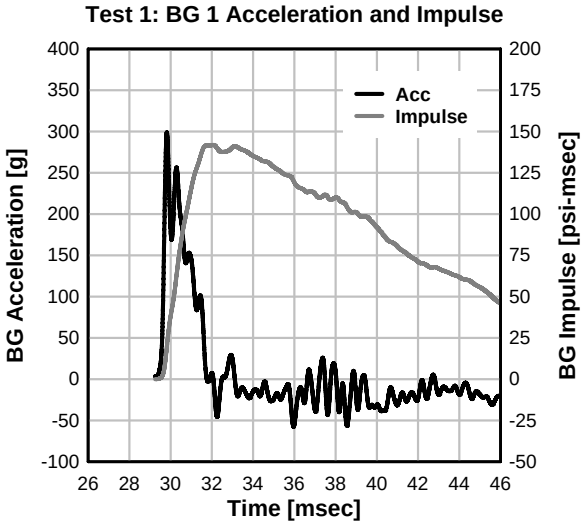
Test 1: BG 1 Acceleration and Impulse
Acc
Impulse
BG Acceleration [g]
BG Impulse [psi-msec]
Time [msec]

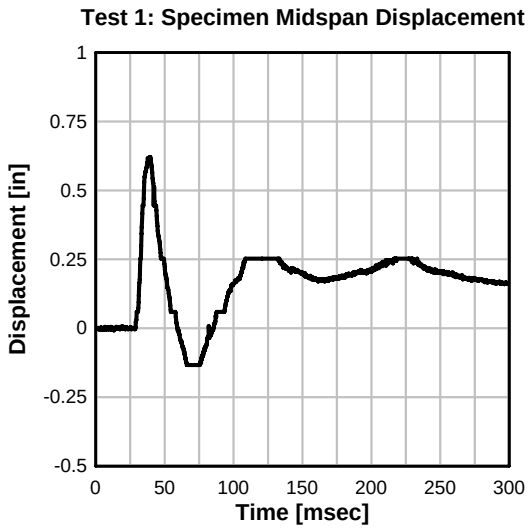
Test 1: Specimen Midspan Displacement
Displacement [in]
Time [msec]
1
0.75
0.5
0.25
0
-0.25
-0.5
0
50
100
150
200
250
300

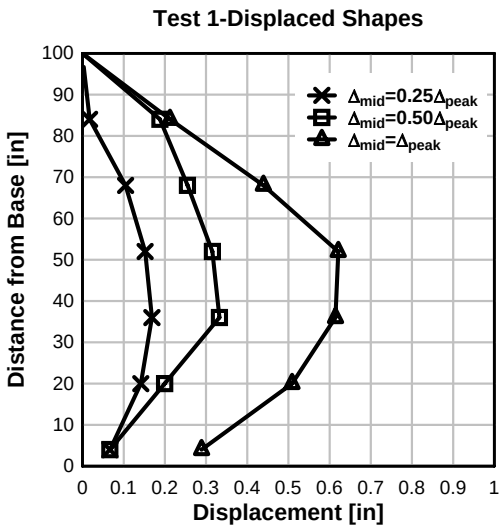
Test 1-Displaced Shapes
Distance from Base [in]
Displacement [in]
Δmid=0.25Δpeak
Δmid=0.50Δpeak
Δmid=Δpeak
100
90
80
70
60
50
40
30
20
10
0
0
0.1
0.2
0.3
0.4
0.5
0.6
0.7
0.8
0.9
1

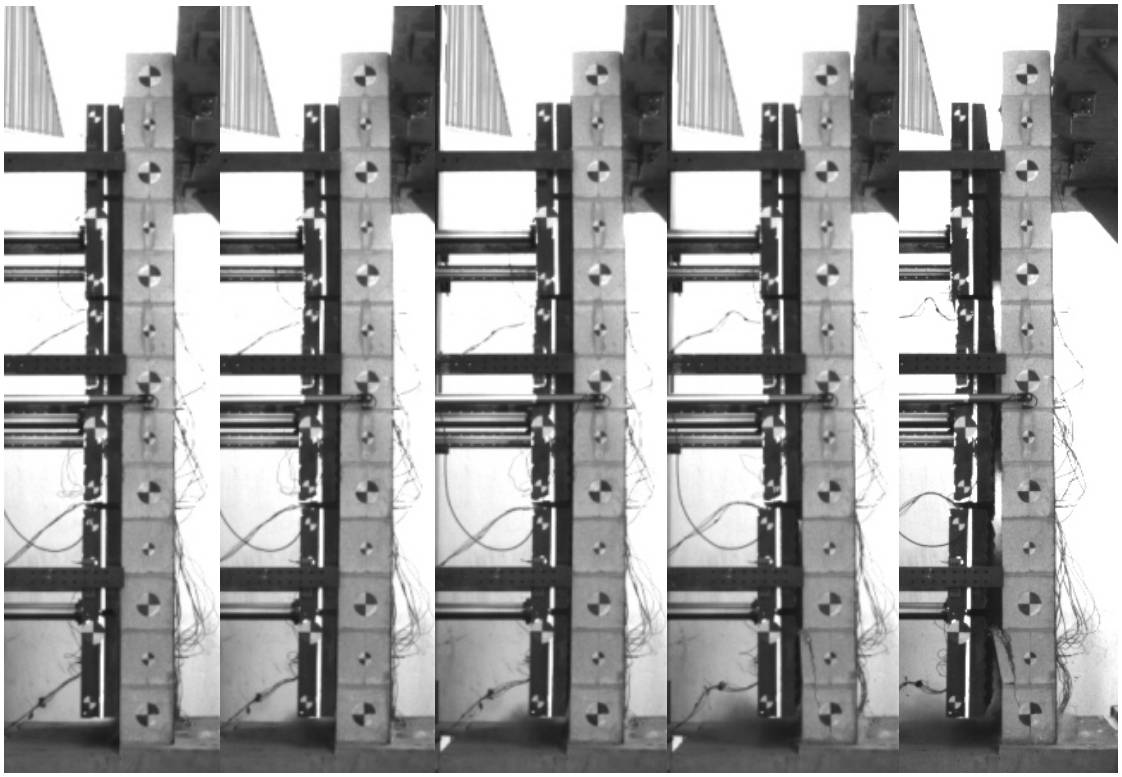

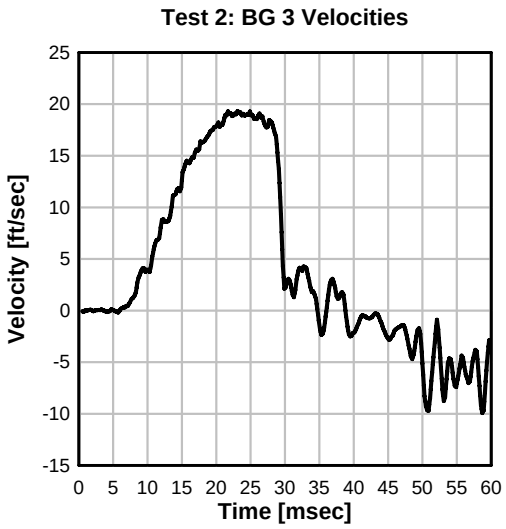
Test 2: BG 3 Velocities
Velocity [ft/sec]
Time [msec]

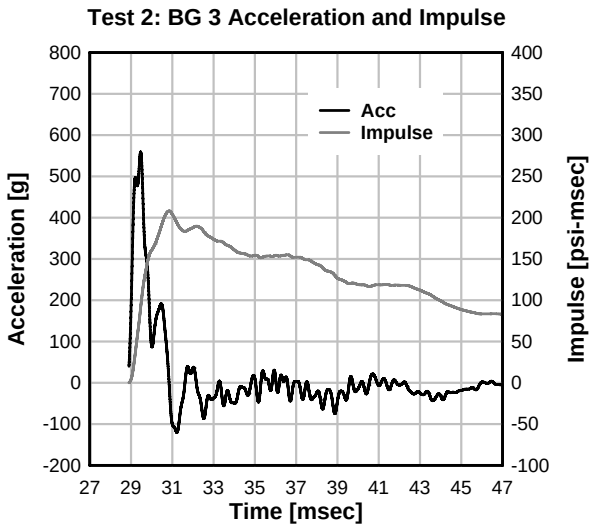
Test 2: BG 3 Acceleration and Impulse
Acc
Impulse
Acceleration [g]
Impulse [psi-msec]
Time [msec]

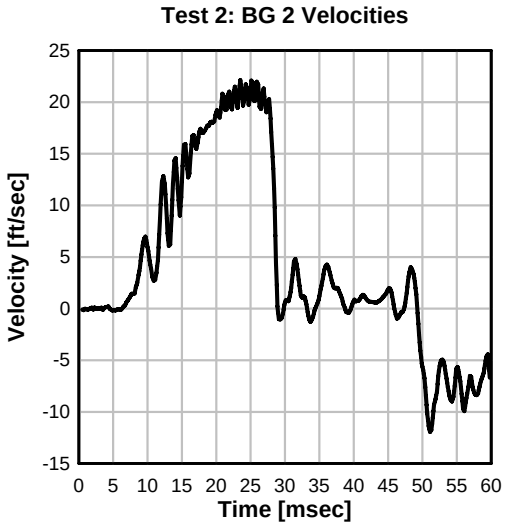
Test 2: BG 2 Velocities
Velocity [ft/sec]
Time [msec]

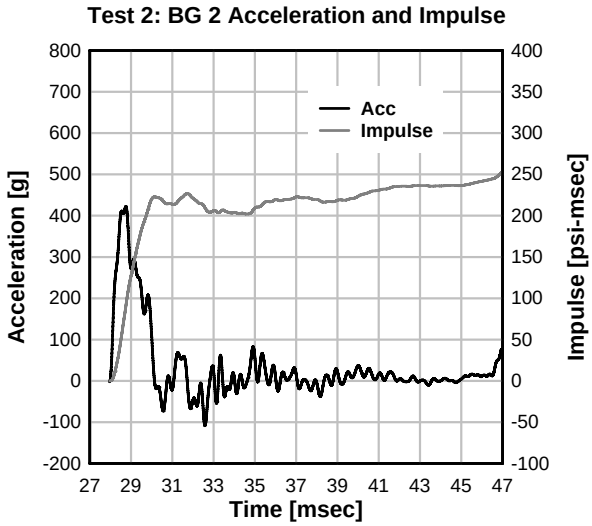
Test 2: BG 2 Acceleration and Impulse
Acc
Impulse
Acceleration [g]
Impulse [psi-msec]
Time [msec]

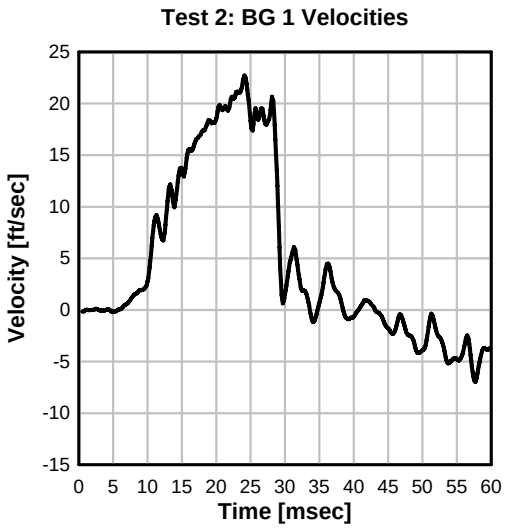
Test 2: BG 1 Velocities
Velocity [ft/sec]
Time [msec]

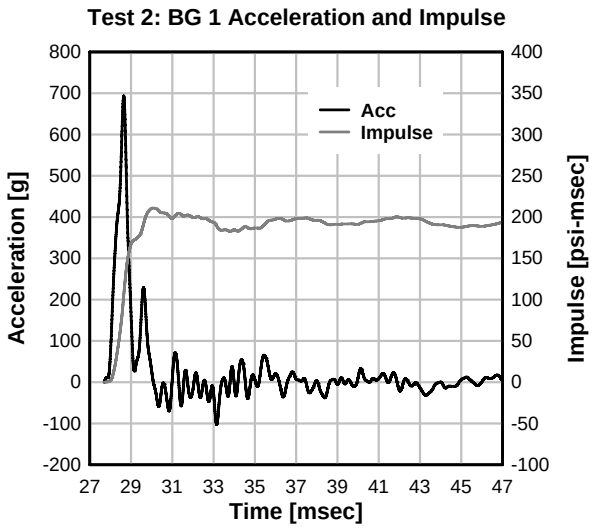
Test 2: BG 1 Acceleration and Impulse
Acc
Impulse
Acceleration [g]
Impulse [psi-msec]
Time [msec]

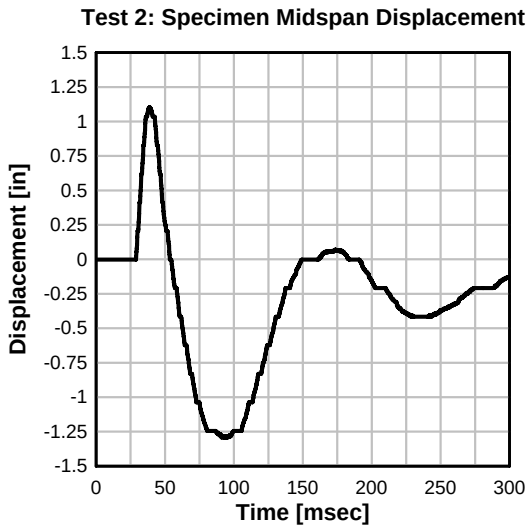
Test 2: Specimen Midspan Displacement
Displacement [in]
Time [msec]
1.5
1.25
1
0.75
0.5
0.25
0
-0.25
-0.5
-0.75
-1
-1.25
-1.5
0
50
100
150
200
250
300

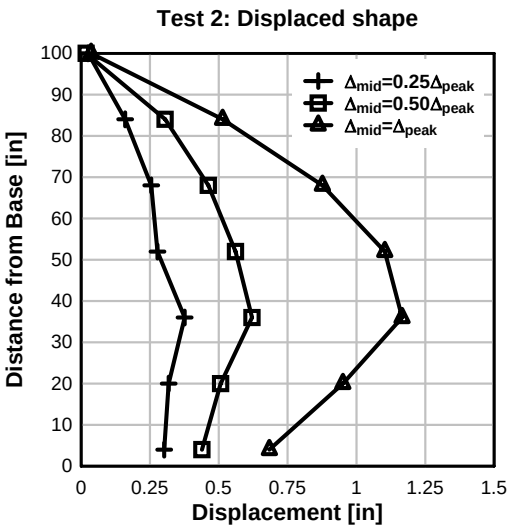
Test 2: Displaced shape
Distance from Base [in]
Displacement [in]
Δmid=0.25Δpeak
Δmid=0.50Δpeak
Δmid=Δpeak
100
90
80
70
60
50
40
30
20
10
0
0
0.25
0.5
0.75
1
1.25
1.5

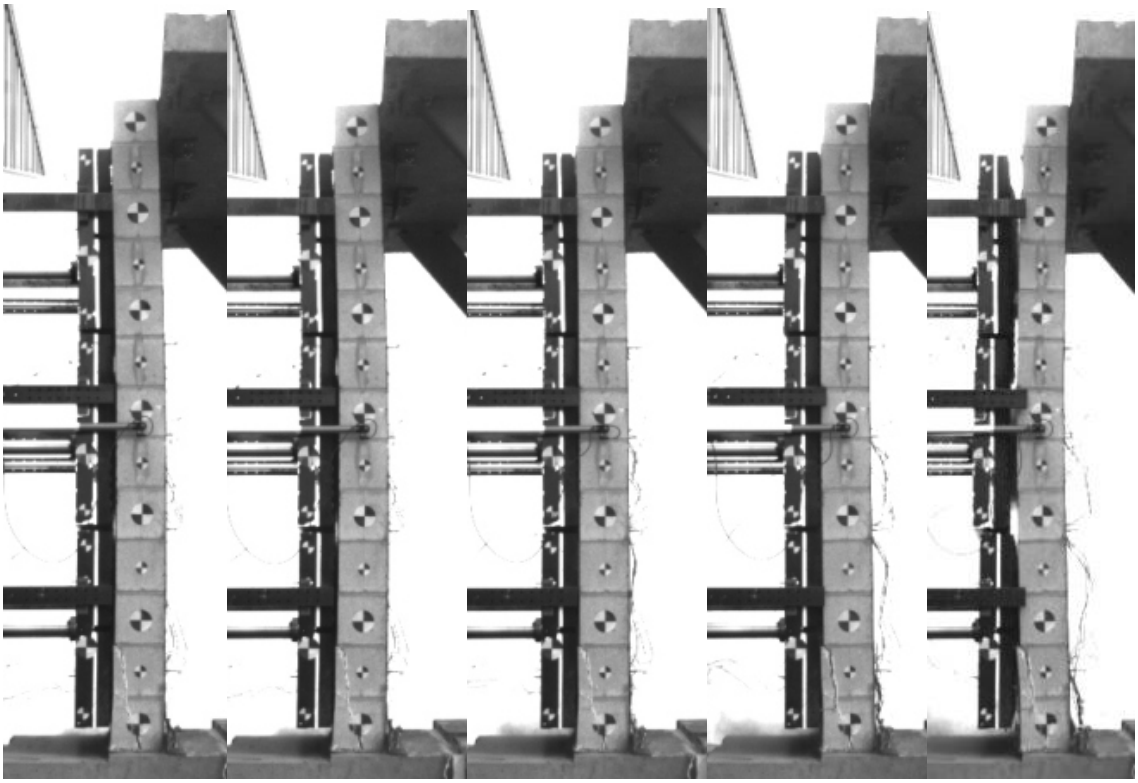

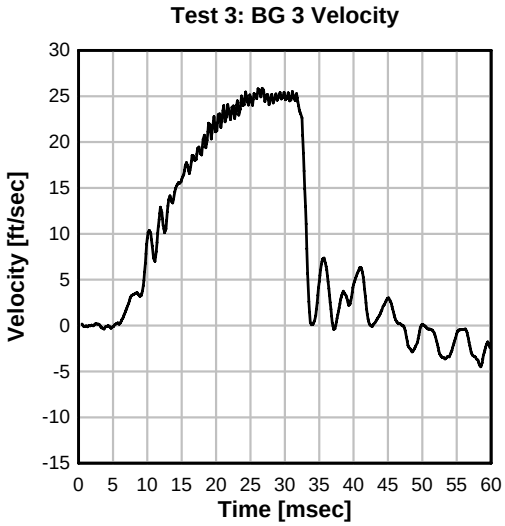
Test 3: BG 3 Velocity
Velocity [ft/sec]
Time [msec]

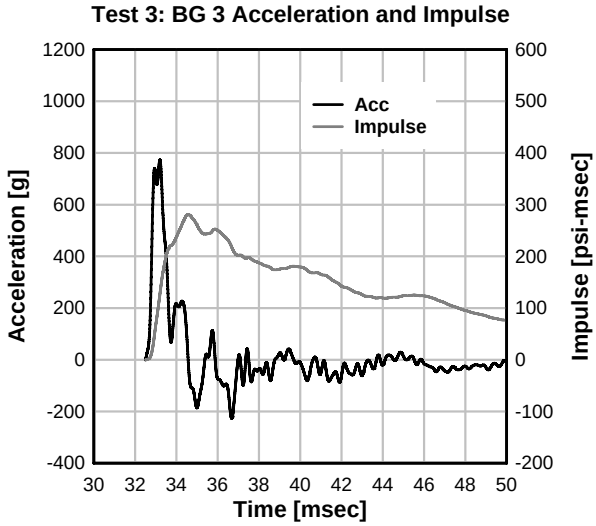
Test 3: BG 3 Acceleration and Impulse
Acc
Impulse
Acceleration [g]
Impulse [psi-msec]
Time [msec]

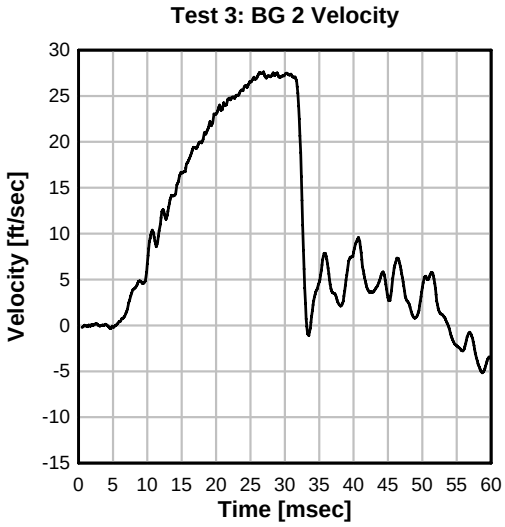
Test 3: BG 2 Velocity
Velocity [ft/sec]
Time [msec]

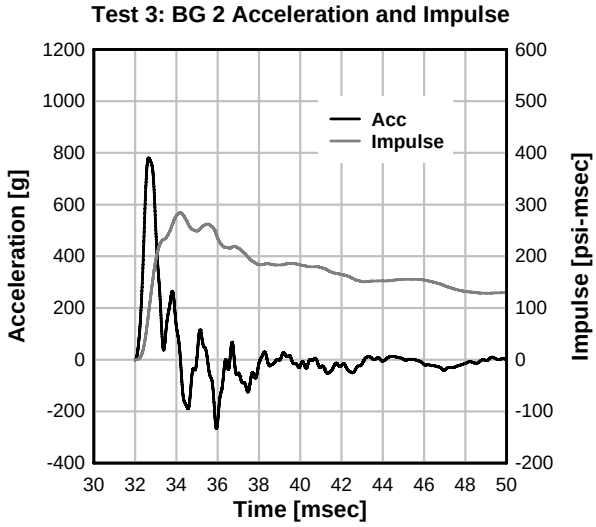
Test 3: BG 2 Acceleration and Impulse
Acc
Impulse
Acceleration [g]
Impulse [psi-msec]
Time [msec]

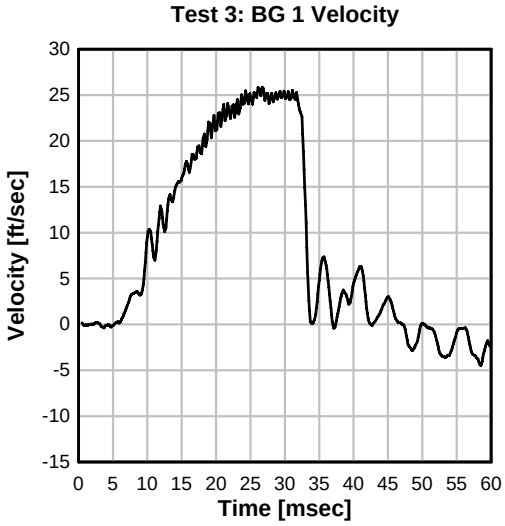
Test 3: BG 1 Velocity
Velocity [ft/sec]
Time [msec]

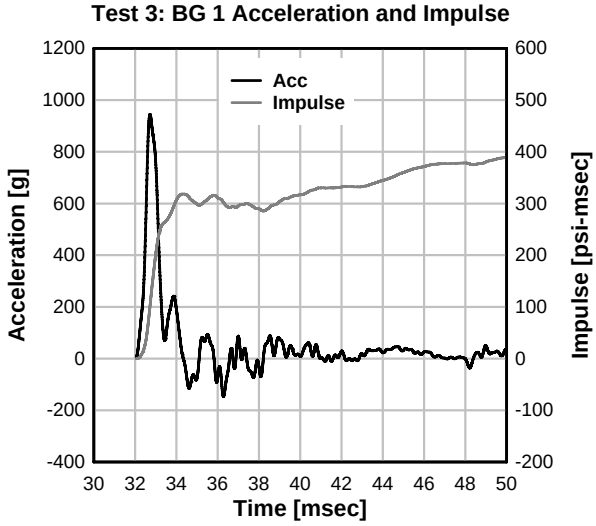
Test 3: BG 1 Acceleration and Impulse
Acc
Impulse
Acceleration [g]
Impulse [psi-msec]
Time [msec]

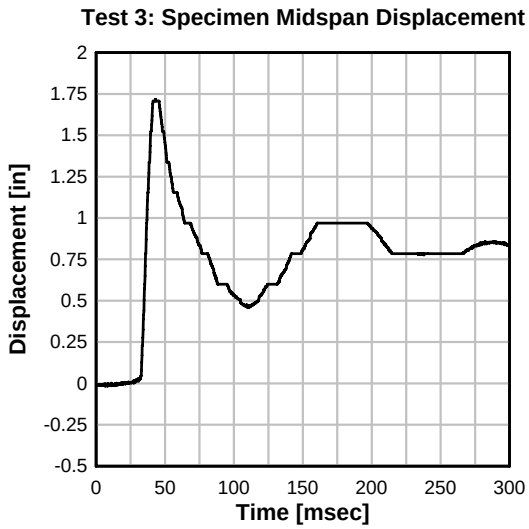
Test 3: Specimen Midspan Displacement
Displacement [in]
Time [msec]
2
1.75
1.5
1.25
1
0.75
0.5
0.25
0
-0.25
-0.5
0
50
100
150
200
250
300

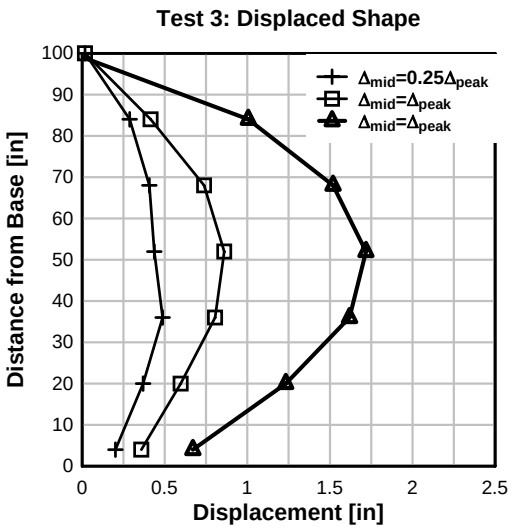
Test 3: Displaced Shape
Distance from Base [in]
Displacement [in]
Δmid=0.25Δpeak
Δmid=Δpeak
Δmid=Δpeak
100
90
80
70
60
50
40
30
20
10
0
0
0.5
1
1.5
2
2.5

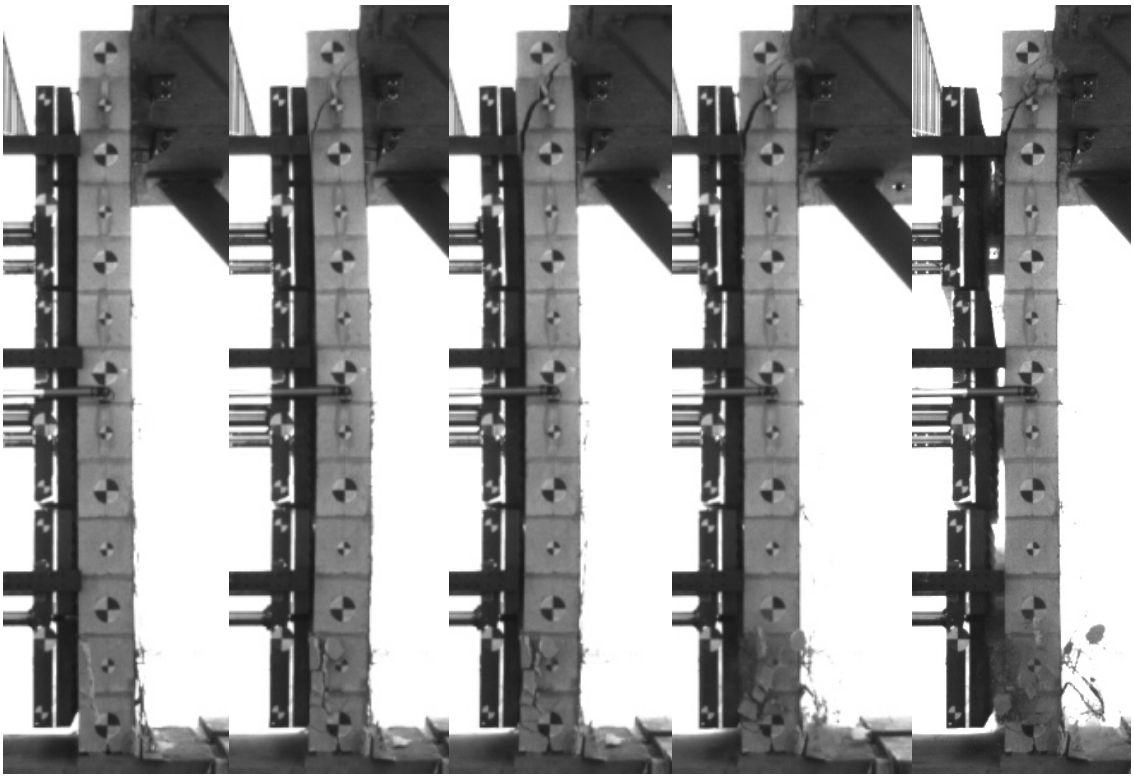

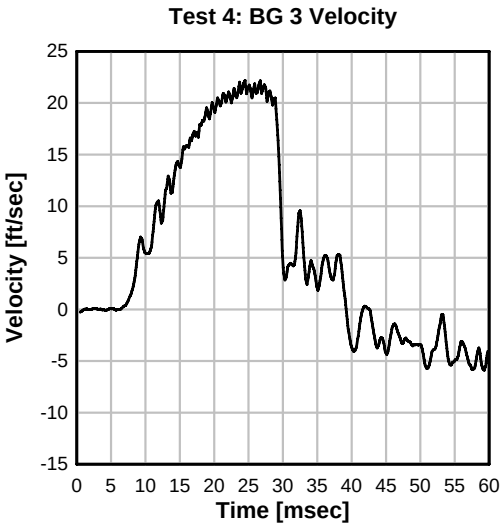
Test 4: BG 3 Velocity
Velocity [ft/sec]
Time [msec]

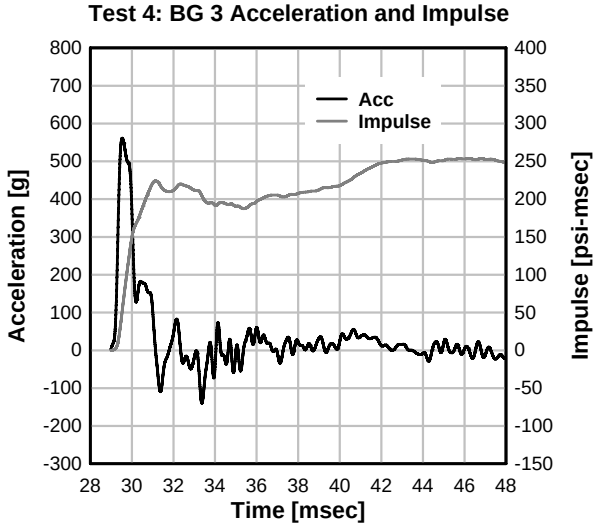
Test 4: BG 3 Acceleration and Impulse
Acc
Impulse
Acceleration [g]
Impulse [psi-msec]
Time [msec]

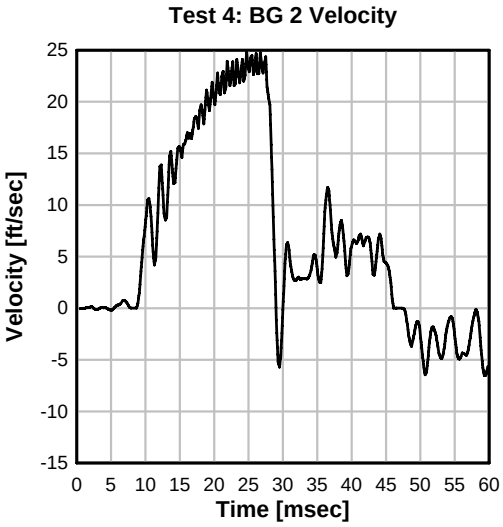
Test 4: BG 2 Velocity
Velocity [ft/sec]
Time [msec]

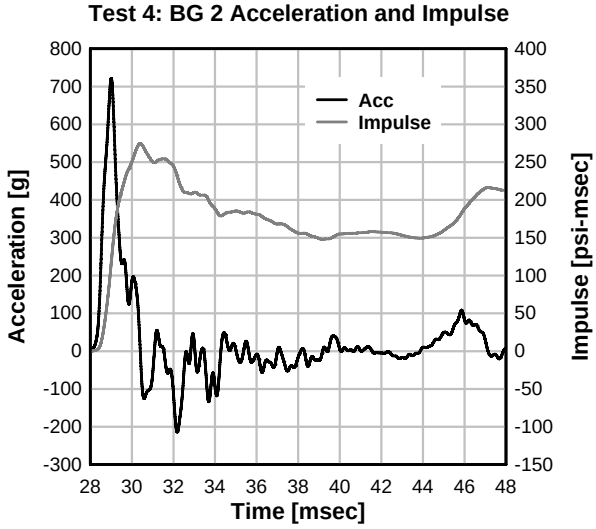
Test 4: BG 2 Acceleration and Impulse
Acc
Impulse
Acceleration [g]
Impulse [psi-msec]
Time [msec]

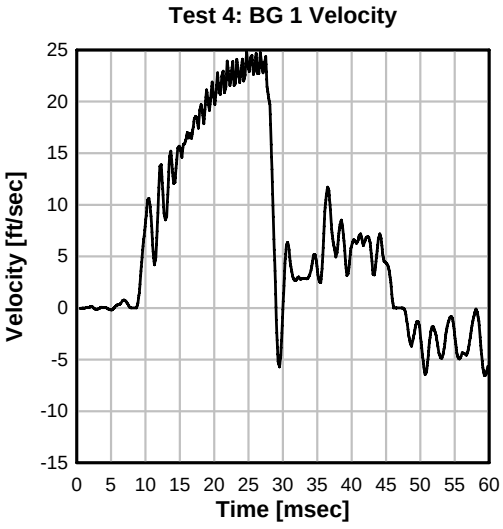
Test 4: BG 1 Velocity
Velocity [ft/sec]
Time [msec]

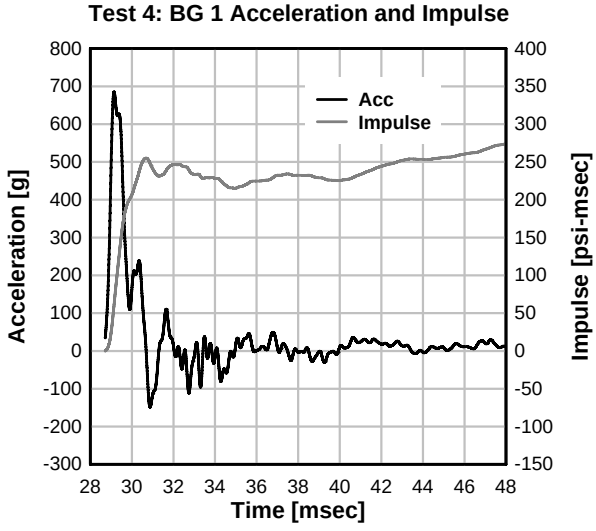
Test 4: BG 1 Acceleration and Impulse
Acc
Impulse
Acceleration [g]
Impulse [psi-msec]
Time [msec]

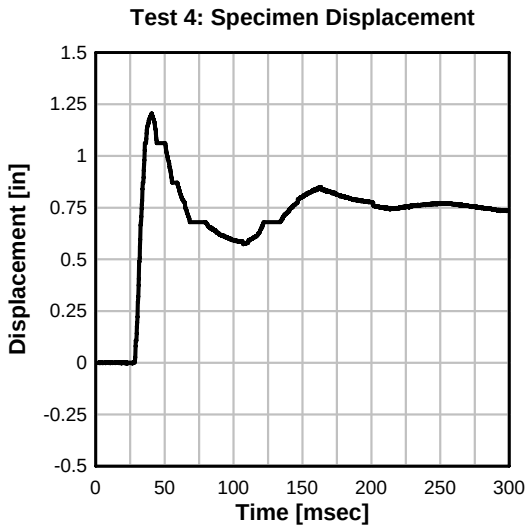
Test 4: Specimen Displacement
Displacement [in]
Time [msec]
1.5
1.25
1
0.75
0.5
0.25
0
-0.25
-0.5
0
50
100
150
200
250
300

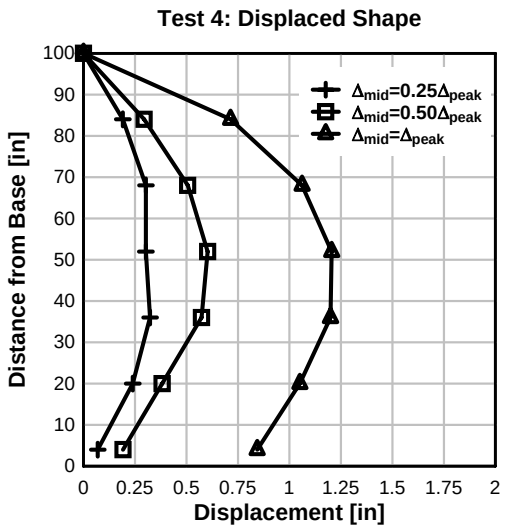
Test 4: Displaced Shape
Distance from Base [in]
Displacement [in]
Δmid=0.25Δpeak
Δmid=0.50Δpeak
Δmid=Δpeak
100
90
80
70
60
50
40
30
20
10
0
0
0.25
0.5
0.75
1
1.25
1.5
1.75
2

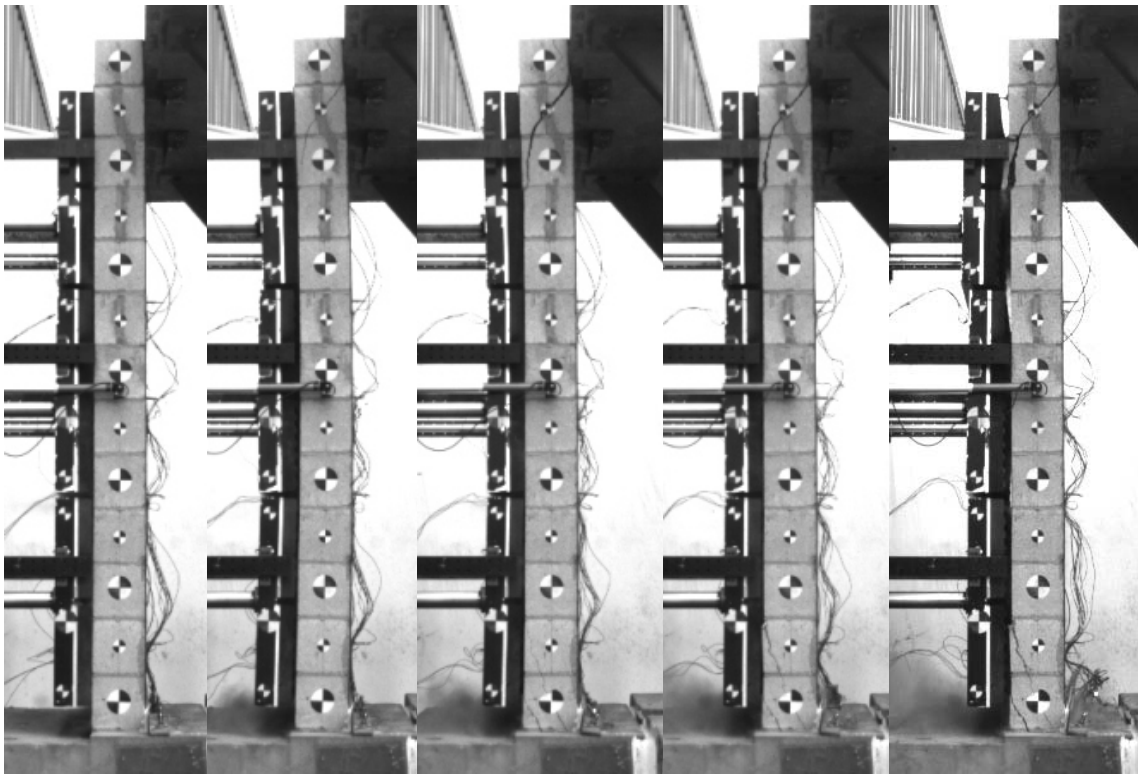

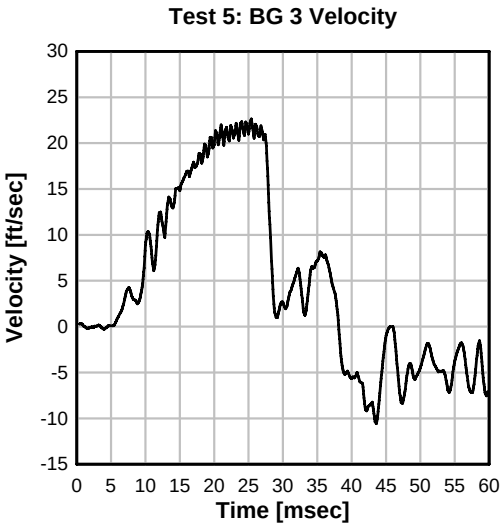
Test 5: BG 3 Velocity
Velocity [ft/sec]
Time [msec]

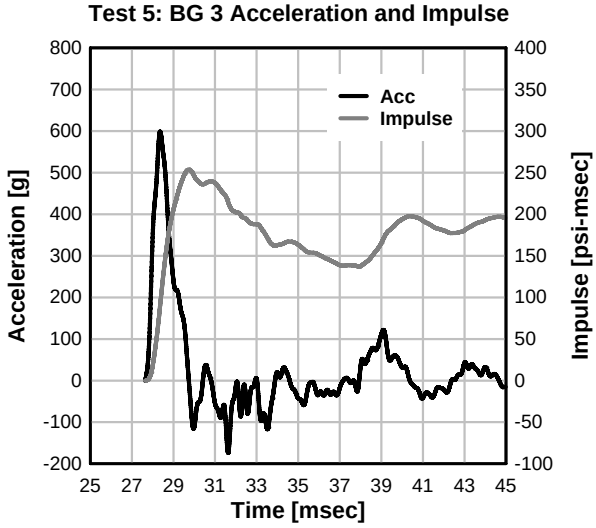
Test 5: BG 3 Acceleration and Impulse
Acc
Impulse
Acceleration [g]
Impulse [psi-msec]
Time [msec]

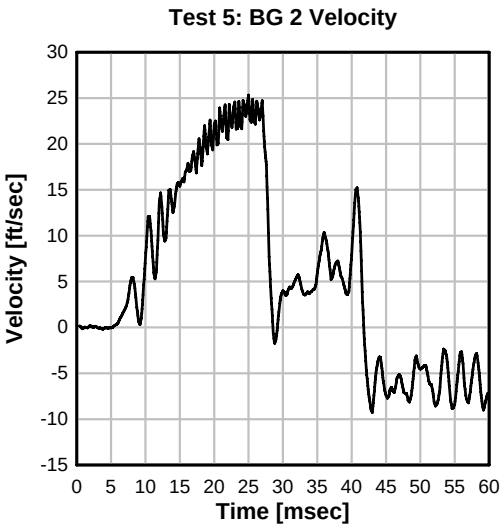
Test 5: BG 2 Velocity
Velocity [ft/sec]
Time [msec]

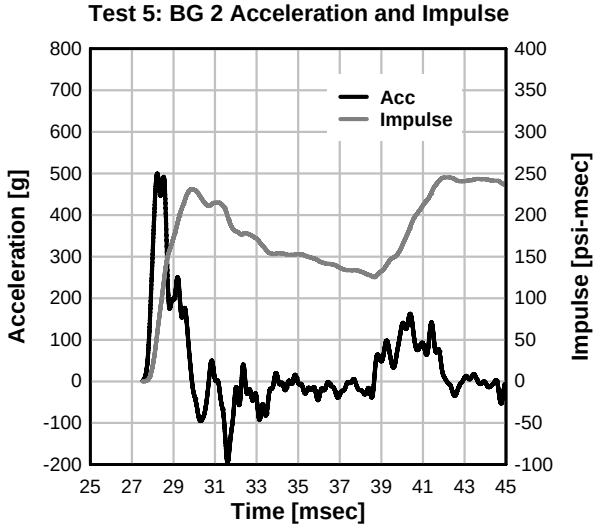
Test 5: BG 2 Acceleration and Impulse
Acc
Impulse
Acceleration [g]
Impulse [psi-msec]
Time [msec]

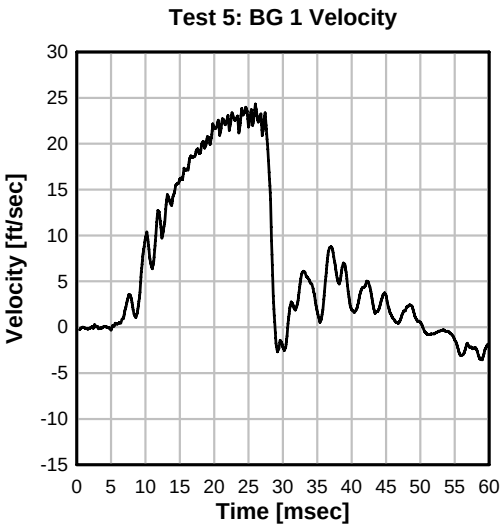
Test 5: BG 1 Velocity
Velocity [ft/sec]
Time [msec]

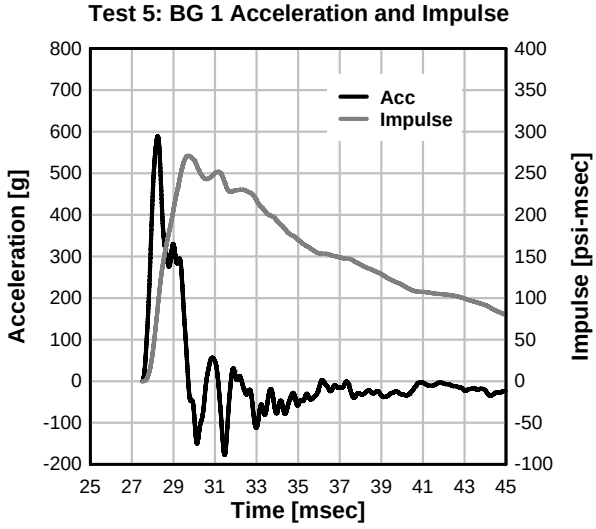
Test 5: BG 1 Acceleration and Impulse
Acc
Impulse
Acceleration [g]
Impulse [psi-msec]
Time [msec]

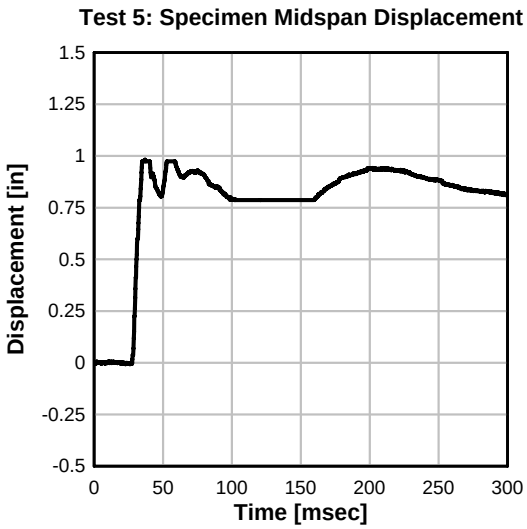
Test 5: Specimen Midspan Displacement
Displacement [in]
Time [msec]
1.5
1.25
1
0.75
0.5
0.25
0
-0.25
-0.5
0
50
100
150
200
250
300

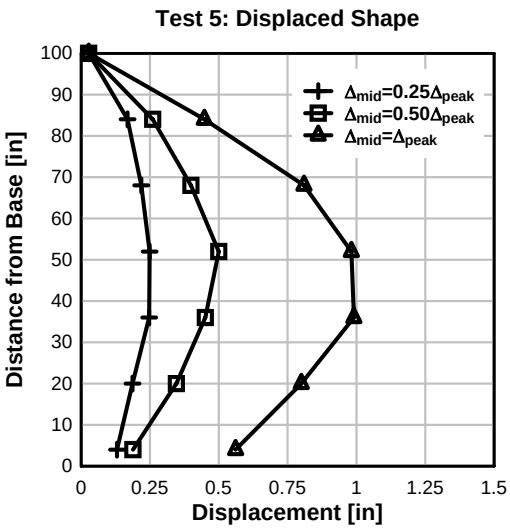
Test 5: Displaced Shape
Distance from Base [in]
Displacement [in]
Δmid=0.25Δpeak
Δmid=0.50Δpeak
Δmid=Δpeak
100
90
80
70
60
50
40
30
20
10
0
0
0.25
0.5
0.75
1
1.25
1.5

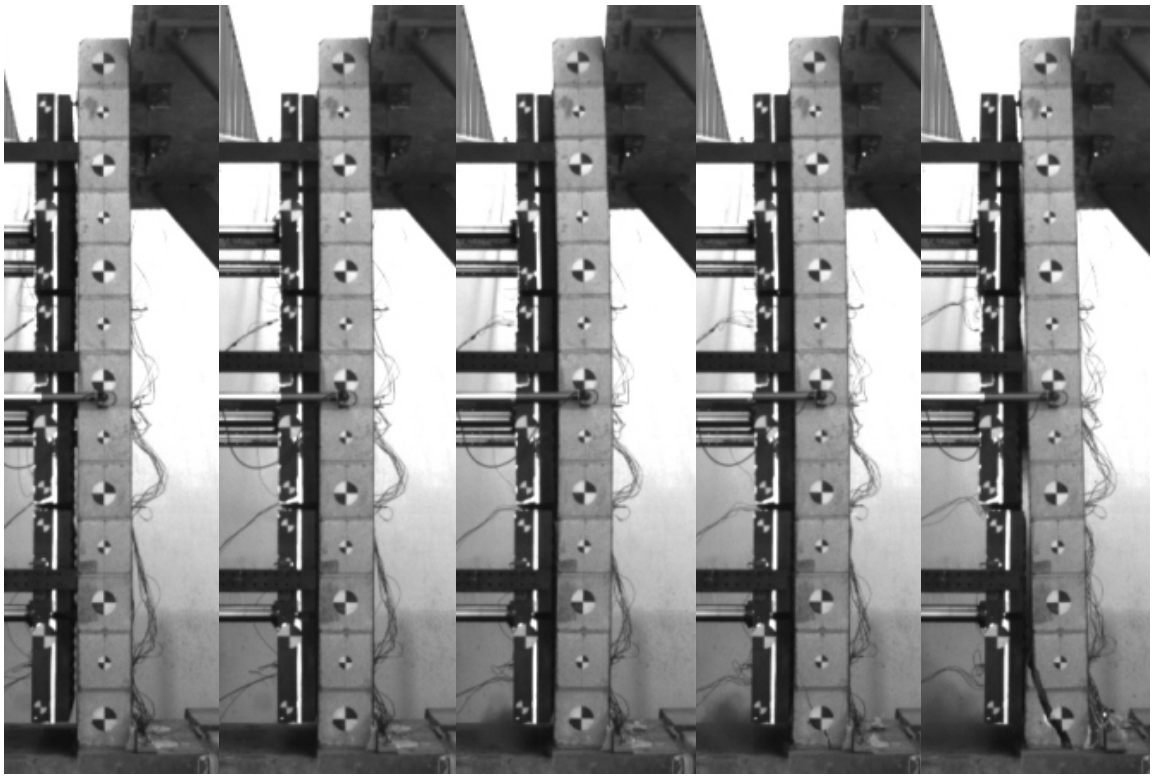

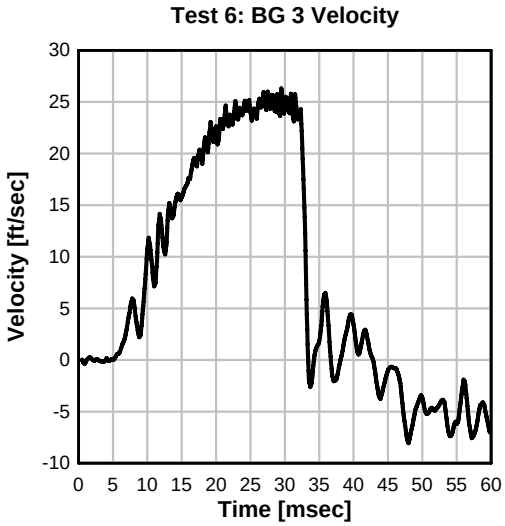
Test 6: BG 3 Velocity
Velocity [ft/sec]
Time [msec]

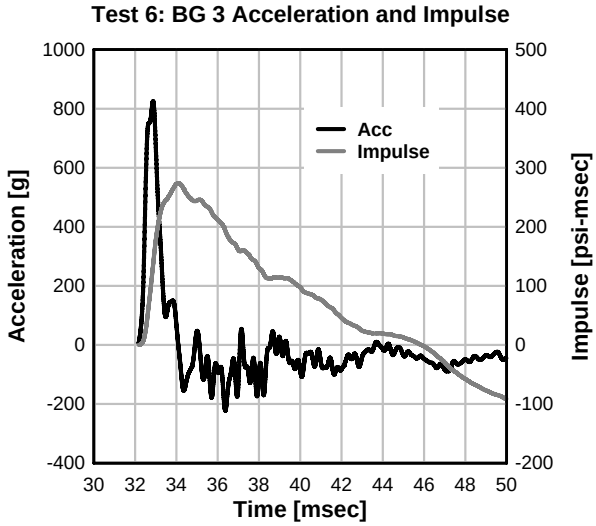
Test 6: BG 3 Acceleration and Impulse
Acc
Impulse
Acceleration [g]
Impulse [psi-msec]
Time [msec]

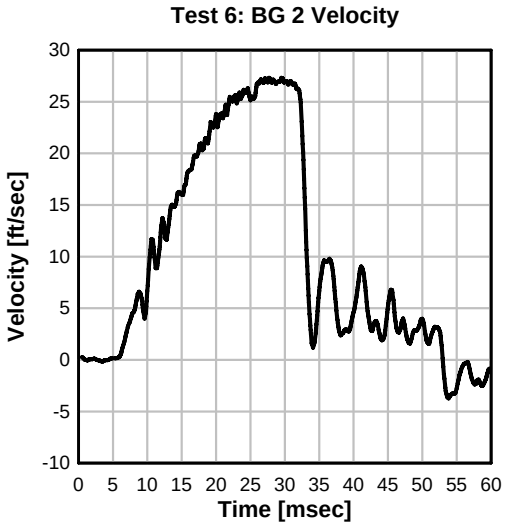
Test 6: BG 2 Velocity
Velocity [ft/sec]
Time [msec]

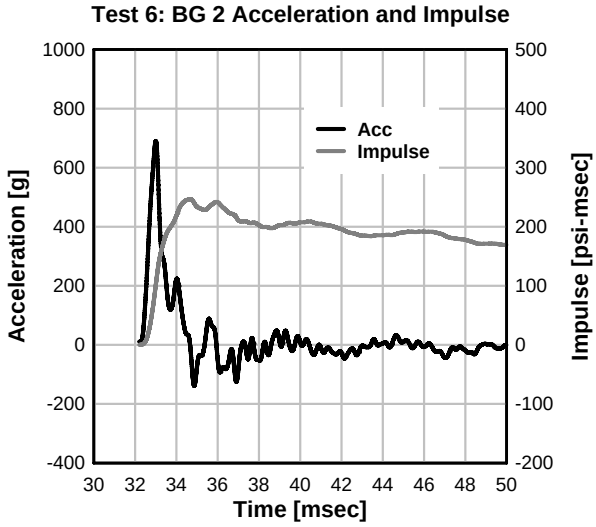
Test 6: BG 2 Acceleration and Impulse
Acc
Impulse
Acceleration [g]
Impulse [psi-msec]
Time [msec]

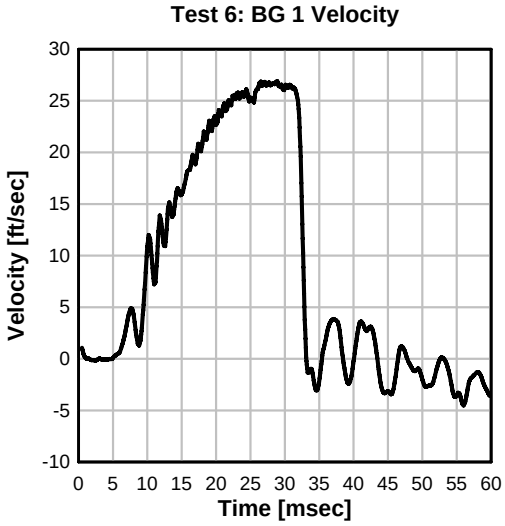
Test 6: BG 1 Velocity
Velocity [ft/sec]
Time [msec]

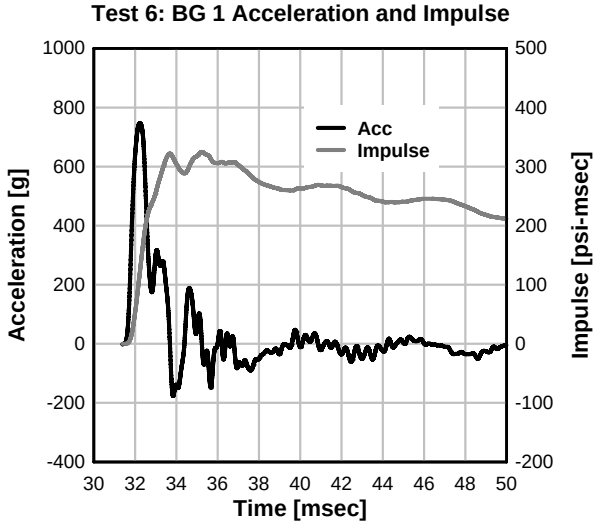
Test 6: BG 1 Acceleration and Impulse
Acc
Impulse
Acceleration [g]
Impulse [psi-msec]
Time [msec]

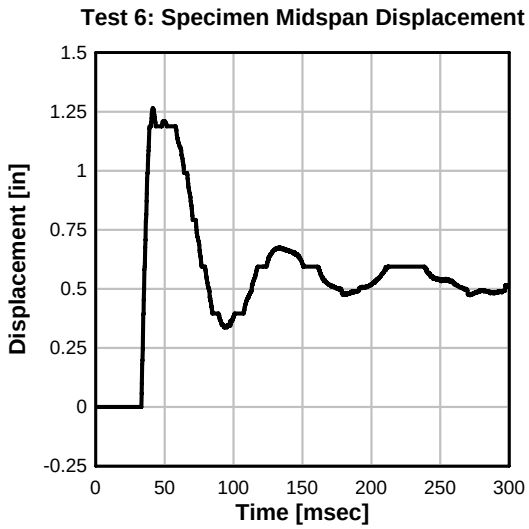
Test 6: Specimen Midspan Displacement
Displacement [in]
Time [msec]
1.5
1.25
1
0.75
0.5
0.25
0
-0.25
0
50
100
150
200
250
300

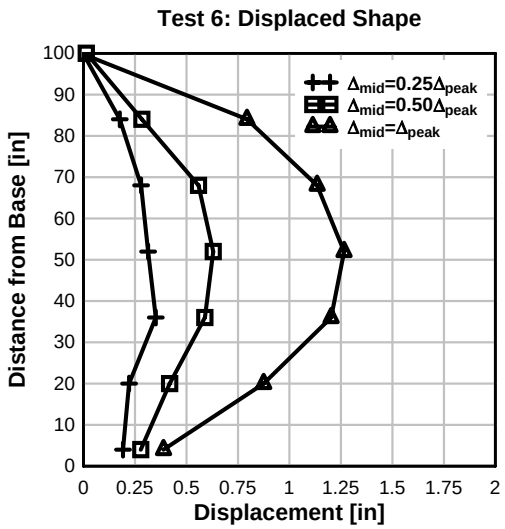
Test 6: Displaced Shape
Distance from Base [in]
Displacement [in]
Δmid=0.25Δpeak
Δmid=0.50Δpeak
Δmid=Δpeak
100
90
80
70
60
50
40
30
20
10
0
0
0.25
0.5
0.75
1
1.25
1.5
1.75
2

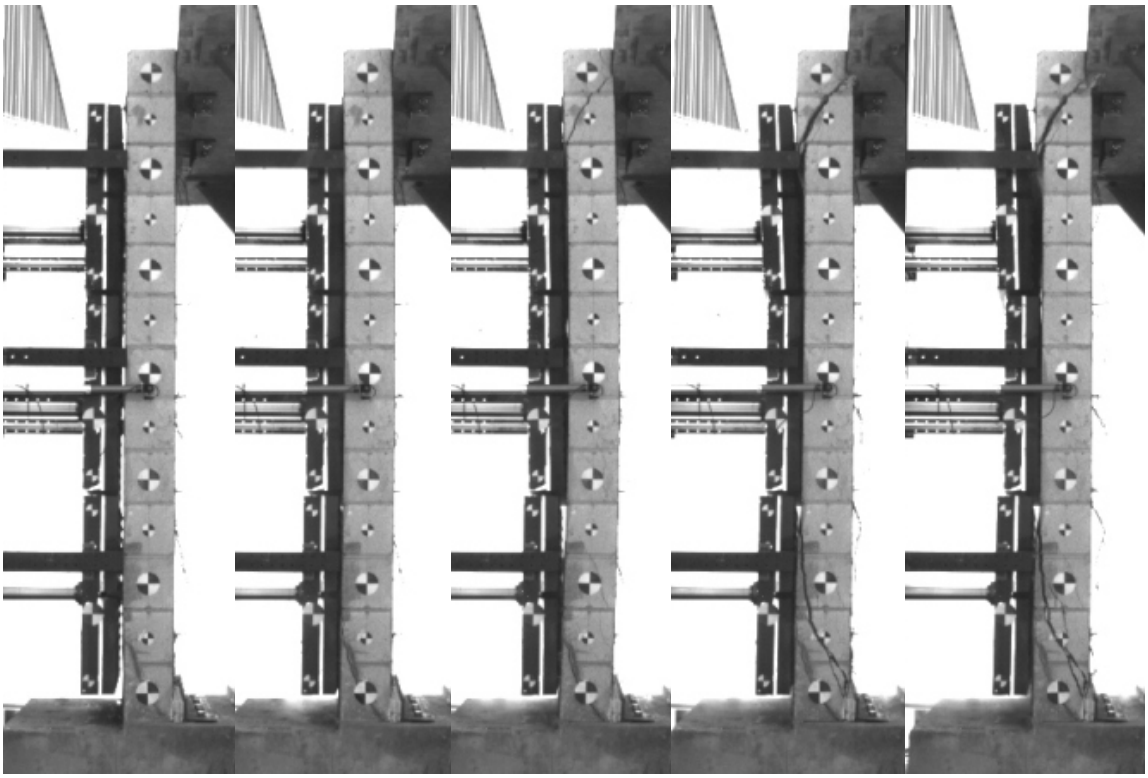

APPENDIX B

This appendix contains test and analytical results from the multiple test series on RC walls with frangible panels that is described in Chapter 5. Plots of load versus displacement are included from the quasi-static tests performed in the first series. For each blast simulator test there are plots of velocity time histories for each BG, acceleration/impulse time histories for each BGs, a displacement time history at the specimen midspan, and specimen displaced shapes at three different times including the time at which the specimen reached peak midspan displacement. Also included for each test is a sequence of photos captured by the high speed camera video. Additional plots are included that compare the results from finite element analyses with the experimental results. For each test there is a plot that compares midspan displacement time histories between the model and the experiment. Comparisons of the displaced shapes for the analysis and the experiments are also plotted for each test.

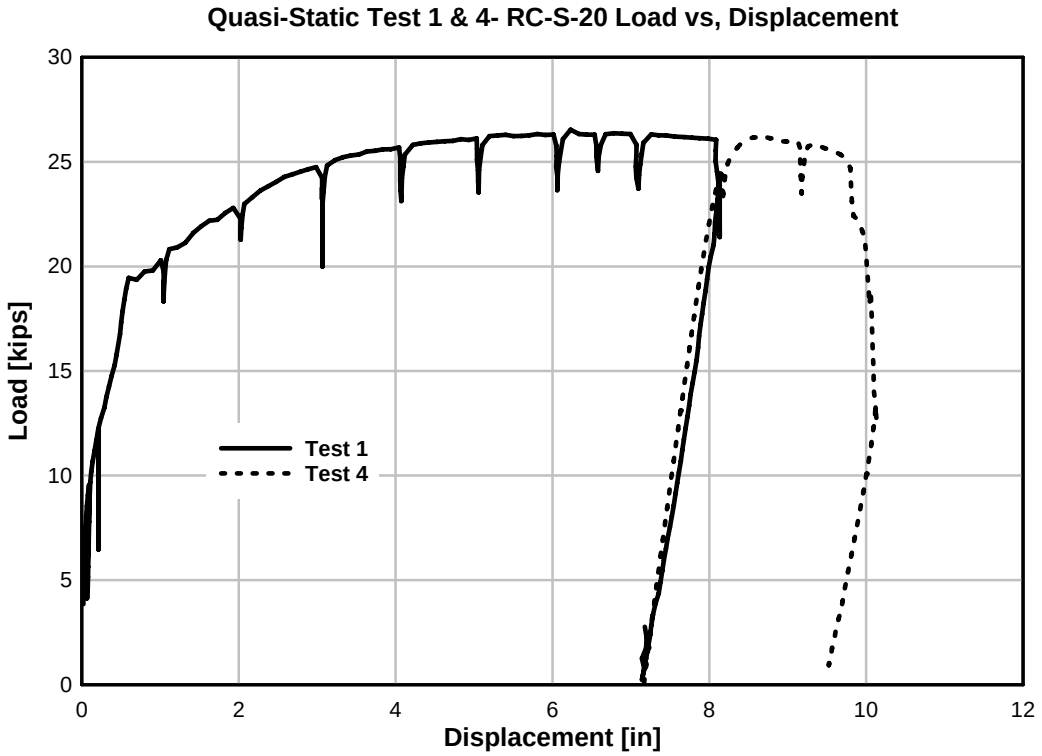
Quasi-Static Test 1 & 4- RC-S-20 Load vs, Displacement
Load [kips]
Displacement [in]
Test 1
Test 4
0
5
10
15
20
25
30
0
2
4
6
8
10
12

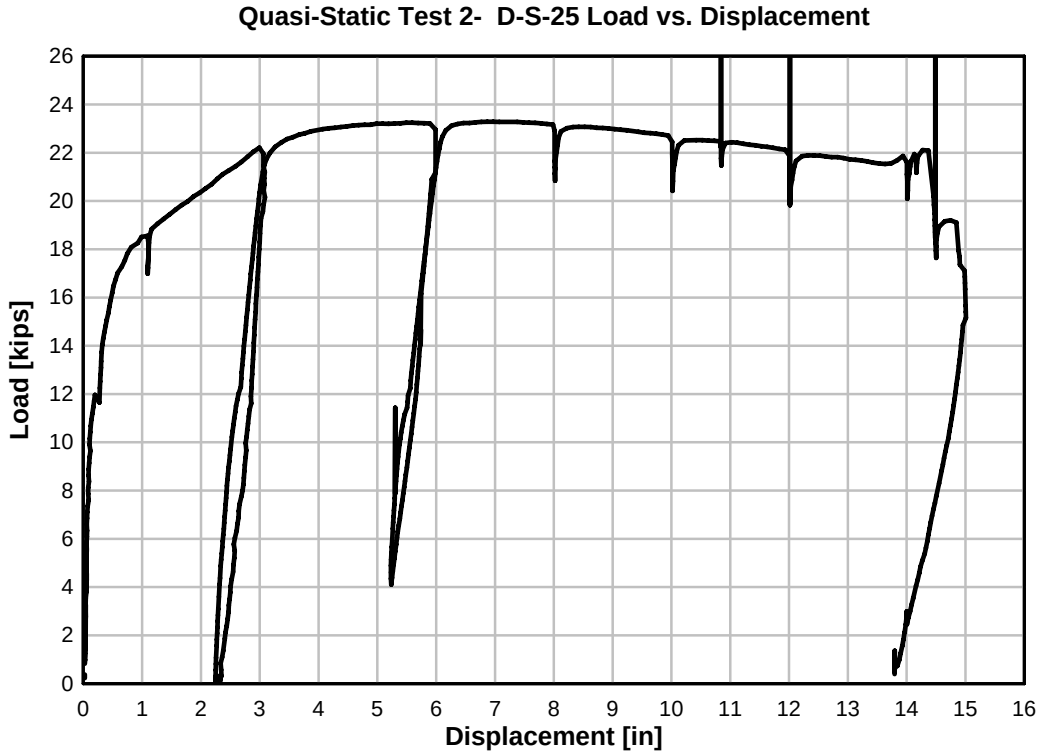
Quasi-Static Test 2- D-S-25 Load vs. Displacement
Load [kips]
Displacement [in]
0
2
4
6
8
10
12
14
16
18
20
22
24
26
0
1
2
3
4
5
6
7
8
9
10
11
12
13
14
15
16

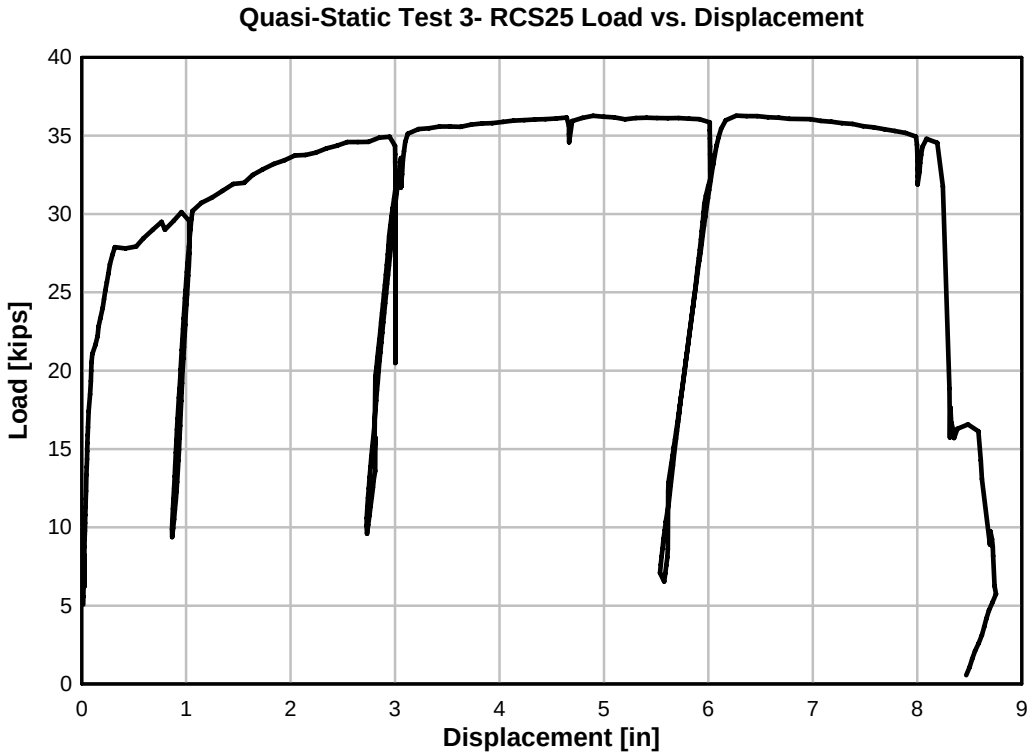
Quasi-Static Test 3- RCS25 Load vs. Displacement
Load [kips]
Displacement [in]
0
5
10
15
20
25
30
35
40
0
1
2
3
4
5
6
7
8
9

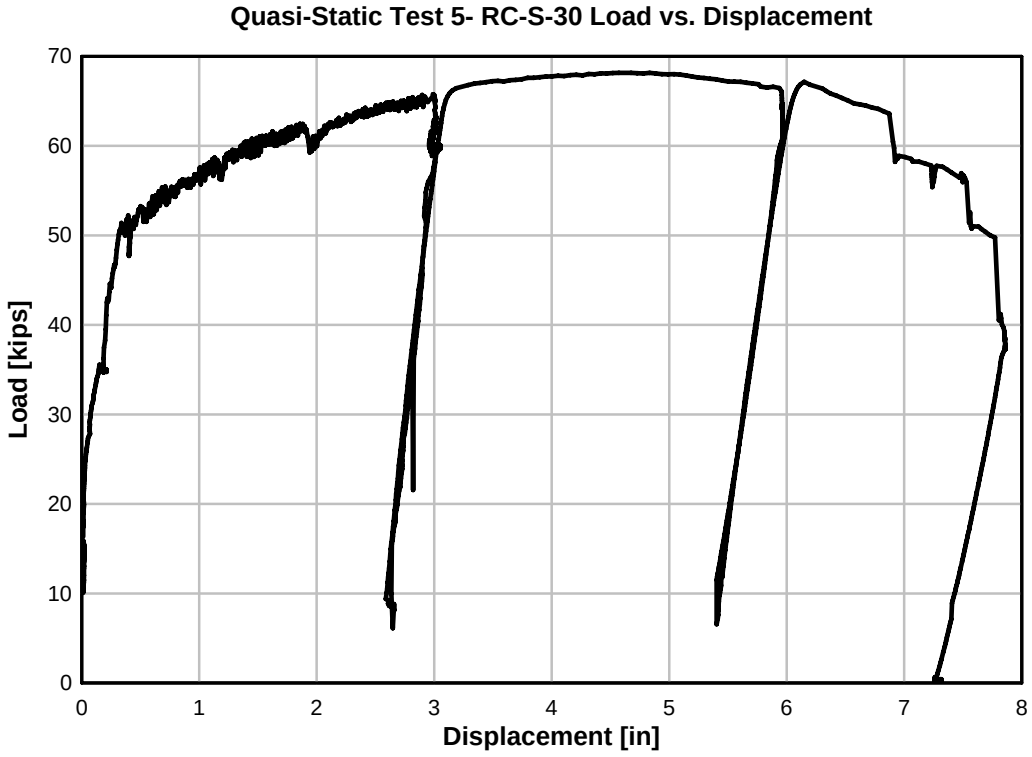
Quasi-Static Test 5- RC-S-30 Load vs. Displacement
Load [kips]
Displacement [in]
0
10
20
30
40
50
60
70
0
1
2
3
4
5
6
7
8

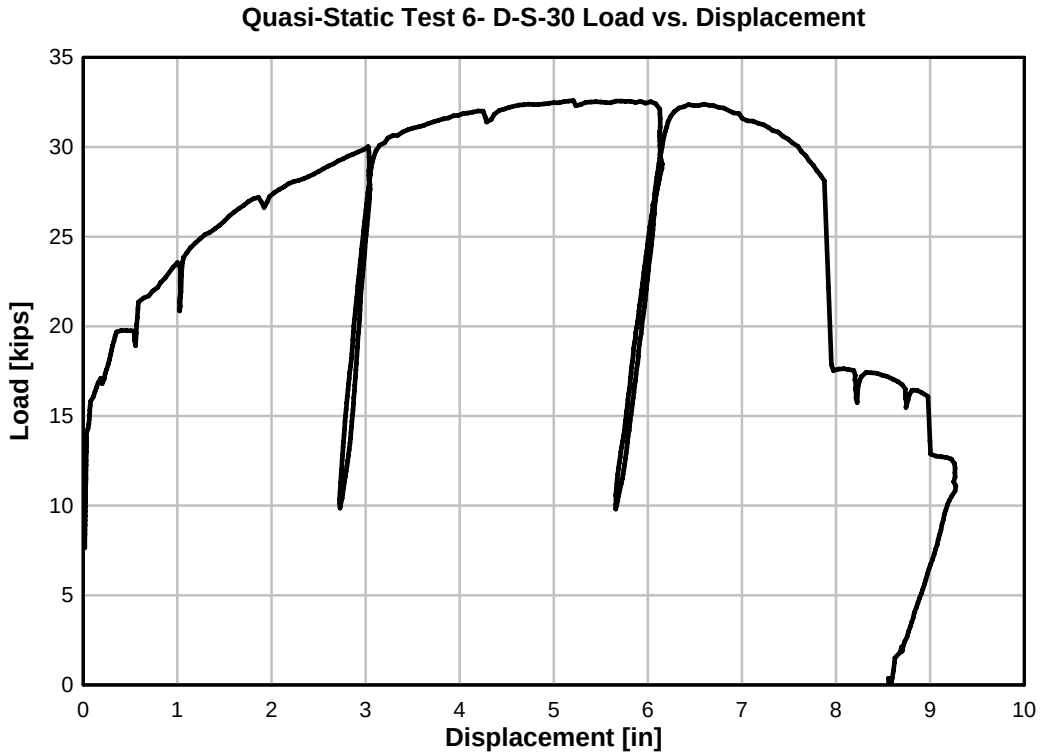
Quasi-Static Test 6- D-S-30 Load vs. Displacement
Load [kips]
Displacement [in]
0
5
10
15
20
25
30
35
0
1
2
3
4
5
6
7
8
9
10

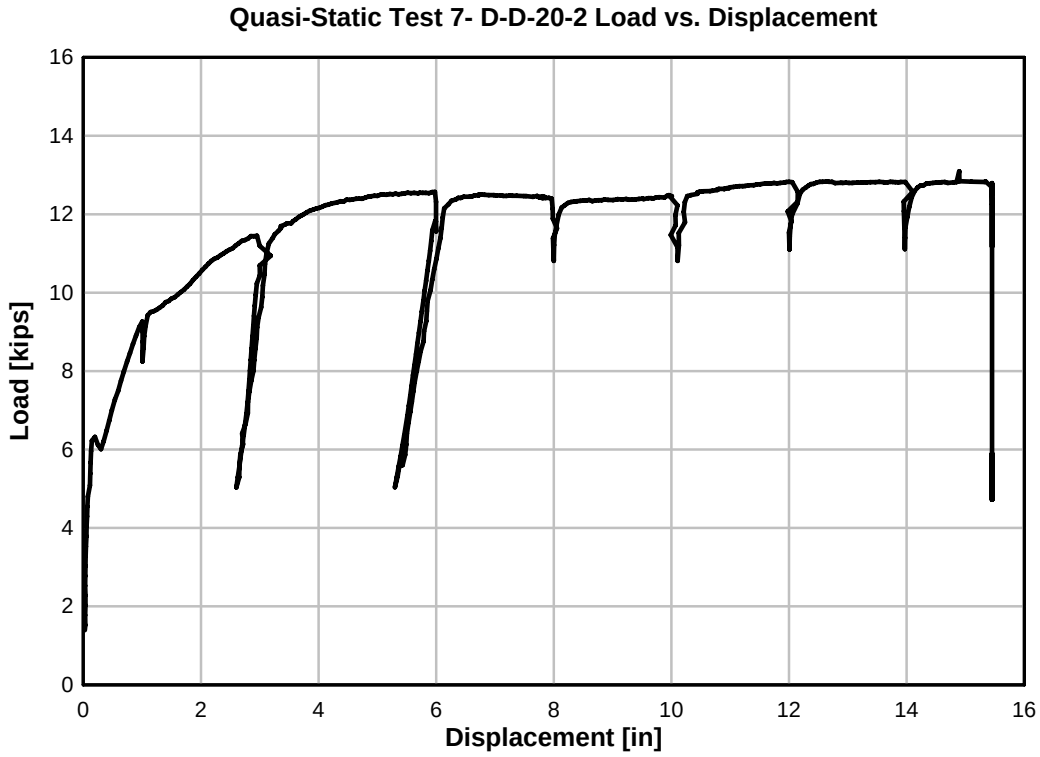
Quasi-Static Test 7- D-D-20-2 Load vs. Displacement
Load [kips]
Displacement [in]
0
2
4
6
8
10
12
14
16
0
2
4
6
8
10
12
14
16

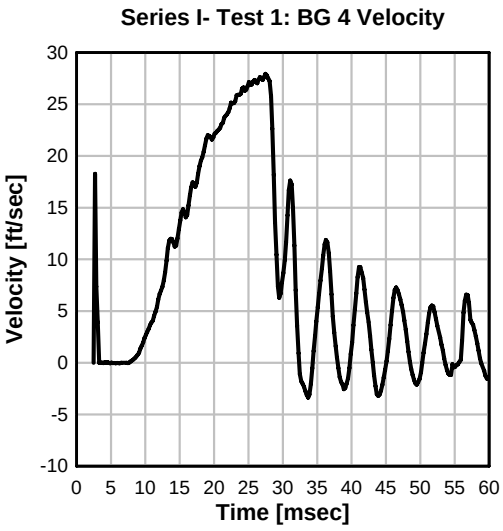
Series I- Test 1: BG 4 Velocity
Velocity [ft/sec]
Time [msec]

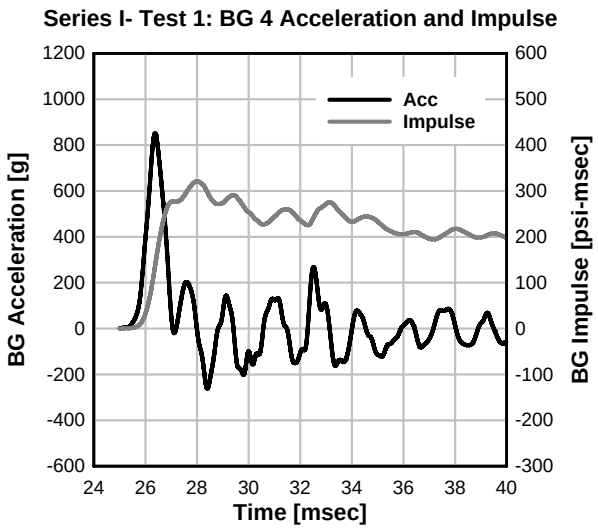
Series I- Test 1: BG 4 Acceleration and Impulse
Acc
Impulse
BG Acceleration [g]
BG Impulse [psi-msec]
Time [msec]

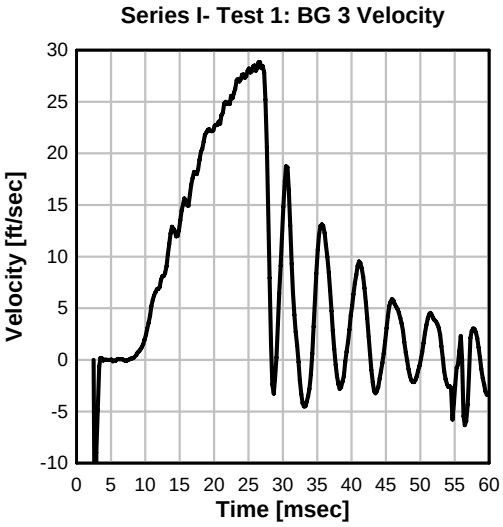
Series I- Test 1: BG 3 Velocity
Velocity [ft/sec]
Time [msec]

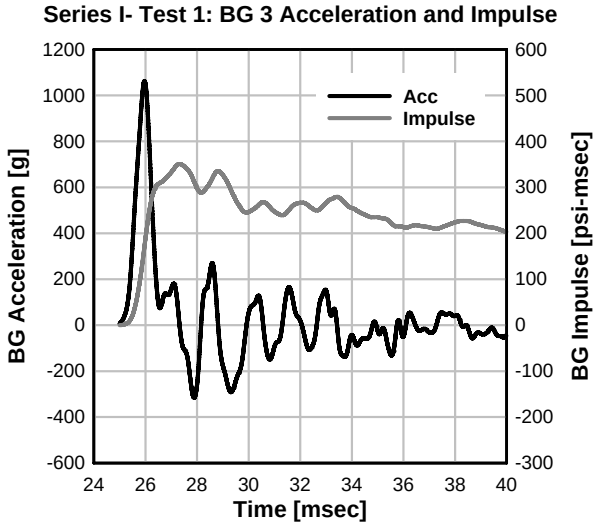
Series I- Test 1: BG 3 Acceleration and Impulse
Acc
Impulse
BG Acceleration [g]
BG Impulse [psi-msec]
Time [msec]

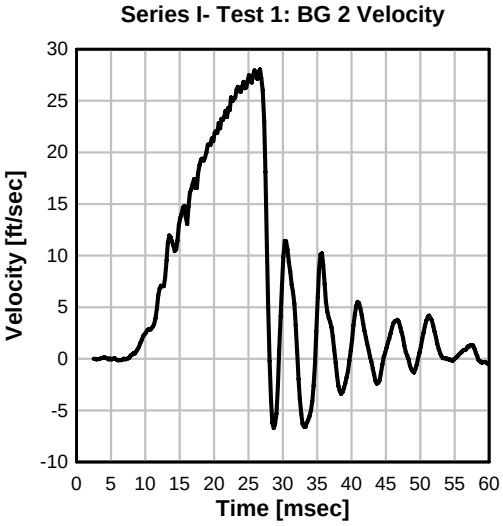
Series I- Test 1: BG 2 Velocity
Velocity [ft/sec]
Time [msec]

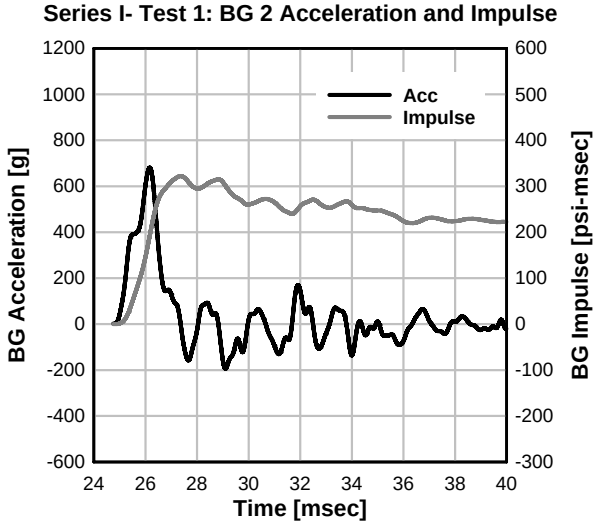
Series I- Test 1: BG 2 Acceleration and Impulse
Acc
Impulse
BG Acceleration [g]
BG Impulse [psi-msec]
Time [msec]

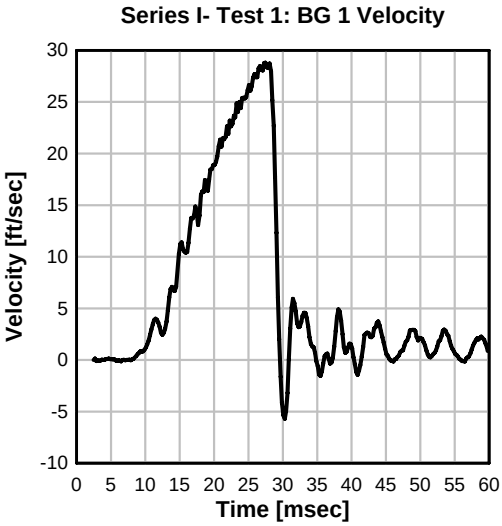
Series I- Test 1: BG 1 Velocity
Velocity [ft/sec]
Time [msec]

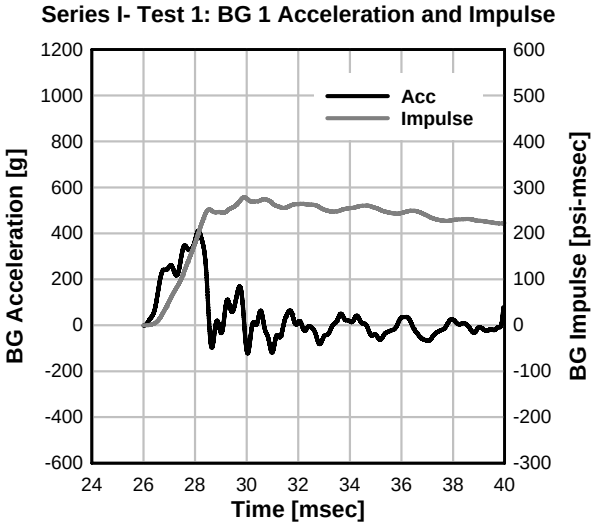
Series I- Test 1: BG 1 Acceleration and Impulse
Acc
Impulse
BG Acceleration [g]
BG Impulse [psi-msec]
Time [msec]

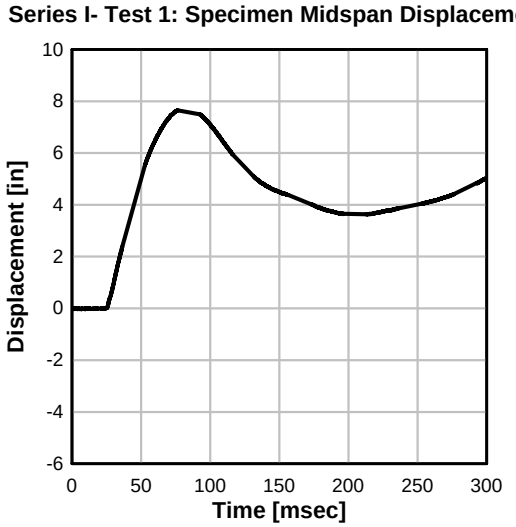
Series I- Test 1: Specimen Midspan Displacement
Displacement [in]
Time [msec]

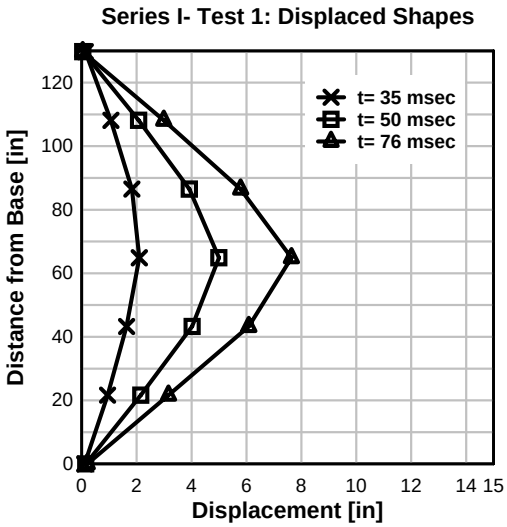
Series I- Test 1: Displaced Shapes
t= 35 msec
t= 50 msec
t= 76 msec
Distance from Base [in]
Displacement [in]

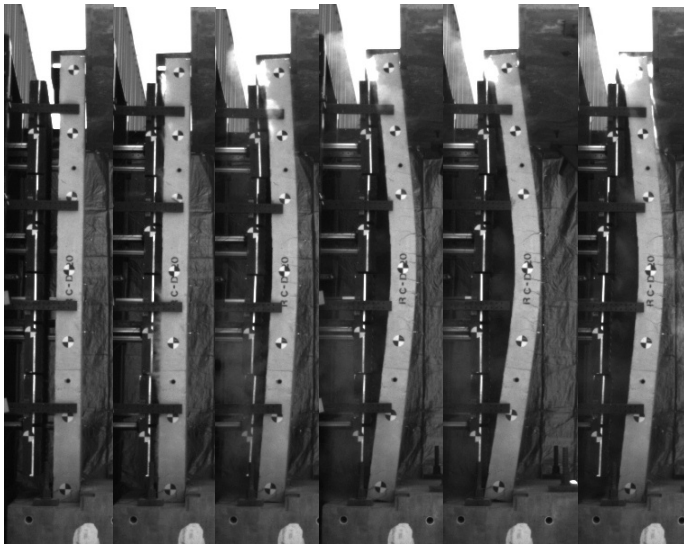

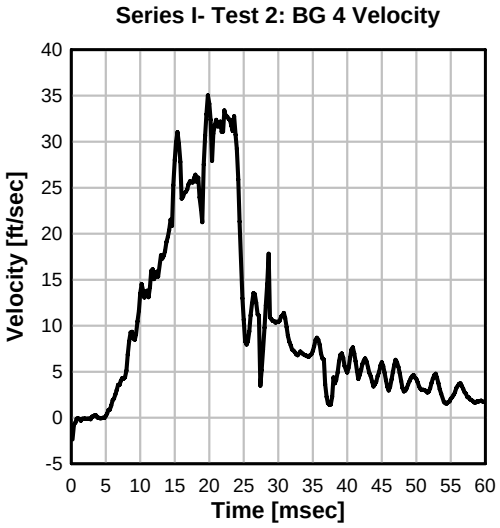
Series I- Test 2: BG 4 Velocity
Velocity [ft/sec]
Time [msec]

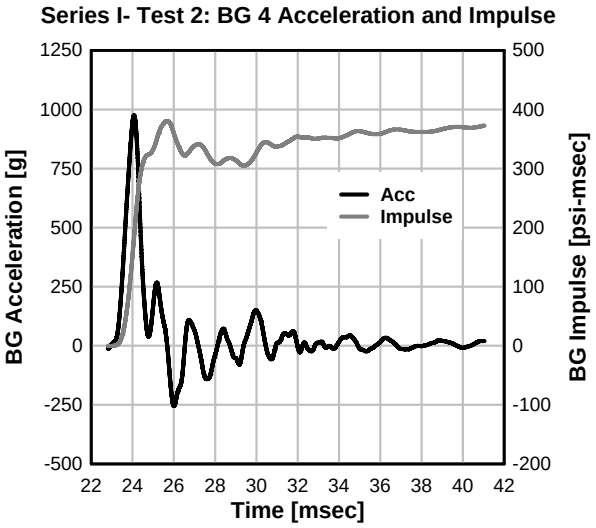
Series I- Test 2: BG 4 Acceleration and Impulse
BG Acceleration [g]
BG Impulse [psi-msec]
Acc
Impulse
Time [msec]

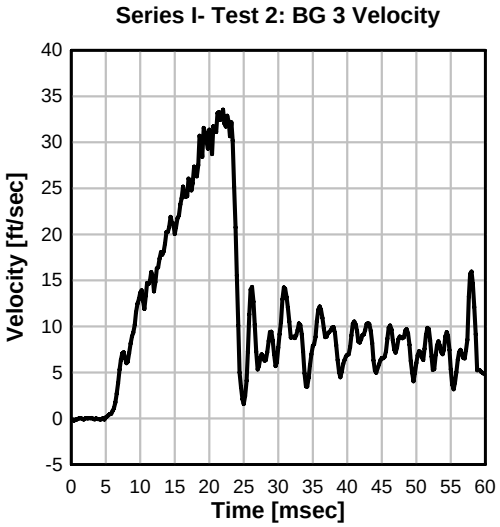
Series I- Test 2: BG 3 Velocity
Velocity [ft/sec]
Time [msec]

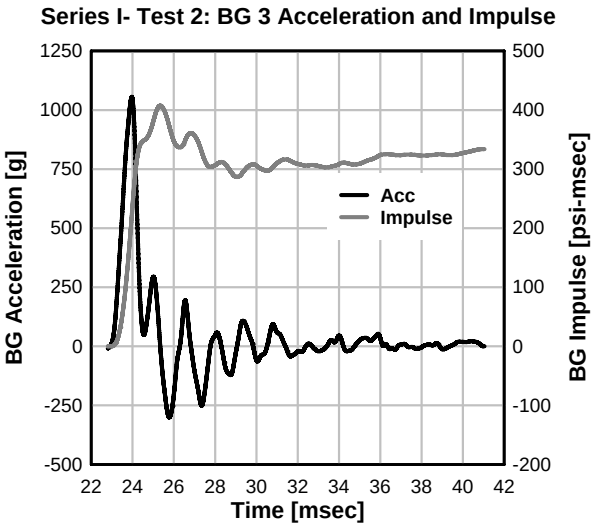
Series I- Test 2: BG 3 Acceleration and Impulse
BG Acceleration [g]
BG Impulse [psi-msec]
Acc
Impulse
Time [msec]

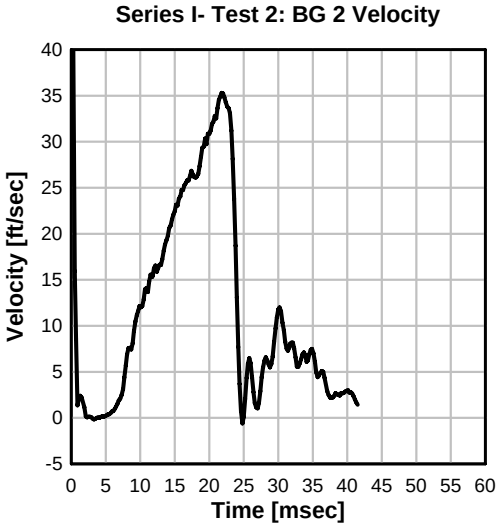
Series I- Test 2: BG 2 Velocity
Velocity [ft/sec]
Time [msec]

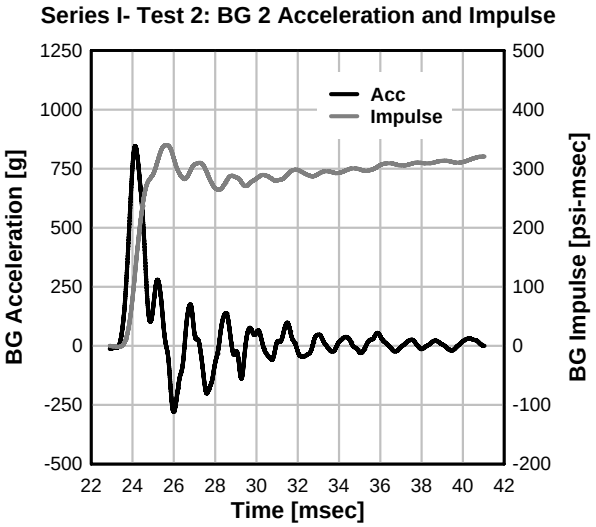
Series I- Test 2: BG 2 Acceleration and Impulse
BG Acceleration [g]
BG Impulse [psi-msec]
Acc
Impulse
Time [msec]

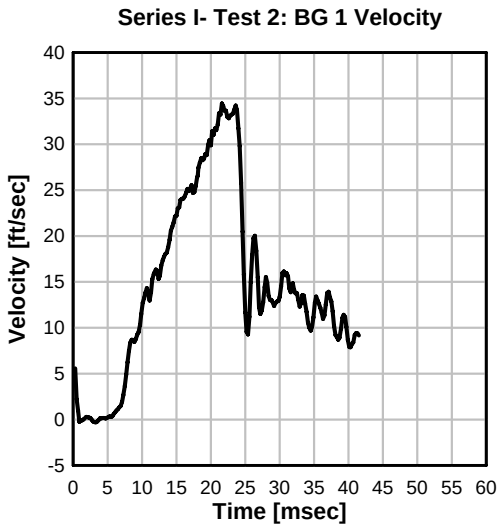
Series I- Test 2: BG 1 Velocity
Velocity [ft/sec]
Time [msec]

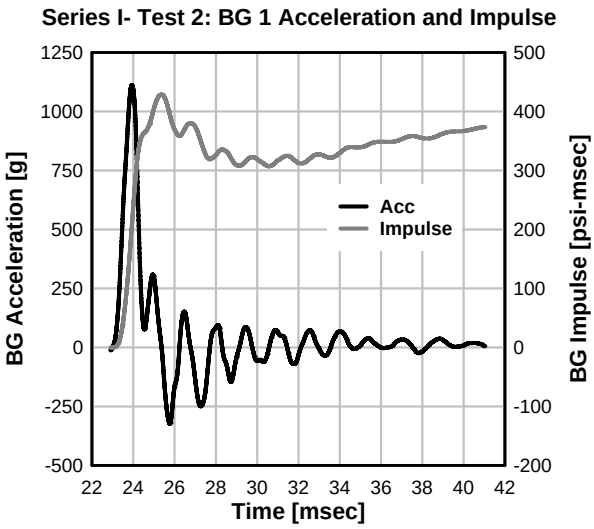
Series I- Test 2: BG 1 Acceleration and Impulse
BG Acceleration [g]
BG Impulse [psi-msec]
Acc
Impulse
Time [msec]

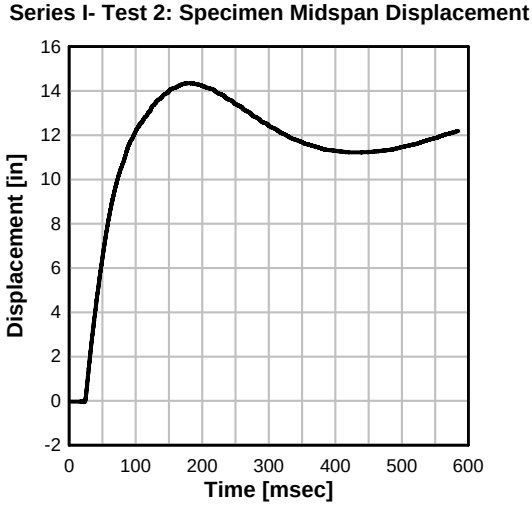
Series I- Test 2: Specimen Midspan Displacement
Displacement [in]
Time [msec]

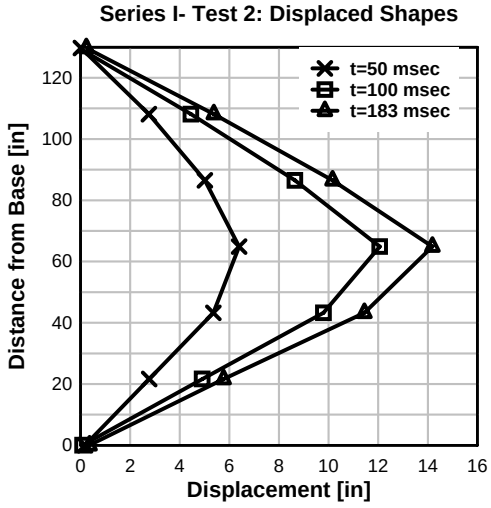
Series I- Test 2: Displaced Shapes
t=50 msec
t=100 msec
t=183 msec
Distance from Base [in]
Displacement [in]

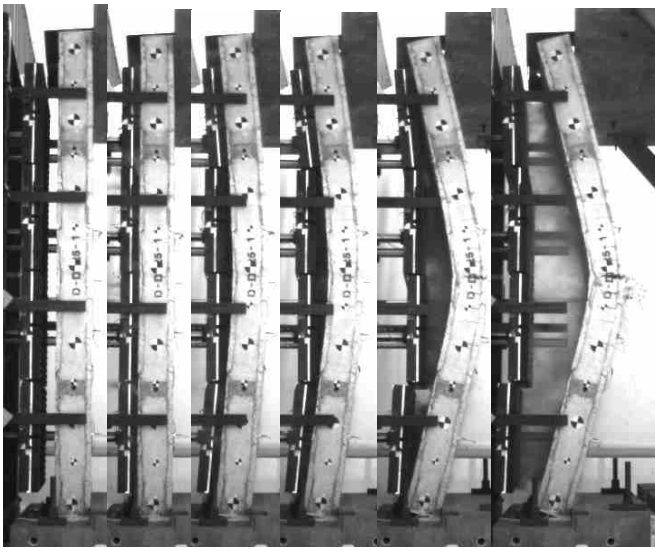

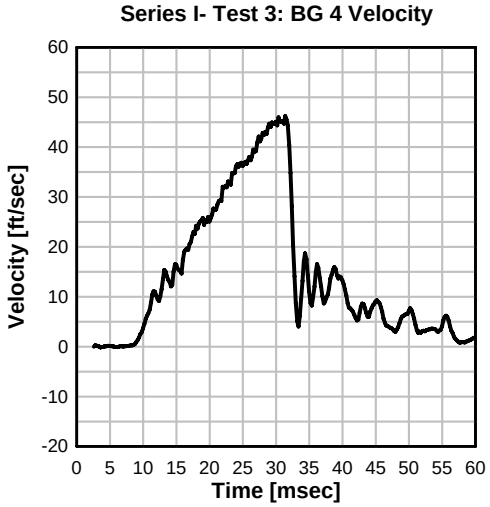
Series I- Test 3: BG 4 Velocity
Velocity [ft/sec]
Time [msec]

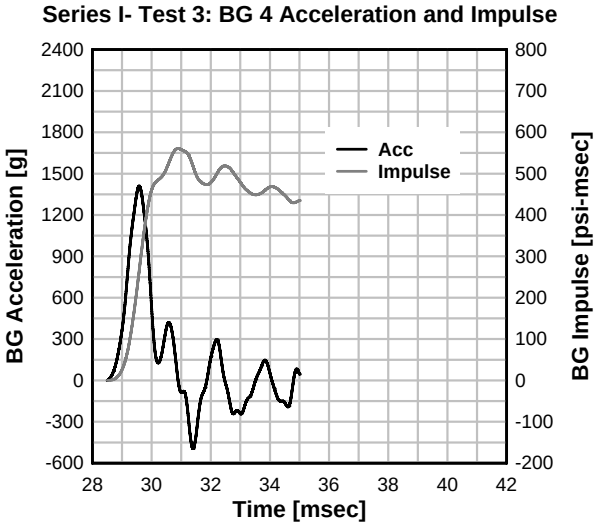
Series I- Test 3: BG 4 Acceleration and Impulse
BG Acceleration [g]
BG Impulse [psi-msec]
Acc
Impulse
Time [msec]

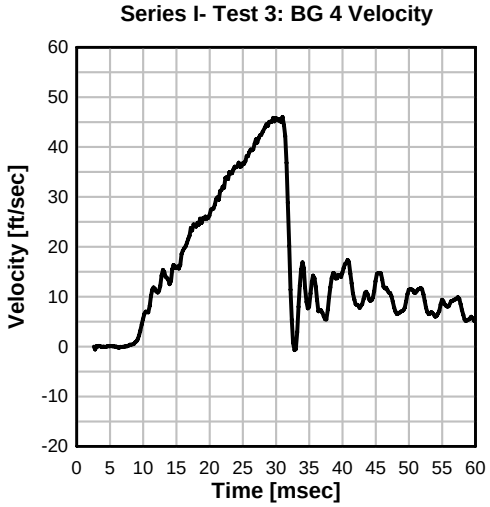
Series I- Test 3: BG 4 Velocity
Velocity [ft/sec]
Time [msec]

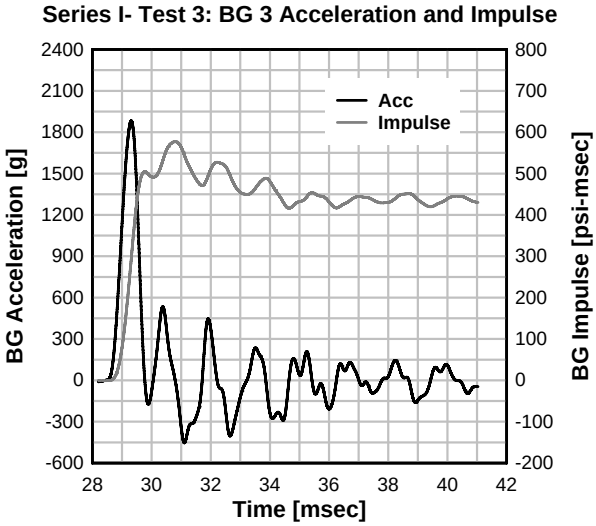
Series I- Test 3: BG 3 Acceleration and Impulse
BG Acceleration [g]
BG Impulse [psi-msec]
Acc
Impulse
Time [msec]

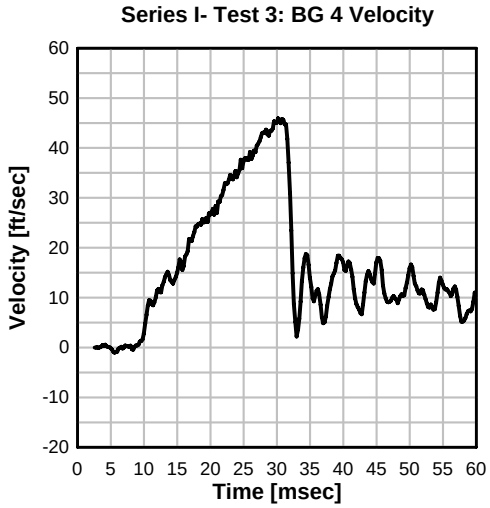
Series I- Test 3: BG 4 Velocity
Velocity [ft/sec]
Time [msec]

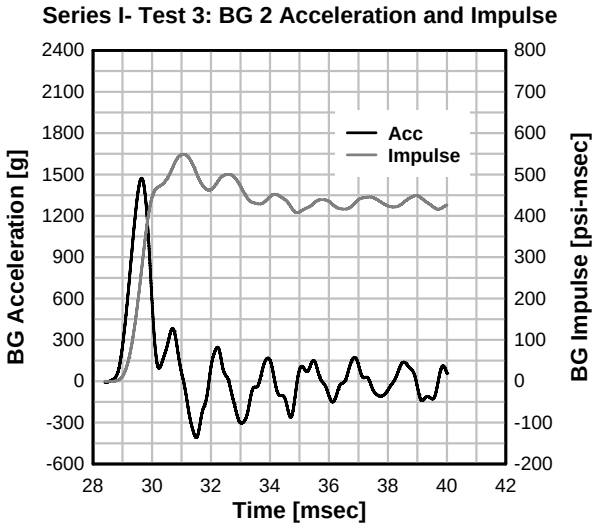
Series I- Test 3: BG 2 Acceleration and Impulse
BG Acceleration [g]
BG Impulse [psi-msec]
Acc
Impulse
Time [msec]

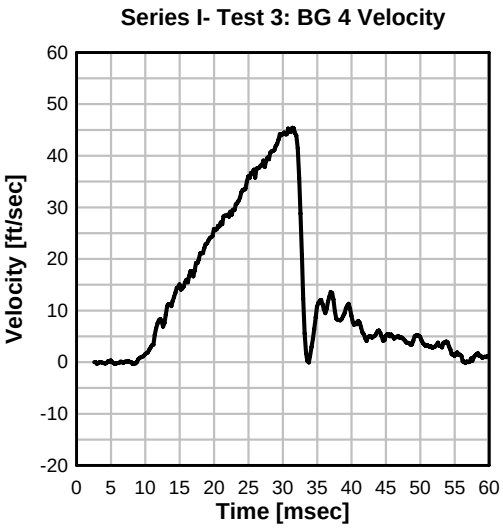
Series I- Test 3: BG 4 Velocity
Velocity [ft/sec]
Time [msec]

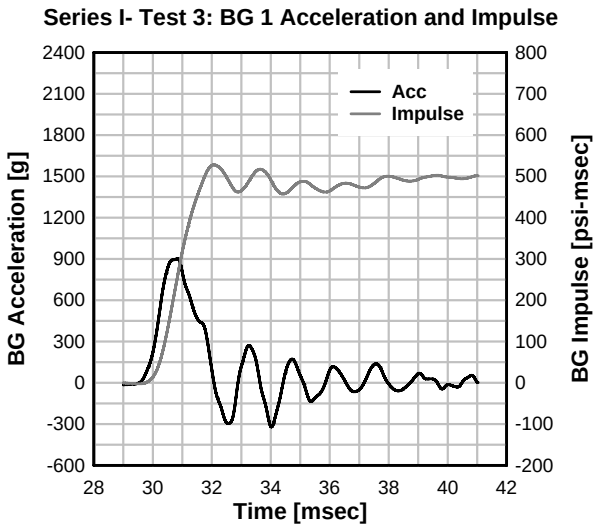
Series I- Test 3: BG 1 Acceleration and Impulse
Acc
Impulse
BG Acceleration [g]
BG Impulse [psi-msec]
Time [msec]

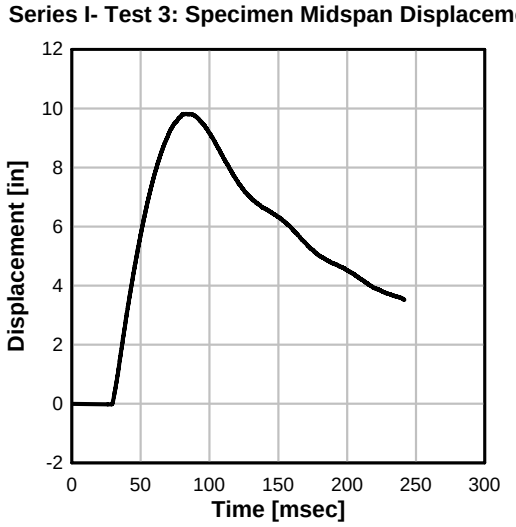
Series I- Test 3: Specimen Midspan Displacement
Displacement [in]
Time [msec]

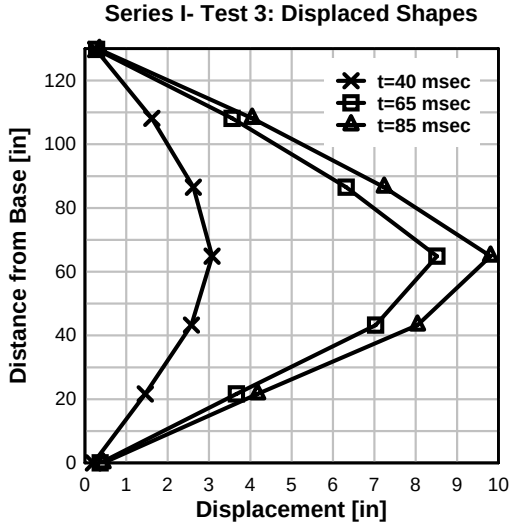
Series I- Test 3: Displaced Shapes
t=40 msec
t=65 msec
t=85 msec
Distance from Base [in]
Displacement [in]

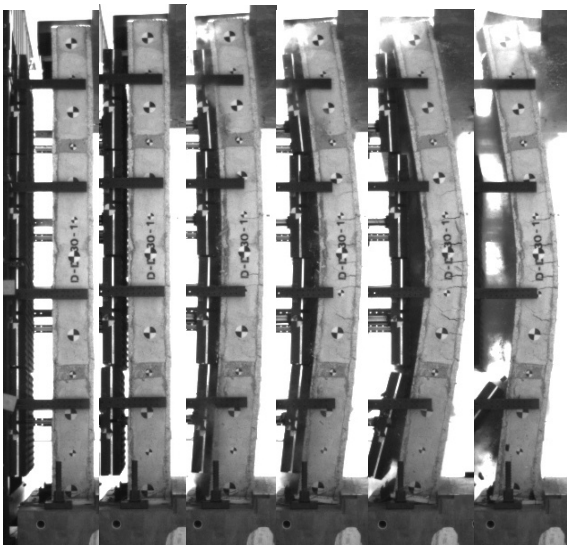

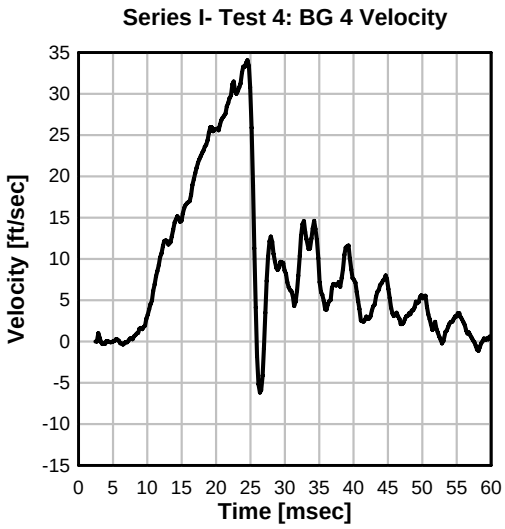
Series I- Test 4: BG 4 Velocity
Velocity [ft/sec]
Time [msec]

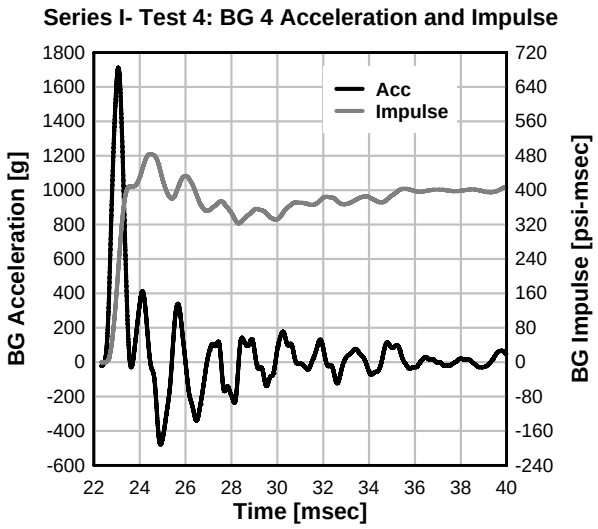
Series I- Test 4: BG 4 Acceleration and Impulse
Acc
Impulse
BG Acceleration [g]
BG Impulse [psi-msec]
Time [msec]

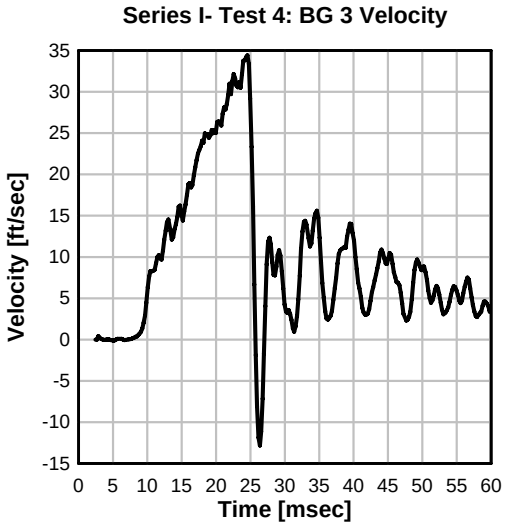
Series I- Test 4: BG 3 Velocity
Velocity [ft/sec]
Time [msec]

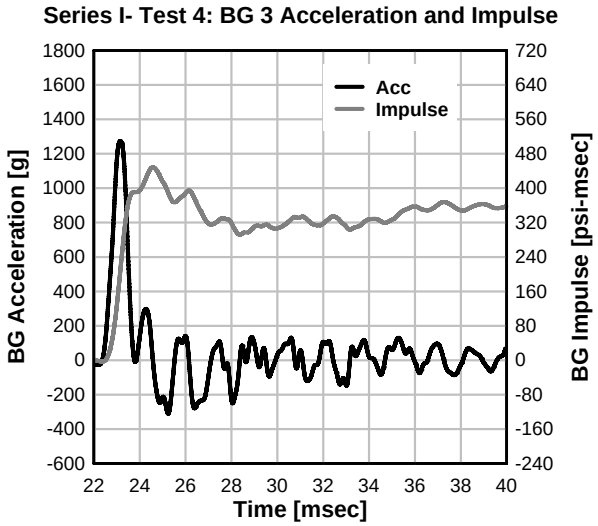
Series I- Test 4: BG 3 Acceleration and Impulse
Acc
Impulse
BG Acceleration [g]
BG Impulse [psi-msec]
Time [msec]

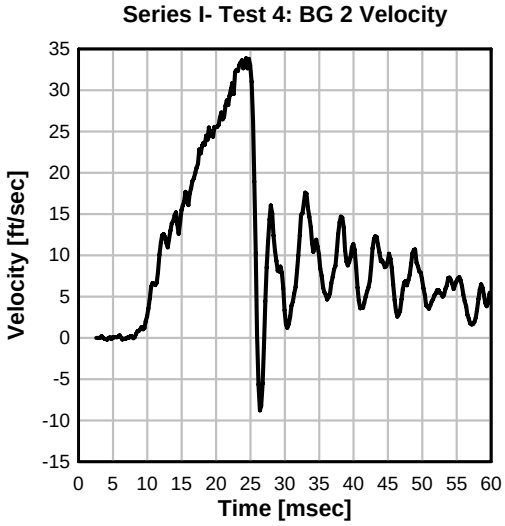
Series I- Test 4: BG 2 Velocity
Velocity [ft/sec]
Time [msec]

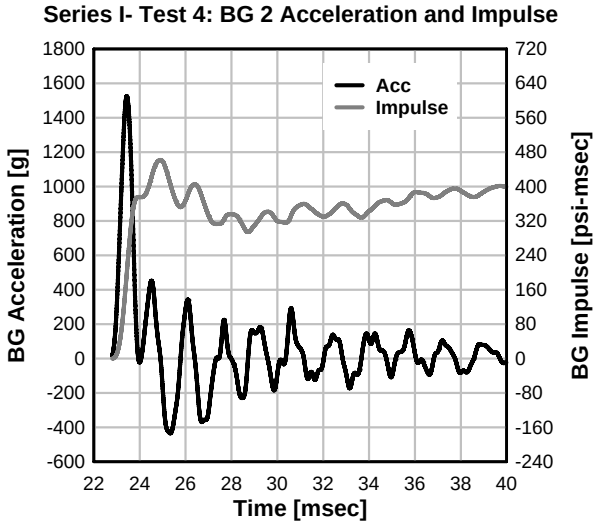
Series I- Test 4: BG 2 Acceleration and Impulse
Acc
Impulse
BG Acceleration [g]
BG Impulse [psi-msec]
Time [msec]

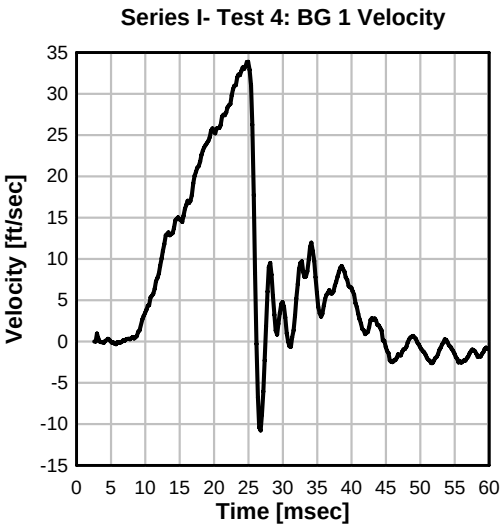
Series I- Test 4: BG 1 Velocity
Velocity [ft/sec]
Time [msec]

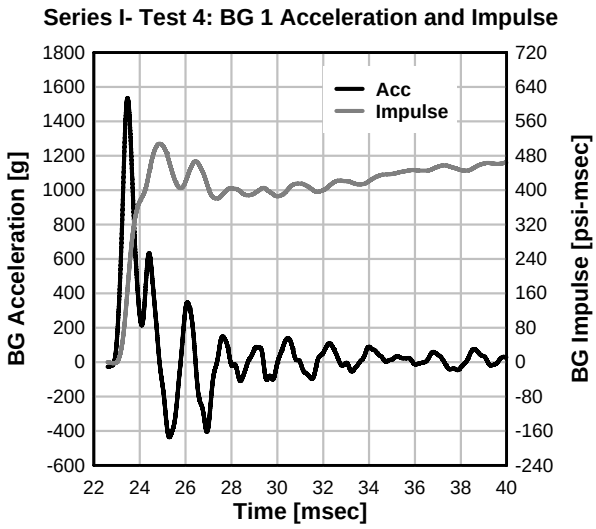
Series I- Test 4: BG 1 Acceleration and Impulse
Acc
Impulse
BG Acceleration [g]
BG Impulse [psi-msec]
Time [msec]

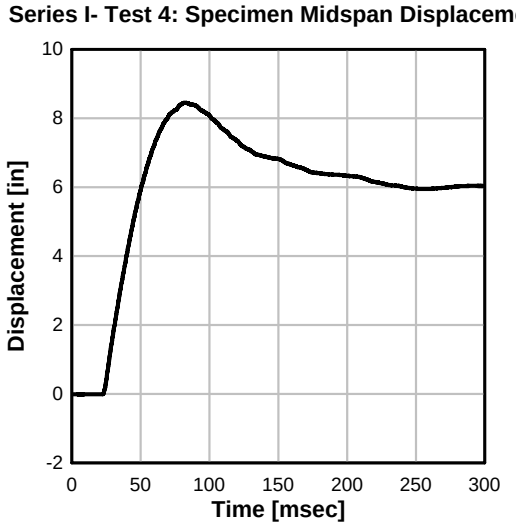
Series I- Test 4: Specimen Midspan Displacement
Displacement [in]
Time [msec]

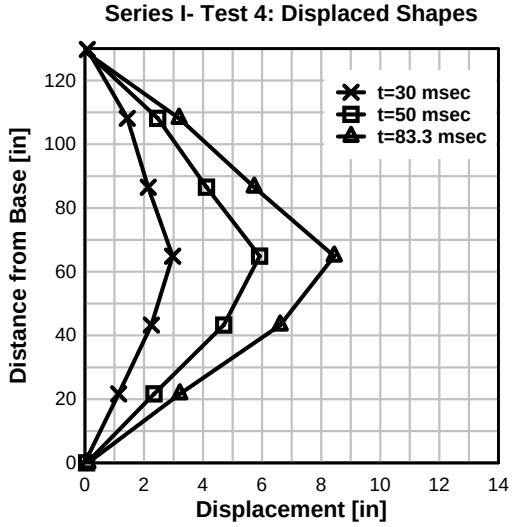
Series I- Test 4: Displaced Shapes
t=30 msec
t=50 msec
t=83.3 msec
Distance from Base [in]
Displacement [in]

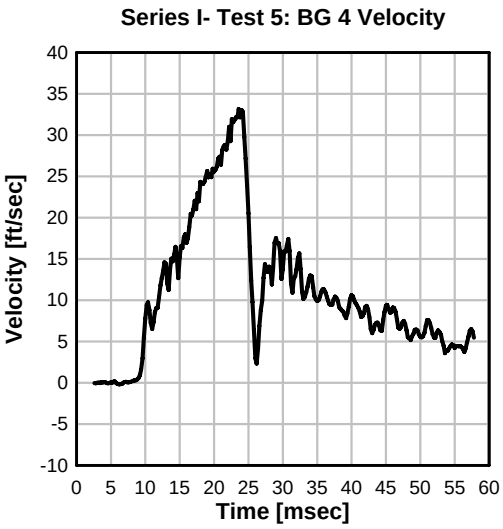
Series I- Test 5: BG 4 Velocity
Velocity [ft/sec]
Time [msec]

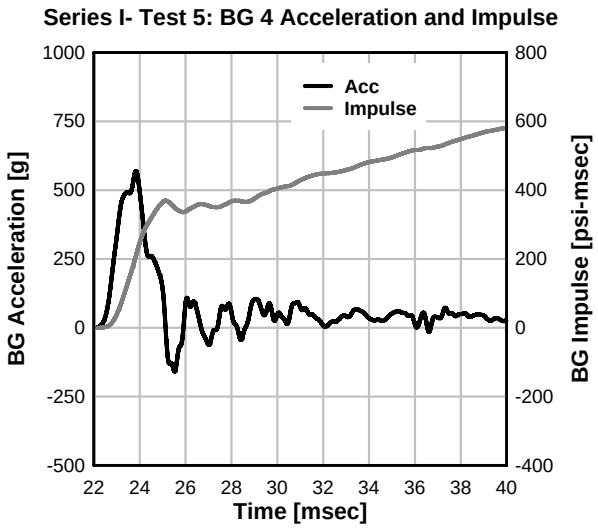
Series I- Test 5: BG 4 Acceleration and Impulse
Acc
Impulse
BG Acceleration [g]
BG Impulse [psi-msec]
Time [msec]

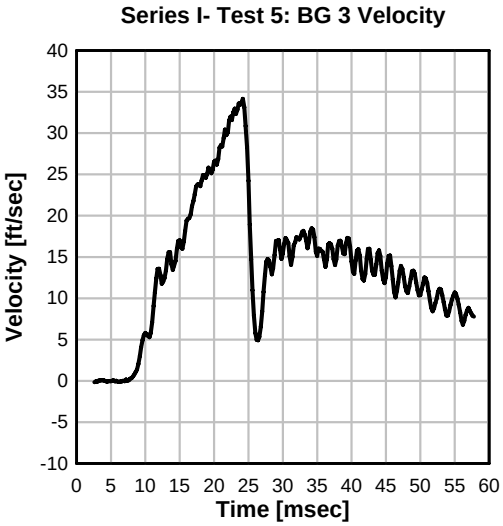
Series I- Test 5: BG 3 Velocity
Velocity [ft/sec]
Time [msec]

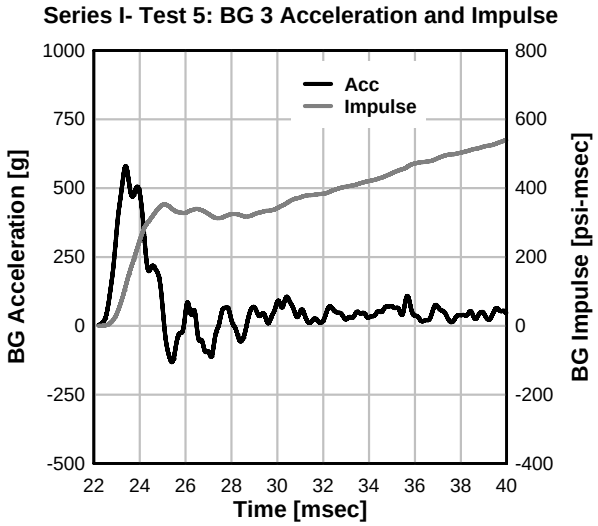
Series I- Test 5: BG 3 Acceleration and Impulse
Acc
Impulse
BG Acceleration [g]
BG Impulse [psi-msec]
Time [msec]

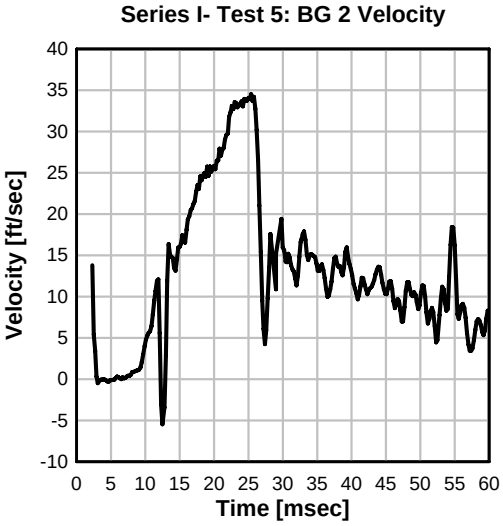
Series I- Test 5: BG 2 Velocity
Velocity [ft/sec]
Time [msec]

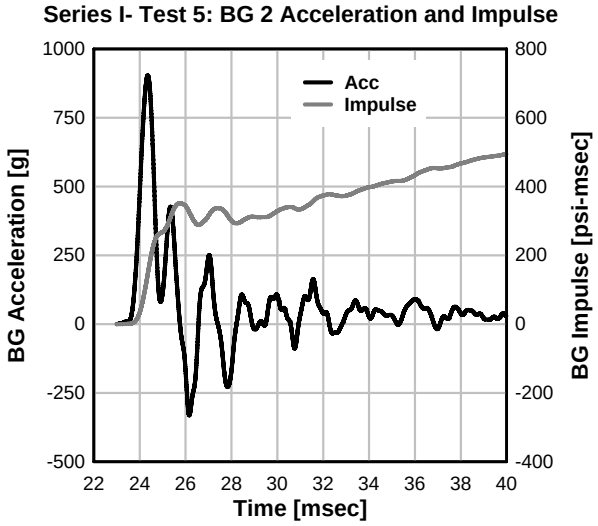
Series I- Test 5: BG 2 Acceleration and Impulse
Acc
Impulse
BG Acceleration [g]
BG Impulse [psi-msec]
Time [msec]

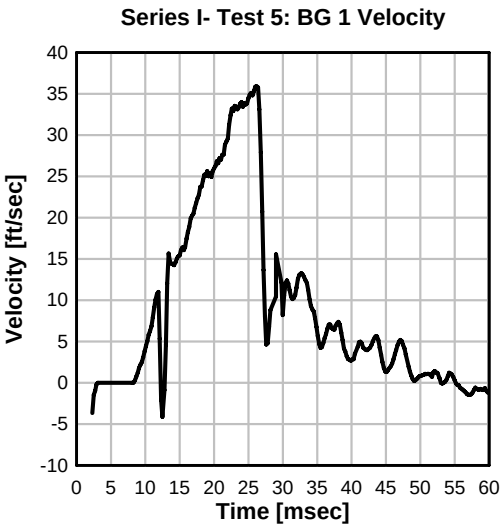
Series I- Test 5: BG 1 Velocity
Velocity [ft/sec]
Time [msec]

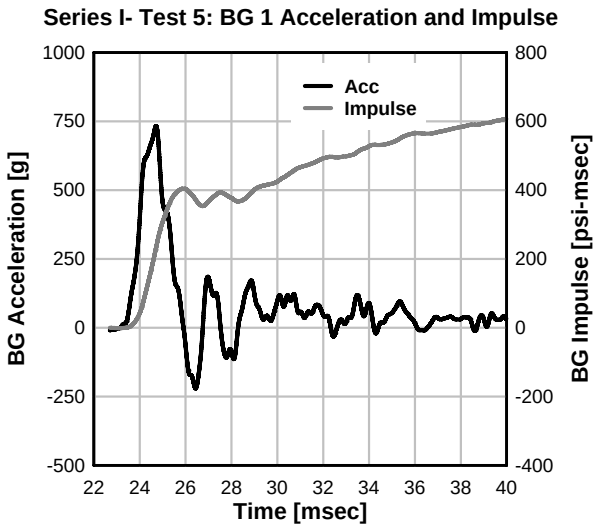
Series I- Test 5: BG 1 Acceleration and Impulse
Acc
Impulse
BG Acceleration [g]
BG Impulse [psi-msec]
Time [msec]

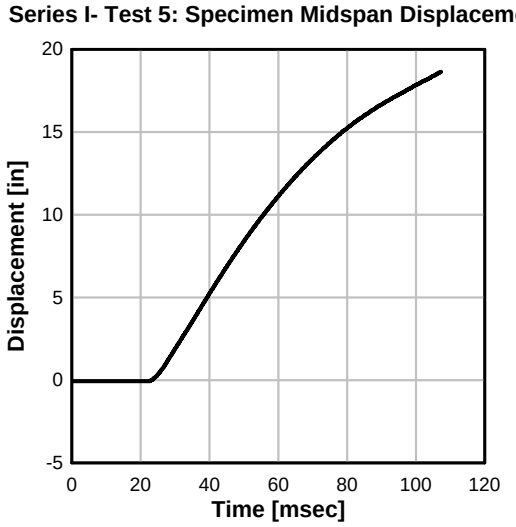
Series I- Test 5: Specimen Midspan Displacement
Displacement [in]
Time [msec]

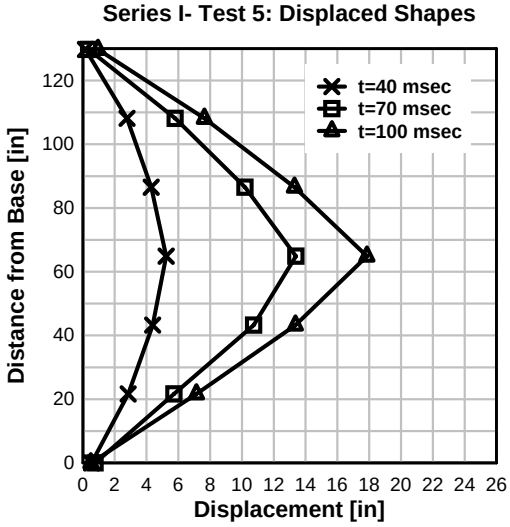
Series I- Test 5: Displaced Shapes
t=40 msec
t=70 msec
t=100 msec
Distance from Base [in]
Displacement [in]

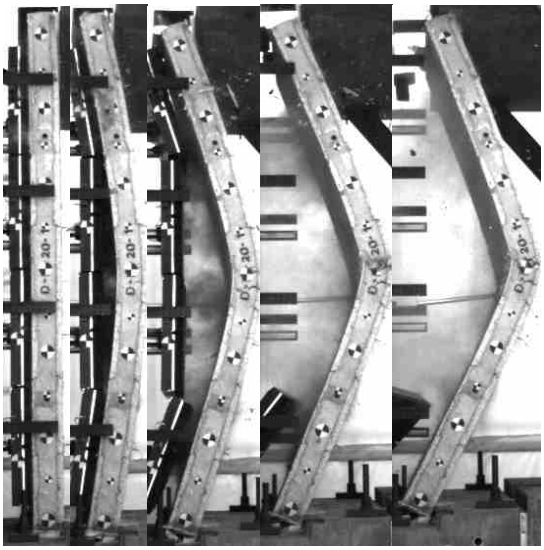

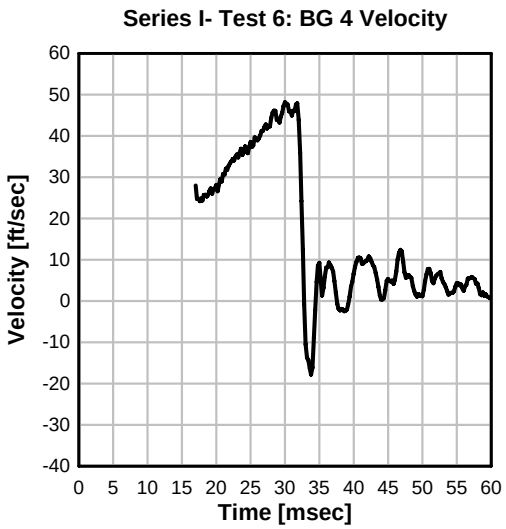
Series I- Test 6: BG 4 Velocity
Velocity [ft/sec]
Time [msec]

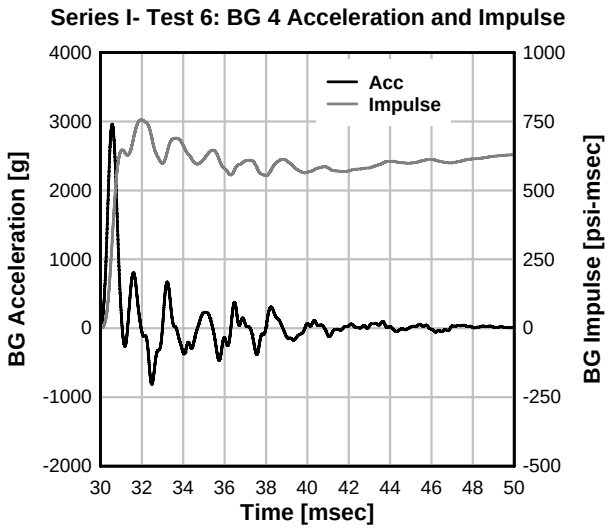
Series I- Test 6: BG 4 Acceleration and Impulse
Acc
Impulse
BG Acceleration [g]
BG Impulse [psi-msec]
Time [msec]

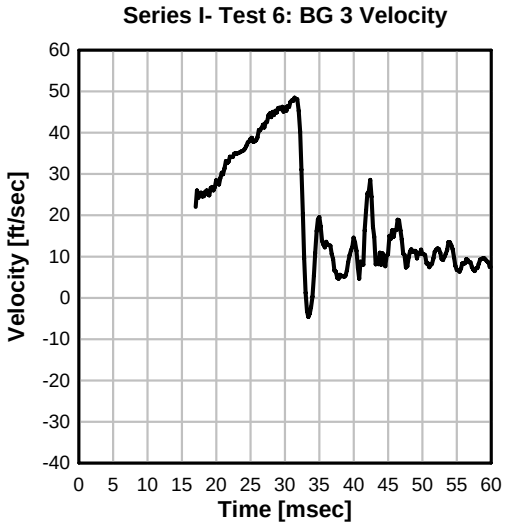
Series I- Test 6: BG 3 Velocity
Velocity [ft/sec]
Time [msec]

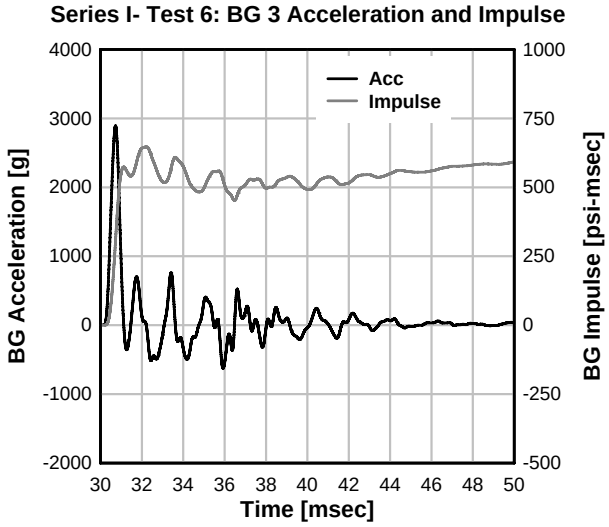
Series I- Test 6: BG 3 Acceleration and Impulse
Acc
Impulse
BG Acceleration [g]
BG Impulse [psi-msec]
Time [msec]

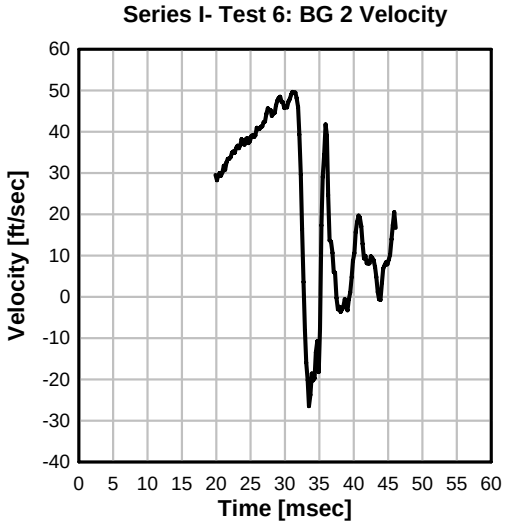
Series I- Test 6: BG 2 Velocity
Velocity [ft/sec]
Time [msec]

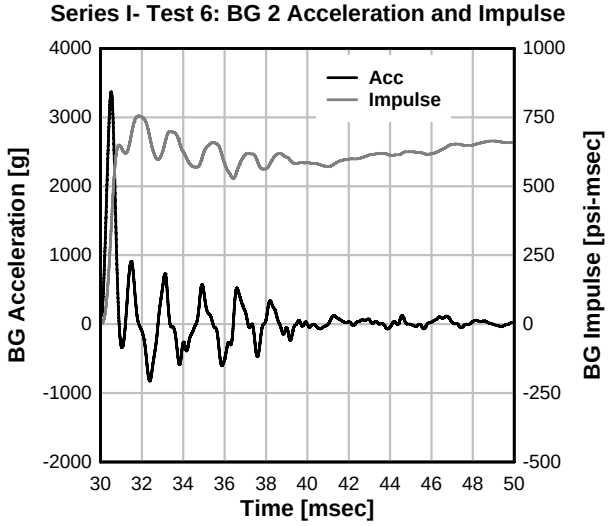
Series I- Test 6: BG 2 Acceleration and Impulse
Acc
Impulse
BG Acceleration [g]
BG Impulse [psi-msec]
Time [msec]

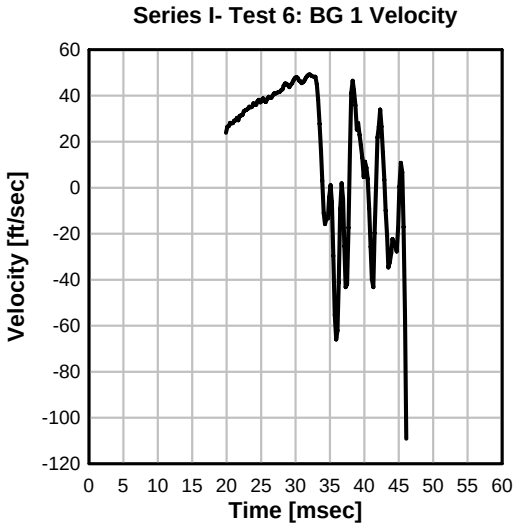
Series I- Test 6: BG 1 Velocity
Velocity [ft/sec]
Time [msec]

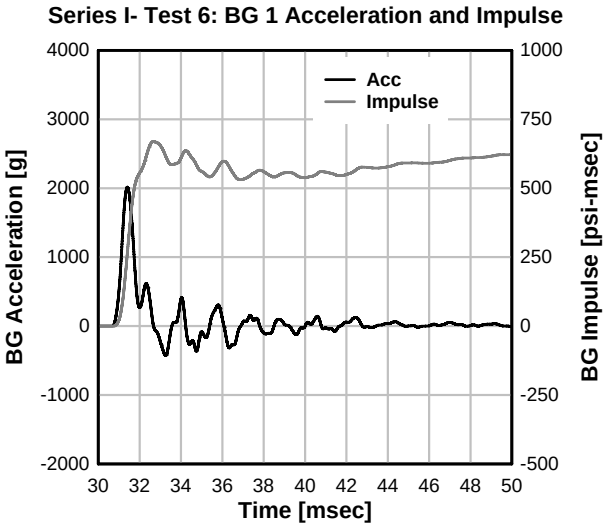
Series I- Test 6: BG 1 Acceleration and Impulse
Acc
Impulse
BG Acceleration [g]
BG Impulse [psi-msec]
Time [msec]

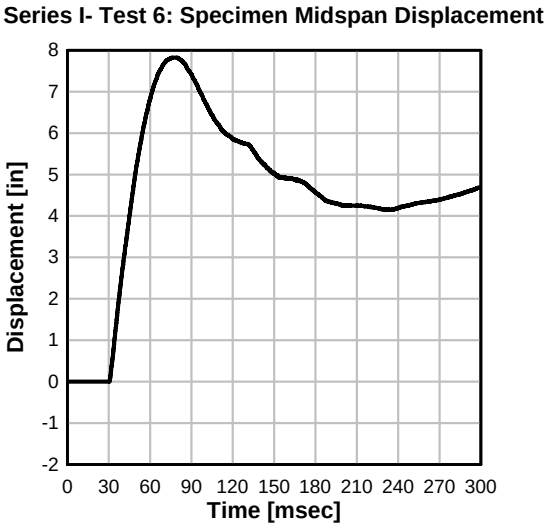
Series I- Test 6: Specimen Midspan Displacement
Displacement [in]
Time [msec]

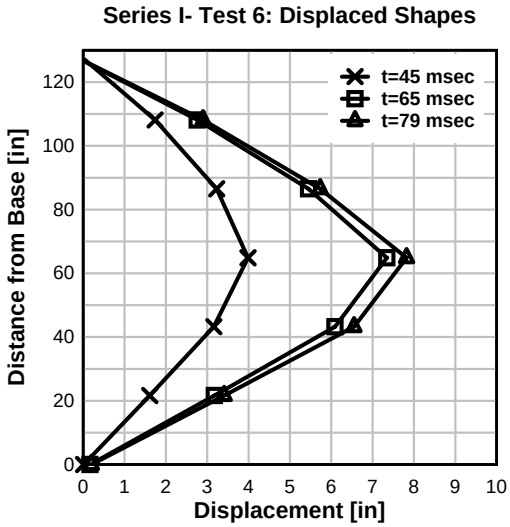
Series I- Test 6: Displaced Shapes
t=45 msec
t=65 msec
t=79 msec
Distance from Base [in]
Displacement [in]

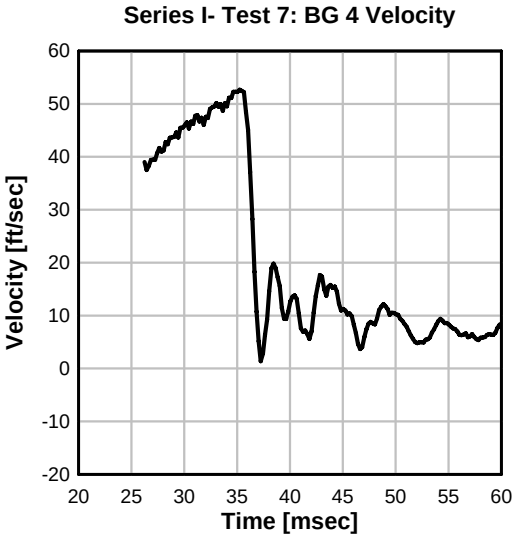
Series I- Test 7: BG 4 Velocity
Velocity [ft/sec]
Time [msec]

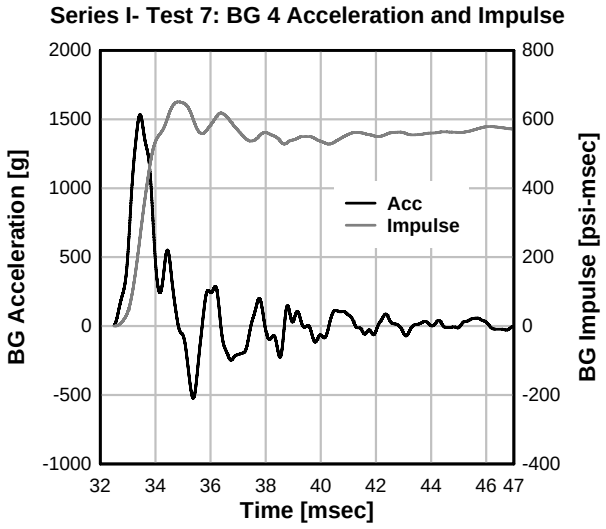
Series I- Test 7: BG 4 Acceleration and Impulse
BG Acceleration [g]
BG Impulse [psi-msec]
Acc
Impulse
Time [msec]

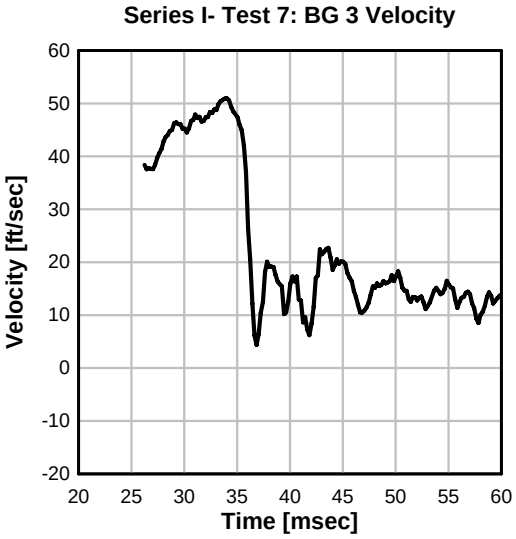
Series I- Test 7: BG 3 Velocity
Velocity [ft/sec]
Time [msec]

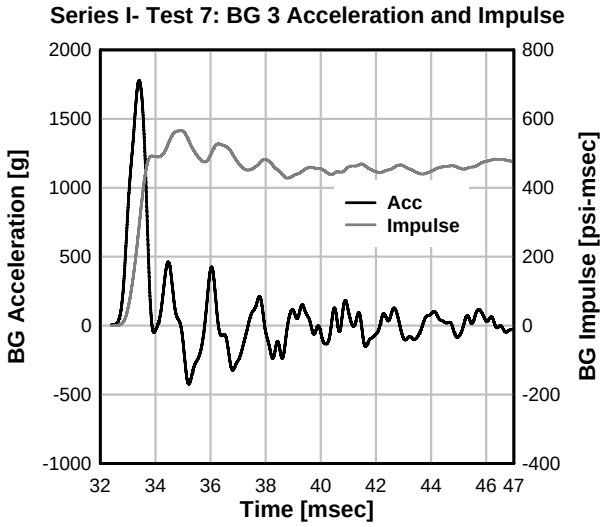
Series I- Test 7: BG 3 Acceleration and Impulse
BG Acceleration [g]
BG Impulse [psi-msec]
Acc
Impulse
Time [msec]

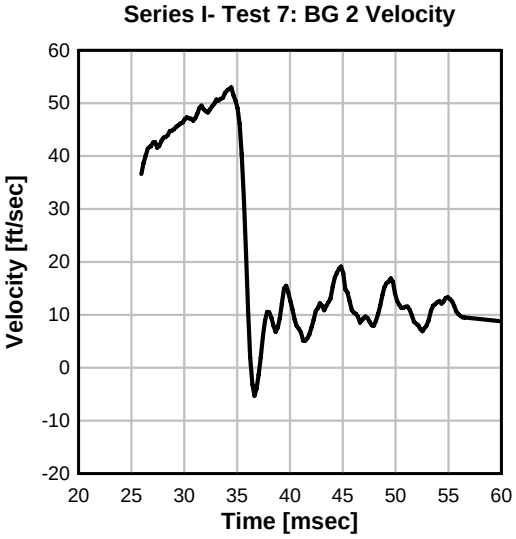
Series I- Test 7: BG 2 Velocity
Velocity [ft/sec]
Time [msec]

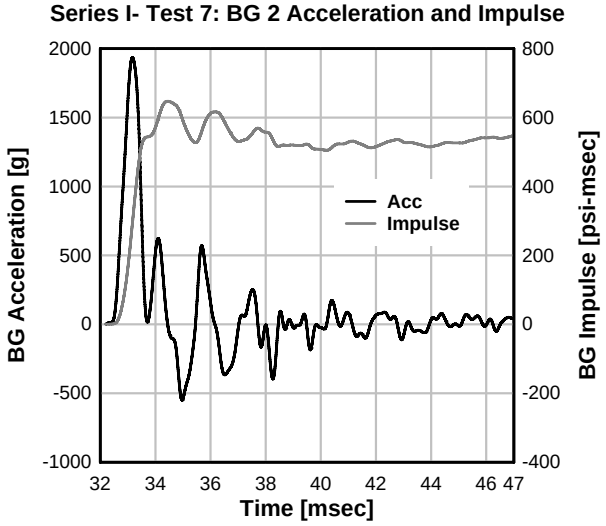
Series I- Test 7: BG 2 Acceleration and Impulse
BG Acceleration [g]
BG Impulse [psi-msec]
Acc
Impulse
Time [msec]

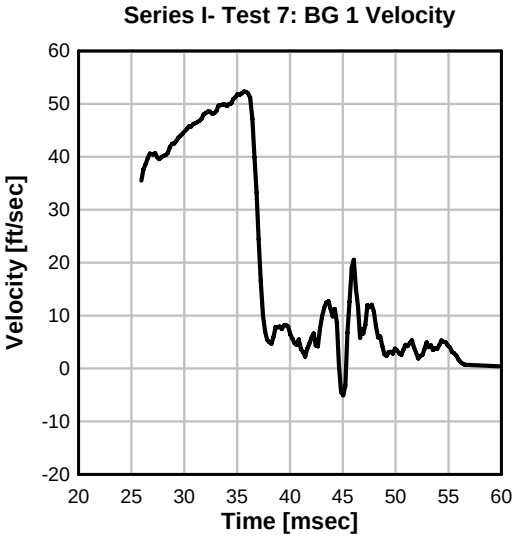
Series I- Test 7: BG 1 Velocity
Velocity [ft/sec]
Time [msec]

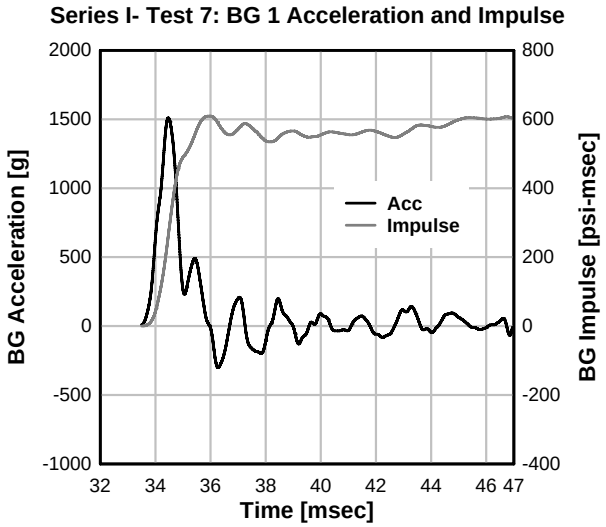
Series I- Test 7: BG 1 Acceleration and Impulse
BG Acceleration [g]
BG Impulse [psi-msec]
Acc
Impulse
Time [msec]

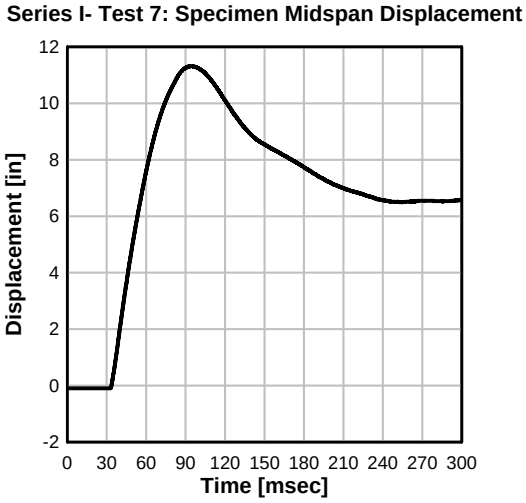
Series I- Test 7: Specimen Midspan Displacement
Displacement [in]
Time [msec]

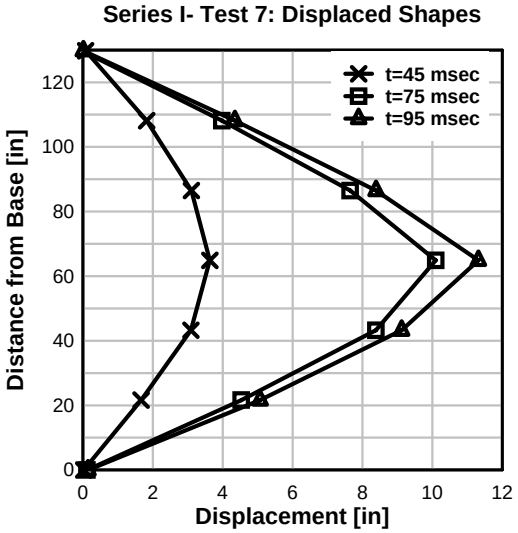
Series I- Test 7: Displaced Shapes
t=45 msec
t=75 msec
t=95 msec
Distance from Base [in]
Displacement [in]

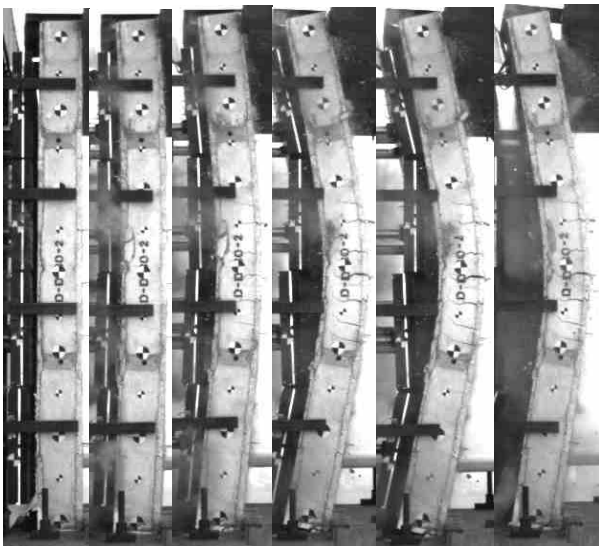

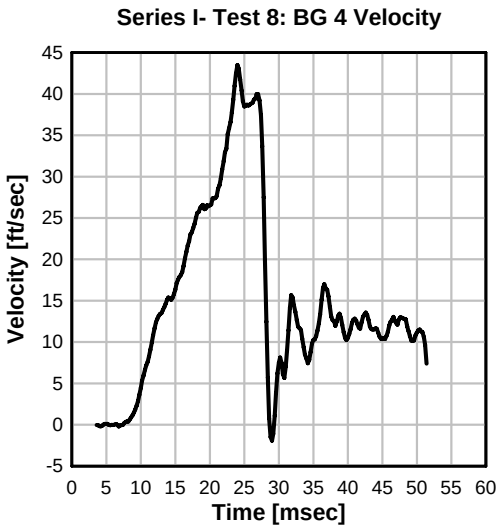
Series I- Test 8: BG 4 Velocity
Velocity [ft/sec]
Time [msec]

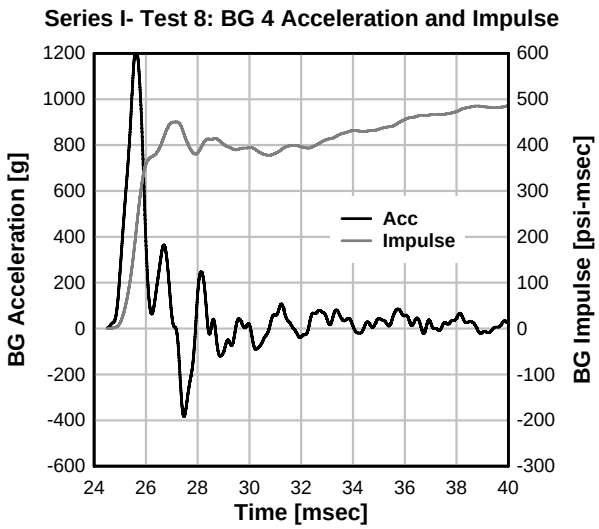
Series I- Test 8: BG 4 Acceleration and Impulse
BG Acceleration [g]
BG Impulse [psi-msec]
Acc
Impulse
Time [msec]

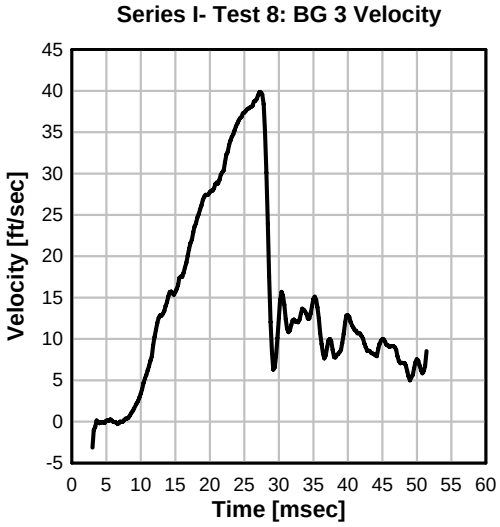
Series I- Test 8: BG 3 Velocity
Velocity [ft/sec]
Time [msec]

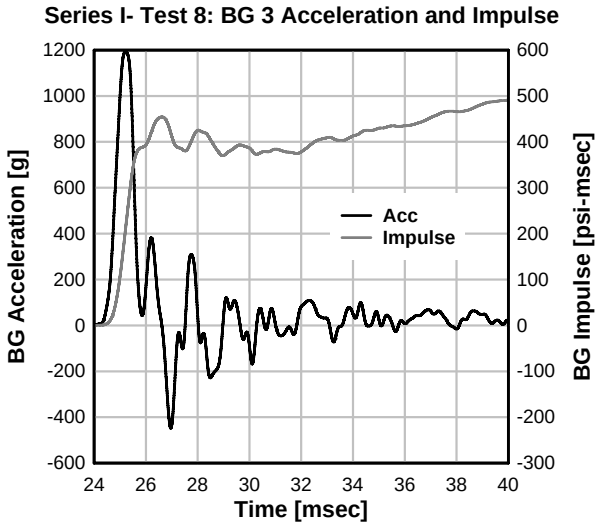
Series I- Test 8: BG 3 Acceleration and Impulse
BG Acceleration [g]
BG Impulse [psi-msec]
Acc
Impulse
Time [msec]

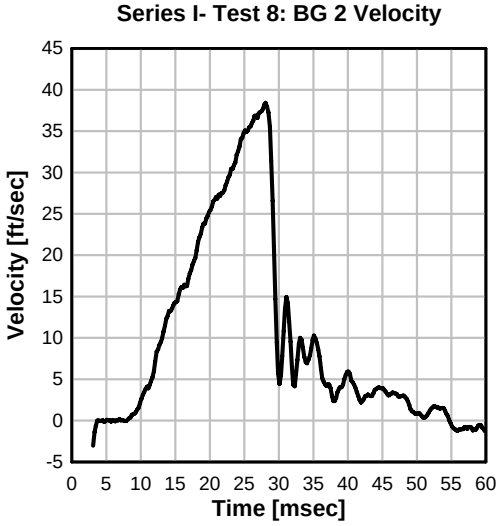
Series I- Test 8: BG 2 Velocity
Velocity [ft/sec]
Time [msec]

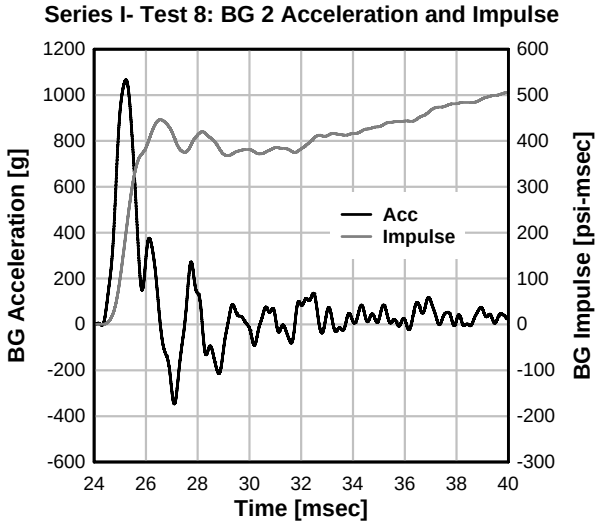
Series I- Test 8: BG 2 Acceleration and Impulse
BG Acceleration [g]
BG Impulse [psi-msec]
Acc
Impulse
Time [msec]

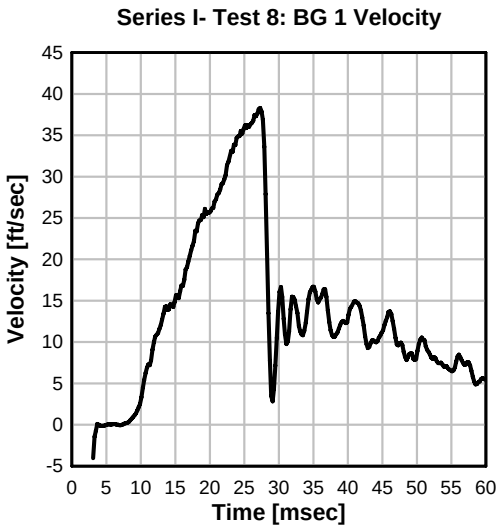
Series I- Test 8: BG 1 Velocity
Velocity [ft/sec]
Time [msec]

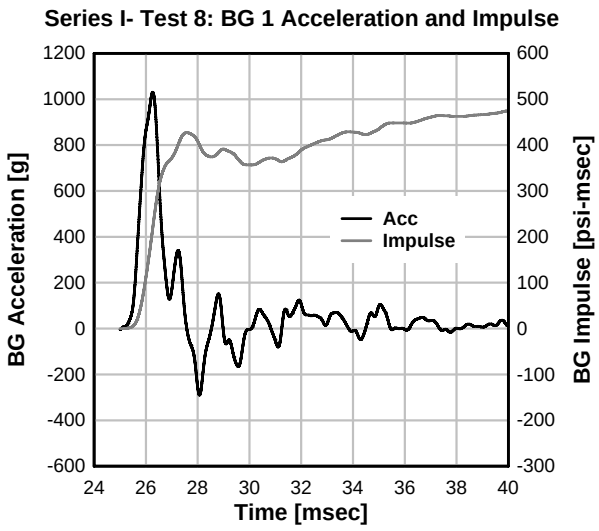
Series I- Test 8: BG 1 Acceleration and Impulse
BG Acceleration [g]
BG Impulse [psi-msec]
Acc
Impulse
Time [msec]

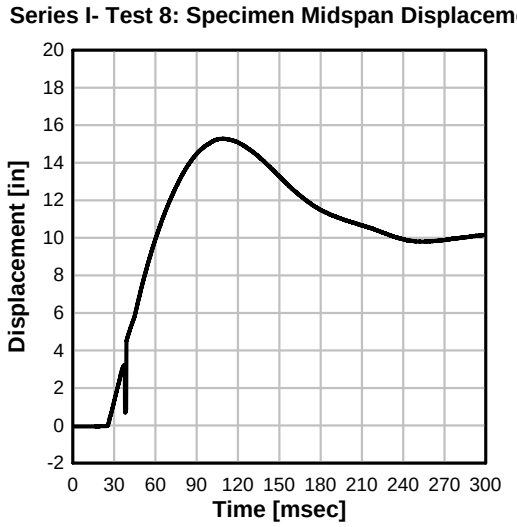
Series I- Test 8: Specimen Midspan Displacement
Displacement [in]
Time [msec]

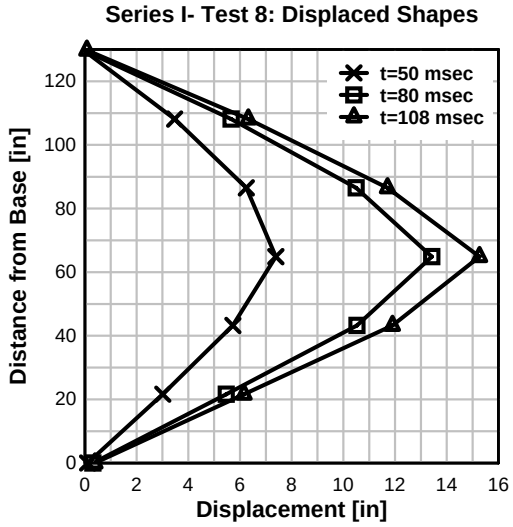
Series I- Test 8: Displaced Shapes
t=50 msec
t=80 msec
t=108 msec
Distance from Base [in]
Displacement [in]

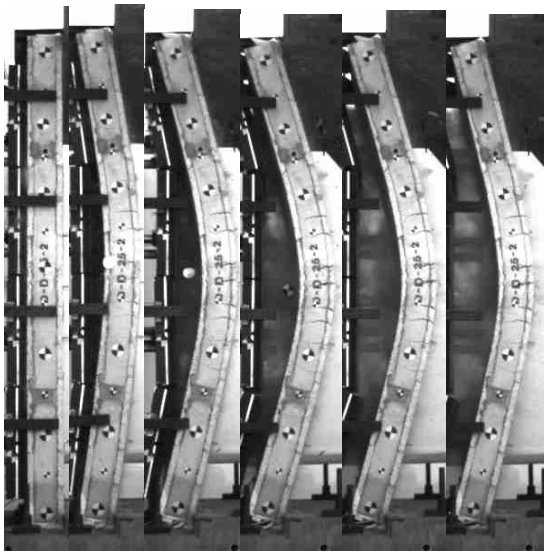

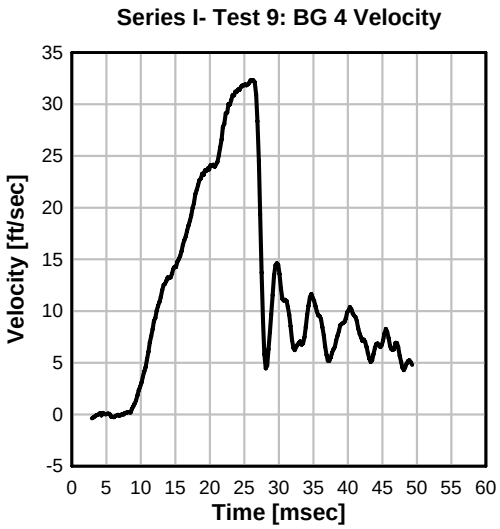
Series I- Test 9: BG 4 Velocity
Velocity [ft/sec]
Time [msec]

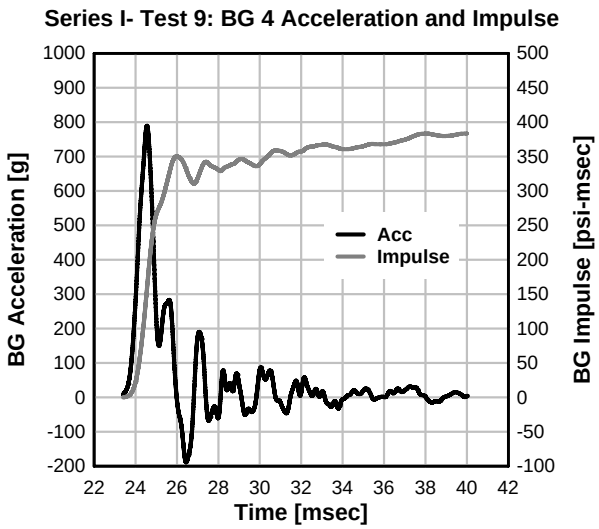
Series I- Test 9: BG 4 Acceleration and Impulse
BG Acceleration [g]
BG Impulse [psi-msec]
Acc
Impulse
Time [msec]

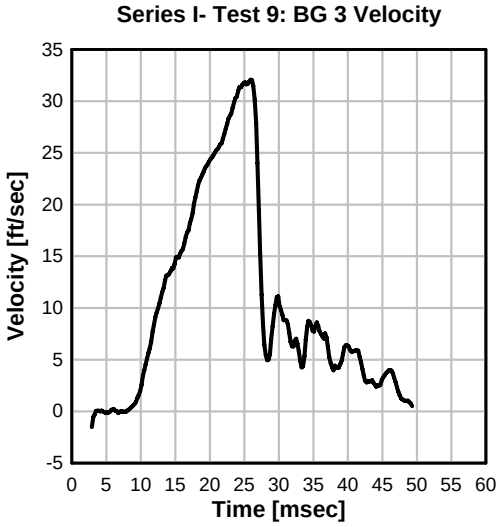
Series I- Test 9: BG 3 Velocity
Velocity [ft/sec]
Time [msec]

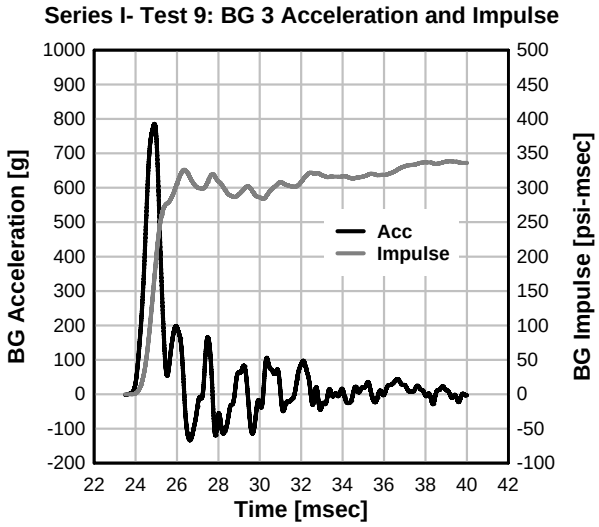
Series I- Test 9: BG 3 Acceleration and Impulse
BG Acceleration [g]
BG Impulse [psi-msec]
Acc
Impulse
Time [msec]

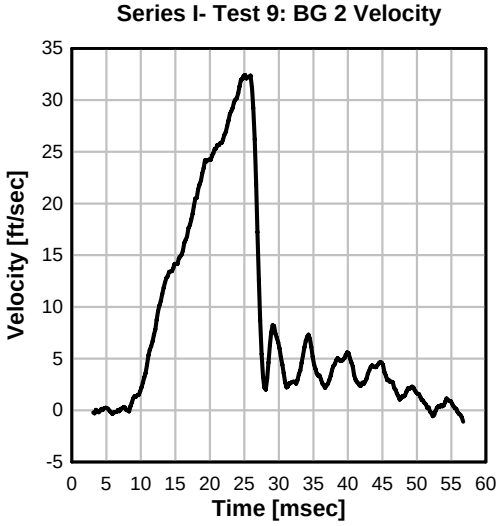
Series I- Test 9: BG 2 Velocity
Velocity [ft/sec]
Time [msec]

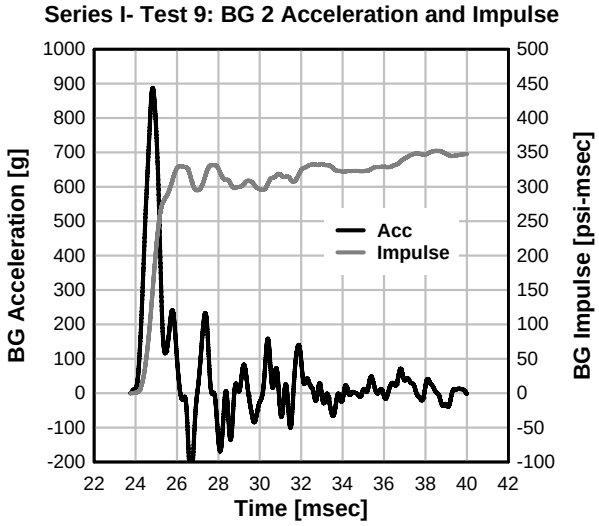
Series I- Test 9: BG 2 Acceleration and Impulse
BG Acceleration [g]
BG Impulse [psi-msec]
Acc
Impulse
Time [msec]

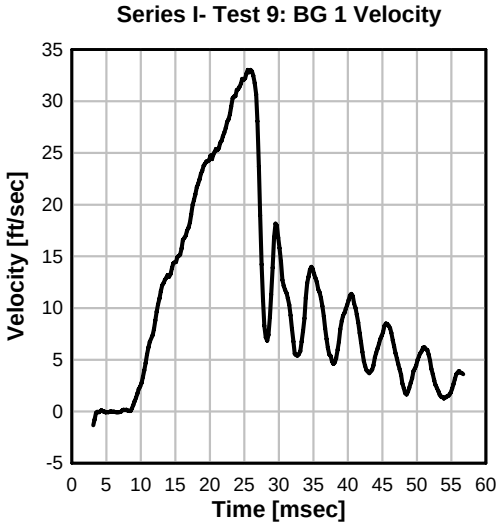
Series I- Test 9: BG 1 Velocity
Velocity [ft/sec]
Time [msec]

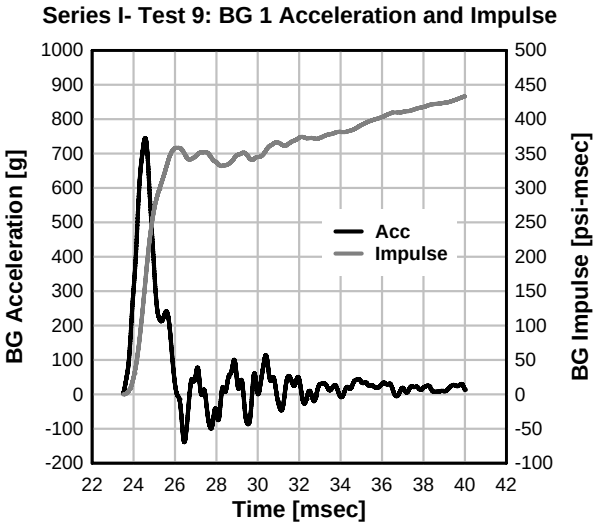
Series I- Test 9: BG 1 Acceleration and Impulse
BG Acceleration [g]
BG Impulse [psi-msec]
Acc
Impulse
Time [msec]

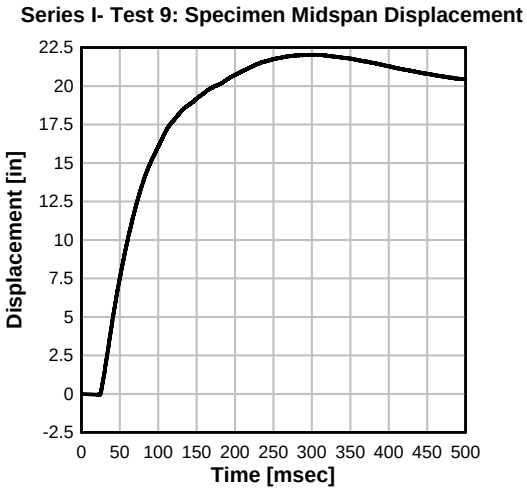
Series I- Test 9: Specimen Midspan Displacement
Displacement [in]
Time [msec]

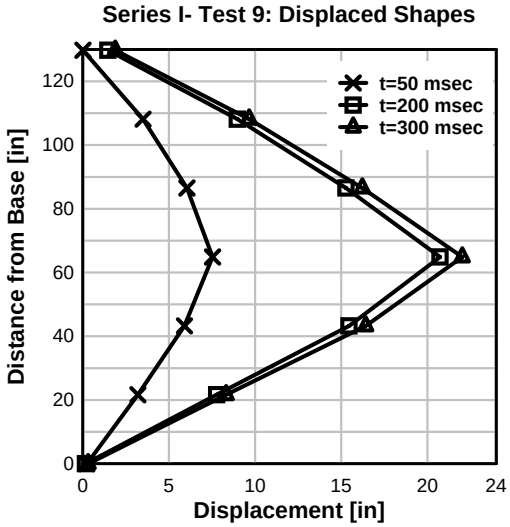
Series I- Test 9: Displaced Shapes
t=50 msec
t=200 msec
t=300 msec
Distance from Base [in]
Displacement [in]

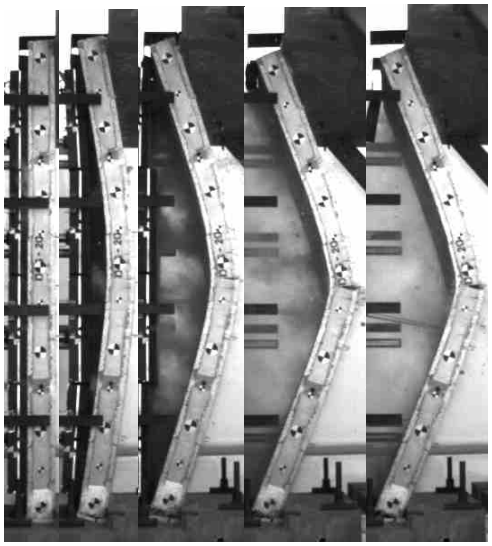

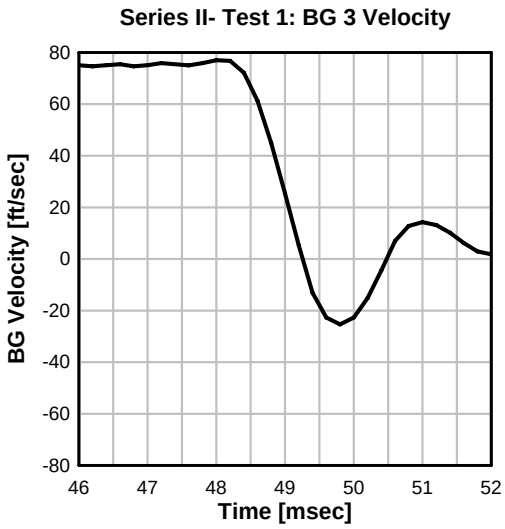
Series II- Test 1: BG 3 Velocity
BG Velocity [ft/sec]
Time [msec]

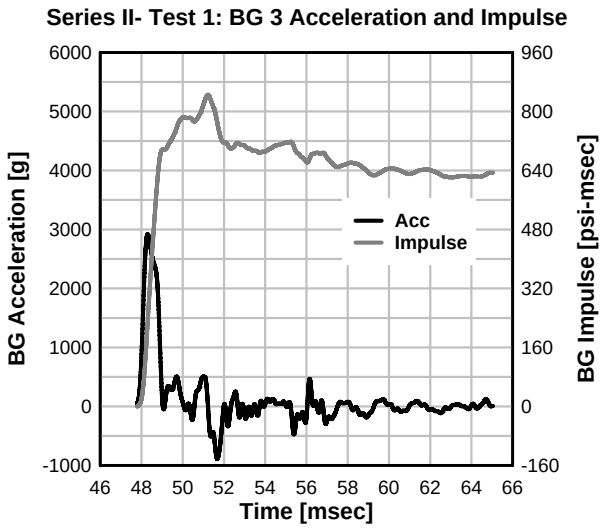
Series II- Test 1: BG 3 Acceleration and Impulse
BG Acceleration [g]
BG Impulse [psi-msec]
Acc
Impulse
Time [msec]

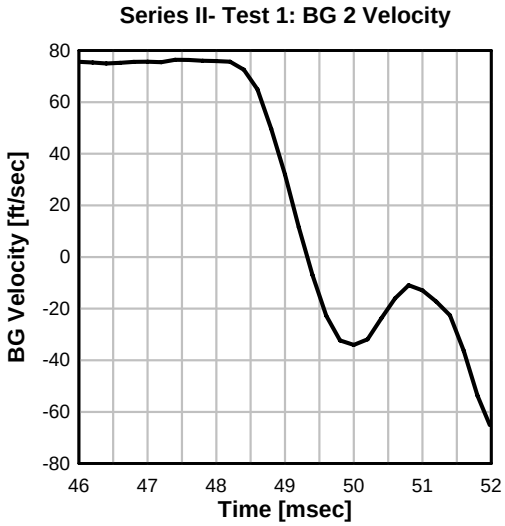
Series II- Test 1: BG 2 Velocity
BG Velocity [ft/sec]
Time [msec]

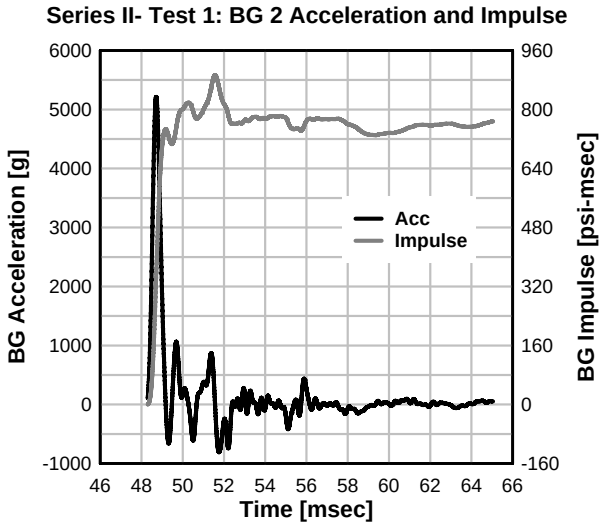
Series II- Test 1: BG 2 Acceleration and Impulse
BG Acceleration [g]
BG Impulse [psi-msec]
Acc
Impulse
Time [msec]

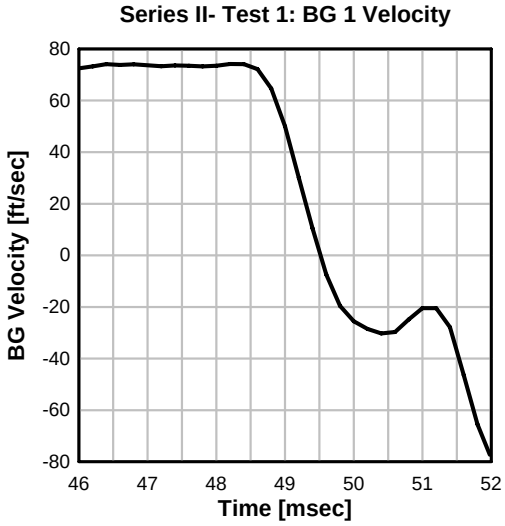
Series II- Test 1: BG 1 Velocity
BG Velocity [ft/sec]
Time [msec]

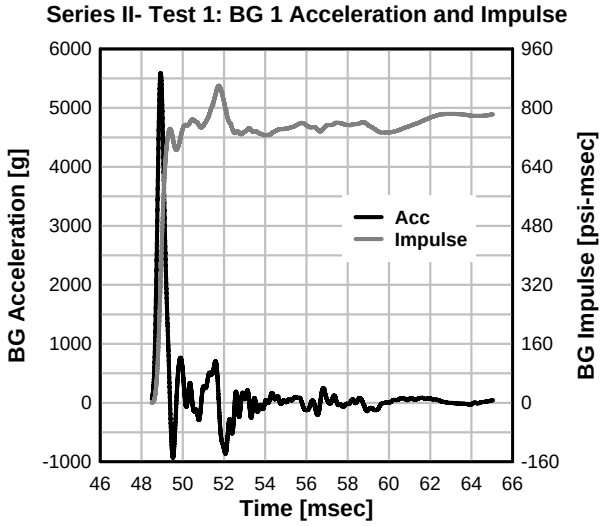
Series II- Test 1: BG 1 Acceleration and Impulse
BG Acceleration [g]
BG Impulse [psi-msec]
Acc
Impulse
Time [msec]

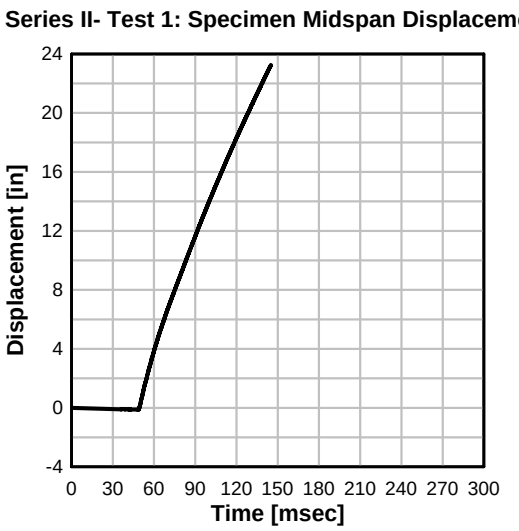
Series II- Test 1: Specimen Midspan Displacement
Displacement [in]
24
20
16
12
8
4
0
-4
0 30 60 90 120 150 180 210 240 270 300
Time [msec]

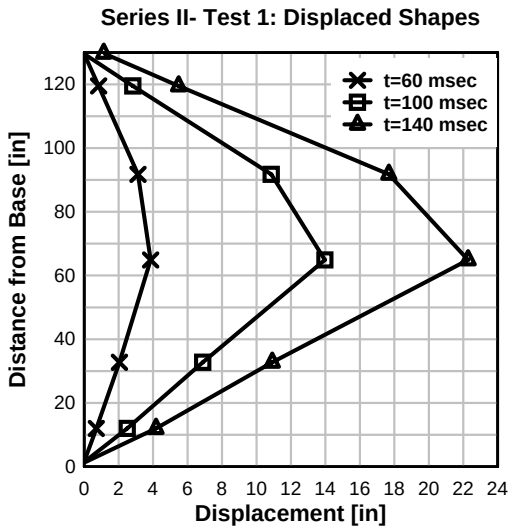
Series II- Test 1: Displaced Shapes
Distance from Base [in]
120
100
80
60
40
20
0
0 2 4 6 8 10 12 14 16 18 20 22 24
Displacement [in]
t=60 msec
t=100 msec
t=140 msec

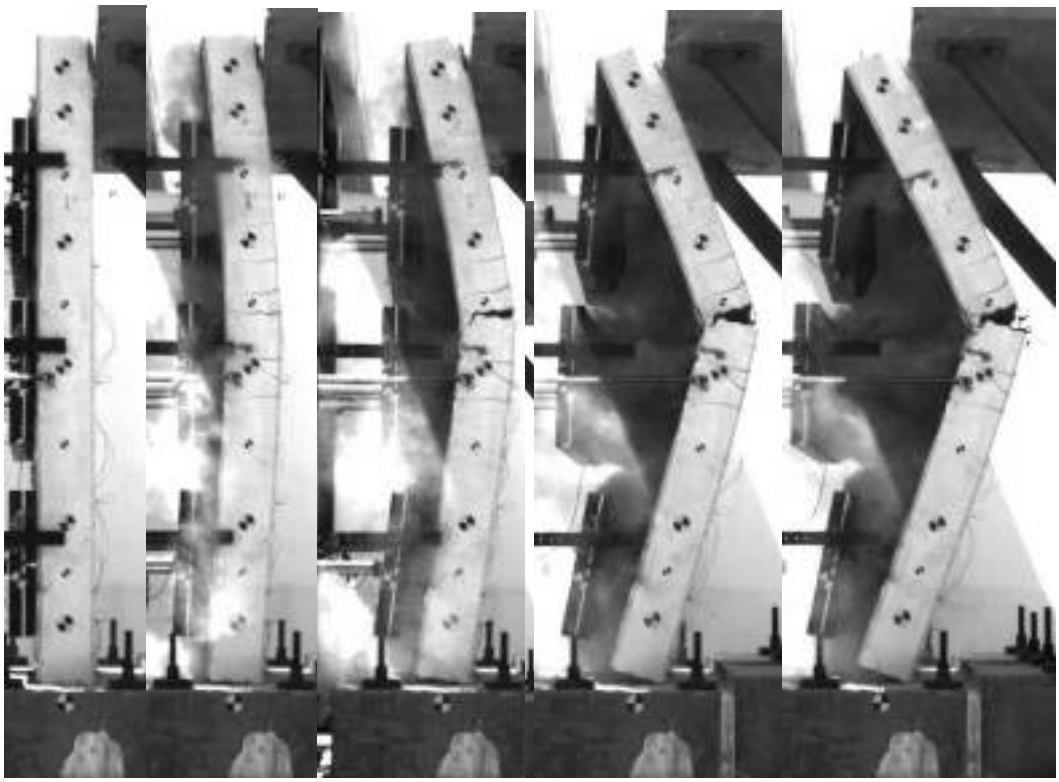

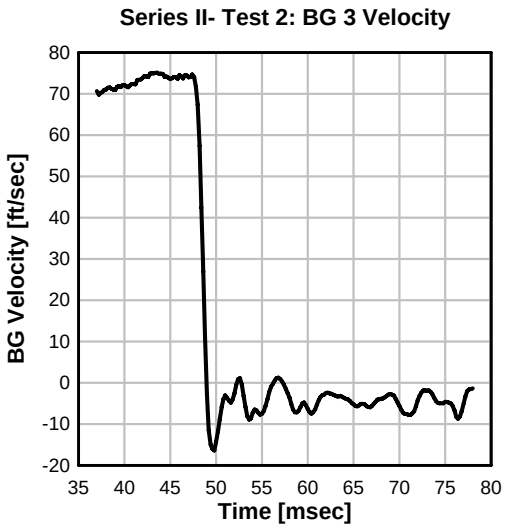
Series II- Test 2: BG 3 Velocity
BG Velocity [ft/sec]
Time [msec]

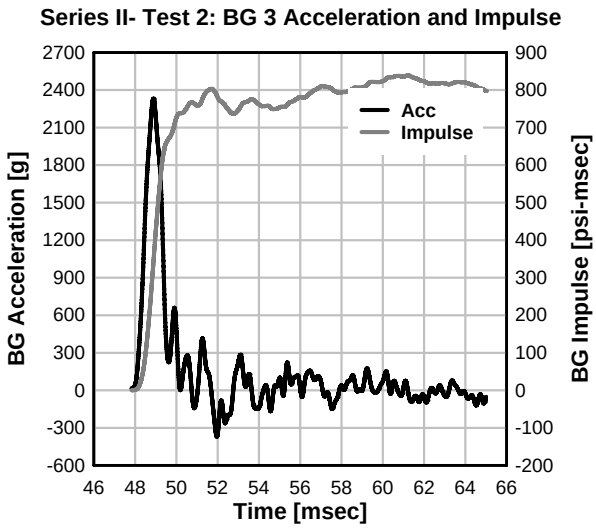
Series II- Test 2: BG 3 Acceleration and Impulse
BG Acceleration [g]
BG Impulse [psi-msec]
Acc
Impulse
Time [msec]

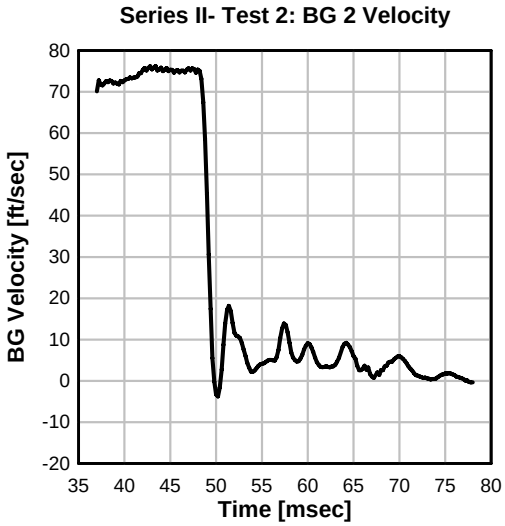
Series II- Test 2: BG 2 Velocity
BG Velocity [ft/sec]
Time [msec]

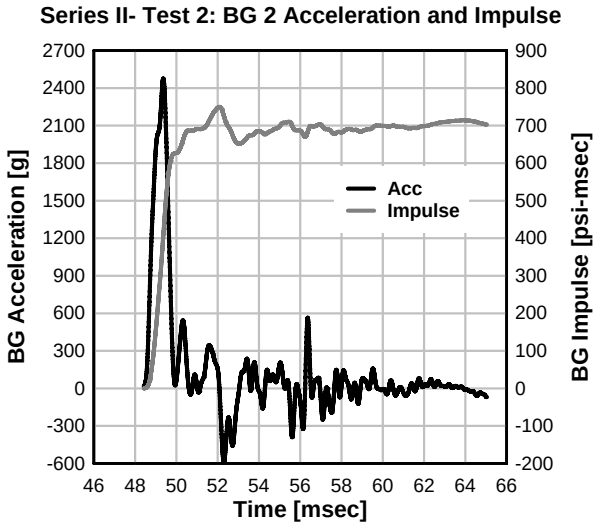
Series II- Test 2: BG 2 Acceleration and Impulse
BG Acceleration [g]
BG Impulse [psi-msec]
Acc
Impulse
Time [msec]

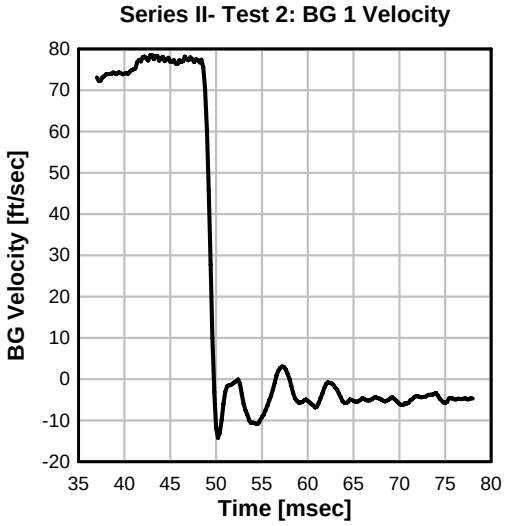
Series II- Test 2: BG 1 Velocity
BG Velocity [ft/sec]
Time [msec]

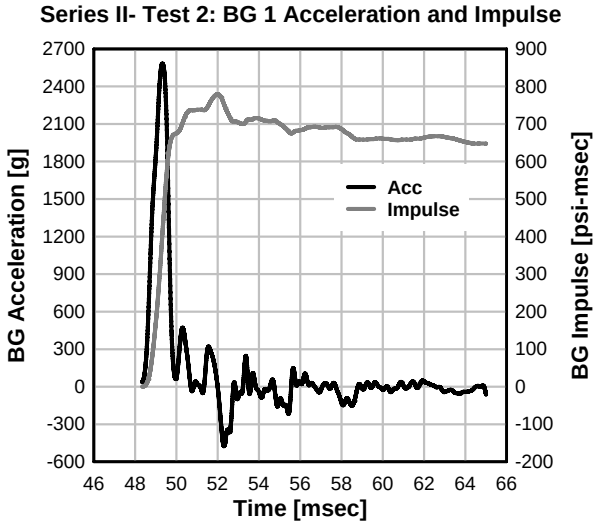
Series II- Test 2: BG 1 Acceleration and Impulse
BG Acceleration [g]
BG Impulse [psi-msec]
Acc
Impulse
Time [msec]

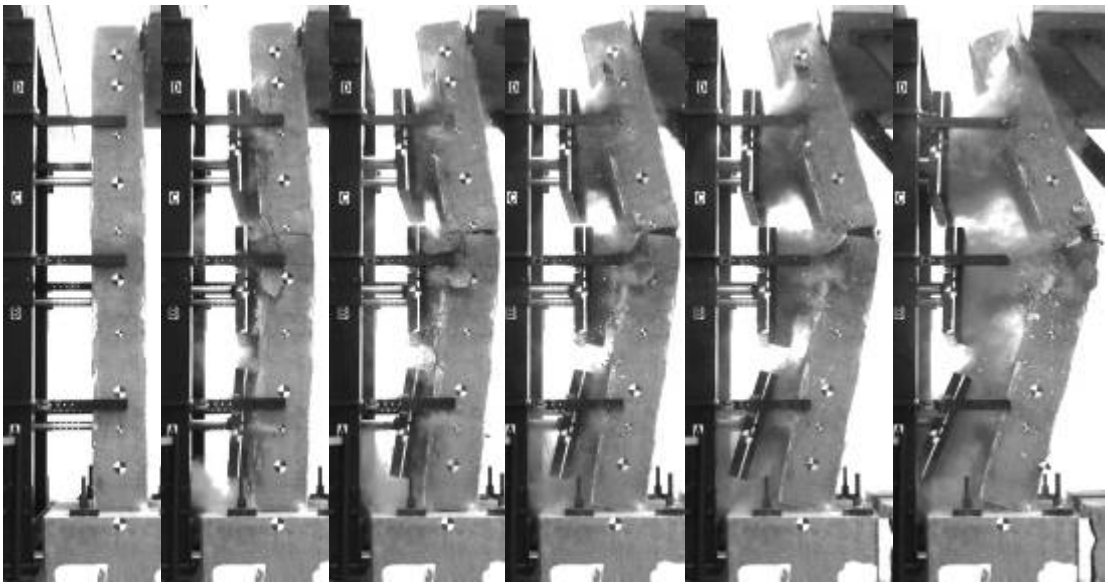

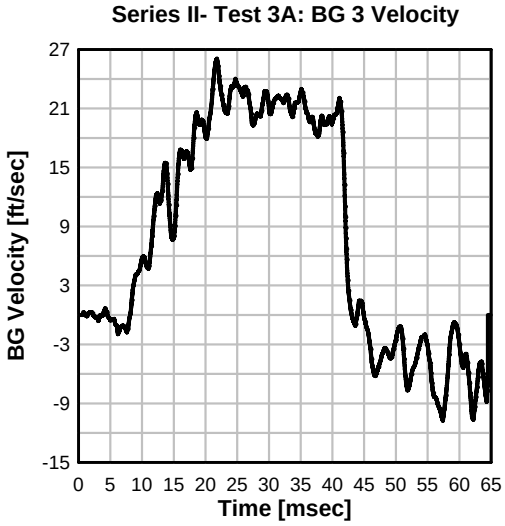
Series II- Test 3A: BG 3 Velocity
BG Velocity [ft/sec]
27
21
15
9
3
-3
-9
-15
0 5 10 15 20 25 30 35 40 45 50 55 60 65
Time [msec]

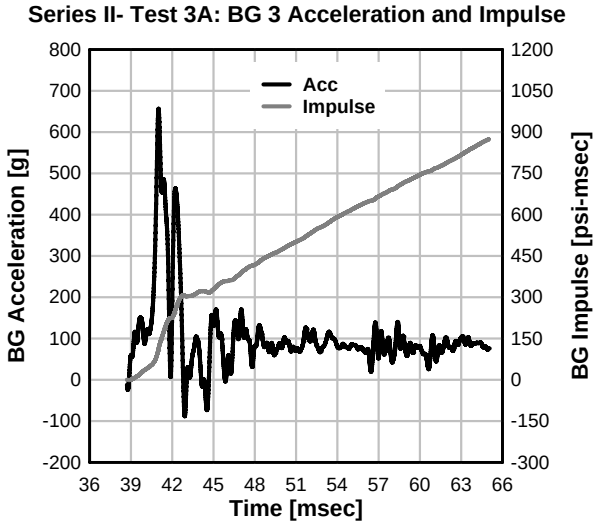
Series II- Test 3A: BG 3 Acceleration and Impulse
Acc
Impulse
BG Acceleration [g]
800
700
600
500
400
300
200
100
0
-100
-200
BG Impulse [psi-msec]
1200
1050
900
750
600
450
300
150
0
-150
-300
36 39 42 45 48 51 54 57 60 63 66
Time [msec]

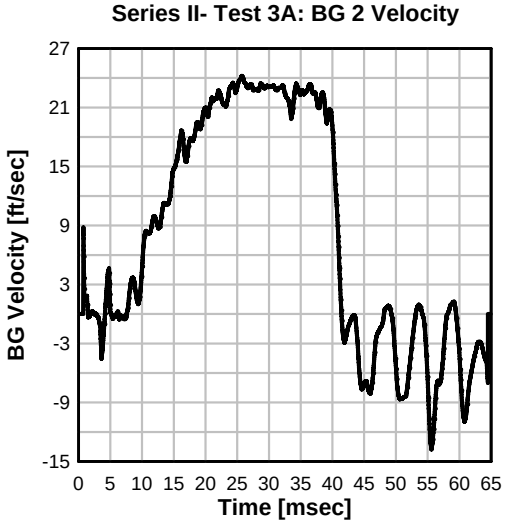
Series II- Test 3A: BG 2 Velocity
BG Velocity [ft/sec]
27
21
15
9
3
-3
-9
-15
0 5 10 15 20 25 30 35 40 45 50 55 60 65
Time [msec]

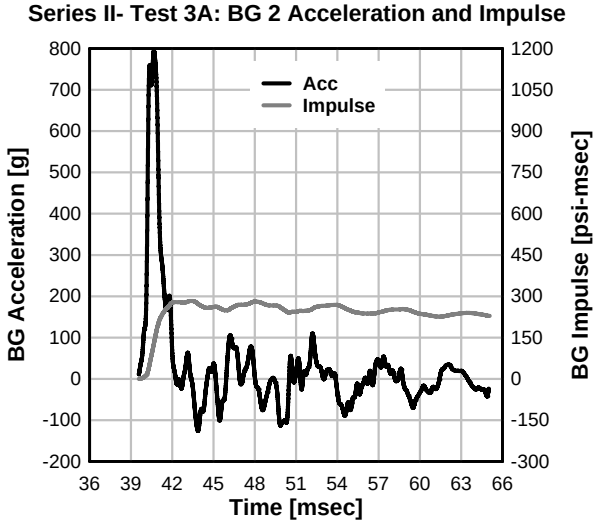
Series II- Test 3A: BG 2 Acceleration and Impulse
Acc
Impulse
BG Acceleration [g]
800
700
600
500
400
300
200
100
0
-100
-200
BG Impulse [psi-msec]
1200
1050
900
750
600
450
300
150
0
-150
-300
36 39 42 45 48 51 54 57 60 63 66
Time [msec]

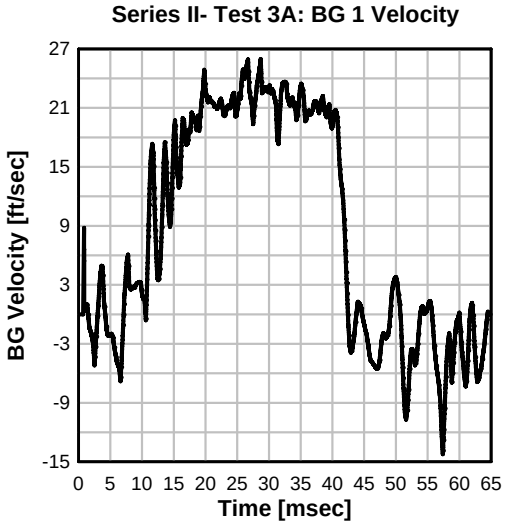
Series II- Test 3A: BG 1 Velocity
BG Velocity [ft/sec]
27
21
15
9
3
-3
-9
-15
0 5 10 15 20 25 30 35 40 45 50 55 60 65
Time [msec]

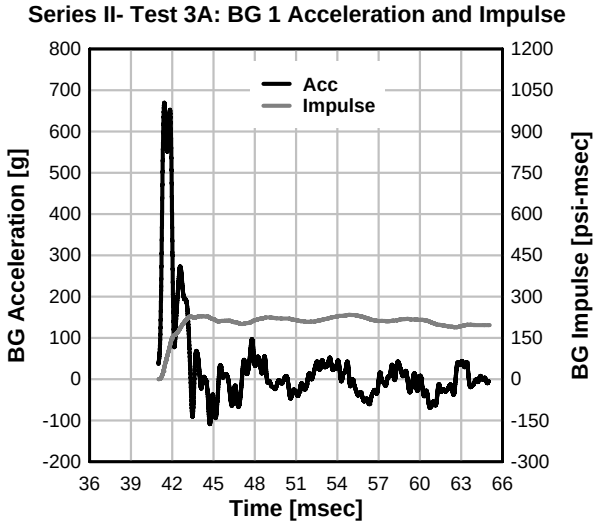
Series II- Test 3A: BG 1 Acceleration and Impulse
Acc
Impulse
BG Acceleration [g]
800
700
600
500
400
300
200
100
0
-100
-200
BG Impulse [psi-msec]
1200
1050
900
750
600
450
300
150
0
-150
-300
36 39 42 45 48 51 54 57 60 63 66
Time [msec]

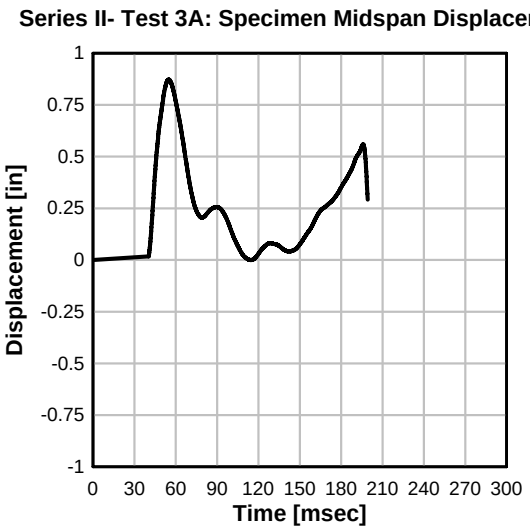
Series II- Test 3A: Specimen Midspan Displacement
Displacement [in]
1
0.75
0.5
0.25
0
-0.25
-0.5
-0.75
-1
0 30 60 90 120 150 180 210 240 270 300
Time [msec]

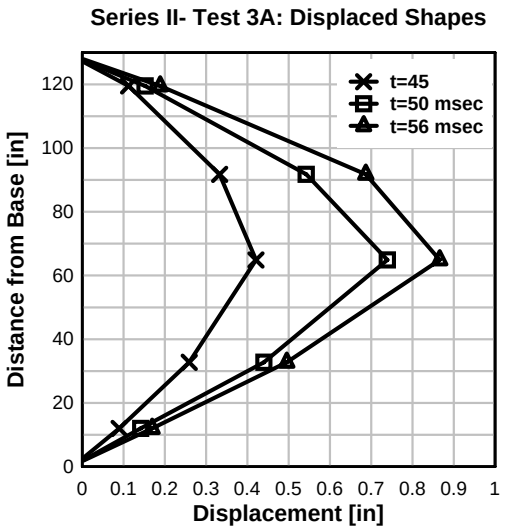
Series II- Test 3A: Displaced Shapes
Distance from Base [in]
120
100
80
60
40
20
0
0 0.1 0.2 0.3 0.4 0.5 0.6 0.7 0.8 0.9 1
Displacement [in]
t=45
t=50 msec
t=56 msec

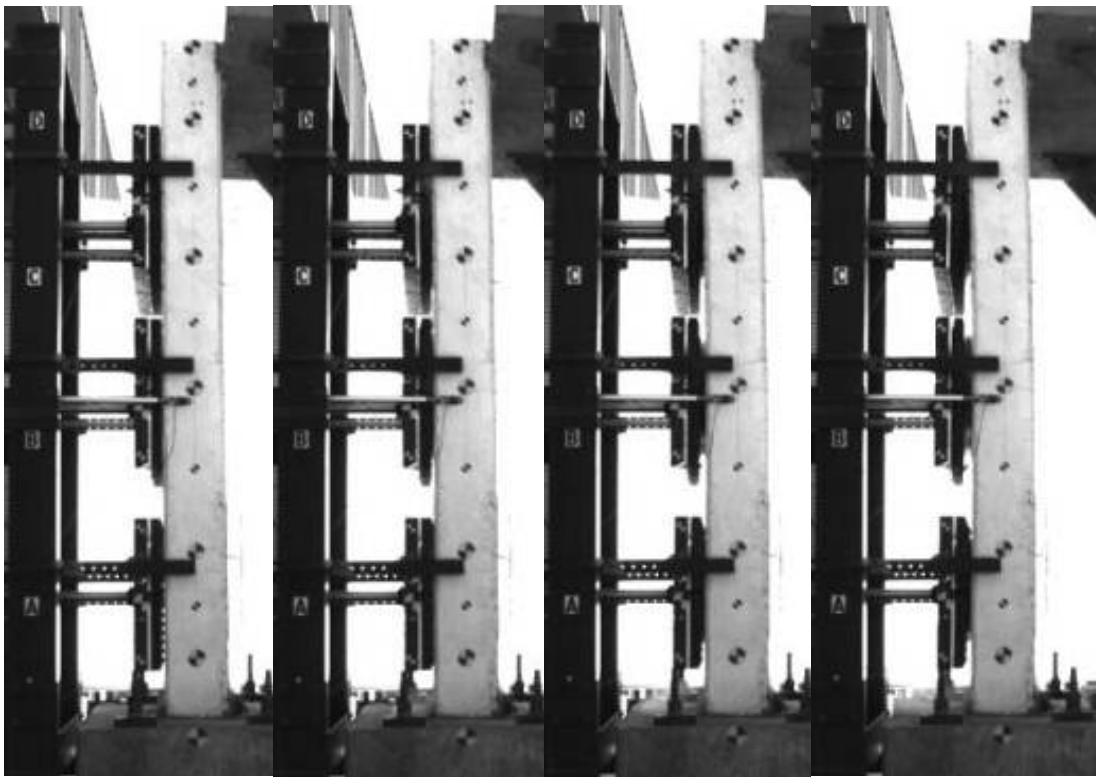

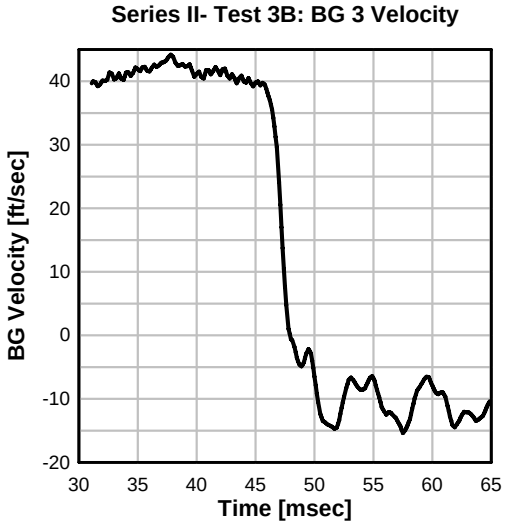
Series II- Test 3B: BG 3 Velocity
BG Velocity [ft/sec]
Time [msec]

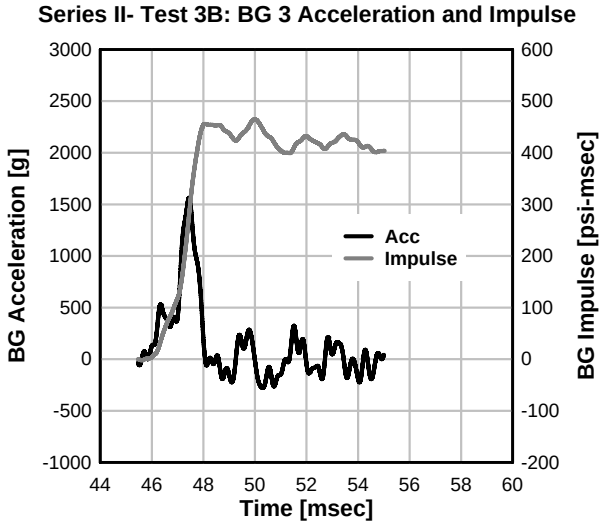
Series II- Test 3B: BG 3 Acceleration and Impulse
BG Acceleration [g]
BG Impulse [psi-msec]
Acc
Impulse
Time [msec]

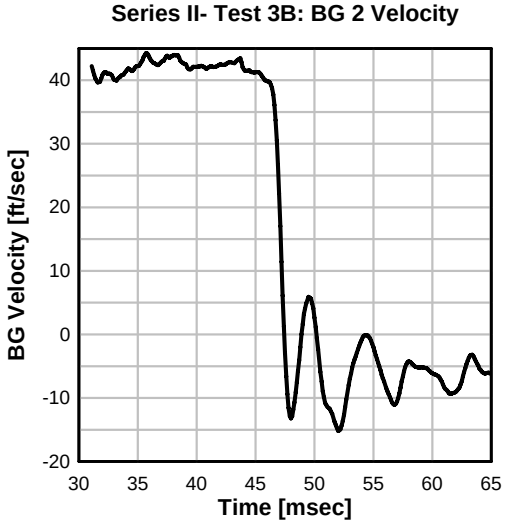
Series II- Test 3B: BG 2 Velocity
BG Velocity [ft/sec]
Time [msec]

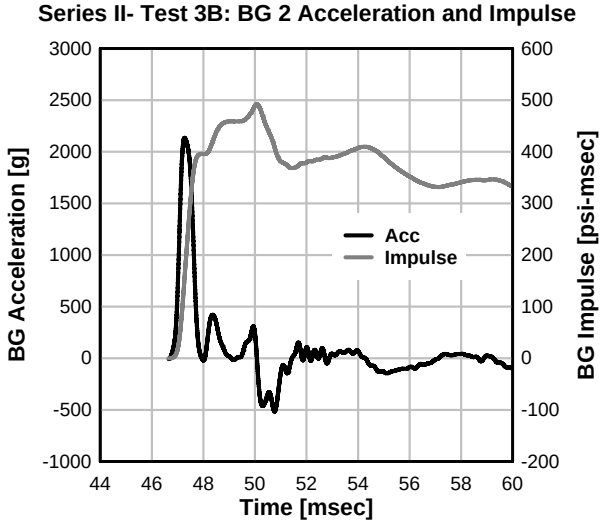
Series II- Test 3B: BG 2 Acceleration and Impulse
BG Acceleration [g]
BG Impulse [psi-msec]
Acc
Impulse
Time [msec]

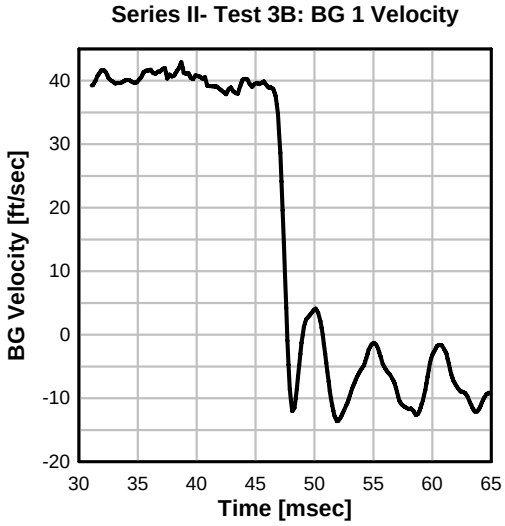
Series II- Test 3B: BG 1 Velocity
BG Velocity [ft/sec]
Time [msec]

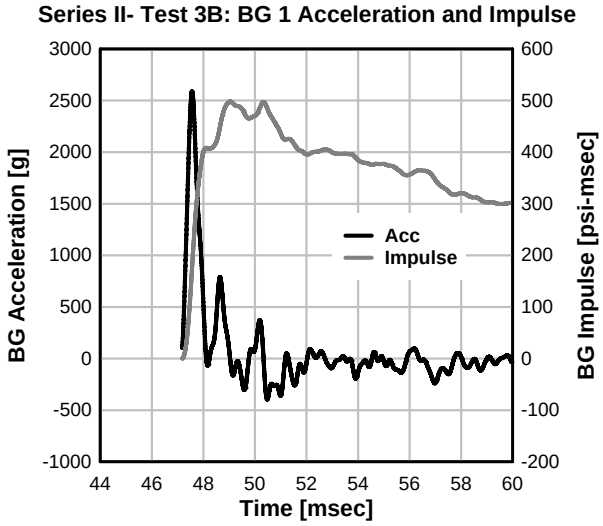
Series II- Test 3B: BG 1 Acceleration and Impulse
BG Acceleration [g]
BG Impulse [psi-msec]
Acc
Impulse
Time [msec]

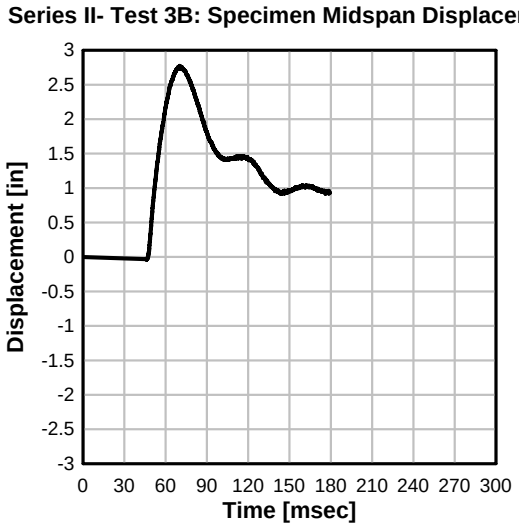
Series II- Test 3B: Specimen Midspan Displacement
Displacement [in]
Time [msec]
3
2.5
2
1.5
1
0.5
0
-0.5
-1
-1.5
-2
-2.5
-3
0 30 60 90 120 150 180 210 240 270 300

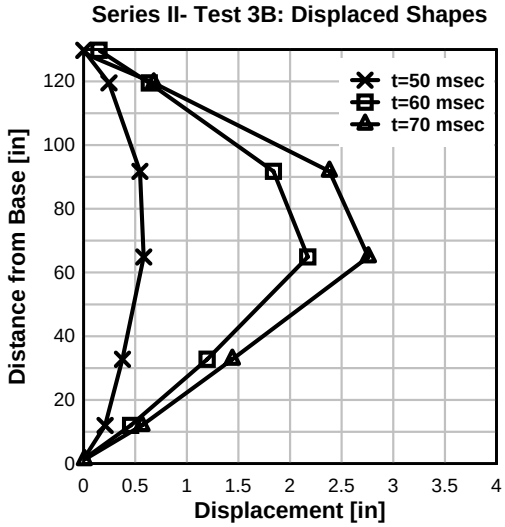
Series II- Test 3B: Displaced Shapes
Distance from Base [in]
Displacement [in]
t=50 msec
t=60 msec
t=70 msec
120
100
80
60
40
20
0
0 0.5 1 1.5 2 2.5 3 3.5 4

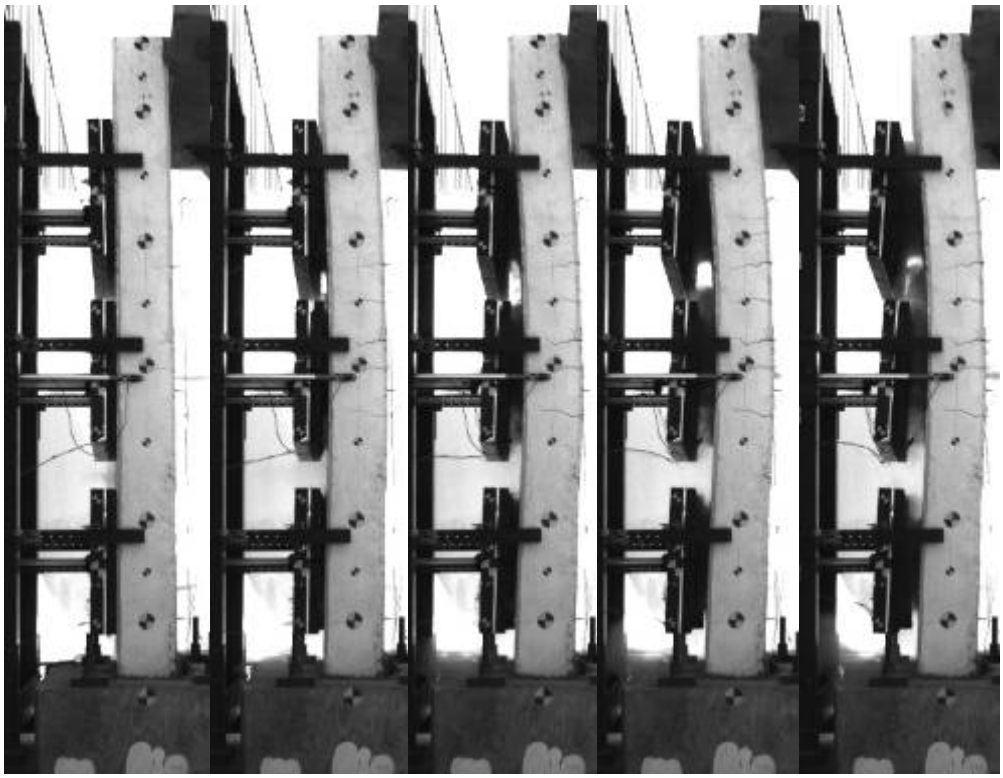

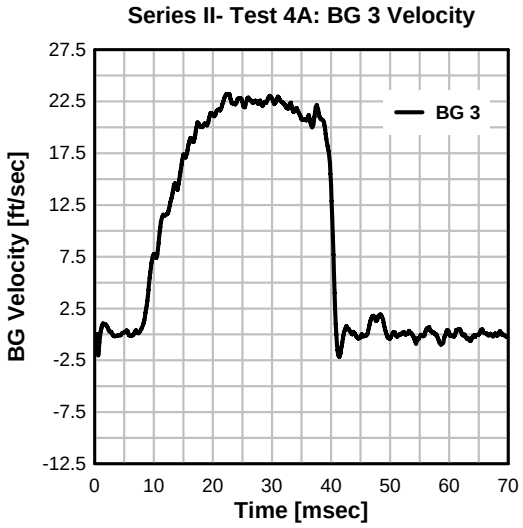
Series II- Test 4A: BG 3 Velocity
BG 3
BG Velocity [ft/sec]
Time [msec]

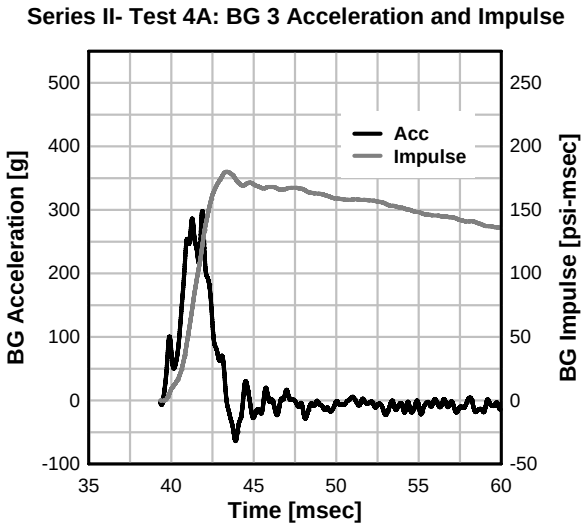
Series II- Test 4A: BG 3 Acceleration and Impulse
Acc
Impulse
BG Acceleration [g]
BG Impulse [psi-msec]
Time [msec]

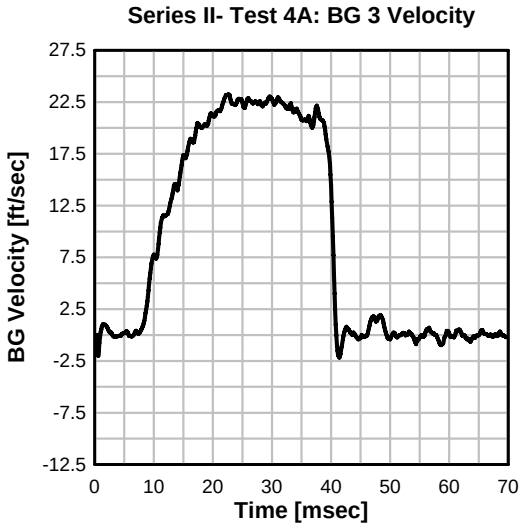
Series II- Test 4A: BG 3 Velocity
BG Velocity [ft/sec]
Time [msec]

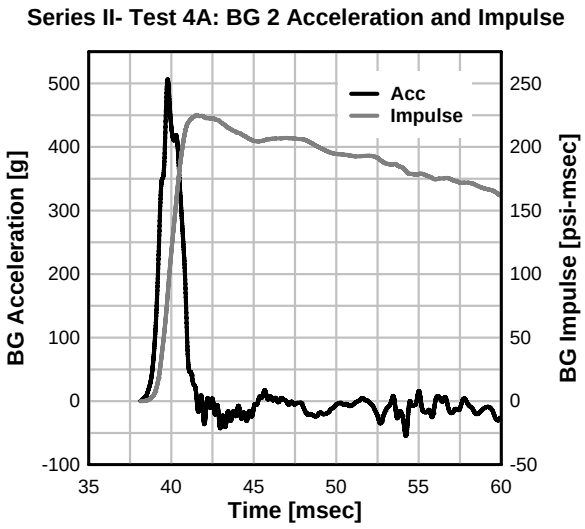
Series II- Test 4A: BG 2 Acceleration and Impulse
Acc
Impulse
BG Acceleration [g]
BG Impulse [psi-msec]
Time [msec]

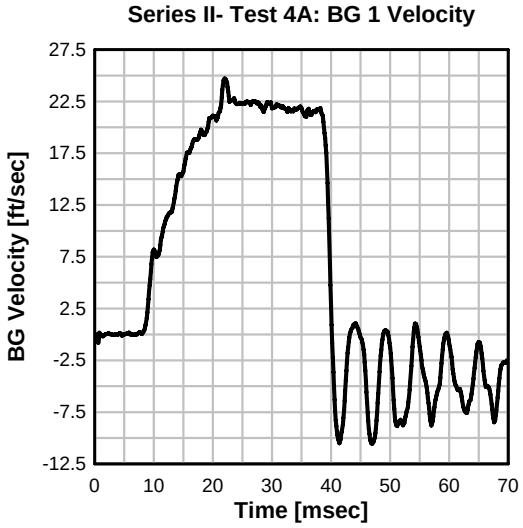
Series II- Test 4A: BG 1 Velocity
BG Velocity [ft/sec]
Time [msec]

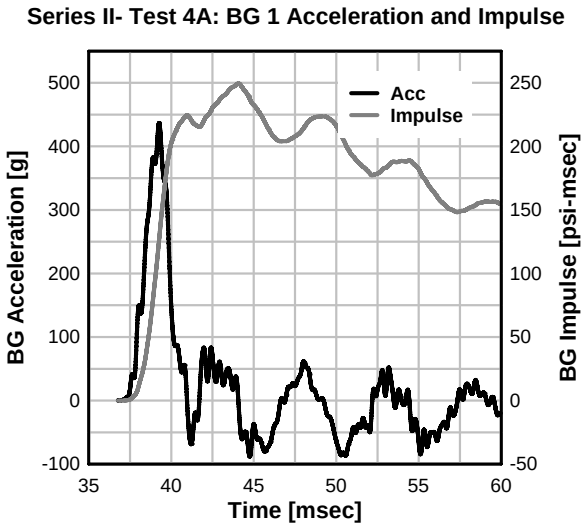
Series II- Test 4A: BG 1 Acceleration and Impulse
Acc
Impulse
BG Acceleration [g]
BG Impulse [psi-msec]
Time [msec]

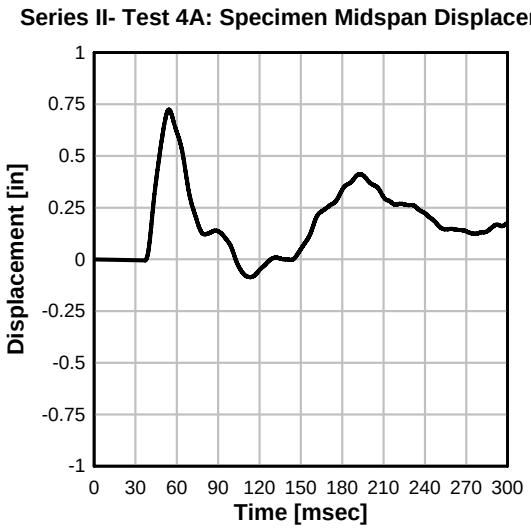
Series II- Test 4A: Specimen Midspan Displacement
Displacement [in]
1
0.75
0.5
0.25
0
-0.25
-0.5
-0.75
-1
0 30 60 90 120 150 180 210 240 270 300
Time [msec]

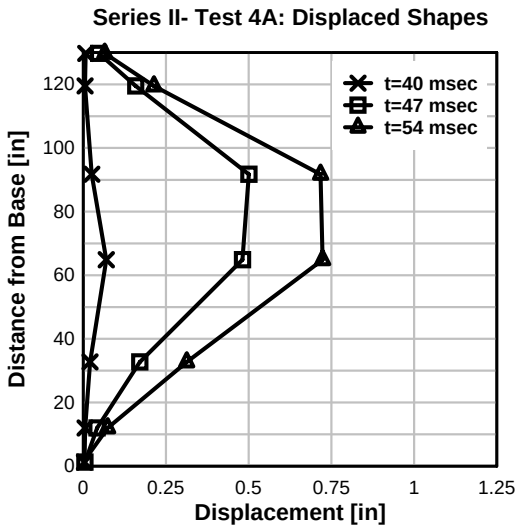
Series II- Test 4A: Displaced Shapes
Distance from Base [in]
120
100
80
60
40
20
0
0 0.25 0.5 0.75 1 1.25
Displacement [in]
t=40 msec
t=47 msec
t=54 msec

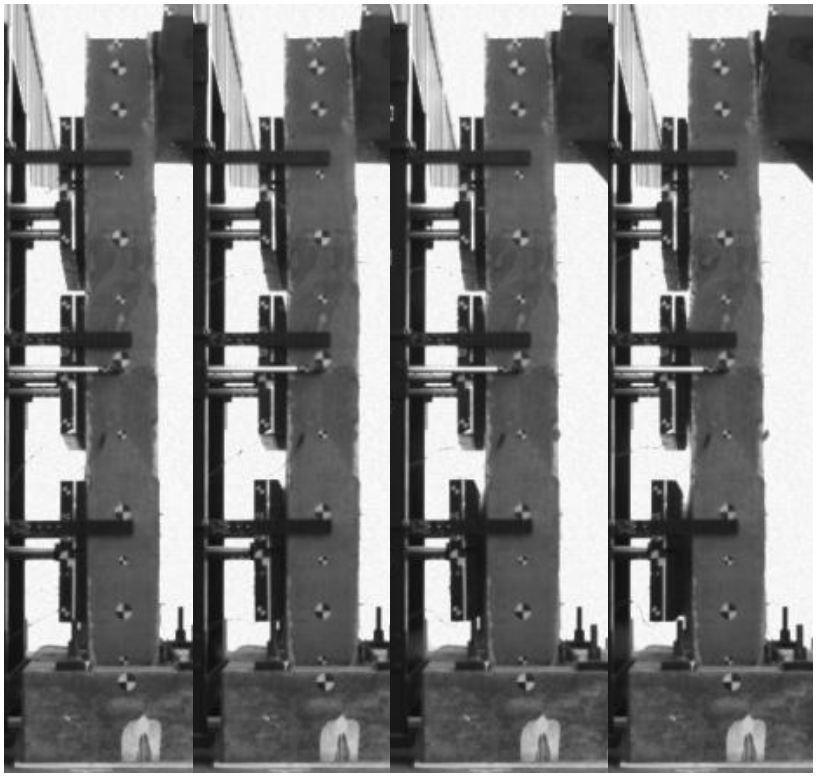

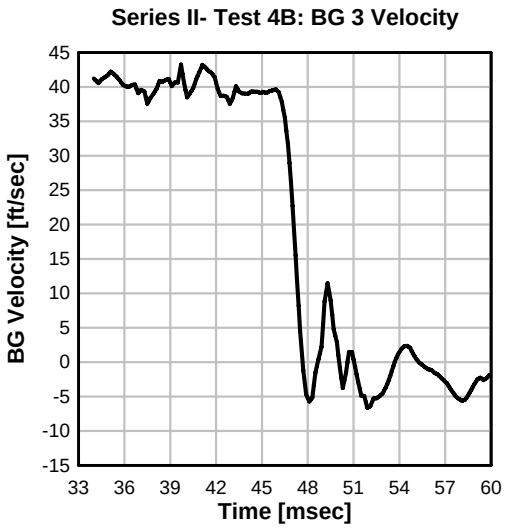
Series II- Test 4B: BG 3 Velocity
BG Velocity [ft/sec]
Time [msec]

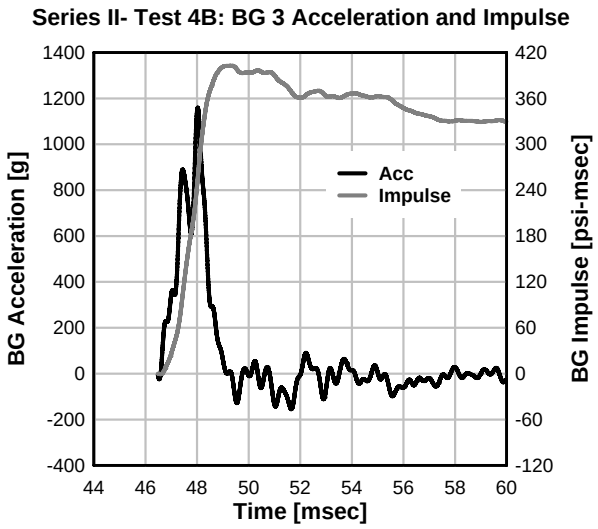
Series II- Test 4B: BG 3 Acceleration and Impulse
BG Acceleration [g]
BG Impulse [psi-msec]
Acc
Impulse
Time [msec]

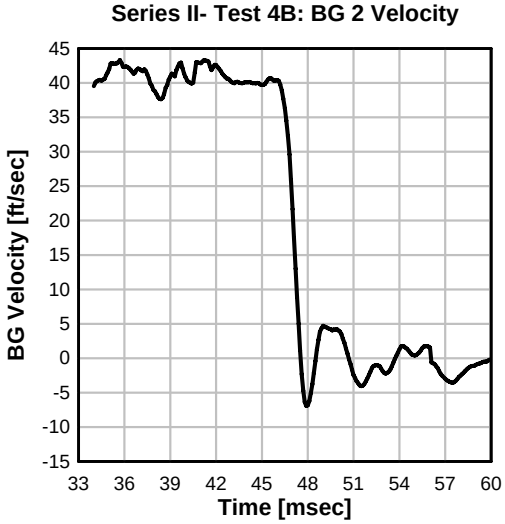
Series II- Test 4B: BG 2 Velocity
BG Velocity [ft/sec]
Time [msec]

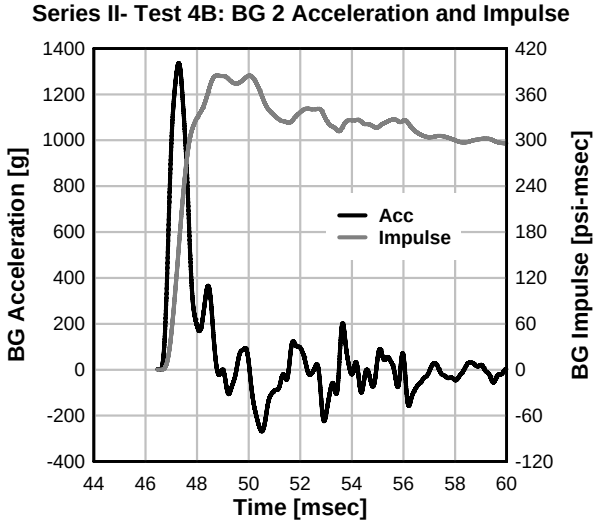
Series II- Test 4B: BG 2 Acceleration and Impulse
BG Acceleration [g]
BG Impulse [psi-msec]
Acc
Impulse
Time [msec]

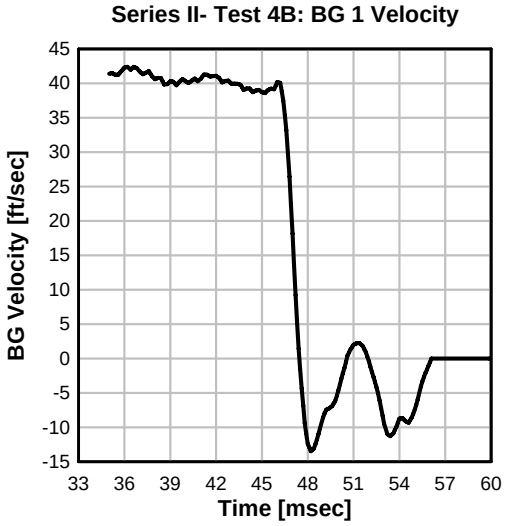
Series II- Test 4B: BG 1 Velocity
BG Velocity [ft/sec]
Time [msec]

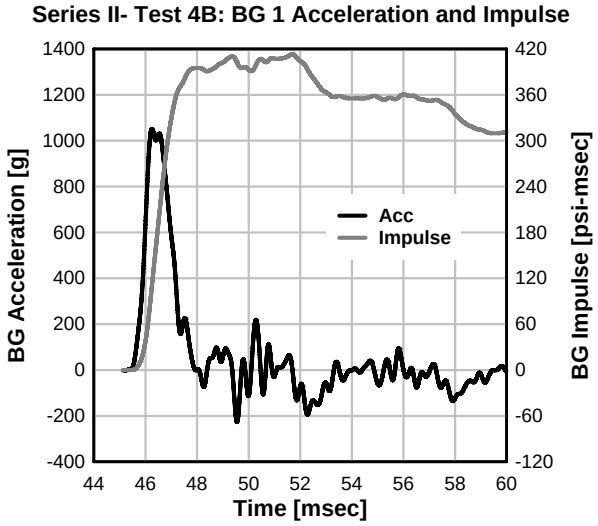
Series II- Test 4B: BG 1 Acceleration and Impulse
BG Acceleration [g]
BG Impulse [psi-msec]
Acc
Impulse
Time [msec]

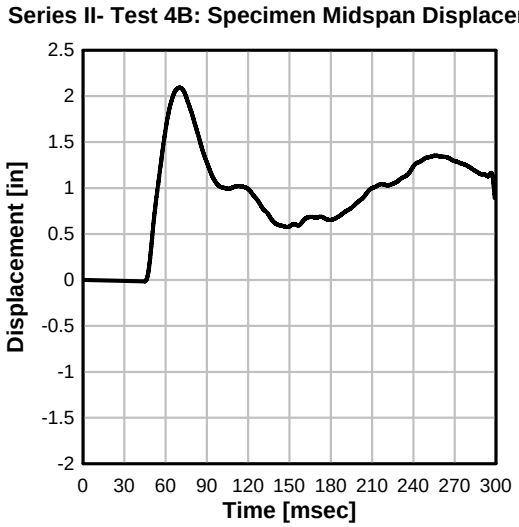
Series II- Test 4B: Specimen Midspan Displacement
Displacement [in]
Time [msec]
2.5
2
1.5
1
0.5
0
-0.5
-1
-1.5
-2
0 30 60 90 120 150 180 210 240 270 300

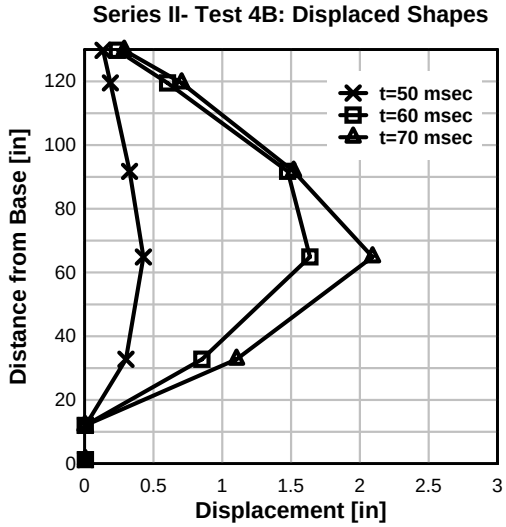
Series II- Test 4B: Displaced Shapes
Distance from Base [in]
Displacement [in]
t=50 msec
t=60 msec
t=70 msec
120
100
80
60
40
20
0
0 0.5 1 1.5 2 2.5 3

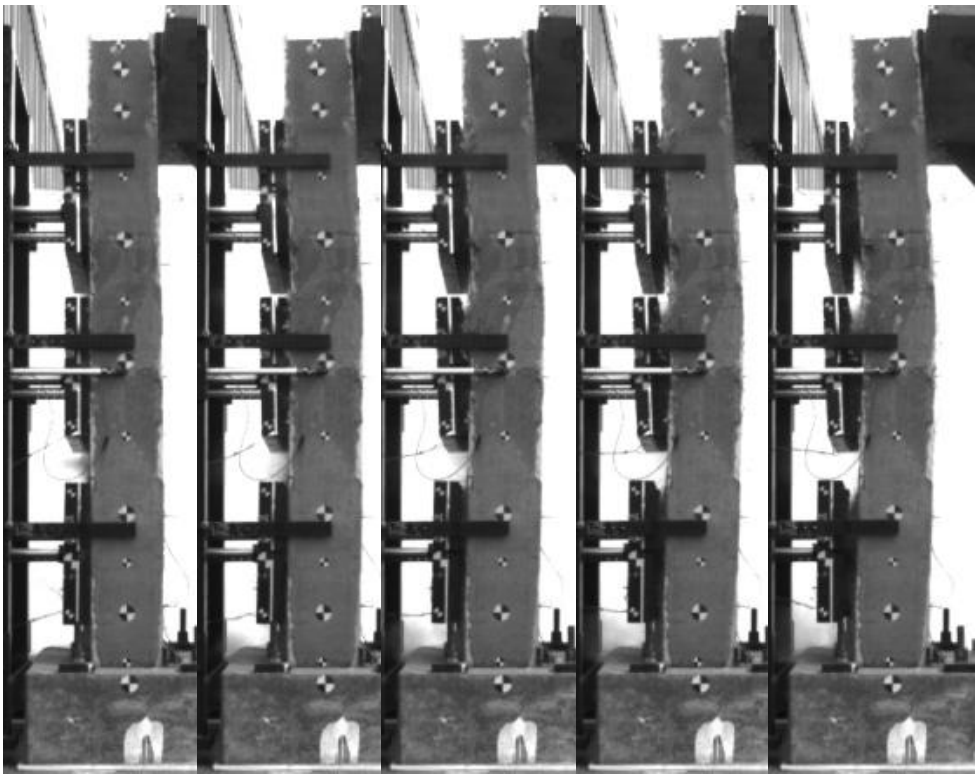

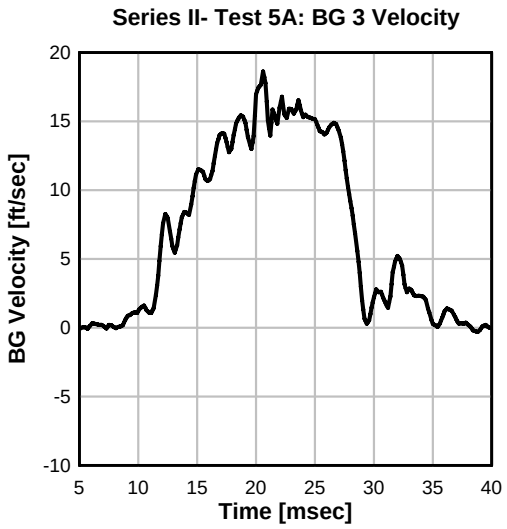
Series II- Test 5A: BG 3 Velocity
BG Velocity [ft/sec]
Time [msec]

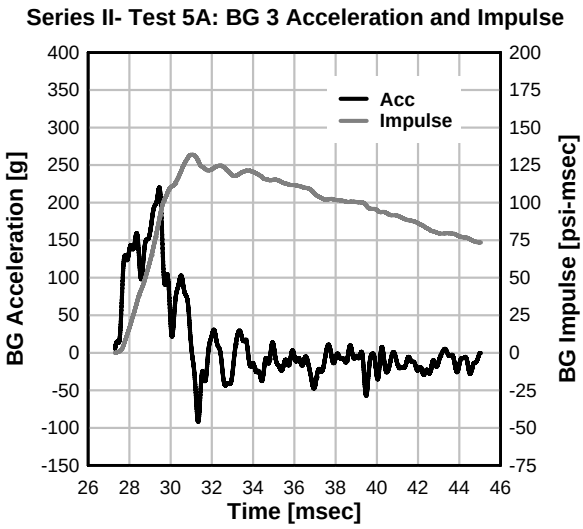
Series II- Test 5A: BG 3 Acceleration and Impulse
Acc
Impulse
BG Acceleration [g]
BG Impulse [psi-msec]
Time [msec]

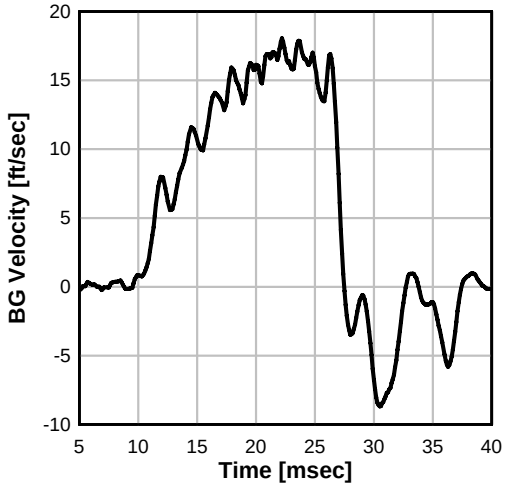
Series II- Test 5A: BG 2 Velocity
BG Velocity [ft/sec]
Time [msec]

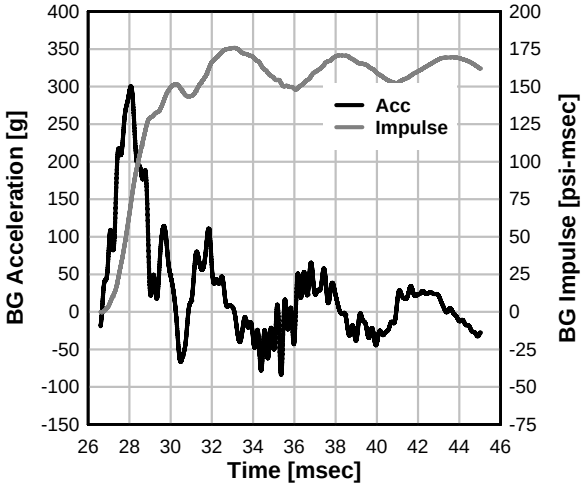
Series II- Test 5A: BG 2 Acceleration and Impulse
Acc
Impulse
BG Acceleration [g]
BG Impulse [psi-msec]
Time [msec]

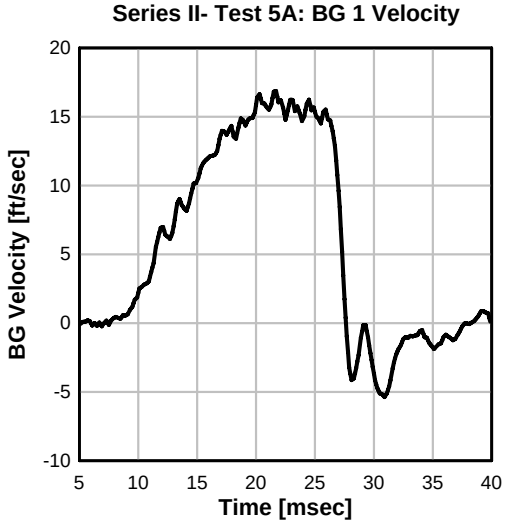
Series II- Test 5A: BG 1 Velocity
BG Velocity [ft/sec]
Time [msec]

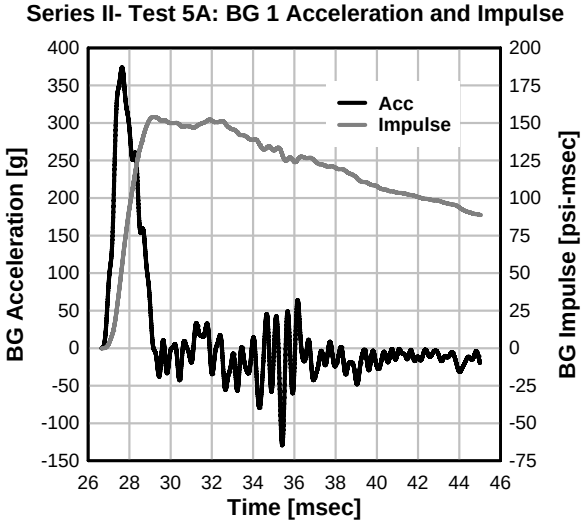
Series II- Test 5A: BG 1 Acceleration and Impulse
Acc
Impulse
BG Acceleration [g]
BG Impulse [psi-msec]
Time [msec]

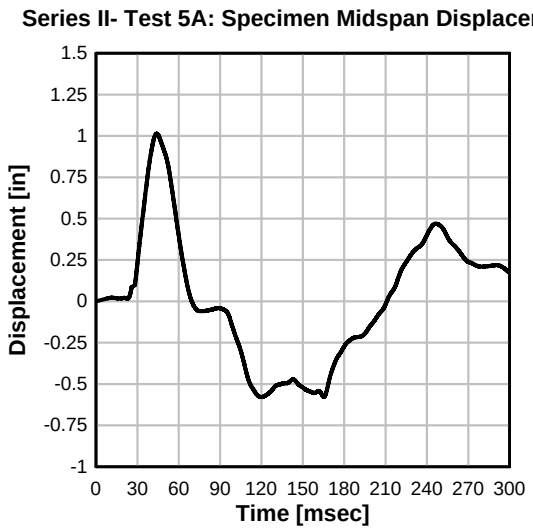
Series II- Test 5A: Specimen Midspan Displacement
Displacement [in]
1.5
1.25
1
0.75
0.5
0.25
0
-0.25
-0.5
-0.75
-1
0 30 60 90 120 150 180 210 240 270 300
Time [msec]

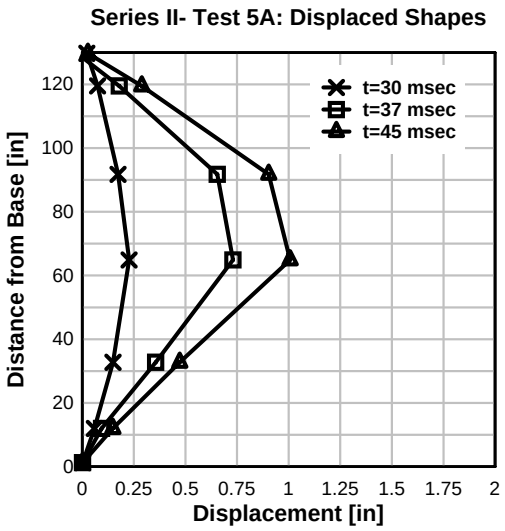
Series II- Test 5A: Displaced Shapes
Distance from Base [in]
120
100
80
60
40
20
0
0 0.25 0.5 0.75 1 1.25 1.5 1.75 2
Displacement [in]
t=30 msec
t=37 msec
t=45 msec

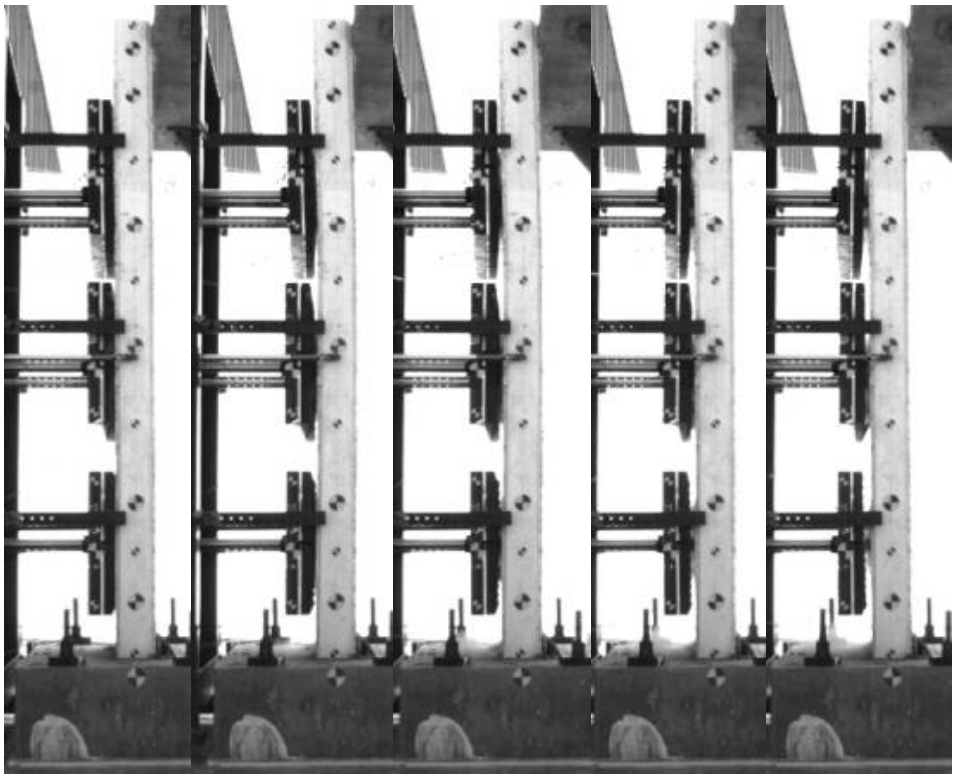

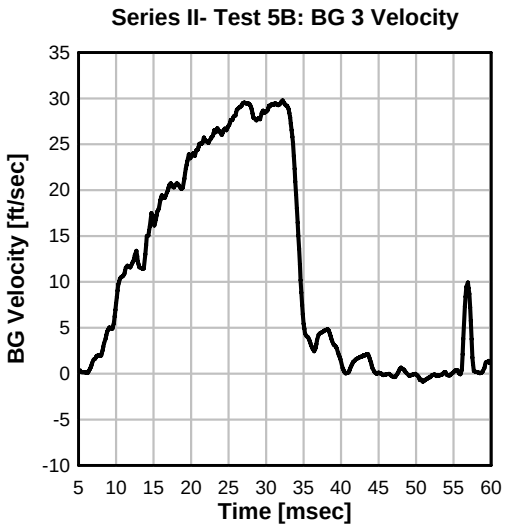
Series II- Test 5B: BG 3 Velocity
BG Velocity [ft/sec]
Time [msec]

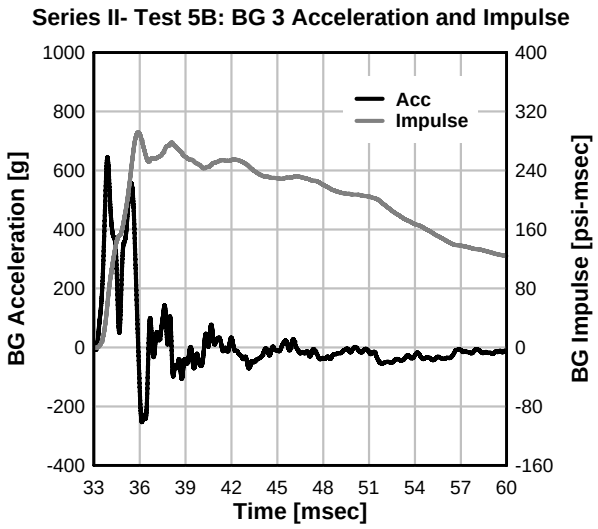
Series II- Test 5B: BG 3 Acceleration and Impulse
Acc
Impulse
BG Acceleration [g]
BG Impulse [psi-msec]
Time [msec]

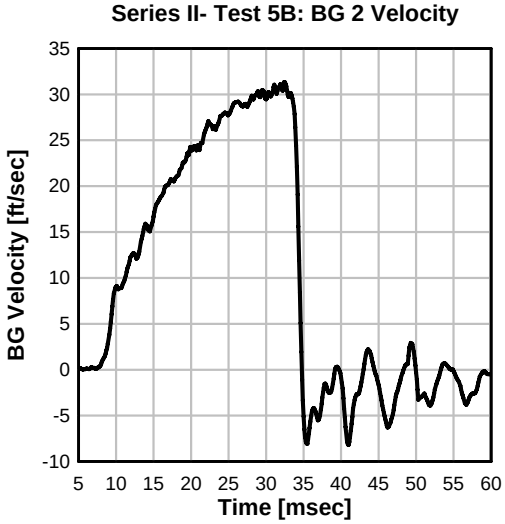
Series II- Test 5B: BG 2 Velocity
BG Velocity [ft/sec]
Time [msec]

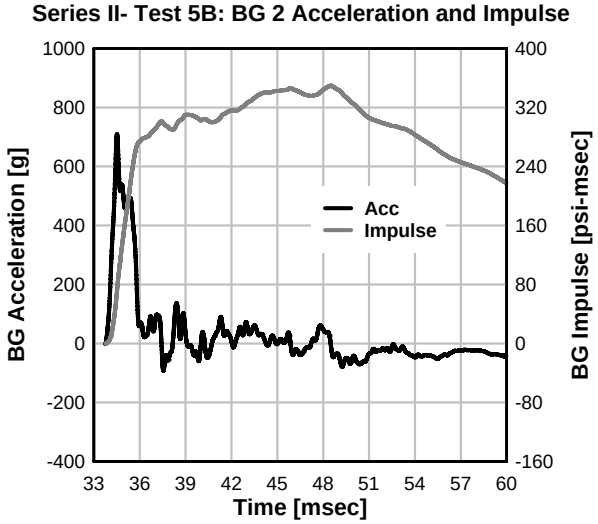
Series II- Test 5B: BG 2 Acceleration and Impulse
Acc
Impulse
BG Acceleration [g]
BG Impulse [psi-msec]
Time [msec]

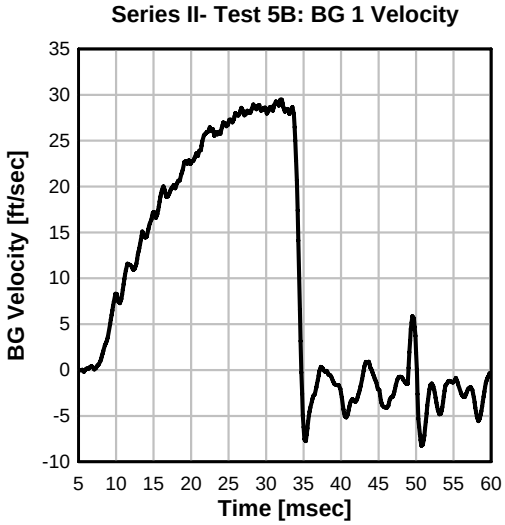
Series II- Test 5B: BG 1 Velocity
BG Velocity [ft/sec]
Time [msec]

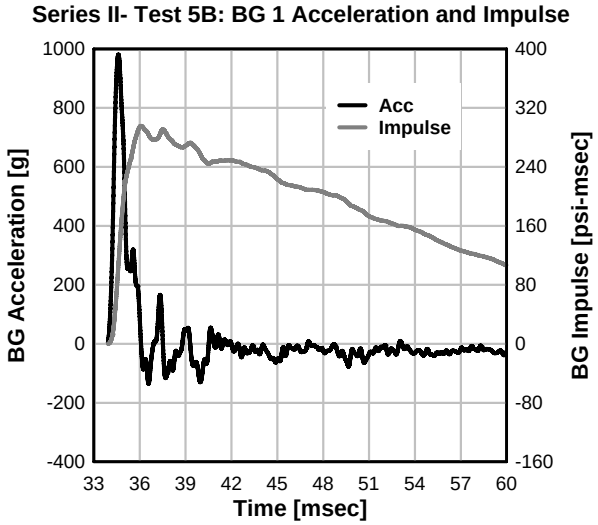
Series II- Test 5B: BG 1 Acceleration and Impulse
Acc
Impulse
BG Acceleration [g]
BG Impulse [psi-msec]
Time [msec]

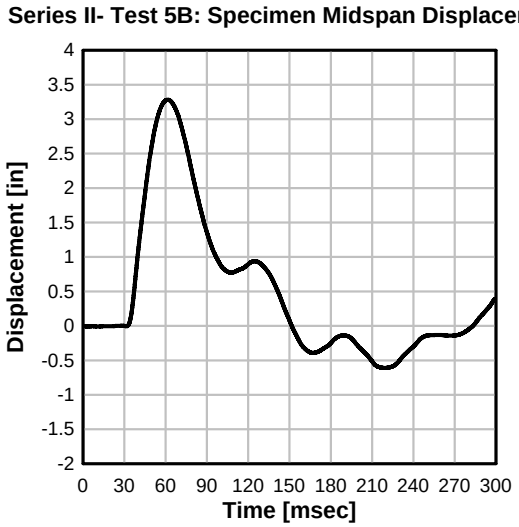
Series II- Test 5B: Specimen Midspan Displacement
Displacement [in]
Time [msec]
4
3.5
3
2.5
2
1.5
1
0.5
0
-0.5
-1
-1.5
-2
0 30 60 90 120 150 180 210 240 270 300

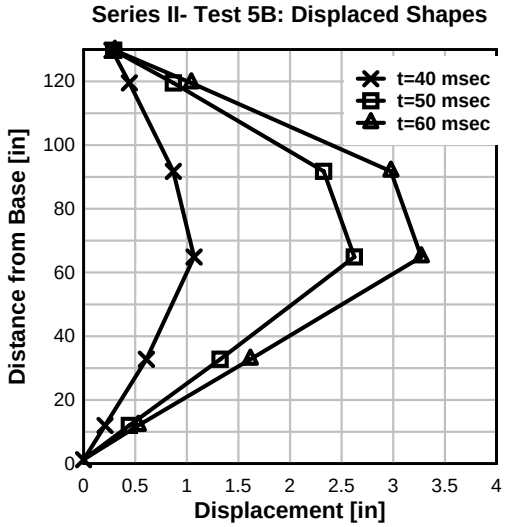
Series II- Test 5B: Displaced Shapes
Distance from Base [in]
Displacement [in]
t=40 msec
t=50 msec
t=60 msec
120
100
80
60
40
20
0
0 0.5 1 1.5 2 2.5 3 3.5 4

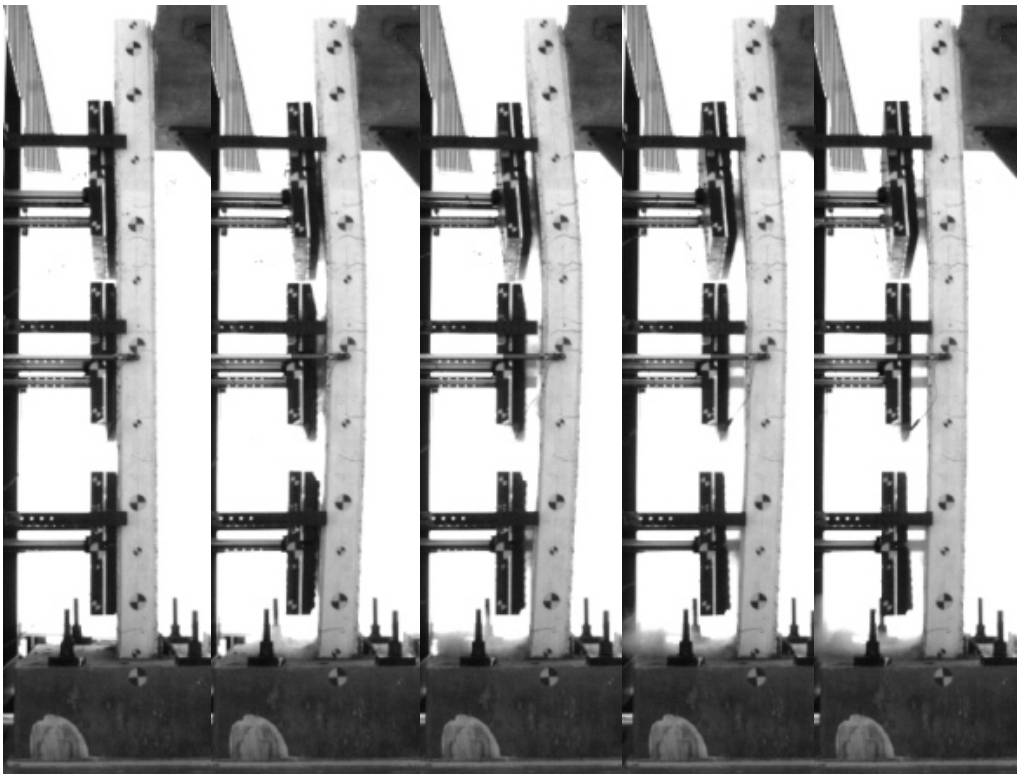

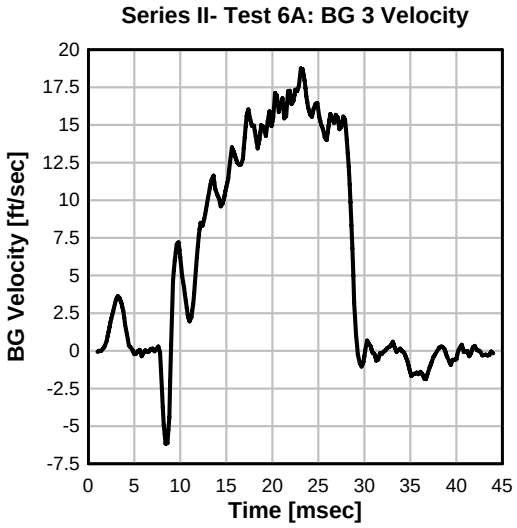
Series II- Test 6A: BG 3 Velocity
BG Velocity [ft/sec]
Time [msec]

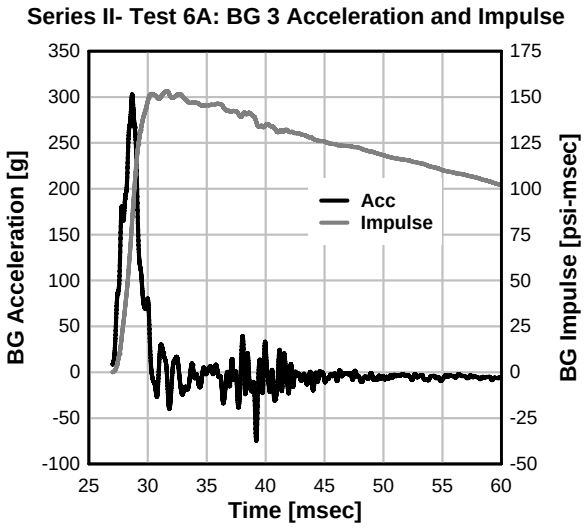
Series II- Test 6A: BG 3 Acceleration and Impulse
BG Acceleration [g]
BG Impulse [psi-msec]
Acc
Impulse
Time [msec]

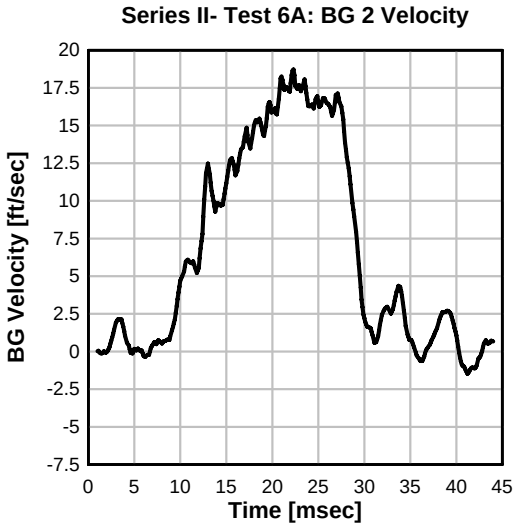
Series II- Test 6A: BG 2 Velocity
BG Velocity [ft/sec]
Time [msec]

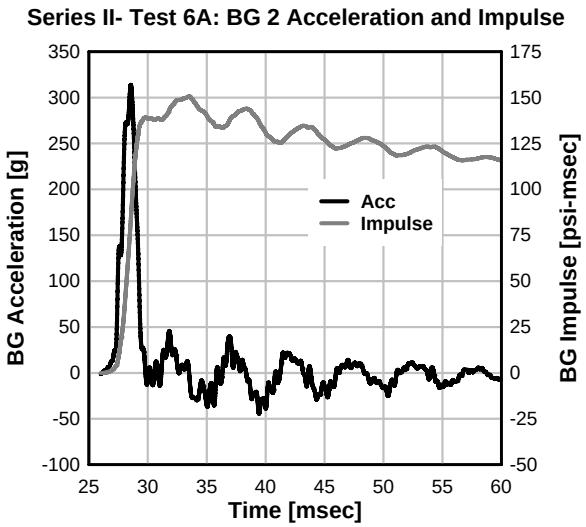
Series II- Test 6A: BG 2 Acceleration and Impulse
BG Acceleration [g]
BG Impulse [psi-msec]
Acc
Impulse
Time [msec]

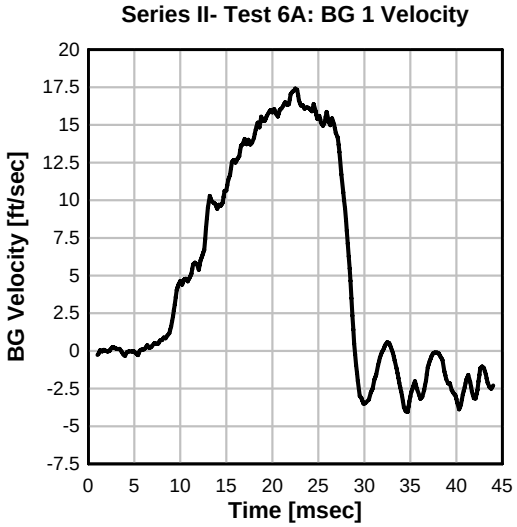
Series II- Test 6A: BG 1 Velocity
BG Velocity [ft/sec]
Time [msec]

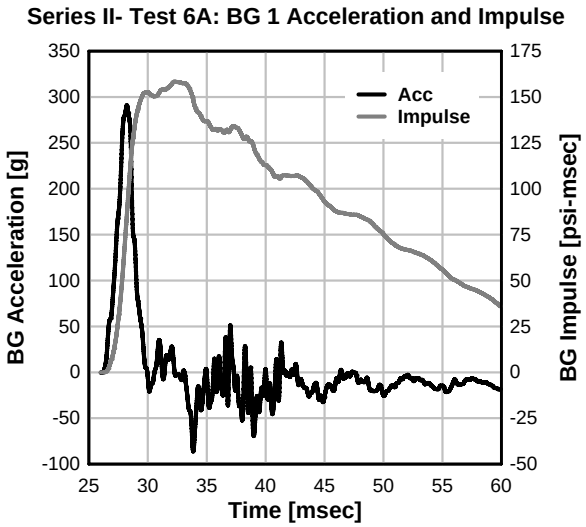
Series II- Test 6A: BG 1 Acceleration and Impulse
BG Acceleration [g]
BG Impulse [psi-msec]
Acc
Impulse
Time [msec]

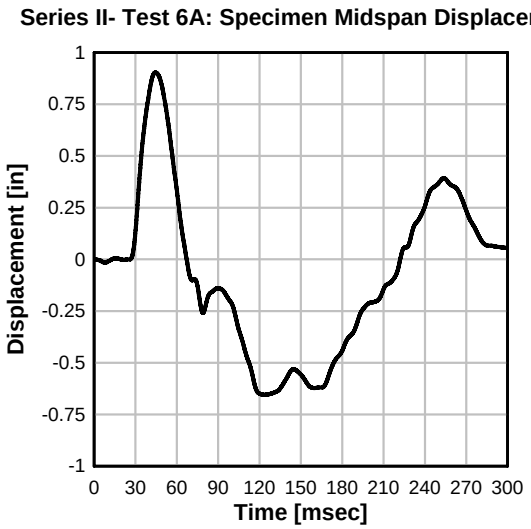
Series II- Test 6A: Specimen Midspan Displacement
Displacement [in]
1
0.75
0.5
0.25
0
-0.25
-0.5
-0.75
-1
0 30 60 90 120 150 180 210 240 270 300
Time [msec]

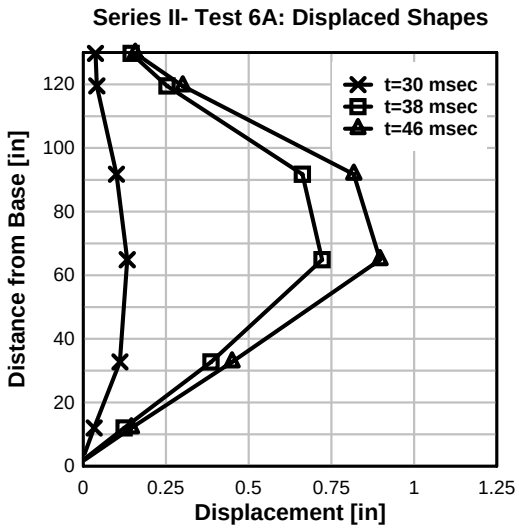
Series II- Test 6A: Displaced Shapes
Distance from Base [in]
120
100
80
60
40
20
0
0 0.25 0.5 0.75 1 1.25
Displacement [in]
t=30 msec
t=38 msec
t=46 msec

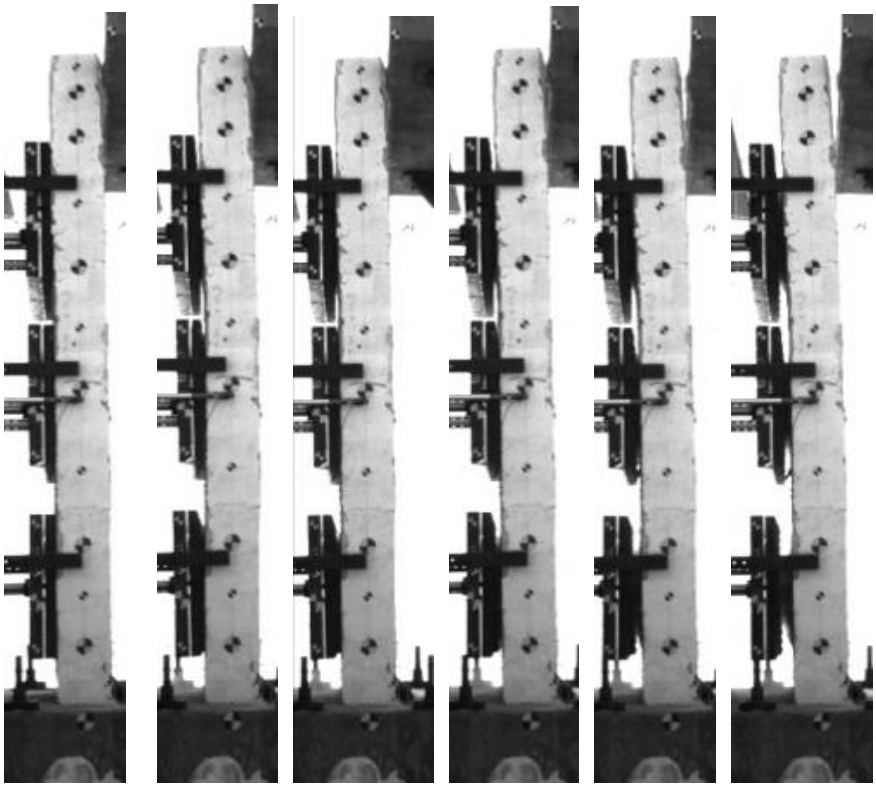

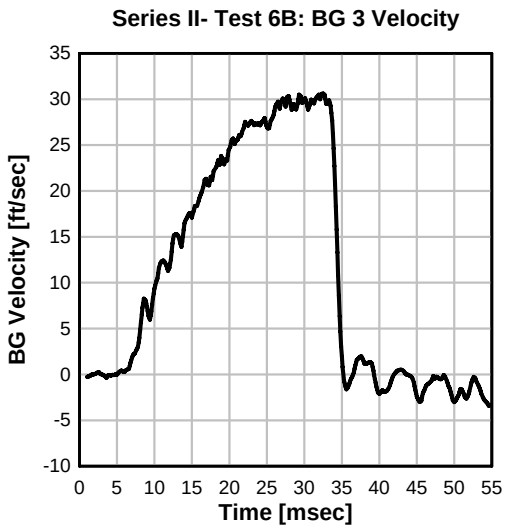
Series II- Test 6B: BG 3 Velocity
BG Velocity [ft/sec]
Time [msec]

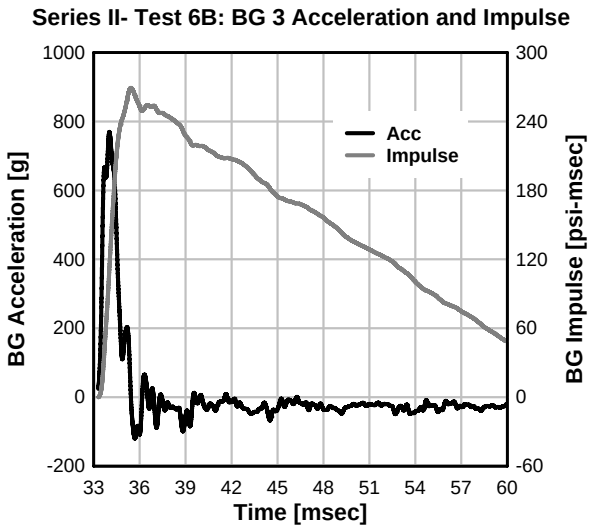
Series II- Test 6B: BG 3 Acceleration and Impulse
BG Acceleration [g]
BG Impulse [psi-msec]
Acc
Impulse
Time [msec]

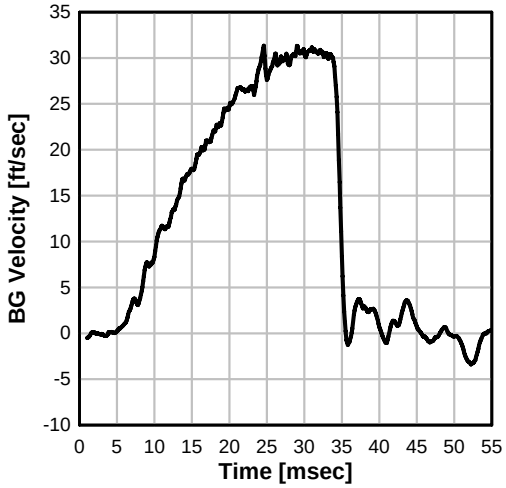
Series II- Test 6B: BG 2 Velocity
BG Velocity [ft/sec]
Time [msec]

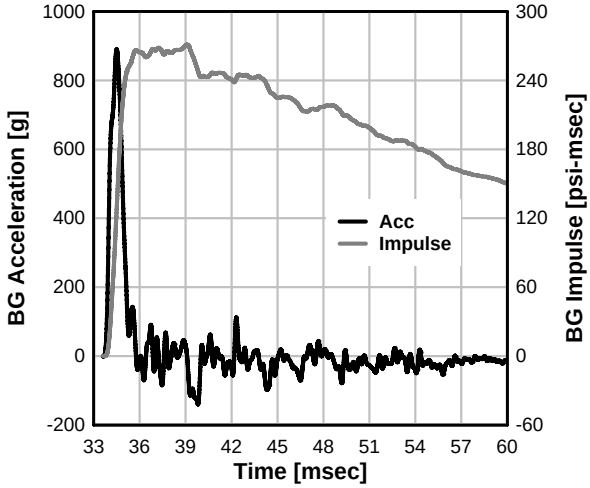
Series II- Test 6B: BG 2 Acceleration and Impulse
BG Acceleration [g]
BG Impulse [psi-msec]
Acc
Impulse
Time [msec]

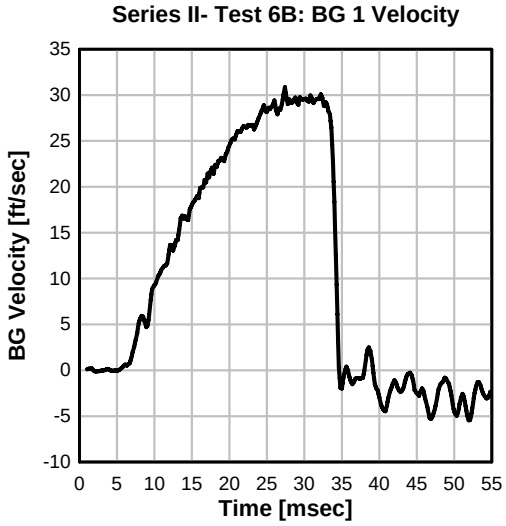
Series II- Test 6B: BG 1 Velocity
BG Velocity [ft/sec]
Time [msec]

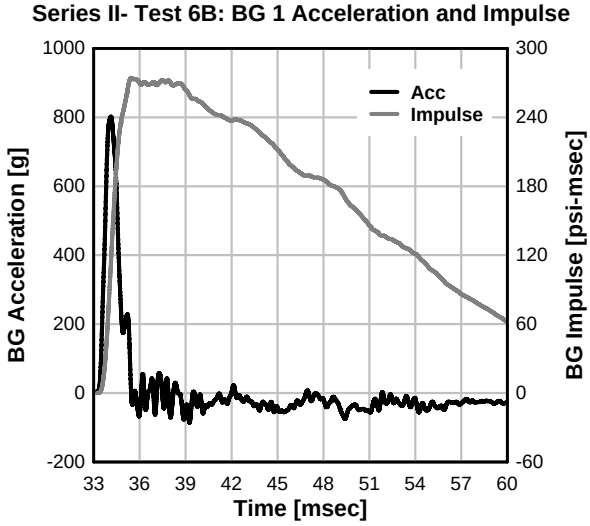
Series II- Test 6B: BG 1 Acceleration and Impulse
BG Acceleration [g]
BG Impulse [psi-msec]
Acc
Impulse
Time [msec]

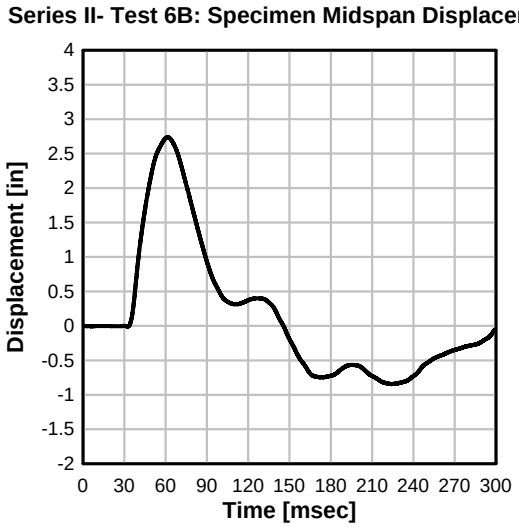
Series II- Test 6B: Specimen Midspan Displacement
Displacement [in]
Time [msec]
4
3.5
3
2.5
2
1.5
1
0.5
0
-0.5
-1
-1.5
-2
0 30 60 90 120 150 180 210 240 270 300

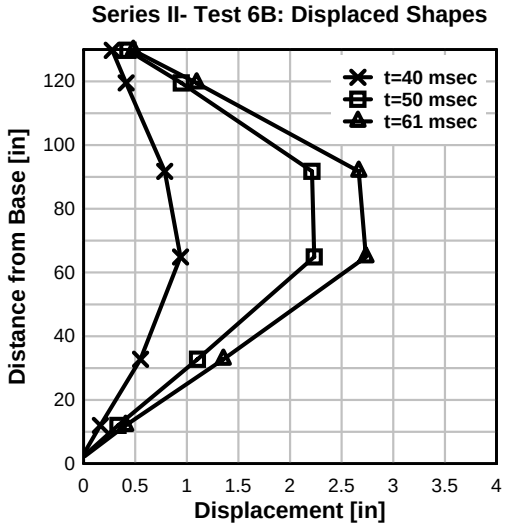
Series II- Test 6B: Displaced Shapes
t=40 msec
t=50 msec
t=61 msec
Distance from Base [in]
Displacement [in]
120
100
80
60
40
20
0
0 0.5 1 1.5 2 2.5 3 3.5 4

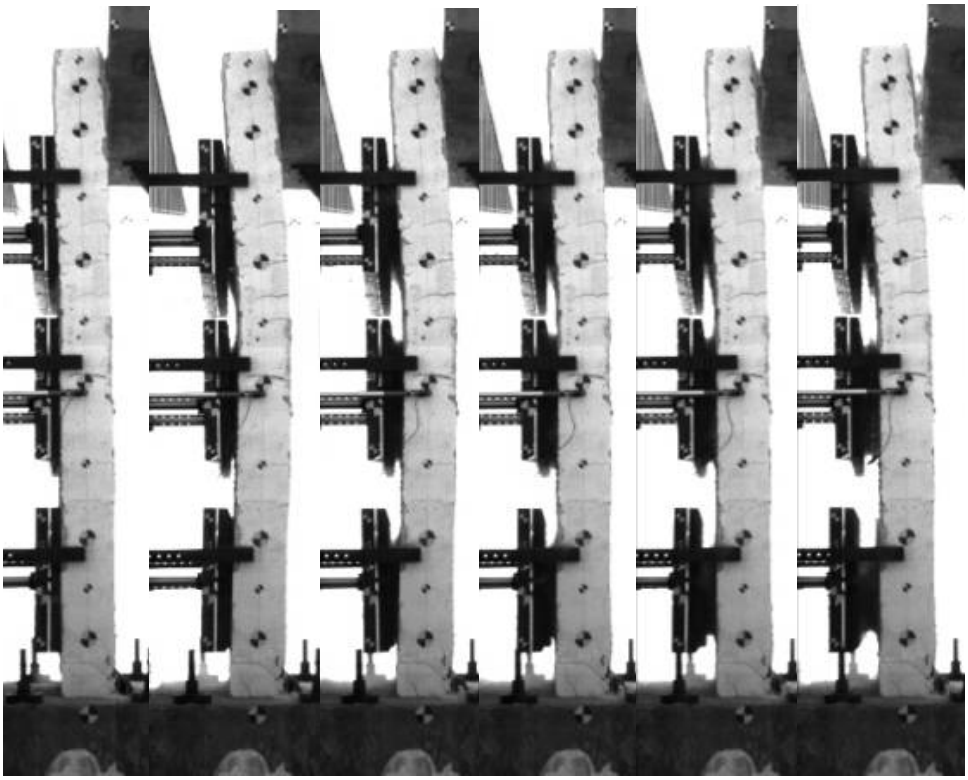

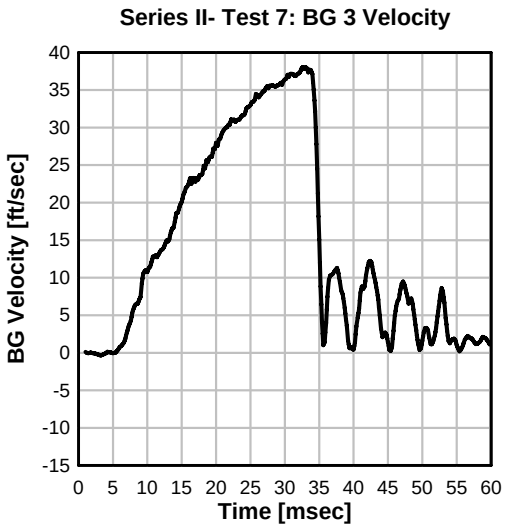
Series II- Test 7: BG 3 Velocity
BG Velocity [ft/sec]
Time [msec]

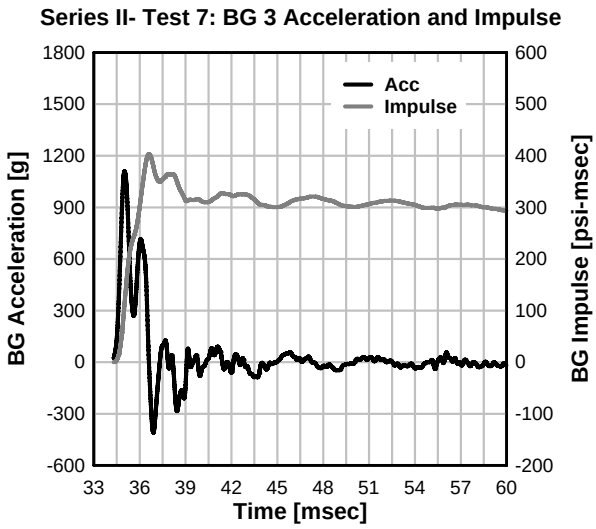
Series II- Test 7: BG 3 Acceleration and Impulse
Acc
Impulse
BG Acceleration [g]
BG Impulse [psi-msec]
Time [msec]

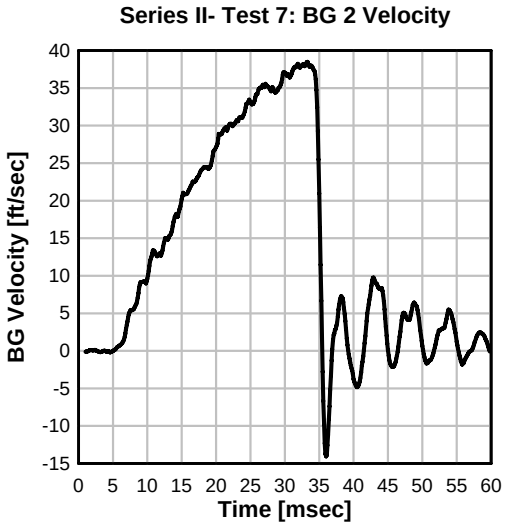
Series II- Test 7: BG 2 Velocity
BG Velocity [ft/sec]
Time [msec]

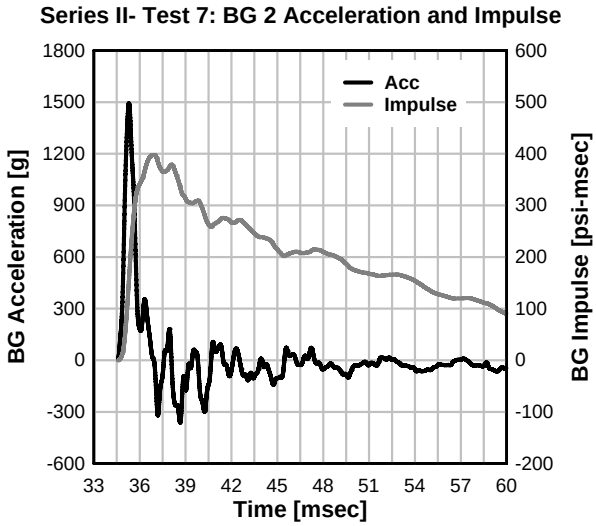
Series II- Test 7: BG 2 Acceleration and Impulse
Acc
Impulse
BG Acceleration [g]
BG Impulse [psi-msec]
Time [msec]

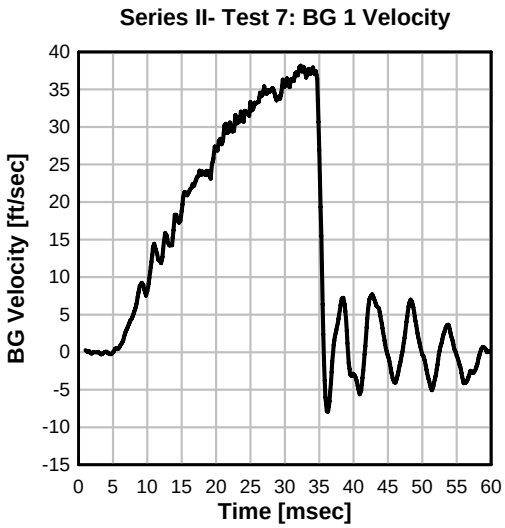
Series II- Test 7: BG 1 Velocity
BG Velocity [ft/sec]
Time [msec]

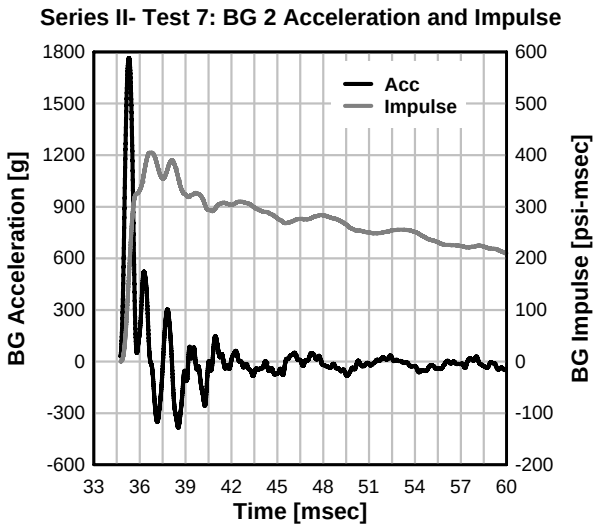
Series II- Test 7: BG 2 Acceleration and Impulse
Acc
Impulse
BG Acceleration [g]
BG Impulse [psi-msec]
Time [msec]

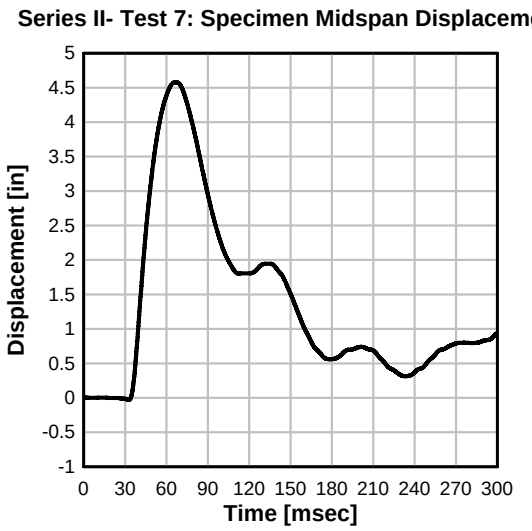
Series II- Test 7: Specimen Midspan Displacement
Displacement [in]
Time [msec]
5
4.5
4
3.5
3
2.5
2
1.5
1
0.5
0
-0.5
-1
0 30 60 90 120 150 180 210 240 270 300

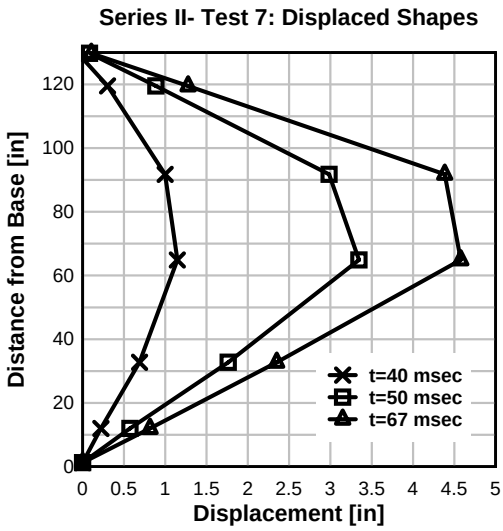
Series II- Test 7: Displaced Shapes
Distance from Base [in]
Displacement [in]
120
100
80
60
40
20
0
0 0.5 1 1.5 2 2.5 3 3.5 4 4.5 5
t=40 msec
t=50 msec
t=67 msec

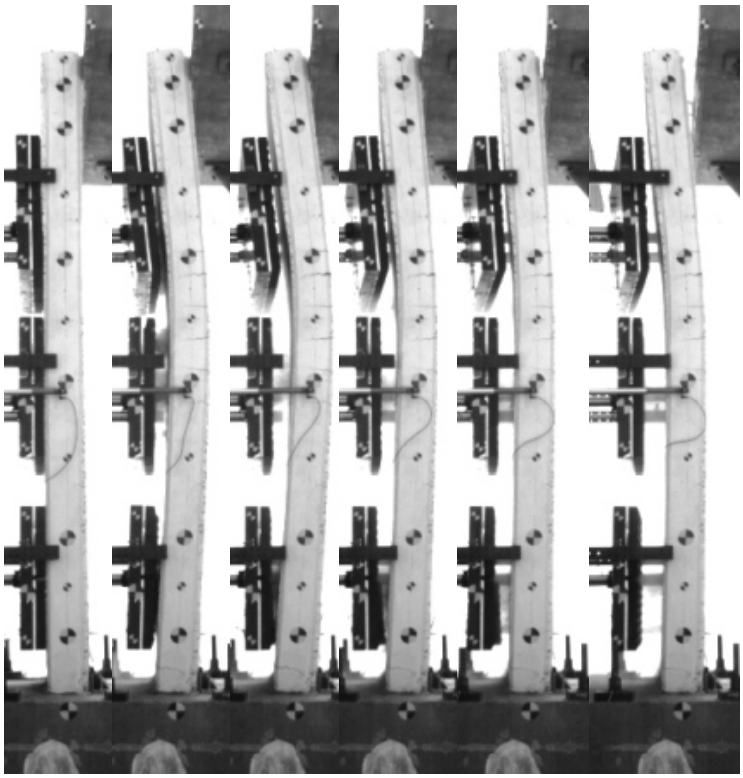

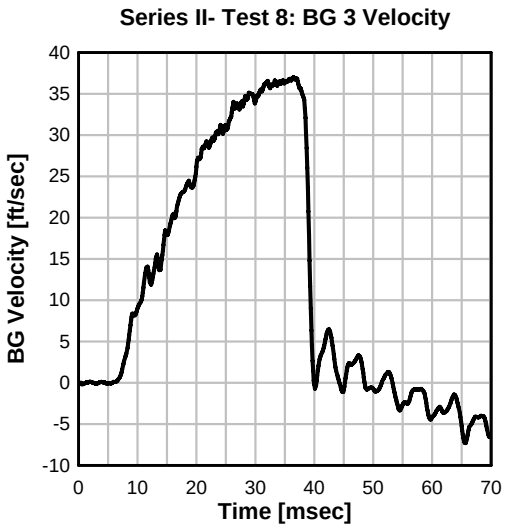
Series II- Test 8: BG 3 Velocity
BG Velocity [ft/sec]
Time [msec]

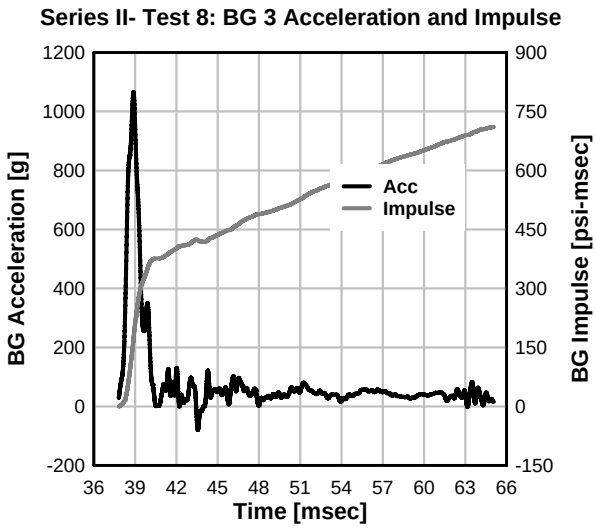
Series II- Test 8: BG 3 Acceleration and Impulse
BG Acceleration [g]
BG Impulse [psi-msec]
Acc
Impulse
Time [msec]

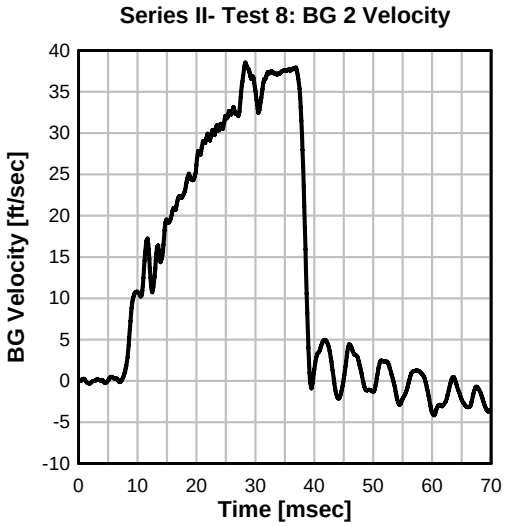
Series II- Test 8: BG 2 Velocity
BG Velocity [ft/sec]
Time [msec]

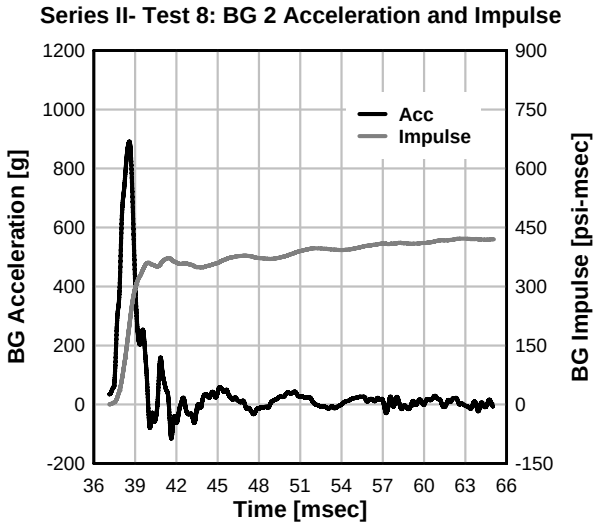
Series II- Test 8: BG 2 Acceleration and Impulse
BG Acceleration [g]
BG Impulse [psi-msec]
Acc
Impulse
Time [msec]

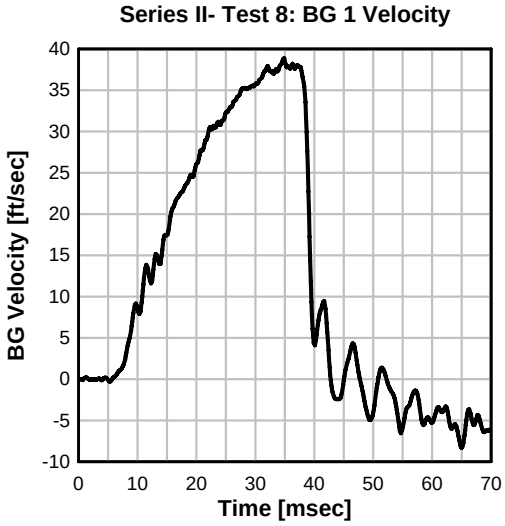
Series II- Test 8: BG 1 Velocity
BG Velocity [ft/sec]
Time [msec]

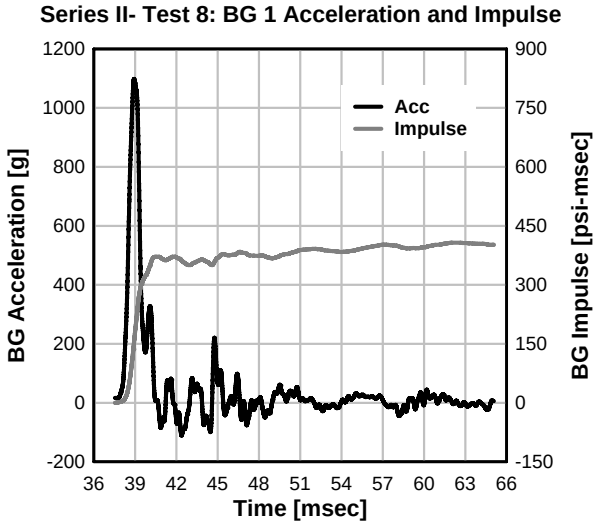
Series II- Test 8: BG 1 Acceleration and Impulse
BG Acceleration [g]
BG Impulse [psi-msec]
Acc
Impulse
Time [msec]

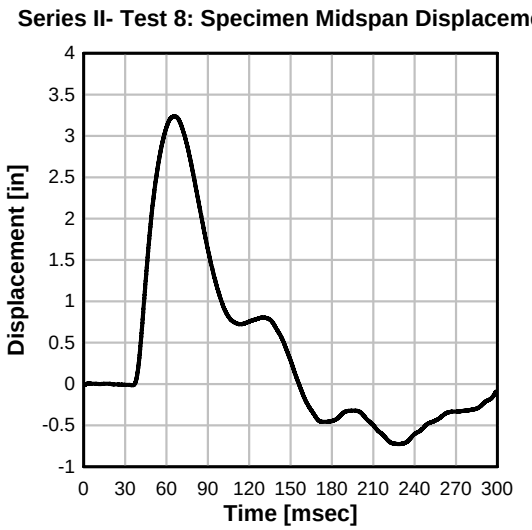
Series II- Test 8: Specimen Midspan Displacement
Displacement [in]
Time [msec]
4
3.5
3
2.5
2
1.5
1
0.5
0
-0.5
-1
0 30 60 90 120 150 180 210 240 270 300

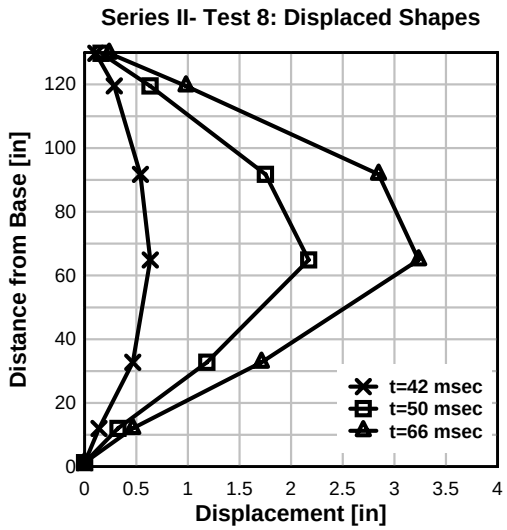
Series II- Test 8: Displaced Shapes
Distance from Base [in]
Displacement [in]
120
100
80
60
40
20
0
0 0.5 1 1.5 2 2.5 3 3.5 4
t=42 msec
t=50 msec
t=66 msec

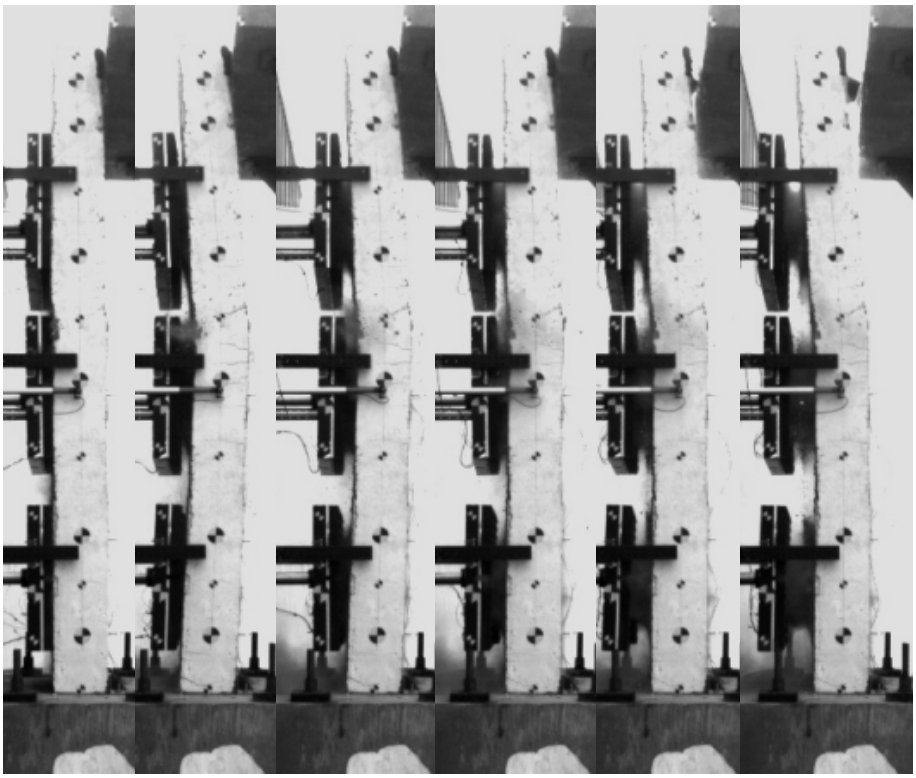

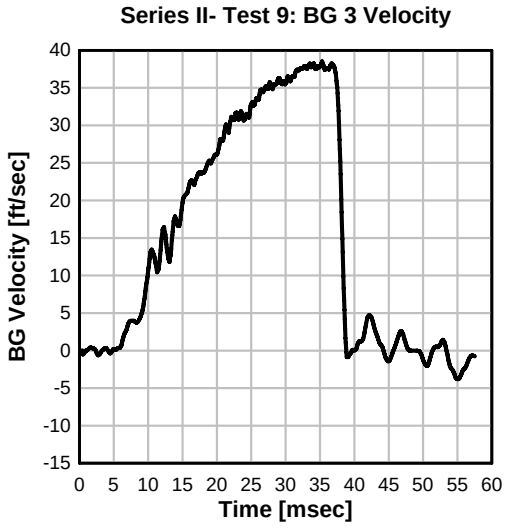
Series II- Test 9: BG 3 Velocity
BG Velocity [ft/sec]
Time [msec]

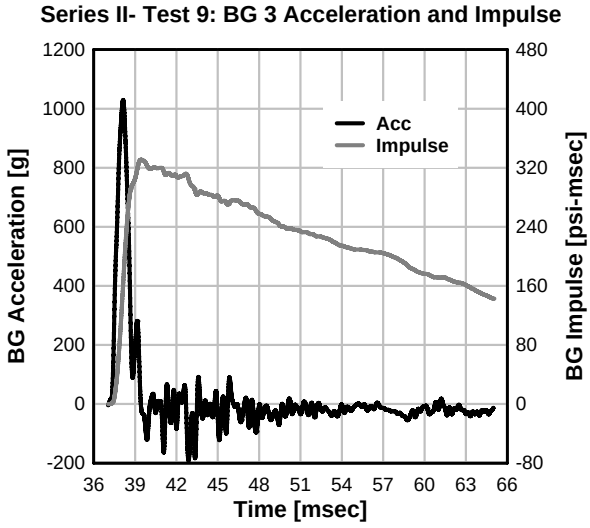
Series II- Test 9: BG 3 Acceleration and Impulse
BG Acceleration [g]
BG Impulse [psi-msec]
Acc
Impulse
Time [msec]

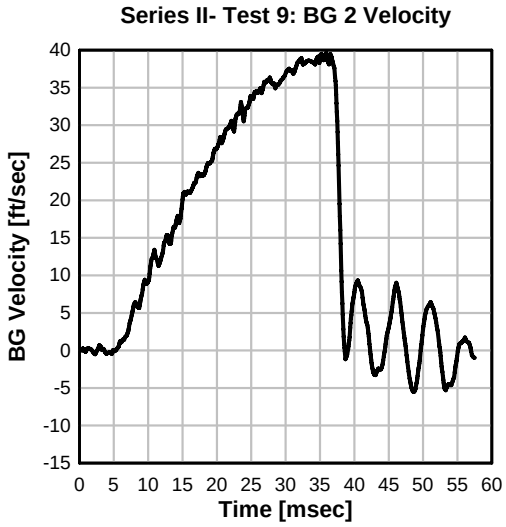
Series II- Test 9: BG 2 Velocity
BG Velocity [ft/sec]
Time [msec]

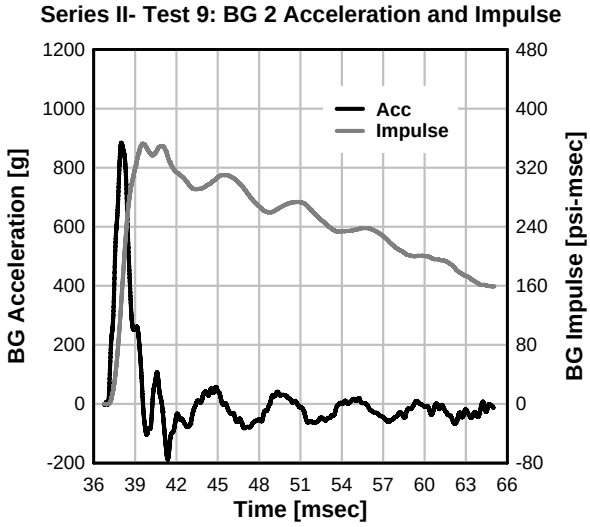
Series II- Test 9: BG 2 Acceleration and Impulse
BG Acceleration [g]
BG Impulse [psi-msec]
Acc
Impulse
Time [msec]

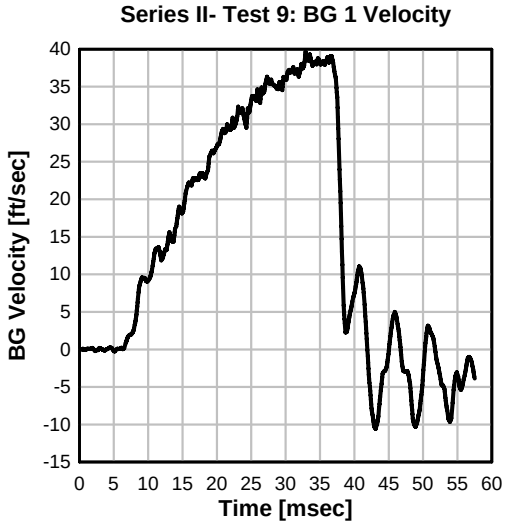
Series II- Test 9: BG 1 Velocity
BG Velocity [ft/sec]
Time [msec]

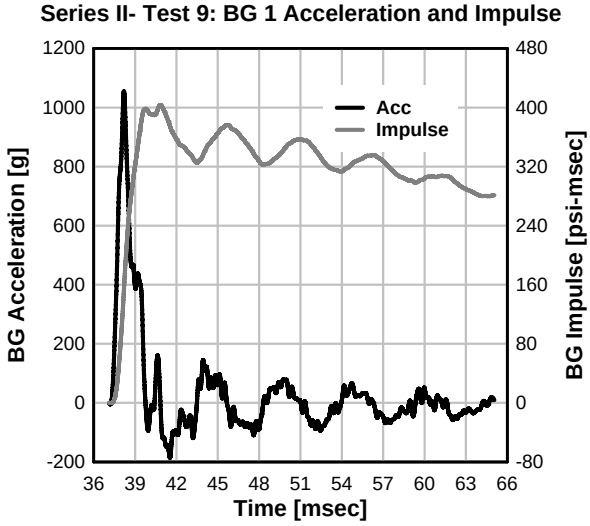
Series II- Test 9: BG 1 Acceleration and Impulse
BG Acceleration [g]
BG Impulse [psi-msec]
Acc
Impulse
Time [msec]

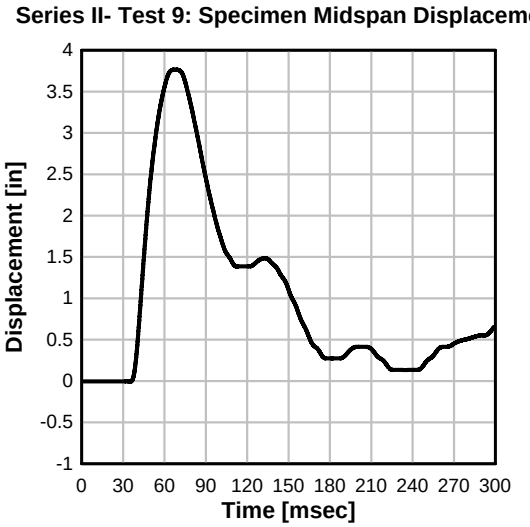
Series II- Test 9: Specimen Midspan Displacement
Displacement [in]
Time [msec]
4
3.5
3
2.5
2
1.5
1
0.5
0
-0.5
-1
0 30 60 90 120 150 180 210 240 270 300

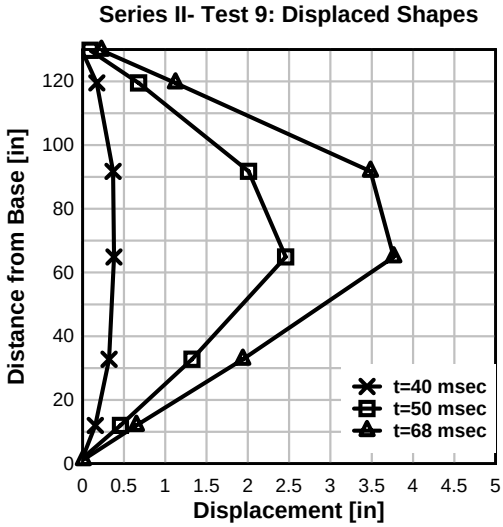
Series II- Test 9: Displaced Shapes
Distance from Base [in]
Displacement [in]
120
100
80
60
40
20
0
0 0.5 1 1.5 2 2.5 3 3.5 4 4.5 5
t=40 msec
t=50 msec
t=68 msec

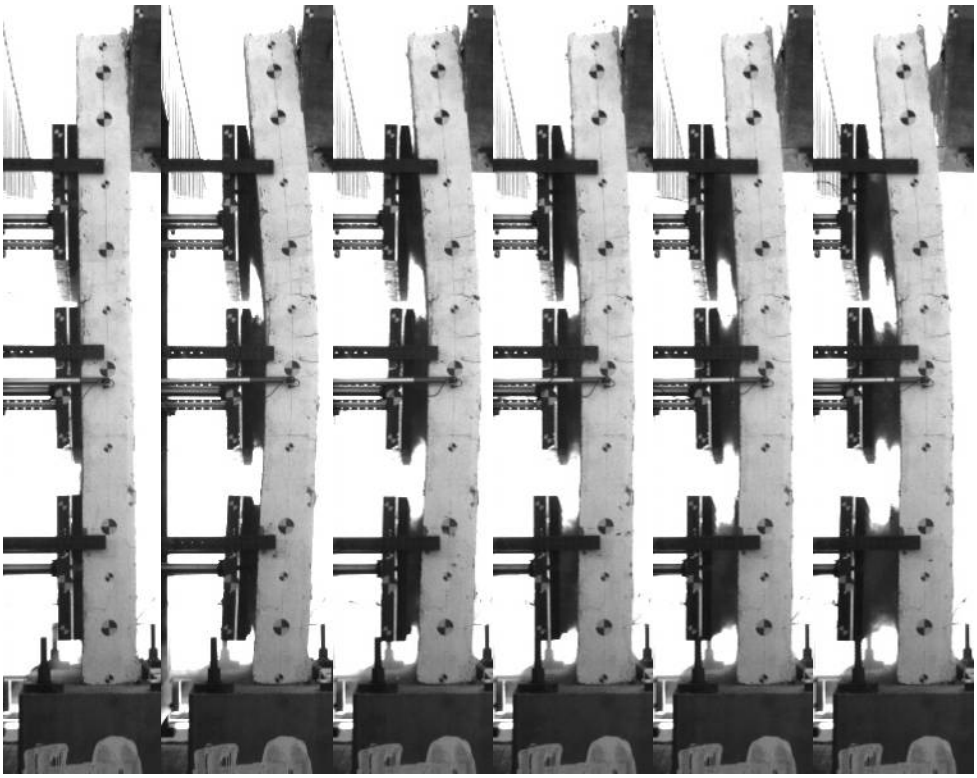

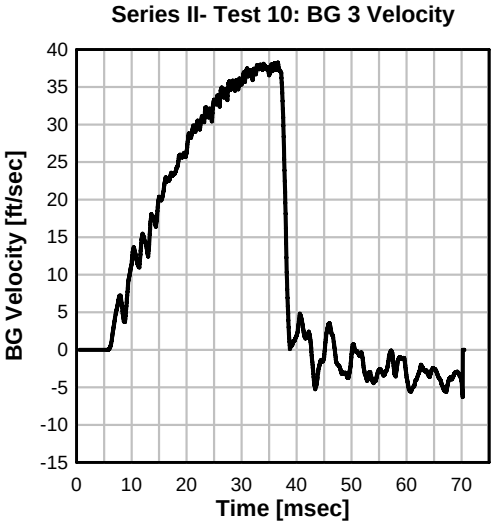
Series II- Test 10: BG 3 Velocity
BG Velocity [ft/sec]
Time [msec]

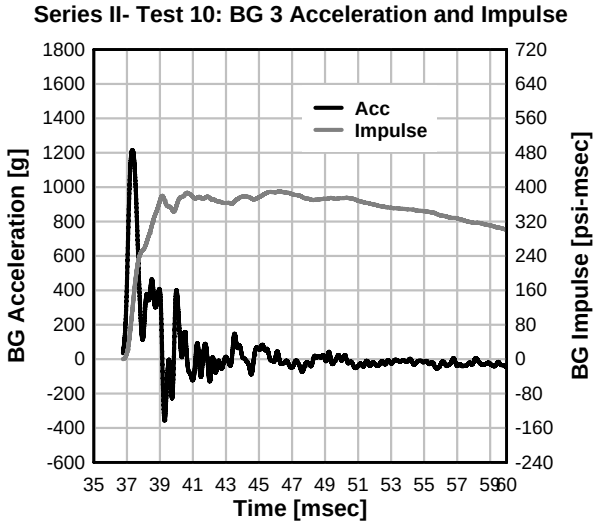
Series II- Test 10: BG 3 Acceleration and Impulse
Acc
Impulse
BG Acceleration [g]
BG Impulse [psi-msec]
Time [msec]

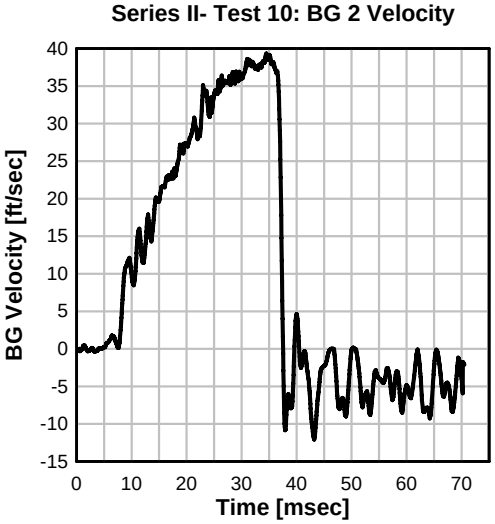
Series II- Test 10: BG 2 Velocity
BG Velocity [ft/sec]
Time [msec]

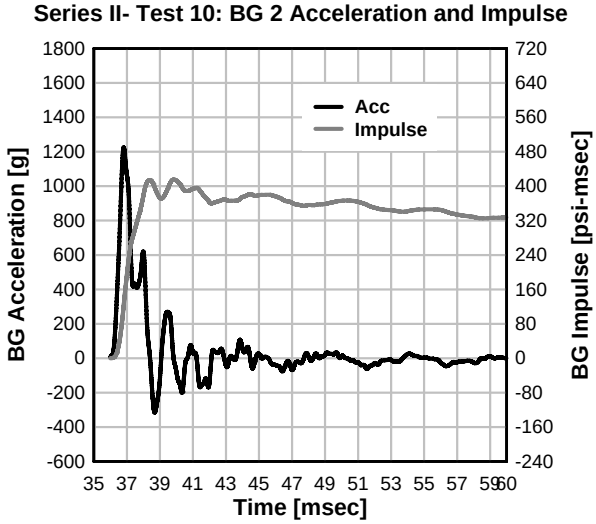
Series II- Test 10: BG 2 Acceleration and Impulse
Acc
Impulse
BG Acceleration [g]
BG Impulse [psi-msec]
Time [msec]

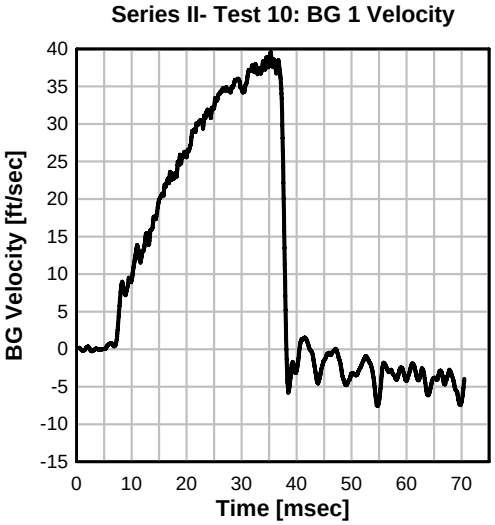
Series II- Test 10: BG 1 Velocity
BG Velocity [ft/sec]
Time [msec]

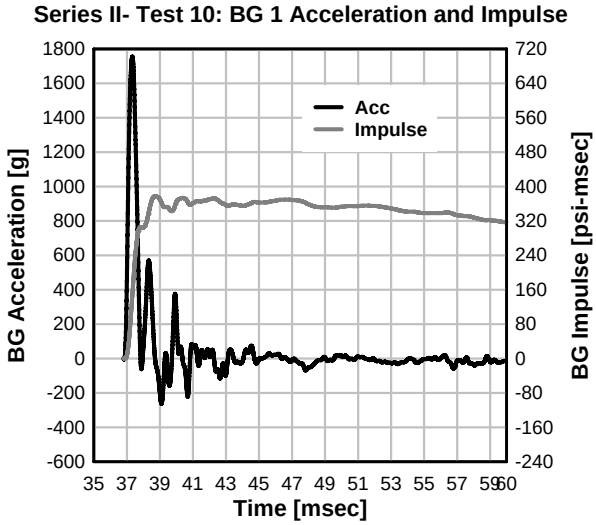
Series II- Test 10: BG 1 Acceleration and Impulse
Acc
Impulse
BG Acceleration [g]
BG Impulse [psi-msec]
Time [msec]

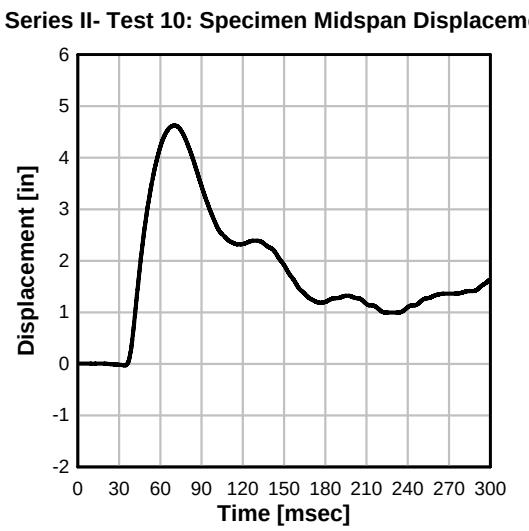
Series II- Test 10: Specimen Midspan Displacement
Displacement [in]
Time [msec]
6
5
4
3
2
1
0
-1
-2
0 30 60 90 120 150 180 210 240 270 300

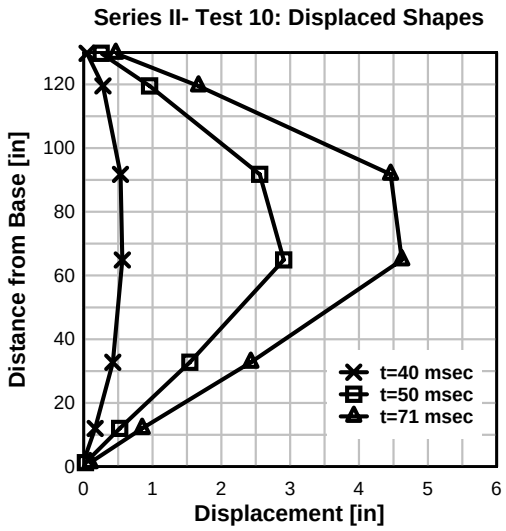
Series II- Test 10: Displaced Shapes
Distance from Base [in]
Displacement [in]
120
100
80
60
40
20
0
0 1 2 3 4 5 6
t=40 msec
t=50 msec
t=71 msec

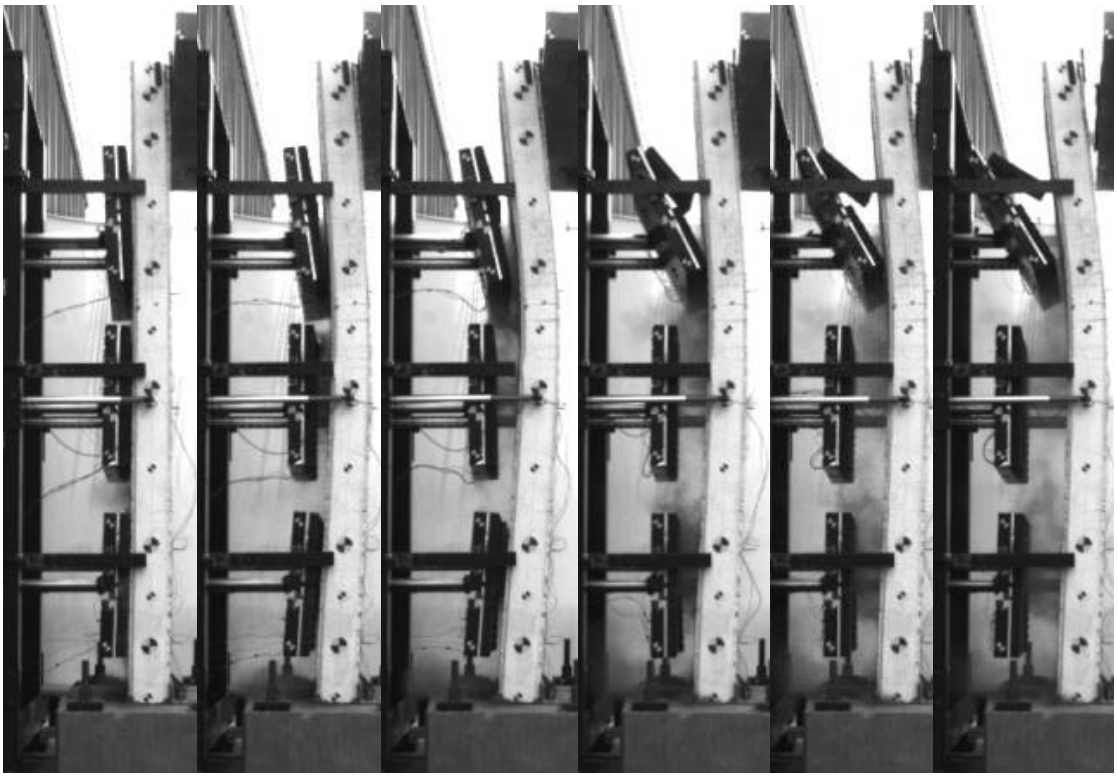

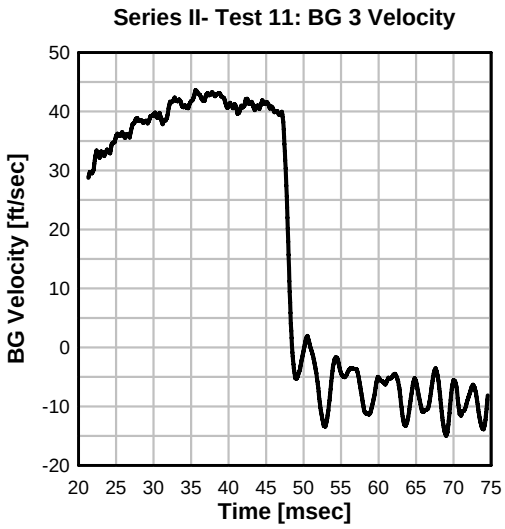
Series II- Test 11: BG 3 Velocity
BG Velocity [ft/sec]
Time [msec]

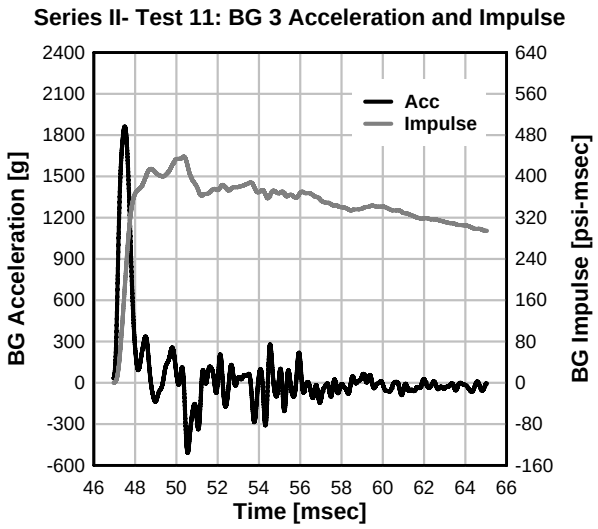
Series II- Test 11: BG 3 Acceleration and Impulse
BG Acceleration [g]
BG Impulse [psi-msec]
Acc
Impulse
Time [msec]

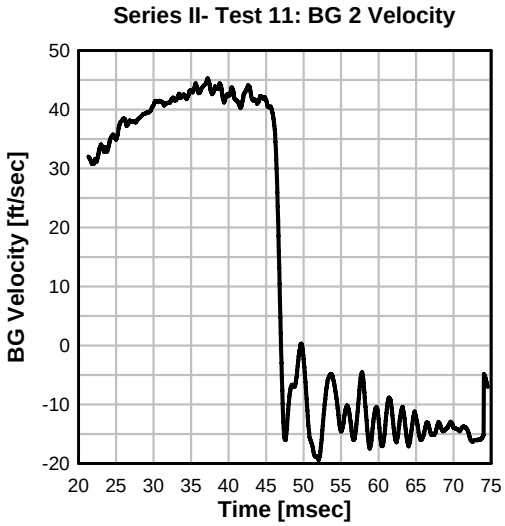
Series II- Test 11: BG 2 Velocity
BG Velocity [ft/sec]
Time [msec]

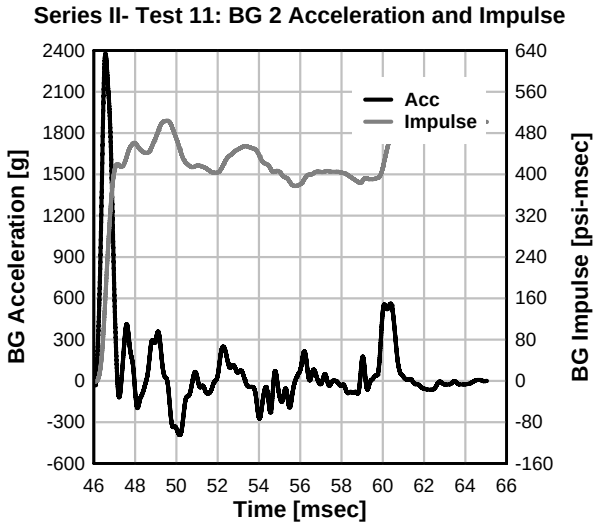
Series II- Test 11: BG 2 Acceleration and Impulse
BG Acceleration [g]
BG Impulse [psi-msec]
Acc
Impulse
Time [msec]

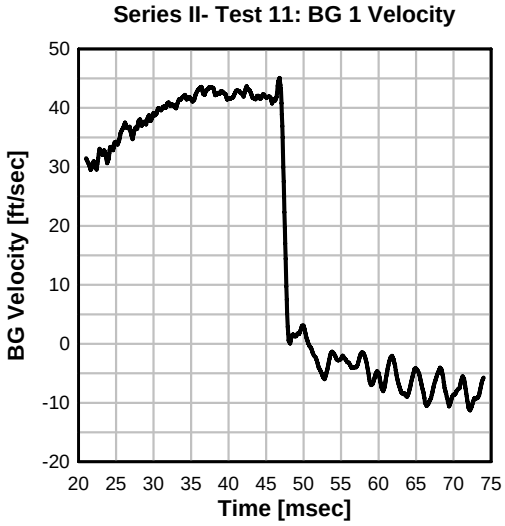
Series II- Test 11: BG 1 Velocity
BG Velocity [ft/sec]
Time [msec]

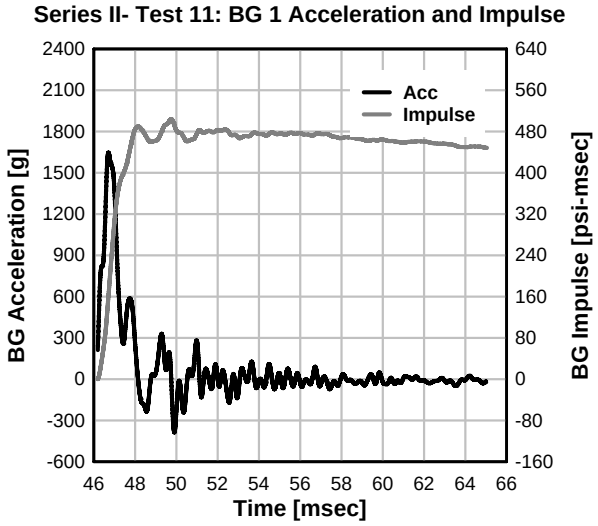
Series II- Test 11: BG 1 Acceleration and Impulse
BG Acceleration [g]
BG Impulse [psi-msec]
Acc
Impulse
Time [msec]

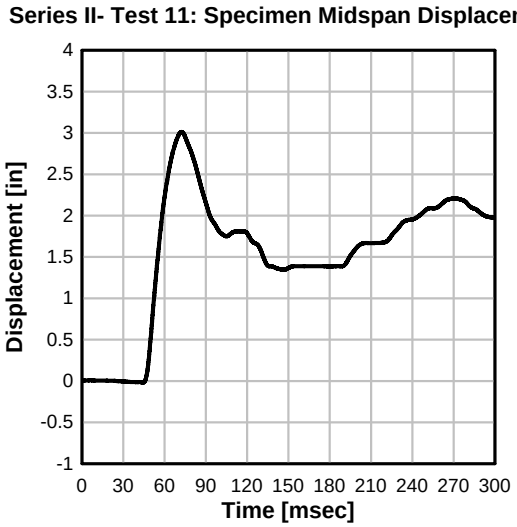
Series II- Test 11: Specimen Midspan Displacement
Displacement [in]
Time [msec]
4
3.5
3
2.5
2
1.5
1
0.5
0
-0.5
-1
0 30 60 90 120 150 180 210 240 270 300

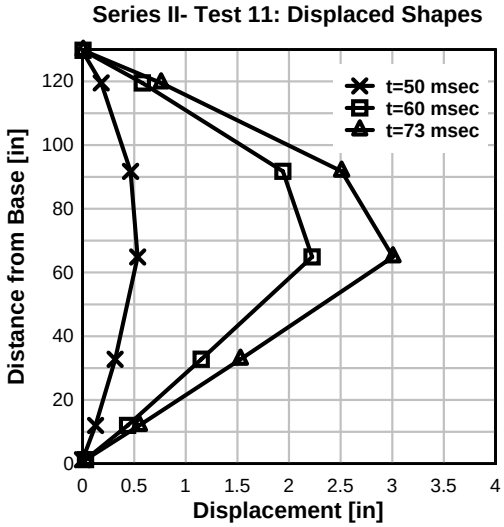
Series II- Test 11: Displaced Shapes
Distance from Base [in]
Displacement [in]
t=50 msec
t=60 msec
t=73 msec
120
100
80
60
40
20
0
0 0.5 1 1.5 2 2.5 3 3.5 4

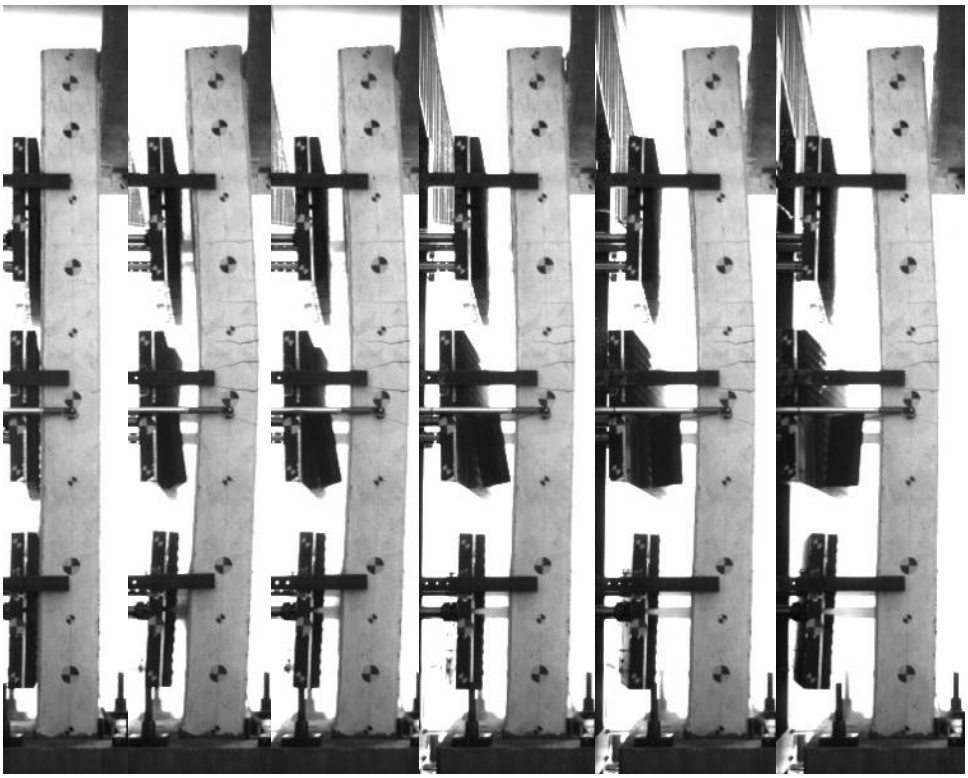

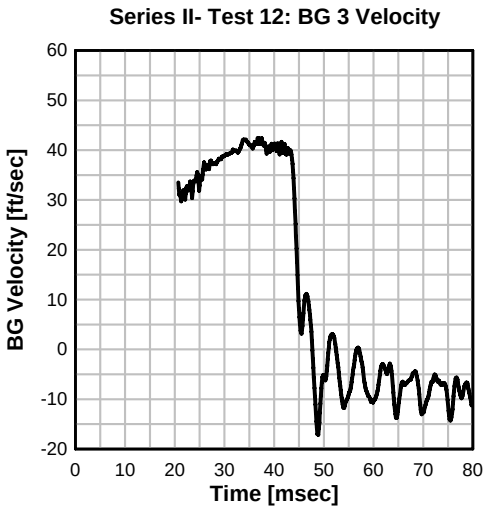
Series II- Test 12: BG 3 Velocity
BG Velocity [ft/sec]
Time [msec]

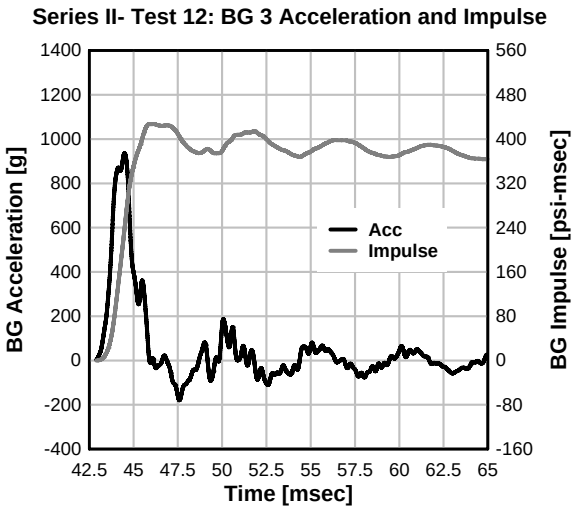
Series II- Test 12: BG 3 Acceleration and Impulse
BG Acceleration [g]
BG Impulse [psi-msec]
Acc
Impulse
Time [msec]

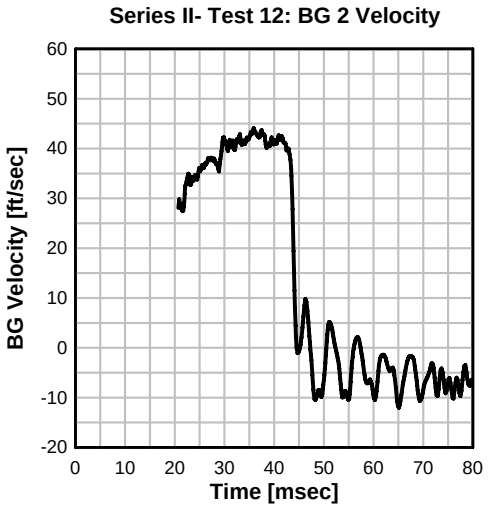
Series II- Test 12: BG 2 Velocity
BG Velocity [ft/sec]
Time [msec]

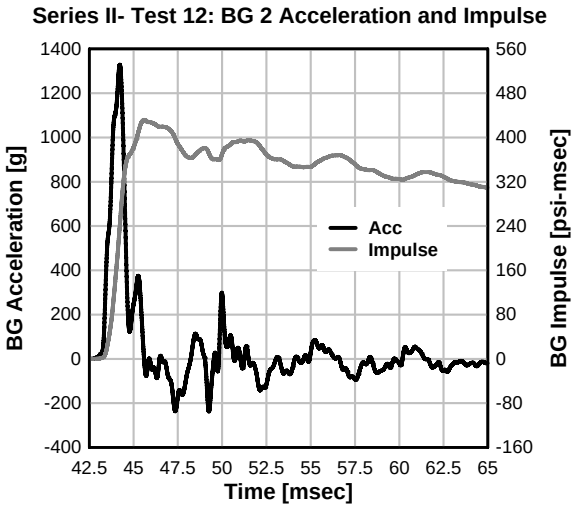
Series II- Test 12: BG 2 Acceleration and Impulse
BG Acceleration [g]
BG Impulse [psi-msec]
Acc
Impulse
Time [msec]

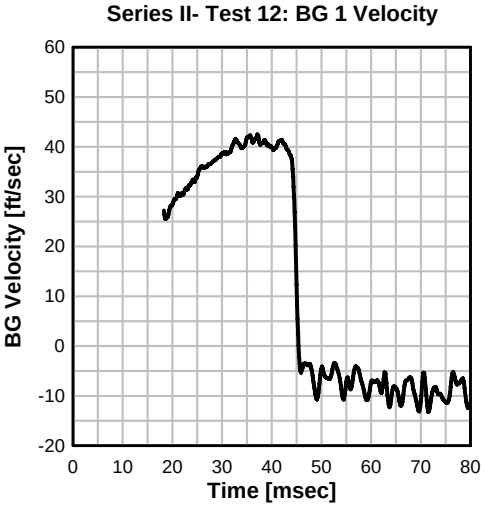
Series II- Test 12: BG 1 Velocity
BG Velocity [ft/sec]
Time [msec]

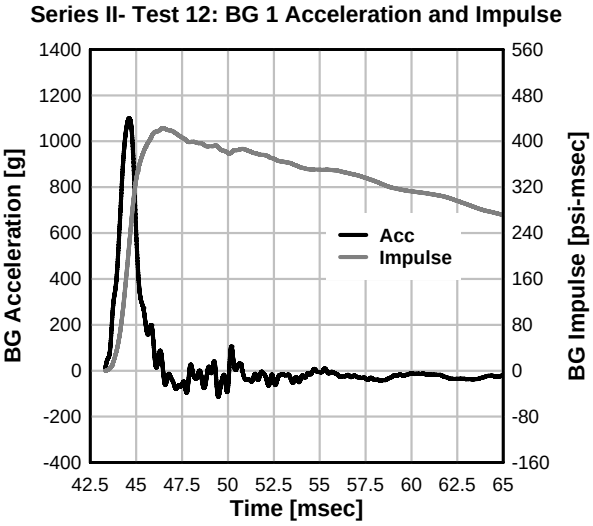
Series II- Test 12: BG 1 Acceleration and Impulse
BG Acceleration [g]
BG Impulse [psi-msec]
Acc
Impulse
Time [msec]

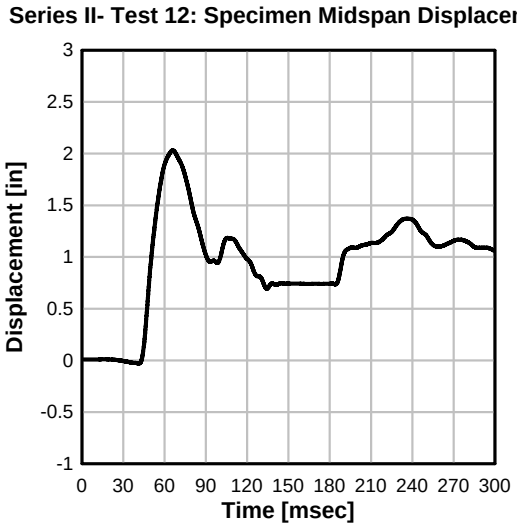
Series II- Test 12: Specimen Midspan Displacement
Displacement [in]
Time [msec]
3
2.5
2
1.5
1
0.5
0
-0.5
-1
0 30 60 90 120 150 180 210 240 270 300

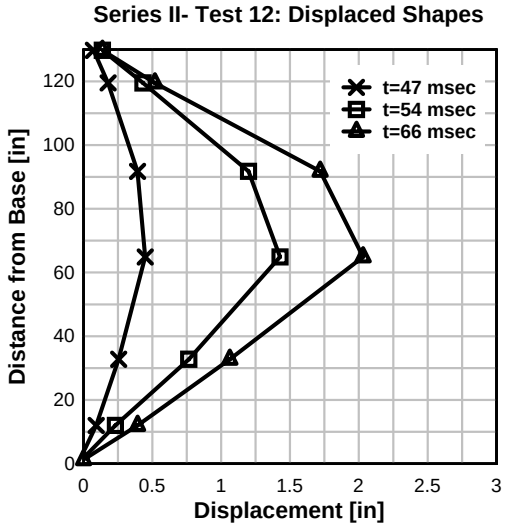
Series II- Test 12: Displaced Shapes
Distance from Base [in]
Displacement [in]
t=47 msec
t=54 msec
t=66 msec
120
100
80
60
40
20
0
0 0.5 1 1.5 2 2.5 3

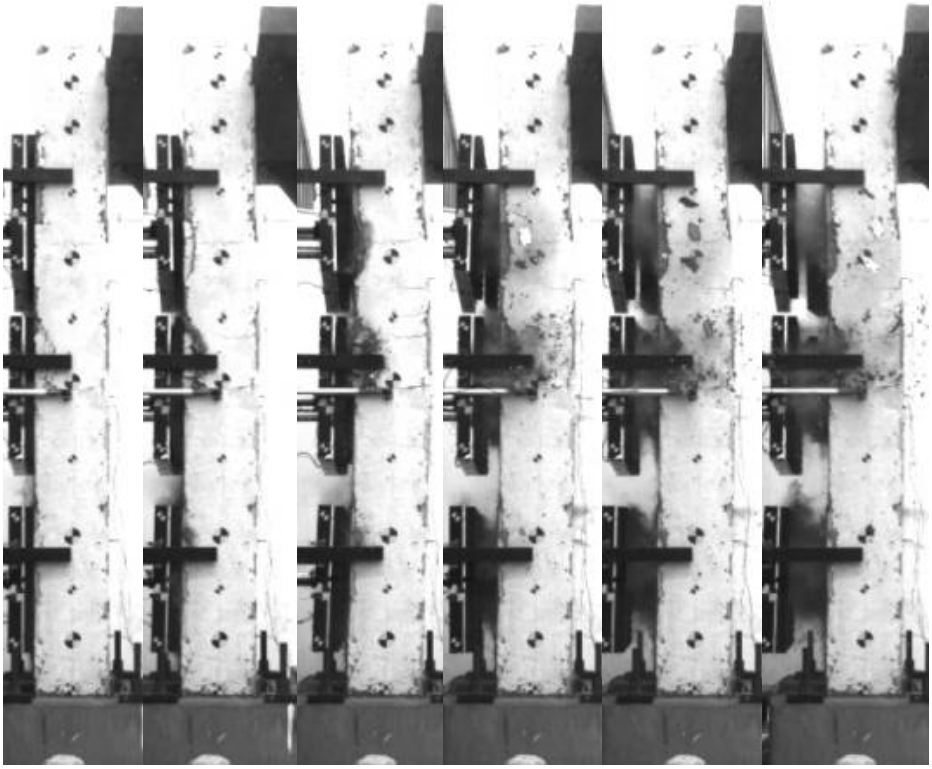

Series I- Test 1: Comparison of Displacement

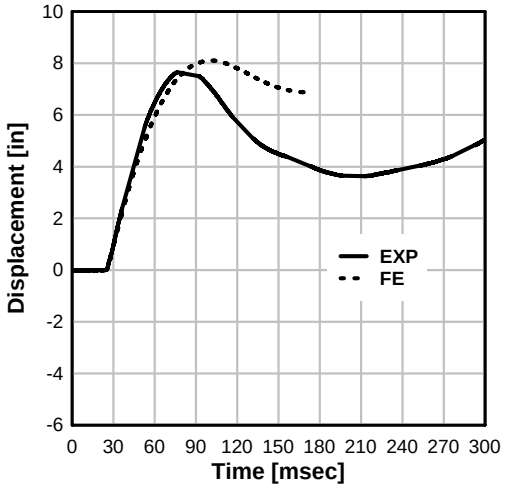

Series I- Test 1: Comparison of Displaced Shapes

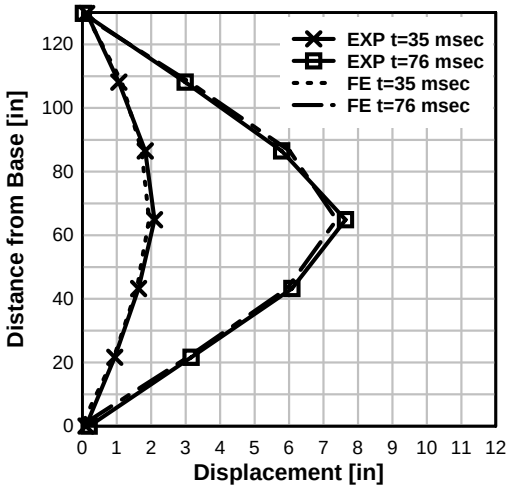

Series I- Test 2: Comparison of Displacement

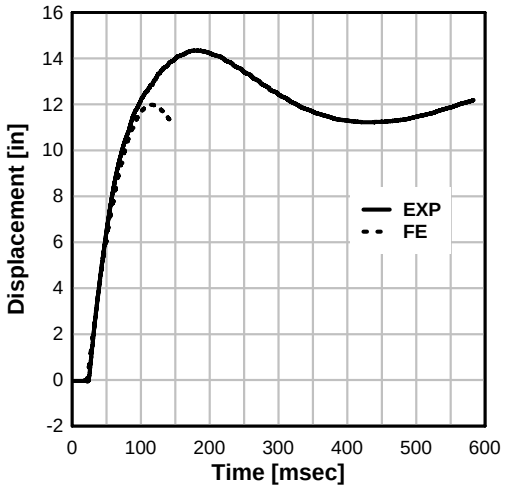

Series I- Test 2: Comparison of Displaced Shapes

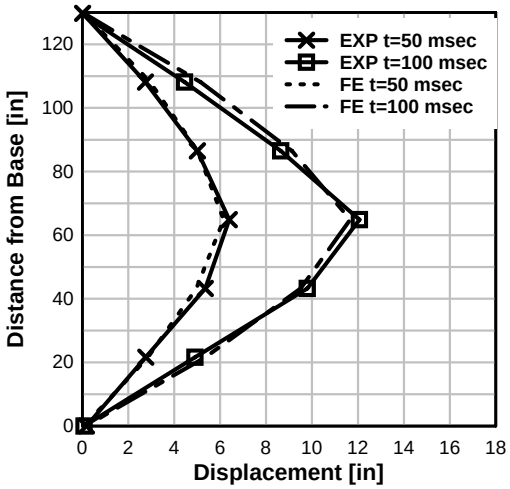

Series I- Test 3: Comparison of Displacement

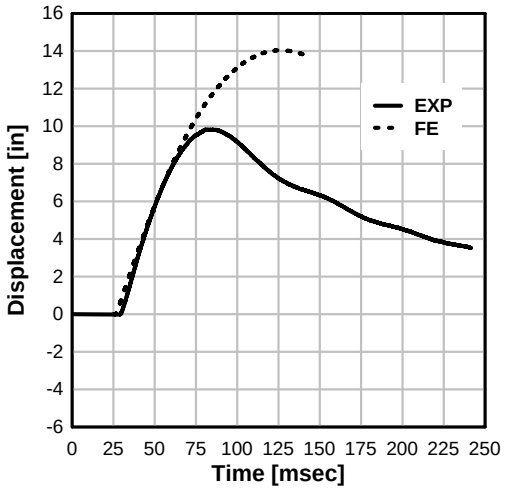

Series I- Test 3: Comparison of Displaced Shapes

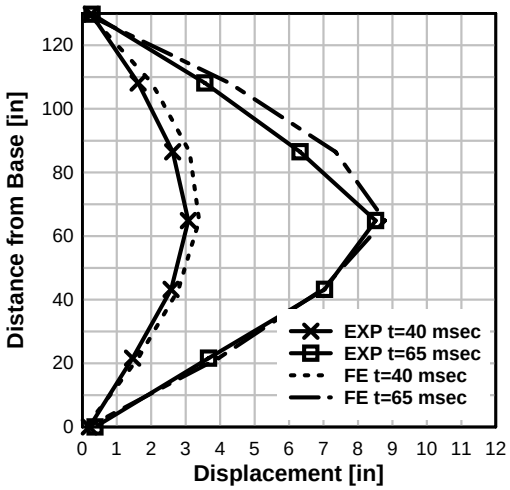

Series I- Test 4: Comparison of Displacement

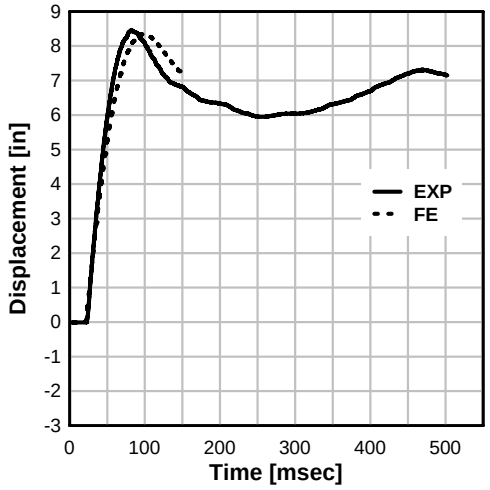

Series I- Test 4: Comparison of Displaced Shapes

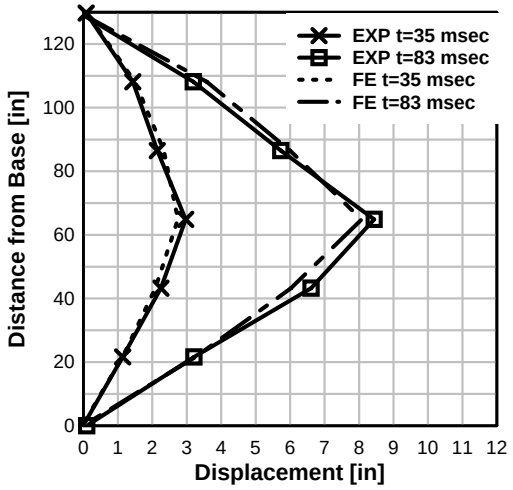

Series I- Test 5: Comparison of Displacement

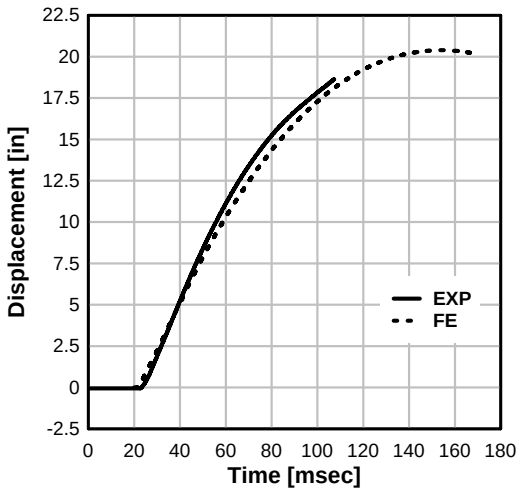

Series I- Test 5: Comparison of Displaced Shapes

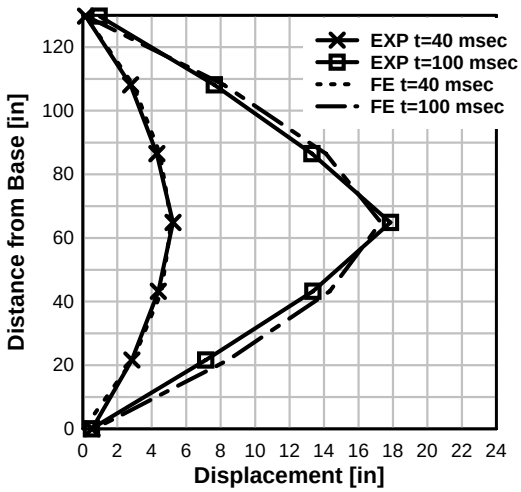

Series I- Test 6: Comparison of Displacement

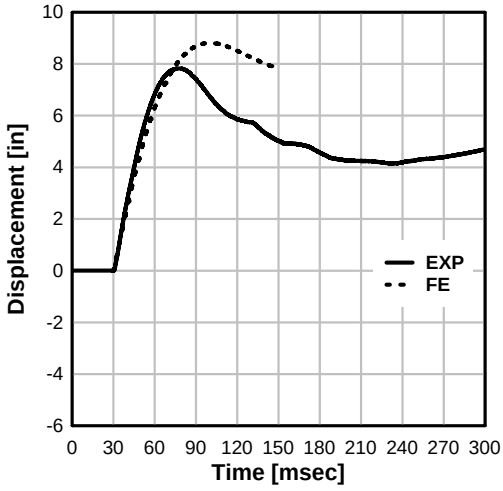

Series I- Test 6: Comparison of Displaced Shapes

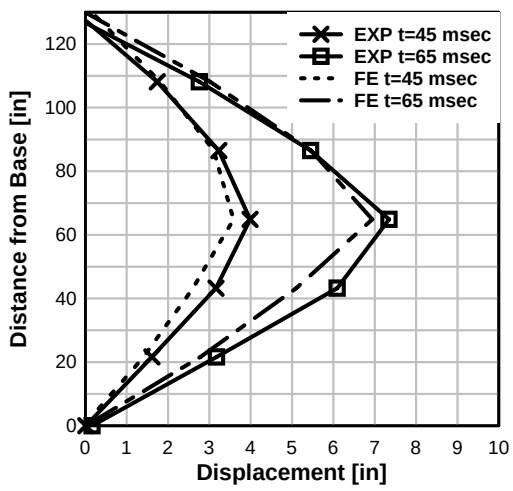

Series I- Test 7: Comparison of Displacement

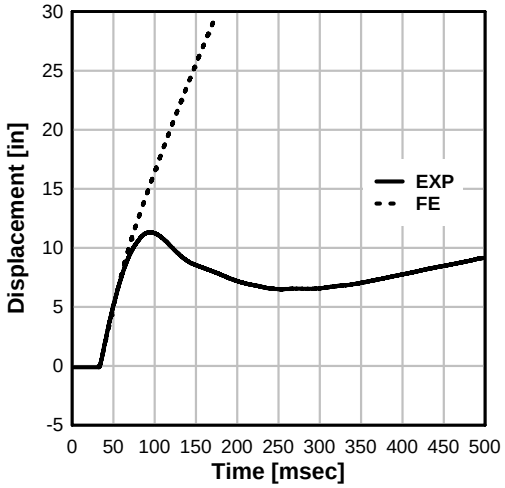

Series I- Test 7: Comparison of Displaced Shapes

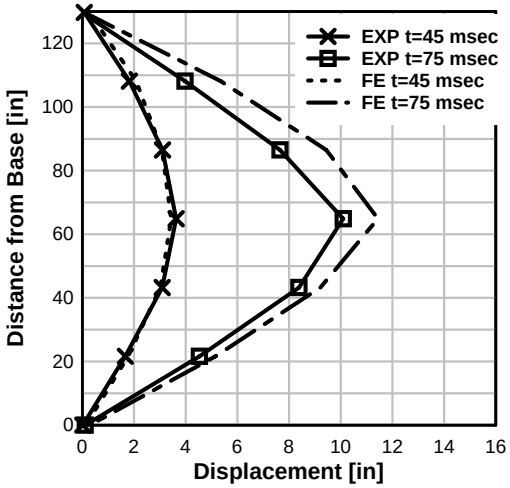

Series I- Test 8: Comparison of Displacement

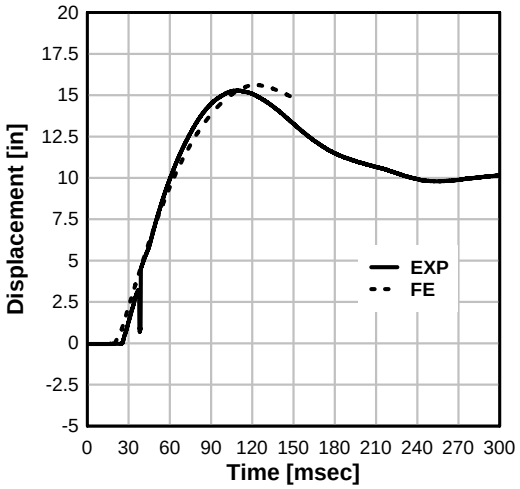

Series I- Test 8: Comparison of Displaced Shapes

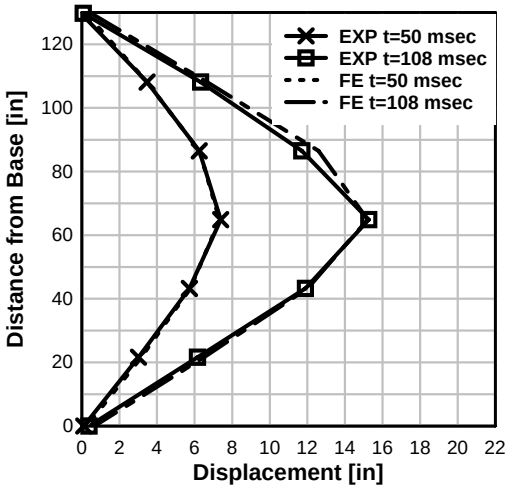

Series I- Test 9: Comparison of Displacement

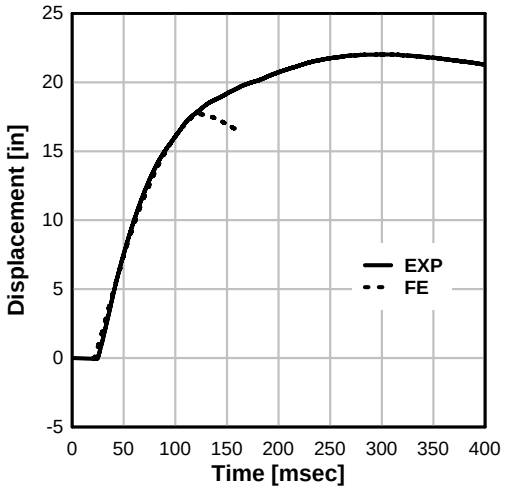

Series I- Test 9: Comparison of Displaced Shapes

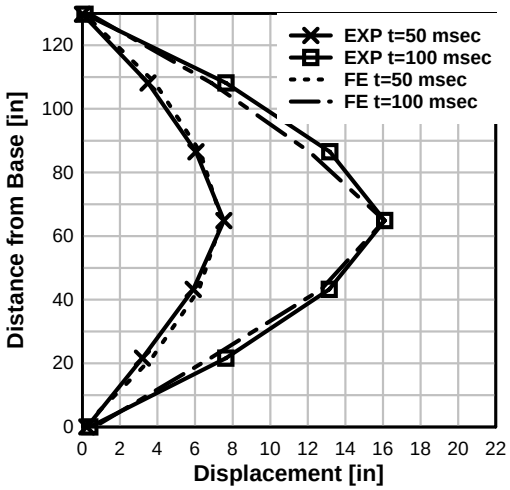

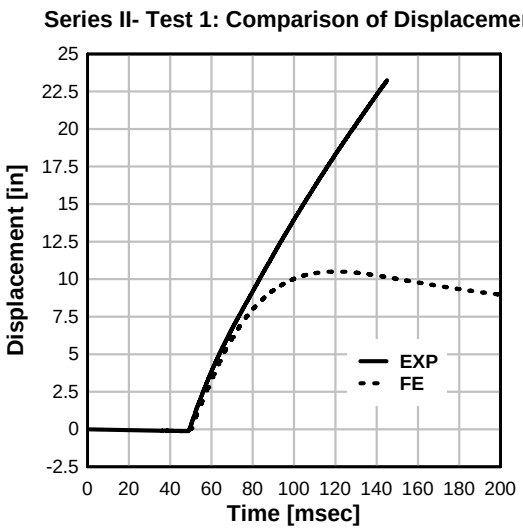
Series II- Test 1: Comparison of Displacement
Displacement [in]
Time [msec]
EXP
FE

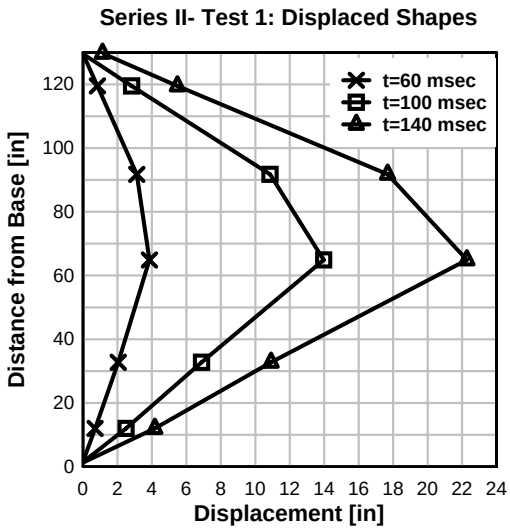
Series II- Test 1: Displaced Shapes
Distance from Base [in]
Displacement [in]
t=60 msec
t=100 msec
t=140 msec

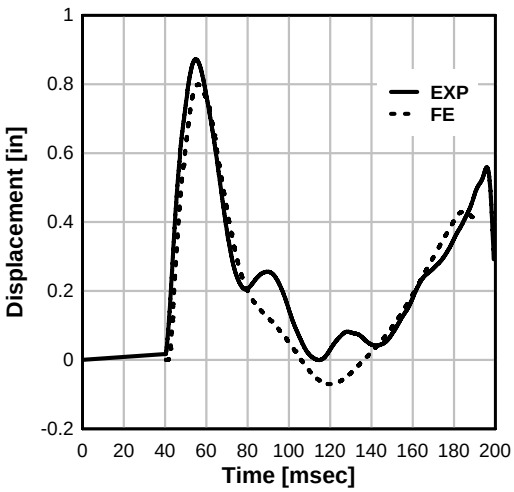
Series II- Test 3A: Comparison of Displacement
Displacement [in]
Time [msec]
EXP
FE

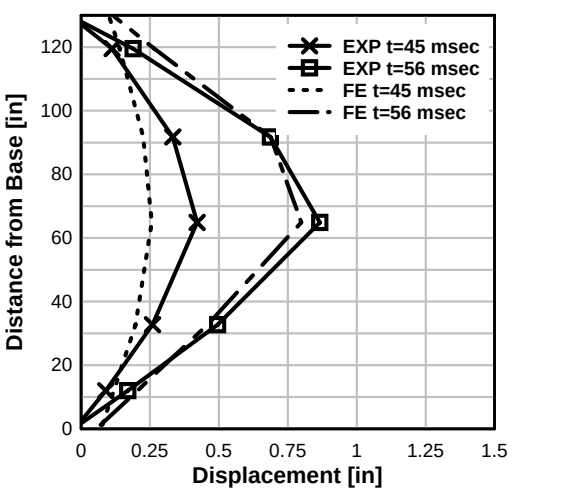
Series II- Test 3A: Comparison of Displaced Shapes
Distance from Base [in]
Displacement [in]
EXP t=45 msec
EXP t=56 msec
FE t=45 msec
FE t=56 msec

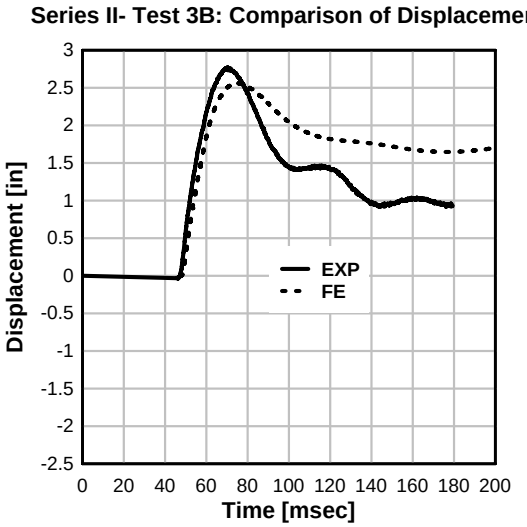
Series II- Test 3B: Comparison of Displacement
Displacement [in]
Time [msec]
EXP
FE

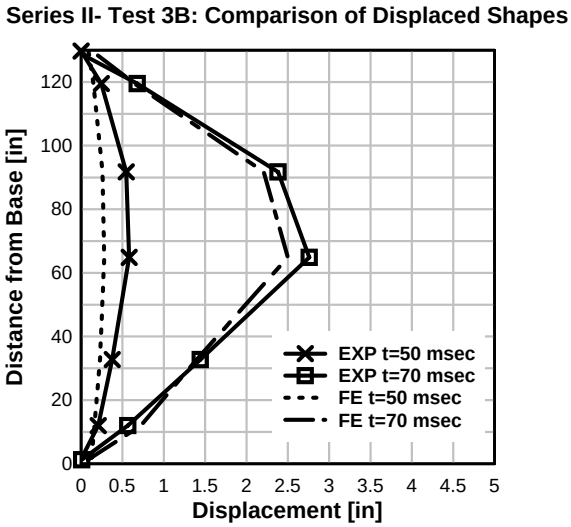
Series II- Test 3B: Comparison of Displaced Shapes
Distance from Base [in]
Displacement [in]
EXP t=50 msec
EXP t=70 msec
FE t=50 msec
FE t=70 msec

Series II- Test 4A: Comparison of Displacement

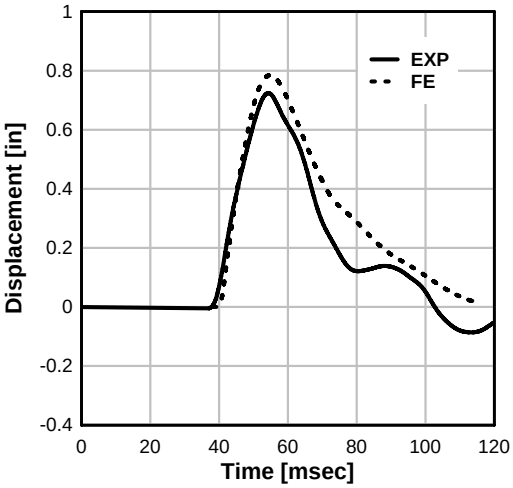

Series II- Test 4A: Comparison of Displaced Shapes

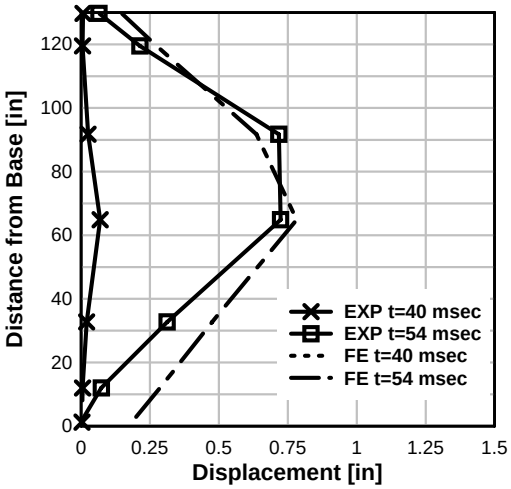

Series II- Test 4B: Comparison of Displacement

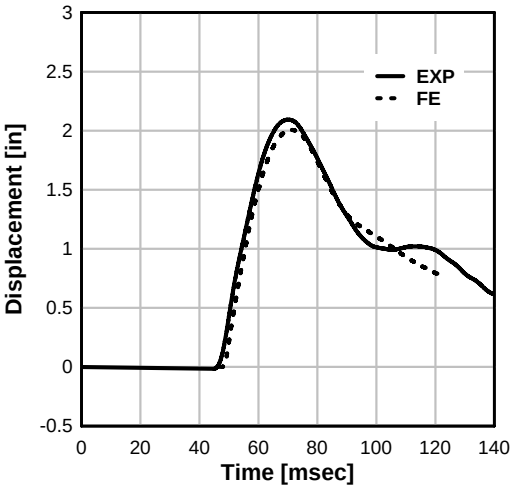

Series II- Test 4B: Comparison of Displaced Shapes

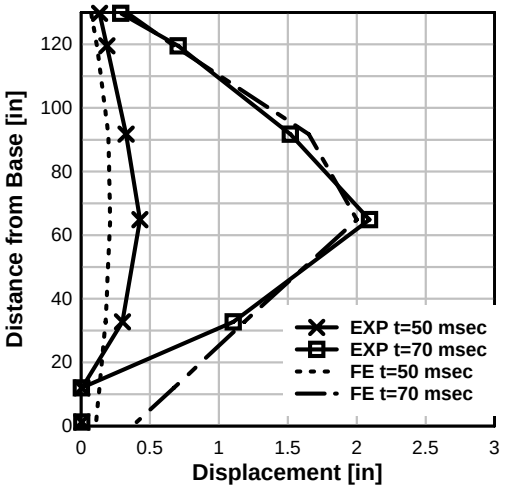

Series II- Test 5A: Comparison of Displacement

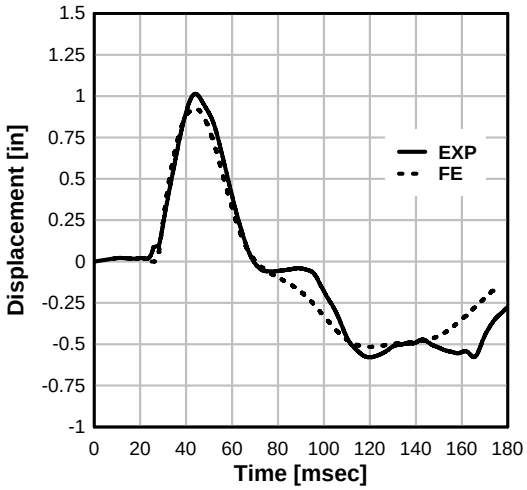

Series II- Test 5A: Comparison of Displaced Shapes

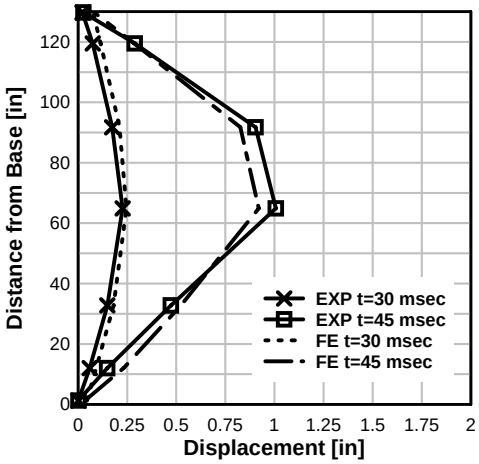

Series II- Test 5B: Comparison of Displacement

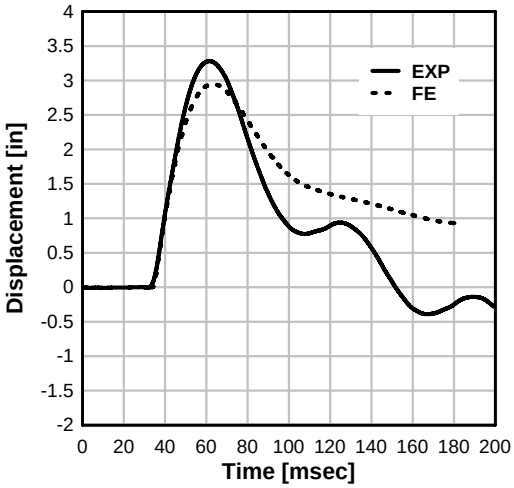

Series II- Test 5B: Comparison of Displaced Shapes

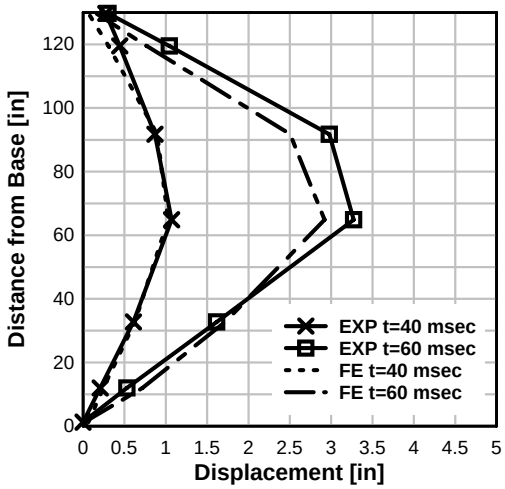

Series II- Test 6A: Comparison of Displacement

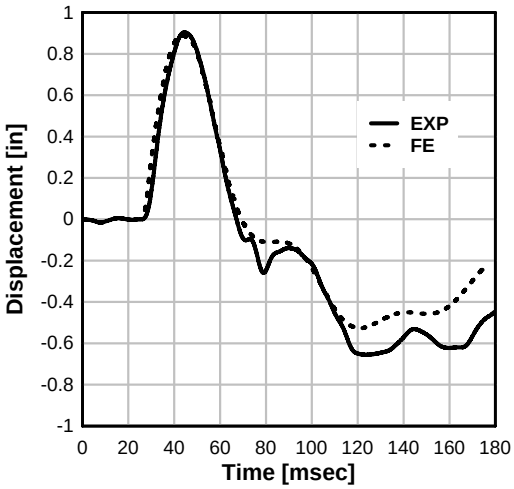

Series II- Test 6A: Comparison of Displaced Shapes

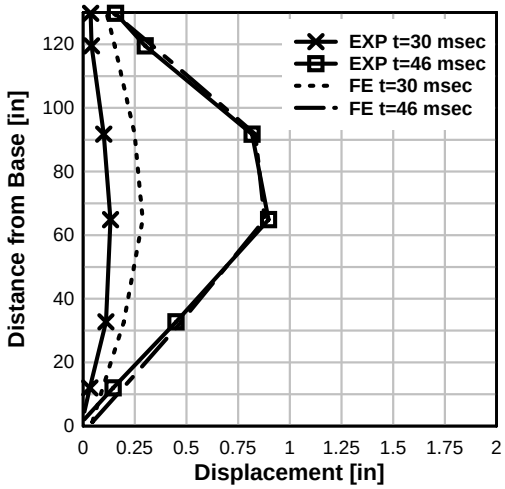

Series II- Test 6B: Comparison of Displacement

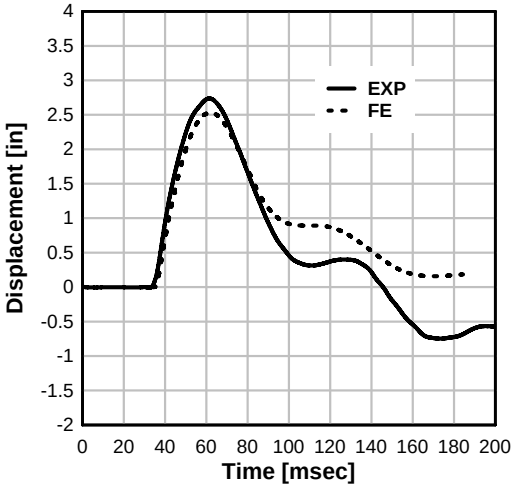

Series II- Test 6B: Comparison of Displaced Shapes

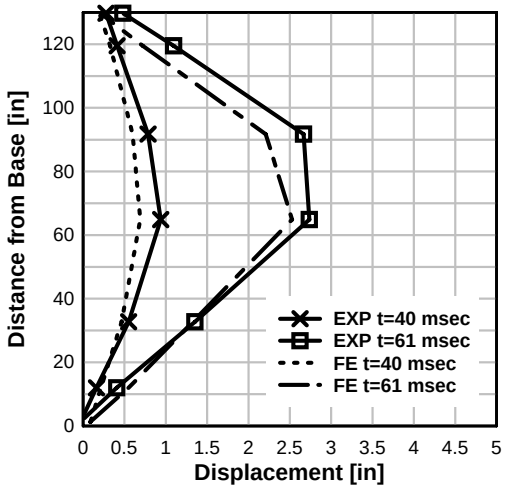

Series II- Test 7: Comparison of Displacement

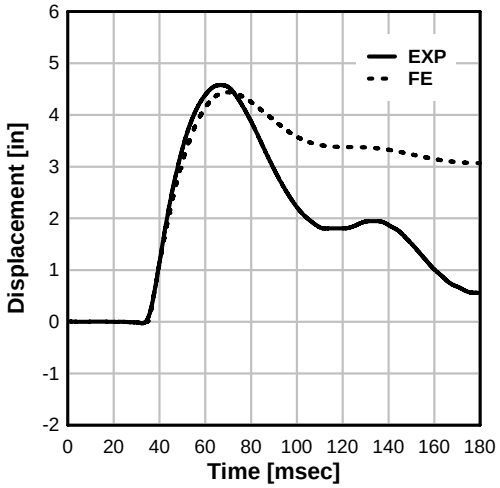

Series II- Test 7: Comparison of Displaced Shapes

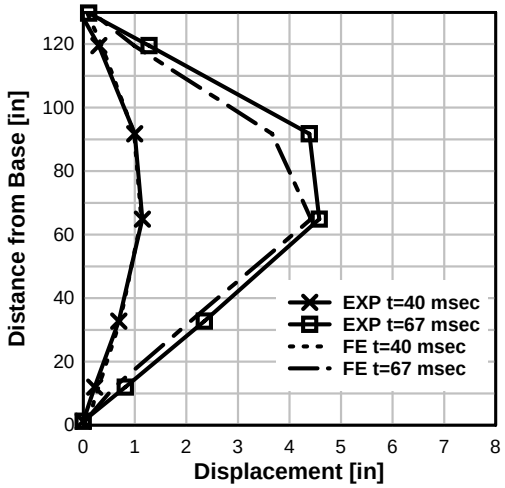

Series II- Test 8: Comparison of Displacement

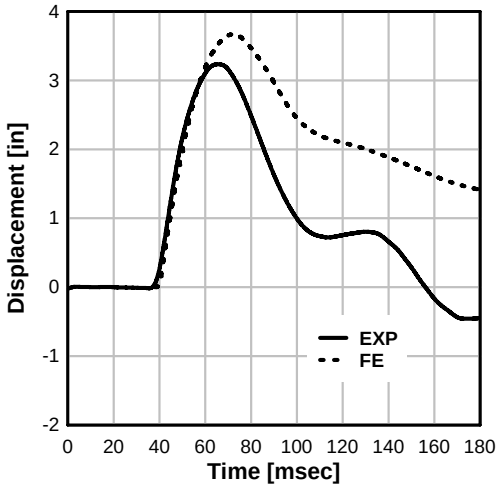

Series II- Test 8: Comparison of Displaced Shapes

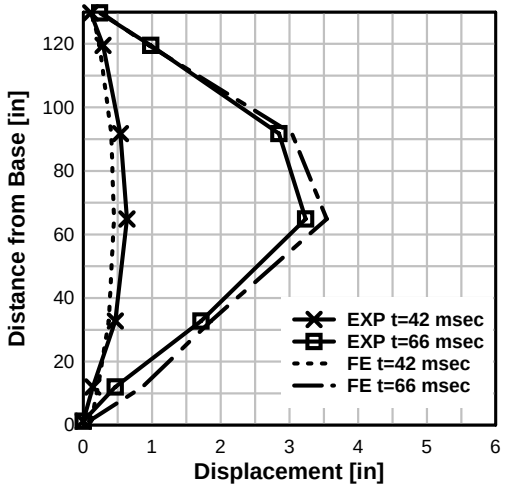

Series II- Test 9: Comparison of Displacement

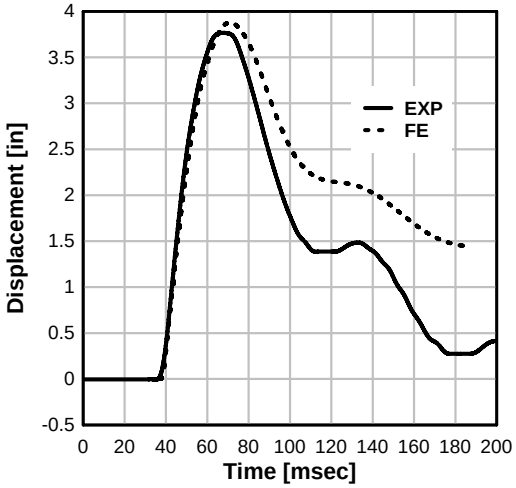

Series II- Test 9: Comparison of Displaced Shapes

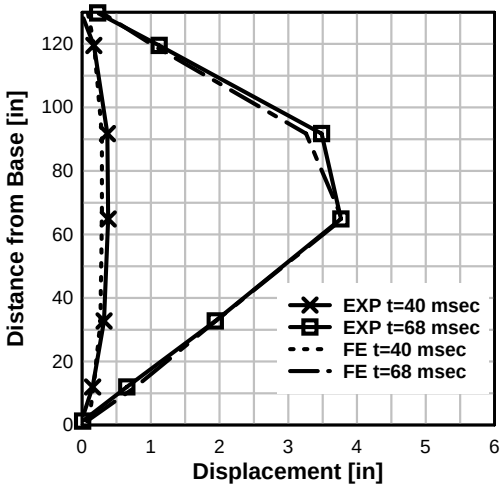

Series II- Test 10: Comparison of Displacement

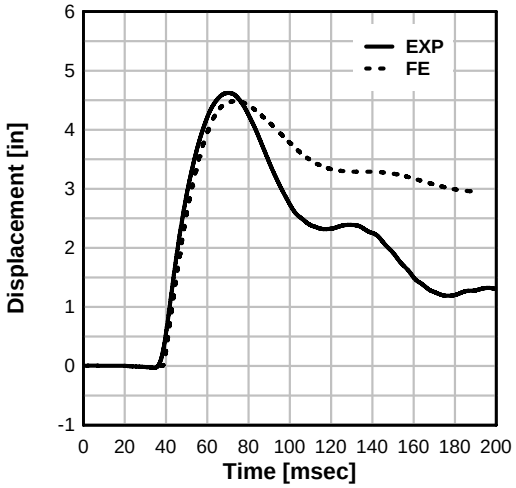

Series II- Test 10: Comparison of Displaced Shapes

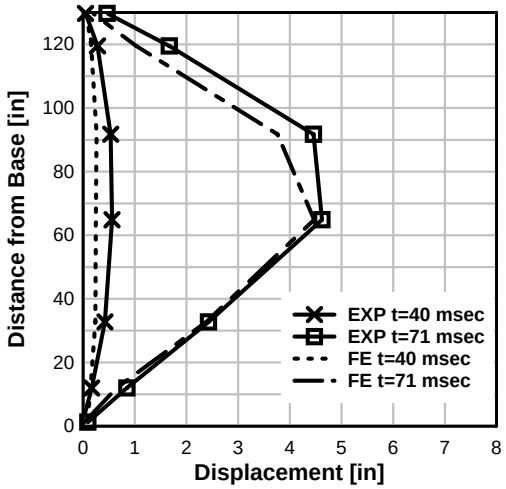

Series II- Test 11: Comparison of Displacement

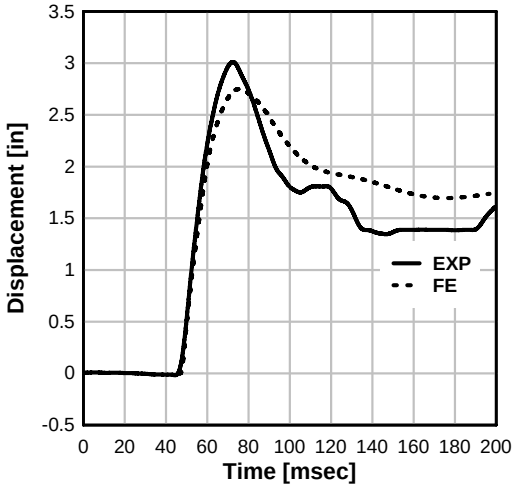

Series II- Test 11: Comparison of Displaced Shapes

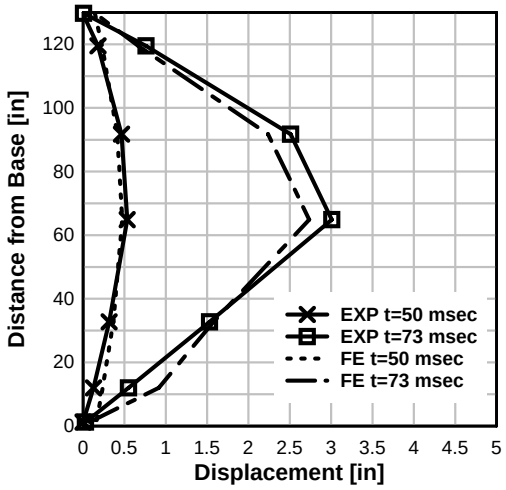

Series II- Test 12: Comparison of Displacement

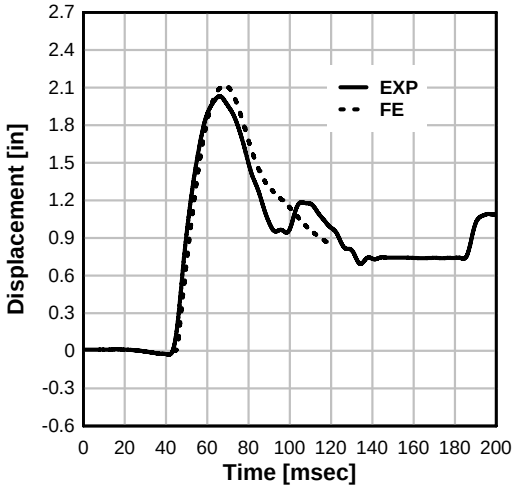

Series II- Test 12: Comparison of Displaced Shapes

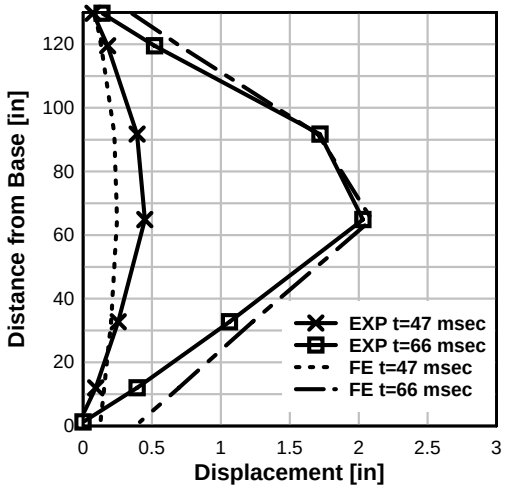

APPENDIX C

This appendix contains test data from the blast simulator test series on URM walls with polyurea catcher systems that is described in Chapter 6. The plots included for each test are velocity time histories for BGs 1-4, acceleration/impulse time histories for BGs 1-4, and displacement/velocity time history at the specimen midspan. Also included for each test is a sequence of photos captured by the high speed camera video.

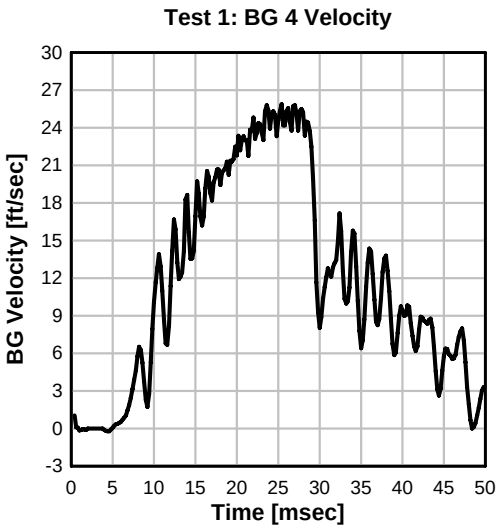
Test 1: BG 4 Velocity
BG Velocity [ft/sec]
Time [msec]

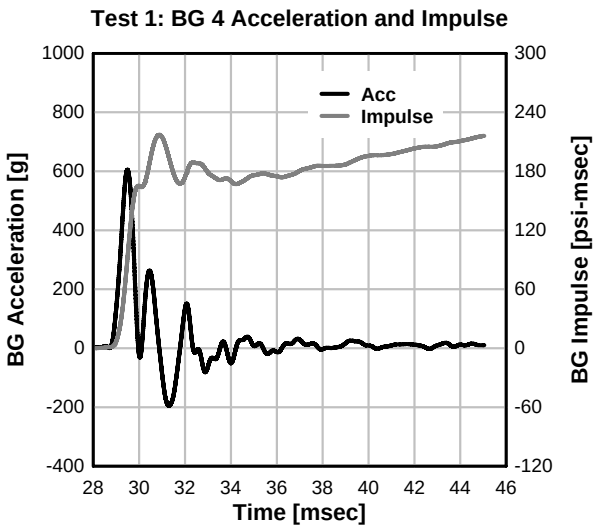
Test 1: BG 4 Acceleration and Impulse
Acc
Impulse
BG Acceleration [g]
BG Impulse [psi-msec]
Time [msec]

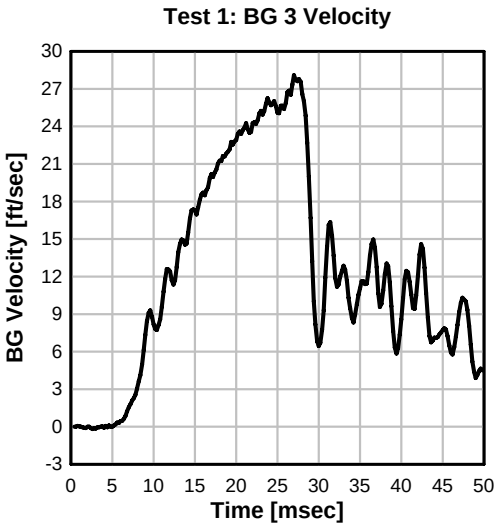
Test 1: BG 3 Velocity
BG Velocity [ft/sec]
Time [msec]

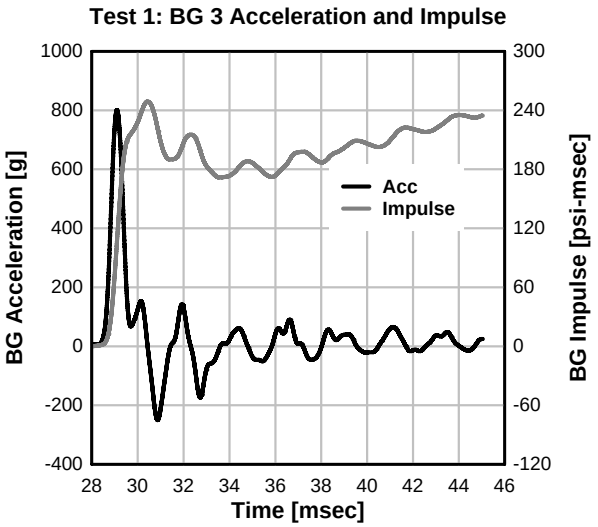
Test 1: BG 3 Acceleration and Impulse
Acc
Impulse
BG Acceleration [g]
BG Impulse [psi-msec]
Time [msec]

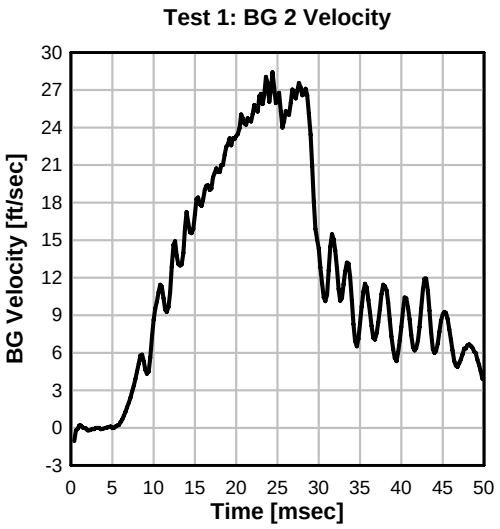
Test 1: BG 2 Velocity
BG Velocity [ft/sec]
Time [msec]

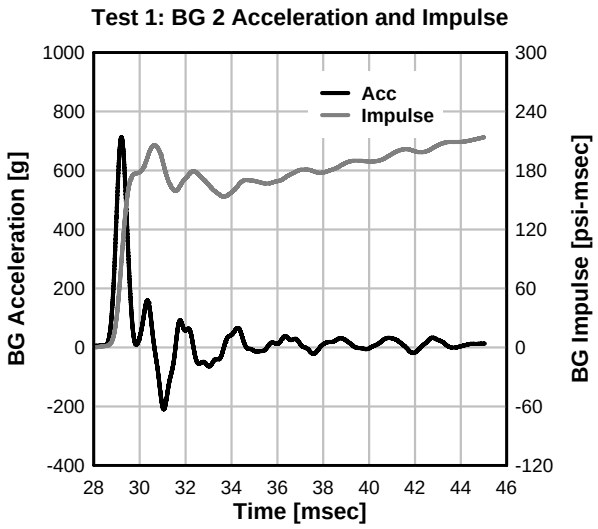
Test 1: BG 2 Acceleration and Impulse
Acc
Impulse
BG Acceleration [g]
BG Impulse [psi-msec]
Time [msec]

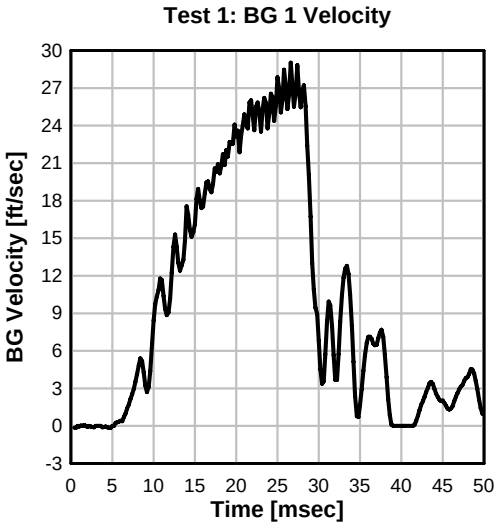
Test 1: BG 1 Velocity
BG Velocity [ft/sec]
Time [msec]

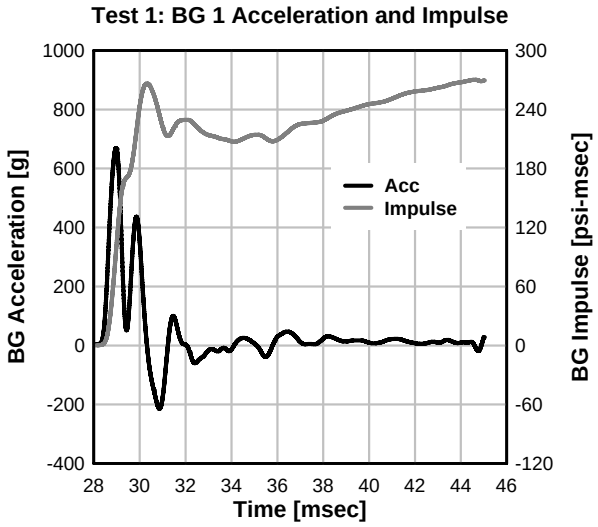
Test 1: BG 1 Acceleration and Impulse
Acc
Impulse
BG Acceleration [g]
BG Impulse [psi-msec]
Time [msec]

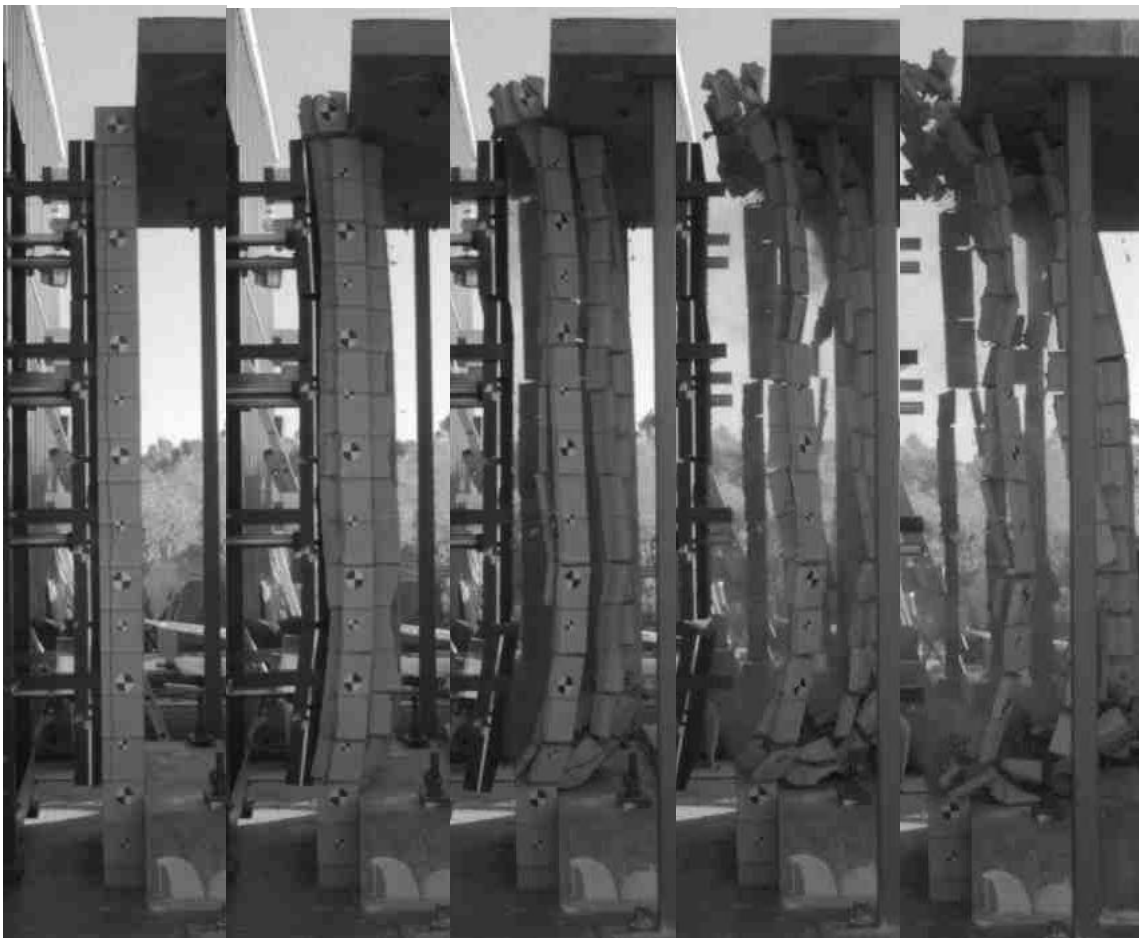

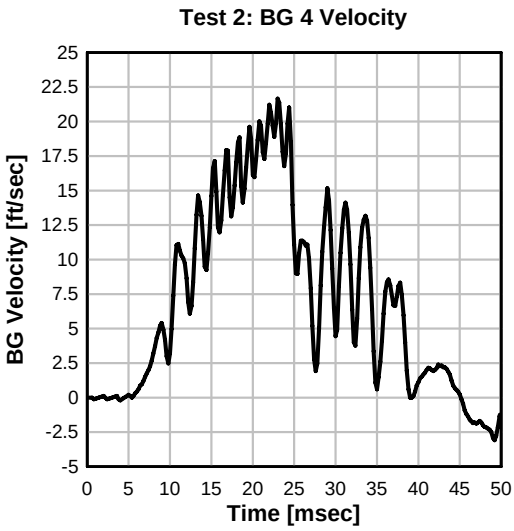
Test 2: BG 4 Velocity
BG Velocity [ft/sec]
Time [msec]

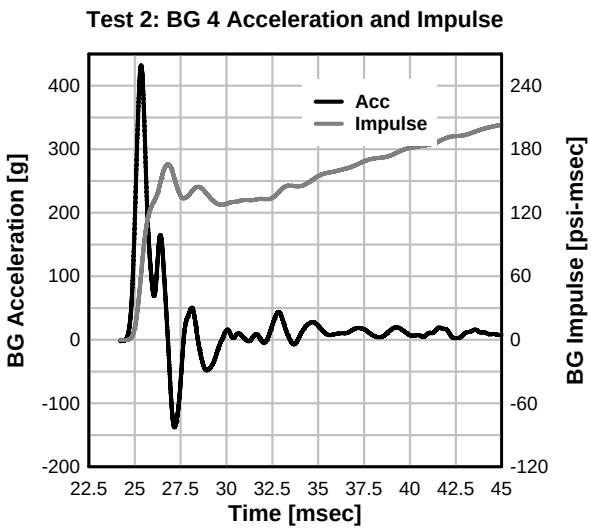
Test 2: BG 4 Acceleration and Impulse
Acc
Impulse
BG Acceleration [g]
BG Impulse [psi-msec]
Time [msec]

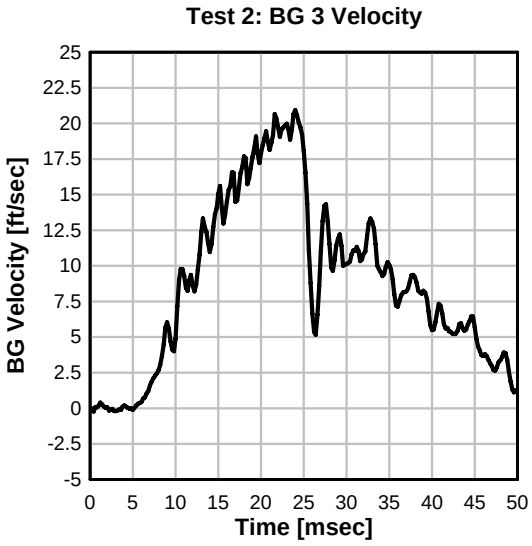
Test 2: BG 3 Velocity
BG Velocity [ft/sec]
Time [msec]

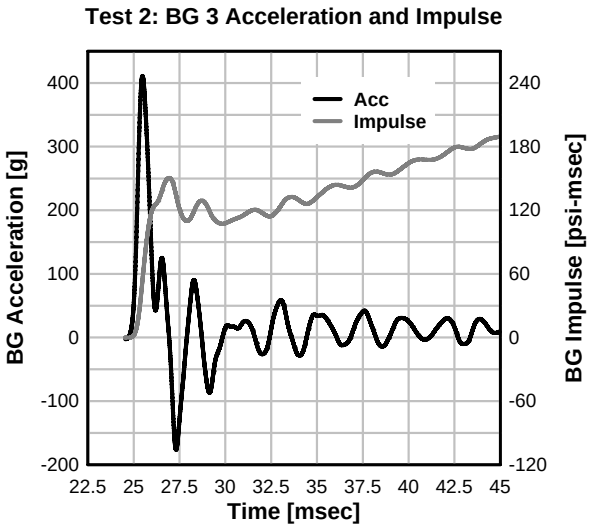
Test 2: BG 3 Acceleration and Impulse
Acc
Impulse
BG Acceleration [g]
BG Impulse [psi-msec]
Time [msec]

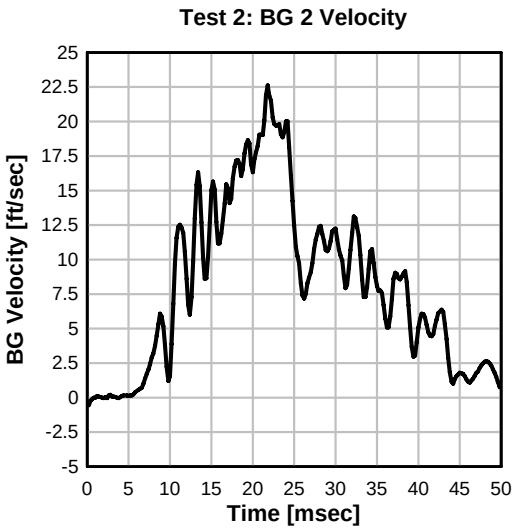
Test 2: BG 2 Velocity
BG Velocity [ft/sec]
Time [msec]

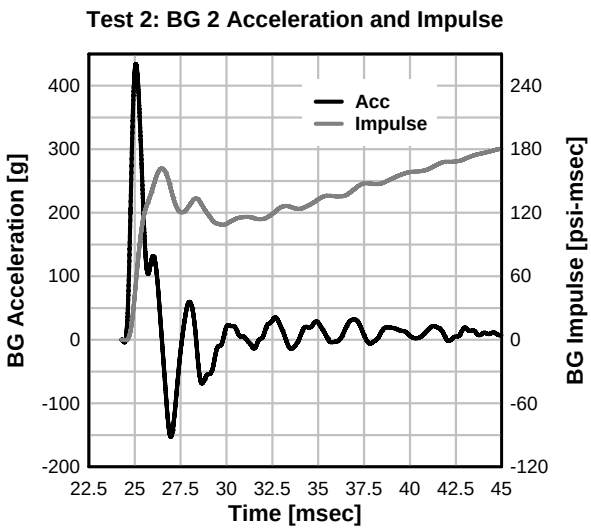
Test 2: BG 2 Acceleration and Impulse
Acc
Impulse
BG Acceleration [g]
BG Impulse [psi-msec]
Time [msec]

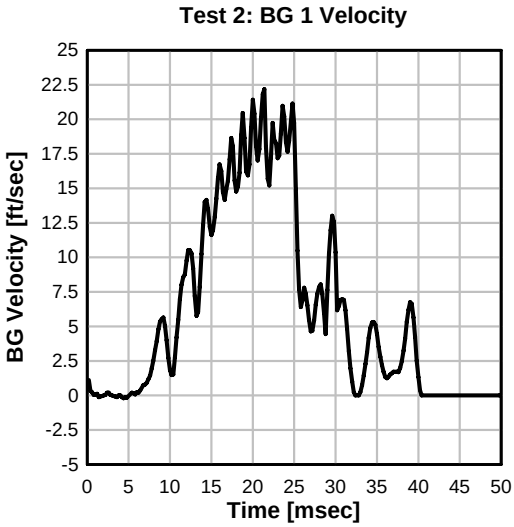
Test 2: BG 1 Velocity
BG Velocity [ft/sec]
Time [msec]

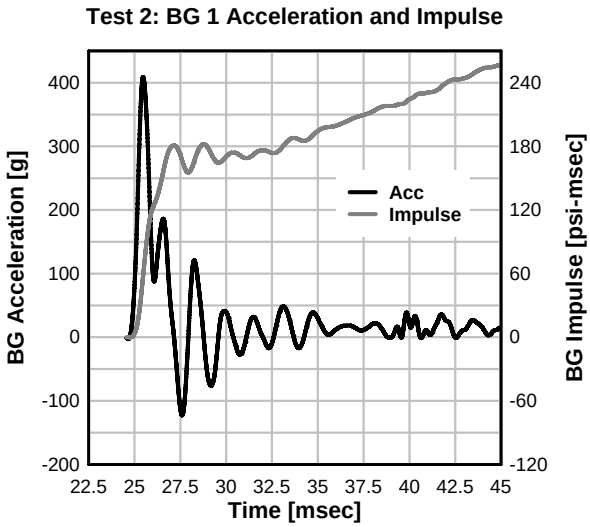
Test 2: BG 1 Acceleration and Impulse
Acc
Impulse
BG Acceleration [g]
BG Impulse [psi-msec]
Time [msec]

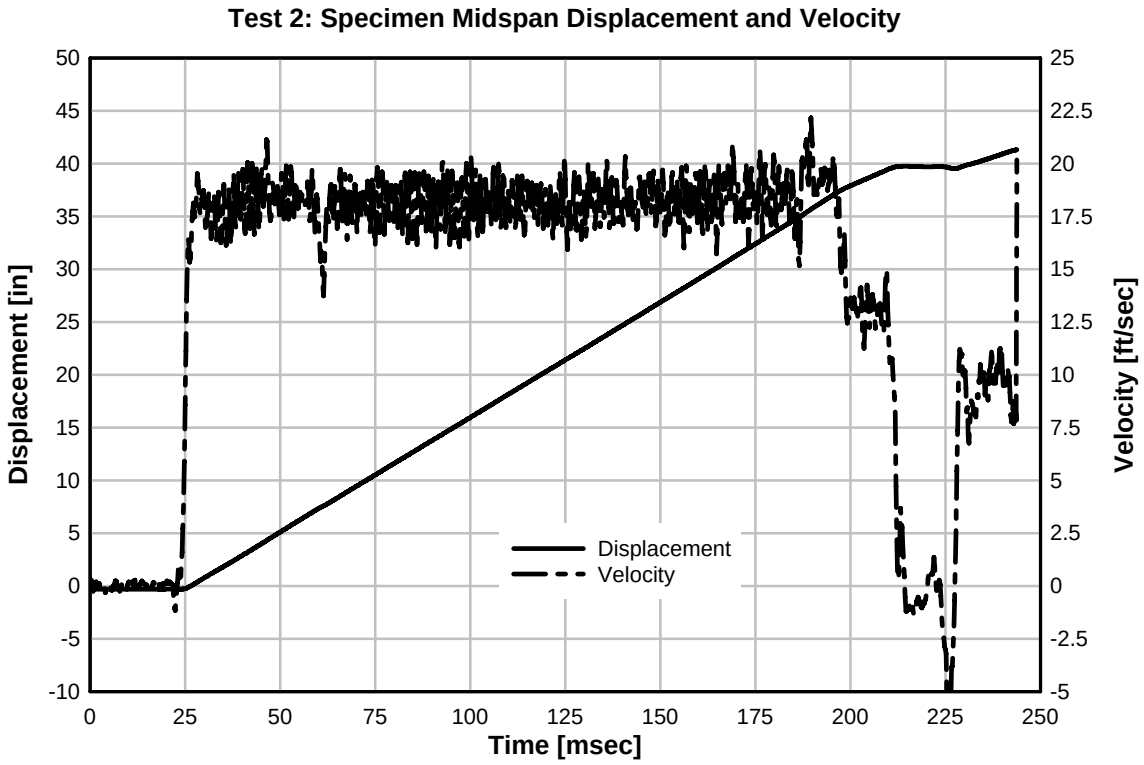
Test 2: Specimen Midspan Displacement and Velocity
Displacement [in]
Velocity [ft/sec]
Time [msec]
Displacement
Velocity
50
45
40
35
30
25
20
15
10
5
0
-5
-10
25
22.5
20
17.5
15
12.5
10
7.5
5
2.5
0
-2.5
-5
0
25
50
75
100
125
150
175
200
225
250

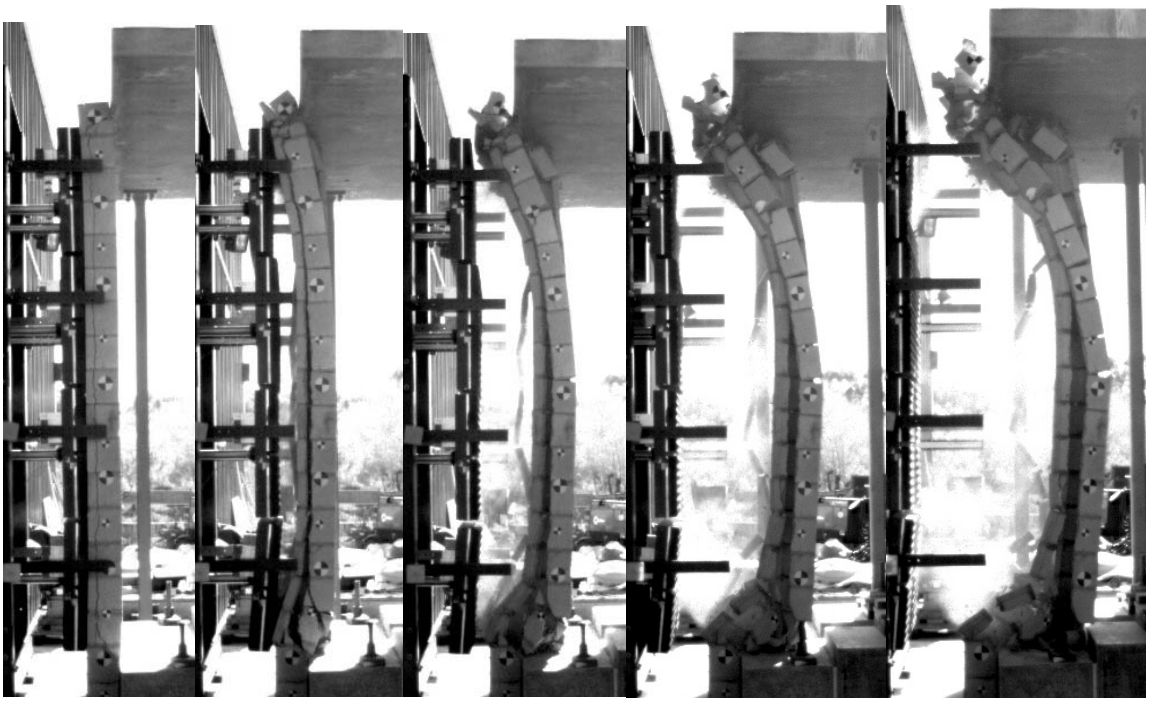

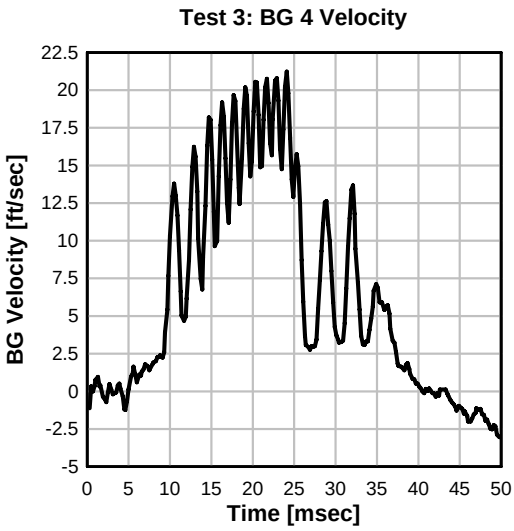
Test 3: BG 4 Velocity
BG Velocity [ft/sec]
Time [msec]

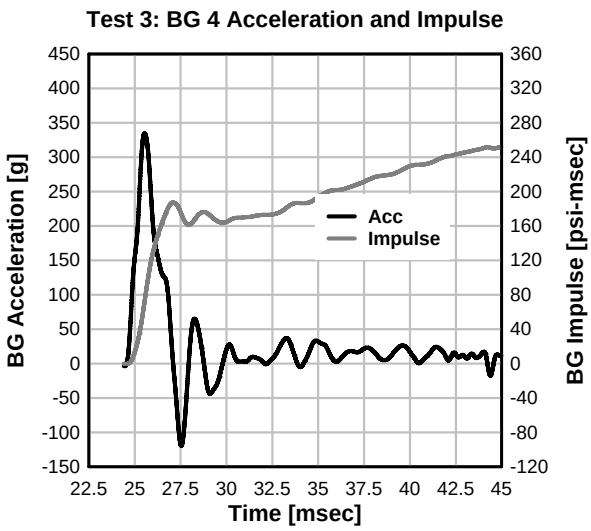
Test 3: BG 4 Acceleration and Impulse
BG Acceleration [g]
BG Impulse [psi-msec]
Acc
Impulse
Time [msec]

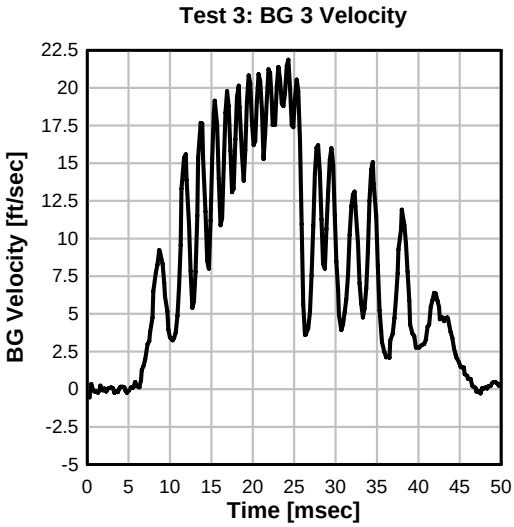
Test 3: BG 3 Velocity
BG Velocity [ft/sec]
Time [msec]

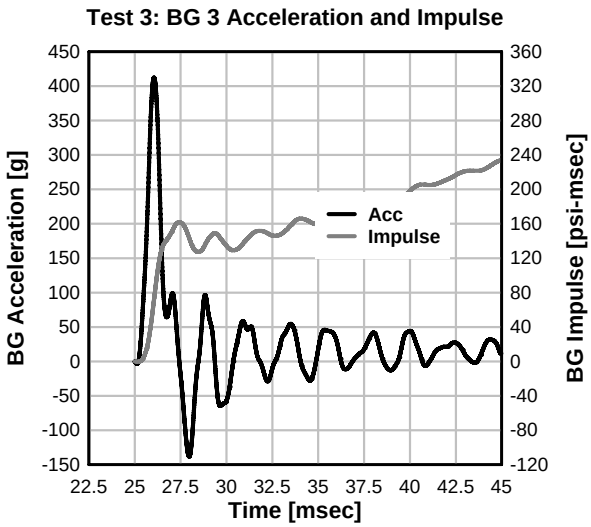
Test 3: BG 3 Acceleration and Impulse
BG Acceleration [g]
BG Impulse [psi-msec]
Acc
Impulse
Time [msec]

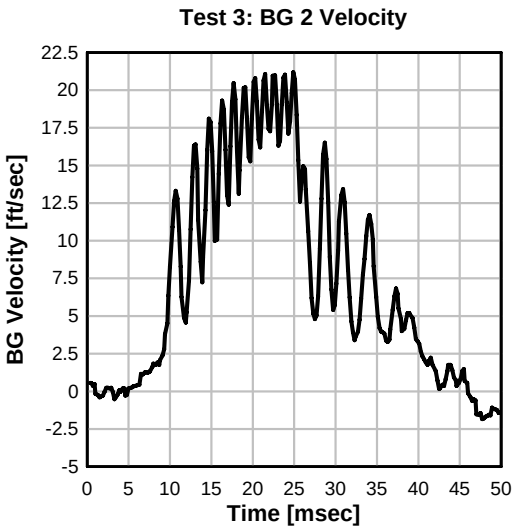
Test 3: BG 2 Velocity
BG Velocity [ft/sec]
Time [msec]

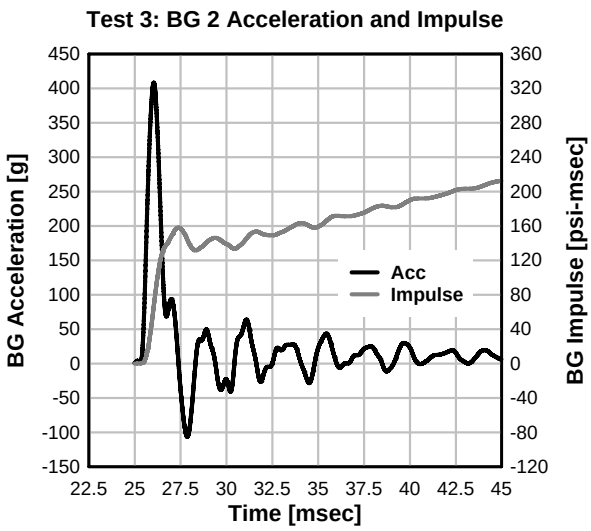
Test 3: BG 2 Acceleration and Impulse
BG Acceleration [g]
BG Impulse [psi-msec]
Acc
Impulse
Time [msec]

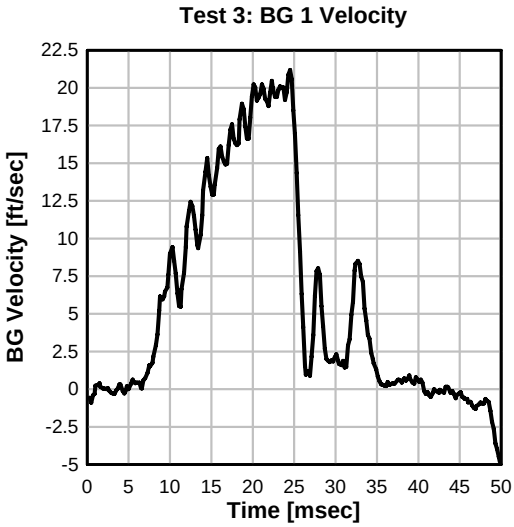
Test 3: BG 1 Velocity
BG Velocity [ft/sec]
Time [msec]

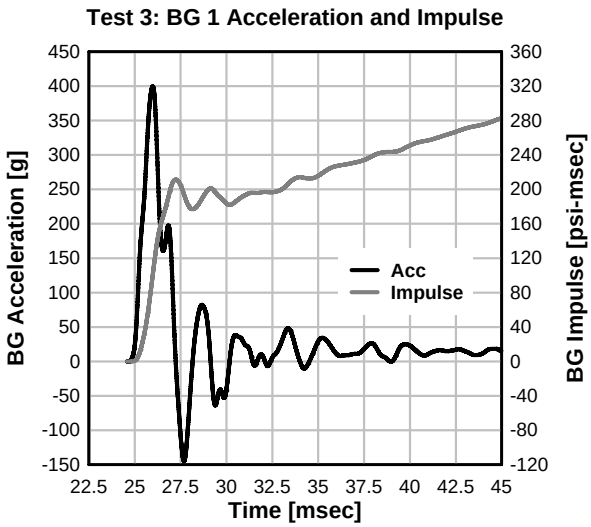
Test 3: BG 1 Acceleration and Impulse
BG Acceleration [g]
BG Impulse [psi-msec]
Acc
Impulse
Time [msec]

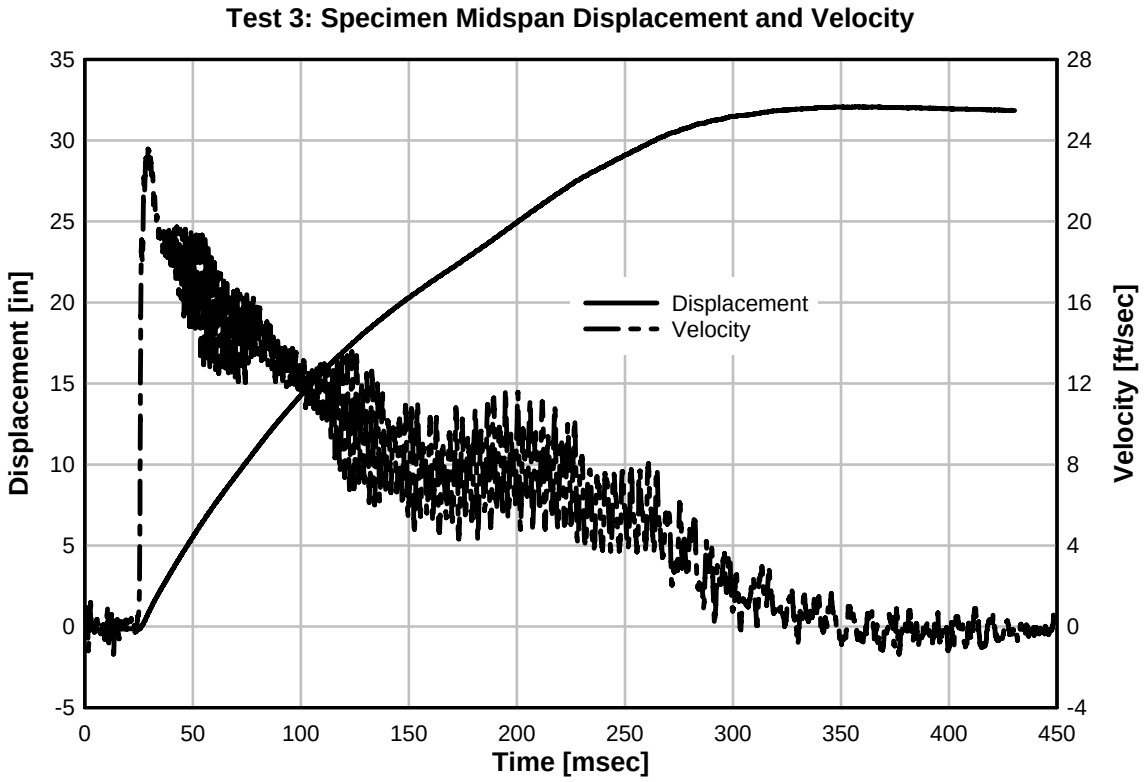
Test 3: Specimen Midspan Displacement and Velocity
Displacement [in]
Velocity [ft/sec]
Time [msec]
Displacement
Velocity
35
30
25
20
15
10
5
0
-5
28
24
20
16
12
8
4
0
-4
0
50
100
150
200
250
300
350
400
450

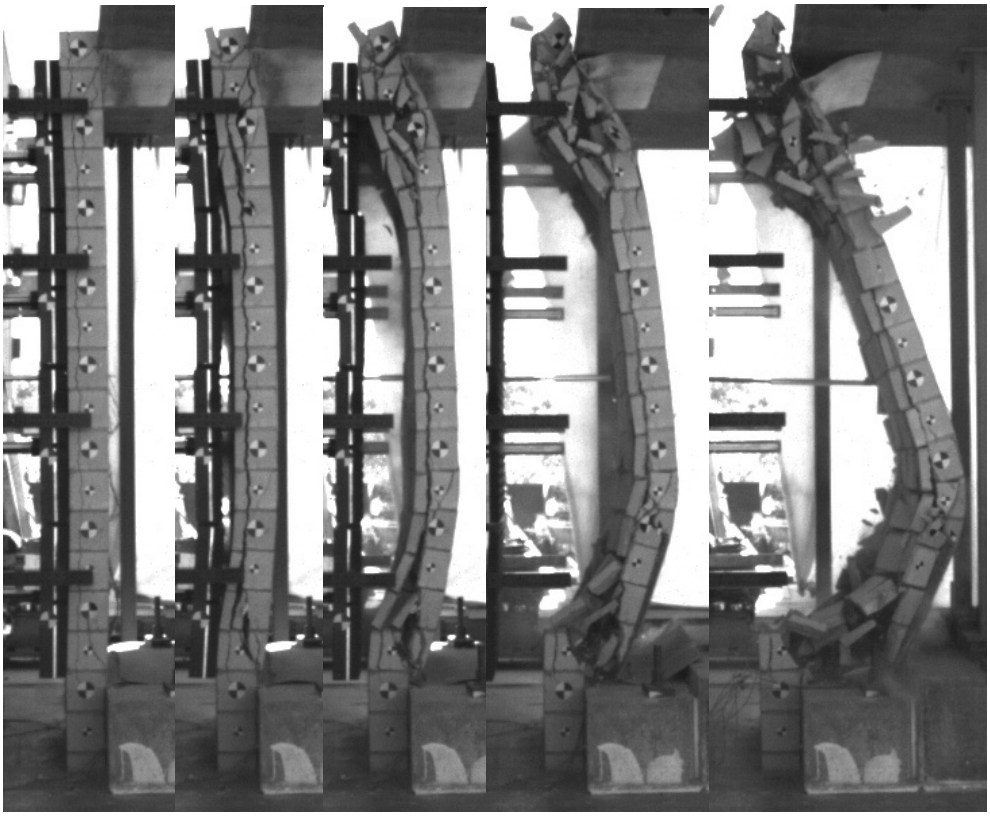

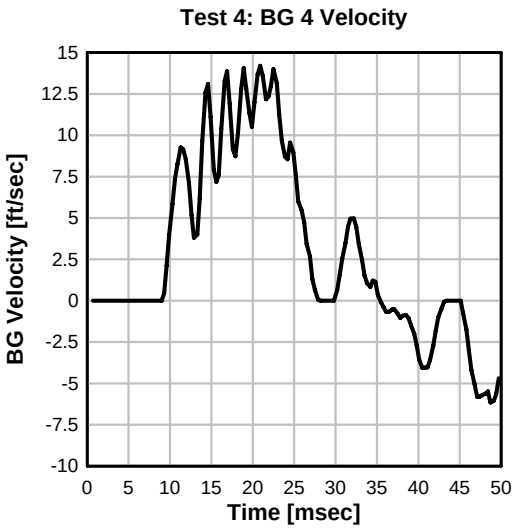
Test 4: BG 4 Velocity
BG Velocity [ft/sec]
Time [msec]

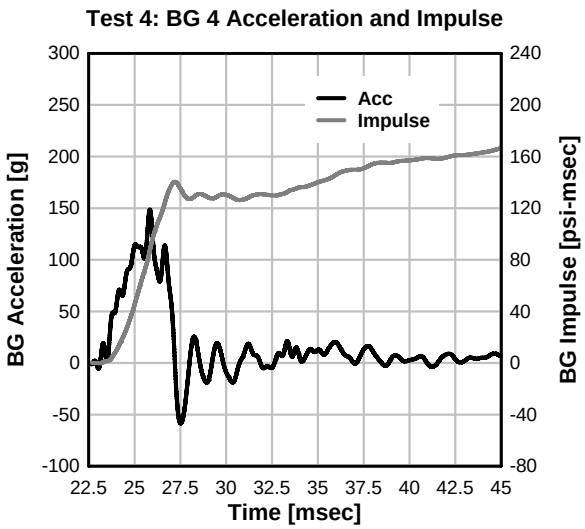
Test 4: BG 4 Acceleration and Impulse
Acc
Impulse
BG Acceleration [g]
BG Impulse [psi-msec]
Time [msec]

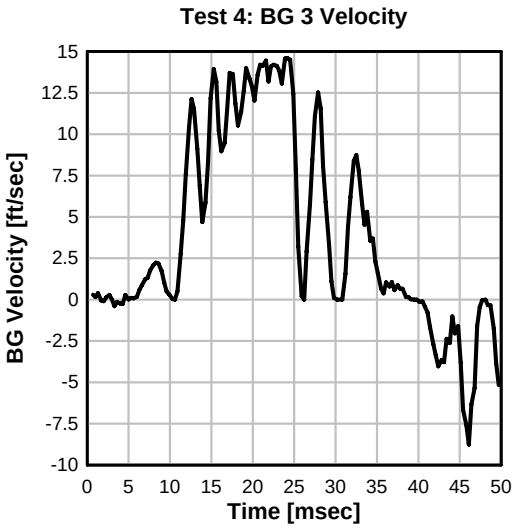
Test 4: BG 3 Velocity
BG Velocity [ft/sec]
Time [msec]

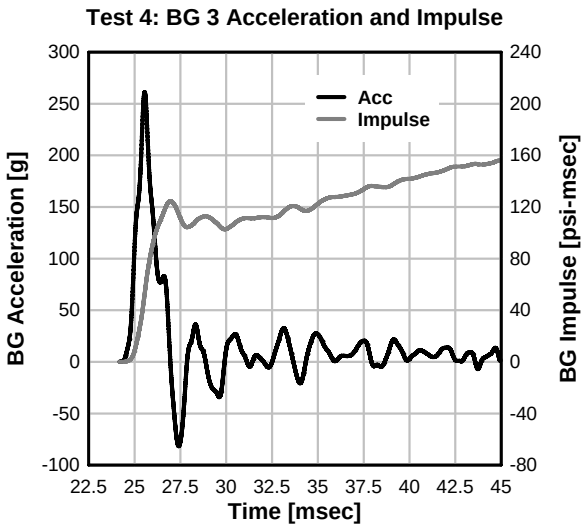
Test 4: BG 3 Acceleration and Impulse
Acc
Impulse
BG Acceleration [g]
BG Impulse [psi-msec]
Time [msec]

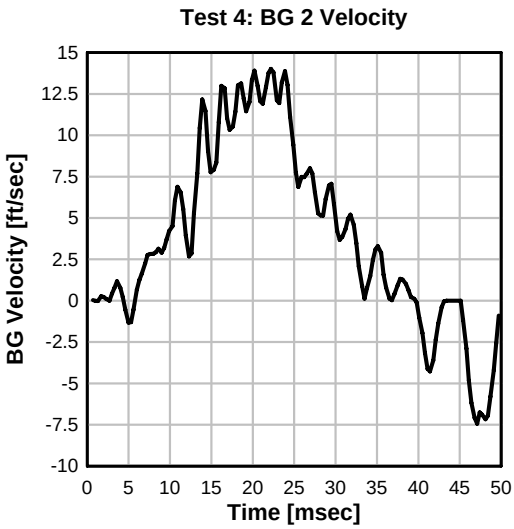
Test 4: BG 2 Velocity
BG Velocity [ft/sec]
Time [msec]

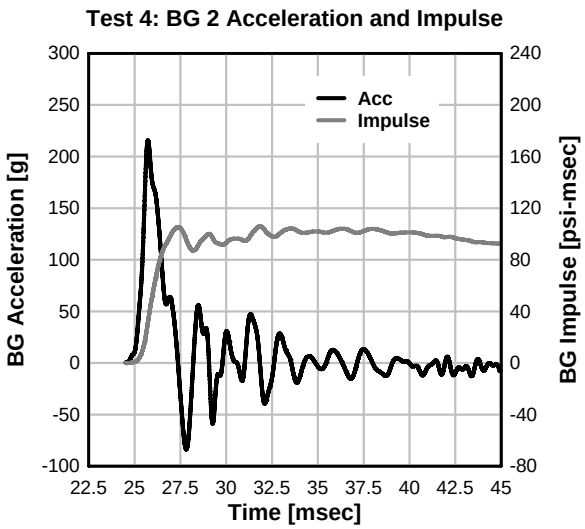
Test 4: BG 2 Acceleration and Impulse
Acc
Impulse
BG Acceleration [g]
BG Impulse [psi-msec]
Time [msec]

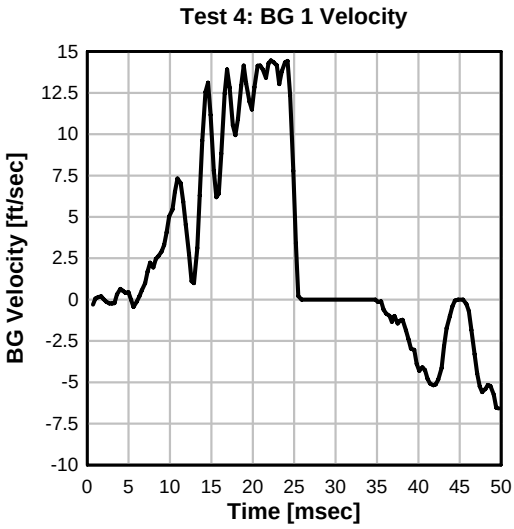
Test 4: BG 1 Velocity
BG Velocity [ft/sec]
Time [msec]

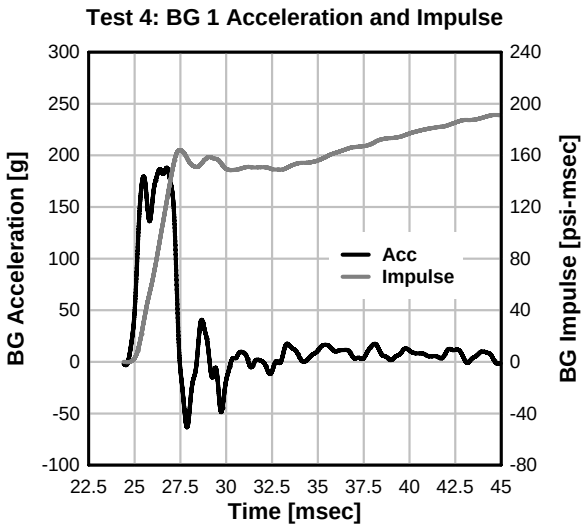
Test 4: BG 1 Acceleration and Impulse
Acc
Impulse
BG Acceleration [g]
BG Impulse [psi-msec]
Time [msec]

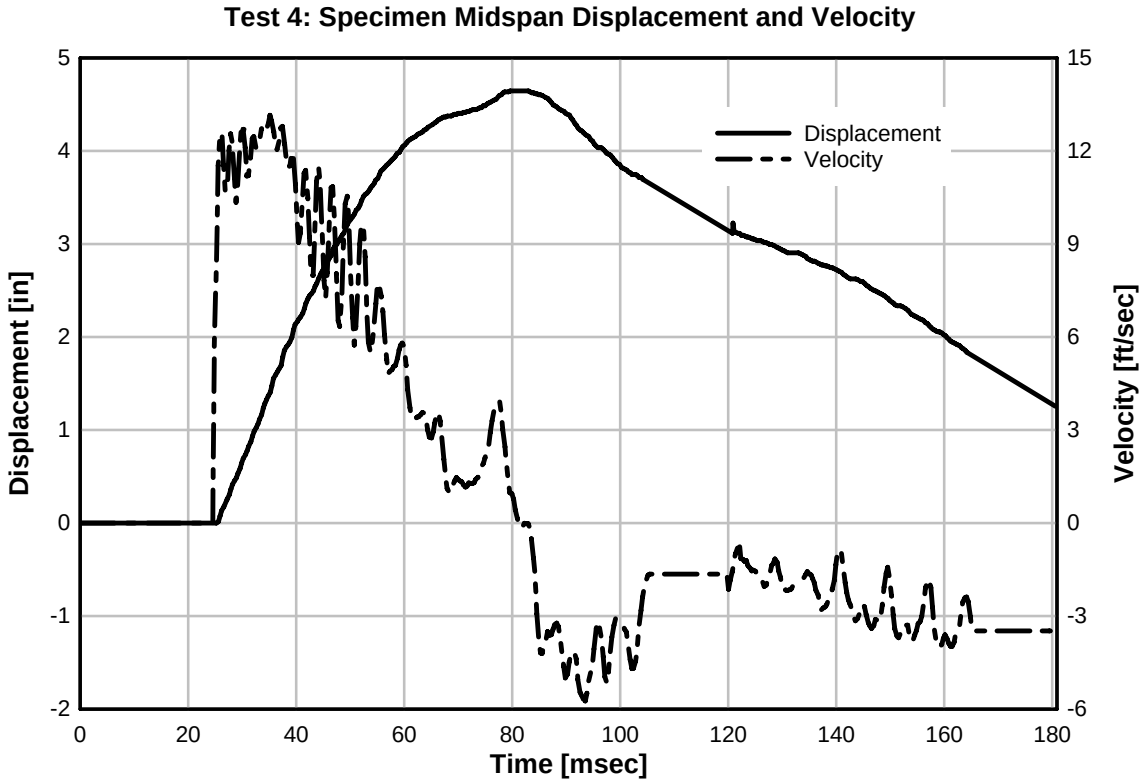
Test 4: Specimen Midspan Displacement and Velocity
Displacement
Velocity
Displacement [in]
Velocity [ft/sec]
Time [msec]
5
4
3
2
1
0
-1
-2
15
12
9
6
3
0
-3
-6
0
20
40
60
80
100
120
140
160
180

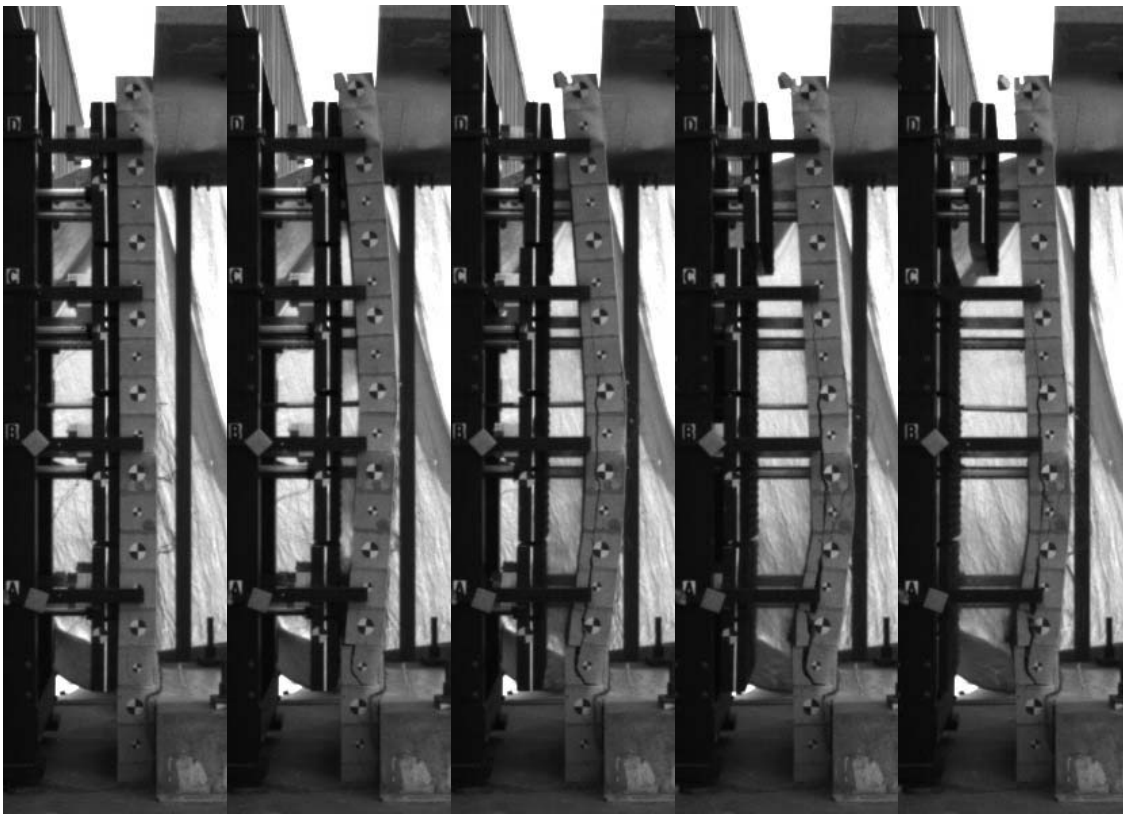

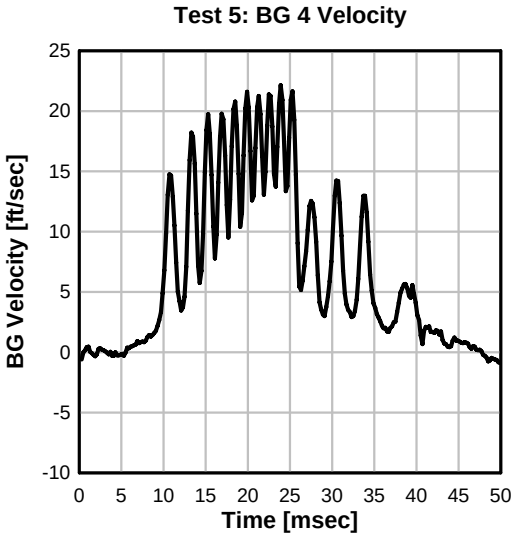
Test 5: BG 4 Velocity
BG Velocity [ft/sec]
Time [msec]

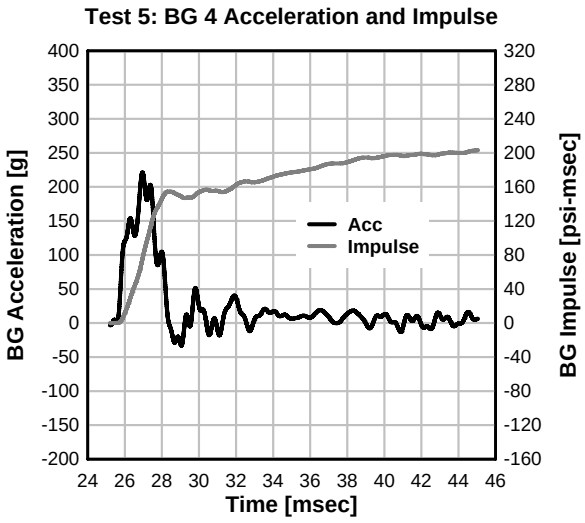
Test 5: BG 4 Acceleration and Impulse
BG Acceleration [g]
BG Impulse [psi-msec]
Acc
Impulse
Time [msec]

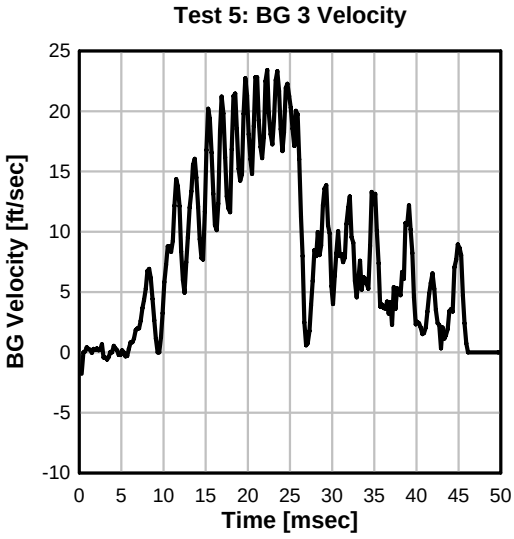
Test 5: BG 3 Velocity
BG Velocity [ft/sec]
Time [msec]

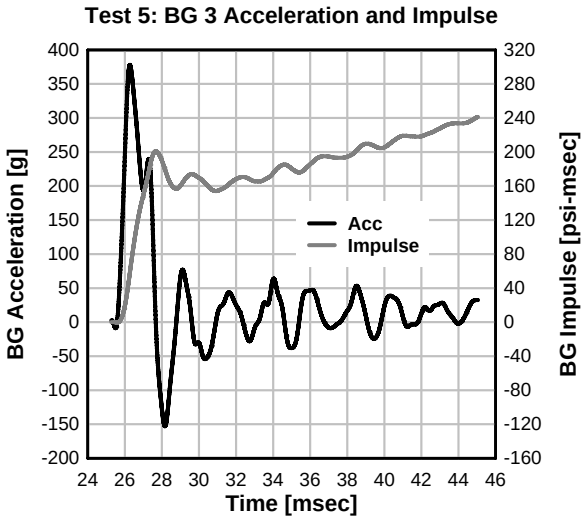
Test 5: BG 3 Acceleration and Impulse
BG Acceleration [g]
BG Impulse [psi-msec]
Acc
Impulse
Time [msec]

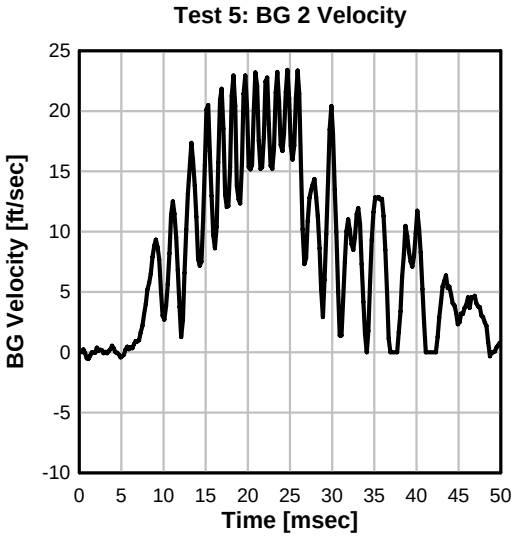
Test 5: BG 2 Velocity
BG Velocity [ft/sec]
Time [msec]

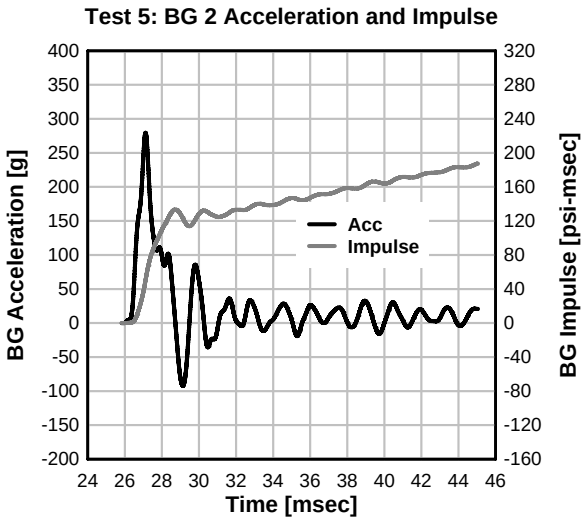
Test 5: BG 2 Acceleration and Impulse
BG Acceleration [g]
BG Impulse [psi-msec]
Acc
Impulse
Time [msec]

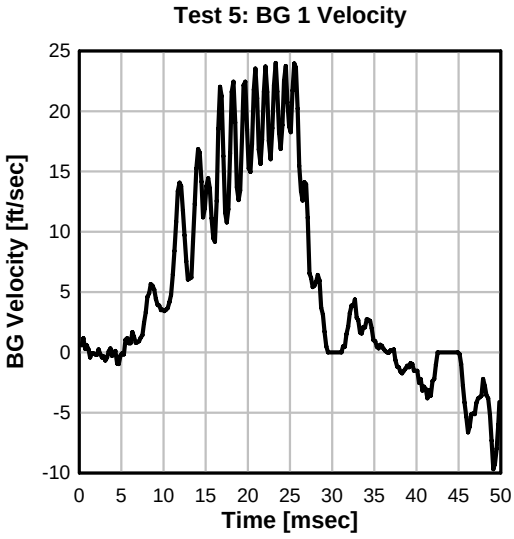
Test 5: BG 1 Velocity
BG Velocity [ft/sec]
Time [msec]

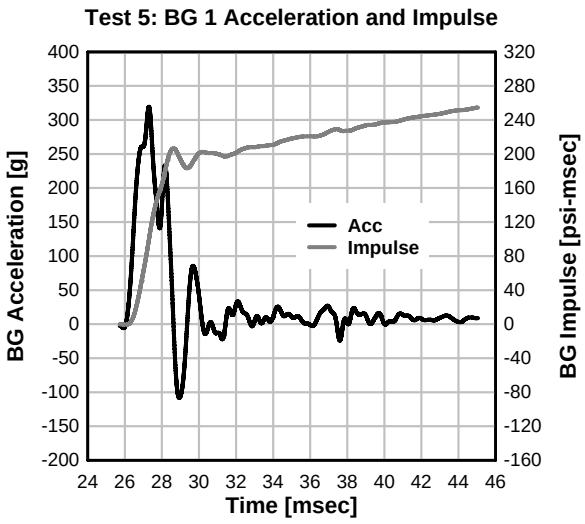
Test 5: BG 1 Acceleration and Impulse
BG Acceleration [g]
BG Impulse [psi-msec]
Acc
Impulse
Time [msec]

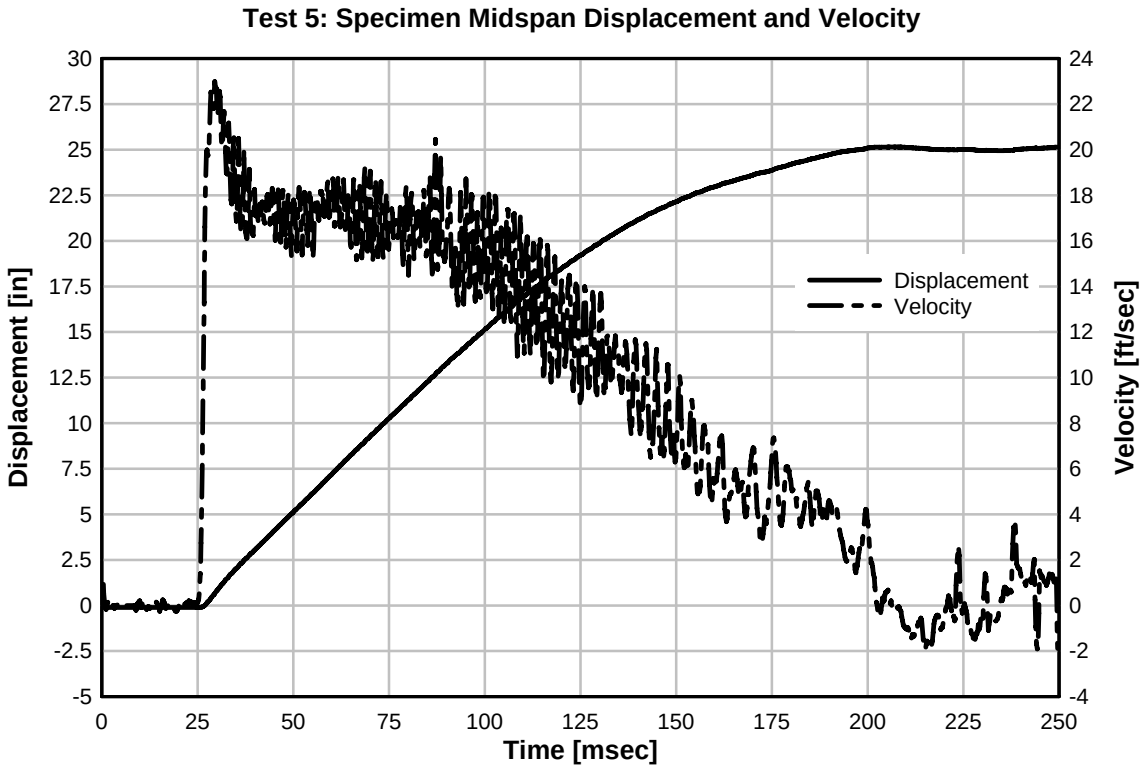
Test 5: Specimen Midspan Displacement and Velocity
Displacement [in]
Velocity [ft/sec]
Time [msec]
Displacement
Velocity
30
27.5
25
22.5
20
17.5
15
12.5
10
7.5
5
2.5
0
-2.5
-5
24
22
20
18
16
14
12
10
8
6
4
2
0
-2
-4
0
25
50
75
100
125
150
175
200
225
250

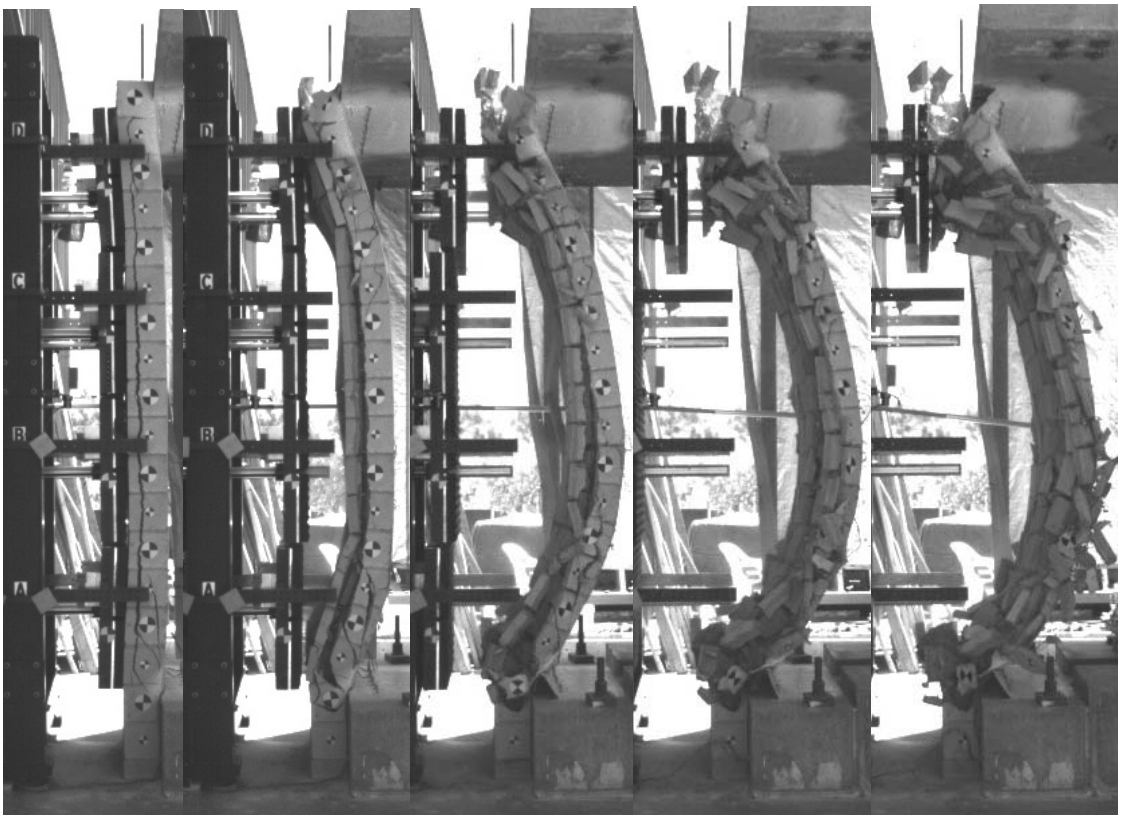

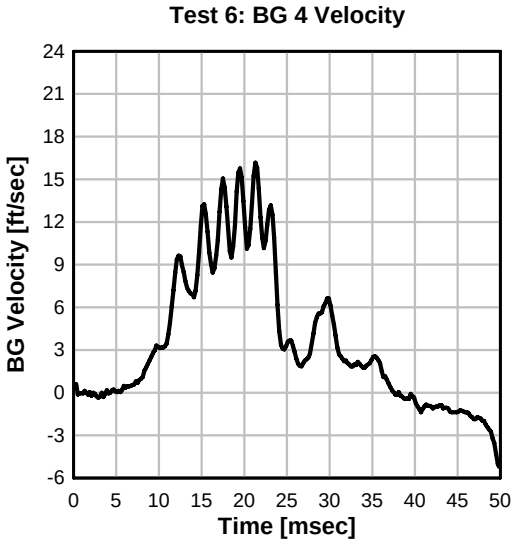
Test 6: BG 4 Velocity
BG Velocity [ft/sec]
Time [msec]

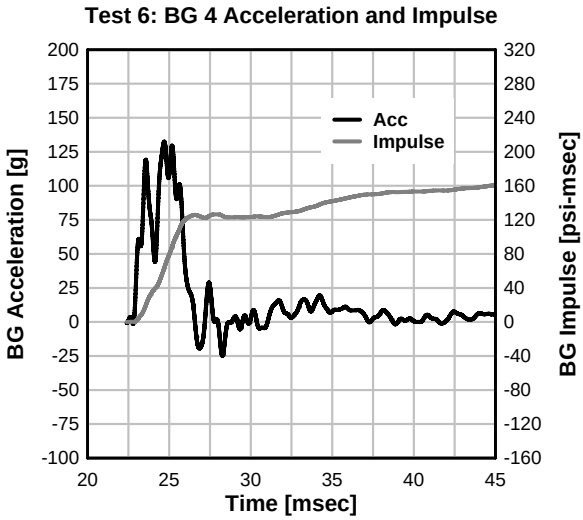
Test 6: BG 4 Acceleration and Impulse
Acc
Impulse
BG Acceleration [g]
BG Impulse [psi-msec]
Time [msec]

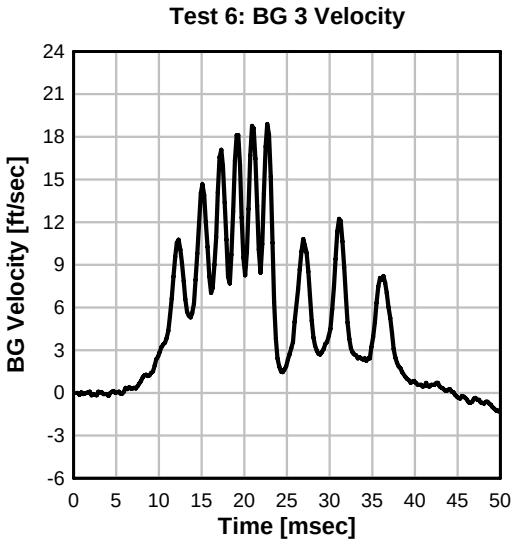
Test 6: BG 3 Velocity
BG Velocity [ft/sec]
Time [msec]

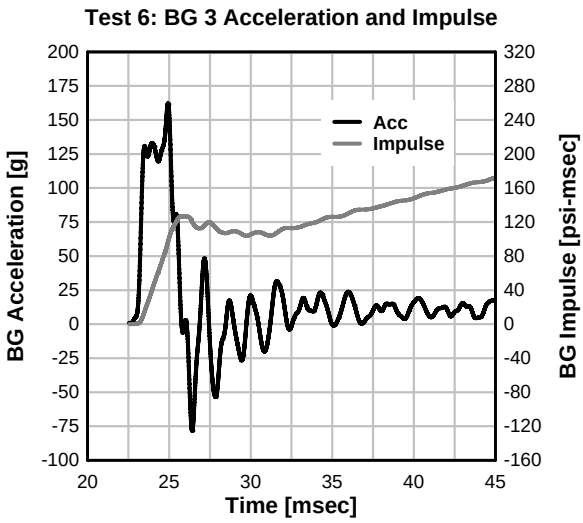
Test 6: BG 3 Acceleration and Impulse
Acc
Impulse
BG Acceleration [g]
BG Impulse [psi-msec]
Time [msec]

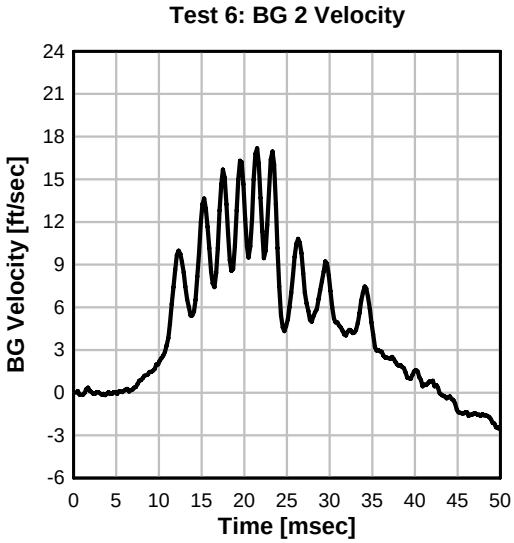
Test 6: BG 2 Velocity
BG Velocity [ft/sec]
Time [msec]

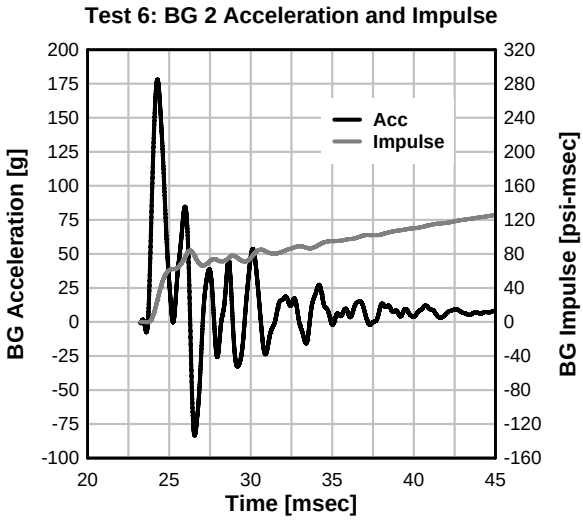
Test 6: BG 2 Acceleration and Impulse
Acc
Impulse
BG Acceleration [g]
BG Impulse [psi-msec]
Time [msec]

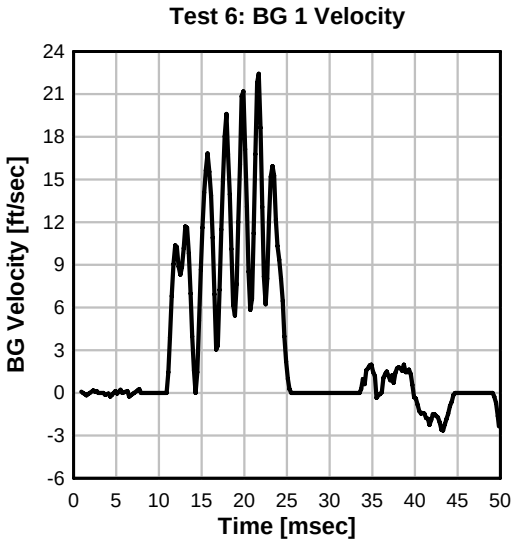
Test 6: BG 1 Velocity
BG Velocity [ft/sec]
Time [msec]

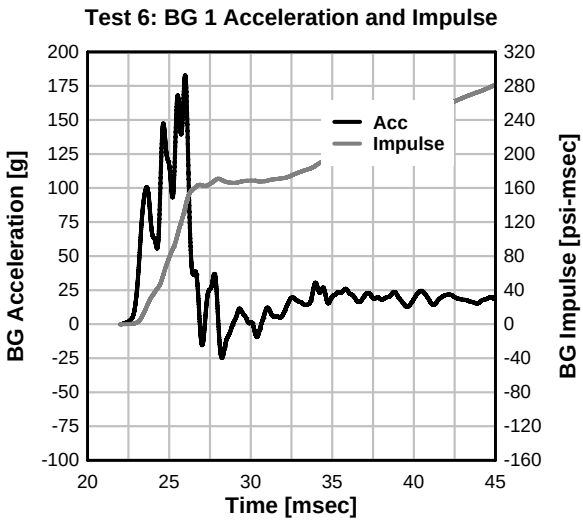
Test 6: BG 1 Acceleration and Impulse
Acc
Impulse
BG Acceleration [g]
BG Impulse [psi-msec]
Time [msec]

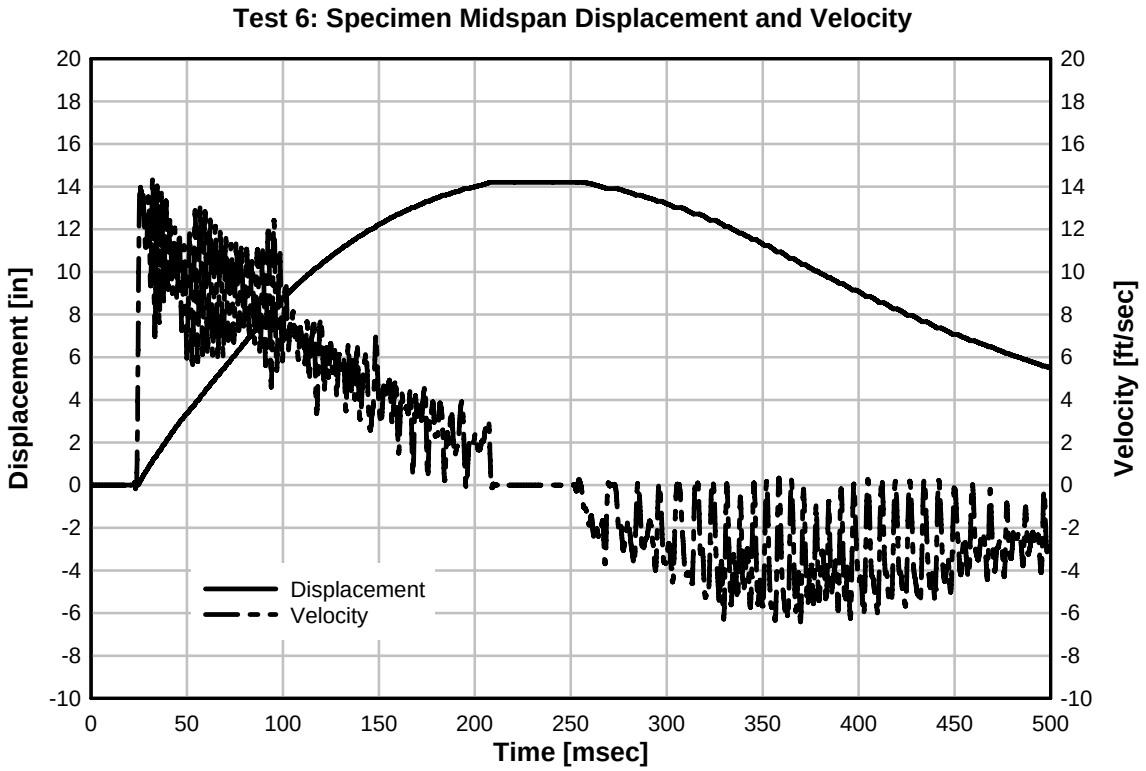
Test 6: Specimen Midspan Displacement and Velocity
Displacement [in]
Velocity [ft/sec]
Time [msec]
Displacement
Velocity
20
18
16
14
12
10
8
6
4
2
0
-2
-4
-6
-8
-10
0
50
100
150
200
250
300
350
400
450
500

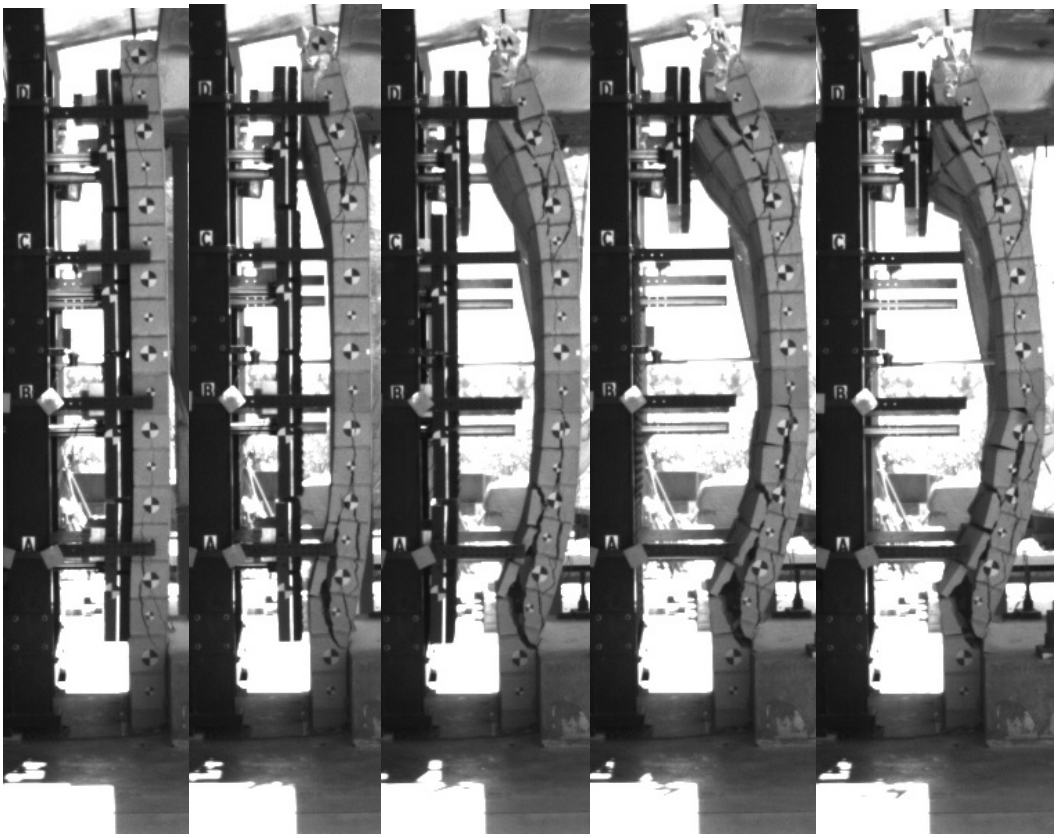

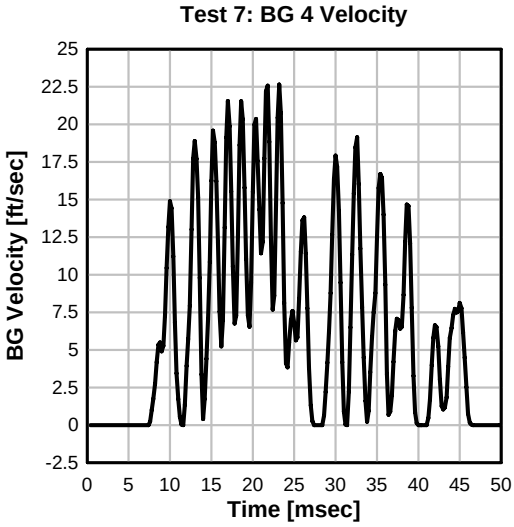
Test 7: BG 4 Velocity
BG Velocity [ft/sec]
Time [msec]

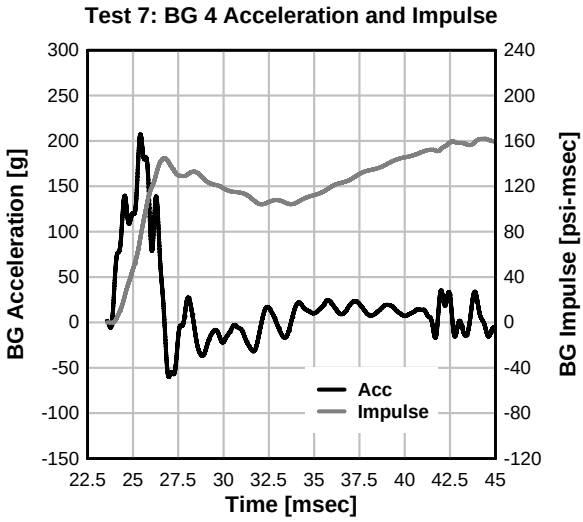
Test 7: BG 4 Acceleration and Impulse
BG Acceleration [g]
BG Impulse [psi-msec]
Acc
Impulse
Time [msec]

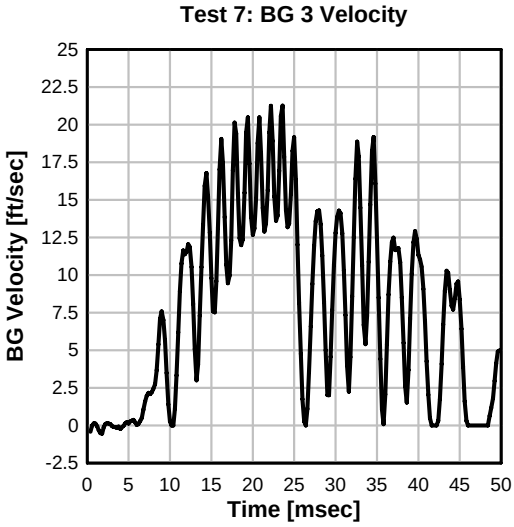
Test 7: BG 3 Velocity
BG Velocity [ft/sec]
Time [msec]

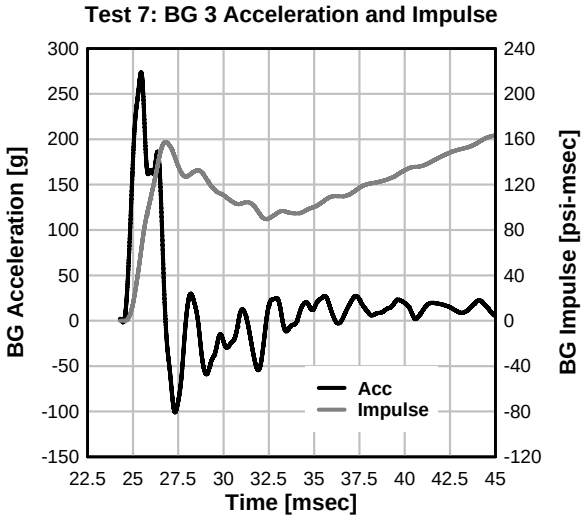
Test 7: BG 3 Acceleration and Impulse
BG Acceleration [g]
BG Impulse [psi-msec]
Acc
Impulse
Time [msec]

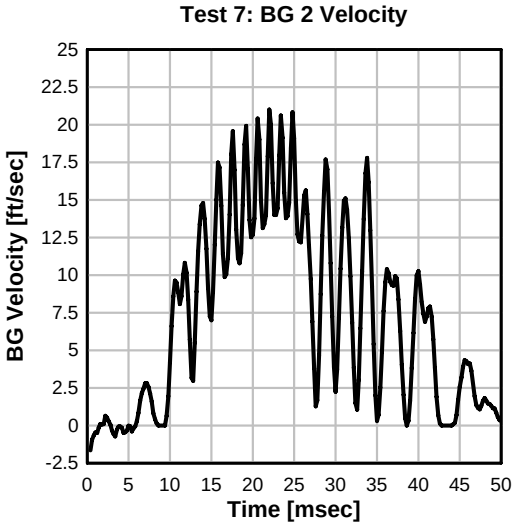
Test 7: BG 2 Velocity
BG Velocity [ft/sec]
Time [msec]

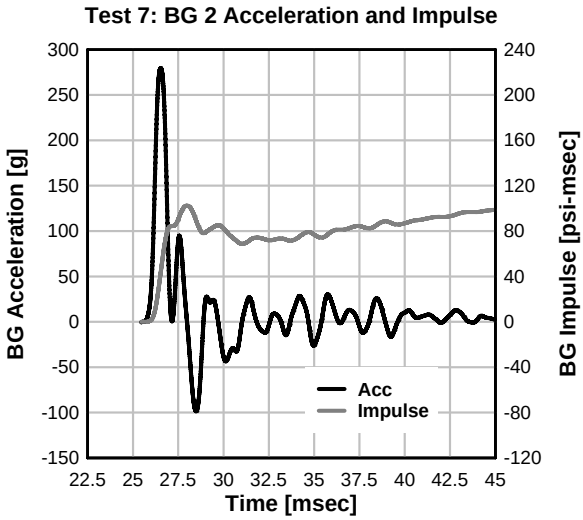
Test 7: BG 2 Acceleration and Impulse
BG Acceleration [g]
BG Impulse [psi-msec]
Acc
Impulse
Time [msec]

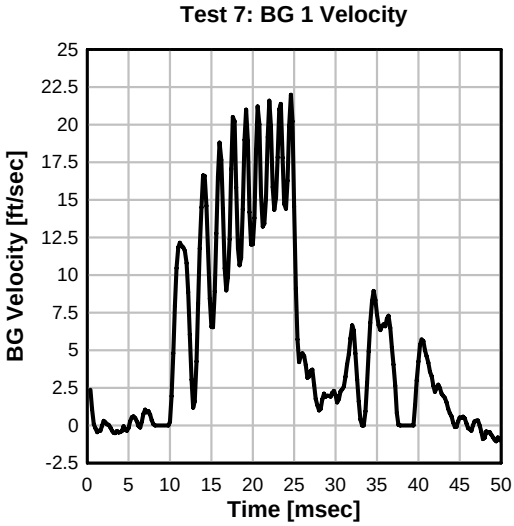
Test 7: BG 1 Velocity
BG Velocity [ft/sec]
Time [msec]

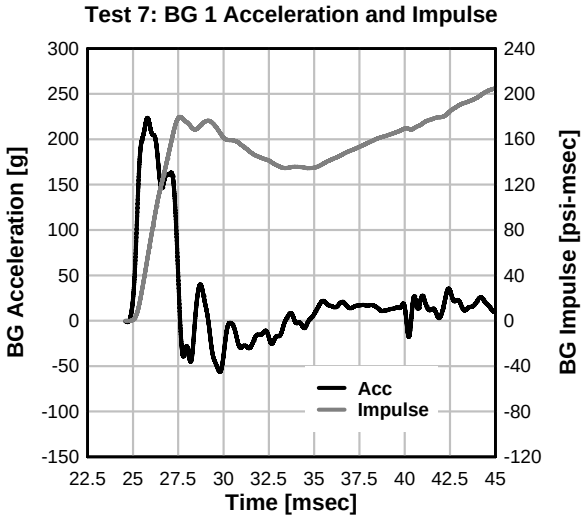
Test 7: BG 1 Acceleration and Impulse
BG Acceleration [g]
BG Impulse [psi-msec]
Acc
Impulse
Time [msec]

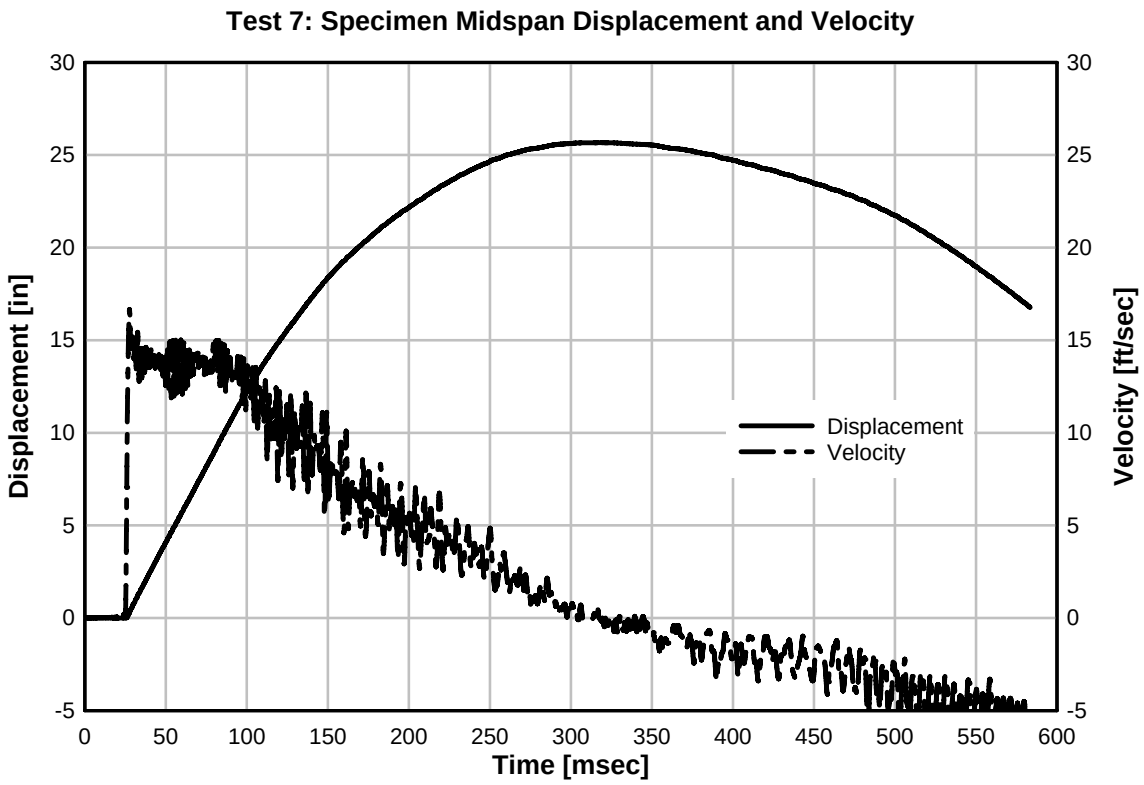
Test 7: Specimen Midspan Displacement and Velocity
Displacement [in]
Velocity [ft/sec]
Time [msec]
Displacement
Velocity
30
25
20
15
10
5
0
-5
0
50
100
150
200
250
300
350
400
450
500
550
600

REFERENCES

1. Hegemier, G., Seible, F., Arnett, K., Rodriguez-Nikl, T., Oesterle, M., Wolfson, J., Gram, M. and Clark, A. (2006). "The UCSD Blast Simulator". in *77th Shock and Vibration Symposium*. Monterey, CA.

2. Mays, G.C. and Smith, P.D. (1995), *Blast effects on buildings : design of buildings to optimize resistance to blast loading*. New York: Thomas Telford.

3. Smith, P.D. and Hetherington, J.G. (1994), *Blast and ballistic loading of structures*. Oxford ; Boston: Butterworth-Heinemann.

4. Conrath, E.J., Krauthammer, T., Marchand, K., A., Mlakar, P., F. and Structural Engineering Institute. (1999), *Structural Design for Physical Security : State of the Practice*. Reston, Va.: Structural Engineering Institute : American Society of Civil Engineers.

5. Brode, H.L. (1955). "Numerical solution of spherical blast waves." *Journal of Applied Physics*. 6, (June).

6. TM 5-1300 (1990). "Structures to Resist the Effects of Accidental Explosions," U.S. Department of the Army.

7. American Institute of Chemical Engineers. Center for Chemical Process Safety. (1996). *Guidelines for evaluating process plant buildings for external explosions and fires*. Center for Chemical Process Safety of the American Institute of Chemical Engineers: New York. pp. xii, 189 p.

8. Baker, Q.A., Tang, M.J., Scheier, E.A. and Silva, G.J. (1996). "Vapor cloud explosion analysis." *Process Safety Progress*. 15, (2) pp. 106-109.

9. Baker, Q.A., Doolittle, C.M., Fitzgerald, G.A. and Tang, M.J. (1998). "Recent developments in the Baker-Strehlow VCE analysis methodology." *Process Safety Progress*. 17, (4) pp. 297-301.

10. Tang, M.J. and Baker, Q.A. (1999). "A new set of blast curves from vapor cloud explosion." *Process Safety Progress*. 18, (4) pp. 235-240.

11. Pierorazio, A.J., Thomas, J.K., Baker, Q.A. and Ketchum, D.E. (2005). "An update to the Baker-Strehlow-Tang vapor cloud explosion prediction methodology flame speed table." *Process Safety Progress*. 24, (1) pp. 59-65.

12. Zeeuwen, J.P. and Wiekema, B.J. (1978). "The Measurement of Relative Reactivites of Combustible Gases". in *Conference on Mechanism of Explosions in Dispersed Energetic Materials*.

13. American Institute of Chemical Engineers. Center for Chemical Process, S. (1994). *Guidelines for evaluating the characteristics of vapor cloud explosions, flash fires, and BLEVEs*. Center for Chemical Process Safety of the American Institute of Chemical Engineers: New York, NY.

14. TM 5-855-1 (1986). "Fundamentals of Protective Design for Conventional Weapons,"

15. Britt, J.R. (1992). ""Enhancements of the BLASTX Code for Blast and Thermal Propagation in Protective Structures: BLASTX Version 2.0." U.S. Army Engineer Waterways Experiment Station.

16. McGlaun, J.M., Thompson, S.L., Kmetyk, L.N. and Elrick, M.G. (1990). "CTH: A Three-Dimensional Shock Wave Physics Code." *International Journal of Impact Engineering*. 10, (1) pp. 351-360.

17. Chopra, A.K. (2001), *Dynamics of structures : theory and applications to earthquake engineering*. 2nd ed. Prentice-Hall international series in civil engineering and engineering mechanics. Upper Saddle River, NJ: Prentice Hall.

18. Biggs, J.M. (1964), *Introduction to structural dynamics*. New York,: McGraw-Hill.

19. Hughes, T.J.R. (2000), *The Finite Element Method : Linear Static and Dynamic Finite Element Analysis*. Mineola, NY: Dover Publications.

20. ACI 318-05 (2005). P.O. Box 9094, Farmington Hills, MI 48333.

21. Chen, W.-F. (1982), *Plasticity in reinforced concrete*. New York: McGraw-Hill.

22. Macgregor, J.G. (1997), *Reinforced Concrete Mechanics and Design*. Third ed. Upper Saddle River, New Jersey: Prentice Hall.

23. William, K.J. and Warnke, E.P. (1975). "Constitutive Model for the Triaxial Behavior of Concrete". in *International Association of Bridge and Structural Engineers, Seminar in Concrete Subjected to Triaxial Stresses*. Bergamo, Italy: IABSE Proceedings.

24. Livermore Software Technology Corporation (2007). *LS-DYNA Keyword User's Manual Version 971*, Livermore, CA

25. Malvar, L.J., Crawford, J.E., Wesevich, J.W. and Simons, D. (1997). "A plasticity concrete material model for DYNA3D." *International Journal of Impact Engineering*. 19, (9-10) pp. 847-873.

26. Oesterle, M.G., Hegemier, G.A. and Seible, F. (2007). ""Ballistic Impact Test Series I & II." TSWG Contracts Deliverable, Contract N41756-05-C-4762, University of California, San Diego, Department of Structural Engineering.

27. Rodriguez-Nikl, T., Gram, M.M., Oesterle, M.G., Hegemier, G.A., Seible, F. and Arnett, K. (2007). "The UCSD Blast Simulator: Experimental Methodology." SSRP 07/05, University of California, San Diego Departement of Structural Engineering.

28. Sallay, J. and Gurtman, G. (2008). "Characterization of Blast Simulator Programmers." Final Report, Science Applications International Corporation.

29. Gurtman, G. and Sallay, J. (2006). "Supporting Computational Analysis for Steel Cellular Bridge Tower: Testing and Programmer Analysis." Memorandum, Science Applications International Corporation.

30. Gurtman, G. and Sallay, J. (2005). "Characterization of UCSD Blast Simulator Programmer Material." Final Report, Science Applications International Corporation.

31. Gent, A.N. and Lindley, P.B. (1959). "The compression of bonded rubber blocks." *Proc. Instn. Mech. Engnrs.* 173, (111).

32. Stanley, M.J., Osowski, J.J. and Leone, M.G. (2000). "Wall Component Test Program: Volume 1." Report No. CT 99-21 for the Defense Threat Reduction Agency,, Energetic Materials Research and Testing Center, (limited distribution).

33. Rodriguez-Nikl, T. (2006). "Experimental simulations of explosive loading on structural components: reinforced concrete columns with advanced composite jackets " PhD Dissertation, Structural Engineering, University of California, San Diego, La Jolla

34. Muszynski, L.C. and Purcell, M.R. (2003). "Use of composite reinforcement to strengthen concrete and air-entrained concrete masonry walls against air blast." *Journal of Composites for Construction*. 7, (2) pp. 98-108.

35. Carney, P. and Myers, J. (2003). "Shear and flexural strengthening of masonry infill walls with FRP for extreme out-of-plane loading, building integration

solutions." *Proceedings of the 2003 architectural engineering conference*, pp. 246-250.

36. Myers, J.J., Belarbi, A. and El-Domiaty, K.A. (2003). "Blast resistance of unreinforced masonry walls retrofitted with fibre reinforced polymers". in *Proceedings of the 9th North American masonry conference*. Clemson, USA.

37. Myers, J.J., Belarbi, A. and El-Domiaty, K.A. (2004). "Blast resistance of FRP retrofitted un-reinforced masonry (URM) walls with and with out arching action." *The Masonry Society Journal*. 22, pp. 9-26.

38. Tan, K.H. (2003). "Blast mitigation using fibre-reinforced polymer systems.". in *Proceedings of the second international symposium on new technologies for urban safety of mega cities in Asia*. Tokyo, Japan.

39. Tan, K.H. and Patoary, M.K.H. (2004). "Strengthening of masonry walls against out-of-plane loads using fiber-reinforced polymer reinforcement." *Journal of Composites for Construction*. 8, (1) pp. 79-87.

40. Baylot, J.T., Bullock, B., Slawson, T.R. and Woodson, S.C. (2005). "Blast Response of Lightly Attached Concrete Masonry Unit Walls." *Journal of Structural Engineering*. 131, (8) pp. 1186-1193.

41. Jones, P.A.S. (1989). "WAC, an analysis program for dynamic loadings on masonry and reinforced concrete walls." MS Thesis, Department of Civil Engineering, Mississippi State University, Mississippi State, Mississippi.

42. Dennis, S.T., Baylot, J.T. and Woodson, S.C. (2002). "Response of 1/4-Scale Concrete Masonry Unit (CMU) Walls to Blast." *Journal of Engineering Mechanics*. 128, (2) pp. 134-142.

43. Urgessa, G., Maji, A. and Brown, J. (2005). "Analysis and testing of blast effects on wall strengthened with GFRP and shotcrete". in *Proceedings of the 50th international SAMPE symposium and exhibition - new horizons for material and processing technologies*. USA.

44. Wesevich, J.W. and Oswald, C.J. (2005). "Empirical based concrete masonry pressure-impulse diagrams for varying degrees of damage". in *ASCE/SEI Structures Congress*. Reston, VA.

45. Stanley, M., Metzger, J. and Martinez, R. (2005). "UL-like testing of commercial off-the-shelf (COTS) products that enhance the blast and ballistic resistance of structures: Quick Look Report 5." TR-05-03, New Mexico Tech, Energetic Material Research and Testing Center, Karagozian & Case, Burbank, CA. (limited distribution).

46. Stanley, M., Metzger, J. and Martinez, R. (2005). "UL-like testing of commercial off-the-shelf products (COTS) that enhance the blast and ballistic resistance of structures: Quick Look Report 6." TR-05-08, New Mexico Tech., Energetic Materials Research and Testing Center, Karagozian & Case, Burbank, CA. (limited distribution).

47. Klingler, R.E., Shing, B.S., Okail, H. and Jo, S. (2008). "NSF NEES small-group project on performance-based design of masonry walls and masonry veneer ". in *Workshop on Masonry in America*. Cancun, Mexico.

48. Collins, M.P. and Porasz, A. (1989). "Shear design for high-strength concrete." *Comite' Euro-International du Beton, Bulletin d' Information*, (193) pp. 77-83.

49. Thorenfeldt, E., Tomaszewicz, A. and Jensen, J.J. (1987). "Mechanical properties of high strength concrete and application in design". in *Symposium on Utilization of High Strength Concrete*. Tapir, Trodheim, Norway.

50. Popovics, S. (1973). "A numerical approach to the compete stress-strain curve of concrete." *Cement and Concrete Research*. 3, (5) pp. 553-599.

51. Paulay, T. and Priestley, M.J.N. (1992), *Seismic Design of Reinforced Concrete and Masonry Buildings*. New York, N.Y.: Wiley.

52. Malvar, L.J. and Crawford, J.E. (1998). "Dynamic increase factors for concrete". in *28th DDESB Explosive Safety Seminar*. Orlando, FL.

53. Magallanes, J.M., Morrill, K.B., Crawford, J.E., Oesterle, M.G. and Hegemier, G.A. (2008). "Finite element models for the analysis and design of CMU walls to blast loads". in *2008 Department of Defence Explosives Safety Seminar*. Palm Springs, CA.

54. Malvar, L.J. and Crawford, J.E. (1998). "Dynamic increase Factors for steel reinforcing bars". in *28th DDESB Explosives Safety Seminar*. Orlando, FL.

55. Uniform building code standards (1997). International Conference of Building Officials., International Conference of Building Officials, Whittier, Calif.

56. CEB-FIP Model Code 90 (1990). Comite Euro-International du Beton - Federation Internationale de la Precontrainte, Redwood Books, Trowbridge, Wiltshire, Great Britain.

57. UFC 4-023-03 (2005). "Unified Facilities Criteria (UFC): Design of Buildings to Resist Progressive Collapse," U. S. Department of Defense.

58. Reid, S.R. and Peng, C. (1997). "Dynamic uniaxial crushing of wood." *International Journal of Impact Engineering*. 19, (6) pp. 531-570.

59. Harrigan, J.J., Reid, S.R. and Peng, C. (1999). "Inertial effects in impact energy absorbing materials and structures." *International Journal of Impact Engineering*. 22, (10) pp. 955-979.

60. Hanssen, A.G., Enstock, L. and Langseth, M. (2002). "Close-range blast loading of aluminum foam panels." *International Journal of Impact Engineering*. 27, (6) pp. 593-618.

61. Sadot, O., Anteby, I., Harush, S., Levintant, O., Nizri, E., Ostraich, B., Schenker, A., Gal, E., Kivity, Y. and Ben-Dor, G. (2005). "Experimental investigation of dynamic properties of aluminum foams." *Journal of Structural Engineering*. 131, (8) pp. 1226-1232.

62. Schenker, A., Anteby, I., Nizri, E., Ostraich, B., Kivity, Y., Sadot, O., Haham, O., Michaelis, R., Gal, E. and Ben-Dor, G. (2005). "Foam-protected reinforced concrete structures under impact: Experimental and numerical studies." *Journal of Structural Engineering*. 131, (8) pp. 1233-1242.

63. Schenker, A., Anteby, I., Gal, E., Kivity, Y., Nizri, E., Sadot, O., Michaelis, R., Levintant, O. and Ben-Dor, G. (2008). "Full-scale field tests of concrete slabs subjected to blast loads." *International Journal of Impact Engineering*. 35, (3) pp. 184-198.

64. Zou, Z., Reid, S.R., Tan, P.J. and Harrigan, J.J. (2009). "Dynamic crushing of honeycombs and features of shock fronts." *International Journal of Impact Engineering*. 36, (1) pp. 165-176.

65. Ma, G.W. and Ye, Z.Q. (2007). "Analysis of foam claddings for blast alleviation." *International Journal of Impact Engineering*. 34, (1) pp. 60-70.

66. Ye, Z.Q. and Ma, G.W. (2007). "Effects of foam claddings for structure protection against blast loads." *Journal of Engineering Mechanics*. 133, (1) pp. 41-47.

67. Li, Q.M. and Meng, H. (2002). "Attenuation of enhancement a one-dimensional analysis on shock transmission in the solid phase of a cellular material." *International Journal of Impact Engineering*. 27, (10) pp. 1049-1065.

68. Malvar, L.J. (1998). "Review of static and dynamic properties of steel reinforcing bars." *ACI Materials Journal*. 95, (5) pp. 609-616.

69. Knox, K.J., Hammons, M.I., Lewis, T.T. and Porter, J.R. (2000). "Polymer materials for structural retrofits." Air Force Research Laboratory.

70. Davidson, J.S., Porter, J.R., Dinan, R.J., Hammons, M.I. and Connell, J.D. (2004). "Explosive Testing of Polymer Retrofit Masonry Walls." *Journal of Performance of Constructed Facilities*. 18, (2) pp. 100-106.

71. Davidson, J.S., Fisher, J.W., Hammons, M.I., Porter, J.R. and Dinan, R.J. (2005). "Failure mechanisms of polymer-reinforced concrete masonry walls subjected to blast." *Journal of Structural Engineering*. 131, (8) pp. 1194-1205.

72. Stanley, M., Metzger, J., Morrill, K.B. and Martinez, R. (2004). "UL-like testing of commercial off-the-shelf (COTS) products that enhance the blast and ballistic resistance of structures: Quick Look Report 3-Test 3." TR-04-50, New Mexico Tech., Energetic Materials Research and Testing Center, Karagozian & Case, Burbank. CA (limited distribution).

73. Stanley, M., Metzger, J., Martinez, R. and Koenig, J. (2005). "UL-like testing of commercial off-the-shelf (COTS) products that enhance the blast and ballistic resistance of structures: Quick Look Report 7-Test 6." TR-05-14.1, New Mexico Tech., Energetic Materials Research and Testing Center, Karagozian & Case, Burbank. CA (limited distribution).

74. Stanley, M., Metzger, J., Martinez, R. and Koenig, J. (2005). "UL-like testing of commercial off-the-shelf (COTS) products that enhance the blast and ballistic resistance of structures: Quick Look Report 8-Test 7." TR-05-18.1, New Mexico Tech., Energetic Materials Research and Testing Center, Karagozian & Case, Burbank. CA (limited distribution).

75. Stanley, M., Metzger, J., Morrill, K.B. and Martinez, R. (2004). "UL-like testing of commercial off-the-shelf (COTS) products that enhance the blast and ballistic resistance of structures: Quick Look Report 2." TR-04-48, New Mexico Tech., Energetic Materials Research and Testing Center, Karagozian & Case, Burbank. CA (limited distribution).

76. Stanley, M., Metzger, J., Morrill, K.B. and Martinez, R. (2005). "UL-like testing of commercial off-the-shelf (COTS) products that enhance the blast and ballistic resistance of structures: Quick Look Report 3-Test 2." TR-04-50, New Mexico Tech., Energetic Materials Research and Testing Center, Karagozian & Case, Burbank. CA (limited distribution).

77. Moradi, L.G., Davidson, J.S. and Dinan, R.J. (2008). "Resistance of membrane retrofit concrete masonry walls to lateral pressure." *Journal of Performance of Constructed Facilities*. 22, (3) pp. 131-142.

78. Moradi, L.G., Davidson, J.S. and Dinan, R.J. (2009). "Response of bonded membrane retrofit concrete masonry walls to dynamic pressure." *Journal of Performance of Constructed Facilities*. 23, (2) pp. 72-80.

79. Connell, J.D. (2002). "Evaluation of elastomeric polymer for retrofit of unreinforced masonry walls subjected to blast." M.S. Thesis University of Alamaba at Birmingham, Birmingham, AL.

80. Thornburg, D.L. (2004). "Development of elastomeric polymer used for external reinforcement of masonry walls subjected to blast." MS Thesis University of Alabama at Birmingham, Birmingham, AL.

81. Laursen, P.T., Seible, F. and Hegemier, G.A. (1995). "Seismic Retrofit and Repair of Reinforced Concrete with Carbon Overlays." SSRP 95/01, University of California, San Diego.